IFMASS 8

FROM FRACTURE MECHANICS TO STRUCTURAL INTEGRITY ASSESSMENT

This monograph contains the lectures presented at the Eighth International Fracture Mechanics Summer School held in Belgrade, Serbia and Montenegro, 23–27 June 2003.

Editors: S. Sedmak and Z. Radaković

Belgrade

2004

This monograph is published with the financial support of the
Serbian Ministry of Science and Environmental Protection, and through
National Project No.1793 (2002–2004): 'Fracture and Damage Mechanics'

Special thanks to Milena Sedmak Vesić for her contribution to this publication.

Jointly published by the
Society for Structural Integrity and Life (DIVK) and
Faculty of Technology and Metallurgy (TMF), University of Belgrade

Edited, reviewed and corrected by:
Prof. Dr Stojan Sedmak
Dr Zoran Radaković

Reviewed by:
Prof. Dr Vitomir Djordjević
Dr Milorad Zrilić

First edition 2004

Circulation:
450 copies

Printed by "Grafički atelje *VULE*", Belgrade.

To contact the Publisher
DIVK (Society for Structural Integrity and Life)
Bul. Vojvode Mišića 43
11000 Belgrade, Serbia and Montenegro
E-mail: divkes@verat.net
http://www.divk.org.yu

CIP – Каталогизација у публикацији
Народна библиотека Србије, Београд

620.172.24(082)
620.169.1(082)
539.42(082)

INTERNATIONAL Fracture Mechanics Summer School (8th ; 2003 ; Belgrade)
From Fracture Mechanics to Structural Integrity Assessment : this monograph contains lectures presented at the Eighth International Fracture Mechanics Summer School held in Belgrade, Serbia and Montenegro, 23–27 June 2003. / editors S.[Stojan] Sedmak, Z.[Zoran] Radaković. – 1st ed. – Belgrade : Society for Structural Integrity and Life (DIVK) : Faculty of Technology and Metallurgy, 2004 (Belgrade : Vule). – 386 str. : ilustr. ; 24 cm

Tiraž 450. – Bibliografija uz svaki rad.

ISBN 86-905595-0-7

a) Металне конструкције – Зборници b) Механика лома – Зборници c) Металне конструкције – Век трајања - Зборници
COBISS.SR–ID 115216140

PREFACE

International Fracture Mechanics Summer Schools have been held from 1980 and have attracted a large number of well-known specialists and participants. Monographs published after every school have been the most effective references in fracture mechanics application for scientists and engineers in former Yugoslavia and Serbia and Montenegro. Previous schools have covered:

1. Introduction to Fracture Mechanics and Fracture-Safe Design (1980)
2. Modern Aspects of Design and Construction of Pressure Vessels and Penstocks (1982)
3. Fracture Mechanics of Weldments (1984)
4. Prospective of Fracture Mechanics Development and Application (1986)
5. The Application of Fracture Mechanics to Life Estimation of Power Plant Components (1989)
6. Service Cracks in Pressure Vessels and Storage Tanks (1991)
7. Experimental and Numerical Methods of Fracture Mechanics in Structural Integrity Assessment (1997)

The Eighth International Fracture Mechanics Summer School was held in Belgrade, Serbia and Montenegro, from June 23 to 27, 2003, and was organized by the Society for Structural Integrity and Life (DIVK), GOŠA Institute, Faculty of Technology and Metallurgy (TMF), in cooperation with the Serbian Ministry of Science and Environmental Protection, City Assembly of Belgrade, Military Technical Institute, and under the auspice of the European Structural Integrity Society – ESIS. Over 100 participants from 13 countries attended, and 25 presentations were given, while 27 participants took part in the satellite event that followed, the Workshop – *New Trends in Fracture Mechanics Application*.

The summer school title “From Fracture Mechanics to Structural Integrity Assessment” enabled to review developments and practical application of fracture mechanics. Lecturers have presented structural integrity problems in various stages as: design and material selection, manufacture and quality assurance, service, maintenance, and repair. These contributions were presented in 4 classified headings:

A. Theoretical background
B. Experiments and testing
C. Service problems
D. The assessment and extension of residual life

The Society for Structural Integrity and Life (DIVK) was established in Belgrade (2001). DIVK members have mostly organized and participated in previous IFMASS. Success of previously organized schools and its importance motivated DIVK to continue with IFMASS 8 in 2003. On meetings held during the 14th European Conference on Fracture (ECF 14) in Cracow (2002), with the participation of Prof. L. Toth (Hungary), the chairman of ESIS Commission TC13: *Education and Training*, Prof. E. Gdoutos (Greece), Prof. D. Angelova (Bulgaria), and Prof. S. Sedmak (Serbia), it was decided to organize IFMASS 8 for South-East European countries.

Joint organization of IFMASS of South-East European countries, under the auspice of the European Structural Integrity Society (ESIS) could be considered as the first step in founding the regional Forum for Structural Integrity of South-East European countries. Recently, at the regional meeting, held in Belgrade, the cooperation in this region is strongly recommended by the governments and encouraged by European Union.

It is concluded that the organization of IFMASS 8 has shown clear interest of the experts from the region in further development and research in structural integrity assessment. All participants wish to contribute in more close and extended cooperation between the experts in the region, with a need to find convenient form for exchange of results in achievements in fracture mechanics and structural integrity assessment through better links between the countries in the region, as well as with the European Structural Integrity Society (ESIS).

The aim of the Forum for Structural Integrity shall be to put together individuals, institutions and countries, interested in cooperative actions for further development of structural integrity, based on scientific achievements and solutions of failures in service and requirements for equipment life extension. In this way the benefit for all parties involved in such an organization can be reached in the most convenient way. In addition, the formal organization can also help in proposing standards and codes of interest for the regional industry, regarding the safety and reliability of equipment, having in mind also the environmental protection. This kind of regional cooperation is broadly accepted and involved in Europe.

We wish to acknowledge the financial support of the Serbian Ministry of Science and Environmental Protection, and through the National Project No.1793 (2002–2004): 'Fracture and Damage Mechanics'.

Belgrade, June 2004 Stojan Sedmak and Zoran Radaković

Contents

Other IFMASS titles

IFMASS 1	*Uvod u mehaniku loma i konstruisanje sa sigurnošću od loma*, Edited by S. Sedmak, published by GOŠA Institute and TMF, Belgrade 1981 (in Serbian)
IFMASS 2	*Savremeni aspekti projektovanja i izrade posuda pod pritiskom i cevovoda*, Edited by S. Sedmak, published by GOŠA Institute and TMF, Belgrade 1982 (in Serbian)
IFMASS 3	*Mehanika loma zavarenih spojeva*, Edited by S. Sedmak, published by GOŠA Institute and TMF, Belgrade 1984 (in Serbian)
IFMASS 4	*Perspektive razvoja i primene mehanike loma*, Edited by S. Sedmak, published by GOŠA Institute and TMF, Belgrade 1986 (in Serbian)
IFMASS 5	*The Application of Fracture Mechanics to Life Estimation of Power Plant Components*, Edited by S. Sedmak, published by EMAS Ltd. and TMF, Belgrade 1990 (in English)
	Primena mehanike loma u oceni preostalog veka komponenti termoenergetske opreme, Edited by S. Sedmak, published by GOŠA Institute and TMF, Belgrade 1991 (in Serbian)
IFMASS 6	*Eksploatacijske prsline u posudama pod pritiskom i rezervoarima*, Edited by S. Sedmak and A. Sedmak, published by TMF, UN European Centre for Peace and Development, and GOŠA Institute, Belgrade 1994 (in Serbian)
IFMASS 7	*Eksperimentalne i numeričke metode mehanike loma u oceni integriteta konstrukcija*, Edited by S. Sedmak and A. Sedmak, published by TMF, GOŠA Institute, and Yugoslav Welding Association, Belgrade 2000 (in Serbian)

PHYSICAL AND MATHEMATICAL ASPECTS OF FRACTURE MECHANICS

Jovo P. Jarić, Faculty of Mathematics, Belgrade, Serbia and Montenegro (S&Mn)
Aleksandar S. Sedmak, Faculty of Mechanical Engineering, Belgrade, S&Mn

INTRODUCTION

That cracks can and do appear in every type of structure is the *raison d'être* of fracture mechanics. What do we mean by "fracture mechanics"? Commonly with most researchers in the field, we define the term in the following way: fracture mechanics is an engineering discipline that quantifies the conditions under which a loaded body can fail due to the extension of a dominant crack contained in that body. This definition is obviously quite general in the sense that it underlies all structural analysis and materials science (Kanninen, [1]). No structural material is exempt from a defected condition, and if it could not fail because of existing defects, it would be pointless to analyze it in any other way. Consequently, each and every structural component is, or could be, a candidate for treatment by fracture mechanics.

Before considering specific nonlinear and dynamic research areas that constitute advanced fracture mechanics, it may be useful to refer to a few significant application areas where fracture mechanics techniques beyond those of Linear Elastic Fracture Mechanics (LEFM) would appear to be required. The examples are applications to nuclear reactor power plant pressure vessels and piping. Probably not more susceptible to subcritical cracking and fracture than it is with other types of engineering structures, because of the catastrophic consequences of a failure, nuclear plant systems have been subjected to an unprecedented degree of scrutiny. Such scrutiny has explored many situations in which applications of LEFM (as conservatively permitted by code procedures) would indicate that failure should occur when in fact experience has demonstrated otherwise. Such observations have led to intense research, focused on the development of nonlinear (e.g., elastic-plastic) and dynamic fracture mechanics methods in order to obtain more realistic assessments of the risk of fracture in nuclear plant components.

1. GRIFFITH'S THEORY

Although fracture mechanics has been developed mainly in the last few decades, one of the basic equations were established already in 1921, by Griffith [2], [3]. He considered an infinite plate of unit thickness with a central transverse crack of length $2a$. The plate is stressed to a stress σ and fixed at its ends (Fig. 1a). The load vs. displacement diagram is given in Fig.1b.

The elastic energy contained in the plate is represented by the area OAB. If the crack extends over a length da, the stiffness of the plate will drop (line OC), which means that some load will be relaxed since the ends of the plate are fixed. Consequently, the elastic energy content will drop to a magnitude represented by area OCB. Crack propagation from a to $a + da$ will result in an elastic energy release equal in magnitude to area OAC.

If the plate were stressed at a higher stress there would be a larger energy release if the crack grew an amount *da*. Griffith stated that crack propagation will occur if the energy released upon crack growth is sufficient to provide all the energy that is required for crack growth. If the latter is not the case, the stress has to be raised. The triangle ODE represents the amount of energy available if the crack would grow.

Griffith's fundamental contributions [2] resolved the infinite crack-tip stress dilemma inherent in the use of the theory of elasticity for cracked structures. But simple estimates, as illustrated in Fig. 2, can be made for the strength of a crystalline solid based on its lattice properties.

This results in a relation for the theoretical tensile strength that is not attained in actuality. Griffith's work was primarily focused on resolving this dichotomy.

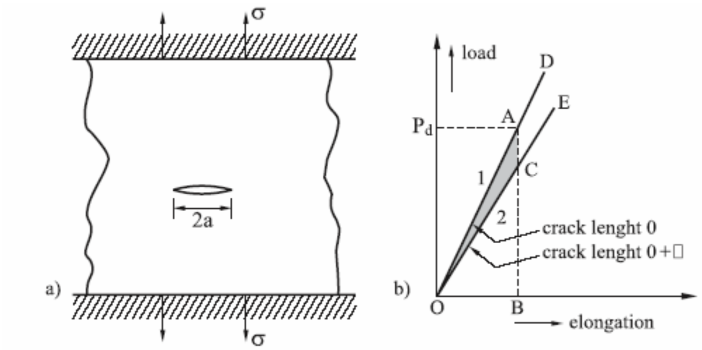

Figure 1. a. Cracked plate with fixed ends; b. Elastic energy

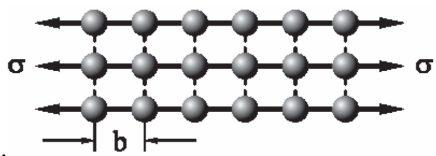

Figure 2. Atomic model for theoretical strength calculations

To approximate the interatomic force-separation law, the function should exhibit three properties:

- an initial slope that corresponds to the elastic modulus E,
- a total work of separation (i.e. area under the curve) that corresponds to the surface energy γ, and
- a maximum value that represents the interatomic cohesive force.

Because the exact form that is selected makes little difference, it is convenient to use a sine function. As can readily be verified, the appropriate relation is then

$$\sigma(x) = \left(\frac{E\gamma}{b}\right)^{1/2} \sin\left[\left(\frac{Eb}{\gamma}\right)^{1/2}\left(\frac{x}{b}\right)\right] \tag{1}$$

where b represents the equilibrium interatomic spacing and x denotes the displacement from the equilibrium separation distance. It follows that the theoretical strength (the maximum value in this relation) is

$$\sigma_{th} = \left(\frac{E\gamma}{b}\right)^{1/2} \tag{2}$$

For many materials $\gamma \cong Eb/40$ so that $\sigma_{th} \cong E/6$. But such a prediction is clearly much in excess of the observed strengths; a result that was explained by Griffith, who traced the discrepancy to the existence of crack-like flaws, by drawing upon the mathematical development of Inglis [4].

Figure 3 shows the results of Griffith's series of experiments on glass fibres having different thickness. As the fibre thickness decreased, the breaking stress (load per unit area) increased. At the limit of large thickness, the strength is that of bulk glass. But of considerable interest is that the theoretical strength is approached at the opposite limit of vanishingly small thickness. This observation led Griffith to suppose that the apparent thickness effect was actually a crack size *a*. Figure 4 illustrates his observation. It is worth mentioning here that this "size effect" is responsible for the usefulness of materials like glass and graphite in fibre composites; that is, the inherent defects can be considerably reduced by using such materials in fibre form bound together by a resin.

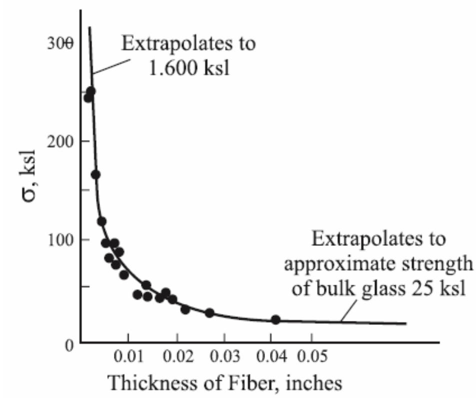

Figure 3. Results of Griffith's experiments on glass fibres

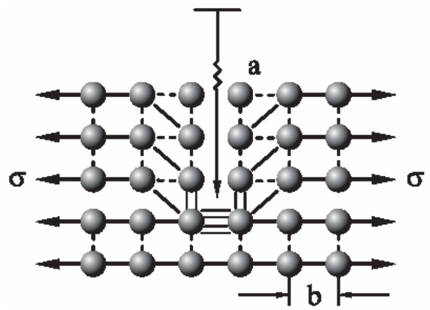

Figure 4. Atomic model with defect for fracture calculations

The basic idea in the Griffith fracture theory is that there is a driving force for crack extension (that results from the release of potential energy in the body) along with an inherent resistance to crack growth. The resistance to crack growth, in glass at least, is associated with the necessity to supply surface energy for the newly formed crack surfaces. Griffith was able to formulate an energy balance approach according to [3]. This has led to a critical condition for fracture that can be written as an equality between the change in potential energy due to an increment of crack growth and the resistance to this growth. For an elastic-brittle material like glass, this is

$$\frac{dW}{dA} - \frac{dU}{dA} = \gamma \tag{3}$$

where W is the external work on the body and U its internal strain energy, γ is the surface energy, and $A = 4Ba$ is the crack surface area for a crack in a body of thickness B.

For a crack in an infinite body subjected to a remote tensile loading normal to the crack (the problem considered by Griffith), only the net change in elastic strain energy needs to be evaluated. Today, this is most conveniently accomplished by making use of a procedure developed by Bueckner [5]. He recognized that the strain energy due to a finite crack is equal to one-half of the work done by stresses (of equal magnitude but opposite in sign to the applied stress) acting on the crack faces. The crack face opening is then given by a Westergaard solution for plane stress [8]; and this is

$$v = \frac{2\sigma}{E}\left(a^2 - x^2\right)^{1/2} \tag{4}$$

where σ is the applied stress and the origin of coordinates is taken at the centre of the crack (Fig. 1). Consequently, for an internal crack, work is done at four separate surface segments. As a result, it is readily shown by using Eq. (4) that

$$W - U = 4B\int_0^a \frac{1}{2}\sigma v(x)\,dx = \frac{\pi a^2 \sigma^2 B}{E} \tag{5}$$

Equation (3) then gives

$$\sigma_f = \left(\frac{2}{\pi}\frac{E\gamma}{a}\right)^{1/2} \tag{6}$$

where σ_f denotes the applied stress that would lead to fracture.

While Eq. (6) was derived for constant applied stress conditions, the same result is also obtained for fixed displacement conditions. Following [6], if the crack is introduced after the load is applied with the grips then being fixed, the total strain energy of the body will be (in plane stress)

$$U = \frac{1}{2}\frac{\sigma^2}{E}V - \pi\frac{\sigma^2 a^2}{E}B \tag{7}$$

where V is the volume of considered body. It can readily be seen that, because $W = 0$ under fixed grip conditions, use of Eq. (3) with $dA = 4Bda$ will again lead to Eq. (6).

The influence of the local crack/structure geometry on the critical applied stress is obvious. For example, if plane strain conditions were taken into account, the E appearing in Eq. (6) would be replaced by $E/(1-\nu^2)$. Further, as shown first by Sneddon [7], the axi-symmetric case of a penny-shaped crack of radius a leads to an expression given by

$$\sigma_f = \left(\frac{\pi}{2}\frac{E}{\left(1-\nu^2\right)^2}\frac{\gamma}{a}\right)^{1/2} \tag{8}$$

which differs by a factor of $(2/\pi)^2$ from the plane strain version of Eq. (6). So, the results for different conditions have the same form of equation and differ only in the value of the numerical factor that appears in them. Recognition of this later provided Irwin with the key in generalizing crack problems to fracture mechanics.

Returning to Griffith's work, the theoretical strength given by Eq. (2) can be combined with the fracture stress given by Eq. (6) to obtain a relation between the theoretical strength and the fracture stress in the presence of a crack. This is

$$\frac{\sigma_f}{\sigma_{th}} \cong \left(\frac{b}{a}\right)^{1/2} \tag{9}$$

Substituting values for bulk glass leads to a value of an inherent crack size of about 0.025 mm. Referring to Fig. 3, it can be seen that when the fibre thickness is reduced below this value (the fibres are flaw-free), the theoretical strength value is approached. This indicates that cracks are the source of the discrepancy between theoretical and observed strength and that quantitative predictions involving them can be made.

2. THE STRESS INTENSITY FACTOR

Irwin's masterstroke was to provide a quantitative relation between the, sometimes mathematically awkward, strain energy release rate, being a global parameter, and the stress intensity factor, being a local crack-tip parameter. Irwin utilized the cracked body solutions of Westergaard [8]. Specifically, Irwin [9] needed two specific relations: for σ_y, the normal stress on the crack, and v, the opening displacement of the crack surfaces. In current notation, these can be written for either plane stress or plane strain by introducing the material parameter κ; defined in terms of Poisson's ratio ν by

$$\kappa = \begin{cases} \dfrac{3-\nu}{1+\nu}, & \text{plane stress} \\ 3-4\nu, & \text{plane strain} \end{cases} \tag{10}$$

Then, the normal stress ahead of the crack and the displacement on the crack surface are given for the Griffith problem by

$$\sigma_y = \frac{x\sigma}{\left(x^2-a^2\right)^{1/2}}, x > a \tag{11}$$

$$\frac{E\nu}{(1+\nu)(k+1)} = \frac{\sigma}{2}\left(a^2-x^2\right)^{1/2}, x > a \tag{12}$$

where x is taken from an origin at the centre of the crack. More convenient relations that are valid very near the crack tip can be obtained by taking $|x| << a$, e.g.

$$\sigma_y \doteq K\left[2\pi(x-a)\right]^{-1/2}, x > a \tag{13}$$

$$v = \frac{(1+\nu)(k+1)}{E}K\left(\frac{a-x}{2\pi}\right)^{1/2}, x > a \tag{14}$$

where K (in tribute to Kies, one of Irwin's collaborators) is the stress intensity factor. K is a geometry-dependent quantity, that has the value $\sigma\sqrt{\pi a}$ for infinite plate.

Supposing that the crack has extended by Δa, Irwin calculated the work required to close it back up to its original length. This amount of work can be equated to the product of the energy release rate and the crack extension increment. Thus,

$$G\Delta a = 2\int_a^{a+\Delta a} \frac{1}{2}\sigma_y(x)v(x-\Delta a)dx \tag{15}$$

Or, by substituting Eqs. (13) and (14) into (15), Irwin obtained

$$G = \frac{1}{4}(1+\nu)(k+1)\frac{K^2}{E} = \frac{K^2}{E'} \tag{16}$$

where $E' = E$ for plane stress and $E' = E/(1-\nu^2)$ for plane strain. Equation (16) provides a replacement for the derivative with respect to crack length of the total strain energy.

Initially, Eq. (16) was perceived only as a convenient means for evaluating G. This is the reason for the appearance of the factor $\sqrt{\pi}$ in expressions for K. The parameter that characterizes the singular behaviour at a crack tip, using Eq. (11) is

$$\lim_{x\to a}\left[2(x-a)\right]^{1/2}\sigma_y(x,0) = \sigma\sqrt{a} \tag{17}$$

which does not include π. Thus, the awkward $\sqrt{\pi}$, incorporated artificially into the definition of K to simplify the calculation of G, is completely unnecessary.

Because the analysis problem was made tractable for practical problems by the use of Eq. (16), it can be said that fracture mechanics as an engineering discipline had its origins in the this procedure. By using complex variable methods, Sih, Paris and Erdogan [10], provided the first collection of stress intensity factors for fracture mechanics practical use. Sih, Paris and Irwin [11] also generalized Eq. (16) for an anisotropic material.

2.1. Atomic simulation of fracture

Fracture by rupture of the interatomic bonds can help to understand fracture toughness origins. Implicit in fracture analyses is the idea that atomic bonds must be ruptured to allow a crack to propagate (Fig. 4). The first quantitative treatment considered interatomic bond rupture, Elliott [12]. Using the linear elastic (continuum!) solution for a cracked body under uniform tension, Elliott evaluated the normal stress and displacement values along a line parallel to the crack plane (Fig. 5), but situated at a small distance $b/2$ into the body. He then plotted the stress at each position as a function of the displacement at that point. The shape of this function turns out to be consistent with interatomic force separation that obeys Hooke's law for small separations, exhibits a maximum, and approaches to zero at large separations, Eq. (1). On the basis of this finding, Elliott formulated a model of two semi-infinite blocks that attract each other with interatomic forces, Fig. 5.

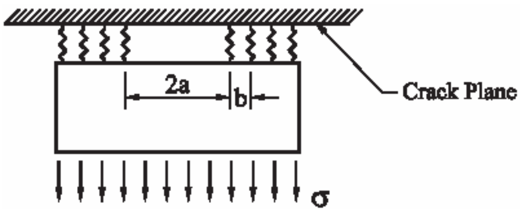

Figure 5. Pseudo-atomic model for fracture mechanics calculations

In this model the distance b between the blocks is taken as the equilibrium interatomic separation distance, and the area under the force-separation curve is set equal to the surface energy γ. The final step is to equate the maximum stress to the critical rupture stress for the material. This gives a relation written in a form like that of Griffith. For plane strain and $\nu = 0.25$, this is

$$\sigma_f = \frac{8}{7}\left(\frac{E\gamma}{a}\right)^{1/2} \tag{18}$$

which can be compared with Eq. (6). It can be seen that, apart from a difference in the numerical constants of only about 1%, these results are identical. Because the approach is based on linear elastic continuum theory (as Elliott recognized), such a result might be regarded as fortuitous. Cribb and Tomkins [13] performed a more direct analysis of the interatomic cohesive forces at the crack tip in a perfectly brittle solid, although finding a result in agreement with Elliott's.

Elliott was concerned also with another aspect of the problem, one that troubles all atomistic and energy balance approaches. Because there is only one point of equilibrium, the crack should close up at all applied stress values that are less than the critical value! Consequently, some physical activity not present in the model (e.g., a missing layer of atoms, gas pressure, and a non-adhering inclusion) must be postulated to assure the existence of the crack, prior to fracture instability. Elliott argued that such a *deus ex machina* would be compatible with his approach. Subsequent researchers simply took the initial displacements of the atoms on the crack plane to be beyond the separation distance corresponding to the maximum cohesive force.

Improvements on continuum-based analyses of discrete atomic-scale events were forthcoming only with the advent of large-scale numerical computation. The first of these may have been that of Goodier and Kanninen [14]; they in effect extended Elliott's model considering two linear elastic semi-infinite solids connected by an array of discrete nonlinear springs spaced a distance b – interatomic separation distance. The crack-tip region in this model is shown in Fig. 6, in which four different analytical forms are selected to represent the interatomic force separation law. In each of these, the initial slope corresponded to the elastic modulus E, with the area under the curve representing the work of separation, equated to the surface energy γ, Eq. (1). For any of these "laws", the solution for the resulting mixed nonlinear boundary condition problem was obtained numerically by monotonically loading the body (with a finite length $2a$ over which the atoms were already supposed to be out-of-range of their counterparts) until the maximum cohesive strength was achieved. Computations performed for a range of crack lengths led to a relation for the fracture stress that can be written as

$$\sigma_f = \alpha \left(\frac{E\gamma}{a} \right)^{1/2} \tag{19}$$

where α is a number having the order of unity. Similarity with Eqs. (6) and (18) is clear.

An obvious shortcoming in the model of Goodier and Kanninen is the limitation to the atomic pairs bridging the crack plane. As later shown by Rice [15], the application of the J–integral to such a problem results in $G = 2\gamma$, regardless of the force law that is used; the difference found for the various choices simply reflects the model discreteness, not the nonlinearity. Recognizing this, Gehlen and Kanninen [16] extended the Goodier-Kanninen treatments by considering the crystal structure at the crack tip. Equilibrium atomic configurations at the tip of a crack in alpha-iron, a body-centred-cubic structure for which interatomic potentials are well known, were determined for different load levels. But, owing to the limited sizes of the model that they were able to employ, the crack growth condition had to be deduced in an artificial way. This work nevertheless also produced a relation of the type given by Eq. (19), again with a constant approximately equal to unity.

Since the number of "free" atoms that Kanninen and Gehlen could admit into their computation was small (about 30), the atomic positions were highly constrained by the linear elastic continuum displacement field in the vicinity of the crack tip. Consequently, the coincidence between their result and that of Griffith is not surprising. This effort was valuable in that the fundamental process responsible for cleavage crack extension was, for the first time, confronted in a realistic way, and no artificial postulates were required to support it. In addition, such a model allows the process of dislocation nucleation, the origin of crack-tip plasticity, to occur naturally. Consequently, it should be possible to delineate the mechanical properties of a material that dictate whether brittle or ductile fracture will occur. Larger models, Gehlen et al. [16], with less rigid constraints in the boundary of the computational model were used, and did indeed permit bond rupture to be possible (Fig. 7), with the origins of dislocation nucleation.

Weiner and Pear [17] first addressed to rapidly propagating cracks in atomic fracture simulation. The development that has much in common with the finite element method is reflected by Ashhurst and Hoover [18]. The calculations of Markworth et al. [19] were based upon body-centred-cubic iron. Reliable interatomic force-separation laws are available for this system and for its interactions with hydrogen and helium atoms. A typical computation is performed by inserting a hydrogen (or helium) atom into the lattice ahead of the crack tip. In contrast to their earlier result, the computation that was carried out shows that the presence of the hydrogen atom causes severe local distortion of the iron crystal, and a relatively small applied stress can bring about a unit of crack advance by bond rupture. In this sense, the iron crystal was indeed "embrittled" by hydrogen. While such a result is intuitively reasonable and probably to be expected, quantitative results can be obtained only through computations such as these.

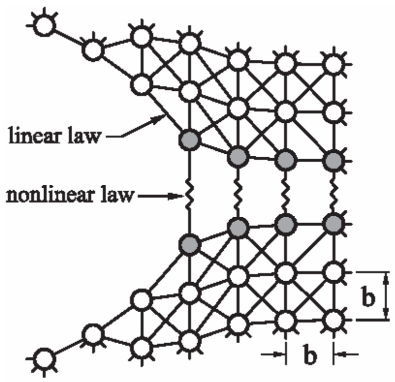

Figure 6. Crack tip in a pseudo-atomic fracture model

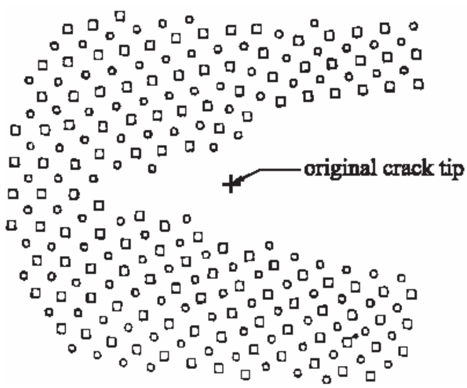

Figure 7. Lattice model of a crack tip in bcc iron showing crack extension

While results such as those of Markworth et al. are encouraging, the prospects for further progress in atomistic simulation of fracture are daunting. The most serious barrier would seem to be the paucity of reliable multi-body interatomic force-separation laws (for the alike as well as for unlike atoms) that can account for temperature effects. Work on the atomic scale will always be handicapped by computer limitations. Compounding this constraint is the ultimate necessity to treat corrosion fatigue that involves low-level, but repeated loadings.

2.2. Simple crack-tip plasticity models

The first quantitative accounting for the effect of the plastic zone at the crack tip seems to be that suggested by Irwin, Kies, and Smith [20]. On the basis that a plastically deformed region cannot support the same level of stress that it could, if yielding did not intervene, they argued that a cracked body is somewhat weaker than a completely elastic analysis would suggest. To account for this within the framework of linear elasticity, they supposed that the effect would be the same as if the crack length were slightly enlarged. Thus, a plasticity-modified stress intensity factor for a crack in an infinite medium can be written as

$$K = \sigma\sqrt{\pi\left(a + r_y\right)} \tag{20}$$

where r_y is supposed to be the measure of plastic zone size, e.g. the radius of a circular zone.

Estimates of r_y can be obtained in a variety of ways. Perhaps the simplest is to take $2r_y$ as the point on the crack line where $\sigma_y = \sigma_Y$ (yield stress). Using Eq. (13) this simple argument gives

$$r_y = \begin{cases} \dfrac{K^2}{2\pi\sigma_Y^2}, \quad \text{plane stress,} \qquad \dfrac{K^2}{6\pi\sigma_Y^2}, \quad \text{plane strain} \end{cases} \tag{21}$$

The distinction arises because σ_Y is taken as the uniaxial tensile yield stress for plane stress while for plane strain it is appropriate to use $\sqrt{3}\,\sigma_Y$ as the parameter governing the plastic zone size. Thus, r_y, is a factor 3 smaller in plane strain than in plane stress. Combining Eqs. (20) and (21) gives (for plane stress)

$$K = \sigma\sqrt{\pi a}\left(1 - \frac{1}{2}\frac{\sigma^2}{\sigma_Y^2}\right)^{1/2} \tag{22}$$

From Eq. (22) it can be seen that this approximate plastic zone correction will be negligible when $\sigma \ll \sigma_Y$, but K will increase to about 40% at applied stresses that are of yield stress magnitude. In plane strain, the correction is generally less than 10%.

Through the use of Eqs. (16), Eq. (22) can be written in terms of the energy release rate. For plane stress conditions, and assuming that $\sigma \ll \sigma_Y$, this relation is

$$G = \frac{\pi\sigma^2 a}{E}\left[1 + \frac{1}{2}\left(\frac{\sigma}{\sigma_Y}\right)^2\right] \tag{23}$$

which is a form once in common use for a plasticity-corrected crack driving force. It will be used here for comparison with the results obtained by COD approach.

2.3. Origin of the COD approach

At about the same time as Irwin and his associates were developing the plasticity enhanced stress intensity factor to broaden the applicability of the linear elastic approach, Wells [21] advanced an alternative concept in the hope that it would apply even beyond general yielding conditions. This concept employs the crack opening displacement (COD) as the parameter governing crack extension. Wells evaluated this parameter using Irwin's plastic zone estimate and the equations for a central crack in an infinite elastic body, by substituting Eq. (21) into Eq. (14) to obtain $\delta = 2v(r_y)$ gives

$$\delta = \alpha\frac{K^2}{E\sigma_Y} \tag{24}$$

Here, α is a numerical factor that in Wells work was equal to $4/\pi$. Wells recognized that the factor $4/\pi$ is inconsistent with an energy balance approach (which would require a factor of unity) and subsequently adopted $\alpha = 1$. Other investigators later found other values of α to be appropriate. Regardless, Eq. (24) shows that the COD approach is entirely consistent with LEFM, where the latter applies. From Eq. (21) and (24) follows

$$r_y = \frac{\delta}{2\pi e_Y} \tag{25}$$

where $e_Y = \sigma_Y/E$ is the uniaxial yield strain. Then, it can be shown that

$$\frac{\delta}{2\pi e_Y a} = \left[2\left(\frac{\sigma_Y}{\sigma}\right)^2 - 1\right]^{1/2} \tag{26}$$

which Wells felt would be acceptable up to $\frac{\sigma_Y}{\sigma} = 0.8$. In the next step, Wells converted Eq. (26) to general yielding conditions, arguing that it is appropriate to assume, although it is not thereby proven, that the crack opening displacement δ will be directly proportional to overall tensile strain e after general yield has been reached.

By assuming that $r_y/a = e/e_Y$, Wells's intuitive argument led to

$$\frac{\delta}{2\pi e_Y a} = \frac{e}{e_Y} \tag{27}$$

which is an approximate post-yield fracture criterion and the basis for the COD method.

While elastic-plastic analyses to determine the plastic region at a crack tip were available, an explicit relation was needed for δ in order to advance the COD concept. This was provided in a key paper published in 1960 by Dugdale [22] in which he developed a closed-form solution applicable for plane stress conditions. Using methods of the complex variable theory of elasticity, developed by Muskhelishvili [23], Dugdale [22] supposed that for a thin sheet, loaded in tension, the yielding will be confined to a narrow band lying along the crack line. Mathematically, this idea is identical to placing internal stresses on the portions of the (mathematical) crack faces near its tips; the physical crack being the remaining stress-free length.

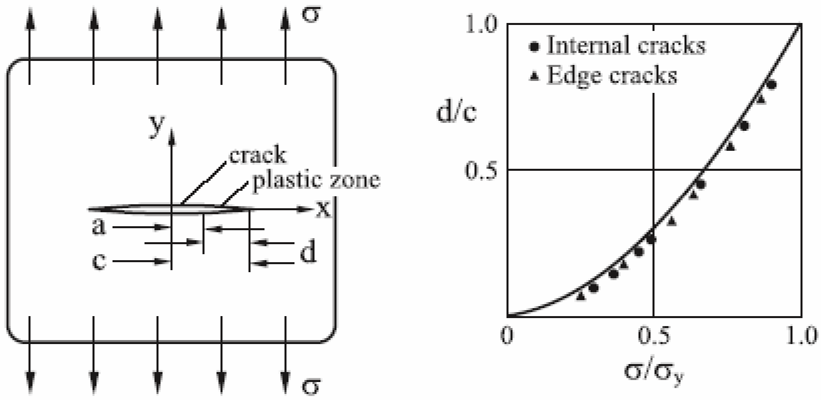

Figure 8. a. The Dugdale model
b. Dugdale's results for the plastic zone size and compared with analysis

The magnitude of the internal stresses in Dugdale's model are taken to be equal to the yield stress of the material. In order to determine the length over which they act, Dugdale postulated that the stress singularity must be abolished. For a crack of length $2a$ in an infinite medium under uniform tension σ, led Dugdale to the relation

$$\frac{a}{c} = \cos\left(\frac{\pi}{2}\frac{\sigma}{\sigma_Y}\right) \tag{28}$$

Here, $c = a + d$, where d (Fig. 8a) denotes the length of the plastic zone at each crack tip. This can also be written as

$$d = 2a\sin^2\left(\frac{\pi}{4}\frac{\sigma}{\sigma_Y}\right) \cong \frac{\pi}{8}\left(\frac{K}{\sigma_Y}\right)^2 \tag{29}$$

where the approximation is valid for small-scale yielding conditions. This can be compared with the expression for r_y, given by Eq. 21. Mathematical similarities between this approach and that of Barenblatt [20] led to the name “Barenblatt–Dugdale” crack theory.

Dugdale obtained experimental results that could be compared with the plastic zone size of Eq. (29) by etching steel sheets, having both internal and edge slits (Fig. 8b).

3. LINEAR ELASTIC FRACTURE MECHANICS

The objective is to sufficiently set theory, principles, and concepts of LEFM. An important goal is also to identify those principles and concepts of LEFM that can be extended or generalized to nonlinear fracture mechanics.

3.1. Stress and displacement fields in the vicinity of a crack tip

The equations governing the linearized theory of elasticity are presented in the following commonly used notation:

- position vector: x (coordinates x_i)
- displacement vector: u (coordinates u_i)
- small strain tensor: ε (coordinates ε_{ij})
- stress tensor: σ (coordinates σ_{ij})
- mass density: ρ.

We consider a body B occupying a regular region V in space, which may be bounded or unbounded, with interior V, closure $\bar{V}$ and boundary S. The system of equations governing the motion of a homogeneous, isotropic, linearly elastic body consists of the stress equations of motion, Hooke’s law and the strain-displacement relations:

$$\sigma_{ij,j} + \rho f_i = \rho \ddot{u}_i \tag{30}$$

$$\sigma_{ij} = \lambda \varepsilon_{kk} \delta_{ij} + 2\mu \varepsilon_{ij} \tag{31}$$

$$\varepsilon_{ij} = \frac{1}{2}\left(u_{i,j} + u_{j,i}\right) \tag{32}$$

respectively. Here and further we adopt the Einstein’s summation convention over two repeated indices.

If the strain-displacement relations are substituted into Hooke’s law and the expressions for the stresses are subsequently substituted in the stress-equations of motion, we obtain the displacement from equations of motion

$$\mu u_{i,jj} + (\lambda + \mu) u_{j,ji} + \rho f_i = \rho \ddot{u}_i \tag{33}$$

Equations (30)–(33) must be satisfied at every interior point of the undeformed body B, i.e. in the domain V. In general, we require

$$u_i(x,t) \in C^2(V \times T) \cap C^1(\nabla \times T) \tag{34}$$

$$f_i(x,t) \in C(V \times T) \tag{35}$$

where T is an arbitrary interval of time.

On the surface S of the undeformed body, boundary conditions must be prescribed. The following boundary conditions are most common:

- Displacement boundary conditions: three components u_i are prescribed on the boundary.
- Traction boundary conditions: three components t_i are prescribed on the boundary with unit normal n. Through Cauchy’s formula

$$t_{(n)i} = \sigma_{ji} n_j \tag{36}$$

this case actually corresponds to conditions on three components of the stress tensor.

- Displacement boundary conditions on part S_I of the boundary and traction boundary conditions on the remaining part $S - S_I$.

To complete the problem statement we define initial conditions; in V we have at time $t = 0$: $u_i(x,0) = \overline{u}_i(x)$, $\dot{u}_i(x,0) = \overline{v}_i(x)$.

Mathematical difficulties in solving general equations of elasticity call for the solutions for, more or less, wide classes of special cases. Such are, for example, the class of one-dimensional problems and plane elasticity problems, which incorporate two practically important cases:

- the deformation of a long cylinder by forces, the same in all planes, applied to its lateral surface and lying in planes perpendicular to the generatrices of the cylinder;
- the deformation of a plate by force lying in its plane and applied to its perimeter.

3.1.1. One-dimensional problems

If the body forces and the components of the stress tensor depend on one spatial variable, say x_1, the stress-equations of motion reduce to

$$\sigma_{i1,1} + \rho f_i = \rho \ddot{u}_i \tag{37}$$

Three separate cases can be considered.

Longitudinal strain. Only the longitudinal displacement $u_1(x_1, t)$ does not vanish. The one strain component is $\varepsilon_{11} = \dfrac{\partial u_1}{\partial x_1}$. By employing

$$\sigma_{ij} = \lambda \varepsilon_{kk} \delta_{ij} + 2\mu \varepsilon_{ij} \tag{38}$$

the components of the stress tensor are obtained as

$$\sigma_{11} = (\lambda + 2\mu) u_{1,1}, \; \sigma_{22} = \sigma_{33} = \lambda u_{1,1} \tag{39}$$

and the equation of motion is

$$(\lambda + 2\mu) u_{1,11} + \rho f_1 = \rho \ddot{u}_1 \tag{40}$$

Longitudinal stress. The longitudinal normal stress σ_{11}, which is a function of x_1 and t only, is the one non-vanishing stress component. Equating the transverse normal stresses σ_{22} and σ_{33} to zero, we obtain the following relations

$$\varepsilon_{22} = \varepsilon_{33} = -\frac{\lambda}{2(\lambda + \mu)} = -\nu \varepsilon_{11} \tag{41}$$

where ν is Poisson's ratio. Subsequent substitution of these results in the expression for σ_{11} yields

$$\sigma_{11} = E \varepsilon_{11} \tag{42}$$

where constant E is Young's modulus

$$E = \frac{\mu(3\lambda + 2\mu)}{\lambda + \mu} \tag{43}$$

The equation of motion follows by substitution of (42) in (37).

Shear. In this case the displacement is in a plane normal to the x_1 – axis,

$$\mathbf{u} = u_2(x_1, t)\mathbf{j} + u_3(x_1, t)\mathbf{k}$$

The stresses are

$$\sigma_{21} = \mu u_{2,1}\,,\ \sigma_{31} = \mu u_{3,1}$$

Clearly, the equations of motion reduce to uncoupled wave equations for u_2 and u_3, respectively.

3.1.2. Two-dimensional problems

In two-dimensional problems the body forces and the components of the stress tensor are independent of one of the coordinates, say x_3. The stress equations of motion can be derived from

$$\sigma_{ij,j} + \rho f_1 = \rho \ddot{u}_1 \tag{44}$$

by setting $\dfrac{\partial}{\partial x_3} \equiv 0$. The system of equations will split up into two uncoupled systems:

$$\sigma_{3\beta,\beta} + \rho f_3 = \rho \ddot{u}_3 \tag{45}$$

and

$$\sigma_{\alpha\beta,\beta} + \rho f_\alpha = \rho \ddot{u}_\alpha \tag{46}$$

Greek indices can assume values 1 and 2 only.

3.1.3. Antiplane shear

Deformation described by displacement distribution $u_3(x_1,x_2,t)$ is called antiplane shear deformation. The corresponding stress components follow from Hooke's law as

$$\sigma_{3\beta} = \mu u_{3,\beta} \tag{47}$$

Eliminating $\sigma_{3\beta}$ from Eqs. (45) and (47) we find that $u_3(x_1,x_2,t)$ is governed by the scalar wave equation

$$\mu u_{3,\beta\beta} + \rho f_3 = \rho \ddot{u}_3 \tag{48}$$

3.1.4. In-plane shear

Two separate cases are described by Eq. (46).

Plane strain. In plane strain deformation all field variables are independent of x_3 and the displacement in the x_3–direction vanishes identically. Hooke's law then yields the following relations:

$$\sigma_{\alpha\beta} = \lambda_{\gamma,\gamma}\delta_{\alpha\beta} + \mu\left(u_{\alpha,\beta} + u_{\beta,\alpha}\right) \tag{49}$$

$$\sigma_{33} = \lambda u_{\gamma,\gamma} \tag{50}$$

where Greek indices can assume the values 1 and 2 only.

Elimination of $\sigma_{\alpha\beta}$ from (46) and (49) leads to

$$\mu u_{\alpha,\beta\beta} + (\lambda + \mu) u_{\beta,\beta\alpha} + \rho f_\alpha = \rho \ddot{u}_{\gamma,\gamma} \tag{51}$$

Plane stress. A two-dimensional stress field is called plane stress if σ_{33}, σ_{23} and σ_{13} are identically zero. From Hooke's law it follows that ε_{33} is related to $\varepsilon_{11} + \varepsilon_{22}$ by

$$\varepsilon_{33} = -\frac{\lambda}{\lambda + 2\mu} u_{\gamma,\gamma} \tag{52}$$

Substitution of (52) into the expression for $\sigma_{\alpha\beta}$ yields

$$\sigma_{\alpha\beta} = \frac{2\mu\lambda}{\lambda+2\mu} u_{\gamma,\gamma}\delta_{\alpha\beta} + \mu\left(u_{\alpha,\beta} + u_{\beta,\alpha}\right) \tag{53}$$

Substituting (53) into (46), we obtain the displacement equations of motion. As far as the governing are concerned, the difference between plane strain and plane stress is merely a matter of different constant coefficients. It should be noted that Eq. (52) implies a linear dependence of u_3 on the coordinate x_3.

3.2. Linear elastic crack-tip fields

Except for brittle materials, any loading of a cracked body is accompanied by inelastic deformation in the vicinity of the crack tip due to stress concentrations. The elastic analysis of a real cracked body must depend on the inelastic deformation region, being small compared to the crack size and which is included in the concept of linear elastic fracture mechanics (LEFM).

Essential LEFM concepts are demonstrated for plane elasticity problems. Let the crack plane lie in the x_1x_3–plane and take the crack front to be parallel to the x_3–axis. For plane problems the stress and displacement fields are functions of x_1 and x_2 only. The deformations due to the three primary loading modes are illustrated in Fig. 9. Mode I is the opening or tensile mode where the crack faces symmetrically with respect to the x_1x_2–and x_1x_3–planes. In Mode II, the sliding or in-plane shearing mode, the crack faces slide relative to each other symmetrically about the x_1x_2–plane, but anti-symmetrically with respect to the x_1x_3–plane. In the tearing or antiplane mode, Mode III, the crack faces also slide relative to each other but anti-symmetrically with respect to the x_1x_2 and x_1x_3–planes. In dislocation theory these three modes correspond, respectively, to wedge, edge, and screw dislocations.

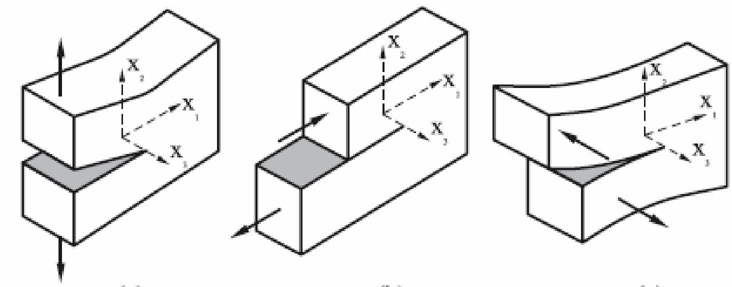

Figure 9. Basic loading modes for a cracked body: a. opening (I); b. sliding (II); c. tearing (III)

These fields govern the fracture process occurring at the crack tip, and the crack-tip fields are developed for the three modes of loading in a homogeneous, isotropic, linear elastic material.

3.2.1. The antiplane problem

Because of its relative simplicity, the antiplane Mode III problem, wherein $u_1 \equiv u_2$ and $u_3 = u_3(x_1,x_2)$, is considered first. Equation (32) yields the following non-zero strain components

$$\varepsilon_{3\alpha} = \frac{1}{2} u_{3,\alpha} \tag{54}$$

Therefore, according to Eq. (47) and (54) the nontrivial stress components are

$$\sigma_{3\alpha} = 2\mu\varepsilon_{3\alpha} \tag{55}$$

Finally, the only relevant equation of equilibrium in the absence of body forces is

$$\sigma_{3\alpha,\alpha} = 0 \tag{56}$$

Equations (54)–(56) can be combined to yield Laplace's equation

$$u_{3,\alpha\alpha} = \nabla^2 u_3 = 0 \tag{57}$$

where $\nabla^2 = \dfrac{\partial^2}{\partial x_1^2} + \dfrac{\partial^2}{\partial x_2^2}$ is the two-dimensional Laplacian operator.

Equation (58) and other planar elasticity problems can be solved by complex variable method. The complex variable z is defined by $z = x_1 + ix_2$ or, in polar coordinates $z = re^{i\theta}$, where $i = \sqrt{-1}$. The overbar is used to denote the complex conjugate; e.g. $\overline{z} = x_1 - ix_2 = re^{-i\theta}$. It follows that

$$x_1 = \Re(z) = \frac{z+\overline{z}}{2} \qquad x_2 = \Im(z) = \frac{z-\overline{z}}{2} \tag{58}$$

where $\Re$ is the real and $\Im$ the imaginary part. By chain rule differentiation is

$$2\frac{\partial}{\partial z} = \frac{\partial}{\partial x_1} - i\frac{\partial}{\partial x_2}, \quad 2\frac{\partial}{\partial \overline{z}} = \frac{\partial}{\partial x_1} + i\frac{\partial}{\partial x_2} \tag{59}$$

$$4\frac{\partial^2}{\partial z \partial \overline{z}} = \frac{\partial^2}{\partial x_1^2} + \frac{\partial^2}{\partial x_2^2} = \nabla^2 \tag{60}$$

Let $f(z)$ be a holomorphic function of the complex variable z, which can be written as

$$f(z) = u(x_1, x_2) + iv(x_1, x_2) \tag{61}$$

where u and v are real functions of x_1 and x_2. It is possible to write

$$\begin{aligned} \frac{\partial f}{\partial x_1} &= \frac{\partial f}{\partial z}\frac{\partial z}{\partial x_1} = f'(z), \\ \frac{\partial f}{\partial x_2} &= \frac{\partial f}{\partial z}\frac{\partial z}{\partial x_2} = if'(z) \end{aligned} \tag{62}$$

where the prime is used to denote a differentiation with respect to the argument of the function:

$$f'(z) = \frac{\partial f}{\partial x_1} = -i\frac{\partial f}{\partial x_2}$$

whence upon the substitution of Eq. (62) yields

$$\frac{\partial u}{\partial x_1} + i\frac{\partial v}{\partial x_1} = \frac{\partial u}{\partial x_2} - i\frac{\partial v}{\partial x_2}.$$

Equating real and imaginary parts we obtain the Cauchy-Riemann equations

$$\frac{\partial u}{\partial x_1} = \frac{\partial v}{\partial x_2}, \quad \frac{\partial v}{\partial x_1} = -\frac{\partial u}{\partial x_2}$$

which may be combined to yield

$$\nabla^2 u = \nabla^2 v = 0$$

Thus, the real and imaginary parts of any holomorphic function are solutions to Laplace's equation.

Therefore, the solution of Eq. (57) can be written as

$$u_3 = \frac{1}{\mu}\left[f(z) + f(\overline{z}) \right] \tag{63}$$

where $f(\overline{z})$ = $u(x_1,x_2) - iv(x_1,x_2)$ is the complex conjugate of $f(z)$. Introducing Eq. (63) into Eq. (54) and employing Eq. (62) we find that

$$\varepsilon_{31} = \frac{1}{2\mu}\left[f'(z) + \overline{f}'(\overline{z}) \right], \quad \varepsilon_{32} = \frac{1}{2\mu}\left[f'(z) - \overline{f}'(\overline{z}) \right] \tag{64}$$

Combining Eq. (55) and (64) one can write

$$\sigma_{31} - i\sigma_{32} = 2f'(z) \tag{65}$$

Let the origin of the x_1, x_2, x_3 coordinate system be located at the tip of a crack, lying along the negative x_1–axis as shown in Fig. 10. Attention is focused upon a small region D containing the crack tip and no other singularities. The dominant character of the stress and displacement fields in D is sought. Consider the holomorphic function

$$f(z) = Cz^{\lambda+1}, \; C = A + iB \tag{66}$$

where A, B and λ are real constants. For finite displacements at the crack tip ($|z| = r = 0$), $\lambda > -1$.

The substitution of Eq. (66) into Eq. (65) yields

$\sigma_{31} - i\sigma_{32} = 2(\lambda+1)Cz^{\lambda} = 2(\lambda+1)r^{\lambda}(A+iB)(\cos\lambda\theta + i\sin\lambda\theta)$, whence

$$\sigma_{31} = 2(\lambda+1)r^{\lambda}(A\cos\lambda\theta - B\sin\lambda\theta), \quad \sigma_{32} = -2(\lambda+1)r^{\lambda}(A\cos\lambda\theta + B\sin\lambda\theta) \tag{67}$$

The boundary condition of traction free crack surfaces produces $\sigma_{32} = 0$ on $\theta = \pm\pi$, so

$A\sin\lambda\pi + B\cos\lambda\pi = 0, \quad A\sin\lambda\pi B\cos\lambda\pi = 0$

To avoid the trivial solution, the determinant of coefficients must vanish. This leads to $\sin 2\lambda\pi = 0$, which for $\lambda > 1$ has the roots $\lambda = -\frac{1}{2}$, for n/2, n = 0, 1, 2,...

Of the infinite set of functions of the form of Eq. (66) that yield traction free crack surfaces within D, the function with $\lambda = -\frac{1}{2}$ for which $A = 0$ provides the most significant contribution to the crack-tip fields. For this case Eq. (67) and (63) become, respectively,

$$\begin{Bmatrix} \sigma_{31} \\ \sigma_{32} \end{Bmatrix} = \frac{K_{III}}{(2\pi r)^{1/2}} \begin{Bmatrix} -\sin(\theta/2) \\ \cos(\theta/2) \end{Bmatrix} \tag{68}$$

$$u_3 = \frac{2K_{III}}{\mu}\left(\frac{r}{2\pi}\right)^{1/2} \sin(\theta/2) \tag{69}$$

where B has been chosen such that

$$K_{III} \lim_{r\to 0}\left\{ (2\pi r)^{1/2} \sigma_{32}\big|_{\theta=0} \right\} \tag{70}$$

The quantity K_{III} is referred to as the Mode III stress intensity factor, which is established by the far field boundary conditions and is a function of the applied loading and cracked body geometry. Whereas, the stresses associated with the other values of λ are finite at the crack tip, the stress components of Eq. (68) have an inverse square root singularity at the crack tip. It is clear that the latter components will dominate as the crack tip is approached. In this sense Eq. (68) and (69) represent the asymptotic forms of the elastic stress and displacement fields.

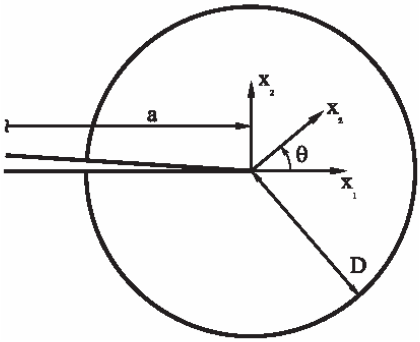

Figure 10. Crack tip region and coordinate system

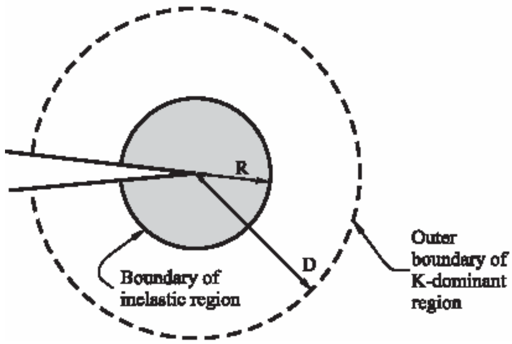

Figure 11. Basis of linear elastic fracture mechanics

3.2.2. The plane problem

Before discussing methods for determining the stress intensity factor and its role in LEFM, the asymptotic fields for the plane strain problem, wherein $u_1 = u_1(x_1,x_2)$, $u_2 = u_2(x_1,x_2)$, and $u_3 = 0$, will be developed. According to Eq. (32) the strain components ε_{3I} will vanish. It follows from Eq. (31) that $\sigma_{3\alpha} = 0$ and

$$\varepsilon_{\alpha\beta} = \frac{1+\nu}{E}\left(\sigma_{\alpha\beta} - \nu\delta_{\alpha\beta}\sigma_{\gamma\gamma}\right) \tag{71}$$

where $\sigma_{\alpha\beta} = \sigma_{\alpha\beta}(x_1,x_2)$. In the absence of body forces, equilibrium equations Eq. (30), reduce to

$$\sigma_{\alpha\beta,\alpha} = 0 \tag{72}$$

and the nontrivial compatibility equation $e_{ijk}e_{pqr}\varepsilon_{jq,kr} = 0$ becomes

$$\varepsilon_{\alpha\beta,\alpha\beta} - \varepsilon_{\alpha\alpha,\beta\beta} = 0 \tag{73}$$

The equilibrium equations will be identically satisfied if the stress components are expressed in terms of the Airy's stress function, $\Psi = \Psi(x_1,x_2)$, such that

$$\sigma_{\alpha\beta} = -\Psi_{,\alpha\beta} + \Psi_{,\gamma\gamma}\delta_{\alpha\beta} \tag{74}$$

After the introduction of Eq. (74) into Eq. (71) the compatibility equation requires that the Airy function satisfies the biharmonic equation

$$\Psi_{,\alpha\alpha\beta\beta} = \nabla^2\left(\nabla^2\Psi\right) = 0 \tag{75}$$

Noting that $\nabla^2\Psi$ satisfies Laplace's equation, one can write, analogous to the antiplane problem, that

$$\nabla^2\Psi = 4\frac{\partial^2\Psi}{\partial z\partial\bar{z}} = f(z) + f(\bar{z}) \tag{76}$$

where $f(z)$ is a holomorphic function. Eq. (76) can be integrated to yield the real function

$$\Psi = \frac{1}{2}\left[\bar{z}\Omega(z) + z\bar{\Omega}(\bar{z}) + \omega(z) + \bar{\omega}(\bar{z})\right] \tag{77}$$

where $f(z)$ and $\omega(z)$ are holomorphic functions.

The substitution of Eq. (77) into Eq. (74) permits writing

$$4\frac{\partial^2\Psi}{\partial z\partial\bar{z}}=\sigma_{11}+\sigma_{22}=2\left[\Omega'(z)+\bar{\Omega}'\bar{\bar{\Omega}}'(\bar{z})\right] \tag{78}$$

$$4\frac{\partial^2\Psi}{\partial\bar{z}^2}=\sigma_{22}-\sigma_{11}-2i\sigma_{12}=2\left[z\bar{\Omega}''(\bar{z})+\bar{\omega}''(\bar{z})\right] \tag{79}$$

$$\sigma_{22}-i\sigma_{12}=\Omega'(z)+\bar{\Omega}'(\bar{z})+z\bar{\Omega}''(\bar{z})+\bar{\omega}''(\bar{z}) \tag{80}$$

Let

$$D=u_1+iu_2 \tag{81}$$

define the complex displacement. Consequently,

$$2\frac{\partial D}{\partial\bar{z}}=\varepsilon_{11}-\varepsilon_{22}+2i\varepsilon_{12} \tag{82}$$

$$\frac{\partial D}{\partial z}+\frac{\partial\bar{D}}{\partial\bar{z}}=\varepsilon_{11}+\varepsilon_{22} \tag{83}$$

The introduction of the stress-strain relation, Eq. (71), into the preceding equations and the employment of Eqs. (78)–(80) provide

$$2\mu\frac{\partial D}{\partial\bar{z}}=-\left[z\bar{\Omega}''+\omega''(\bar{z})\right] \tag{84}$$

$$\frac{2\mu}{1-2\nu}\left(\frac{\partial D}{\partial z}+\frac{\partial\bar{D}}{\partial\bar{z}}\right)=2\left[\Omega'+\bar{\Omega}'(\bar{z})\right] \tag{85}$$

Integrating Eq. (84) and (85) we obtain relation for rigid body complex displacement

$$2\mu D=\kappa\Omega(z)-z\bar{\Omega}'-\bar{\omega}'(\bar{z}) \tag{86}$$

$$\kappa=3-4\nu \tag{87}$$

This complex variable formulation is also valid for generalized plane stress, if

$$\kappa=\frac{3-\nu}{1+\nu} \tag{88}$$

To examine the character of the Mode I stress and displacement fields, the coordinate system origin is positioned at the crack tip. Due to symmetry with respect to the crack plane, the solution of the form

$$\Omega=Az^{\lambda+1}\qquad\omega'=Bz^{\lambda+1} \tag{89}$$

where A, B, and λ are real constants, is chosen. For non-singular displacements at the crack tip, $\lambda>-1$. The introduction of Eq. (89) into Eq. (80) yields

$$\sigma_{22}-i\sigma_{12}=(\lambda+1)r^{\lambda}\begin{Bmatrix}A\left[2\cos\lambda\theta+\lambda\cos(\lambda-2)\theta\right]+B\cos\lambda\theta-\\-i\left[A\lambda\sin(\lambda-2)\theta+B\sin\lambda\theta\right]\end{Bmatrix} \tag{90}$$

which must vanish for $\theta=\pm\pi$. Consequently,

$$A(2+\lambda)\cos\lambda\pi+B\cos\lambda\pi=0\qquad A\lambda\sin\lambda\pi+B\sin\lambda\pi=0$$

for which a nontrivial solution exists if $\sin 2\lambda\pi=0$, or, equivalently,

$$\lambda=-\frac{1}{2}\text{, for n/2, n = 0, 1, 2,...}$$

The dominant contribution to the crack-tip stress and displacement fields occurs for $\lambda = -\frac{1}{2}$, for which $A = 2B$. As in the antiplane problem, an inverse square root stress field singularity exists at the crack tip. Substituting Eq. (89) with $A = 2B$ and $\lambda = -\frac{1}{2}$ into Eq. (78), (86) and (90), it is

$$\begin{Bmatrix} \sigma_{11} \\ \sigma_{12} \\ \sigma_{13} \end{Bmatrix} = \frac{K_I}{(2\pi r)^{1/2}} \cos(\theta/2) \begin{Bmatrix} 1-\sin(\theta/2)\sin(3\theta/2) \\ \sin(\theta/2)\cos(3\theta/2) \\ 1+\sin(\theta/2)\sin(3\theta/2) \end{Bmatrix} \tag{91}$$

$$\begin{Bmatrix} u_1 \\ u_2 \end{Bmatrix} = \frac{K_I}{(2\mu)\left(\frac{r}{2\pi}\right)^{1/2}} \begin{Bmatrix} \cos(\theta/2)\left[\kappa-1+2\sin^2(\theta/2)\right] \\ \sin(\theta/2)\left[\kappa+1-2\cos^2(\theta/2)\right] \end{Bmatrix} \tag{92}$$

The Mode I stress intensity factor K_I is defined by

$$K_I = \lim_{r\to 0}\left\{(2\pi r)^{1/2}\,\sigma_{22}\,|_{\theta=0}\right\} \tag{93}$$

When this is repeated with A and B being pure imaginary, the Mode II fields

$$\begin{Bmatrix} \sigma_{11} \\ \sigma_{12} \\ \sigma_{13} \end{Bmatrix} = \frac{K_{II}}{(2\pi r)^{1/2}} \begin{Bmatrix} -\sin(\theta/2)\left[2+\cos(\theta/2)\cos(3\theta/2)\right] \\ \cos(\theta/2)\left[1-\sin(\theta/2)\sin(3\theta/2)\right] \\ \sin(\theta/2)\cos(\theta/2)\cos(3\theta/2) \end{Bmatrix} \tag{94}$$

$$\begin{Bmatrix} u_1 \\ u_2 \end{Bmatrix} = \frac{K_{II}}{(2\mu)\left(\frac{r}{2\pi}\right)^{1/2}} \begin{Bmatrix} \sin(\theta/2)\left[\kappa+1+2\sin^2(\theta/2)\right] \\ -\cos(\theta/2)\left[\kappa-1-2\cos^2(\theta/2)\right] \end{Bmatrix} \tag{95}$$

are obtained, where

$$K_{II} = \lim_{r\to 0}\left\{(2\pi r)^{1/2}\,\sigma_{12}\,|_{\theta=0}\right\} \tag{96}$$

is the Mode II stress intensity factor for plane strain $\sigma_{33} = \nu(\sigma_{11}+\sigma_{22})$ whereas $\sigma_{33} = 0$ for plane stress.

3.2.3. Fracture criterion

It bears repeating that the foregoing stress and displacement fields for the three modes of loading represent the asymptotic fields as $r\to 0$ and may be viewed as the leading terms in the expansions of these fields about the crack tip. The applied loading σ, the crack length a, and perhaps other dimensions of the cracked body will affect the strength of these fields only through the stress intensity factor; that is, $K = K(\sigma, a)$. When using these expressions, a sufficiently small neighbourhood of the crack tip is considered, where only the leading terms are dominant. In Fig. 11, a measure of the characteristic size of this "K–dominant" neighbourhood is marked as D.

Since the elastic stress field is of the singular nature, there is an inelastic region surrounding the crack tip where the processes of void nucleation, growth, and coalescence in ductile fracture occur. Let R be a representative dimension of this inelastic region. An estimate for R can be obtained, say, for Mode I by equating σ_{22} to the yield stress σ_Y, at $r = R$ and $\theta = 0$, so that

$$R\frac{1}{2\pi}\left(\frac{K_I}{\sigma_Y}\right)^2 \tag{97}$$

Within this region the linear elastic solution is invalid. It is not possible, therefore, to characterize directly the fracture process with a linear elastic formulation. This is not essential provided the inelastic region is confined to the K–dominant region. The situation where R is small compared to D and any other geometrical dimension is referred to as small-scale yielding.

The elastic analysis indicates that the distributions of stress and strain within the K–dominant region are the same regardless of the configuration and loading. Thus, given two bodies with different size cracks and different loadings of the same mode, but otherwise identical, then the near tip stress and deformation fields will be the same if the stress intensity factors are equal. Consequently, the stress intensity factor characterizes the load or deformation experienced by the crack tip and is a measure of the propensity for crack extension or of the crack driving force. If crack growth is observed to initiate in the first body at a critical stress intensity factor, then crack extension in the second body can be expected when its stress intensity factor attains the same critical value. Therefore, within the confines of small-scale yielding, the LEFM fracture criterion for incipient crack growth can be expressed as

$$K(\sigma, a) = K_c \tag{98}$$

where K_c is the critical value of the stress intensity factor K and is a measure of the materials resistance to fracture.

In general the structural integrity assessment of a cracked component requires a comparison of the crack driving force, as measured by the stress intensity factor K, and the materials fracture toughness, K_c. An assessment involves either determining the critical loading to initiate growth of a known crack or in establishing the critical crack size for a specified loading.

3.2.4. The stress intensity factor

Because of the difficulties in satisfying the boundary conditions for finite bodies, only a limited number of closed-form solutions exist. Nevertheless, when the size of the crack is small compared to other dimensions of the body, the crack can be viewed as being in an infinite body. In this case there are standard techniques for establishing the stress intensity factor.

4. PATH INDEPENDENT J INTEGRAL

Considerable mathematical difficulties accompany the determination of concentrated strain fields near notches and cracks, especially in nonlinear materials. An approximate analysis of strain-concentration problems is possible by a method which bypasses this detailed solution of boundary-value problems. The approach is first to identify a line integral which has the same value for all integration paths surrounding notch tip in two-dimensional deformation fields of linear or nonlinear elastic materials. The choice of a near-tip path directly relates the integral to the locally concentrated strain field.

The primary interest in discussing nonlinear materials lies with elastic-plastic behaviour of metals, particularly in relation to fracture. This behaviour is best modelled through incremental stress-strain relations, but formulating a path integral for incremental plasticity analogous to that for elastic materials has failed. Thus a “deformation” plasticity theory is used and the phrase “elastic-plastic material” denotes a nonlinear elastic material exhibiting a linear Hookean response for stress within a yield surface and a nonlinear hardening response for those outside.

4.1. Definition of path independent J integral

So far, it has been assumed implicitly that crack tip plasticity is so small that linear elastic fracture mechanics (LEFM) apply. If so, the energy release rate is not affected by the plastic deformation at the crack tip, and G follows from the elastic stress field. The energy release rate is influenced by the crack tip plastic zone, if the latter cannot be considered negligibly small.

Rice [15] laid the ground work for the bulk of the applications in elastic-plastic fracture mechanics and for crack-tip characterization in a variety of other applications.

Consider a homogeneous body of linear or nonlinear elastic material free of body forces and subjected to a two-dimensional deformation field (plane strain, generalized plane stress, antiplane strain) so that all stresses σ_{ij} depend only on two Cartesian coordinates $x_1(=x)$ and $x_2(=y)$. Suppose the body contains a notch of the type shown in Fig. 12, having, at surfaces parallel to x–axis, a rounded tip denoted by the arc Γ_i. A straight crack is a limiting case.

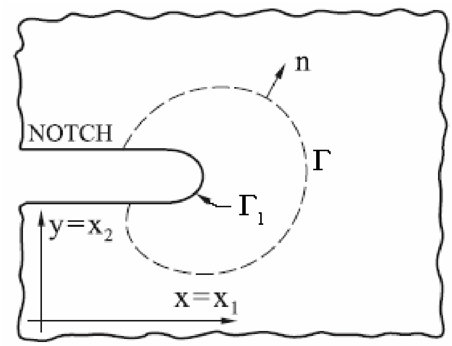

Figure 12. Flat surfaced notch in two-dimensional deformation field (all stresses depend only on x and y). Γ is any curve surrounding the notch tip; Γ_i denotes the curved notch tip

Now consider the integral J defined by

$$J = \int_{\Gamma} \left(W dy - \mathbf{T} \frac{\partial u}{\partial x} ds \right) \tag{99}$$

where the strain-energy density W is defined by

$$W = W(x, y) = W(\varepsilon) = \int_0^t \sigma_{ij} \, d\varepsilon_{ij} \tag{100}$$

and where $\varepsilon = [\varepsilon_{ij}]$ – is the infinitesimal strain tensor.

Here Γ is a curve surrounding the notch tip, the integral being evaluated in a counterclockwise sense starting from the lower flat notch surface and continuing along the path Γ to the upper surface. $\mathbf{T}$ is the traction vector defined according to outward normal along Γ, $T_i = \sigma_{ij} n_j$, $\mathbf{u}$ is the displacement vector, and ds is an element of arc length along Γ. To prove path independency, consider any closed curve Γ^* enclosing an area A^* in a two-dimensional deformation field free of body forces. Application of Green’s theorem gives

$$\int_{\Gamma^*}\left(Wdy - T_i\frac{\partial u}{\partial x}ds\right) = \int_{A^*}\left[\frac{\partial W}{\partial x} - \frac{\partial}{\partial x_j}\left(\sigma_{ij}\frac{\partial u_i}{\partial x}\right)\right]dx\,dy$$

Differentiating the strain-energy density, making use of (31), we have

$$\frac{\partial W}{\partial x} = \frac{\partial W}{\partial \varepsilon_{ij}}\frac{\partial \varepsilon_{ij}}{\partial x} = \sigma_{ij}\frac{\partial \varepsilon_{ij}}{\partial x} = \frac{1}{2}\sigma_{ij}\left[\frac{\partial}{\partial x}\left(\frac{\partial u_i}{\partial x_j}\right) + \frac{\partial}{\partial x}\left(\frac{\partial u_j}{\partial x_i}\right)\right] = \sigma_{ij}\frac{\partial}{\partial x_j}\left(\frac{\partial u_i}{\partial x}\right)$$

since $\sigma_{ij} = \sigma_{ji}$, $= \frac{\partial}{\partial x_j}\left(\sigma_{ij}\frac{\partial u_i}{\partial x}\right)$ (since $\frac{\partial \sigma_{ij}}{\partial x_j} = 0$)

The area integral of this equation vanishes identically, and thus

$$\int_{\Gamma^*}\left(Wdy - \mathbf{T}\frac{\partial \mathbf{u}}{\partial x}ds\right) = 0 \text{ for any closed curve } \Gamma^* \tag{101}$$

Consider any two paths Γ_1 and Γ_2 surrounding the notch tip, as does Γ in Fig. 12. Transverse Γ_2 in the counter-clockwise sense continues along the lower flat notch surface to the starting point where Γ_1 intersects the notch. This describes a closed contour so that the integral of $Wdy - \mathbf{T}\cdot(\partial\mathbf{u}/\partial x)ds$ vanishes. But $\mathbf{T} = 0$ and $dy = 0$ on the portions of path along the flat notch surfaces. Thus the integral along counter-clockwise Γ_1 and the integral along counter-clockwise Γ_2 sum up to zero. J has the same value when computed by integrating along either Γ_1 or Γ_2, and path independent is proven. We assume, of course, that the area between curves Γ_1 and Γ_2 is free of singularities.

By taking Γ close to the notch tip, the integral depends only on the local field. So, the path may be shrunk to the lip Γ_1 (Fig. 12) of a smooth-ended notch and since $\mathbf{T} = 0$

$$J = \int_{\Gamma_1} W\,dy \tag{102}$$

so that J is an averaged measure of the strain on the notch tip. The limit is not meaningful for a sharp crack. Nevertheless, since an arbitrarily small curve Γ may then be chosen surrounding the tip, the integral may be made to depend only on the crack tip singularity in the deformation field. The utility of the method rests in the fact that alternate choices of integration paths often permit a direct evaluation of J. The J integral is identical in form to a static component of the "energy momentum tensor" introduced by Eshelby [25] to characterize generalized forces on dislocations and point defects in elastic fields.

4.2. Evaluation of the *J* Integral

The J integral may be evaluated almost by inspection for the configurations shown in Fig. 13, useful in illustrating the relation to potential energy rates. In Fig. 13a, a semi-infinite flat-surfaced notch in an infinite strip of height h, loads are applied by clamping the upper and lower surfaces of the strip so that the displacement vector $\mathbf{u}$ is constant on each clamped boundary.

Take Γ to be the dashed curve shown, which stretches out to $x = \pm\infty$. There is no contribution to J from the portion of Γ along the clamped boundaries, since $dy = 0$ and $\partial\mathbf{u}/\partial x = 0$. It is also at $x = -\infty$, $W = 0$ and $\partial\mathbf{u}/\partial x = 0$. The entire contribution to J comes from the portion of Γ at $x = +\infty$, and since $\partial\mathbf{u}/\partial x = 0$, then

$$J = W_\infty h \tag{103}$$

where W_∞ is the constant strain-energy density at $x = +\infty$.

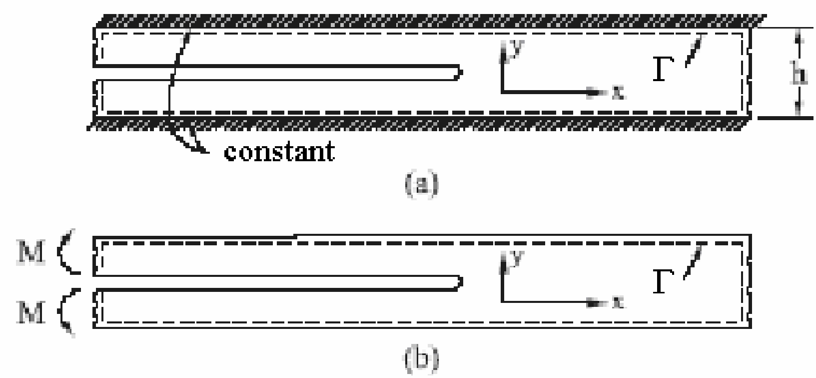

Figure 13. Two special configurations of infinite strips with semi-infinite notches, for which J integral is readily evaluated along the dashed-line paths Γ'. (a) Constant displacements imposed by clamping boundaries, and (b) pure bending of beam-like arms.

Now consider the similar configuration in Fig. 13b, with loads applied by couples M per unit thickness on the beamlike arms so a state of pure bending (all stresses vanishing except σ_{xx}) results at $x = -\infty$. For the contour Γ shown by dashed line, no contribution to J occurs at $x = +\infty$ as W and **T** vanish there, and no contribution occurs for portions of Γ along the upper and lower surfaces of the strip as dy and **T** vanish. In that case J is given by the integral across the beam arms at $x = -\infty$ and on this portion of Γ, $dy = -ds$, $\mathbf{T}_y = 0$, and $\mathbf{T}_x = \sigma_{xx}$. We end up integrating

$$\sigma_{xx}\frac{\partial u_x}{\partial x} - W = \sigma_{xx}\varepsilon_{xx} - W = \sigma_{ij}\varepsilon_{ij} - W = \int_0^{\sigma} \varepsilon_{ij}\, d\sigma_{ij} = \Omega \tag{104}$$

across the two beam arms, where Ω is the complementary energy density. Thus, letting $\Omega_b(M)$ be the complementary energy per unit length of beam arm per unit thickness for a state of pure bending under moment per unit thickness M

$$J = 2\Omega_b\left(M\right) \tag{105}$$

4.3. Small scale yielding in elastic-plastic materials

Consider a narrow notch or crack in a body loaded so as to induce a yielded zone near the tip that is small in size compared to geometric dimensions such its notch length, unnotched specimen width (ligament), and so on. The situation envisioned has been termed "small-scale yielding", and a boundary-layer style formulation of the problem [26] is employed to discuss the limiting case. The essential ideas are illustrated with reference to Fig. 14. Symmetrical loading about the narrow notch are imagined to induce a deformation state of plane strain. First, consider the linear elastic solution, when the notch is presumed to be a sharp crack. Employing polar coordinates r, θ with origin at the crack tip, the form of stresses in the vicinity of the tip are known ([27], [28]) to exhibit a characteristic inverse square-root dependence on r:

$$\sigma_{ij} = \frac{K_I}{\left(2\pi r\right)^{1/2}} f_{ij}\left(\theta\right) \text{ + other terms which are bounded at the crack tip} \tag{106}$$

Here K_I is the stress intensity factor and the set of functions $f_{ij}(\theta)$ are the same for all symmetrically loaded crack problems. For an isotropic material

$$f_{xx} = \cos(\theta/2)\left[1-\sin(\theta/2)\sin(3\theta/2)\right]$$
$$f_{yy} = \cos(\theta/2)\left[1+\sin(\theta/2)\sin(3\theta/2)\right] \tag{107}$$
$$f_{xy} = f_{yx} = \sin(\theta/2)\cos(\theta/2)\cos(3\theta/2)$$

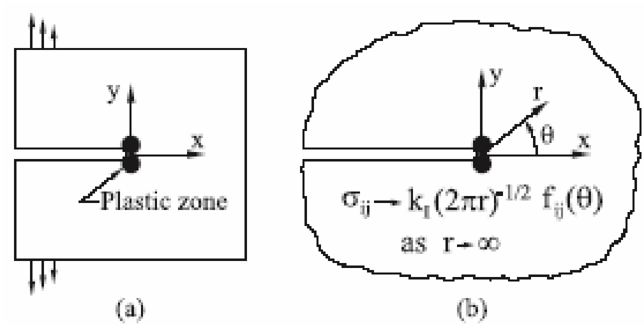

Figure 14. (a) Small-scale yielding near a narrow notch or crack in an elastic- plastic material. (b) The actual configuration is replaced by a semi-infinite notch or crack in an infinite body; actual boundary conditions are replaced by the requirement of on asymptotic approach to the linear elastic crack tip singularity stress field.

Now suppose the material is elastic-plastic and the load level is sufficiently small so that a yield zone forms corresponding to small-scale yielding, Fig. 14a. One anticipates that the elastic singularity governs stresses at distances from the notch root that are large compared to yield zone and root radius dimensions, but still small compared to characteristic geometric dimensions such as notch length. The actual configuration in Fig. 14a is then replaced by the simpler semi-infinite notch in an infinite body, Fig. 14b,

$$\sigma_{ij} \to \frac{K_I}{(2\pi r)^{1/2}} f_{ij}(\theta) \text{ as } r \to 0, \tag{108}$$

where K_I is the stress intensity factor from the linear elastic crack solution. Such boundary–layer solutions for cracks are mathematically exact in the plastic region – only to the first non-vanishing term of a Taylor expansion of complete solutions in the applied load. But comparison [26] with complete solutions indicates that the boundary–layer approach is an accurate approximation up to one half of net section yielding load levels. We now evaluate the integral J from the boundary–layer solution, taking Γ to be a large circle of radius r in Fig. 13b:

$$J = r\int_{-\pi}^{+\pi}\left[W(r,\theta)\cos\theta - \mathbf{T}(r,\theta)\frac{\partial \mathbf{u}}{\partial x}(r,\theta)\right]d\theta \tag{109}$$

By path independence we may let $r \to \infty$ and since W is quadratic in strain in the elastic region, only the asymptotically approached inverse square-root elastic-stress field contributes. Working out the associated plane-strain deformation field, one finds

$$J = \frac{1-\nu^2}{E}K_I^2, \text{ for small scale yielding} \tag{110}$$

where E is Young's modulus and ν is Poisson's ratio.

Primarily, we will later deal with one configuration, the narrow notch or crack of length $2a$ in a remotely uniform stress field σ_∞, Fig. 15. In this case [28]

$$K_I = \sigma_\infty (\pi a)^{1/2}$$

and

$$J = \frac{\pi(1-\nu^2)}{E}\sigma_\infty^2 a\,, \text{ for small scale-yielding} \tag{111}$$

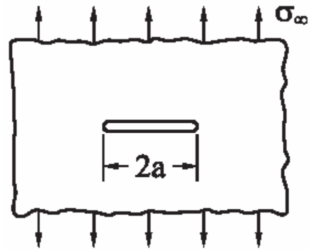

Figure 15. Narrow notch or crack of length $2a$ in infinite body; uniform remote stress σ_∞.

For plane stress, the same result holds for J with $1-\nu^2$ replaced by unity. The same computation may be carried out for more general loading. Letting K_I, K_{II}, and K_{III} be elastic stress-intensity factors [28] for the opening, in-plane sliding, and anti-plane sliding (tearing) modes, respectively, of notch tip deformation, one readily obtains

$$J = \frac{1-\nu^2}{E}\left(K_I^2 + K_{II}^2\right) + \frac{1-\nu^2}{E}K_{III}^2 \quad \text{(small-scale yielding)} \tag{112}$$

4.3.1. Interpretation in terms of energy comparisons for notches of neighbouring size

Let A' denote the cross section and Γ' the bounding curve of a two-dimensional elastic body. The potential energy per unit thickness is defined as

$$P = \int_{A'} W dx\, dy - \int_{\Gamma''} \mathbf{T}\cdot\mathbf{u}\, ds \tag{113}$$

where Γ'' is that portion of Γ' on which tractions $\mathbf{T}$ are prescribed. Let $P(\ell)$ denote the potential energy of a body containing a flat-surfaced notch as in Fig. 11. with tip at $x = \ell$. We compare this with the energy $P(\ell + \Delta\ell)$ of an identically loaded body which is similar in every respect except that the notch is now at $x = \ell + \Delta\ell$, the shape of the curved tip Γ_t, being the same in both cases. Then one may show that

$$J = -\lim_{\Delta l \to 0} \frac{P(\ell + \Delta\ell) - P(\ell)}{\Delta\ell} = -\frac{\partial P}{\partial \ell} \tag{114}$$

is the rate of decrease of potential energy with respect to notch size (see Rice, [29]). Upper equations provide a check. For loading by imposed displacements only, as in Fig. 14(a), the potential energy equals the strain energy so that Eq. (103) results. Similarly, the potential energy equals minus the complementary energy for loading by traction only as in Fig. 14b, so that Eq. (106) results. Equation (113) is the linear elastic energy-release rate given by Irwin [28], reflecting the fact that a small nonlinear notch tip zone negligibly affects the overall compliance of a notched body.

J. W. Hutchinson [30], has noted that an energy-rate line integral proposed by Sanders [31] for linear elasticity may be rearranged so as to coincide with the J integral form. The connection between energy rates and locally concentrated strains on a smooth-ended notch tip, as in Eqs. (103) and (115), has been noted first by Thomas [32] and later by Rice and Drucker [33] and Bowie and Neal [34]. Since subsequent results on strain concentrations will be given in terms of J, means for its determination in cases other than those represented by Equations (103)–(112) are useful. In particular, the compliance testing method of elastic fracture mechanics [28] is directly extendable through Eq. (114) to nonlinear materials. Also, highly approximate analyses may be employed since only overall compliance changes enter the determination of J. For example, the Dugdale model [35] may be employed to estimate the derivation of J from its linear elastic value in problems dealing with large-scale plastic yielding near a notch. Once having determined J (approximately), the model may be ignored and methods of the next sections employed to discuss local strain concentrations.

Such estimates of J are given in reference [29] for the two models just noted. As anticipated, deviations from the linear elastic value show little sensitivity to the particular model employed.

It can be shown that the interpretation of J as the rate of the potential energy change for nonlinear constitutive behaviour plays key role for fracture analysis in elastic-plastic conditions. Here, we will focus on the role played by J in unifying linear elastic fracture mechanics. By taking Γ as a contour that circumscribes the cohesive zone in Barenblatt's model, Rice has found that

$$J = \int_0^{\delta_t} \sigma(\delta)\, d\delta \tag{115}$$

where σ denotes the cohesive stress and δ_t is the separation distance at the crack tip. At the onset of fracture δ_t must be equal to δ_c, the out-of-range interatomic separation distance. Then, the right-hand side of Eq. (115) would be twice the surface energy. Thus, for fracture, $J_c = 2\gamma$. This relation strongly suggests that, for linear elastic conditions, J and G are equivalent.

This equivalence can also be shown directly through an energy release rate interpretation of J, which results in

$$J = -\frac{\partial \Pi}{\partial a} \equiv G \tag{116}$$

where Π denotes the potential energy of the cracked body. From this finding Rice was able to conclude that:

"...the Griffith theory is identical to a theory of fracture based on atomic cohesive forces, regardless of the force-attraction law, so long as the usual condition is fulfilled that the cohesive zone be negligible in size compared to characteristic dimensions".

Finally, Rice [35] also applied the J–integral to the Dugdale model. The result is just the same as Eq. (116) provided $\sigma(\delta)$ is taken equal to σ_Y. The result is simply

$$J = \sigma_Y \delta_t \tag{117}$$

where δ_t is the crack-tip opening displacement. Equations (116) and (117) taken together with Eq. (115) show the equivalence of all fracture mechanics parameters under linear elastic conditions.

However, this will not be true for a growing crack. Crack advance in an elastic-plastic material involves elastic unloading and non-proportional loading around the crack tip. Neither of these processes is adequately accommodated by deformation theory.

Nonetheless, the energy-based definition of J given by Eq. (117) has been very useful in mathematical analyses, both in determining critical J values from experimental load–deflection records and for component fracture predictions.

REFERENCES

1. Kanninen, M.F., *Advanced fracture mechanics*, Oxford Engineering Science Series, Oxford University Press. (1985)
2. Griffith, A.A, *The Phenomena of Rupture and Flow in Solids*, Philosophical Transactions of the Royal Society of London, A221, pp. 163–197, (1921); and *The Theory of Rupture*, Proceedings of the First International Conference of Applied Mechanics, Delft. (1924)
3. Griffith, A.A, *The Theory of Rupture*, Proceedings of the First International Conference of Applied Mechanics, Delft, pp. 55–63, Biezeno and Burgers ed. Waltman. (1925)
4. Inglis, C.E., *Stresses in a Plate Due to the Presence of Cracks and Sharp Corners*, Transactions of the Institute of Naval Architects, 55, pp. 219–241. (1913)
5. Bueckner, H.F., *The Propagation of Cracks and the Energy of Elastic Deformation*, Transactions of the American Society of Mechanical Engineers, 80, pp. 1225–1230. (1958)
6. Erdogan, F., *Stress Intensity Factors*, Journal of Applied Mechanics, 50, pp. 992–1002. (1983)
7. Sneddon, I.N., *The Distribution of Stress in the Neighborhood of a Crack in an Elastic Solid*, Proceedings of the Royal Society of London, A187, pp. 229–260. (1946)
8. Westergaard, H.M., *Bearing Pressures and Cracks*, Transactions of the American Society of Mechanical Engineers, 61, pp. A49–A53. (1939)
9. Irwin, G.R., *Analysis of Stresses and Strains Near the End of a Crack Traversing a Plate*, Journal of Applied Mechanics, 24, pp. 361–364. (1957)
10. Sih, G.C., Paris, P.C., and Erdogan, F., *Crack Tip Stress-Intensity Factors for Plane Extension and Plate Bending Problems*, Journal of Applied Mechanics, 29, pp. 306–312. (1962)
11. Sih, G.C., Paris, P.C., and Irwin, G.R., *On Cracks in Rectilinearly Anisotropic Bodies*, International Journal of Fracture Mechanics, 1, pp. 189–203. (1965)
12. Elliott, H.A., *An Analysis of the Conditions for Rupture Due to Griffith Cracks*, Proceedings of the Physical Society, 59, pp. 208–223. (1947)
13. Cribb, J.L., and Tomkins, B., *On the Nature of the Stress at the Tip of a Perfectly Brittle Crack*, Journal of the Mechanics and Physics of Solid, 15, pp. 135–140. (1967)
14. Goodier, J.N., *Mathematical Theory of Equilibrium Cracks*, Fracture, H. Liebowitz (ed.), Vol. II, Academic, New York, pp. 1–66. (1968)
15. Rice, J.R., *A Path Independent Integral and the Approximate Analysis of Strain Concentration by Notches and Cracks*, Journal of Applied Mechanics, 35, pp. 379–386. (1968)
16. Gehlen, P.C., and Kanninen, M.F., *An Atomic Model for Cleavage Crack Propagation in Alpha Iron*, Inelastic Behavior of Solids, M.F. Kanninen et al.(ed.), McGraw-Hill, New York, pp. 587–603. (1970)
17. Weiner, J.H., and Pear, M., *Crack and Dislocation Propagation in an Idealized Crystal Model*, Journal of Applied Physics, 46, pp. 2398–2405. (1975)
18. Ashurst, W.T., and Hoover, W.G., *Microscopic Fracture Studies in the Two-dimensional Triangular Lattice*, Physical Review B, 14, pp. 1465–1473. (1976)
19. Markworth, J.A., Kahn, L.R., Gehlen, P.C., and Hahn, G.T., *Atomistic Computer Simulation of Effects of Hydrogen and Helium on Crack Propagation in BCC Iron*, Res. Mechanica, 2, pp. 141–162. (1981)
20. Irwin, G.R, Kies, J.A., and Smith, H.L., *Fracture strengths relative to onset and arrest of crack propagation*, Proceed. of the American Society for Testing Materials, 58, pp. 640–657. (1958)
21. Wells, A.A., *Applications of fracture mechanics at and beyond general yielding*, British Welding Journal, 10, pp. 563-570. (1963)
22. Dugdale, D.S., *Yielding of steel sheets containing slits*, Journal of the Mechanics and Physics of Solids, 8, pp. 100-108. (1960)
23. Muskhelisvili, N.I., *Some Basic Problems in the Mathematical Theory of Elasticity*, Nordhoff, the Netherlands. (1954)
24. Barenblatt, G.I., *The Mathematical Theory of Equilibrium of Crack in Brittle Fracture*, Advances in Applied Mechanics, 7, pp. 55–129. (1962)

25. Eshelby, J.D., *The Continuum Theory of Lattice Defects*, Solid State Physics, Vol.3, Academic Press. (1956)
26. Rice, J.R., *The Mechanics of Crack Tip Deformation and Extension by Fatigue*, Fatigue Crack Growth, ASTM Spec. Tech. Publ., p.415. (1967)
27. Williams, M.L., *On the Stress Distribution at the Base of a Stationary Crack*, Journal of Applied Mechanics, Vol. 24, No.1, Trans. ASME, Vol. 79, Mar. 1957, pp. 109-114.
28. Irwin, G.R., *Fracture Mechanics*, Structural Mechanics (Proceeding of first Naval Symposium), Pergamon Press. (1960)
29. Rice, J.R., *Mathematical Analysis in the Mechanics of Fracture*, Treatise on Fracture, Vol.2, ed. Liebowitz, H., Academic Press.
30. Hutchinson, J.W., *Fundamentals of the Phenomenological Theory of Nonlinear Fracture Mechanics*, Journal of Applied Mechanics, 50, pp. 1042–1051. (1983)
31. Sanders, J.L., *On the Griffith - Irwin Fracture Theory*, Journal of Applied Mechanics, Vol.27, No.2, Trans. ASME, Vol. 82, Series E, June 1960, pp. 352– 352.
32. Thomas, A.G., *Rupture of Rubber, II, The Strain Concentration at an Incision*, Journal of Polymer Science, Vol. 18. (1955)
33. Rice, J.R., Drucker, D.C., *Energy Changes in Stressed Bodies Due to Void and Crack Growth*, International Journal of Fracture Mechanics, Vol.3, No.1. (1967)
34. Bowie, O.L., Neal, D.M., *The Effective Crack Length of an Edge Notch in a Semi-Infinite Sheet Under Tension*, International Journal of Fracture Mechanics.
35. Rice, J.R., *Stresses Due to a Sharp Notch in a Work-Hardening Elastic-Plastic Material Loaded by Longitudinal Shear*, Journal of Applied Mechanics, Vol.34, No.2, Trans. ASME, Vol. 89, Series E, June 1967, pp. 287–298.

DAMAGE MECHANICS - BASIC PRINCIPLES

Dušan P. Krajčinović, Arizona State University, Tempe, Arizona, USA
Dragoslav M. Šumarac, Civil Engineering Faculty, Belgrade, S&Mn

INTRODUCTION

The origin of Damage Mechanics dates in 1958, after the celebrated paper of L. M. Kachanov [1]. Since then, Krajčinović, Chow, Lemaitre, Chaboche, Murakami, Bazant were among others who helped the development in this field. There are two basic approaches. The first one is the so-called phenomenological, and the other- the physical.

In the next paragraph, a simple loose bundle parallel bar system will be presented for the purpose of explaining the essential feature of this theory. In the second section, the composite material with the circular cracks will be outlined within the framework of Damage Mechanics. The third paragraph is devoted to material, damaged with elliptical cracks. The example of a repaired bridge is also presented.

1. LOOSE BUNDLE PARALLEL BAR SYSTEM

This paragraph represents a part of the paper written by D. Krajčinović et al., [2]. Consider the simplest approximation of a perfectly brittle solid by a loose bundle parallel bar system assuming that:

- all extant links share equally in carrying the external tensile load F regardless of their position within the system;
- all N links have identical stiffness $k = K/N$ and elongations u;
- all links remain elastic until they rupture (Fig. 1, Fig. 2); and
- the rupture strength f_r of links is a random variable defined by a prescribed probability density distribution $p(f_r)$.

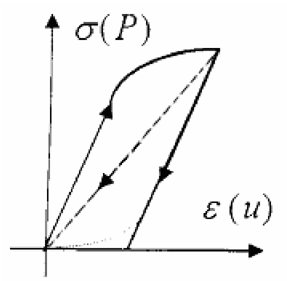

Figure 1. σ–ε diagram for ductile and brittle material

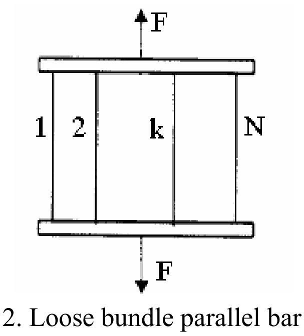

Figure 2. Loose bundle parallel bar system

Application of a loose bundle parallel bar system implicitly assumes that the damage evolution and ultimately the failure are attributable primarily to the existence of the regions of inferior toughness within the material. Local stress concentrations are therefore assumed to have a second-order effect on the structural response.

During the deformation of the system subjected to a quasi-statically incremented external tensile load F, the tensile forces in individual links f_i (i=1 to N) keep increasing. When the force f_i in a link exceeds its strength f_{ri} the link ruptures releasing its force.

The released force is distributed quasi-statically and equally to all extant links. Consequently, the deformation process is characterized by the sequential ruptures of individual links. On the system scale rupture of individual links is observed as gradually decreasing (system) stiffness.

Since each link is perfectly elastic until it ruptures (Fig. 1), the force-displacement relation for the i-th link is,

$$f_i = \frac{K}{N} u = ku \quad \text{if} \quad 0 \le ku > f_i \qquad f_i = 0 \quad \text{if} \quad ku \ge f_{ri} \tag{1}$$

The equilibrium equation for the system is then:

$$F = \sum_{i=1}^{N} f_i = Ku\left(1 - \frac{n}{N}\right) = Ku\left(1 - D\right) \tag{2}$$

where n is the number of ruptured links (at a given magnitude of the externally applied tensile force F). The fraction of ruptured links,

$$D = \frac{n}{N} \tag{3}$$

is accumulated damage on the macro-scale. In absence of ductile phenomena and residual strains, D fully defines the state of the material and quantifies the level of degradation of the material stiffness and, perhaps, even the residual load bearing capability.

Maximum force to which the system can be subjected (i.e., macro failure in a force-controlled test) occurs when the tangent modulus reduces to zero, i.e., when:

$$\frac{dF}{du} = 0, \quad \text{for} \quad u = u_m \tag{4}$$

In unloading, the force-displacement relation is simply,

$$F = K\left(1 - D_u\right)u \tag{5}$$

where D_u=*const* is the system damage at the point at which the unloading commenced (at the highest recorded force F, Fig. 2). Consequently, the system unloads along the current (secant) stiffness $\overline{K} = K(1 - D_u)$, i.e., along a line connecting the point at which the unloading started and the origin of the F–u space. After the unloading is completed, no residual strain is retained in the system.

1.1. Thermodynamic analysis

The energy E used on the rupture of links is equal to the difference between the mechanical work of the externally applied tensile force F and the energy of elastic deformation that would be released in the course of subsequent unloading, i.e.

$$E = W - U = \int_0^u F du - \frac{1}{2} F u \tag{6}$$

Geometrically, the energy E is equal to the area (dotted in Fig. 3) contained within the loading (ascending) and unloading (descending) segments of the force-displacement curve.

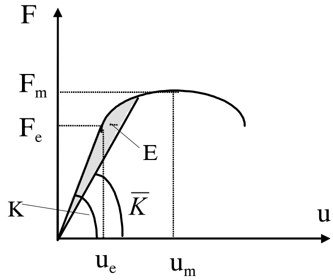

Figure 3. The force-displacement diagram

Consider the Helmholtz free energy of the entire system $\Phi = \Phi(u,D,T)$. Using the first law of thermodynamics and restricting considerations to isothermal processes ($T = const > 0$), the free energy change rate, during loading by monotonically increasing tensile force F, can be written in the usual form (Rice, [3], Schapery, [4]),

$$\dot{\Phi} = F\dot{u} - T\Lambda \tag{7}$$

where Λ is the irreversible entropy production rate. The second law of thermodynamics requires that $\Lambda \geq 0$.

Let the free energy be equal to zero in the initial, unruptured and unloaded state ($D = 0$, $F = 0$). The free energy of a state defined by load $F > 0$ and damage $D > 0$ is then equal to the work done in transforming the body from its initial to current state along an imagined reversible and isothermal path. Following arguments analogous to those in Rice [3], related thermodynamic analysis of the quasi-static growth of Griffith cracks, a loaded state in which at least some of the links are ruptured ($D > 0$), can be created by an imagined sequence of two steps: first, $n = DN$ links are ruptured quasi-statically pulling against the cohesive forces keeping together two adjacent layers of atoms, and second, stretching elastically the extant links until the requested state of deformation u is arrived at. The work associated with this sequence is,

$$\Phi = E_\gamma + U \tag{8}$$

$$E_\gamma = 2A\int_{\gamma_{\min}}^{\gamma_r} \gamma_r p(\gamma_r) d\gamma_r \tag{9}$$

is the energy of free surface, created by rupturing n links, and γ_r is the link dependent specific surface energy, A denotes the initial unruptured cross-section area of the whole system. The linear elastic fracture mechanics suggests that the surface energy is a quadratic function of the force in the link at its rupture. Under this assumption and after lengthy calculations, as is shown in Krajčinović et al. [2], energy of free surface is:

$$E_\gamma = 2aA\left[f_{\min}^2 D + f_{\min}(\Delta f) D^2 + \frac{1}{3}(\Delta f)^2 D^3 \right] \tag{10}$$

The rate of change of density of Helmholz free energy is therefore

$$\dot{\phi} = \left[K(1-D)u \right]\dot{u} + \left\{ -\frac{1}{2}Ku^2 + 2aA\left[f_{\min} + (\Delta f D) \right]^2 \right\}\dot{D} \tag{11}$$

Comparing (11) and (7) it follows that $F = K(1–D)u$ and

$$T\Lambda = \left(\frac{1}{2}Ku^2 - 2A\gamma_r \right)\dot{D} \tag{12}$$

In (12), γ_r is the surface energy of the link rupturing at the displacement level u. Introduce

$$\Gamma = -\frac{\partial U}{\partial D} = \frac{1}{2} K u^2 \tag{13}$$

i.e., the energy release rate associated with the damage progression $\dot{D}$, as the driving force needed to rupture the links causing the damage, and

$$R = 2A\gamma_r \tag{14}$$

as the current resistive force. Equation (12) and the requirement of a non-negative entropy production rate ($\Lambda \geq 0$) consequently give

$$(\Gamma - R)\dot{D} \geq 0 \tag{15}$$

which is already written in the Eq. (12).

1.2. Conjugate measures of damage and associated affinities

The rate of energy used in the rupturing process is from (6),

$$\dot{E} = \dot{W} - \dot{U} = \left(F - \frac{\partial U}{\partial u} \right) \dot{u} - \frac{\partial U}{\partial D} \dot{D} \tag{16}$$

Since $F = \partial U / \partial u$,

$$\dot{E} = -\frac{\partial U}{\partial D} \dot{D} = \Gamma \dot{D} \tag{17}$$

where Γ is the thermodynamic force or affinity conjugate to damage variable D. Since

$$U = \frac{1}{2} F u = \frac{1}{2} K (1 - D) u^2 \tag{18}$$

it follows that

$$\Gamma = \frac{1}{2} K u^2 \tag{19}$$

as already established in (13). Geometrically, Γ is numerically equal to the area of the triangle doted in Fig. 4a.

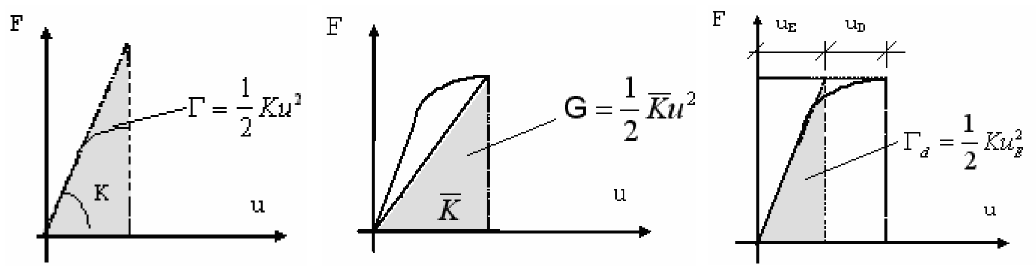

a) b) c)

Figure 4. Thermodynamic force (affinities) conjugate to damage variables a) D; b) **D;** c) d

Introduce now a new damage variable by defining its rate of change relative to the current number of the unruptured links ($N - n$),

$$\dot{\mathbf{D}} = \frac{\dot{n}}{N - n} \tag{20}$$

Integrating (20) from the initial (n = 0) to the current state (n > 0), it follows that

$$\mathbf{D} = \ln\frac{N}{N-n} \tag{21}$$

The logarithmic measure (21) was first used by Janson and Hult [5]. In analogy with the strain measure commonly used in the theory of plasticity, damage variable (21) can be referred to as a logarithmic damage. Since $0 \le n \le N$, it follows that $0 \le \mathbf{D} \le \infty$. Recall that the previous damage variable $D = n/N$ is defined in the interval $0 \le D \le 1$. The relations between the two measures of damage D and $\mathbf{D}$ and their rates $\dot{D}$ and $\dot{\mathbf{D}}$ are:

$$D = 1 - \exp(-\mathbf{D}) = \mathbf{D} - \frac{1}{2!}\mathbf{D}^2 + \frac{1}{3!}\mathbf{D}^3 - \ldots \tag{22}$$

$$\dot{\mathbf{D}} = \frac{1}{1-D}\dot{D}, \quad \dot{D} = \exp(-\mathbf{D})\dot{\mathbf{D}} \tag{23}$$

Using the initial unruptured area A and current unruptured area $\overline{A} = (1-D)A$, the introduced damage variables and their rates can be expressed as,

$$D = \frac{A - \overline{A}}{A}, \quad \dot{D} = -\frac{\dot{\overline{A}}}{A} \tag{24}$$

$$\mathbf{D} = \ln\frac{A}{\overline{A}}, \quad \dot{\mathbf{D}} = -\frac{\dot{\overline{A}}}{\overline{A}} \tag{25}$$

For infinitesimally small accumulated damages ($n << N$, $D << 1$), the distribution between two damage measures disappears, i.e. $\mathbf{D} \cong D$ and $\dot{\mathbf{D}} = \dot{D}$.

The thermodynamic force (affinity) $\mathbf{G}$ conjugate to damage variable (flux) $\mathbf{D}$ is obtained from

$$\dot{E} = \Gamma\dot{D} = \mathbf{G}\dot{\mathbf{D}} \tag{26}$$

such that

$$\mathbf{G} = \exp(-\mathbf{D})\Gamma = (1-D)\Gamma = \frac{1}{2}\overline{K}u^2 \tag{27}$$

In Equation (27)

$$\overline{K} = \exp(-\mathbf{D})K = (1-D)K \tag{28}$$

is the current elastic stiffness of the system, reflecting the already recorded damage.

Geometrically $\mathbf{G}$ is the area of the dotted triangle shown in Fig.4b. It is, in fact identically equal to currently available elastic energy U, i.e., $\mathbf{G} = U$.

The entropy inequality (15) can now be expressed in terms of the damage variable D as

$$\left(\mathbf{G} - \mathbf{R}\right)\dot{\mathbf{D}} = \left(\frac{1}{2}\overline{K}u^2 - 2\overline{A}\gamma_r\right)\dot{\mathbf{D}} \tag{29}$$

where $\mathbf{R} = 2\overline{A}\gamma_r$ is the corresponding resistance force, while $\overline{A}$ is the cross-section area currently available to carry the external applied tension force. For continuing damage ($\dot{\mathbf{D}} \ge 0$), (29) therefore requires $\mathbf{G} > \mathbf{R}$. If the entire energy used in the rupturing process is transformed into the free surface, $\mathbf{G} = \mathbf{R}$.

Other measures of (large) damage and conjugate affinities can be introduced, similarly as in large strain continuum mechanics, Hill [6]. For example, the "Lagrangian type" damage can be defined by,

$$D_L = \frac{A^2 - \overline{A}^2}{2A^2} = \frac{N^2 - (N-n)^2}{2N^2} = D - \frac{1}{2}D^2 \tag{30}$$

Similarly, a damage variable,

$$d = \frac{A - \overline{A}}{\overline{A}} = \frac{n}{N-n} = \frac{D}{1-D} \tag{31}$$

is the number (n) of ruptured bars per current number of unruptured bars ($N - n$). The "Eulerian type" damage parameter can be then defined as

$$D_E = \frac{A^2 - \overline{A}^2}{2\overline{A}^2} = \frac{N^2 - (N-n)^2}{2(N-n)^2} = d + \frac{1}{2}d^2 \tag{32}$$

The affinities to D_L and D_E follow from (26):

$$\Gamma_L = \frac{1}{1-D}\Gamma, \qquad \Gamma_E = \frac{1}{1+d}\Gamma_d \tag{33}$$

where $\Gamma_d = (1 - D)^2\Gamma$ is the affinity conjugate to damage variable d. If the total displacement u is decomposed into its elastic and damage parts, by defining elastic component as displacement that would correspond to current force if no damage was produced ($u_E = F/K$, Fig. 4c), then

$$u = u_E + u_D\,, \quad u_E = (1 - D)u \quad \text{and} \quad u_D = Du \tag{34}$$

The affinity Γ_d can then be expressed as

$$\Gamma_d = \frac{1}{2}Ku_E^2 \tag{35}$$

representing the accumulated strain energy associated with the elastic component of displacement u_E. Geometrically, Γ_d is equal to the dotted triangle shown in Fig. 4c.

2. DAMAGE DUE TO PRESENCE OF MICROCRACKS

In this paragraph, attention will be focused on micromechanical theories with the example of thermal damage growth in composite materials. For phenomenological damage theories the readers are advised to read the paper Chow and Chen [7].

2.1. Compliance of the cracked body with the circular cracks

Due to presence and increase of the crack, the compliance of the body containing circular slits would increase as well. Firstly the compliance due to presence of a single circular crack would be derived, and after that due to presence of many cracks.

Consider the circular crack (Fig. 5) under plane stress condition. From Cotterell and Rice [8], for small α ($\alpha \to 0$), taking only linear term in α, the stress intensity factors (SIF) are:

$$K_I = \sqrt{\pi a}\left(\sigma_2' - \frac{3}{2}\alpha\sigma_6'\right) = \sqrt{\pi a}\left(\sigma_2' - \frac{3}{2}\frac{a}{R}\sigma_6'\right) \tag{36}$$

$$K_{II} = \sqrt{\pi a}\left[\sigma_6' + \left(\sigma_2' - \frac{1}{2}\sigma_1'\right)\alpha\right] = \sqrt{\pi a}\left[\sigma_6' + \left(\sigma_2' - \frac{\sigma_1'}{2}\right)\frac{a}{R}\right] \tag{37}$$

where Voigt's notation was used:

$$\sigma_2' = \sigma_{yy}'; \quad \sigma_1' = \sigma_{xx}'; \quad \sigma_6' = \sigma_{xy}' \tag{38}$$

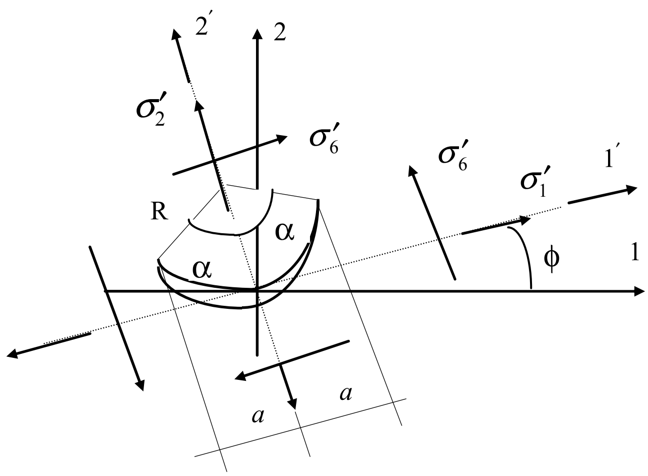

Figure 5. Circular crack in the global and local coordinates

Potential energy increase due to presence of a single crack is obtained by fracture mechanics models from (36) and (37) as,

$$\psi^{*(k)} = \int_{-a}^{+a} \frac{K_I^2 + K_{II}^2}{E} da = \frac{\pi a^2}{E}\left[(\sigma_2')^2 \left(1+\frac{a^2}{2R^2}\right) + (\sigma_1')^2 \frac{a^2}{8R^2} - \sigma_1'\sigma_2' \frac{a^2}{2R^2} - \right. \\ \left. -\sigma_1'\sigma_6' \frac{2a}{3R} - \sigma_2'\sigma_6' \frac{2a}{3R} + (\sigma_6')^2 \left(1 + \frac{9}{8}\frac{a^2}{R^2}\right)\right] \tag{39}$$

The increase of the compliances due to presence of one crack are obtained by differentiating expression (39) with the governing stresses in the form,

$$S_{ij}^{*(k)'} = \frac{\partial^2 \psi^{*(k)}}{\partial^2 \sigma_i' \partial^2 \sigma_j'} \tag{40}$$

Substituting (39) into (40) yields to,

$$S_{ij}^{*(k)'} = \frac{2\pi a^2}{E}\left[\frac{a^2}{8R^2}\delta_{1i}\delta_{1j} - \frac{1}{4}\frac{a^2}{4R^2}(\delta_{1i}\delta_{2j} + \delta_{2i}\delta_{1j}) + \left(1 + \frac{a^2}{2R^2}\right)\delta_{2i}\delta_{2j} - \right. \\ \left. -\frac{1}{3}\frac{a}{R}\left(\delta_{1i}\delta_{6j} + \delta_{6i}\delta_{1j}\right) - \frac{1}{3}\frac{a}{R}\left(\delta_{2i}\delta_{6j} + \delta_{6i}\delta_{2j}\right) + \left(1 + \frac{9}{8}\frac{a^2}{R^2}\right)\delta_{6i}\delta_{6j} \right] \tag{41}$$

In the case of straight crack ($R \to \infty$, or $a/R \to 0$), from (41) it follows,

$$S_{ij}^{*(k)'} = \frac{2\pi a^2}{E}(\delta_{2i}\delta_{2j} + \delta_{6i}\delta_{6j}) \tag{42}$$

which is a very well known expression see Šumarac, Krajčinović [9]. Compliances (41) are in the local coordinate system. Using transformation rule,

$$S_{ij}^{*(k)} = S_{mn}^{*(k)'} g_{mi} g_{nj} \tag{43}$$

where transformation matrix g_{ij} is given by Horii and Nemat-Nasser [11], as

$$g_{ij} = \begin{bmatrix} \cos^2\theta & \sin^2\theta & \sin 2\theta \\ \sin^2\theta & \cos^2\theta & -\sin 2\theta \\ -\frac{1}{2}\sin 2\theta & \frac{1}{2}\sin 2\theta & \cos 2\theta \end{bmatrix} \tag{44}$$

Substituting (44) into (43) it is finally obtained

$$\begin{aligned} S_{ij}^{*(k)'} = \frac{2\pi a^2}{E}\Bigg[& \frac{a^2}{8R^2} g_{1i}g_{1j} - \frac{1}{4}\frac{a^2}{4R^2}\left(g_{1i}g_{2j} + g_{2i}g_{1j}\right) + \left(1 + \frac{a^2}{2R^2}\right) g_{2i}g_{2j} - \\ & - \frac{1}{3}\frac{a}{R}\left(g_{1i}g_{6j} + g_{6i}g_{1j}\right) - \frac{1}{3}\frac{a}{R}\left(g_{2i}g_{6j} + g_{6i}g_{2j}\right) + \left(1 + \frac{9}{8}\frac{a^2}{R^2}\right) g_{6i}g_{6j} \Bigg] \end{aligned} \tag{45}$$

It is very easy to calculate particular values of the compliance from the expression (45) which represents the contribution due to presence of one crack. In the case of many cracks, the total compliance would be, Krajčinović [12],

$$\overline{S}_{ij} = S_{ij}^0 + S_{ij}^* \tag{46}$$

where S_{ij} is the compliance of the undamaged material, and $S_{ij}{}^*$ stands for the increase of the compliance due to presence of all cracks,

$$S_{ij}^* = N \int_{R_{\min}}^{R_{\max}} \int_{\theta_{\min}}^{\theta_{\max}} S_{ij}^{*(k)}(R,\theta) p(R) p(\theta) dR d\theta \tag{47}$$

where N is the number of cracks per unit area (unit cell), see Horii, Nemat-Nasser, 1983 [11], and Šumarac, Krajčinović [13]. Taking for simplicity that the distribution of orientations of cracks is uniform, i.e. $\phi_{\min} = 0$ and $\phi_{\max} = \pi$, and extending the same for the crack (aggregate) radius R, it will be:

$$p(\theta) = \frac{1}{\pi}; \qquad p(R) = \frac{1}{R_{\max} - R_{\min}} \tag{48}$$

Introducing (45) and (48) into (47), and taking governing coefficients of matrix g_{ij} for $S_{11}{}^*$, after lengthy integration and algebra it is obtained

$$S_{11}^* = \frac{\omega}{E}\left(1 + \frac{a^2}{R_{\max}R_{\min}}\right) \tag{49}$$

where

$$\omega = N\pi a^2 \tag{50}$$

is the measure of the damage, see Krajčinović [11], Šumarac, Krajčinović [13]. For the straight crack, $(a^2/R_{\max}R_{\min}) \to 0$, it follows,

$$S_{11}^* = \frac{\omega}{E} \tag{51}$$

which is identical to the results obtained in the two above mentioned papers. From (46) and (49), taking for $S_{11} = 1/E$, it follows,

$$\frac{\bar{E}}{E} = \frac{1}{1 + N\pi a^2 (1 + a^2 / R_{\max}R_{\min})} \tag{52}$$

The expression (52) is derived using Taylor (dilute concentration) model (see Šumarac, Krajčinović [13]).

2.2. Damage of plain concrete due to thermal incompatibility of concrete components (TICC)

The phenomenon of thermal incompatibility of concrete components (TICC) is a very important issue in design and maintenance of concrete structures. This is a serious problem in climates with large temperature amplitude change (desert-like climate) and for concrete structures exposed to fire. The investigation is focused on the aggregate with the coefficient of thermal expansion (CTE) α_a smaller than CTE of the cement paste (α_c). The same procedure could be applied for any particular composite, where herein explained and accepted assumptions could be applied.

In order to determine the degradation of material, which is formed from components with different CTE, the basic problem, shown in Fig. 6, should be solved. The aggregate with the CTE α_a is embedded in the hardened cement paste with the CTE α_c. For simplicity, it will be assumed that Young's modules of two materials are equal, $E_a = E_c = E$. Only the case of the plane stress will be considered. Due to temperature increase $\theta = T - T_0$, the stress in both aggregate and cement paste would occur, because of the mismatch of the CTE, $\alpha_a < \alpha_c$. This phenomenon is referred to as TICC (Venecanin [14]). The way how to determine the stresses in the aggregate and cement paste can be found in papers: Šumarac [15], and Šumarac, Krasulja [16]. Within the aggregate the stresses are constant,

$$\sigma_{xx} = \sigma_{\theta\theta} = \frac{E(\alpha_c - \alpha_a)}{2}\theta \tag{53}$$

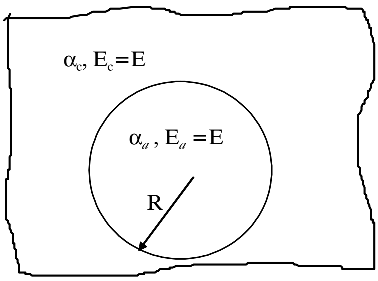

Figure 6. Aggregate as a thermal inclusion

The stresses in the cement paste are:

$$\sigma_{xx} = \frac{E(\alpha_c - \alpha_a)}{2}\theta\frac{R^2}{r^2}, \quad \sigma_{\theta\theta} = \frac{E(\alpha_c - \alpha_a)}{2}\theta\frac{R^2}{r^2} \quad (r \geq R) \tag{53a}$$

where r is the distance measured from the centre of the aggregate**.** Due to stresses given by (53) and (53a), cracks will occur, or already existing, will grow at the interface of aggregate and cement paste.

In this lecture, small circular crack (small in comparison with the radius of the aggregate) would be considered. This assumption leads to very simple analytical expressions, suitable for the closed form integration. A more accurate approach is presented in the paper written by Ju [17], considering arbitrary size of the crack. The solution in this case is numerical.

From the paper Cotterell and Rice [8], the stress intensity factors for a slightly curved crack due to stress σ_{rr} given by (53) are (see Šumarac [15], Šumarac, Krasulja [16]):

$$K_I = \frac{1}{\sqrt{\pi a}} \int_{-a}^{a} \sigma_{rr} \sqrt{\frac{a+t}{a-t}} dt = \sigma_{rr} \sqrt{\pi a}\ ; K_{II} = \frac{1}{\sqrt{\pi a}} \int_{-a}^{a} \frac{1}{2} \alpha \sigma_{rr} \sqrt{\frac{a+t}{a-t}} dt = \frac{1}{2} \alpha \sigma_{rr} \sqrt{\pi a} \tag{54}$$

Once the stress intensity factors are known, strain energy release rate by fracture mechanics is easily obtained from (54) as,

$$G = \frac{K_I^2 + K_{II}^2}{E} = \pi a \sigma_{rr} \left(1 + \frac{\alpha^2}{4} \right) = \pi a \sigma_{rr} \left(1 + \frac{a^2}{4R^2} \right) \tag{55}$$

The next step requires the experimentally obtained resistance or $\Re$ curve. The procedure for obtaining $\Re$ curve for softening materials, such as concrete, can be found in Foote et al. [18]. In the absence of exact $\Re$ curve for the interfacial circular crack, between the aggregate and the cement paste, it will be assumed that

$$\Re = R^2 C^2 \pi \frac{(a - a_0)^2 a}{R^2} \left(1 + \frac{a^2}{4R^2} \right) \tag{56}$$

where C is constant to be determined. The crack stability criterion of fracture mechanics is:

$$G = \Re \quad \text{and} \quad \frac{\partial G}{\partial R} \geq \frac{\partial \Re}{\partial a} \tag{57}$$

Substituting (55) and (56) into (57) it is obtained:

$$a = a_0 + \frac{\sigma_{rr}}{C} = a_0 + \frac{E(\alpha_c - \alpha_a)}{2} \theta \tag{58}$$

The expression (58) represents the crack size a as a function of temperature θ. Comparing the experimental and theoretical results, it is found that constant C (the dimension $\sqrt{\mathrm{MN}}/\mathrm{m}^2$) can be approximated as

$$C = 50 \frac{E(\alpha_c - \alpha_a)}{a_0} \tag{59}$$

Substituting (59) into (58) and the obtained result into (51), finally,

$$\frac{\bar{E}}{E} = \frac{1}{1 + 0.094(1 + 0.01\theta)^2 + 0.003016(1 + 0.01\theta)^4} \tag{60}$$

The following values are taken for calculating relation (60): $N = 7500$ cracks/m^2, $\alpha_c = 25.4 \times 10^{-6} (°\mathrm{C})^{-1}$, $\alpha_a = 11.9 \times 10^{-6} (°\mathrm{C})^{-1}$ (see Venecanin [14]), and $R_{min} = 0.4$ cm, $R_{max} = 3.1$ cm (obtained from the grading curves and aggregate mix). The initial, average length of crack is taken to be $a_0 = 0.2$ cm. The relation (60) is valid only for $\theta = T - T_0 > 0$, where $T_0 = 20°$C. For $T = 20°$C (referent temperature), the material is undamaged.

Experimental results are explained in the paper Šumarac, Krasulja [16], here only briefly presented. The experimental tests for this research comprise the thermal treatment of two series of specimens, produced of concrete with two different aggregates. The first group of specimens, marked CL, was made of concrete with crushed limestone aggregate, and in the second, marked as RA, river aggregate was used. Six specimens in each series were thermally treated, exposing them to the following temperatures: 20, 55, 90, 125, and 160°C. Thermal treatment commenced at 180 days concrete age and was performed in "Hereaus–Votsch" VUK 500 clima chamber. Procedure was completely identical for both groups-series of specimens. Prior to putting them into the chamber, specimens were allowed to air dry for several days.

Properties of concrete, measured by non-destructive methods on all specimens, every 24 hours are: resonant frequency (f) and mass measuring. The expression from which the dynamic modulus of elasticity is calculated reads,

$$E = 4\gamma f^2 l^2 \quad \text{(MPa)} \tag{61}$$

where γ is the density of concrete (kg/m^3), f is resonant frequency (Hz), and l the length of specimen (m). Resonant frequency data were obtained by CNS-electronics "ERUDITE" equipment. Results for dynamic modulus of elasticity, obtained from expression (61) and from measured data, are presented in Fig. 7. Usually, it was assumed that concrete with the river aggregate would be more resistant to temperature increase, and the concrete with limestone aggregate could have exhibited changes caused by the TICC effect. In Fig. 7, temperature exposure has a quite perceptible influence on both concretes. The decrease in dynamic modulus of elasticity was recorded for both concretes. From Fig. 7 one can notice that concrete made with river aggregate showed a slightly slower degradation rate. At the end of thermal treatment (160°C), the value of E decreased for concrete with RA for 25.4%, while for concrete with CL for 27.2%. Such drop of basic mechanical and deformational properties is somewhat surprising, since temperatures below 160°C are not considered high for concrete.

From comparison of theoretical results obtained by expression (60) and dimensionless values obtained from experimental results (61), it is evident that the agreement is good for the entire range of investigated temperatures (Fig. 7). The discrepancy between theoretical and experimental results is less than 3%.

Finally it is concluded that this study, theoretically and experimentally, confirms that moderate temperature change can cause substantial degradation of concrete properties.

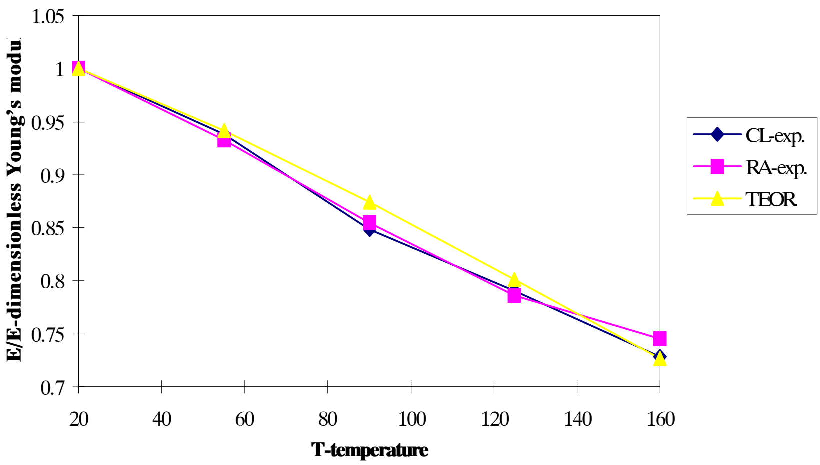

Figure 7. Comparison of theoretical and experimental results

2.3. Plane sheet weakened by elliptical void

Consider the problem of the elliptic cylinder ($a_3 \to \infty$) (Fig. 8.) embedded in the elastic isotropic material with the same elastic parameters E (Young's modulus) and ν (Poisson's ratio). Eshelby, in his 1957 paper [19], referred to "eigenstrains" as stress-free transformation strains. He proved that the uniform "eigenstrain" $\varepsilon_{ij}^{*'}$ within the elliptical inclusion, cause the uniform "eigenstresses" $\sigma_{ij}^{*'}$ in the same region (see also Mura [20]):

$$\sigma_{11}^{*'} = \frac{\mu}{1-\upsilon}\left\{-2+\frac{a_2^2+2a_1a_2}{(a_1+a_2)^2}+\frac{a_2}{a_1+a_2}\right\}\varepsilon_{11}^{*'}+\frac{\mu}{1-\upsilon}\left\{\frac{a_2^2}{(a_1+a_2)^2}-\frac{a_2}{a_1+a_2}\right\}\varepsilon_{22}^{*'}-$$
$$-\frac{2\mu\upsilon}{1-\upsilon}\frac{a_1}{a_1+a_2}\varepsilon_{33}^{*'}$$
$$\sigma_{22}^{*'} = \frac{\mu}{1-\upsilon}\left\{-2+\frac{a_1^2+2a_1a_2}{(a_1+a_2)^2}+\frac{a_1}{a_1+a_2}\right\}\varepsilon_{22}^{*'}+\frac{\mu}{1-\upsilon}\left\{\frac{a_1^2}{(a_1+a_2)^2}-\frac{a_1}{a_1+a_2}\right\}\varepsilon_{11}^{*'}- \tag{62}$$
$$-\frac{2\mu\upsilon}{1-\upsilon}\frac{a_2}{a_1+a_2}\varepsilon_{33}^{*'}$$
$$\sigma_{33}^{*'} = -\frac{2\mu\upsilon}{1-\upsilon}\frac{a_1}{a_1+a_2}\varepsilon_{11}^{*'}-\frac{2\mu\upsilon}{1-\upsilon}\frac{a_2}{a_1+a_2}\varepsilon_{22}^{*'}-\frac{2\mu}{1-\upsilon}\varepsilon_{33}^{*'}$$
$$\sigma_{12}^{*'} = -\frac{2\mu}{1-\upsilon}\frac{a_1a_2}{(a_1+a_2)^2}\varepsilon_{12}^{*'},\quad \sigma_{23}^{*'} = -2\mu\frac{a_2}{a_1+a_2}\varepsilon_{23}^{*'},\quad \sigma_{31}^{*'} = -2\mu\frac{a_2}{a_1+a_2}\varepsilon_{31}^{*'}$$

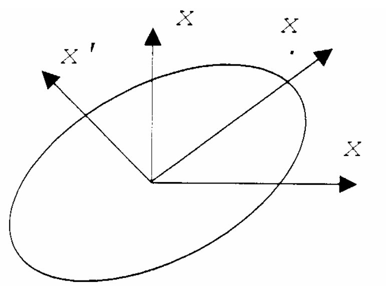

Figure 8. Global and local (primed) coordinate system of an elliptical void (inclusion)

In the above expressions, $a_1 = a$ and $a_2 = \alpha a$ are half-axes of the elliptical region, while μ and ν are the shear modulus and Poison's ratio, respectively. According to equivalent inclusion method (Mura [20]), the total stress within the elliptical region under far field stresses σ_{ij}', and one that is caused by the "eigenstrain" given by expressions (62) should be zero everywhere in the elliptical region, if the region should represent the void:

$$\sigma_{11}' + \sigma_{11}^{*'} = 0,\qquad \sigma_{22}' + \sigma_{22}^{*'} = 0,\qquad \sigma_{12}' + \sigma_{12}^{*'} = 0 \tag{63}$$

Expression (63) is written for plane stress condition. Substituting governing values from expression (62) into (63), leads to the system of equations with respect to unknown "eigenstrains" $\varepsilon_{11}^{*'}$, $\varepsilon_{22}^{*'}$ and $\varepsilon_{12}^{*'}$. The solution of the system of equations is:

$$\varepsilon_{11}^{*'} = \frac{1-\upsilon}{2\mu}\left[(1+2\alpha)\sigma_{11}' - \sigma_{22}'\right],\ \varepsilon_{22}^{*'} = \frac{1-\upsilon}{2\mu}\left[\frac{2+\alpha}{a}\sigma_{22}' - \sigma_{11}'\right],\ \varepsilon_{12}^{*'} = \frac{1-\upsilon}{2\mu}\frac{(1+\alpha)^2}{\alpha}\sigma_{12}' \tag{64}$$

Once the $\varepsilon_{ij}^{*'}$ are known, the increase of the strain energy of the body, due to presence of elliptical void is obtained as:

$$\Delta W = -\frac{1}{2}V\sigma_{ij}'\varepsilon_{ij}^{*'} = -\frac{1}{2}\pi a_1 a_2 \sigma_{ij}'\varepsilon_{ij}^{*'} \tag{65}$$

Substituting (64) into (65) yields to:

$$\Delta W = \frac{\pi\alpha a^2}{2E}\left[(1+2\alpha)(\sigma'_{11})^2 - 2\sigma'_{11}\sigma'_{22} + \frac{(2+\alpha)}{\alpha}(\sigma'_{22})^2 + \frac{2(1+\alpha)^2}{\alpha}(\sigma'_{12})^2\right] \tag{66}$$

Differentiating (66) twice with respect to stresses, yields to the compliances:

$$S'^{(k)*}_{ij} = \frac{\partial^2 W}{\partial\sigma'_i \partial\sigma'_j} \tag{67}$$

where Voigt notation, $\sigma'_1 = \sigma'_{11}$, $\sigma'_2 = \sigma'_{22}$ and $\sigma'_6 = \sigma'_{12}$ is used. Also in expression (67), (k) refers to a single elliptical void and (*) stands for the increase of the governing value of the compliance, due to presence of the void. Once the compliances $S'^{(k)*}_{ij}$, in the local coordinate system are determined, by using the transformation rule (Horii, Nemat-Nasser [11]), the compliances in the global coordinate system $S_{ij}^{(k)*}$, can be determined.

2.4. Mean field theory (uniform distribution of voids)

In the case of many voids, the total compliance would be (Horii, Nemat-Nasser [11]; Šumarac, Krajčinović [9]):

$$\overline{S}_{ij} = S_{ij} + \widehat{S}^*_{ij} \tag{68}$$

In the above expression (*) refers to the increase of the value due to presence of voids, and S_{ij} is the compliance matrix of the undamaged (virgin) material.

In the case of Taylor model, system of Eqs. (68) leads to:

$$\frac{\overline{E}^{tm}}{E} = \frac{1}{1+\omega(\alpha^2+\alpha+1)}, \quad \frac{\overline{\nu}^{tm}}{\nu} = \frac{1+\dfrac{\omega\alpha}{\nu}}{1+\omega(\alpha^2+\alpha+1)} \tag{69}$$

In the case of self-consistent model, equations (68) are:

$$\frac{1}{\overline{\overline{E}}} = \frac{1}{E} + \frac{\omega}{\overline{\overline{E}}}(\alpha^2+\alpha+1), \qquad -\frac{\overline{\nu}}{\overline{\overline{E}}} = -\frac{\nu}{E} - \frac{\omega}{\overline{\overline{E}}}\alpha \tag{70}$$

Their solution is:

$$\frac{\overline{E}^{sc}}{E} = 1-\omega(\alpha^2+\alpha+1), \quad \frac{\overline{\nu}^{sc}}{\nu} = 1-\omega(\alpha^2+\alpha+1) + \frac{\omega\alpha}{\nu} \tag{71}$$

The total overall compliance for matrix in the case of self-consistent approximation for uniform distribution of elliptical voids is:

$$\frac{\overline{S}^{sc}_{ij}}{S_{ij}} = \begin{bmatrix} \dfrac{1}{1-\omega A} & -1-\dfrac{\omega\alpha}{\nu(1-\omega A)} & 0 \\ -1-\dfrac{\omega\alpha}{\nu(1-\omega A)} & \dfrac{1}{1-\omega A} & 0 \\ 0 & 0 & \dfrac{1+\nu-\omega\nu A+\omega\alpha}{(1+\nu)(1-\omega A)} \end{bmatrix} \tag{72}$$

3. DAMAGE AND REPAIR OF THE PIVNICA BRIDGE

Damage of the Pivnica bridge, stretching across the river Ibar on the railroad route Belgrade–Thessaloniki, has been considered with the models in this paper. The bridge was destroyed by NATO, during the bombing campaign in Yugoslavia, in 1999. Rebuilding of the bridge was performed using one temporary support at the place of most severe damage. The two new spans were built in factory, and other damage was repaired on site. The static and dynamic characteristics of rebuilt structure are analysed, based on damage mechanics and theory of structures. It is shown that for more amount of damage, the structure of the bridge becomes more compliant, or in another words, the period of free vibration is slightly increased. The problem of material fatigue, especially in parts which have undergone low cycle fatigue is shortly outlined.

Figure 9. The destroyed Pivnica bridge

The Pivnica bridge was hit two times. The first bombshell hit the middle part of bridge, but the bridge did not collapse. The second projectile hit the diagonal above support, and then the bridge fell into the river (Fig. 9). Due to impact, the bottom members were plastically deformed. Additionally, there was a lot of damage due to bomb shrapnel. Holes in the members can be approximated as ellipses. In the first section, it has been explained in detail, how the decrease of Young's modulus can be expressed in terms of damage, see Eqs. (69) and (71).

It should be noted that for reconstructing the bridge, 75 tons of steel was spent. The total weight of the bridge (Fig. 9) is 440 tons. In Fig. 10, the static scheme for finite element method (FEM) is shown.

3.1. Dynamic characteristics of the reconstructed bridge

All static and dynamic characteristics are analysed using FEM procedure. First step was to find free vibrations for first three modes. They are: T_1 = 0.731 s, T_2 = 0.2491 s, T_3 = 0.1212 s. For the damaged bridge it is calculated $\omega = 0.1$, $\omega = 0.2$ and $\omega = 0.3$ for the two spans of bottom members, and four spans of top members. For instance, in case of $\omega = 0.3$, $T_2(\omega = 30\%) = 0.2551$ s. This result is expected. The structure is damaged, when period of vibrations is larger.

3.2. Problem of fatigue

It is well known that railway bridges are designed against the high cycle fatigue. During the bombardment some elements were destroyed, neighbouring parts suffered low cycle fatigue. It was not possible to change all elements. It is important to check the behaviour of elements, which suffered low cycle fatigue, but are still a part of the structure. This is especially important during winter, when temperatures are well below zero.

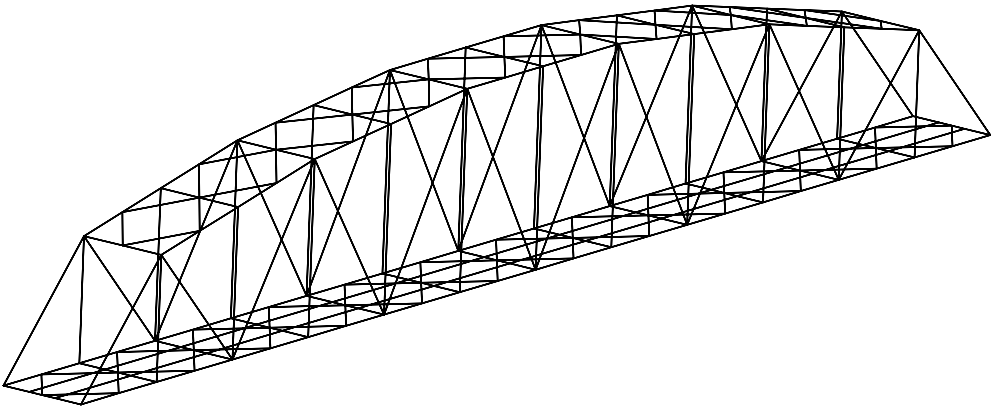

Figure 10. Reconstructed Pivnica bridge–static scheme

Figure 11. The reconstructed Pivnica bridge

4. CONCLUSIONS

Damage mechanics, as a new branch of mechanics, already found its place in some codes for design and maintenance of engineering structures. The airplane industry, which was the first to incorporate damage parameters in design, where damage tolerance is the issue which is now well established among researchers and engineers. It spread its importance from airplane industry to other areas of engineering, such as mechanical, civil, mining, etc. It was developed by using some elements of the Theory of Plasticity and Fracture Mechanics, and has its own principles and assumptions, but in many cases it should be combined with the two already mentioned theories, as shown in this paper.

Problems, such are localization in quasi-brittle materials, fatigue of metals, and failure of composites, are some of those that cannot be solved successfully without the application of Damage Mechanics. With further developments of basic principles and, particularly, with the development of computational Damage Mechanics, it continues to spread its importance.

ACKNOWLEDGMENTS

The authors gratefully acknowledge the financial support provided by SFS to the Department of Civil Engineering, University of Belgrade, through the grant SGR.4.05. 0278.5, which has made this work possible.

REFERENCES

1. Kachanov, L. M., *Time of the Rupture Process under Creep Conditions*, T.V.Z. Akad. Nauk., SSR, Otd. Tech. Nauk, 9, 26-31. (1958)
2. Krajčinović, D., Lubarda, A.V., Šumarac, D., *Fundamental Aspects of Brittle Cooperative Phenomena-Effective Continua Models*, Mechanics of Materials, 15, 99-115. (1993)
3. Rice, J.R., *Thermodynamics of the quasi-static growth of Griffith cracks*, Journal Mech. Phys. and Solids, 26, pp. 61–78. (1978)
4. Shapery, R.A., *A theory of mechanical behaviour of elastic media with growing damage and other changes in structures*, J. Mech. Phys. Solids, 38, 215-253. (1990)
5. Janson, J., Hult, J., *Fracture mechanics and damage mechanics a combined approach*, J. mechanique appliquee, vol.1, 1, pp. 69-84. (1977)
6. Hill, R., *Aspects of invariance in solids mechanics*, Advances in Applied Mechanics, C.S. Yih, ed., Vol. 18, Academic Press, N.Y., pp. 1-75. (1978)
7. Chow, C.L., Chen, X.F., *An isotropic model of damage mechanics based on edochronic theory of plasticity*, Int. J. Fract. 55, pp. 115-130. (1992)
8. Cotterell, B., Rice, J.R., *Slightly Curved or Kinked Cracks*, Int. J. Fract., 16: 155-169. (1980)
9. Šumarac, D., Krajčinović, D., *A Mesomechanical Model for Brittle Deformation Processes: Part II*, J. Appl. Mech., 56, pp. 57-62. (1989)
10. Krajčinović, D., Šumarac, D., *A Mesomechanical Model for Brittle Deformation Processes: Part I*, J. Appl. Mech., 56, pp. 51-56. (1989)
11. Horii, H., Nemat-Nasser, S., *Overall Moduli of Solids with Micro-Cracks: Load Induced Anisotropy*, J. Mech. Phys. Solids, 31, pp. 155-171. (1983)
12. Krajčinović, D., *Damage Mechanics*, Mech. Mater., 8, pp. 117-197. (1989)
13. Šumarac, D., Krajčinović, D., *A Self-consistent Model for Microcracks Weakened Solids*, Mech. Mater., 6, pp. 39-52. (1987)
14. Venecanin, S., *Thermal Incompatibility of Concrete Components and Thermal Properties of Carbonate Rocks*, ACI Mater. J., 87, pp. 602-607. (1990)
15. Šumarac, D., *Damage of the Particulate Composite due to Thermal Internal Stresses*, ECF11, Mechanisms and Mech. of Damage and Failure, Vol.III, Ed. J. Petit, ESIS, pp. 1913-1918. (1996)
16. Šumarac, D., Krasulja, M., *Damage of Plain Concrete due to Thermal Incompatibility of its Phases*, Int. J. Damage Mech. (1997)
17. Ju, J.W., *A Micromechanical Damage Model for Uniaxially Reinforced Composites Weakened by Interfacial Arc Microcracks*, J. Appl. Mech., 58, pp. 923-930. (1991)
18. Foote, M.L.R., Mai, W.Y., Cotterell, B., *Crack Growth Resistance Curves in Strain-Softening Materials*, J. Mech. Phys. Solids, 34, pp. 593-607. (1986)
19. Eshelby, J.D., *The determination of the elastic field of an ellipsoidal inclusion and related problems*, Proc. Roy. Soc., A241, pp. 376-396. (1957)
20. Mura, T., *Micromechanics of defects in solids*, Martinus Nijhoff Publishers. (1987)

BASIC FATIGUE CONCEPTIONS AND NEW APPROACHES TO FATIGUE FAILURE

Donka G. Angelova, University of Chemical Technology & Metallurgy, Sofia, Bulgaria

In memoriam to Dr Bryan Burns

INTRODUCTION

Although in the very beginning of 1900s Ewing and Humfrey described the fatigue behaviour of metals, revealing the appearance of slip bands and microscopic defects, which grew slowly, there was not any mathematical concept about fatigue development and failure. Even when Inglis and Griffith presented analytical models of fracture in brittle solids, each in his own way, using stress (Inglis [1]) and energy (Griffith [2]) approaches, their mathematical tools didn't offer a direct transition to the fatigue failure of metallic materials. Almost three decades later a big success came through the Irvin analyses [3], introducing now the well-known stress intensity factor, K. In the early 1960s, Paris, Gomez and Anderson [4] suggested the specific presentation "fatigue crack growth rate da/dN against stress intensity factor range ΔK" for constant amplitude fatigue loading. In the beginning of the 1970s, Elber [5] showed the phenomenon of crack closure under cyclic tensile loads and, in the middle of the same decade, Pearson [6] emphasized the significant role of crack size, defined later as "short crack problem". Then in the 1980s, two basic short crack models appeared, known as the Brown-Hobson model [7, 8] and the Navarro-de los Rios model [9]. The first one described fatigue crack growth rate through decreasing crack growth falls at fatigue thresholds, clearly defined by Miller [10]. The second model presented crack growth rate through decreasing crack growth fluctuations, occurring continuously up to complete failure. Some modifications of these models were introduced during the 1990s, as that for corrosion fatigue, Akid-Murtaza [11,12], later revised by Angelova-Akid in an attempt to describe physically small crack growth, separately from short crack growth, by a new equation [13], and improved for the cases of crack coalescence by Brown, Gao and Miller [14, 15]. Fatigue from defects, and especially inclusions, is another field showing a different face of failure development through so-called optically-dark-area growth and offering the Marukami-Endo's method (1980-2002) of the square-area-parameter fatigue model [16]. But although major advances have been made in all these areas, the application of fatigue concepts to different practical situations is highly individual and often involves empirical and semi-empirical approaches, including a great number of specifying constants.

An alternative approach to the successive forms of the Brown-Hobson model is proposed by Angelova-Akid [17]. This approach adopts normalized parameters describing corrosion fatigue behaviour of metals in non-dimensional terms, applied to some fatigue characteristics as pit and crack size, crack growth rate and cycles. A further development of the alternative approach of normalized parameters reveals a specific tendency of metal fatigue behaviour, expressed analytically as a relation between the crack growth rate and a non-dimensional characterizing function and graphically, as an almost straight line. The non-dimensional characterizing function is firstly mentioned by Angelova [18], where the linear presentation of fatigue is called "natural fatigue tendency". But, there the function is involved only by its final form and without any details either, about its mathematical obtaining, or its physical sense. The present lecture involves detailed mathematical, parametrical and dimensional analyses on these elements. Thus, it reveals the energy nature of the proposed new function, which turns it into *energy normalized fatigue function*. Also it suggests a more precise further development of the idea of the *natural fatigue tendency or ability of metals and alloys* widening the range of its applications to different steels and non-ferrous alloys as well as to a bigger variety of different testing conditions.

1. MATERIALS AND FATIGUE TEST RESULTS

Materials selected for the present study are divided into three groups.

A-Group

- Low-carbon roller-quenched tempered steel, RQT501 [17];
- Medium carbon steel [7, 8] and high-strength spring steel, existing results [11, 12];
- AISI 4140 steel, existing results [19];
- Martensitic 2.1/4Cr-1Mo Steel (commercial designation AISI A542 Class 2), existing results [20];
- CMV Steel, existing results [21].

B-Group

- N18 Ni based superalloy, existing results [22].

C-Group

- Al7010-T7451 alloy, existing results [23];
- Ti-48Al-2Mn-2Nb alloy, existing results [24].

The results from all fatigue tests described in the above mentioned papers are shown as it has been originally done by their authors in form of two kinds of multitudes, *L* and *M*, located at the right hand-side in Figs. 1–9. In these figures the original graphic presentation of *L* and *M* is of the kind:

(i) crack growth rate, *da/dN* vs. crack length, *a*, or in log-log terms log*da/dN* vs. log*a*;

(ii) crack growth rate, *da/dN* vs. stress intensity factor range, ΔK, or log*da/dN* vs. logΔK.

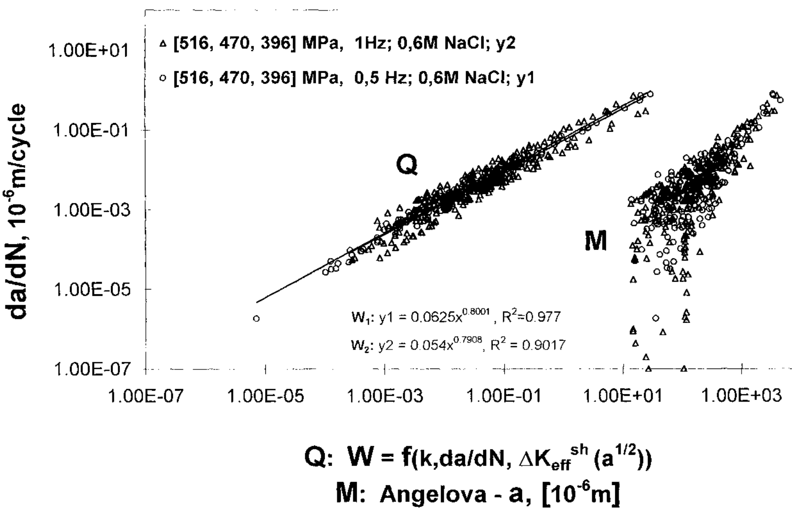

Figure 1. Short fatigue cracks in RQT501 steel under tension-tension loading at $R = 0.1$ (Angelova and Akid, 1999) [17]

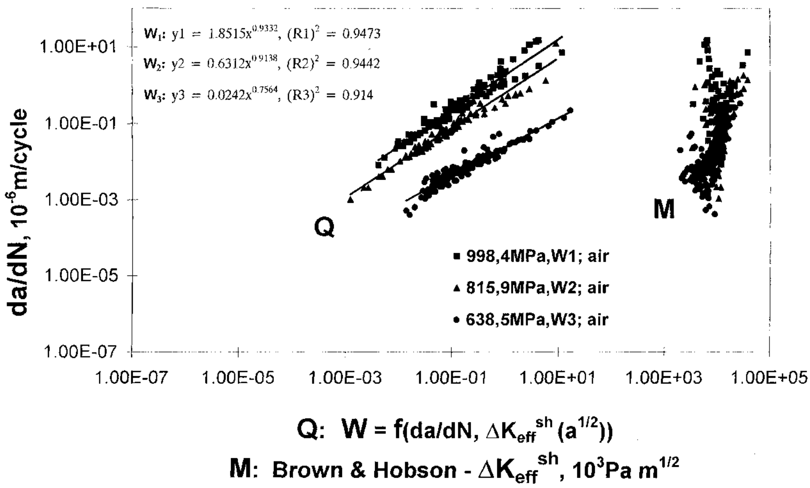

Figure 2. Short fatigue cracks in medium carbon steel under push-pull at R = –1 (Brown and Hobson, 1986) [7]

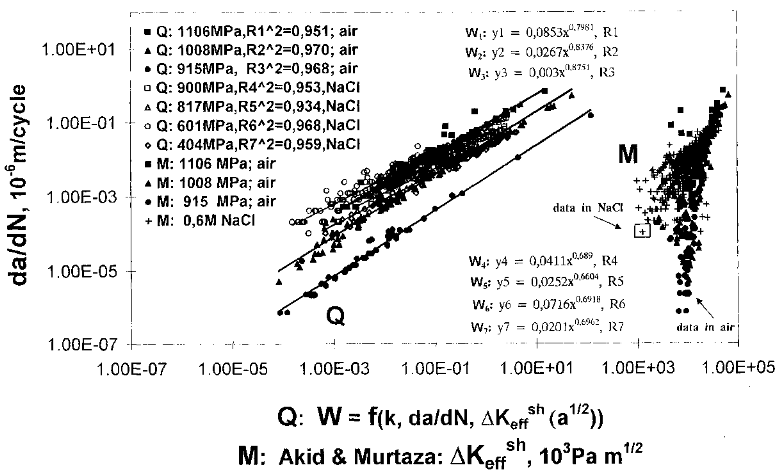

Figure 3. Short fatigue crack in high-strength spring steel under fully reversed torsion (Akid and Murtaza) [11]

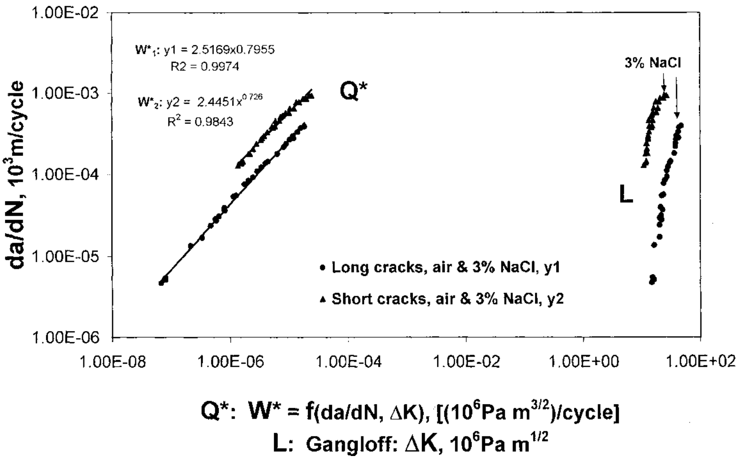

Figure 4. Sort and long fatigue cracks in 4140 steel subjected to air & 3% NaCl (Gangloff, 1981) [19]

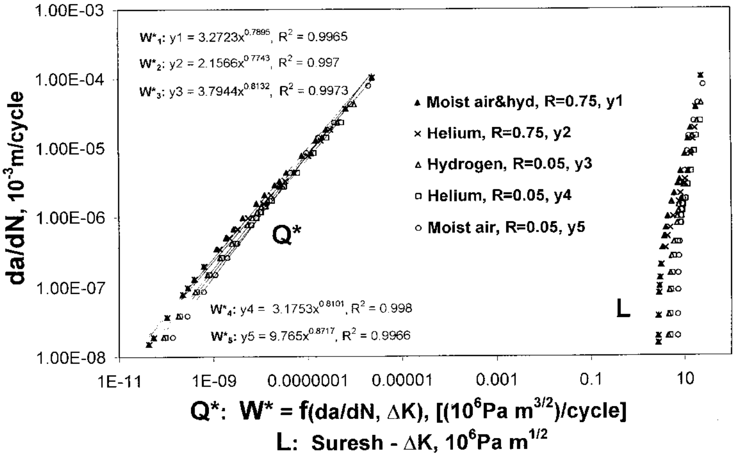

Figure 5. Fatigue in 2.1/4Cr-1Mo steel (AISI A542 Class 2) (Suresh, Zamiski &Ritchie, 1981) [20]

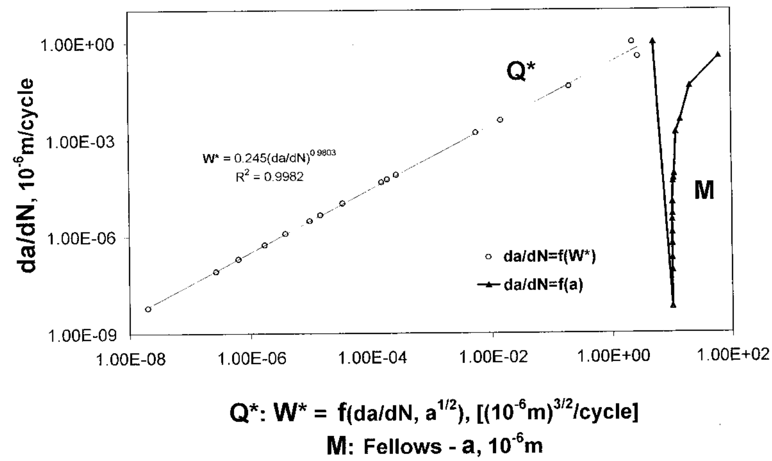

Figure 6. Fretting fatigue in CMV steel (Fellows, Nowell, Hills, 1997) [21]

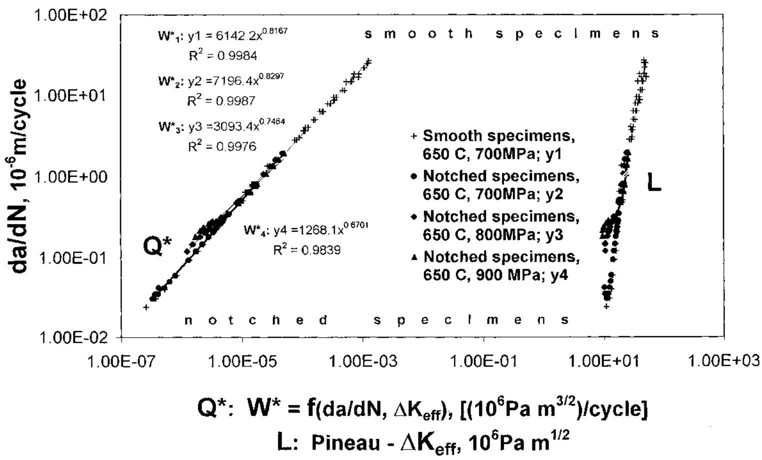

Figure 7. Short fatigue cracks in N 18 Ni based superalloy (Pineau, Sansoz, Brethes, 1998) [22]

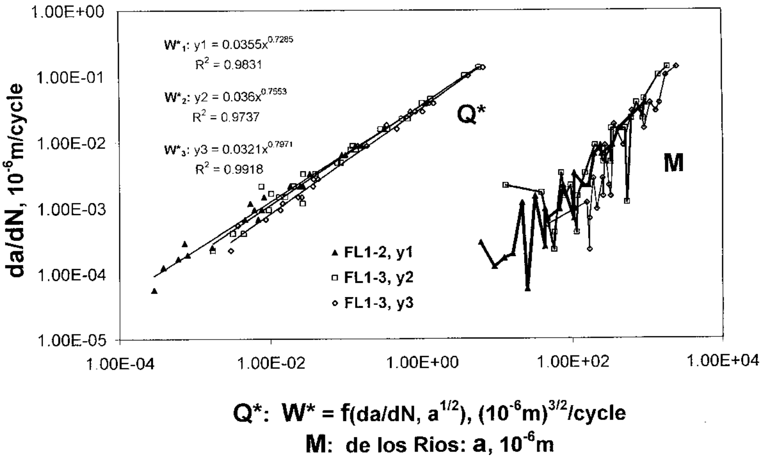

Figure 8. Fatigue in Al7010-T7451 alloy under random loading (Rios and Wei, 1998) [23]

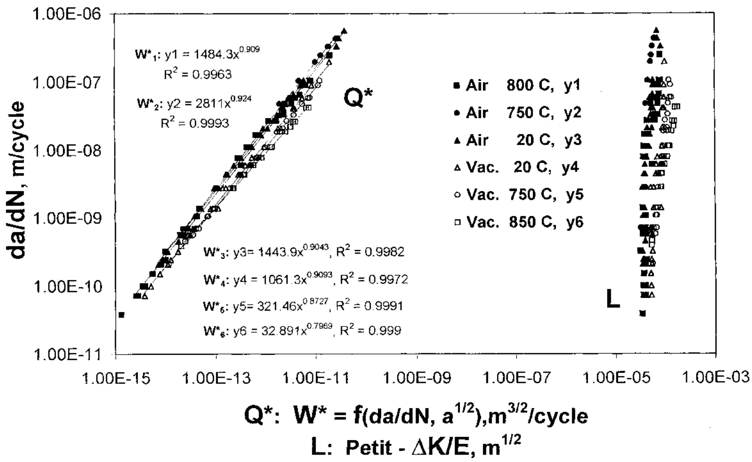

Figure 9. Fatigue in Ti-48Al-2Mn-2Nb alloy (Petit, Tonneau, Henaff, Mabru, 1988) [24]

2. AN ALTERNATIVE APPROACH FOR DESCRIBING METAL FATIGUE BEHAVIOUR. Analysis and discussion

Now we will present a completely new approach to fatigue phenomenon. This is an alternative approach, which can show immediately and in a simple way the very important comparison between the fatigue characteristics of different materials in terms of short and/or long fatigue cracks, and can allow using a wider range of different-sized and different-shaped specimens. This approach introduces a new graphic presentation that plots crack growth rate log*da/dN* against normalized fatigue function log $\Delta W_{(a/N)}$; the new presentation uses normalized parameters as follow:

- normalized defect growth rate, $(da/dN)/(a_f/N_f)$;
- normalized stress range, $\Delta\sigma/\Delta\sigma_{FL}$;
- normalized characterizing fatigue function, $\Delta W_{(a/N)} = k\dfrac{da}{dN}\Delta K$.

Firstly, we will remember that the original presentation of crack growth rate, *da/dN*, uses the intervals Δa and ΔN, $\Delta a/\Delta N \underset{\Delta\to 0}{\to} da/dN$, and an eventual transition from ordinary to normalized parameters may be expressed as:

$$\frac{\Delta a}{\Delta N}\frac{\Delta N_{f0}}{\Delta a_{f0}} \to \frac{\Delta a}{\Delta N}\frac{N_f}{a_f} \tag{1}$$

where a_f and N_f are the final length of the major crack and the number of cycles to failure, respectively.

Secondly, we will analyze the normalized characterizing fatigue function $\Delta W_{(a/N)}$, $\Delta W_{(a/N)} = k\frac{da}{dN}\Delta K$. As a first step to its mathematical obtaining in the form $k\frac{da}{dN}\Delta K$, we will reveal the well established stress influence on fatigue crack growth introducing a function that includes as a multiplication, both the normalized crack growth rate from (1), and the normalized stress range $\Delta\sigma/\Delta\sigma_{FL}$:

$$\frac{\Delta a}{\Delta N}\frac{\Delta N_{f0}}{\Delta a_{f0}}\frac{\Delta\sigma}{\Delta\sigma_{FL}} \to \frac{\Delta a}{\Delta N}\frac{N_f}{a_f}\frac{\Delta\sigma}{\Delta\sigma_{FL}} \tag{2}$$

where $\Delta\sigma_{FL}$ is the stress range at the fatigue limit in air for a given material. Then we can represent the multiplication (2) as follows

$$\frac{\Delta a}{\Delta N}\frac{N_f}{a_f}\frac{\Delta\sigma}{\Delta\sigma_{FL}} = \frac{\Delta a}{\Delta N}\frac{N_f}{\sqrt{a_f}}\frac{\Delta\sigma}{\Delta\sigma_{FL}\sqrt{a_f}} = \frac{\Delta a}{\Delta N}\frac{N_f}{\sqrt{a_f}}\frac{F\Delta\sigma\sqrt{\pi}}{F\Delta\sigma_{FL}\sqrt{\pi a_f}} = \frac{\Delta a}{\Delta N}\frac{N_f}{\sqrt{a_f}}\frac{k_1\Delta\sigma}{\Delta K_{FL}} \tag{3}$$

where $k_1 = F\sqrt{\pi}$ is a constant, F is the known finite size correction factor, and $\Delta K_{FL} = F\Delta\sigma_{FL}\sqrt{\pi a_f} = const$ is the maximum value of the stress intensity factor range at the fatigue limit for $a \equiv a_f$. Then, if we multiply (3) by the square root of the normalized crack length $\sqrt{a/a_f}$ to produce another stress intensity factor range, $\Delta K = F\Delta\sigma\sqrt{\pi a}$, the expression (3) turns into

$$\begin{aligned}\frac{\Delta a}{\Delta N}\frac{N_f}{a_f}\frac{\Delta\sigma}{\Delta\sigma_{FL}}\sqrt{\frac{a}{a_f}} &= \frac{\Delta a}{\Delta N}\frac{N_f}{\sqrt{a_f}}\frac{k_1\Delta\sigma}{\Delta K_{FL}}\frac{\sqrt{a}}{\sqrt{a_f}} = \frac{\Delta a}{\Delta N}\frac{N_f}{\sqrt{a_f}}\frac{\Delta K}{\Delta K_{FL}\sqrt{a_f}} = \\ &= \frac{\Delta a}{\Delta N}\frac{N_f}{a_f}\frac{\Delta K}{\Delta K_{FL}} = \frac{\Delta a}{\Delta N}k\Delta K \underset{\Delta\to 0}{\to} \frac{da}{dN}k\Delta K = k\frac{da}{dN}\Delta K\end{aligned} \tag{4}$$

where $k\frac{da}{dN}\Delta K$ is the final form of the normalized characterizing fatigue function $\Delta W_{(a/N)} = k\frac{da}{dN}\Delta K$, and $k = \frac{N_f}{a_f}\frac{1}{\Delta K_{FL}}$ $\left(\frac{\text{cycle}}{\text{m}^{3/2}\text{Pa}}\right)$ is a normalizing constant in general sense, whose parameters can be flexible in terms of their replacing by other parameters, more convenient for other cases. For example, in the case of constant-amplitude fatigue we can also use $k_{K_{\max}} = \frac{N_f}{a_f}\frac{1}{K_{\max}(a_f)}$.

On the other hand, the expression (2) may be discussed in another way

$$\frac{\Delta a}{\Delta N}\frac{N_f}{a_f}\frac{\Delta\sigma}{\Delta\sigma_{FL}}=\left(\frac{\Delta a}{\Delta N}\frac{\Delta\sigma}{a_f}\right)\frac{N_f}{\Delta\sigma_{FL}}=k_2\left(\frac{\Delta a}{\Delta N}\frac{\Delta\sigma}{a_f}\right),\ \text{or}$$

$$\frac{\Delta a}{\Delta N}\frac{N_f}{a_f}\frac{\Delta\sigma}{\Delta\sigma_{FL}}=\frac{\Delta a}{\Delta t\nu}\frac{t_f\nu}{a_f}\frac{\Delta\sigma}{\Delta\sigma_{FL}}=\frac{k_2}{\nu}\left(\frac{\Delta a}{\Delta t}\frac{\Delta\sigma}{a_f}\right)=k_3\left(\frac{\Delta a}{\Delta t}\frac{\Delta\sigma}{a_f}\right)$$

$$k_2=\frac{N_f}{\Delta\sigma_{FL}}\ \left(\frac{\text{cycle}}{\text{Pa}}\right);\quad k_3=\frac{t_f}{\Delta\sigma_{FL}}\ \left(\frac{\text{s}}{\text{Pa}}\right) \tag{5}$$

where $t\nu$ substitutes N. The physical sense of both kinds of expressions located in brackets of (5) can be evaluated clearer after some transformations:

$$\frac{\Delta a}{\Delta N}\frac{\Delta\sigma}{a_f}\left(\frac{\text{m}}{\text{cycle}}\frac{\text{Pa}}{\text{m}}\right)=\frac{\Delta a}{\Delta N}\frac{\Delta\sigma}{a_f}\left[\frac{1}{\text{cycle}}\frac{1}{\text{m}}\left(\text{m}\frac{\text{J}}{\text{m}^3}\right)\right]\xrightarrow[\text{Appendix}]{(4\text{A})}\frac{1}{\Delta N}\frac{\Delta W_{E_{th}}}{V_f}\left(\frac{\text{J}}{\text{m}^3\,\text{cycle}}\right)$$

$$\text{and}\quad \frac{\Delta a}{\Delta t}\frac{\Delta\sigma}{a_f}\left(\frac{\text{m}}{\text{s}}\frac{\text{Pa}}{\text{m}}\right)=\frac{\Delta a}{\Delta t}\frac{\Delta\sigma}{a_f}\left[\frac{1}{\text{s}}\frac{1}{\text{m}}\left(\text{m}\frac{\text{J}}{\text{m}^3}\right)\right]\xrightarrow[\text{Appendix}]{(4\text{A})}\frac{1}{\Delta t}\frac{\Delta W_{E_{th}}}{V_f}\left(\frac{\text{J}}{\text{m}^3\text{s}}\right) \tag{6}$$

It makes obvious now that the expressions (6) represent an energy change or portion, namely, the potential energy decrease of ΔW_{Eth}, necessary for crack growth of Δa [m], per *cycle* or *second* and per *unit volume of energy exchange* around the growing crack a, as it is shown dimensionally in (6), and parametrically in Griffith-theory sense through (1A)–(4A) in Appendix.

Thus, equations (5) can be rewritten as:

$$\frac{\Delta a}{\Delta N}\frac{N_f}{a_f}\frac{\Delta\sigma}{\Delta\sigma_{FL}}=k_2\left(\frac{\Delta a}{\Delta N}\frac{\Delta\sigma}{a_f}\right)\xrightarrow[(6)]{}k_2\left(\frac{1}{\Delta N}\frac{\Delta W_{E_{th}}}{V_f}\right)$$

$$\frac{\Delta a}{\Delta N}\frac{N_f}{a_f}\frac{\Delta\sigma}{\Delta\sigma_{FL}}=k_3\left(\frac{\Delta a}{\Delta t}\frac{\Delta\sigma}{a_f}\right)\xrightarrow[(6)]{}k_3\left(\frac{1}{\Delta t}\frac{\Delta W_{E_{th}}}{V_f}\right) \tag{7}$$

Considering (4) as a multiplication of (2) (through its form (3)) and the square root of normalized crack length, $\sqrt{(a/a_f)}$, we have to multiply (5), or its final form (7), by $\sqrt{(a/a_f)}$, which will give us the same result as that obtained in (4) under the condition $\Delta \rightarrow 0$:

$$\frac{da}{dN}\frac{N_f}{a_f}\frac{\Delta\sigma}{\Delta\sigma_{FL}}\frac{\sqrt{a}}{\sqrt{a_f}}\xleftarrow[\Delta\leftarrow 0]{}\frac{\Delta a}{\Delta N}\frac{N_f}{a_f}\frac{\Delta\sigma}{\Delta\sigma_{FL}}\frac{\sqrt{a}}{\sqrt{a_f}}\ ,$$

$$\frac{\Delta a}{\Delta N}\frac{N_f}{a_f}\frac{\Delta\sigma}{\Delta\sigma_{FL}}\frac{\sqrt{a}}{\sqrt{a_f}}=\left(\frac{\Delta a}{\Delta t}\frac{\Delta\sigma}{a_f}\right)\frac{t_f}{\Delta\sigma_{FL}}\frac{\sqrt{a}}{\sqrt{a_f}}=\left(\frac{\Delta a}{\Delta t}\frac{\Delta\sigma}{a_f}\right)\frac{t_f}{\Delta K_{FL}}\frac{F\sqrt{\pi}}{1}\left(\sqrt{a}\right)\frac{\sigma_{\max}}{\sigma_{\max}}=$$

$$=\left(\frac{\Delta a}{\Delta t}\frac{\Delta\sigma}{a_f}\right)\frac{t_f}{\Delta K_{FL}}\left(\frac{K_{\max}}{\sigma_{\max}}\right)\xrightarrow[\substack{(10\text{A})\\ \text{Appendix}}]{a\rightarrow a_f}\left(\frac{\Delta a}{\Delta t}\frac{\Delta\sigma}{a_f}\right)\frac{t_f}{\Delta K_{FL}}\left(\frac{K_c}{\sigma_{\max}}\right)\underset{\substack{(8\text{A}-9\text{A})\\ \text{Appendix}}}{=} \tag{8}$$

$$\underset{\substack{(8\text{A}-9\text{A})\\ \text{Appendix}}}{=}\left(\frac{\Delta a}{\Delta t}\frac{\Delta\sigma}{a_f}\right)\frac{t_f}{\Delta K_{FL}}\left(\frac{\sqrt{\text{G}_\text{c}E'}}{\sigma_{\max}}\right)\underset{\substack{(6\text{A}-7\text{A})\\ \text{Appendix}}}{=}\left(\frac{\Delta a}{\Delta t}\frac{\Delta\sigma}{a_f}\right)\frac{t_f}{\sigma_{\max}}\frac{\sqrt{2\gamma_s E'}}{\Delta K_{FL}}$$

$$\left\{\left(\frac{\Delta a}{\Delta t}\frac{\Delta\sigma}{a_f}\right)\frac{t_f}{\sigma_{\max}}\right\}\frac{1}{\Delta K_{FL}}\sqrt{2\gamma_s E'}\ \left[\left\{\left(\frac{\mathrm{J}}{\mathrm{sm}^3}\right)\frac{\mathrm{s}}{\mathrm{Pa}}\right\}\frac{1}{\mathrm{Pa}\sqrt{\mathrm{m}}}\sqrt{\frac{\mathrm{JPa}}{\mathrm{m}^2}}\right]=$$

$$=\left\{\left(\frac{\Delta a}{\Delta t}\frac{\Delta\sigma}{a_f}\right)\frac{t_f}{\sigma_{\max}}\right\}\frac{1}{\Delta K_{FL}}\sqrt{2\gamma_s E'}\ \left[\left\{\left(\frac{\mathrm{J}}{\mathrm{sm}^3}\right)\frac{\mathrm{sm}^2\mathrm{m}}{\mathrm{Nm}}\right\}\frac{1}{\mathrm{Pa}\sqrt{\mathrm{m}}}\mathrm{Pa}\sqrt{\mathrm{m}}\right]\xrightarrow[(6)]{}$$

$$\xrightarrow[(6)]{}\left\{\left(\frac{\Delta W_{E_{th}}}{(\Delta t)}\right)\frac{t_f}{W_{\max}}\right\}\frac{1}{\Delta K_{FL}}\sqrt{2\gamma_s E'}\ \left[\left\{(\mathrm{J})\frac{1}{\mathrm{J}}\right\}(1)\right]=k_4\left\{\left(\frac{\Delta W_{E_{th}}}{(\Delta t)}\right)\frac{t_f}{W_{\max}}\right\}\ [1]$$

where $\sigma_{\max}=\dfrac{W_{\max}}{V_f}$, because it is by definition $\sigma=\dfrac{W}{V}$; then $\dfrac{\Delta W_{E_{th}}}{V_f}\Big/\dfrac{W_{\max}}{V_f}=\dfrac{\Delta W_{E_{th}}}{W_{\max}}$, $k_4=\dfrac{\sqrt{2\gamma_s E'}}{\Delta K_{FL}\left(a_f\right)}$; G is the energy release rate, and γ_s is the free surface energy per unit surface area.

So, the transformations in (8) lead to

$$\begin{aligned}&k\frac{\Delta a}{\Delta N}\Delta K=\frac{\Delta a}{\Delta N}\frac{N_f}{a_f}\frac{\Delta\sigma}{\Delta\sigma_{FL}}\frac{\sqrt{a}}{\sqrt{a_f}}\xrightarrow[a\to a_f]{}k_4\left(\frac{\Delta W_{E_{th}}}{\Delta t}\right)\frac{t_f}{W_{\max}}=\\&=k_4\left(\frac{\Delta W_{E_{th}}}{\Delta N}\right)\frac{N_f}{W_{\max}}\xrightarrow[k_4\to 1]{}\left(\frac{\Delta W_{E_{th}}}{\Delta N}\right)\frac{N_f}{W_{\max}}=\left(\frac{\Delta W_{E_{th}}}{\Delta t}\right)\frac{t_f}{W_{\max}}\end{aligned}\tag{9}$$

Both expressions $\left(\dfrac{\Delta W_{E_{th}}}{\Delta t}\right)\dfrac{t_f}{W_{\max}}$ and $\left(\dfrac{\Delta W_{E_{th}}}{\Delta N}\right)\dfrac{N_f}{W_{\max}}$ from (9) represent a normalized energy change or portion, namely, the normalized potential energy decrease of $\Delta W_{E_{th}}/W_{\max}$, necessary for crack growth of Δa, per *second* or *cycle*. Here the normalizing parameter is the maximum energy $W_{\max}$, corresponding to $\sigma_{\max}$.

Considering the transition $\Delta\to 0$ applied to $\Delta a/\Delta N$ in (8) and (9) as $k\dfrac{\Delta a}{\Delta N}\Delta K\xrightarrow[\Delta\to 0]{}$ $k\dfrac{da}{dN}\Delta K$, in terms of time or cycles two new forms of (9) are obtained

$$\begin{aligned}&1.\ k\frac{da}{dN}\Delta K\xrightarrow[a\to a_f]{}k_4\left(\frac{\Delta W_{E_{th}}}{\Delta t}\right)\frac{t_f}{W_{\max}}\xrightarrow[k_4\to 1]{}\left(\frac{\Delta W_{E_{th}}}{\Delta t}\right)\frac{t_f}{W_{\max}}\\&2.\ k\frac{da}{dN}\Delta K\xrightarrow[a\to a_f]{}k_4\left(\frac{\Delta W_{E_{th}}}{\Delta N}\right)\frac{N_f}{W_{\max}}\xrightarrow[k_4\to 1]{}\left(\frac{\Delta W_{E_{th}}}{\Delta N}\right)\frac{N_f}{W_{\max}}\end{aligned}\tag{10}$$

The results from (4), and from (9) through final forms (10) allow proposing an energy normalized (non-dimensional), characterizing fatigue function $\Delta W_{(a/N)}$ as:

$$\Delta W_{(a/N)}=k\frac{da}{dN}\Delta K\xrightarrow[a\to a_f]{}\left\{k_4\left(\frac{\Delta W_{E_{th}}}{\Delta t}\right)\frac{t_f}{W_{\max}}=k_4\left(\frac{\Delta W_{E_{th}}}{\Delta N}\right)\frac{N_f}{W_{\max}}\right\}\tag{11}$$

or even (when we have not enough data, i.e. for a_f and N_f to omit $k = \frac{N_f}{a_f}\frac{1}{\Delta K_{FL}}$ calculated for a_f and N_f :

$$\Delta W^*_{(a/N)} = \frac{da}{dN}\Delta K \xrightarrow[a \to a_f]{} \frac{k_4}{k}\left\{\left(\frac{\Delta W}{\Delta t}\right)\frac{t_f}{W_{\max}} = \left(\frac{\Delta W}{\Delta N}\right)\frac{N_f}{W_{\max}}\right\} =$$

$$= const\left\{\left(\frac{\Delta W}{\Delta t}\right)\frac{t_f}{W_{\max}} = \left(\frac{\Delta W}{\Delta N}\right)\frac{N_f}{W_{\max}}\right\} \tag{12}$$

$$const = k_4/k = \frac{\sqrt{2\gamma_s E'}}{\Delta K_{FL}}\frac{a_f \Delta K_{FL}}{N_f} = \sqrt{2\gamma_s E'}\frac{a_f}{N_f}$$

It is very important to note that we proved the energy nature of the fatigue function $\Delta W_{(a/N)}$ in terms of tendency under the condition of final failure $a \to a_f$, and hence in Griffith-theory sense.

The new presentation "*da/dN* against $\Delta W_{(a/N)}$ or $\Delta W^*_{(a/N)}$" (using the analytical forms (11) or (12)) is shown in Figs. 1–9 as a family of lines *Q* or *Q** with their equations *y(x)* and corresponding correlation coefficients R^2. At the same time for comparative analyses, as mentioned above, Figs. 1–9 incorporate the original results of the quoted data from [7–8, 11–12, 17, 19–24], which are located at the right-hand side in each graph as:

- the multitude of data points *M*, plotted as *da/dN* against crack length, *a*, or stress intensity factor, ΔK,
- the family of sigmoid curves ***L*,** where it is possible, plotted as *da/dN* against conventional ΔK in its different versions.

The new presentation reveals some common features:

- All sets of data, using the proposed plots "crack growth rate, *da/dN* (m/cycle), against energy normalized fatigue function, $\Delta W_{(a/N)}$, or its form $\Delta W^*_{(a/N)}$ ($m^{3/2}$Pa/cycle)" show an almost linear positioning of the data points for the given stress range, under all chosen conditions of different environments, frequencies, temperatures, *B*–ratios, smooth and notched specimens, constant and random amplitudes, tests for short and long cracks, simple and fretting fatigue. As the normalized fatigue function $\Delta W_{(a/N)}$ represents a kind of normalized energy, it means that in terms of normalized energies, crack growth rate is a linear function of normalized potential energy decrease, necessary for crack growth.
- For all 33 sets of data shown in Figs. 1–9, the correlation coefficients of the corresponding lines (crack growth rate *da/dN* against $\Delta W_{(a/N)}$ or $\Delta W^*_{(a/N)}$) are very high, higher than 0.9. Their distribution is as follows: in 29 cases they are higher than 0.95 and just in 4, higher than 0.94, 0.93, 0.91, 0.9. In more details the exact results are: in 17 cases the correlation coefficients are higher than 0.99; in 4, higher than 0.98; in 4, higher than 0.97; in 3, higher than 0.96; in 5, higher than 0.95, 0.94, 0.93, 0.91, 0.9. At the same time, the results for the correlation coefficients of the Paris–regime lines (*da/dN* against ΔK in its different versions) in only 4 cases show the correlation coefficients higher than 0.95 [17, 20], while in the other cases, described in [7–8, 11–12, 19, 21–24] these coefficients belong to intervals [0.00008, 0.344], [0.354, 0.577], [0.651, 0.823], 0.14. This reveals that even for cases of non–Paris fatigue behaviour, when the correlation coefficients for the traditional ΔK presentations are very low and unsatisfactory, the corresponding coefficients of the proposed $\Delta W_{(a/N)}$ – presentation are high enough to

define almost straight lines. This gives us certain hope that using the new energy normalized characterizing fatigue function, $\Delta W_{(a/N)}$, or its modification $\Delta W^*_{(a/N)}$, we can reduce the data readings of the basic fatigue parameters during each test. Therefore we can shorten fatigue testing times and offer more precise models and predictions of metal fatigue, applying laboratory results to real members of constructions with higher reliability.

CONCLUSIONS

A new energy normalized characterizing fatigue function $\Delta W_{(a/N)}$ is proposed which adopts normalized parameters of defect growth rate and stress intensity factor range, and its physical sense is of normalized potential energy decrease, necessary for crack growth per second, or cycle. The proposed function takes part in a new presentation of fatigue data "crack growth rate *da/dN* against normalized fatigue function $\Delta W_{(a/N)}$ or its modification $\Delta W^*_{(a/N)}$ and shows linear behaviour, called "natural fatigue tendency or ability," which is expressed as an almost straight line and corresponds to a given stress range under different fatigue conditions. The natural fatigue tendency reveals an eventual way of linearization of fatigue behaviour (in terms of the proposed new function $\Delta W_{(a/N)}$ and new presentation of fatigue crack growth data) and suggests more precise and faster assessment prediction and comparison of fatigue development in different metals and alloys.

The proposed function is illustrated on nine metallic materials, steels and non-ferrous alloys, under a wide variety of fatigue conditions of environment, stress state range and ratio, frequency, short and long crack testing, use of smooth and notched specimens, experiments on simple and fretting fatigue.

REFERENCES

1. Inglis, C.E., *Stress in a plate due to the presence of cracks and sharp corners*, Transactions of the Institute of Naval Architects, 55, pp. 219-241. (1913)
2. Griffith, A.A., *The phenomenon of rupture and flow in solids*, Philosophical Transaction of the Royal Society, London A221, pp. 163-197. (1921)
3. Irwin, G.R., *Analysis of stresses and strains near the end of a crack traversing a plate*. Journal of Applied Mechanics, 24, pp. 361-364. (1957)
4. Paris, P.C., Gomez, M.P., and Anderson, W.P., *A rational analytic theory of fatigue*, The Trend in Engineering, 13, pp. 9-14. (1961)
5. Elber, W., *Fatigue crack closure under cyclic tension*, Engineering Fracture Mechanics, 2, pp. 37-45. (1970)
6. Pearson, S., *Initiation of fatigue cracks in commercial aluminum alloys and the subsequent propagation of very short cracks*, Engineering Fracture Mechanics, 7, pp. 235-247. (1975)
7. Hobson, P.D., Brown, M., Rios, E.R., *Short fatigue cracks*, ECF Publication 1, Mechanical Engineering Publications, London, pp. 441-459. (1986)
8. Hobson, P.D., *The growth of short fatigue cracks in a medium carbon steel*, Ph.D. Thesis, University of Sheffield, UK. (1985)
9. Navarro, A., Rios, E.R., *A model of short fatigue crack propagation with an interpretation of the short long crack transition*, Fatigue Fract. Engng Mater. Struct., 10, pp. 169-186. (1987)
10. Miller, K.J., *Materials science perspective of metal fatigue resistance*, Mater. Sci. Tech., 9, pp. 453-462. (1993)
11. Murtaza, G., Akid, R., *Modelling short fatigue crack growth in a heat-treated low-alloy steel*, Int. J. Fatigue, 17 (3), pp. 207-114. (1995)
12. Murtaza, G., *Short fatigue crack growth in a high strength spring steel*, Ph.D. Thesis, University of Sheffield, UK. (1992)
13. Angelova, D., Akid, R., *A note on modelling short fatigue crack behaviour*, Fatigue Fract. Engng Mater. Struct., 21, pp. 771-779. (1998)

14. Gao, N., Brown, M.W., Miller, K.J., *Short crack coalescence and growth in 316 stainless steel subjected to cyclic and time dependant deformation I*, Fatigue Fract. Engng Mater. Struct., 18, pp. 1407-1422. (1995)
15. Gao, N., Brown, M.W., Miller, K.J., *Short crack coalescence and growth in 316 stainless steel subjected to cyclic and time dependant deformation II*, Fatigue Fract. Engng Mater. Struct., 18, pp. 1423-1441. (1995)
16. Murakami, Y., *Metal Fatigue: Effects of Small Defects and Nonmetallic Inclusions*, Elsevier. (2002)
17. Angelova, D., Akid, R., *A normalization of corrosion fatigue behaviour: an example using an offshore structural steel in chloride environments*. Fatigue Fract. Engng Mater. Struct., 22, pp. 409-420. (1999)
18. Angelova, D., *A new normalized characterizing fatigue function*, The 13th European Conference on Fracture - ECF 13 “Fracture Mechanics: Applications and Challenges,” San Sebastian, Spain, Abstracts Volume, pp. 128. (2000)
19. Gangloff, R.P., *The criticality of crack size in aqueous corrosion fatigue*, Res Mechanica Letters, 1, pp. 299-306. (1981)
20. Suresh, S., *Fatigue of Materials*, Cambridge University Press, Cambridge, UK. (1998)
21. Fellows, L.J., Nowell, D., Hill, D.A., *Analysis on crack initiation and propagation in fretting fatigue: the effective initial floaw size methodology*, Fatigue Fract. Engng Mater. Struct., 20, pp. 61-70. (1997)
22. Sansoz, F., Brethes, B., Pineau, A., *Short fatigue crack propagation from notches in N18 Ni based superalloy*, The 12th Bienniel European Conference on Fracture ECF-12 “Fracture from Defects,” Sheffield, UK, pp. 61-66. (1998)
23. Wei, L., Rios, E.R., *Micro-fracture mechanics based modelling of fatigue crack growth in aluminium alloy Al7010-T7451 under random loading*, The 12th Bienniel European Conference on Fracture ECF-12 “Fracture from Defects,” Sheffield, UK, pp. 37-42. (1998)
24. Tonneau, A., Henaff, G., Mabru, C., Petit, J., *Fatigue crack propagation in FeAl and TiAl alloys as influenced by environment and temperature*, The 12th Bienniel European Conference on Fracture ECF-12 “Fracture from Defects,” Sheffield, UK, pp. 103-108. (1998)

APPENDIX

Characterization of fatigue crack growth under both elastic and elastic-plastic conditions uses some parameters and approaches to fracture at monotonic loading with the existing connections and equivalencies between them, or so-called linear elastic and non-linear elastic-plastic fracture mechanics implications for fatigue. The parameters and approaches used in the present study and the connections and equivalencies between them are concerned with the following.

1. The pioneering theory of Griffith as a base of modern theories of fracture

The Griffith theory formulates criteria for the unstable growth of a crack under conditions of a balance between changes in mechanical and surface energies in the region of crack developing. After Griffith [2], the decrease in potential energy of the system W_p with a through-thickness crack of length $2a$, located at the centre of a large brittle plate of uniform thickness B, which is subjected to a constant far-field tensile stress σ, can be represented as

$$W_p = -\frac{\pi a^2 \sigma^2 B}{E'} \tag{1A}$$

or

$$-a^2\sigma^2 = \frac{W_p E'}{\pi B}\left[\frac{(\mathrm{J})\,\mathrm{Pa}}{\mathrm{m}}\right] = \frac{W_p}{\pi B}(E' A_{\perp B})\frac{1}{A_{\perp B}}\left[\frac{\mathrm{J}}{\mathrm{m}_B}\left(\frac{\mathrm{J}}{\left(\mathrm{m}^3 = \mathrm{m}_B(\mathrm{m}_a)^2\right)}(\mathrm{m}_a)^2\right)\frac{1}{(\mathrm{m}_a)^2}\right] =$$

$$= \left(\frac{W_p}{\pi B}(E' A_{\perp B})\frac{1}{A_{\perp B}}\right)\left[\frac{\mathrm{J}}{\mathrm{m}_B}\left(\frac{\mathrm{J}}{\mathrm{m}_B}\right)\frac{1}{\mathrm{m}_a{}^2}\right] = k_{th}\left(\frac{W_p}{B}(E_{th} A_{\perp B})\frac{1}{A_{\perp B}}\right)\left[\left(\frac{\mathrm{J}}{\mathrm{m}_B}\right)^2\frac{1}{\mathrm{m}_a{}^2}\right] =$$

$$= k_{th}\left(\frac{W_p}{B}\left(\frac{W_{th}}{B}\right)\frac{1}{A_{\perp B}}\right)\left[\left(\frac{\mathrm{J}}{\mathrm{m}_B}\right)^2\frac{1}{\mathrm{m_a}^2}\right] \tag{2A}$$

or

$$\frac{W_p E'}{\pi B}\left[\frac{(\mathrm{J})\,\mathrm{Pa}}{\mathrm{m}}\right] = -k_{th}\frac{\left(\sqrt{W_p E_{th}}\right)^2}{B}\left[\frac{\mathrm{J}^2}{(\mathrm{m}_B\mathrm{m}_a)^2}\right]$$

$$\text{and}\quad \frac{W_p E'}{\pi B}\left[\frac{(\mathrm{J})\,\mathrm{Pa}}{\mathrm{m}}\right] = -k_{th}\frac{\left(\sqrt{W_p W_{th}}\right)^2}{B^2}\frac{1}{A_{\perp B}}\left[\frac{\mathrm{J}^2}{(\mathrm{m}_B\mathrm{m}_a)^2}\right] \tag{3A}$$

where:

- $E' = \dfrac{E}{1-\nu^2}$ for plane strain and $E' = E$ for plane stress;
- E is Young's modulus and ν is Poisson's ratio;
- $\pi a^2 B = A_{\perp B} B = V$ is the region of energy spread around the growing crack a, introduced by Griffith as a volume of a cylinder with parameters a and B, where the mentioned balance between the changes in mechanical and surface energies is in effect, and owing to this is named "volume of energy exchange around growing crack"; here a is an effective length of the growing crack, measured as the smallest distance between its tips; when $a \to a_f$, $V \to V_f$;
- $E_{th} = k_{th}{}^1 E$ (where $k_{th}{}^1$ adopts usually a value of $1/2\pi$ or 0.1) is the theoretical strength and dimensionally, energy per unit volume – this defines $W_{th} = E_{th}(V = BA_{\perp B})$ as the total energy corresponding to E_{th} in the crack region V; $k_{th} = f(k_{th}{}^1)$ is an equalizing constant;
- among the dimensions in (2A), (m_B) and (m_a) mean *meter* measured, respectively, alongside the thickness of the plate B, and at the plate surface considering the crack area $A_{\perp B} = \pi a^2$ which is perpendicular to B, so (m_a) is connected with $\sqrt{(A_{\perp B})}$.

Thus, the equation (2A), accordingly to (3A), can be shown in its two forms:

$$-(a\sigma)^2 = -a^2\sigma^2 = k_{th}\frac{W_p E_{th}}{B}\left[\frac{\mathrm{J}^2}{\mathrm{m}^4}\right] = k_{th}\frac{W_p W_{th}}{B(V = BA_{\perp B})}\left[\frac{\mathrm{J}^2}{\mathrm{m}^4}\right]$$

$$a\sigma = k_{th}\sqrt{\frac{W_p E_{th}}{B}}\left[\frac{\mathrm{J}}{\mathrm{m}^2}\right] = k_{th}\sqrt{\frac{W_p}{B}\frac{W_{th}}{BA_{\perp B}}}\left[\frac{\mathrm{J}}{\mathrm{m}_B\mathrm{m}_a}\right] = \frac{W_{E_{th}}}{A_{\mathrm{II}B}}\left[\frac{\mathrm{J}}{\mathrm{m}^2}\right] \tag{4A}$$

where $W_{E_{th}} = \sqrt{(W_p W_{th})}$, and $A_{\mathrm{II}B} = B\sqrt{(A_{\perp B})}$.

These forms reveal two things. Firstly, the expression $a^2\sigma^2$ can be discussed as proportional to the square value of the energy W_{th} (corresponding to the theoretical strength E_{th} that by definition, and for our case, has to be reached for fracturing every volume unity of a perfect plate with the same size as the already introduced one with the through-thickness crack a), decreased by a coefficient W_p/W_{th} reading a drop of W_{th} for the system with a crack. This drop reaches the potential energy W_p, represented by (1A), so for the plate with a crack a, the expression W_pW_{th}, appearing in (4A), replaces W_{th}^2, describing the fracture of an eventual perfect plate. Secondly, the multiplication $a\sigma$ is the geometrical mean energy $\sqrt{(W_pW_{th})}$ of W_{th} and W_p per unit crack surface area A_{IIB}, or W_{Eth}/A_{IIB} (J/m^2).

The surface energy of the system with the through-thickness crack a is

$$W_s = 2(2aB)\gamma_s = 2A\gamma_s \tag{5A}$$

where $A_{IIB} = 2aB \equiv A$ is one of the crack surfaces alongside B, and γ_s is the free surface energy per unit surface area.

Finally, the total energy of the crack system using (1A) and (5A) is $U = W_p + W_s$, and the critical condition for the onset of crack growth suggested by Griffith, $dU/dA = 0$, (where $A = 2aB$). This leads to the so called *Griffith critical stress for fracture initiation*, $\sigma_f^2 = \frac{2E'\gamma_s}{\pi a}$ or $\sigma_f^2 = \frac{2E'(\gamma_s + \gamma_p)}{\pi a}$, where the latter is known as Orowan's extension for metals including the plastic work per unit area of crack surface created, γ_p.

The Griffith theory represented in this current Appendix note (1) is not directly valid for an application to cyclic loading, as it has been especially founded for a constant far-field tensile stress σ, but it can be applied to the cyclic conditions in terms of final failure and in sense of some equivalencies marked below.

2. The equivalence between Griffith's model and Irwin's approach introducing the energy release rate *G*

Irwin defined the energy release rate G as

$$G = -\frac{dW_p}{dA} \tag{6A}$$

and the Griffith criterion can be expressed in terms of the critical G

$$G = \frac{\pi\sigma^2 a}{E'} = 2\gamma_s \tag{7A}$$

A further consideration of (6A) and (7A) gives a succession of equations $G = -\frac{1}{2B}\frac{dW_p}{da} = \frac{\pi\sigma^2 a}{E'}$, $-\frac{1}{2B}dW_p = \frac{\pi\sigma^2 a}{E'}da$, and finally $W_p = -k'\frac{B\pi\sigma^2 a^2}{E'}$, leading to the same result for the potential energy W_p, given in (1A) – both expressions differ only by a numerical constant k'.

3. The direct equivalence of the stress intensity factor, *K* (providing a unique characterization of the near-tip fields under small-scale yielding conditions) to the energy approach, based on the energy release rate, *G*

The energy release rate G and the stress intensity factors K_{I}, K_{II} and K_{III} (for the three different modes) are uniquely related, and for the general three-dimensional case, involving plane strain and anti-plane strain loading, it can be expressed as

$$G = \frac{(1-\nu^2)}{E}\left(K_{\mathrm{I}}^2 + K_{\mathrm{II}}^2\right) + \frac{(1+\nu)}{E}K_{\mathrm{III}}^2 \tag{8A}$$

and, for plane stress as,

$$G = \frac{1}{E}\left(K_{\mathrm{II}}^2 + K_{\mathrm{II}}^2\right) \qquad (9A)$$

4. The cyclic loading characterization

The cyclic loading characteristics can be represented through the monotonic loading ones as the following replacements:

- the stress range $\Delta\sigma$ replaces σ, $\Delta\sigma \to \sigma$;
- the stress intensity factor range ΔK replaces K, $\Delta K \to K$;
- the crack tip opening displacement range $\Delta\delta$ replaces δ, $\Delta\delta \to \delta$, where $\Delta\delta_t \approx \dfrac{\Delta K_{\mathrm{I}}^2}{2\sigma_y E}$;
- the J-integral range ΔJ replaces J, $\Delta J \to J$.

In context of notes 2, 3, and 4, it is important to mention that there is a connection between the cyclic loading characteristics, and especially ΔK, and in terms, for example of final failure, it leads to the above mentioned equivalence of K and G, and finally to the Griffith criterion re-phrased in terms of G. A real fatigue example can be the final regime of crack growth after the Paris regime, where the fatigue crack growth rate becomes significantly higher and the influence of stress R–ratio increases as

$$K_{\max} \underset{a \to a_f}{\to} K_c \ (K_{\max} \underset{a \to a_f}{\to} K_{\mathrm{I}c} \text{ in plane strain) or } K_{\max} = \frac{\Delta K}{(1-R)} \underset{a \to a_f}{\to} K_c \qquad (10A)$$

leading to $K_c = f(G_c)$ and (7A).

SOME PROBLEMS OF CRACKS ON BIMATERIAL INTERFACE

Ružica R. Nikolić, Faculty of Mechanical Engineering, Kragujevac, S&Mn
Jelena M. Veljković, DP Zastava Mašine, Kragujevac, S&Mn

INTRODUCTION

The scientific understanding of the mechanics of crack initiation and crack growth in bimaterial interfaces is essential for the effective study of failure processes in advanced materials such as composites and ceramics. A very important failure mechanism in fibre or whisker reinforced ceramic composites, for example, is the debonding between the matrix and the reinforcing phase. This debonding process may either take place quasi-statically or dynamically, depending on the nature of the loads that the composite structure is subjected to.

The earliest study of interfacial failure appears to be by Williams [1], who examined the local fields near the tip of a traction free semi-infinite interfacial crack, lying between two perfectly bonded elastic half spaces. He observed that, unlike in homogeneous materials, the interfacial crack exhibits an oscillatory stress singularity. Since then, Sih and Rice [2], and Rice and Sih [3], have provided explicit expression for the near tip stresses and related them to remote elastic stress fields. The works of Erdogan [4] and England [5] have also further examined two-dimensional singular modes for single or multiple crack configurations in bimaterial systems. Recent progress in interfacial fracture includes work by Rice [6], Hutchinson and Suo [7], and Shih [8], Liu, Lambros and Rosakis [9], Veljković [10], Veljković and Nikolić [11, 12].

1. ELASTIC FRACTURE MECHANICS CONCEPT FOR INTERFACIAL CRACK

The near tip linear elastic stress field for the crack along an interface between dissimilar materials is considered. The simplest model of such cracks are surfaces across which no tractions are transmitted. Solutions of that model predict material inter-penetration, close to crack tip. That feature can be ignored in interpreting the solutions, because the predicted contact zone is small, compared to relevant physical sizes.

The specific problem of crack lying along bimaterial interface of isotropic material is presented in Fig. 1. Let a material with Young's modulus E_1 and Poisson's ratio ν_1 occupy the upper half-plane, $y > 0$, and let material with E_2 and ν_2 occupy the lower half-plane, $y < 0$. The two materials are bonded along the positive x-axis, and the crack lies along the negative x-axis.

The near tip stress field for an interface crack between the two dissimilar isotropic materials is a linear combination of two types of fields: a coupled oscillatory field defined by a complex stress intensity factor K, and a non-oscillatory field scaled by a real stress intensity factor K_{III}. The near stress field for an interface crack has the form:

$$\sigma_{\alpha\beta} = \frac{1}{\sqrt{2\pi r}}\left[\mathrm{Re}(Kr^{i\varepsilon})\Sigma^{\mathrm{I}}_{\alpha\beta}(\theta,\varepsilon) + \mathrm{Im}(Kr^{i\varepsilon})\Sigma^{\mathrm{II}}_{\alpha\beta}(\theta,\varepsilon) + K_{\mathrm{III}}\Sigma^{\mathrm{III}}_{\alpha\beta}(\theta)\right] \tag{1}$$

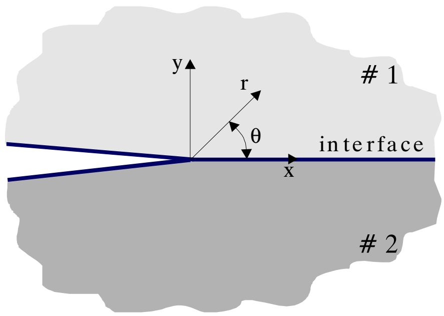

Figure 1. Interface crack between two dissimilar materials.

Here r and θ are polar coordinates and α, $\beta = x, y, z$, $\Sigma_{\alpha\beta}{}^{\mathrm{I,II,III}}(\theta)$ are the angular functions, which correspond to tensile tractions, in-plane shear tractions and anti-plane shear tractions across the interface, respectively, so that the tractions at a distance r ahead of the crack tip take the form:

$$(\sigma_{yy} + i\sigma_{xy})_{\theta=0} = \frac{Kr^{i\varepsilon}}{\sqrt{2\pi r}} \qquad (\sigma_{yz})_{\theta=0} = \frac{K_{\mathrm{III}}}{\sqrt{2\pi r}} \tag{2}$$

and in this sense, $\Sigma_{\alpha\beta}{}^{\mathrm{I,II,III}}(\theta)$ may be said to correspond to modes I, II and III of the crack growth. The angular function $\Sigma_{\alpha\beta}{}^{\mathrm{I,II}}(\theta)$ for material–1 takes the form:

$$\begin{aligned}
\Sigma_{rr}^{\mathrm{I}}(\theta) &= -\frac{\operatorname{sh}\varepsilon(\pi-\theta)}{\operatorname{ch}\varepsilon\pi}\cos\frac{3\theta}{2} + \frac{e^{-\varepsilon(\pi-\theta)}}{\operatorname{ch}\varepsilon\pi}\cos\frac{\theta}{2}\left(1+\sin^2\frac{\theta}{2}+\varepsilon\sin\theta\right)\\
\Sigma_{\theta\theta}^{\mathrm{I}}(\theta) &= \frac{\operatorname{sh}\varepsilon(\pi-\theta)}{\operatorname{ch}\varepsilon\pi}\cos\frac{3\theta}{2} + \frac{e^{-\varepsilon(\pi-\theta)}}{\operatorname{ch}\varepsilon\pi}\cos\frac{\theta}{2}\left(\cos^2\frac{\theta}{2}-\varepsilon\sin\theta\right)\\
\Sigma_{r\theta}^{\mathrm{I}}(\theta) &= \frac{\operatorname{sh}\varepsilon(\pi-\theta)}{\operatorname{ch}\varepsilon\pi}\sin\frac{3\theta}{2} + \frac{e^{-\varepsilon(\pi-\theta)}}{\operatorname{ch}\varepsilon\pi}\sin\frac{\theta}{2}\left(\cos^2\frac{\theta}{2}-\varepsilon\sin\theta\right)\\
\Sigma_{rr}^{\mathrm{II}}(\theta) &= \frac{\operatorname{ch}\varepsilon(\pi-\theta)}{\operatorname{ch}\varepsilon\pi}\sin\frac{3\theta}{2} - \frac{e^{-\varepsilon(\pi-\theta)}}{\operatorname{ch}\varepsilon\pi}\sin\frac{\theta}{2}\left(1+\cos^2\frac{\theta}{2}-\varepsilon\sin\theta\right)\\
\Sigma_{\theta\theta}^{\mathrm{II}}(\theta) &= -\frac{\operatorname{ch}\varepsilon(\pi-\theta)}{\operatorname{ch}\varepsilon\pi}\sin\frac{3\theta}{2} - \frac{e^{-\varepsilon(\pi-\theta)}}{\operatorname{ch}\varepsilon\pi}\sin\frac{\theta}{2}\left(\sin^2\frac{\theta}{2}+\varepsilon\sin\theta\right)\\
\Sigma_{r\theta}^{\mathrm{II}}(\theta) &= \frac{\operatorname{ch}\varepsilon(\pi-\theta)}{\operatorname{ch}\varepsilon\pi}\cos\frac{3\theta}{2} + \frac{e^{-\varepsilon(\pi-\theta)}}{\operatorname{ch}\varepsilon\pi}\cos\frac{\theta}{2}\left(\sin^2\frac{\theta}{2}+\varepsilon\sin\theta\right)\\
\Sigma_{rz}^{\mathrm{I,II}}(\theta) &= \Sigma_{z\theta}^{\mathrm{I,II}}(\theta) = 0, \qquad \Sigma_{zz}^{\mathrm{I,II}}(\theta) = \nu\left(\Sigma_{rr}^{\mathrm{I,II}}(\theta) + \Sigma_{\theta\theta}^{\mathrm{I,II}}(\theta)\right)
\end{aligned} \tag{3}$$

For material–2, everywhere simply replace $-\pi$ with π, and vice-versa. The mode III functions $\Sigma_{\alpha\beta}{}^{\mathrm{III}}(\theta)$ are the same as for a homogeneous solid:

$$\begin{aligned}
&\Sigma_{rr}^{\mathrm{III}}(\theta) = \Sigma_{\theta\theta}^{\mathrm{III}}(\theta) = \Sigma_{r\theta}^{\mathrm{III}}(\theta) = \Sigma_{zz}^{\mathrm{III}}(\theta) = 0,\\
&\Sigma_{rz}^{\mathrm{III}}(\theta) = \sin\frac{\theta}{2}, \quad \Sigma_{\theta z}^{\mathrm{III}}(\theta) = \cos\frac{\theta}{2}
\end{aligned} \tag{4}$$

Figures 2 and 3 show angular variations of stresses for an arbitrary bimaterial combination.

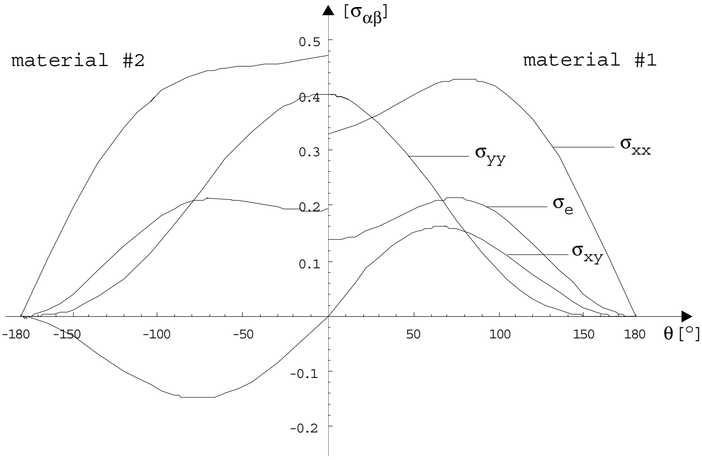

Figure 2. Angular variations of stress for arbitrary bimaterial combination, Eq. (1), by use of programme package Mathematica

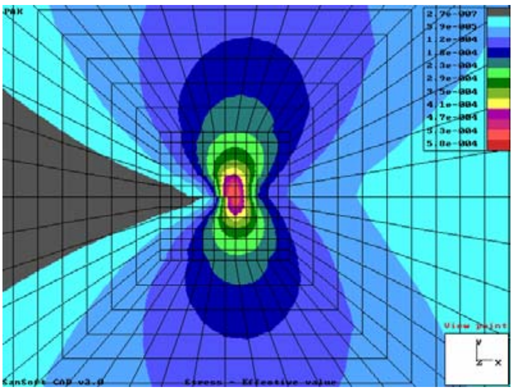

Effective stress

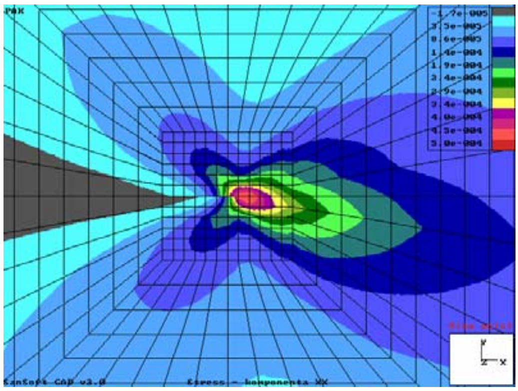

stress σ_{xx}

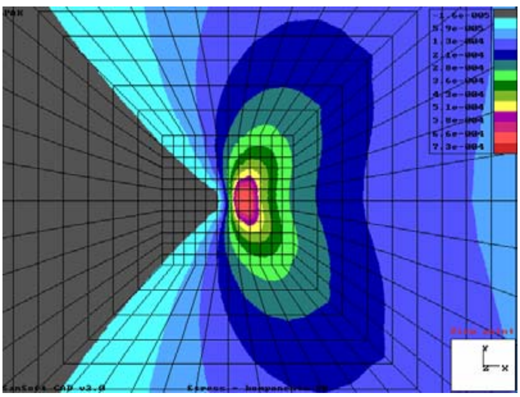

stress σ_{yy}

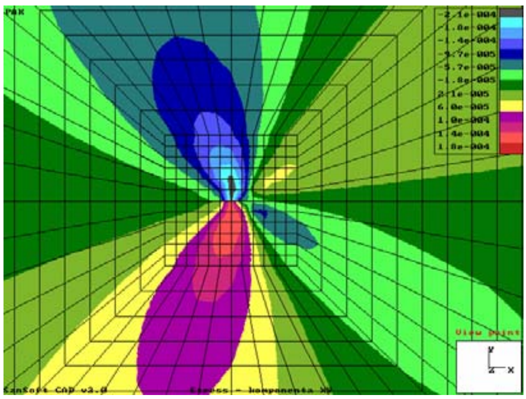

stress σ_{xy}

Figure 3. Angular variations of stresses for arbitrary bimaterial combination (program PAK)

Stress jump across the interface is a characteristic feature of the interface crack, as shown in Figs. 2 and 3. The stress component σ_{xx} is taken to be discontinuous across the bond line at $y = 0$, while the strain component ε_{xx} is continuous along such a line, i.e.,

$$(\varepsilon_{xx})_1 = (\varepsilon_{xx})_2 \tag{5}$$

From the strain–stress relations (Hooke's law) it follows that:

$$(\sigma_{xx})_2 = \frac{E_2}{E_1}(\sigma_{xx})_1 + \left(\nu_2 - \nu_1 \frac{E_2}{E_1}\right)\sigma_{yy} \tag{6}$$

for plane stress conditions, and

$$(\sigma_{xx})_2 = \frac{E_2}{E_1}\left(\frac{1-\nu_1^2}{1-\nu_2^2}\right)(\sigma_{xx})_1 + \left(\frac{\nu_2}{1-\nu_2} - \frac{\nu_1(1+\nu_2)}{1-\nu_2^2}\nu_1 \frac{E_2}{E_1}\right)\sigma_{yy} \tag{7}$$

for plane strain conditions.

There is no unique physical interpretation for bimaterial interfacial crack, such as in the case of homogeneous materials. Namely, symmetry and anti-symmetry modes are entirely separated for homogeneous material. For interface crack, the symmetry and anti-symmetry modes are coupled. However, angular functions $\Sigma_{\alpha\beta}^{\mathrm{I,II}}(\theta)$ also depend on elastic properties of the bimaterial combination through the parameter ε. The parameter ε is called the *bielastic constant* or the *oscillatory index*, and is given by:

$$\varepsilon = \frac{1}{2\pi}\ln\left(\frac{1-\beta}{1+\beta}\right) \tag{8}$$

Here β is one of two Dundurs parameters:

$$\alpha = \frac{\mu_2(\kappa_1+1)-\mu_1(\kappa_2+1)}{\mu_2(\kappa_1+1)+\mu_1(\kappa_2+1)}, \qquad \beta = \frac{\mu_2(\kappa_1-1)-\mu_1(\kappa_2-1)}{\mu_2(\kappa_1+1)+\mu_1(\kappa_2+1)} \tag{9}$$

where: μ_i is the shear modulus, $\kappa_i = 3-4\nu_i$ for the plane strain, and $\kappa_i = (3-\nu_i)/(1+\nu_i)$ for the plane stress and ν_i is Poisson's ratio, and subscripts 1 and 2 refer to materials 1 and 2, respectively.

In Eq. (1), K_{III} presents the mode III stress intensity factor, which has the same form as for homogeneous solid. As opposite to homogeneous material, where mode I and II factors are separated (K_{I} and K_{II}), there is a single complex intensity factor K for the in-plane modes. In-plane modes are coupled together for interfacial crack. The two stress intensity factors have different dimensions K = [stress]·[length]$^{1/2-i\varepsilon}$ and K = [stress]·[length]$^{1/2}$.

The complex stress intensity factor is a property of interface cracks. That complex stress intensity factor has the generic form:

$$K = YT\sqrt{L}\,L^{-i\varepsilon}e^{-i\psi} \tag{10}$$

where T is a magnitude of stress, applied due to the specimen load, L is a characteristic length (crack length, layer thickness), Y is a dimensionless real positive quantity, and ψ is the phase angle of $KL^{i\varepsilon}$, though it is often called the phase angle of the complex stress intensity factor, or the phase angle of the applied load. Both Y and ψ are dependent on applied load in general, on ratios of elastic modules and of characteristic cracked body sizes.

Considering Eqs. (1) and (2), one may conclude that for bimaterial case, K_{I} and K_{II} are not constant. In fact, these variables are functions of r, denoted as K_1 and K_2 are given by:

$$\begin{aligned} K_1 &= K_{\mathrm{I}}(r) \equiv \mathrm{Re}(Kr^{i\varepsilon}) = YT\sqrt{L}\cos\left[\psi - \varepsilon\ln(L/r)\right] \\ K_2 &= K_{\mathrm{II}}(r) \equiv \mathrm{Im}(Kr^{i\varepsilon}) = YT\sqrt{L}\sin\left[\psi - \varepsilon\ln(L/r)\right] \end{aligned} \tag{11}$$

Evidently, the ratio $\sigma_{yx}/\sigma_{yy} = K_2/K_1 = \mathrm{tg}[\psi - \varepsilon\ln(L/r)]$ varies with r near the tip. The quantity $\psi - \varepsilon\ln(L/r)$ is the local phase angle of the field.

To better characterize phase angles variation with distance, i.e. the so-called phase index, it is helpful to write the interface traction vector in the following way:

$$\mathbf{t} = \{t_1, t_2, t_3\} = \{\sigma_{yx}, \sigma_{yy}, \sigma_{yz}\} \tag{12}$$

For $t = t_1 + i \cdot t_2$, it is:

$$t = |t| e^{i\psi_r} = \frac{K r^{i\varepsilon}}{\sqrt{2\pi r}} \tag{12'}$$

the phase angle ψ_r is a measure of the ratio of the normal to in-plane shear tractions at a distance r ahead of the crack tip. When the distance changes from r_1 to r_2, the phase angle changes:

$$\psi_{r_1} - \psi_{r_2} = \varepsilon \ln\left(\frac{r_2}{r_1}\right) \tag{13}$$

Convenient for a wide range of materials, the phase angle variation with distance is the quantity $(180/\pi)\varepsilon\ln(10) = \varepsilon^*$. It has the interpretation as the phase change in degrees for a decade increase in distance. As an example, for $\varepsilon = 0.05$ as for glass/Al_2O_3 interface, the phase index is $\varepsilon^* = 6.6°$. For $\varepsilon = 0$ the mode mixity can be defined in the usual way. When all the three modes are present, the mode mixity is fully specified by two solid angles, ψ and ϕ, in the space of the interface traction vector $\mathbf{t} = \{\sigma_{yx}, \sigma_{yy}, \sigma_{yz}\}$:

$$\mathrm{tg}\psi = \left(\frac{\sigma_{yx}}{\sigma_{yy}}\right)_{r\to 0} \qquad \cos\phi = \left(\frac{\sigma_{yz}}{|\mathbf{t}|}\right)_{r\to 0} \tag{14}$$

An equivalent definition can be given in (K_{I}, K_{II}, K_{III}) space as:

$$\mathrm{tg}\psi = \frac{K_{\mathrm{II}}}{K_{\mathrm{I}}} \qquad \cos\phi = \frac{K_{\mathrm{III}}}{\sqrt{K_{\mathrm{I}}^2 + K_{\mathrm{II}}^2 + K_{\mathrm{III}}^2}} \tag{15}$$

The angles ψ and ϕ are presented in Fig. 4. These definitions also apply to cracks in homogeneous materials.

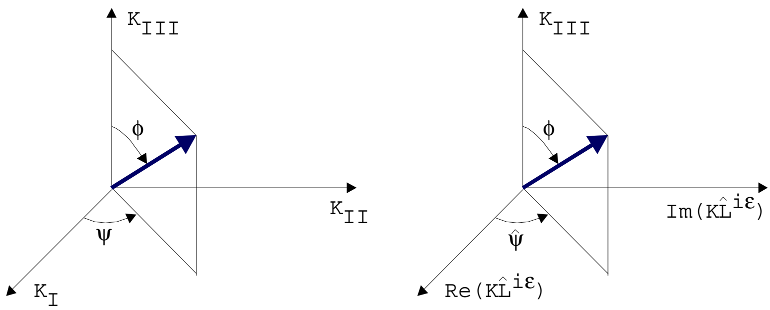

Figure 4. Mode mixity defined as solid angles in K space: (a) for $\varepsilon = 0$, (b) for $\varepsilon \neq 0$.

For $\varepsilon \neq 0$ tension and shear effects are inseparable near the interface crack tip. A measure of the relative proportion of shear to normal tractions (or mode II to mode I) requires the specification of a characteristic length quantity $\hat{L}$. For oscillatory fields the mode mixity is uniquely specified by:

$$\mathrm{tg}\hat{\psi} = \left(\frac{\sigma_{yx}}{\sigma_{yy}}\right)_{r\to \hat{L}} \qquad \cos\phi = \left(\frac{\sigma_{yz}}{|\mathbf{t}|}\right)_{r\to 0} \tag{16}$$

The length $\hat{L}$ is arbitrary, but must be invariant for a specific material pair, i.e. $\hat{L}$ must be independent of the overall specimen sizes and specimen types. A length between the inelastic zone size and the specimen size is a sensible choice of $\hat{L}$. For example, $\hat{L}$ = 100 μm is suitable for many brittle bimaterial specimens in the laboratory research.

Using the stress field (1), or the tractions in (2), the mode mixity $\hat{\psi}$ and ϕ, can also be defined in K space, Fig. 4:

$$\mathrm{tg}\,\hat{\psi} = \frac{\mathrm{Im}(K\hat{L}^{i\varepsilon})}{\mathrm{Re}(K\hat{L}^{i\varepsilon})} \quad \cos\phi = \frac{K_{\mathrm{III}}}{\sqrt{|K|^2 + K_{\mathrm{III}}^2}} \tag{17}$$

A consequence of the oscillatory field is that the traction ratio t_1/t_2 varies slowly as r moves away from the tip. Let $\hat{\psi}_1$ and $\hat{\psi}_2$ be associated with $\hat{L}_1$ and $\hat{L}_2$, respectively. Based on the first of two Eqs. (17), it can be written:

$$\hat{\psi}_2 - \hat{\psi}_1 = \varepsilon \ln\left(\frac{\hat{L}_2}{\hat{L}_1}\right) \tag{18}$$

what would not make a big difference for various $\hat{L}$'s. For example, for an epoxy/glass interface ε= 0.06, for the mode mixity change of ten, the change in distance amounts to $\hat{\psi}_2 - \hat{\psi}_1$ = 7.9°.

From the above discussion, it can be concluded that the near tip stress field for bimaterial interface crack for mode mixity is dependent on the phase angle of the load. In Fig. 5, the hoop stress is plotted against the angle θ for several phase angles.

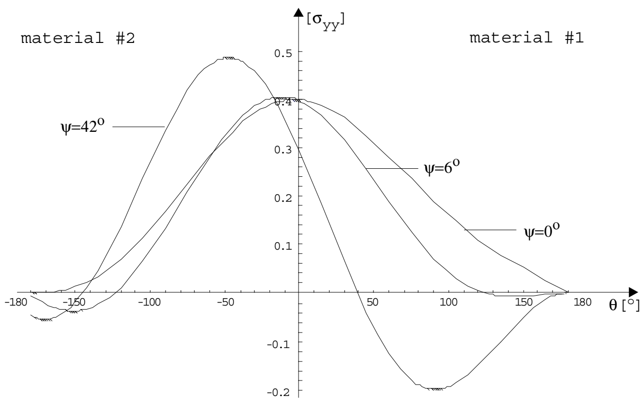

Figure 5. Angular variation of hoop stress for several phase angles.

Let δ_α denote components of the relative displacement between the two initially coincident points along the crack faces. For isotropic solids:

$$\delta_y + i\delta_x = \frac{1}{(1+2i\varepsilon)\,\mathrm{ch}(\pi\varepsilon)} \cdot \frac{4Kr^{i\varepsilon}}{E^*}\sqrt{\frac{2r}{\pi}}, \quad \delta_z = \frac{2K_{\mathrm{III}}}{\mu^*}\sqrt{\frac{2r}{\pi}} \tag{19}$$

where

$$\frac{2}{E^*} = \frac{1}{E_1'} + \frac{1}{E_2'}, \qquad \frac{2}{\mu^*} = \frac{1}{\mu_1} + \frac{1}{\mu_2} \tag{20}$$

and $E' = E/(1-\nu^2)$ for plane strain and $E' = E$ for plain stress.

The energy release rate is related to K and K_{III} by:

$$G = \frac{1}{\mathrm{ch}^2(\pi\varepsilon)} \cdot \frac{|K|^2}{E^*} + \frac{K_{\mathrm{III}}^2}{2\mu^*} \tag{21}$$

Overlapping of the crack faces and contact in isotropic bimaterials does not involve the mode III field. The present discussion is confined to the coupled in-plane modes. According to Eq. (19) interpenetration of the crack faces, $\delta_y < 0$, will occur at sufficiently small r. Writing $\delta = \delta_y + i\delta_x$ and using (19) one obtains:

$$\delta_y = |\delta| \cos\left[\psi - \mathrm{arctg}(2\varepsilon) - \varepsilon \ln\left(\frac{L}{r}\right)\right] \tag{22}$$

The contact zone size, if it is sufficiently small with respect to crack size L, is estimated to be the largest r for which the opening gap δ_y just turns negative. For $\varepsilon > 0$:

$$r_C = L e^{-\frac{\frac{\pi}{2} + \psi - \mathrm{arctg}(2\varepsilon)}{\varepsilon}} \tag{23}$$

For $\varepsilon < 0$, just replace ε with –ε, and ψ with $-\psi$ in Eq. (23). As an example, if L = 1 cm, $|\psi| \leq \pi/4$ and $|\varepsilon| \leq 0.03$, then $r_C < 1$⊕, which is smaller than all physically relevant length scales.

We may conclude from the above discussion that the crack tip state is characterized by the complex K, if $r_C/L \ll 1$; Rice [6] has suggested using $r_C/L < 0.01$. Combining this condition with Eq. (23) leads to the following range of ψ, in which K is applicable:

$$\text{for } \varepsilon > 0 \quad -\pi/2 + 6.6\varepsilon < \psi < \pi/2 + 2\varepsilon \tag{24}$$

$$\text{for } \varepsilon < 0 \quad -\pi/2 + 2\varepsilon < \psi < \pi/2 + 6.6\varepsilon \tag{25}$$

In the above equations arctg(2ε) is approximated by 2ε.

Let r_k denote the characteristic radius of the region controlled by Eq. (1). Then r_k will be some function of relevant dimensions of the crack geometry. At distances sufficiently close to the tip; the field, Eq. (1), does not apply because of the presence of:

- a material non-linear zone (plasticity) r_p;
- a contact zone r_C; and/or
- small-scale heterogeneities and irregularities r_i (grains, voids, micro-cracks, inter-diffusion zones). If those zones and/or irregularities are sufficiently small compared to a characteristic crack dimension L, then an annular region exists:

$$r_k > r \gg r_p, r_C, r_i \tag{26}$$

in which (1) is dominant. In other words, if (26) is satisfied, the complex K uniquely measures the fields in an annular region surrounding the crack tip. Estimates of r_k for finite width crack geometries have been obtained by O'Dowd et al. [13]. Their studies show that:

$$r_k \approx L/10 \tag{27}$$

where L is the shortest of the crack lengths, the uncracked ligament length, the layer thickness or the distance between the crack tip and the point of load application. Combining (26) and (27):

$$L/10 > r_k \gg r_p, r_C, r_i \tag{28}$$

The condition for the existence of a K annulus is:

$$L > 100 \times (r_p, r_C, r_i) \tag{29}$$

Observe that the contact zone size depends on the phase of the applied load but not on its magnitude, (23), while the size scale of irregularities is a property of the bimaterial. In contrast, the plastic zone size is proportional to $|K|^2$, i.e. it scales with the square of the magnitude of the applied load. If the interface is relatively tough or if one material has low yield stress, a sizeable plastic zone can develop before the onset of fracture.

To summarize, note that if the size requirements (29), then concerning the crack geometry, material mismatch and applied loads is communicated to the crack tip through K only. Details that have no effect on K also have no effect on the near tip field since the latter is uniquely characterized by K. Therefore, K provides boundary conditions for the inner region where fracture processes occur, i.e. the onset of fracture can be phrased in terms of K. These arguments are identical to those made for the stress intensity factor in linear elastic fracture mechanics. In LEFM methodology, and in the developing subject of interface fracture mechanics, the underlying idea is the K dominance.

It has been observed in experiments that cracks in isotropic, homogeneous, brittle solid seek to propagate on planes ahead of which local mode I conditions prevail. Consequently, one single parameter, K_{Ic} can be designated to each material to quantify its resistance to fracture. By contrast, whenever planes of low fracture resistance exist, cracks may be trapped on such planes regardless of the local mode mixity. Orthotropic materials, such as composites and brittle crystals, provide examples where definite weak planes exist: longitudinal planes for composites and cleavage planes for crystals. Interfaces offer another example, when they are brittle compared with the substrates. A documented experimental fact is that fracture resistance for such weak planes depends strongly on mode mixity. Therefore, the toughness values at various mode mixities fully characterized the fracture resistance of a weak plane.

For a given mode mixity $\hat{\psi}$ and ϕ, the interface fracture toughness Γ is defined as the energy release rate at onset of crack growth. The fracture toughness $\Gamma(\hat{\psi},\phi)$ is a property of bimaterial interface. The interface toughness curve for an arbitrary interface is shown in Fig. 6.

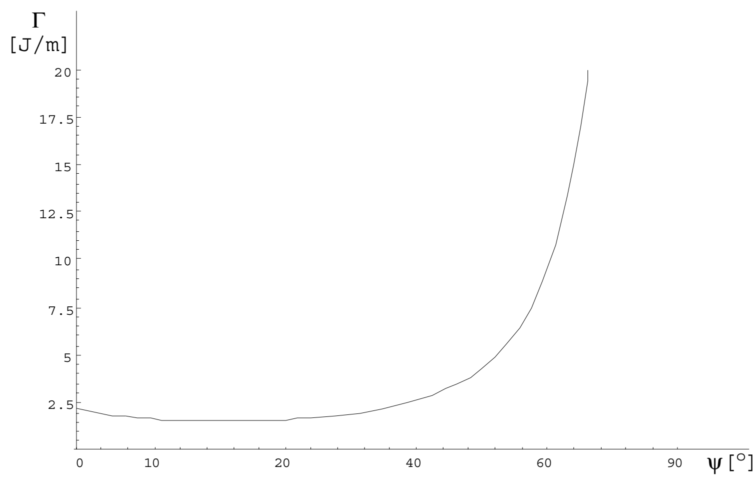

Figure 6. Interface toughness curve

For a given bimaterial interface, $\Gamma(\hat{\psi},\phi)$ is a surface in the K–space, which in principle can be determined directly by experiments. Upon loading, a crack will not propagate unless the driving force reaches the toughness surface, i.e. the mixed mode fracture condition is:

$$G(\hat{\psi},\phi)=\Gamma(\hat{\psi},\phi) \tag{30}$$

The fracture resistance is unambiguously specified by a surface $\Gamma(\hat{\psi},\phi)$ together with a length $\hat{L}$ for the definition $\hat{\psi}$. Specifically, $\Gamma(\hat{\psi},\phi)$ is the critical value of the energy release rate required to advance the crack in the interface under the mode mixity $\hat{\psi}$ and ϕ. Interface fracture toughness of several bimaterial systems has been measured by Wang and Suo [14], Cao and Evans [15], Liechti and Chai [16], and Stout et al. [17].

2. INTERPRETATION OF INTERFACIAL FRACTURE BY THE RICE–THOMSON MODEL

The major difference between a monolithic solid and an interface is that the response of an interface crack depends not only on structure of the interface, but also on the direction of the crack propagation and local loading conditions. The directionality of interfacial cracking may be understood in terms of the competition between dislocation emission from the crack tip and decohesion of the interface [3]. Recently developed Rice–Thomson model significantly helps in understanding the problems of the misorientation and cracking direction dependence of fracture behaviour. This model treated dislocation emission on a slip plane that intersects the crack front, as it will be shortly described.

2.1. The Rice–Thomson model

Immediately ahead of the tip, two different deformation mechanisms are acting, Fig. 7.

The near tip field for stationary cracks is divided into angular sectors in which the stress is constant and changes discontinuously at sector boundaries. The resulting sector arrangement is shown in Fig. 7a and b, for ideally plastic materials with crack tip along the [110] direction. Active slip plane traces are marked within each sector. Regular shear means the zone is parallel to the corresponding slip plane trace (Fig. 7c); kinking shear means the zone is perpendicular to the corresponding slip plane trace (Fig. 7d) and complex shear is a combination of shearing along two slip planes, involving regular or kinking shear, depending on whether the zone is perpendicular or parallel to slip planes trace.

In the ductile configuration the zone of concentrated shearing ahead of the tip corresponds to regular shearing, it can be accomplished by moving dislocation, nucleated at the crack tip along the slip plane, or by activation of a small number of internal sources, which allow dislocation to glide towards and away from the tip along that slip plane. However, the corresponding zone in the brittle orientation requires a kinking shear type mode, which must be accomplished by dislocation dipoles nucleated from a profusion of internal sources, and may not fully relax the crack. When the number of sources is limited or when their activation energy is large it might be difficult to generate and move these types of dislocations, leading to brittle fracture.

The Rice–Thomson model states that the ductile versus brittle response of an interfacial crack is determined by the competition between dislocation emissions from the crack tip and atomic decohesion of the interface. The energy release rate for dislocation emission from the crack tip G_{disl}, and the energy release rate for cleavage, G_{cleav}, are compared to determine whether dislocation emission from the crack tip or atomic decohesion will occur first. If $G_{disl} < G_{cleav}$, then dislocation emission will occur first, thereby blunting the crack tip and reducing the high crack tip stress field required for cleavage. In this case, the interface is interpreted as intrinsically ductile. If $G_{disl} > G_{cleav}$ then atomic decohesion will occur first, thereby producing cleavage-like intergranular brittle fracture. In this case, the interface is judged as intrinsically brittle. This competition process is shown schematically in Fig. 8.

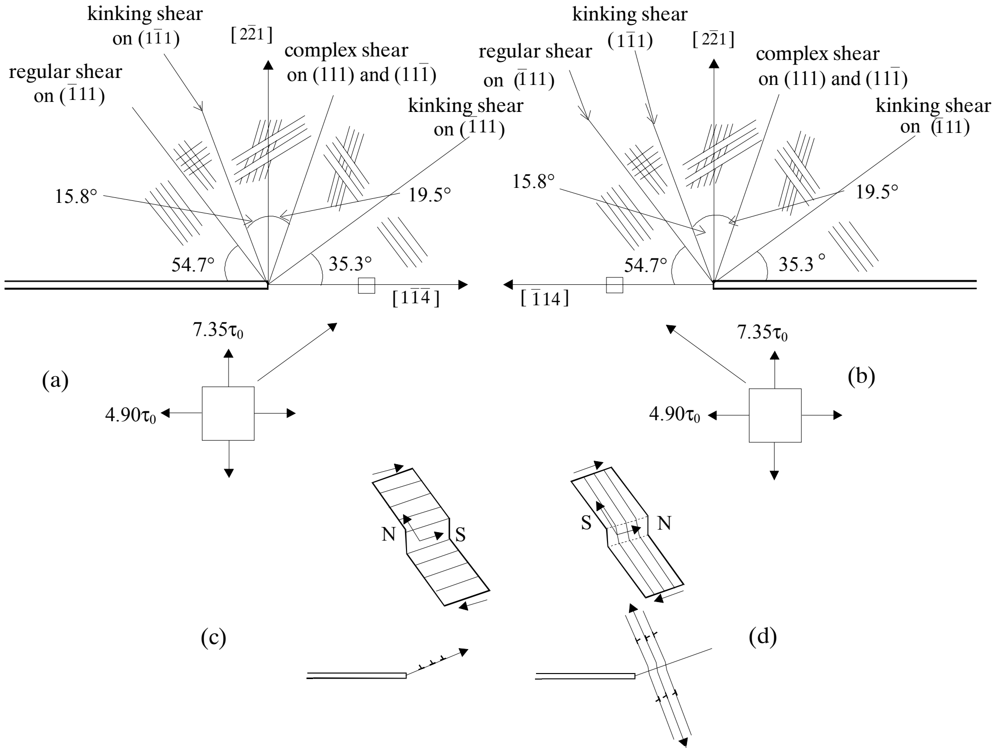

Figure 7. Sector arrangement for ideally plastic material with crack tip along the [110] direction: a) brittle orientation; b) ductile orientation; c) regular shearing mode; d) kinking shearing mode

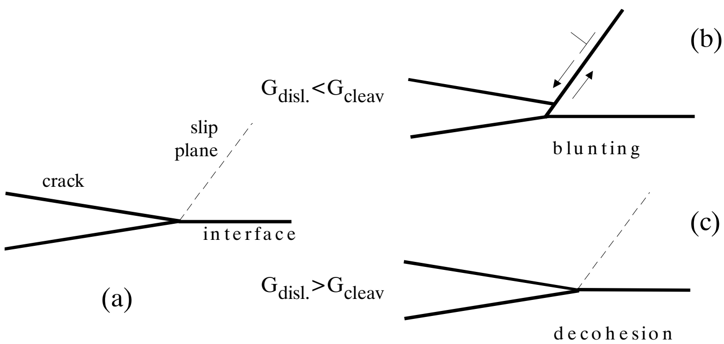

Figure 8. a) Schematic representation of a stationary, atomistically sharp crack; b) the competition between dislocation emission from the crack tip; c) decohesion of the interface ahead of the crack

The competition between cleavage and dislocation emission depends on type of crystal interface and crack growth direction in the interface. These effects are divided into a geometric and a structural factor. The first is a measure of relative orientation of the crack and available slip planes in adjoining crystals and determines the energy release rate for dislocation emission from the crack tip. The second is a measure of the interface structure and determines the propensity for impurity segregation to reduce the decohesion energy of the interface, Wang and Anderson [19].

The energy release rate for cleavage can be calculated from the criterion for crack growth in the absence of plasticity, Rice [21]:

$$G_{cleav} \geq 2\gamma_{int} \tag{31}$$

where $2\gamma_{int}$ is the decohesion energy of the interface and is the reversible work of separating against atomic cohesive forces, the interface along which the crack grows.

Detailed thermodynamic analyses have shown that if the separation process is rapid, compared to the diffusion time scales for the solute in the bulk or along the interface, so that the grain boundary excess Γ remains unchanged, the reversible work of separation is given by:

$$2\gamma_{int} \cong 2\gamma_o - (\Delta g_b - \Delta g_s)\Gamma \tag{32}$$

where $2\gamma_o = 2\gamma_s - \gamma_b$ is the work of separation in absence of an impurity; γ_s and γ_b are, respectively, the surface and grain boundary free energies at $\Gamma = 0$, Δg_s and Δg_b are the segregation energies from the bulk to the surface and to the boundary, Γ is the solute excess in the grain boundary or on the free surface. Each of the terms on the right hand side of Eq. (32) accounts for the structural dependence of the decohesion energy of the interface.

The critical local crack tip loading for dislocation emission can be expressed as a critical energy release rate at which stable equilibrium of dislocation loop becomes unstable. For the simplified geometry adopted in Fig. 9, the dislocation loop shape is described only by a semicircle of radius r. In this case, the condition for spontaneous dislocation emission is obtained by, first, minimizing the total energy of the cracked body with respect to r, and next, finding the condition where the second order derivative of energy changes from positive to negative, Rice [21].

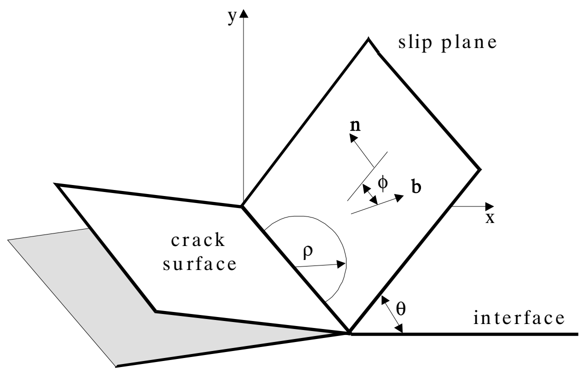

Figure 9. Geometry used for the analysis of dislocation emission on an inclined slip plane

For the case shown in Fig. 9, where the crack tip lies along the intersection of a slip plane and the interface, the terms in the total energy which depend on r are given by:

$$E_{total}(r) = E_{self} + E_{ledge} - W_{stress} \tag{33}$$

where E_{self} is self energy of the loop, including the energy of the dislocation core along the loop and image effects present from the free surfaces of the crack; E_{ledge} is the energy of the ledge created by crack tip blunting due to dislocation emission, and W_{stress} is the

Peach–Koehler type work of expanding the loop through the crack tip stress field. The last term represents the driving force for dislocation emission.

All terms on the right hand side of Eq. (33) depend on the geometry of the crack and available slip systems.

The self energy of a semicircular shear dislocation loop emanating from a crack front, which is contained in an active slip plane, has been shown to be one–half of the energy of a full dislocation loop in an uncracked body plus a term characterized by a correction factor *m*, Rice [21]:

$$E_{self} = \pi r A_o \ln\left(\frac{8r}{e^2 r_o}\right) + \pi r A_o \ln m = \pi r A_o \ln\frac{8rm}{e^2 r_o} \tag{34}$$

where r is the radius of the dislocation loop; r_o is the dislocation core cut-off radius; A_o is the pre-logarithmic energy factor of the loop, determined from the elastic constants of the material; the crystallographic orientation of the loop plane and magnitude b of the Burgers vector, **b**. For the isotropic case A_o is:

$$A_o = \mu b^2 \frac{2-\nu}{8\pi(1-\nu)} \tag{35}$$

where μ is the elastic shear modulus, and ν is Poisson's ratio.

The dependence of self-energy on the crystallographic orientation of the loop is contained in A_o, r_o and m. However, in cases where dislocation motion in a given material is limited to a single family of crystallographic planes, A_o is constant. Value of dislocation core cut-off, r_o, is a function of the line- and Burgers vector orientations. For single family of crystallographic planes, it is reasonable to approximate r_o as a constant.

The strongest orientation dependence enters through m, and is expressed in terms of the angle θ between the inclined slip plane and uncracked extension of the crack plane, and the angle ϕ between the normal to the crack front, and the b-vector, Fig. 9. For a semicircular shear dislocation loop, m has the form Anderson, Wang and Rice [22]:

$$m(\theta,\phi) \cong \exp\left[1.23\cos^2\phi \cdot \ln m_1 + 0.86\sin^2\phi \cdot \ln(2\cos\theta/2)\right] \tag{36}$$

where

$$m_1 = 2\cos\frac{\theta}{2}\exp\left[-\frac{1}{2}\sin\frac{\theta}{2}\sin\frac{3\theta}{2}\right] \tag{37}$$

is a correction factor for a straight edge dislocation, parallel to the crack front and with $\phi = 0$.

Evaluation of the ductile or brittle behaviour of various interface in a given polycrystal will depend on values of θ and ϕ. The self-energy will vary with $m(\theta,\phi)$, and will therefore be a monotonically decreasing function of θ and ϕ.

From the geometry in Fig. 9, the ledge energy per unit length of the blunted crack front is (Wang and Anderson [19]):

$$E_{ledge} = \gamma_{ledge} b\cos\phi\sin\theta \tag{38}$$

where γ_{ledge} is the free energy per unit area of the ledge, and together with the factor $b\cos\phi$ - is the fully formed ledge area per unit length of the blunted crack front. The factor $\sin\theta$ is included to approximate the effect of the proximity of the crack walls to the ledge at low values of θ, (Rice [21]).

An important contribution to the geometric dependence of dislocation emission is from the work, W_{stress}, of the Peach–Koehler force on the expanding loop. This term is calculated by integrating, over the loop area, the product of the resolved shear stress, τ on the slip plane in the direction of **b** times the displacement b. The resolved shear stress produced by a near tip field characterized by local stress intensity factor K may be written as:

$$\tau = \frac{1}{\sqrt{r}}\left[\mathrm{Re}\left(Kr^{i\varepsilon}\right)S_{\mathrm{I}} + \mathrm{Im}\left(Kr^{i\varepsilon}\right)S_{\mathrm{II}} + K_{\mathrm{III}}S_{\mathrm{III}}\right] \tag{39}$$

where r is the distance from the crack tip, and S_α (α = I, II, III) represent the geometric Schmid factors, Anderson, Wang and Rice [22]:

$$\begin{aligned} S_{\mathrm{I}} &= \frac{1}{\sqrt{2\pi}}\Sigma^{\mathrm{I}}_{r\theta}(\theta)\cos\phi \\ S_{\mathrm{II}} &= \frac{1}{\sqrt{2\pi}}\Sigma^{\mathrm{II}}_{r\theta}(\theta)\cos\phi \\ S_{\mathrm{III}} &= \frac{1}{\sqrt{2\pi}}\cos\frac{\theta}{2}\sin\phi \end{aligned} \tag{40}$$

where $\sum^{\mathrm{I}}_{r\theta}(\theta)$ and $\sum^{\mathrm{II}}_{r\theta}(\theta)$ are angular functions:

$$\begin{aligned} \Sigma^{\mathrm{I}}_{r\theta}(\theta) &= \frac{\mathrm{sh}\,\varepsilon(\pi-\theta)}{\mathrm{ch}\,\varepsilon\pi}\sin\frac{3\theta}{2} + \frac{e^{-\varepsilon(\pi-\theta)}}{\mathrm{ch}\,\varepsilon\pi}\sin\frac{\theta}{2}\left(\cos^2\frac{\theta}{2} - \varepsilon\sin\theta\right) \\ \Sigma^{\mathrm{II}}_{r\theta}(\theta) &= \frac{\mathrm{ch}\,\varepsilon(\pi-\theta)}{\mathrm{ch}\,\varepsilon\pi}\cos\frac{3\theta}{2} + \frac{e^{-\varepsilon(\pi-\theta)}}{\mathrm{ch}\,\varepsilon\pi}\cos\frac{\theta}{2}\left(\sin^2\frac{\theta}{2} + \varepsilon\sin\theta\right) \end{aligned} \tag{41}$$

In the case of the dislocation emission from the crack tip, for all r of order **b**, the Burgers vector, or the dislocation loop in consideration, $Kr^{i\varepsilon} \cong Kb^{i\varepsilon}$. Based on this approximation, the loading phase angle ψ, might be defined by

$$Kb^{i\varepsilon} = |K|e^{i\psi'} = \mathrm{ch}\,\pi\varepsilon\sqrt{GE^*}\cdot e^{i\psi'} \tag{42}$$

Here $E^* = 2\bar{E}_1\bar{E}_2\big/\left(\bar{E}_1+\bar{E}_2\right)$; $\bar{E}_i = E_i\big/\left(1-\nu_i^2\right)$; $\psi' = \psi - \varepsilon\ln(L/b)$ is the atomic scale phase angle; L is the characteristic length connected with the dimension of the specimen; ψ is the loading phase angle.

Using (34), (38), (39) and that the critical condition for nucleation of dislocation is determined by rendering the first and second derivatives of E_{total} with respect to r equal to zero, the critical stress intensity factor is given by:

$$\left[\mathrm{Re}\left(Kb^{i\varepsilon}\right)S_{\mathrm{I}} + \mathrm{Im}\left(Kb^{i\varepsilon}\right)S_{\mathrm{II}} + K_{\mathrm{III}}S_{\mathrm{III}}\right]_{disl} = 0.76\frac{A_o}{b}\sqrt{\frac{m}{r_o}}\Lambda \tag{43}$$

where $\Lambda = \exp\left(\dfrac{2\gamma_{ledge}b\cos\Phi\sin\Theta}{\pi A_o}\right) = \exp\left(\dfrac{E_{ledge}}{\pi A_0}\right)$.

The Eq. (43) may be used to observe a directional dependence of crack growth and phase angle effects.

2.2. Application of the Rice–Thomson model to bicrystals and bimaterials

2.2a. Dislocation nucleation and emission from crack tip in copper bicrystals, Fig. 10

In the calculations, the core cut-off is assumed to be equal to the Burgers vector, $r_o = b$. The ledge energy, $\gamma_{ledge} = 0.1\gamma_s$, where γ_s = 1.725 J/m^2 and isotropic elasticity is presumed.

For Cu [110] symmetrically tilted bicrystals (Wang [18]), where the crack front lies along the tilt axis, the likely dislocations to be activated are partial dislocations with $b = a\langle 112\rangle/6$ and $\phi = 60°$ and $\phi = 0°$. The partial dislocations with $\phi = 0°$, such that the Burgers vector is perpendicular to the crack front, have a lower value of energy release rate for dislocation emission then those with $\phi = 60°$ and are favoured to pop out first. However, the partial dislocation with $\phi = 0°$ reaches the stable equilibrium due to the stacking fault cracked. Upon nucleation of partial dislocation with $\phi = 60°$, the stacking fault is removed and the dislocation pair expands unstably from the crack tip.

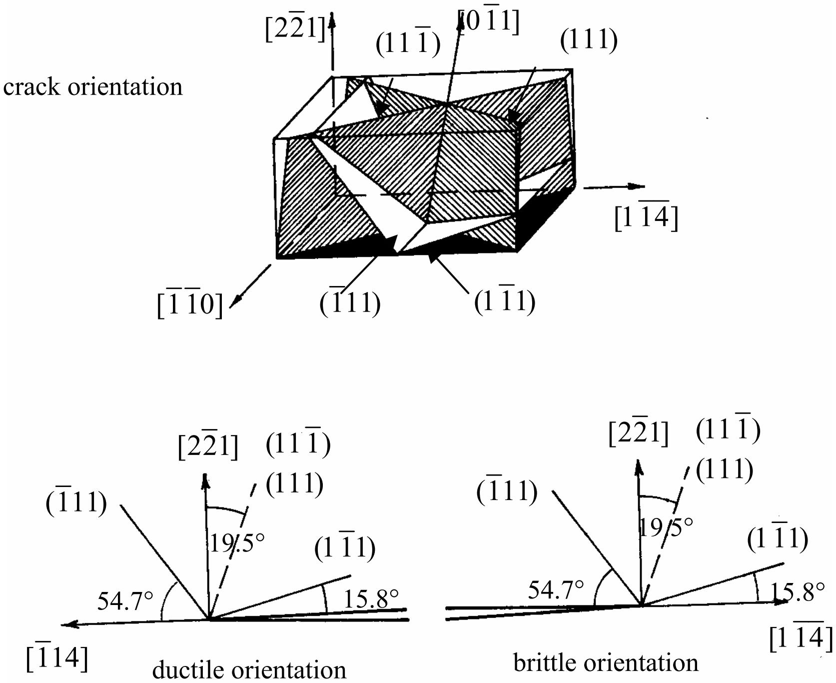

Figure 10. A schematic illustration of the crystallographic configurations in the Cu $\Sigma 9[110](2\bar{2}1)$ bicrystals.

The critical energy release rate for dislocation emission is determined by minimum value of G_{disl} required to nucleate the partials with $\phi = 60°$. The results are shown in Fig. 11.

The directionality observed in $\Sigma 9$ copper bicrystals might be understood by comparing predictions for opposite cracking directions. For cracking in the $[\bar{1}14]$ direction, the most likely dislocation to be activated are partials on the $(1\bar{1}\bar{1})$ slip plane with $\theta = 54.7°$, $\phi = 60°$ and $G_{disl} = 3.8$ J/m^2. If the crack growth direction is reversed in the $[1\bar{1}\bar{4}]$ direction, the most active slip systems remain the same, but in this case, $\theta = 125.3°$ and the predicted value of G_{disl} is 8.3 J/m^2. Dislocation emission is preferred in the $[\bar{1}14]$ direction.

An important observation in Fig. 11 is that crack tip response for $\Sigma 9$ boundary is ductile when the interface crack is initiated by fatigue in the $[\bar{1}14]$(–) direction, but is brittle when the crack is oriented in the opposite (+) direction. This is in agreement with the experimental results.

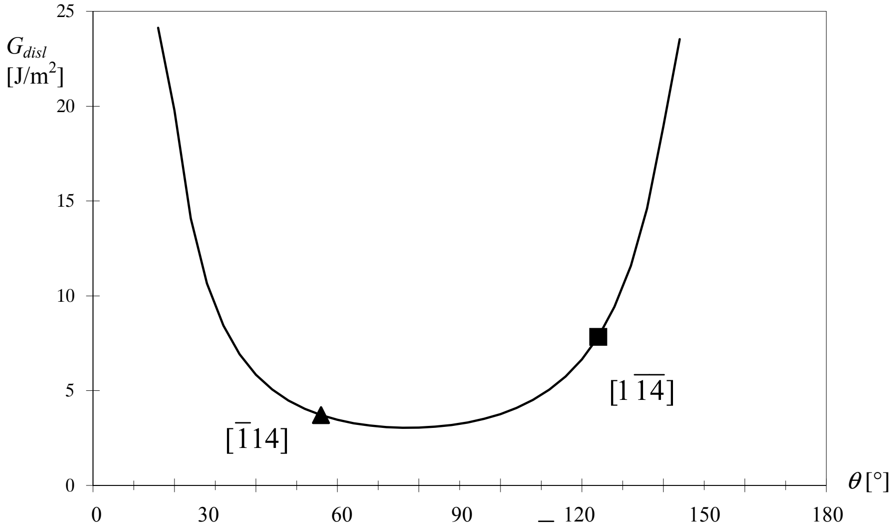

Figure 11. The G_{disl} versus θ for Σ9[110]/($\bar{2}21$) bicrystals and $\phi = 60°$

2.2b. Dislocation nucleation and emission from crack tip in Fe-2.7% Si bicrystals, Fig. 12

For [100] symmetrically tilted Fe bicrystals the likely dislocations to be active from the crack tip lying along [100] might be those with $b = a\langle 111\rangle/2$ and $\phi = 35.26°$ on {110} plane, Wang and Mesarović [20]. The critical G_{disl} versus θ curve predicted by the Rice–Thomson type model is presented in Fig. 13. Here the core cut-off is $r_o = 2/3b$ (dashed line) or $r_o = 1.045b$ (solid line), the ledge energy is $\gamma_{ledge} = 0.4\gamma_s$ and an isotropic elasticity is presumed.

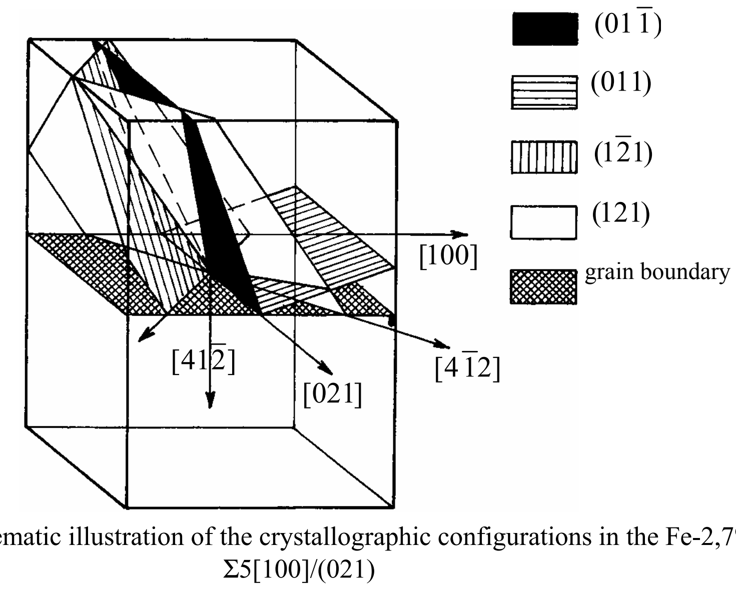

Figure 12. A schematic illustration of the crystallographic configurations in the Fe-2,7% Si Σ5[100]/(021)

Figure 12 shows that when the crack propagates in negative direction, $[01\bar{2}]$, the active slip plane would be $(01\bar{1})$ with $\theta = 71.57°$ and $G_{disl} = 6.3$ J/m^2 for $r_o = 2/3b$, i.e. $G_{disl} = 3.37$ J/m^2 for $r_o = 1.045b$. In the positive direction, $[01\bar{2}]$, the active slip plane would still be $(01\bar{1})$ but in this case $\theta = 108.43°$ and $G_{disl} = 9.6$ J/m^2 for $r_o = 2/3b$, i.e. $G_{disl} = 5.15$ J/m^2 for $r_o = 1.045b$, about twice then in the negative direction. Thus, the crack growth in this bicrystal is expected to be ductile in the negative direction and brittle in the positive direction.

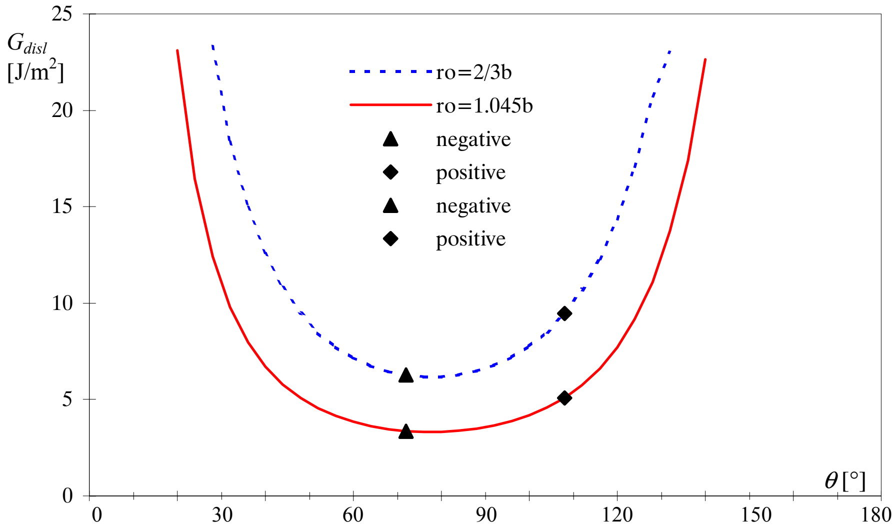

Figure 13. The G_{disl} versus θ for FeΣ5[100]/(021) bicrystals and ϕ = 35.26°

2.2c. Dislocation nucleation and emission from the interfacial crack tip in copper/ sapphire bimaterials, Fig. 14

For the Cu/Al_2O_3 bimaterials system under pure bend conditions, the phase angle is 52° and the atomic scale phase angle is ψ' = –79°, Mesarović and Kysar [23]. Assuming the sapphire is purely elastic and dislocation can only be activated in Cu, the critical energy release rate for dislocation emission from the $(2\bar{2}1)_{Cu}$ crack tip versus θ is presented in Fig. 14.

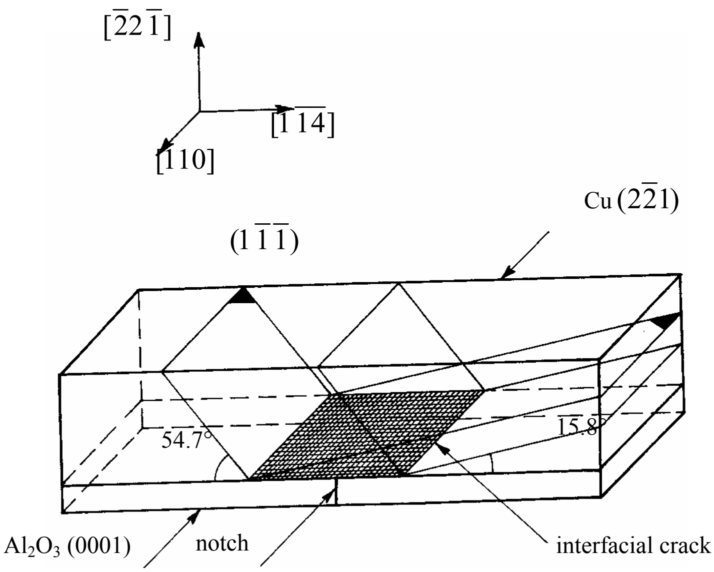

Figure 14. A schematic illustration of the Cu/sapphire specimen

The active slip systems have changed from the $(1\bar{1}\bar{1})$ slip plane to the $(1\bar{1}1)$ slip plane with θ = 125.3° and θ = 15.8°, respectively. Due to the large negative phase angle ψ' = –79°, the $(1\bar{1}\bar{1})$ system are favorable for nucleation, so that θ= 125.3°. From Eq. (57), energy release rate for positive $[1\overline{14}]$ direction is G_{disl} = 0.86 J/m^2. For $(2\bar{2}1)_{Cu}$ interface and negative $[\bar{1}14]$ crack direction, the active slip systems have changed the $(1\bar{1}\bar{1})$ to the $(1\bar{1}1)$ slip plane with θ= 54.7° and θ= 164.2°, respectively. Due to the large negative phase angle ψ' = –79°, the system $(1\bar{1}1)$ are favourable for nucleation, so that θ= 164.2°. From Eq. (43), energy release rate for negative $[\bar{1}14]$ direction is G_{disl} = 4.9 J/m^2.

From Figs. 10 and 15 it may be concluded that the cracking of copper bicrystals is ductile in a negative direction, while in Cu/sapphire bimaterials, cracking behaviour is brittle in the negative direction. As in bicrystals, G_{disl} is a function of θ, but due to mode II loading conditions that are the most in the bimaterials, the minimum value occurs at large values of θ angle, $\theta \approx$ 130°. The minimum value of G_{disl} for bimaterials is much lower then for bicrystals.

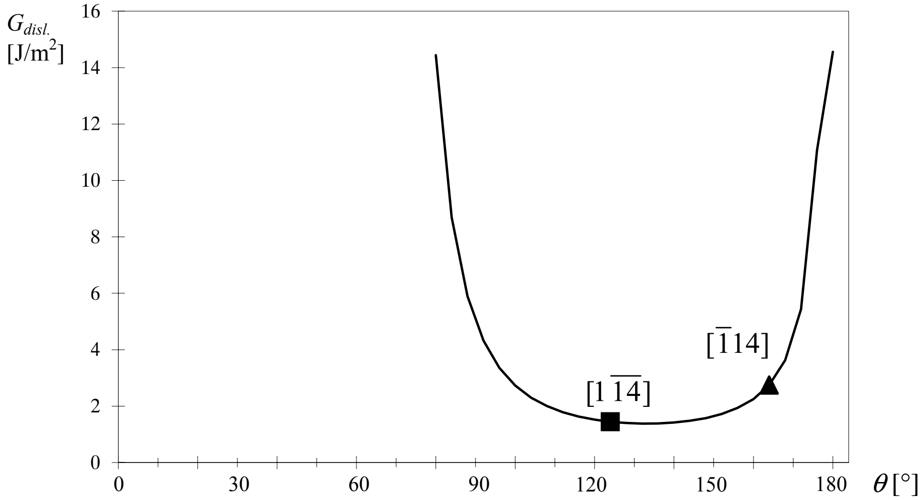

Figure 15. The critical G_{disl} versus θ for Cu/sapphire interfaces loaded in pure bending. The atomic scale phase angle is –79°.

The phase angle effect plays an important role in bimaterial systems. The phase angle effect is shown in Fig. 16, which gives G_{disl} versus ψ' for various slip plane inclination angles. Solid lines correspond to angles associated with direction $[1\overline{14}]$ and dashed lines correspond to angles associated with direction $[\bar{1}14]$. Comparison of curves at ψ'= 0° and ψ'= 79° shows that favoured directions for dislocation emission reverse when the phase angle is altered.

Crack tip fields for the crack along the interface between elastically dissimilar solids are characterized by one real and one complex stress intensity factor, where the latter couples two of the classically separate crack tip modes.

The variation of the local phase angle, indicating stress field mode coupling, at the near atomic scale of dislocation nucleation, is an important aspect of the problem.

The dislocation problem arises in evaluating the competition between atomically brittle decohesion and plastic blunting at interfacial crack tips. Results confirm that both the properties of the interface and the direction of attempted cracking along it are important for the outcome of that competition; the latter arises because of the different stressing of slip systems, associated with different direction of cracking.

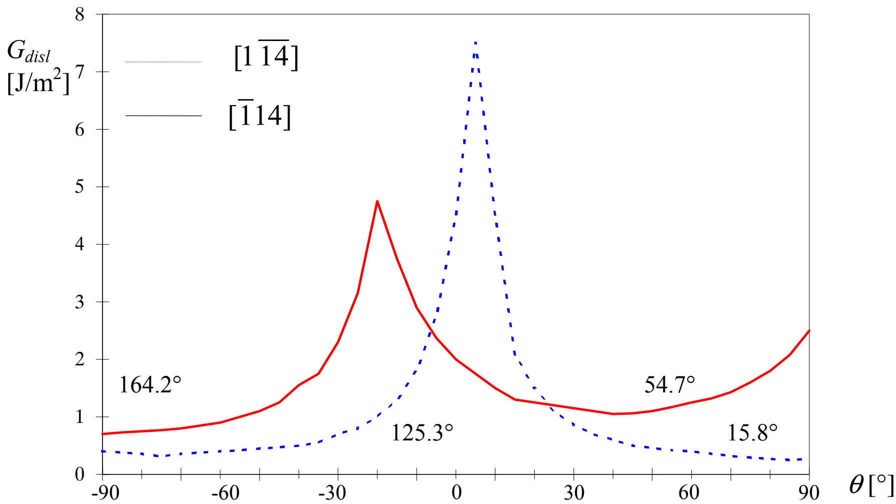

Figure 16. G_{disl} versus ψ' for Cu/sapphire bimaterials. The numbers attached are inclination angles θ of the potentially active slip planes

3. INTERFACE CRACKS IN BILAYERS

Results from section 1 are used to analyse a semi-infinite interface crack between two isotropic elastic layers under generalized edge loading conditions, Fig. 17, Bagchi and Evans [24]. The problem shown in Fig. 17c is a superposition of problems shown in Fig. 10a and b.

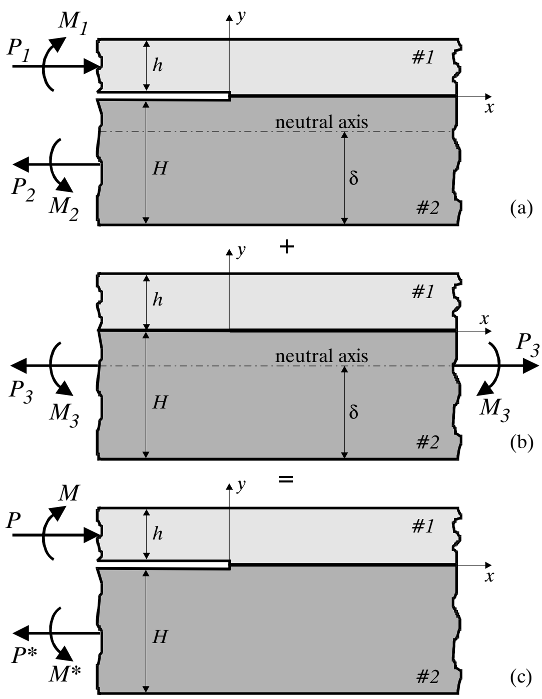

Figure 17. Superposition scheme for the bimaterial structure with generalized edge loading

Force and moment equilibrium dictate that (Suo and Hutchinson [25]):

$$P_1 - P_2 - P_3 = 0 \tag{44}$$

$$M_1 - M_2 + P_1\left(\frac{h}{2} + H - \delta\right) + P_2\left(\delta - \frac{H}{2}\right) - M_3 = 0 \tag{45}$$

Only four among these six loading parameters are actually independent. These are P_1, P_3, M_1 and M_3. The number of independent load parameters can be further reduced to only two, through superposition (Fig. 17). These parameters are force and moment:

$$\begin{aligned} P &= P_1 - C_1 P_3 - C_2\frac{M_3}{h} \\ M &= M_1 - C_3 M_3 \end{aligned} \tag{46}$$

where the C's are dimensionless numbers. Following calculations in Bagchi and Evans [24], one obtains the necessary variables for calculating the complex stress intensity factor. Force and moment parameters are then:

$$\begin{aligned} P &= P_1 - \int_{H-\delta}^{H-\delta+h} \sigma_{xx}(y)\,dy \\ M &= M_1 - \int_{H-\delta}^{H-\delta+h} \sigma_{xx}(y)\left[y - \left(H - \delta + \frac{h}{2}\right)\right]dy \end{aligned} \tag{47}$$

and the energy release rate can be computed from the difference between energy stored in the structure per unit length far ahead, and far behind the crack tip:

$$G = \frac{1}{2E_1}\left[\frac{P^2}{Ah} + \frac{M^2}{Ih^3} + 2\frac{PM}{h^2\sqrt{AI}}\sin\gamma\right] \tag{48}$$

with:

$$A = \frac{1}{1+\Sigma(4\eta + 6h^2 + 3\eta^3)}, \quad I = \frac{1}{12(1+\Sigma\eta^3)}, \quad \sin\gamma = 6\Sigma\eta^2(1+\eta)\sqrt{AI} \tag{49}$$

Thus, the corresponding stress intensity factor is:

$$|K|^2 = \left[\frac{P^2}{Ah} + \frac{M^2}{Ih^3} + 2\frac{PM}{h^2\sqrt{AI}}\sin\gamma\right]\frac{p^2}{2} \tag{50}$$

where: $p = \sqrt{\dfrac{1-\alpha}{1-\beta^2}}$

The linearity and dimensional considerations lead to the following general expression:

$$K = \left[a\frac{P}{\sqrt{Ah}} + b\frac{M}{\sqrt{Ih^3}}\right]\frac{p}{\sqrt{2}}h^{-i\varepsilon} \tag{51}$$

where a and b are dimensionless complex numbers, which can be found by substitution of Eq. (50) into (51), yielding:

$$2\sin\gamma = \bar{a}b + a\bar{b} \tag{52}$$

such that:

$$a = e^{i\omega} \quad \text{and} \quad b = -ie^{i(\omega+\gamma)} \tag{53}$$

where ω is a real angular function of α, β and η, tabulated by Suo and Hutchinson [25]. In this paper, their results are substituted by Mathematica program simulation of ω, and it is presented by the following expression:

$$\omega = \frac{1-\eta}{1+\eta}\sqrt{\frac{\beta(1-\alpha)}{\alpha-\beta^2}} \tag{54}$$

Equation (51) can be written as:

$$K = K_1 + iK_2 = \frac{1}{\sqrt{2}}\left(\frac{P}{\sqrt{Ah}} - ie^{i\gamma}\frac{M}{\sqrt{Ih^3}}\right)\frac{p}{\sqrt{2}}h^{-i\varepsilon}e^{i\omega} \tag{55}$$

Taking as the reference length the film thickness h, one obtains:

$$\begin{aligned} K_1 &= \mathrm{Re}\left(Kh^{i\varepsilon}\right) = \frac{p}{\sqrt{2}}\left[\frac{P}{\sqrt{Ah}}\cos\omega + \frac{M}{\sqrt{Ih^3}}\sin\left(\omega+\gamma\right)\right] \\ K_2 &= \mathrm{Im}\left(Kh^{i\varepsilon}\right) = \frac{p}{\sqrt{2}}\left[\frac{P}{\sqrt{Ah}}\sin\omega - \frac{M}{\sqrt{Ih^3}}\cos\left(\omega+\gamma\right)\right] \end{aligned} \tag{56}$$

In accordance with Eq. (21), the mode mixity, at the prescribed length $r = h$ ahead of the crack tip for the planar conditions, is given by:

$$\psi = \mathrm{arctg}\left[\frac{\xi\sin\omega - \cos(\omega+\gamma)}{\cos\omega + \sin(\omega+\gamma)}\right] \tag{57}$$

$$\xi = \frac{Ph}{M}\sqrt{\frac{I}{A}} \tag{58}$$

The mode mixity ψ is plotted in Fig. 18 as a function of α for various film/substrate thickness ratios η. This diagram is obtained with variable ω, calculated by Mathematica program package.

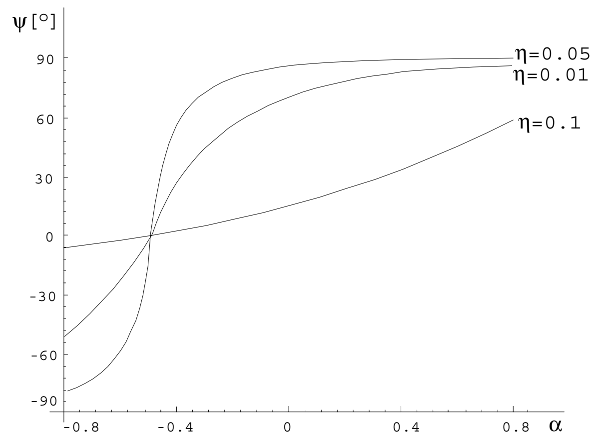

Figure 18. Mode mixity versus parameter α

The mode mixity obtained from (57), for various bimaterial systems, is shown in Fig. 19. This phase angle is small for the bimaterial system, while it takes the value $\psi = 50°$ for the homogeneous case and thin film/substrate systems.

Let us denote the energy release rate for semi-infinite crack along the interface as G_i, (given by Eq. 21, for the planar problem), and the energy release rate for steady-state substrate as G (given by Eq. 47). The ratio G/G_i is shown in Fig. 20 as a function of α for various film/substrate thickness ratios η. This ratio is relatively independent of the bimaterial system properties and it varies between 0.55 and 0.83.

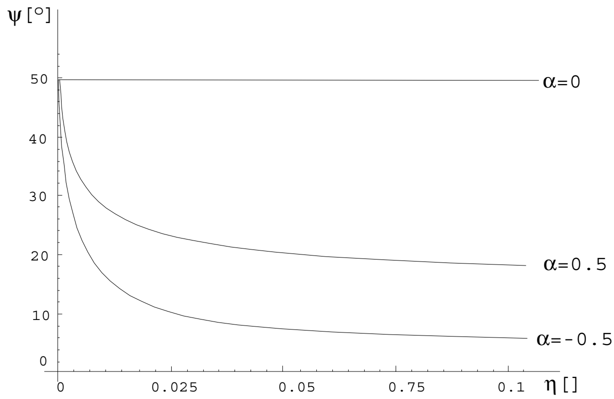

Figure 19. Variations of the mode mixity with thickness ratio η

Let G_C be the substrate toughness and let G_{iC} be the interface toughness. If

$$\frac{G_C}{G_{iC}} > \frac{G}{G_i} \tag{59}$$

the system is more likely to fracture by interface then substrate, and conversely.

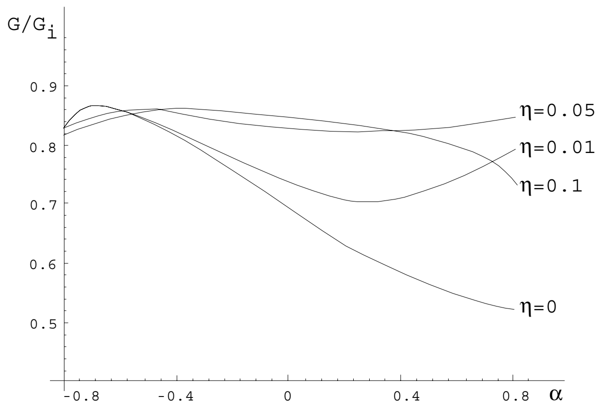

Figure 20. Energy release rate ratio as a function of parameter α

Comparing values of the energy release rate for the substrate or thin film with its values, one can define where the crack is going to propagate: into the substrate, into the thin film, or along the interface. Values of the energy release rate, the stress intensity factor, and mode mixity parameter can be determined in terms of only one dimensionless factor ω, which is a function of sample geometry and materials elastic properties. The thin layers problem, under conditions of residual tensile stresses, gives the appropriate model for solving problems in the area of composite materials manufacturing, electronic devices design, protective coatings problems, as well as for other applications.

REFERENCES

1. Williams, M.L., *On the stress distribution at the base of a stationary crack*, J. Appl. Mech., Vol. 79, pp. 104-109. (1957)
2. Sih, G.C., Rice, J.R., *The bending of plates of dissimilar materials with cracks*, J. Appl. Mech., Vol. 31, pp. 477-482. (1964)
3. Rice, J.R., Sih, G.C., *Plane problems of cracks in dissimilar media*, J. Appl. Mech., Vol. 32, pp. 418-423. (1965)

4. Erdogan, F., *Stress distribution in bonded dissimilar materials with cracks*, J. Appl. Mech., Vol. 32, pp. 403-410. (1965)
5. England, A.H., *A crack between dissimilar media*, J. Appl. Mech., Vol. 32, pp. 400-402. (1965)
6. Rice, J.R., *Elastic fracture mechanics concepts for interfacial cracks*, J. Appl. Mech., Vol. 55, pp. 98-103. (1988)
7. Hutchinson, J.W., Suo, Z., *Mixed mode cracking in layered materials*, Applied Mechanics, 29. (1992)
8. Shih, C.F., *Cracks on bimaterial interfaces: Elasticity and plasticity aspects*, Material Science and Engineering, A143. (1991)
9. Liu C., Lambros, J., Rosakis, A.J., *Highly transient elastodynamic crack growth in bimaterial interface: higher order asymptotic analysis and optical experiments*, J. Mech. Phys. Solids, 41. (1993)
10. Veljković, J., *Analysis of crack propagation on the bimaterial interface*, MS, Faculty of Mechanical Engineering, Kragujevac. (1998)
11. Veljković, J.M., Nikolić, R.R., *Edge effect on the coating delamination*, Fatigue 2003, 7-9th April 2003, Cambridge, UK. (2003)
12. Veljković, J.M., Nikolić, R.R., *Application of the interface crack concept to problem of a crack between the thin layer and the substrate*, Facta Universitatis, Series: Mechanics, Automatic Control and Robotics, Vol. 3, No.13, 2003, pp. 573-581. (2003)
13. O'Dowd, N.P., *Mixed-mode fracture mechanics of brittle/ductile interfaces*, Miss-Matching of Welds, ESIS 17, Mechanical Engineering Publications, London, pp. 115-128. (1994)
14. Wang, J.S., Suo, Z., *Experimental determination of interfacial toughness curves using Brazilian - nut sandwiches*, Acta Metall., 38, pp. 1279-1290. (1990)
15. Cao, H.C., Evans, A.G., *An experimental study of the fracture resistance on bimaterial interface*, Mech. Mater., 7, pp. 295-305. (1989)
16. Liechti, K.M., Chai, Y.-S., *Asymmetric shielding in interfacial fracture under in plane shear*, J. Appl. Mech., Vol. 28. (1991)
17. Stout, M.G., O'Dowd, N.P., Shih, C.F., *Fracture toughness of alumina/niobium interfaces: experiments and analysis*, Philosoph. Mag., 66, pp. 1037-1064. (1992)
18. Wang, J.S., *Fracture behavior of embrittled f.c.c. metal bicrystals and its misorientation dependence: Part I - experimental*, Acta Metall., Vol. 39, pp. 779-792. (1991)
19. Wang, J.S., Anderson, P.M., *Fracture behavior of embrittled f.c.c. metal bicrystals and its misorientation dependence: Part II - theory and analysis*, Acta Metall., Vol. 39. (1991)
20. Wang, J.S., Mesarović, S.Dj., *Directional dependence of corrosion fatigue of Fe-2.7% Si alloy bicrystals*, Acta Metall., Vol. 43, pp. 3837-3849. (1995)
21. Rice, J.R., *Tensile crack tip fields in elastic-ideally plastic crystals*, Mechanics of Materials 6, pp. 317-335. (1987)
22. Anderson, P.M., Wang, J.S., Rice, J.R., *Thermodynamic and mechanical models of interfacial embrittlement*, MECH, 131. (1988)
23. Mesarović, S.Dj., Kysar, J.W., *Continuum aspects of directionally dependent cracking of an interface between copper and alumina crystals*, Mechanics of Materials, pp. 272-280. (1996)
24. Bagchi, A., Evans, A.G., *The mechanics and physics of thin film decohesion and its measurement*, Interface Science, 3. (1996)
25. Suo, Z., Hutchinson, J.W., *Interface crack between two elastic layers*, Int. J. Fracture, Vol. 43, pp. 1-18. (1990)

A CONTRIBUTION OF FRACTURE MECHANICS TO MATERIAL DESIGN

Aleksandar N. Radović, Nenad A. Radović, Faculty of Technology and Metallurgy, Belgrade, S&Mn

INTRODUCTION

Failure of component/structure can be attributed to numerous reasons, as showed in Fig. 1. Causes of failure shown in Fig. 1 can be classified in two groups, i.e. causes driven by design activities (positions 2 and 3) and causes driven by fabrication procedure in all steps (positions 1, and 4 to 6). It can be concluded that major reasons for failure are related to fabrication, service, and maintenance, i.e. activities depending on "human factor". This latter behaviour can be improved by implementation of quality assurance and better operating and controlling organization. On the other hand, about 29.3% of all failures are caused by poor design or standards. Therefore, this segment was in the focus of research, primarily due to high price of very responsible constructions (nuclear and power plants, space and air industry, military applications).

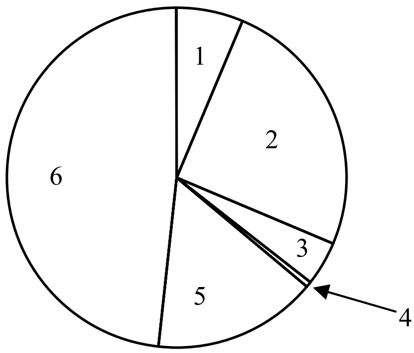

Figure 1. Causes for failure of steel structures; 1-poor quality of material (6.3%); 2-inappropriate project solution (design) (25.1%); 3-doubtful standards (4.2%); 4-inappropriate strength/properties (0.4%); 5-irresponsible manipulation, service, and maintenance (15.7%); 6-errors in fabrication and finalization of component/structures (48.3%), [1]

Material design is usually based on following requirements:

- mechanical properties: strength (YS–yield strength and/or UTS–ultimate tensile strength), elongation, deflection, toughness;
- technological properties (weldability, formability, machinability);
- physical properties (corrosion resistance, wear resistance, electrical/thermal conductivity).

Traditional design implements the safety factor (SF) as a safety measure of a construction. The allowed stresses were calculated from the YS (or UTS) and SF ratio. This approach was rational only for structures in which plastic yielding was expected to occur, i.e. when no brittle fracture was expected.

The YS to UTS ratio was also used, due to the "strength reserve" between values of YS and UTS, i.e. if plastic yielding ocurrs, large strain and strength increase can be measured. This approach is almost abandoned, because, for example, microalloyed steels have much higher YS in comparison to C or C-Mn steels, while the UTS is of similar values. These steels have strongly questioned the reliability of design relations and calculation. Both approaches have not answered to the need for safe design against brittle fracture.

It was A.A. Griffith who introduced in 1920 both the presence of defects, named cracks, and the first quantitative relationship for cracked solid materials. During the next 80 years, modifications and improvements of Griffith's early work has established fracture mechanics as a reliable methodology for quantification prediction of service behaviour of both material and component. Of course, since there is no perfect methodology, fracture mechanics should be used, bearing in mind all its limitations.

Fracture condition for an infinite plate with through-thickness crack is given by [2-4]:

$$K_{\mathrm{I}c} = \sigma\sqrt{\pi a} \tag{1}$$

where:

$K_{\mathrm{I}c}$ – minimal critical stress intensity factor, as	σ – design stress, introduced by	a – allowable flaw size or flaw detection sensitivity of equipment for
material property	service conditions	defects introduced during fabrication

This relationship may be used in one of several ways to design against a component failure. Its significance lies in the fact that the designer must make a decision – what is the most important feature in component service and design: certain materials properties; the design stress level as affected by many factors; or the crack size that can be tolerated for safe operation of the part. After making the decision, i.e. specifying two parameters in Eq. 1, the third parameter is easily calculated. This simple equation has imposed a major challenge to all material scientists. Development of material with, as high as possible, $K_{\mathrm{I}c}$ was in the focus. In Tables 1 and 2, the roles of major alloying elements in steels and (as an example) one Al alloy [2], are listed.

Table 1. Role of major alloying elements in steels [1]

Element	Role
C	Extremely potent hardenability agent and solid solution strengthener; carbides also provide strengthening but serve to nucleate cracks
Ni	Extremely potent toughening agent; lowers transition temperature; hardenability agent; austenite stabilizer
Cr	Provides corrosion resistance in stainless steel; hardenability agent in quenched and tempered steels; solid solution strengthener; strong carbide former
Mo	Hardenability agent in quenched and tempered steels; suppresses tempering embrittlement; solid solution strengthener; strong carbide former
Si	Deoxidizer; increases yield point and transition temperature when present in solid solution
Mn	Deoxidizer; forms MnS, which precludes hot cracking, caused by grain-boundary melting of MnS films; lowers transition temperature
Co	Used in maraging steels to enhance martensite formation and precipitation kinetics
Ti	Strong carbide and nitride former, stabilizer in stainless steels
V	Strong carbide and nitride former
Nb	Strong carbide and nitride former, stabilizer in stainless steels
Al	Strong deoxidizer; forms AlN, which pins grain boundaries and keeps ferrite grain size small. AlN formation also serves to remove N from solid solution, thereby lowering lattice resistance to dislocation motion and lowering transition temperature

It is clear that the increase of toughness in steel requires known mechanisms: grain refinement and/or alloying with Ni. On the other hand, toughness is not the only requirement for one material. Therefore, development of material that can meet all requirements together with reasonably low cost is the eternal question and challenge. The response of material scientists in the previous century and the contribution of fracture mechanics will be described on the development of steel.

Table 2. Role of major alloying elements in aluminium alloy 7178-T6 [1]

Element	Role
Zn	Found in Guinier-Preston zone and subsequently in $MgZn_2$ precipitates; strong precipitation-hardening agent
Mg	Some Mg_2Si formation, but mostly found in $MgZn_2$ precipitates and in solid solution
Cu	Exists in solid solution, in $CuAl_2$, and in Cu-Al-Mg type precipitates, and also in Al_7Cu_2Fe intermetallic compound
Fe	Initially reacts to form Al-Fe-Si intermetallic compiounds; impurity
Si	Initially reacts to form Al-Fe-Si intermetallic compiounds, prior to be replaced by Cu. Also forms Mg_2Si
Cr	Combines with Al and/or Mg to form fine precipitates which serve to grain refine
Mn	Exact role not clear
Sc	Grain refiner
RE	Grain refiners

The first and the oldest type of steel used as structural steels are plain carbon steels. The increase in strength was based on increase in carbon content. Carbon in Fe is a solid solution, with limited solubility. During deformation, as a result of applied stress, dislocations through their movement interact with obstacles, what in turn requires increase of applied strength for further deformation. Influence of carbon content on transition temperature in carbon steels is shown in Fig. 2 [5].

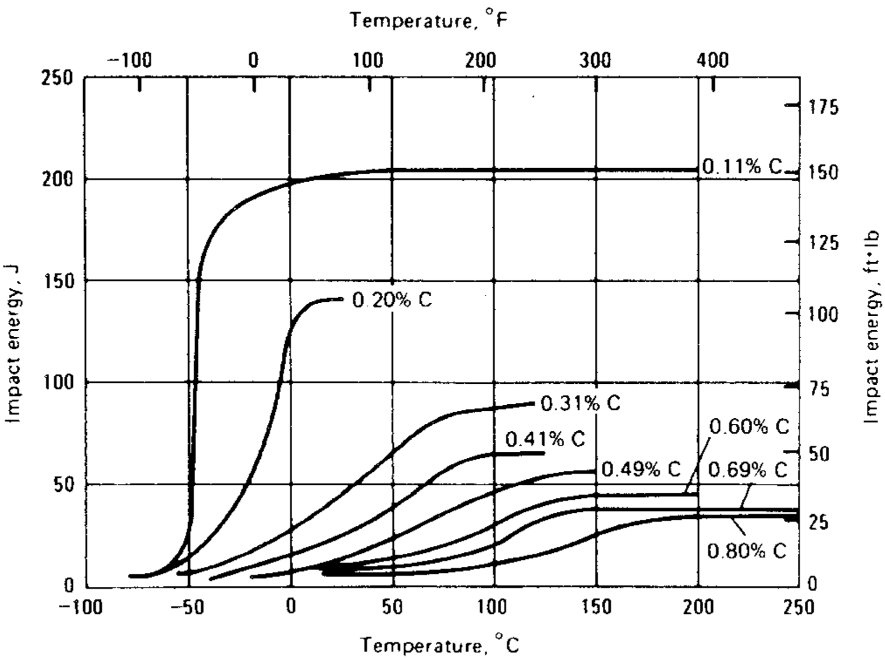

Figure 2. Influence of carbon content on transition temperature in steels [5]

It is clear that increase of carbon content increases transition temperature and lowers the upper shelf of impact toughness. In these steels, the microstructure depends on carbon content, and is mainly ferritic or ferritic–pearlitic, and in some cases even bainitic. Increase of carbon provides increase in carbide fraction. Carbides (cementite) are elongated with very sharp tips. They act as stress concentrators, decreasing toughness. Also, due to the low level of technology, it was not possible to remove S and P from the steel matrix during processing. Sulphur forms a low melting eutectic with Fe, distributed as a thin film on grain boundaries, leading to fracture. Influence of sulphur content on the transition temperature in carbon steels is shown in Fig. 3 [2].

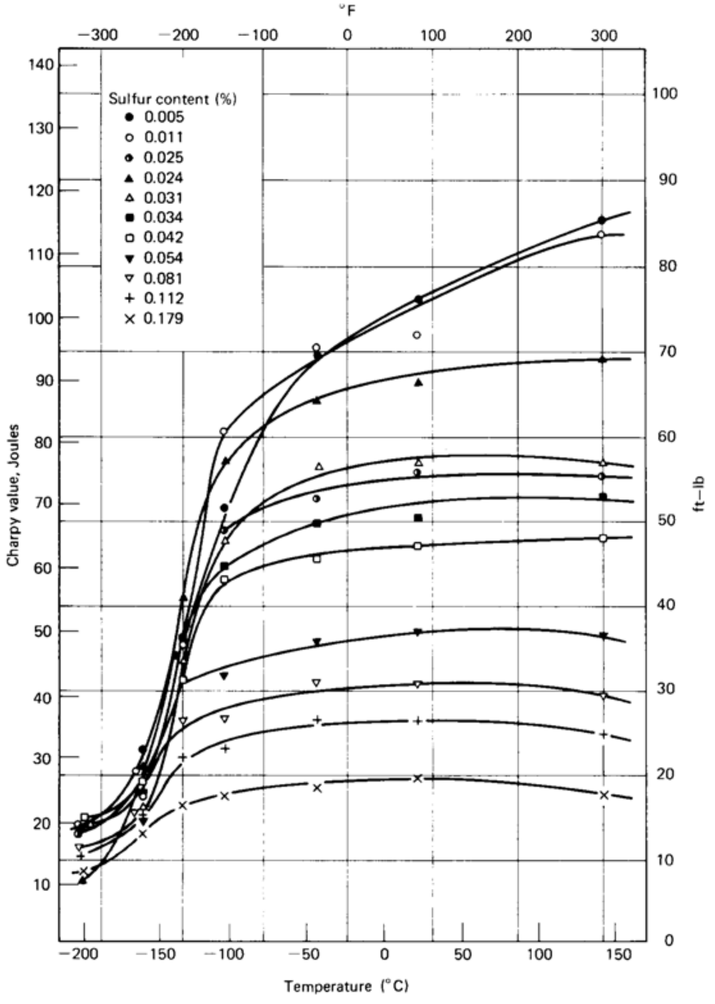

Figure 3. Influence of sulphur content on transition temperature in steels [2]

Increase of sulphur content has the same feature as the increase of carbon content. The requirement for steels with the, as low as possible, level of impurities has become a permanent challenge up to today! Generally speaking, increase of strength in plain C–steels, only due to increase in carbon could not deal with three major problems: low toughness and low transition temperature, poor weldability, and enormous weight of the construction itself. Also, in steels with more than 0.8% C, cementite is introduced, and can in some cases lead to formation of a carbide net, characterized by very sharp edges, behaving as stress concentrators.

As it can be seen from Fig. 2, for structural components that require improved mechanical properties (higher toughness), only low carbon steel can be used, but its strength is relatively low. Therefore, larger cross-sections should be used, what in turn leads to increase in weight of the construction and introduction of a third stress component. To overmatch these problems it was necessary to produce a new type of steel, C-Mn steels. Introduction of manganese had several roles: formation of sulphur containing inclusions, additional solid-solution strengthening, and lowering of the carbon level in steel, i.e. the carbon equivalent.

Manganese is substitutionally soluted in Fe, but the effect on strengthening is not pronounced since it depends on differences in atomic size. Mn and Fe are neighbouring elements in the periodic table. In structural steels, the content of Mn is in most cases limited to 1.5–1.7%, while larger content leads to increase of A_{r3} temperature and nucleation of pro-eutectoid ferrite [6]. In other steels, the Mn content may be as high as 12%. The influence of Mn on transition temperature in C-Mn steels is shown in Fig. 4, [7].

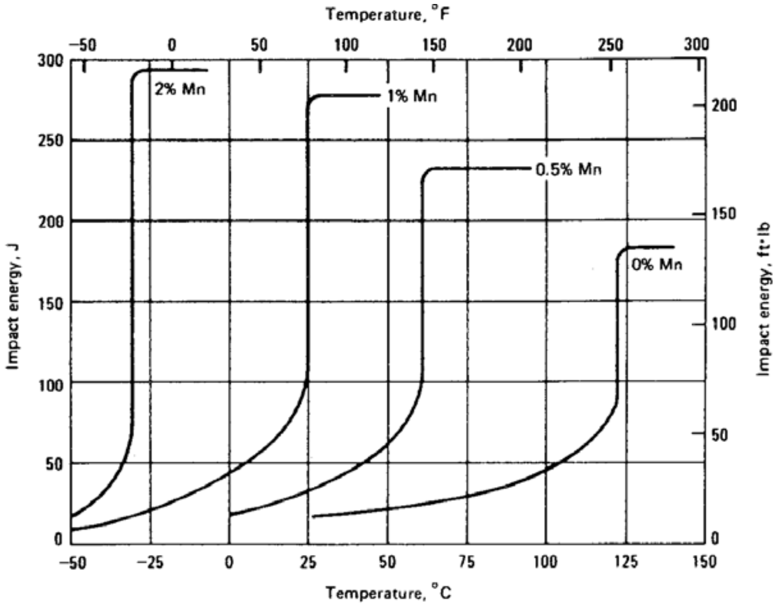

Figure 4. Influence of manganese on transition temperature in C-Mn steels

Increase of Mn content decreases transition temperature to very low temperatures. The main mechanism lies in the formation of MnS (manganese–sulphide). Manganese and sulphur have strong chemical affinity, leading to spontaneous formation of MnS inclusion during solidification of steel. The simplest way to completely remove S from the solid solution is the addition of sufficient amounts of Mn. This role of Mn ensured significant rise in toughness in low carbon steels, with exceptions in some medium carbon quenched and tempered steels. During further metal working, MnS inclusions can become elongated (rolling) or fractured and dispersed (forging). Presence of long elongated MnS inclusions in as-rolled steels is very dangerous, since the edges behave as stress concentrators, leading to fracture or to lamellar tearing in welded constructions. The next task was to eliminate sulphides as critical particles. The solution was additionally alloyed with Ca or rare earth elements (RE). This improvement was directly based on knowledge provided by fracture mechanics, i.e. addition of Ca primarily influences the shape of MnS. This feature is shown in Fig. 5 [1].

After rolling, MnS becomes elongated, with very sharp tip. This shape leads to behaviour close to stress concentration. On the other hand, in Ca-treated steels, during solidification, MnS starts to grow spherically. During both hot and cold deformation, due to higher Young's modulus, Ca treated particles remain spherical. This approach has been ever since of great practical importance, since it has focused attention on particle shape instead on the overall level of impurities. Therefore, since spherical second-phase particles are not critical for stress concentration, toughness is improved, without any influences on other mechanical properties. In modern structural steels, sulphur content is close to 0.0050%.

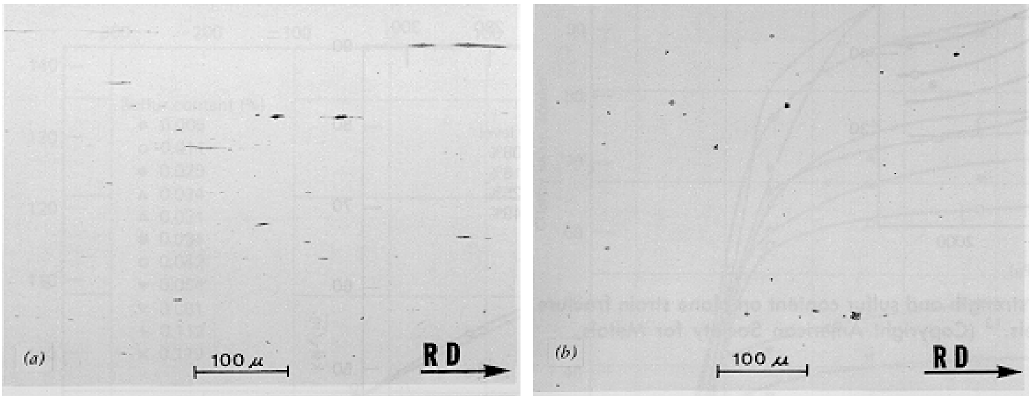

Figure 5. Shape of MnS after rolling (RD-rolling direction): (a) no Ca added; (b) addition of Ca [1]

The next problem steel producers faced was the presence of free oxygen, originating from air blowing in converter, or in furnace. In order to eliminate oxygen it was necessary to modify the chemical composition by adding a specific chemical element with strong affinity to oxygen. The answer came from the diagram of stability of oxides. Usually, Si or Al were used in an amount, estimated from the last chemical composition analysis during steel production (ladle after converter). This procedure introduced a new type of steels, so called killed steels, since oxide formation prevents bubbling of liquid metal. Furthermore, addition of Al became more interesting due to some observations showing that in some Al-killed steels at grain boundaries precipitation of AlN occurred, decreasing grain boundary mobility. This was observed in steels in which Al was added in high amount; air-blowing (instead of oxygen, nowadays) led to reasonable presence of nitrogen and strong affinity between Al and N. This was the first empirical case of grain boundary control, but significant industrial application did not follow. On one hand, physical metallurgy defined mechanisms of deformation strengthening and recrystallization, and on the other hand, it has been a great effort to choose elements from the periodic table that behave similarly to Al, but with much better control.

At first, on the laboratory scale, and later on full industrial scale, completely new steels were introduced, alloyed with Nb, Ti, V, Zr, B and other elements. In these steels, large increase in strength is due to addition of very small amounts of listed elements. Chronological use of microalloying (MA) elements in steels is given in Fig. 6 [8].

Prevailing of any element can be attributed to the price and advantages for thermomechanical processing. In microalloyed steels the small addition of alloying elements lead to intensive grain refinement and/or precipitation hardening due to precipitation of stable carbides, nitrides or carbonitrides.

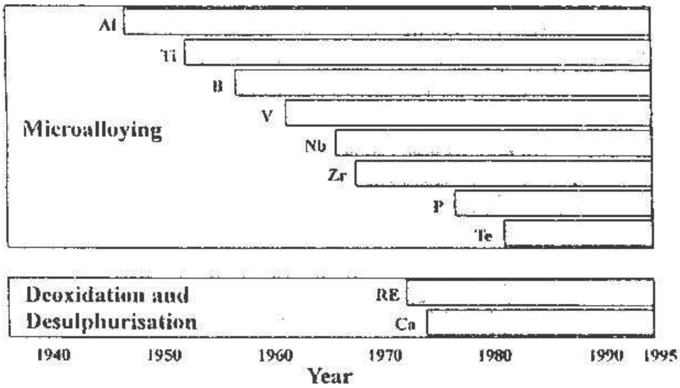

Figure 6. Chronological development of the use of microalloying (MA) elements in steels [8]

The main motives for developing MA steels were: significant increase in strength, resulting in either lowered construction weight or increased carrying capacity; thermo-mechanical treatment, a demand on the world market for steels with good weldability for pipelines, for which was not possible to use the "traditional" way to increase strength and toughness by heavier alloying- and carbon content. The microstructure of MA steels after hot working is typically fine-grained and consists of small and homogenous ferrite (α) grains. Small amount of cementite is also present (low pearlite steels are also used), together with fine dispersed carbonitride particles that can be observed only on electron microscope. The influences of niobium content and grain size on transition temperature in microalloyed steels are shown in Figs. 7 and 8, respectively.

Theoretically, the best combination of strength and toughness is obtained in fine grained steel by homogeneous distribution of dislocations in the homogenous mixture of two phases. One phase should be precipitated within the other (combination of coherent and semi-coherent precipitates) in the matrix, with grain size less than 1 μm [11]. This is an ideal case that can be achieved only in limited aspects in microalloyed steels, while, it is more pronounced in quenched and tempered (Q + T) steels. Since, Q + T steels contain some other elements, the role of nickel is of the greatest importance. The influence of nickel on transition temperature in steels is shown in Fig. 9 [12].

Figure 10 shows mechanisms for crack arrest in materials, indicating possible ways for improvement of toughness. Crack deflection and meandering are the dominant mechanisms of crack propagation in steels, confirming the experience that the best combination of strength and toughness is observed in quenched and tempered steels.

Crack arrest in these steels is caused by extended energy required for fracturing of carbides. Since carbides have large Young's modulus, the energy spent for their fracture is very high. This mechanism is positive, but costs of these steels are extremely high, and the processing window is very narrow. Both facts have determined very limited use of quenched and temepered (Q + T) steels. Therefore, large scale production of materials with similar microstructure was needed. The answer to FM demands was established in the mid-sixties in the last century. As discussed earlier, the steels are called microalloyed, due to very small addition of strong carbide and nitride forming elements: Nb, V, and Ti.

The first phase in producing (Q + T) steels is quenching, aimed to create martensite (supersaturated solution of carbon in the Fe matrix). Further tempering is aimed at: stress relieving; eliminating retained austenite; and precipitation of carbides (usually those of Cr and/or Mo and V). The carbides are nucleated both on grain boundaries and within grains. Finally, this microstructure consists of mixed ferrite and carbides. Significant number of very fine and closely distributed second phase particles enables a strong dispersion-hardening effect. On the other hand, large particles at long distances diminish the effect.

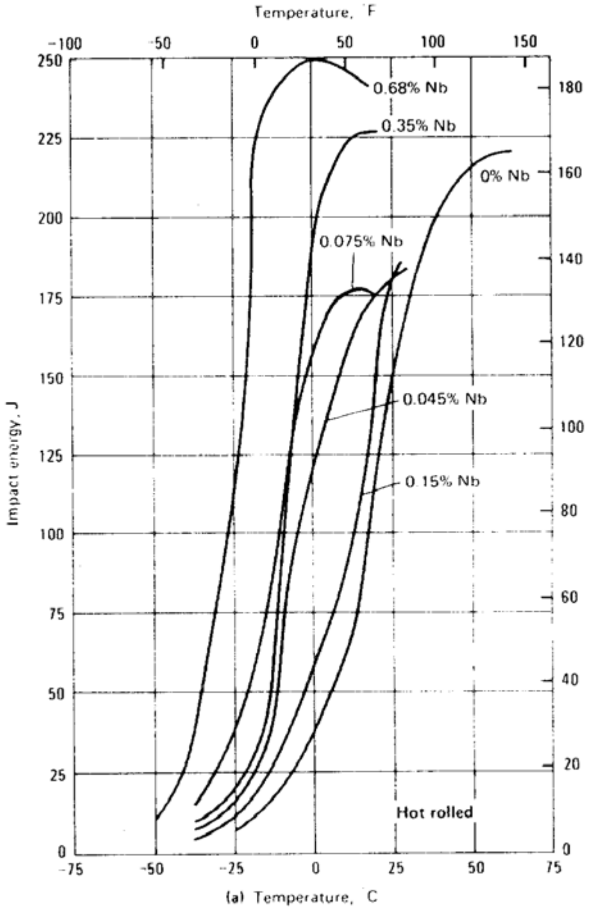

Figure 7. Influence of niobium content on transition temperature in steels [9]

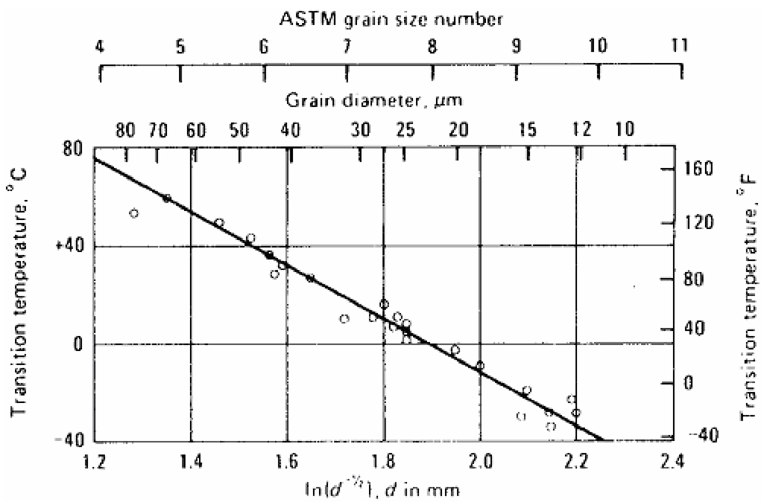

Figure 8. Influence of grain size on transition temperature [10]

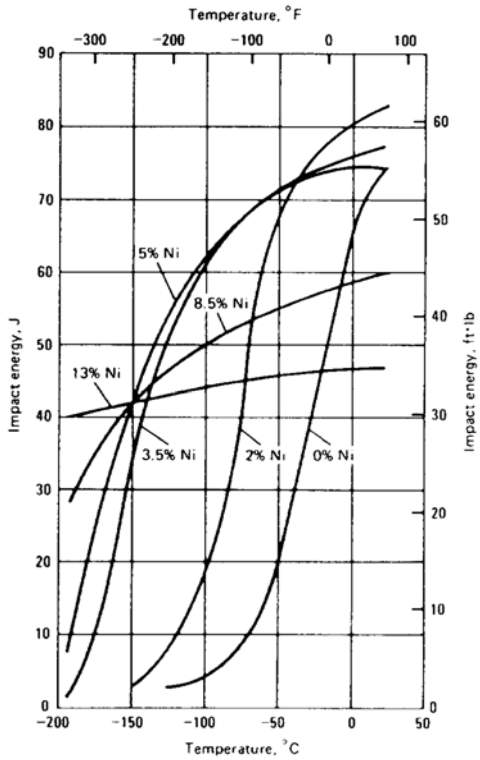

Figure 9. Influence of nickel content on transition temperature in steels [12]

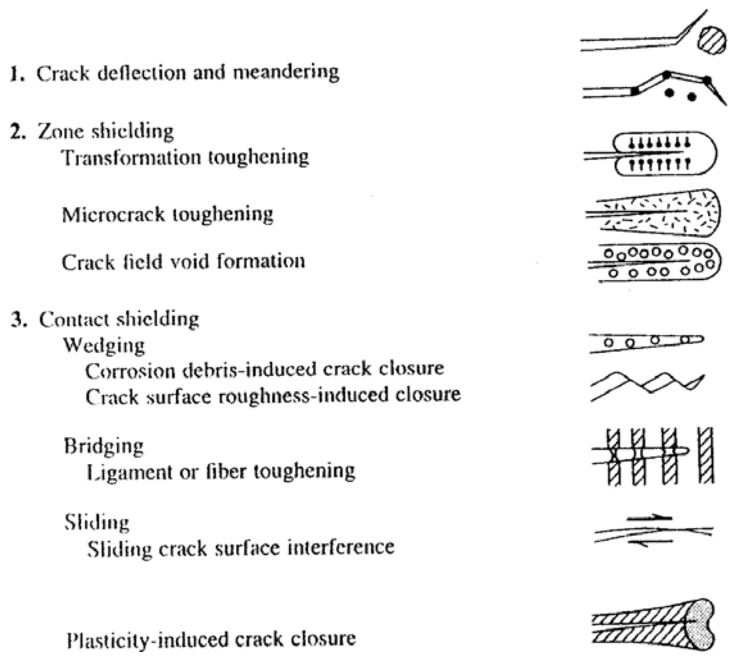

Figure 10. Mechanisms of crack arrest in materials, [1]

As an example of design of a new steel type are steels with intermetallic phases. These steels contain needle-like martensite laths, smaller than 1 μm, providing high YS and toughness level. Properties can not be further improved by additional alloying with C or N.

Since needlelike martensite can be obtained only in very low carbon content, further increase of YS is possible only by controlled precipitation of intermetallics. This area requires knowledge of some new: two-, three- or even multiple alloying element systems and this research will generate itself, [11].

The measures for technological improvement are, [13]:

- Cleanness of steel. The state of the art of steel making technology can produce very clean steel in terms of N + O + S + P < 50 ppm. Clean steel improves toughness of both base metal and heat affected zone (HAZ).
- Inclusion shape control. Even though S content is lowered to 10 ppm, it is not possible to avoid formation of MnS in the central segregation zone. As pointed out previously, MnS tends to elongate, and behaves as a stress concentrator and lowers the toughness.
- Centerline segregation in slab. The continuously cast slab always has centerline segregation, characterized with higher concentration of Mn, C, P, and S. The intensity of centerline segregation can be reduced by cleaner steel, by reduction of slab thickness during steel casting and accelerated cooling, or by combination of these processes.
- Slab reheating temperature. Reheating temperature in furnace must provide both homogenous grain size and dissolution of alloying elements.
- Accelerated cooling. It increases the undercooling and nucleation rate, enabling additional refinement. One result is the absence of a clear yield point, due to bainitic transition.

The development of steel as a structural material is summarized in Figs. 11 [14] and 12 [15].

Each new generation of steel follows the direction to both decrease the transition temperature and increase the yield point. Also, this development had to be accompanied with improvements in weldability and formability. Development of steels for pipelines, i.e., had to be accompanied by improvements in weldability (Fig. 12), therefore, the carbon content is very low, while good toughness and a high yield point is achieved by complex alloying (by combination of Nb, V, and Ti).

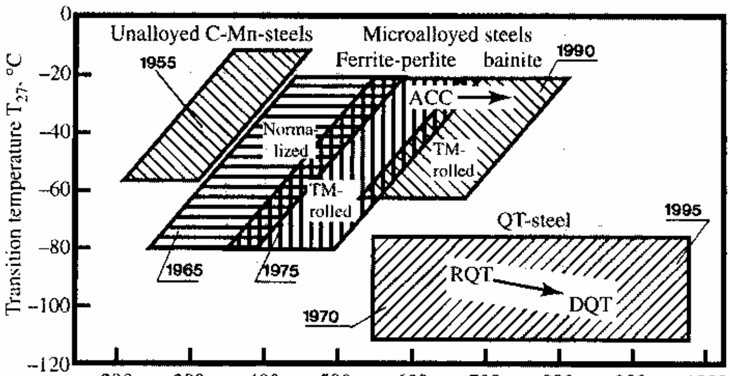

Figure 11. Schematic interrelationship between the yield strength and the transition temperature T_{27} for different steels [14]

Another contribution of fracture mechanics is described in development of medium carbon microalloyed steels for sucker rod applications in oil industry, [16]. This rod is subjected to heavy dynamic loading in a very aggressive environment. Therefore, the requirements are very strict. On the other hand, the presence of acicular ferrite considerably improves toughness, due to the shape of ferrite grains, and due to the fact that bainite brings corrosion resistance. A new steel containing 0.030% C, 0.33% Si, 1.5% Mn, 0.1% V, 0.012% N, 0.01% Ti has been designed for this purpose. Rods are connected by thread, thus, absence of welding has allows a relatively high carbon content. Figures 13 and 14, in respect, show the temperature effect on CVN impact energy and microstructures. Steel was produced by hot forging with subsequent cooling on still air.

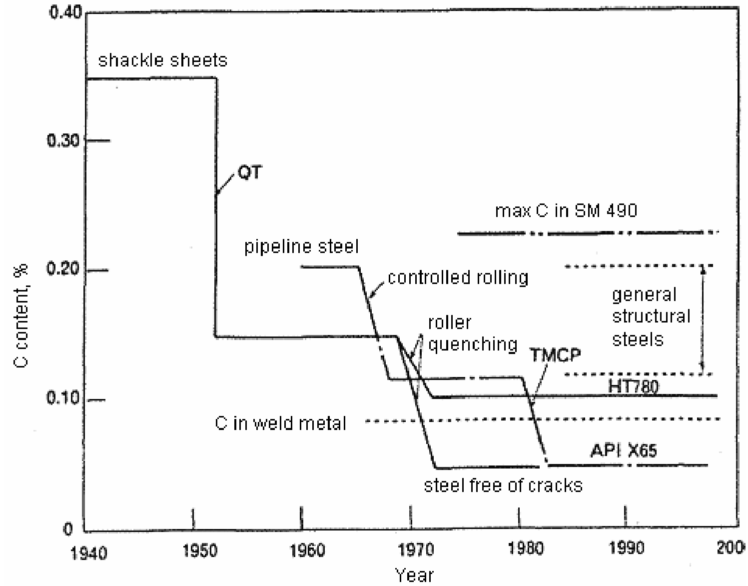

Figure 12. Change of carbon content in structural steels during its development, [15]

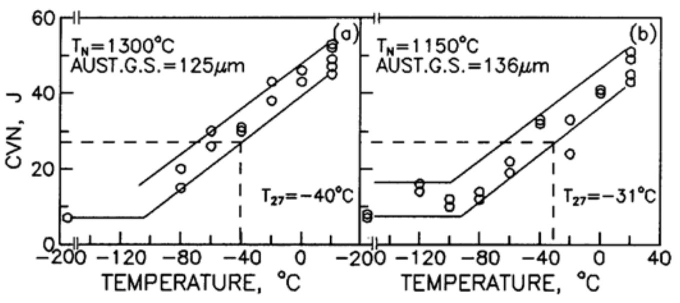

Figure 13. The effect of temperature on CVN impact energy of medium-carbon V-microalloyed steel, [16]

Figure 14. Microstructure of tested steel with MnS-VN inclusion and INI-intragranularly nucleated ferrite, [16]

The very low transition temperature, in spite that this is not a Q + T steel, is due to dominant presence of acicular ferrite. It is suggested that non-metallic particles are necessary for nucleation of acicular ferrite. The extent of nucleation depends on composition, crystal structure, and also on number, size and interparticle distance. The second condition is the grain size at annealing temperature, i.e. grains should have some optimal size, rather larger than smaller, because larger grains will decrease temperature of austenitic decomposition to the temperature range in which acicular ferrite is a dominant structure. Hardenability has a similar role. Second phase particles are usually oxides and/or nitrides or sulphides; MnS particles served as preferential places for precipitation of VN, which has an extremely great potential for nucleation of intragranular pro-eutectoid ferrite (intergranularly nucleated ferrite–INI), which in turn serves as a nucleation site for acicular ferrite. Therefore, even considerable high content of sulphur (130 ppm) has not deteriorated the toughness, i.e. nucleation of acicular ferrite would not be possible without MnS particles. This conclusion is very important for further practice in design of materials.

Based on knowledge of fracture mechanics, particles in steel are not only considered in the direction of smaller content of impurities, but more to the *control* of shape and distribution of second phase particles. It is much easier and reasonably cheaper to control the shape of inclusions, than to produce very low S steel. If the shape of second phase is modified into a sphere, than negligible stress concentration will occur, and presence of inclusions can be sometimes neglected or even necessary.

CONCLUSION

Fracture mechanics had introduced the relation between material properties, service conditions and defects in structures, originating from fabrication. In the area of materials design, fracture mechanics have improved the quantification of both shape and size of inclusion/second phase particles, allowing a less conservative approach to design, i.e. practical dealing in material production with the aim to produce materials with acceptable impurity content, distributed in controlled shape and size. This approach has opened a whole new area, both in materials design and methods for detecting defects in materials.

REFERENCES

1. Перельмутер, А.В., Автоматическая Сварка, 9-10, 107-112. (2000)
2. Hertzberg, R.W., *Deformation and Fracture Mechanics of Engineering Materials*, J. Wiley and Sons, New York. (1996)
3. Knott, J.F., *Fundamentals of Fracture Mechanics*, Butterwords, London. (1973)
4. Drobnjak, Dj., Lecture notes, Faculty of Technology and Metallurgy, Belgrade. (1996)
5. Burns, K.W., Pickering, F.B., Journal of the Iron and Steel Institute, 202, pp. 899-906. (1964)
6. Palmiere, E.J., Garcia, C.I., DeArdo, A.J., *Processing, Microstructure and Properties of Microalloyed and Other Modern High Strength Low Alloyed Steels*, The Iron and Steel Society, Warrendale, Pa, pp. 113-133. (1992)
7. Allen, N.P. et al., Journal of the Iron and Steel Institute, 174, pp. 108-120. (1953)
8. Mueschenborn, W. et al., Microalloying 95, Ed. M. Korchynsky, The Iron and Steel Society, Warrendale, Pa, pp. 35-48. (1995)
9. Philips, R., Duckworth, W., Copley, F.E.L., Journal of the Iron and Steel Institute, 202, pp. 593-600. (1964)
10. Petch, N.J., *Fracture*, ed. B.L. Averbach et al., Technology Press, Cambridge, Mass. pp. 54-67. (1959)
11. Hougardy, H.P., Stahl und Eisen, 119, pp. 85-90. (1999)
12. Roe, G.L., *Notch toughness of steels*, Metals Handbook 9th Edition, Vol.1, pp. 689-709. (1978)
13. Tanaka, T., Microalloying 95, Ed. M. Korchynsky, The Iron and Steel Society, Warrendale, Pa, pp. 165-181. (1995)
14. Prediction of Steel Production for Year 2000 (in Swedish), Stetsen, 59, No.2, pp. 4-10. (2000)
15. Yurioka, N., Document IIW IX-1963-2000 (2000)
16. Drobnjak, Dj., Koprivica, A., Fundamentals and Application of Microalloying Forging Steels, Ed. Chester J. van Tyne, G. Krauss and D. Matlock, TMS, Warrendale, Pa, pp. 93-106. (1996)

FRACTURE MECHANICS STANDARD TESTING

Stojan Sedmak, Society for Structural Integrity and Life, Belgrade, S&Mn
Zijah Burzić, Military Technical Institute, Belgrade, S&Mn

1. FUNDAMENTALS OF FRACTURE TOUGHNESS TESTING

Fracture toughness testing is based on the experiments performed to determine critical values of strain energy release rate or stress intensity factor. The precracked specimen of standard geometry is loaded until it breaks and the recorded data for load and displacement can be used to calculate the fracture corresponding parameter from developed formulae. To understand exactly what measurements are made in standard practice and why precise limitations are put on specimen dimensions and testing conditions to give valid results, it is necessary to review the development of precracked specimens testing from the first experiments carried out by Irwin [1]. It is also to emphasize that, using the same type of specimen and the same procedure, different fracture parameters can be determined for brittle and stable (partial or total) crack growth.

1.1. Testing of thin sheet

In the experiments Irwin intended to test his theory of fast fracture, in which the failure stress σ_F of an infinite body with a central crack of length $2a$ is given by:

$$\sigma_F = \sqrt{\frac{EG_{crit}}{\pi a}} \tag{1}$$

in plane stress; G_{crit} is the critical value of the strain energy release rate at fracture and E– elasticity modulus. The equivalent expression for critical stress intensity factor K_{crit} is

$$K_{crit} = \sigma_F \sqrt{\pi a} \tag{2}$$

To simulate this situation, Irwin chose to test large, centrally-cracked thin sheets of aluminium. Irwin allowed for the fact that the stress-free boundaries were not at infinity by employing a relationship between stress intensity factor and applied stress of the form:

$$K = \sigma \sqrt{W \tan\left(\frac{\pi a}{W}\right)} \tag{3}$$

where W is the specimen width. It can be seen that, when (a/W) is very small, the function in the square root tends to πa, as for an infinite body.

Irwin obtained the results shown in Fig. 1, which clearly indicate that σ_F is inversely proportional to $\sqrt{(a)}$. The value of G_{crit} calculated from the results is about 130 kJm^{-2}, i.e. about five orders of magnitude greater than the surface energy of aluminium. The relationship in Fig. 1 enabled to design against fracture using fracture mechanics.

This analysis rests on the assumption that the behaviour is elastic and so the specimen's dimensions must be larger than the extent of plasticity before fracture. In addition to aluminium alloys, similar experiments were carried out on titanium alloys, maraging steels, and other high-strength steels, that supported well the theoretical approach.

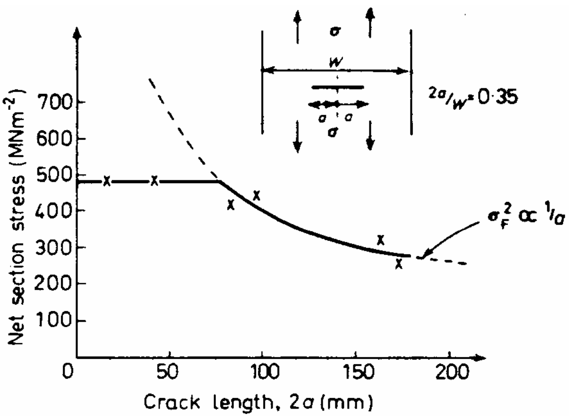

Figure 1. Net-section stress at instability vs. crack length for 7075 alloy T 6, [2]

1.2. The dependence of fracture toughness on thickness

The results in Fig. 2 [2] show a large variation in toughness for experiments carried out with an aluminium alloy (7075-T6) of different specimen thickness. Three regions in the toughness curve: A, B, and C can be recognized, taking into account the fracture profiles and stress-displacement curves form obtained in each region (Fig. 2b). The fractures are classified as "slant" or "square", depending on whether the macroscopic fracture surface is at 45° to the tensile axis or normal to it. The second curve in Fig. 2a indicates how the proportion of square fracture varies with specimen thickness: up to the maximum of the toughness curve (region A) fractures are completely slant, in thick specimens (region C) they are generally square, and for intermediate thickness, they are of "mixed-mode".

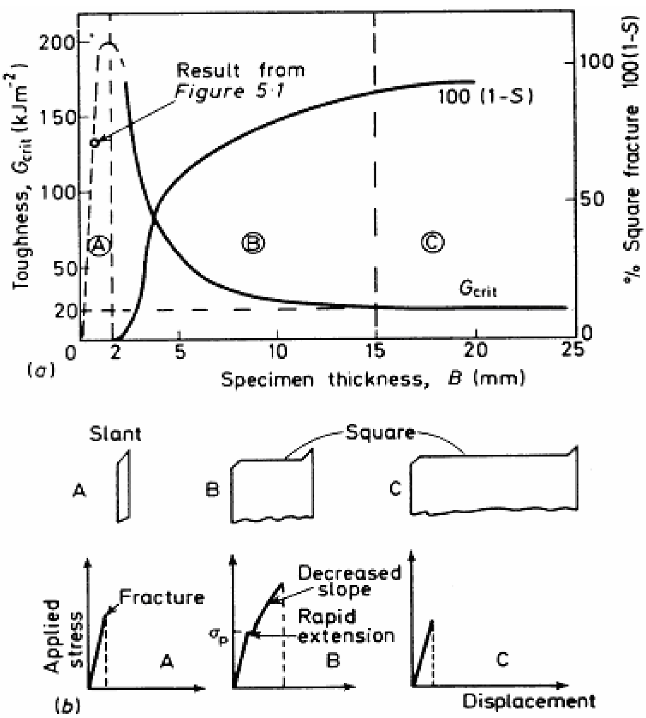

Figure 2. (a) Variation of toughness with thickness for 7075 Alloy - T6
(b) Fracture profiles and stress-displacement curves typical of regions A, B and C [2]

1.2.1. Fracture in thin sheet

In region A (Fig. 2a and b) the specimens are very thin and show increasing toughness with thickness due to plane stress condition: the stress in the thickness direction tends to zero. The load-displacement curve is linear up to fracture and the fracture is 100% slant. In that case yielding occurs on through-thickness planes at 45°, in the direction of maximum shear stress, crack tip must move forward by an antiplane strain mechanism. It can do this only because, in practical testing configuration, some buckling and twisting allows the specimen's halves above and below the fracture plane to be displaced laterally.

1.2.2. Plane strain fracture

In region C (Fig. 2), specimens are rather thick so that all the load-bearing cross-section deforms in plane strain. Fracture propagates in the centre under critical crack tip conditions and any differences in behaviour of the specimen edges are insignificant in determining failure conditions for the specimen as a whole. Load increase is linear until a critical (low) value is reached, when fast failure occurs. The fracture of very thick specimens, region C, occurred with total instability at loads corresponding to a virtually constant toughness value and fracture appearance is almost completely square, with very small proportions of slant ("shear lips") at the edges. The central region of a thick test-piece deforms under approximately plane strain conditions (Fig. 3). Then, the strain in thickness direction is zero, and when yielding occurs around a crack tip, high constraints are set up, and a triaxial stress state develops. This stress state enhances the initiation of fracture. The high value of maximum tensile stress below the notch may promote any cracking mechanisms to which the material is prone. If crack extension occurs when the strain in the region immediately ahead of the crack tip achieves a critical value, an effect of triaxial stress can arise through changes that it may make on the strain gradient in this region. For a given crack opening displacement, the plastic zone size in plane stress (specimen edges) is much larger than in plane strain (specimen mid-thickness), since yielding spreads under a shear stress component which includes full value of local tensile stress.

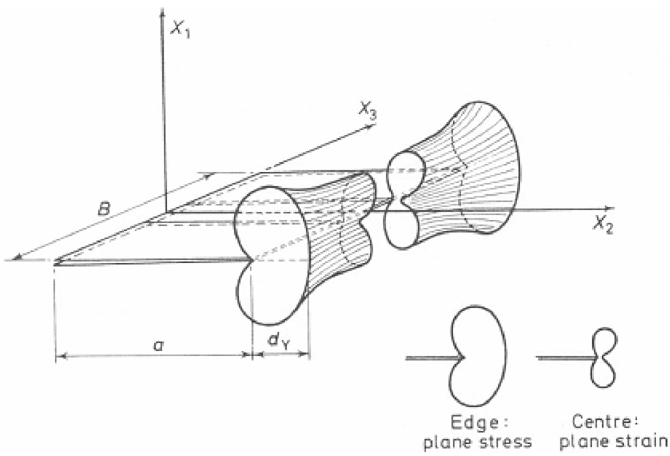

Figure 3. Plastic zone ahead of crack in a plate of finite thickness [2]

1.2.3. The intermediate range

In region B, the fracture behaviour is complicated. The specimen is neither so thin that failure occurs by the sliding-off mechanism as in region A, nor so thick that it fails by a completely "plane-strain" square fracture. Its thickness is such that the central and edge regions are of comparable size. The sequence of events is indicated by the load–displacement trace in Fig. 2b. The load on a specimen is raised to a value, F_P (corresponding to the stress σ_P – Fig. 2b), at which some square fracture can form in the centre of the thickness. In a very thick test piece, such fracture would spread catastrophically because it would occupy a large part of the thickness, but, in the intermediate range, due to side-ligaments of the cross-section, the total instability does not occur. The load–displacement curve may show a sudden extension for constant or even decreasing load if the square fracture tunnels ahead rapidly ("pop-in"). If the square fracture does not advance so rapidly, its presence will be detected only by a change in the compliance of the testpiece. The crack is longer; so the load–deflection curve exhibits a decreased slope. The effects are shown in Fig. 2b.

As the load is raised above F_P, the central square fracture tunnels into the centre of the testpiece and perhaps also spreads slightly in the through-thickness direction. The side ligaments can be sheared apart when sufficient displacement at the crack tip is attained and the total crack advances in a composite fashion: the square fracture tunnelling ahead and dragging the slant (shear lips) with it.

It is important to realise that, as the crack grows under increasing load, the plastic zone ahead of the crack tip grows bigger and is therefore more easily able to relax the through-thickness stress. Less of the thickness therefore deforms in plane strain and the proportion of square fracture decreases. At the thin end of the range, the initial square fracture occupies only a small proportion of the thickness cross-section; as it tunnels forward, the plastic zone size becomes large with respect to plate thickness; the through-thickness stress is relaxed; and final instability is achieved at a load, F_F, large enough to operate a sliding mechanism for separation, analogous to that in region A. The sequence of events illustrated in Fig. 4 is quite consistent, both with fracture appearance of broken specimens and with the observed load–displacement records. The fracture load is lower than that for a thinner specimen, because the testpiece, at instability, contains a longer crack.

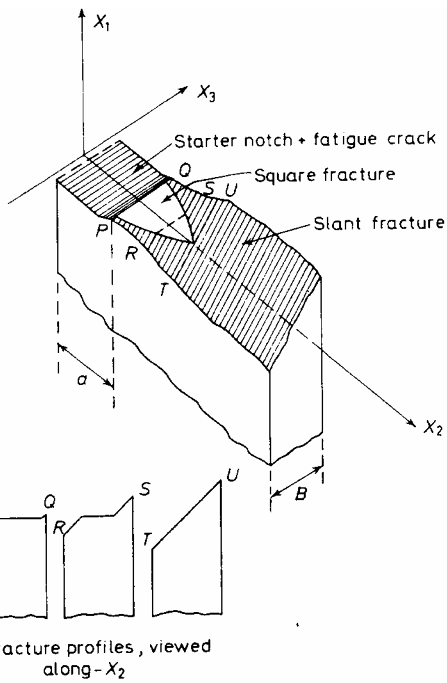

Figure 4. Development of slant fracture in region B [2]

At the thick end of the intermediate range, the side ligaments bear a much smaller proportion of the total load applied to the specimen and so final instability follows the initiation "pop-in" more rapidly, provided that the test is carried out under load control (a "soft" system). The fracture profile at instability is now a mixture of slant and square. Under displacement control, a rapid "pop-in" can cause the load to relax.

1.2.4. Conclusions on thickness effects

In regions B and C (Fig. 2) the central part deforms under conditions close to those of plane strain deformation: the side faces can support no stress normal to the free surface and deform in plane stress. High tensile stresses and a concentrated strain gradient are present ahead of the crack tip in the centre; on the sides the stresses are much lower and the strain is spread over a larger plastic zone. In the centre "plane strain pop-ins" are produced at a critical value of stress intensity: whether the fracture of the testpiece as a whole proceeds very fast at this stress, or at a higher value, depends on the proportion of the cross-section occupied by the shear lips.

The peak of the toughness curve occurs at a thickness of approximately 2 mm. For thicker specimens, an increasing proportion of square fracture is produced, and the total fracture toughness drops. To provide an upper bound for the curve which shows how the proportion of square fracture varies with thickness, one can assume that the shear lips are of constant size (i.e. 2×1 mm) in specimens of all thicknesses.

The next assumption to be examined is that the "pop-ins" are occurring under plane strain conditions. The assumption rests first on the constancy of the widths of the shear lips at the initiation of square fracture, implying that the increase of stress in thickness direction from zero at the free side surfaces to the plane strain value in the centre of the piece occurs over a constant distance, and secondly on behaviour of the "laminate", such that both "plane strain" and "plane stress" fractures occur under uniquely defined conditions. But, there is no guarantee that a square fracture is characteristic of plane strain over all its thickness. In mild steel, macroscopically square fractures have been shown to occur at loads which decrease with increasing thickness until constancy is achieved, when plane strain conditions are met [2]. In the aluminium alloys, a square "pop-in" may occur in relatively thin sheet at a critical stress intensity greater than the limiting value, so that the toughness of the material for true plane strain conditions is overestimated.

The total fracture toughness of a specimen in the intermediate range is composed of contributions from both the slant and square components. Estimation of the subsequent toughness is not simple, because, as the crack tip advances under constant load, the strain energy release rate increases and more driving force for accelerating fracture is available, yet the plastic zone size, and area that will fracture by high energy shearing, also increases, so that more work is required to cause failure.

2. DEVELOPMENT OF STANDARD FRACTURE TESTING

The introduction of standard procedures for determination of crack parameters has been necessary for practical application of fracture mechanics. For different crack parameters (stress intensity factor, crack opening displacement, J integral, final stretch zone) and different situations in which they can be applied, different standards had been accepted. In practical use of fracture mechanics standards one has to account with their limited applicability. The first limitation is connected with the size of specimens and transferability of obtained results to the full scale structure, because the stress state in specimen and component can differ. The second limitation concerns the structure design stage. The existence of crack can not be accepted in design requirements, so it is not possible to assess the crack significance in design stage, but fracture toughness properties can be applied in material selection in a proper way. For that, the application of standards for crack parameters determination is directed to the situations of detected cracks of defined size and position in structures, mainly during service, and only rarely in inspection of new structures. Regular control and inspections in service are introduced to assess the existence of damages, which could eventually reduce the structural safety in next service. The repair of these damages is in many cases the condition for further exploitation of structure. In welded structures, for example, cracks, as most dangerous damages, are not allowed by standards. In that case only fitness-for-purpose criteria can be applied, proving that the present crack is not significant for given load and operational condition. Fitness-for-purpose assessment requires the critical value of crack parameter that is determined by fracture mechanics standard test methods. Fracture case studies are the next example in which standards for crack parameter evaluation are applicable. Mostly, cracks are responsible for fracture occurrence and the data of crack parameters must be involved in the analysis [3].

First drafts for fracture mechanics standards occurred in late sixties. American Society for Testing and Materials (ASTM) announced tentative standard ASTM E399-70T [4], and British Standard Institution (BSI) DD3 draft standard. These both proposals have been accepted, after regular procedure, as standards under the same title: “Standard Test Method for Plane-Strain Fracture Toughness of Metallic Materials” and nowadays are available as ASTM E399, respectively BS 5447 (which is now included in the new BS7448 standard) [5].

Some time after the first fracture mechanics standard draft DD3, BSI announced new draft DD 19 “Standard Test Method for Crack Opening Displacement,” accepted in 1972 as standard BS 5762, and now also included in BS7448.

Fracture mechanics standards, developed by ASTM after ASTM E 399, together with other standards in which cracks are considered, are listed bellow:

- ASTM E561-86: Standard Practice for R–Curve Determination
- ASTM E647-88a: Standard Test Method for Measurement of Fatigue Crack Growth Rate
- ASTM E740-88: Standard Practice for Fracture Testing With Surface–Crack Tension Specimens
- ASTM E812-81 (Reapproved 1988): Standard Test Method for Crack Strength of Slow–Bend Precracked Charpy Specimens of High-Strength Metallic Materials
- ASTM E813-89: Standard Test Method for J_{Ic}, A Measure of Fracture Toughness
- ASTM E992-84 (Reapproved 1989): Standard Practice for Determination of Fracture Toughness of Steels Using Equivalent Energy Methodology
- ASTM E1152-87: Standard Test Method for Determining *J–R* Curve
- ASTM E1221-88: Standard Test Method for Determining Plane-Strain Crack-Arrest Fracture Toughness, K_{Ia}, of Ferritic Steels
- ASTM E1290-89: Standard Test Method for Crack-Tip Opening Displacement (CTOD) Fracture Toughness Measurement
- ASTM E1304-89: Standard Test Method for Plane-Strain (Chevron Notch) Fracture Toughness of Metallic Materials
- ASTM E1737-96: Standard Test Method for *J* Integral Characterization of Fracture
- ASTM E1820-99: Standard Test Method for Measurement of Fracture Toughness
- ASTM E1823-99: Terminology Relating to Fatigue and Fracture Testing

The ASTM E1820-99 standard combines two former standards (E 813 and E 1152), as natural development, since they mainly coincided. Achieved experience and comparison with crack opening measurement enabled significant extension of J integral applicability domain, accepted in new standard for material characterization.

In addition to the given list, several standards are evaluated as important, because they contain interesting definitions or produce interesting results, e.g.:

– ASTM E338-81 (Reapproved 1986): Standard Method of Sharp-Notch Tension Testing of High-Strength Sheet Steel Materials
– ASTM E208-87a: Standard Test Method for Conducting Drop-Weight Test to Determine Nil-Ductility Transition Temperature of Ferritic Steels
– ASTM E436-74 (Reapproved 1986): Standard Method for Drop-Weight Tear Tests of Ferritic Steels
– ASTM E604-83 (Reapproved 1988): Standard Test Method for Dynamic Tear Testing of Metallic Materials

The intention to unify standards, based primarily on the same specimen form and similar testing procedure, is also present in European approach. Based on standard drafts, P1 and P2, published by European Structural Integrity Society (ESIS), standard test method is defined known as:

– EFAM GTP 94: The GKSS test procedure for determining fracture behaviour of materials

Similar, but extended approach, is accepted in British Standards, and new standard,

– BS 7448 "Fracture mechanics toughness tests"

published 1991 in its Part 1. "Methods for determination of K_{Ic}, critical CTOD and critical J values of metallic materials" included former standards BS 5447 and BS 5762, but also J integral determination is added. Part 2, "Methods for determination of K_{Ic}, critical CTOD and critical J values of welds in metallic materials," published 1997, prescribes procedures for fracture mechanics testing of welded joints. In the next elaboration are: Part 3, for determination of dynamic fracture toughness and Part 4, for determination resistance (R) curves of fracture toughness.

Yugoslav standards for crack parameter are defined in the late eighties. They are:

– JUS C.A4.083 – *Mehanička ispitivanja materijala. Osnovni pojmovi i veličine u mehanici loma* (Mechanical testing of materials. Basic terms and values in fracture mechanics.)
– JUS C.A4.084 – *Mehanička ispitivanja. Ispitivanje žilavosti loma pri ravnoj deformaciji (K_{Ic})*. (Mechanical testing. Plane strain fracture toughness testing (K_{Ic})).

The necessity to introduce JUS standard for crack parameters is given in "Codes for technical norms for stationary pressure vessels" (*Sl. list SFRJ, 16/83*), in which for pressure vessels classes I and II the value of crack parameter for selected material is required, in the form of plane strain fracture toughness K_{Ic} or crack opening displacement COD, depending on material thickness and strength.

3. TERMS AND VALUES IN FRACTURE TESTING

The terms and values of importance for pre-cracked specimen testing are presented here according to standard JUS C.A4.083. Other terms, that can help to understand fracture mechanics testing and analysis of test results, can be found in cited standards.

3.1. Configuration of crack

The crack in a component or specimen could be (Fig. 5):

– through crack, passing from one to the other component edge (a);
– surface crack, visible only on one part of component surface) (b);
– embedded crack, located in component inner and not visible (c).

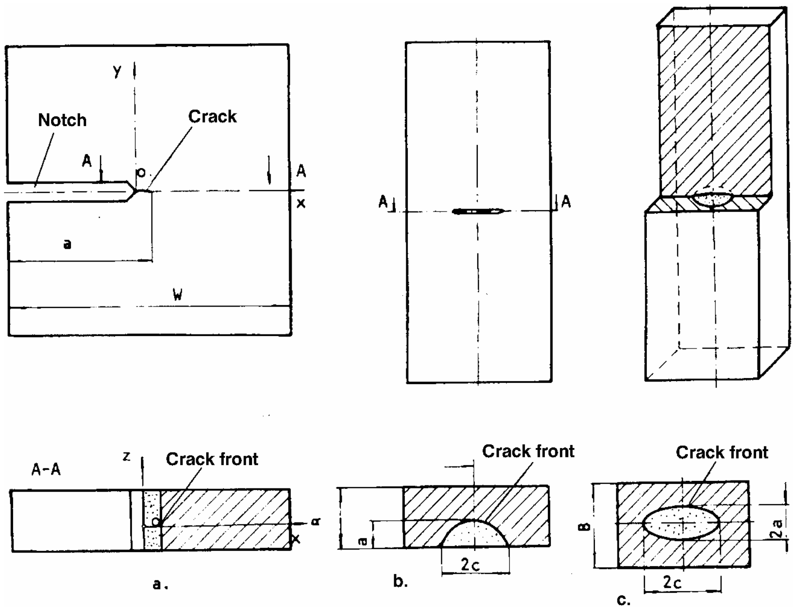

Figure 5. Through crack (a), surface crack (b), and embedded crack (c) in component (specimen)

3.2. Stresses, strains and displacements, crack parameters

Standard test methods require detailed description of stress field ahead crack tip (Fig. 6). Two stress states are of importance. The first is triaxial stress state, in which all three principal normal stress components are acting, constraining deformation to only two directions – plane strain. Empirical condition for plane strain is given by

$$B = 2.5 \frac{K_{\mathrm{I}}^2}{\sigma_Y^2} \tag{4}$$

Here, B stands for specimen (component) thickness, K_{I} for stress intensity factor, σ_Y for effective yield stress, the average value of yield strength and ultimate tensile strength.

Plane stress is the stress state for which Eq. (4) is not fulfilled, that means only two normal stress components ("plane") are applied. Strain components in all three directions corresponded to the load of that kind and will be established in thin plates.

It is to make a difference between stress state in cracked components and general stress state of crack-free component, having in mind stress concentration around crack.

Fracture mechanics defined three basic modes of crack extension: opening (Mode I), sliding (Mode II), and shearing (Mode III) (Fig. 7), with corresponding displacements v (I), u (II) and w (III). Opening is the most critical mode for crack extension, and for that it is accepted in standards for fracture mechanics testing.

Stress intensity factor K_{I} presents the intensity of stress field ahead of an ideal crack (stress field singularity) for Mode I (opening) and is defined as:

$$K_{\mathrm{I}} = \lim_{r \to 0} \left[\sigma_y (2\pi r)^{1/2} \right] \tag{5}$$

where σ_y is a stress component that mostly contributes to crack opening (Fig. 6), and r the distance from crack tip of a point in which stress component is determined.

In accordance with mode I displacement v–crack opening displacement (COD) is defined in Fig. 8, in which W is specimen width, a initial (fatigue) crack length, and $W - a$

initial ligament value. Bend angle is designated by α, and the value $r(W-a)$, added to crack length a, determines the actual rotation centre. The value of crack mouth opening displacement (CMOD), designated by $2v_m$, is measured by positioning of clip gauge in knives of thickness z. The next analysis enabled to define crack tip opening displacement (CTOD), for which symbol δ is accepted. For known size of initial crack a and CMOD value, the answer whether fracture will take place before or after full scale yielding can be obtained according to ligament size (the distance to opposite side from crack tip). If the ligament is small, plastic zone will be formed across it before critical value of COD (δ_c) at crack tip is reached and fracture is ductile; if ligament is large, critical value δ_c is reached first (before net section yielding) and fracture is brittle. Since in both cases the value of COD is almost the same, it is possible to use COD as a crack parameter.

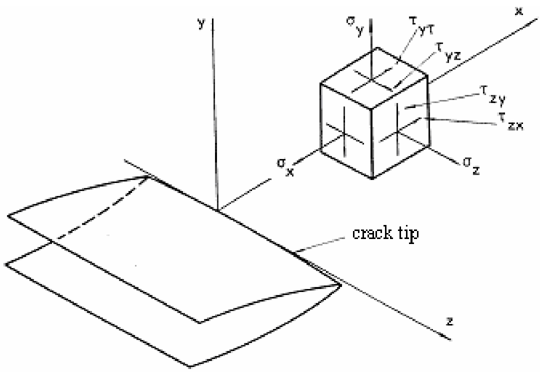

Figure 6. The components of elastic stress field ahead crack tip

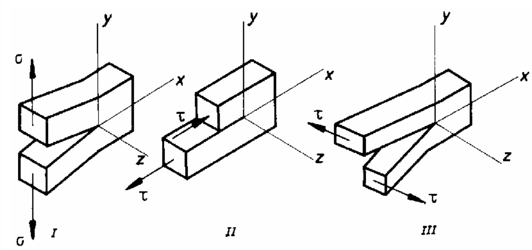

Figure 7. Modes of crack front displacement: opening (I), sliding (II), tearing (III)

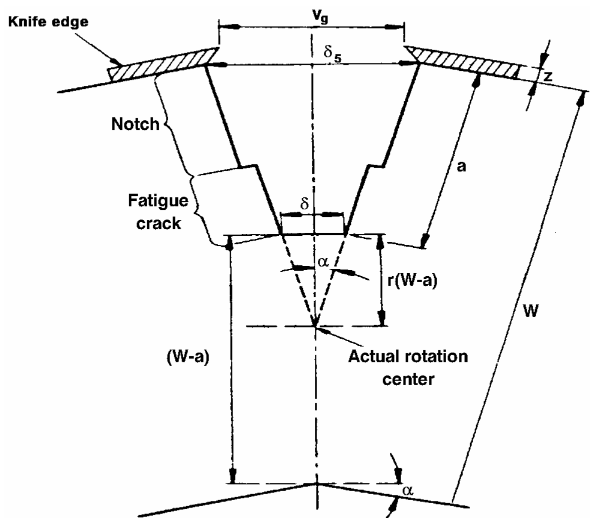

Figure 8. Geometrical dependencies for COD determination on three point bend specimen

Cottrell defined critical crack opening displacement δ_c for plane stress condition and Mode I loading in the form:

$$\delta_c = \frac{8R_{eh}a}{\pi E}\ln\left[\sec\left(\frac{\pi\sigma_c}{2R_{eh}}\right)\right] \tag{6}$$

where σ_c is fracture stress, and R_{eh} yield strength.

When plastic zone of significant size is established in the crack tip region, it is not more possible to describe stress and strain fields by a single parameter, as it was the case with critical stress intensity factor K_{Ic} (Fig. 9).

The specimen will behave as its compliance is greater of that corresponding to crack size due to the effect of blunted crack, surrounded by elastically deformed material (Fig. 9–III). This effect can be expressed by the value r_y:

$$r_Y = \frac{\alpha}{2\pi}\frac{K_{\mathrm{I}}^2}{\sigma_Y^2} \tag{7}$$

In Eq. (7) the coefficient $\alpha = 1$ for plane stress, and $\alpha = (1/3 \text{ to } 1/4)$ for plane strain.

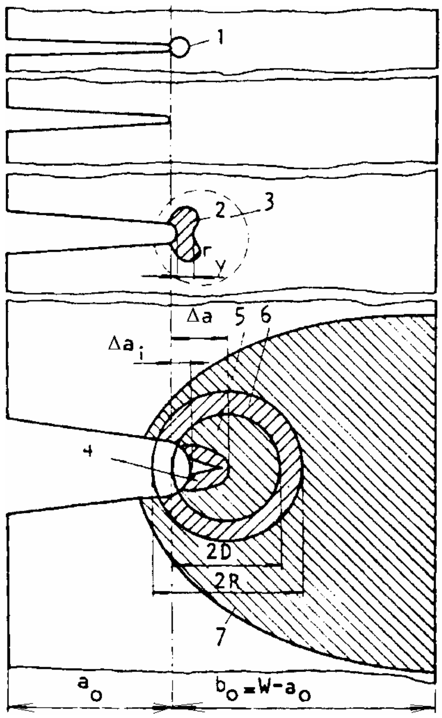

Figure 9. The scheme of plastic deformation development around crack tip in a central part of the specimen for different load levels
I–Initial stage (1-plastic zone, visible after unloading); II–Stage of relaxation (relaxed residual stress around crack tip); III–Blunting of a crack and small plastically deformed zone (2); 3 is the region in which material behaviour is described by K_{I} value; IV–Stable crack growth (4-zone of elastic unloading; 5-process zone; 6-Hutchinson-Rice-Rosengren zone; 7-zone of large plastic deformation, for net section yielding)

Plastic zone is a region ahead of the crack tip, in which material behaviour is not linear: it is small if surrounded by singular stress field, described by stress intensity factor K_{I} (Fig. 9–III). Plastic zone is large if it is surrounded by material of behaviour not described by K_{I} value. The term net section yielding comprises of yielding spread across the ligament, and full scale yielding denotes yielding spread over the total specimen.

Radius R (Fig. 9–IV) determines the extension of HRR zone, named according to the material behaviour model of Hutchinson-Rice-Rosengren (HRR), in which the state of stress and strain is described by parameter J_{I} (path independent J integral), and in which no relaxation occurs with uniform growth of J integral.

Radius D defines the process zone (fracture process), in which free crack surfaces can be formed from crack tip during crack extension, caused the relaxation of elastic-plastic material during uniform growth of J integral. Radius D is usually small and comparable to initial crack opening in the vicinity of crack tip (Fig. 9–IV).

3.3. Material crack resistance

Material crack resistance is described by above given parameters that are determined by corresponding standard methods.

The general term, fracture toughness, represents a measure of crack growth resistance. This term mostly addresses to fracture mechanics test results, but as a general term it can be also applied for results of pre-cracked or pre-notched specimens, not based on fracture mechanics approach. In this case they can be used as comparative for fracture control according to experience or empirical relationships.

Crack growth resistance is a measure, expressed by stress intensity factor, K_R, crack opening displacement, δ_c, or J integral, J_R, and in some cases by crack driving force, G_R. In practical use, crack driving force is equal to J integral, meaning $G = J$.

The resistance curve (R curve) can be expressed as dependence of crack driving force in the form of some given parameters, and crack extension by stable growth, Δa (Fig. 10).

Plane strain fracture toughness, K_{Ic}, as a crack parameter for brittle fracture, is a critical stress intensity factor in plane strain condition, as described in standards for negligible plastic zone size ahead of the crack tip, if standard requirements regarding specimen size (Eq. 4) and crack are fulfilled. This value is a material property.

In a similar way fracture toughness for plane stress condition, K_c, can be defined, but in that case plane strain condition according to Eq. (4) is not fulfilled; this value is thickness dependent and for that is not a material property.

Additional elements on the R curve (Fig. 10) are important. The first one is the blunting line that approximately describes crack growth by tip blunting before its stable growth. This dependence is linear (Fig. 11), since blunting capacity is determined by final stretch zone size, approximately equal to one half of corresponding crack opening displacement. Crack extension for blunting, Δa_B, is determined, and based on effective yield stress σ_Y:

$$\Delta a_B = \frac{J}{2\sigma_Y} \tag{8}$$

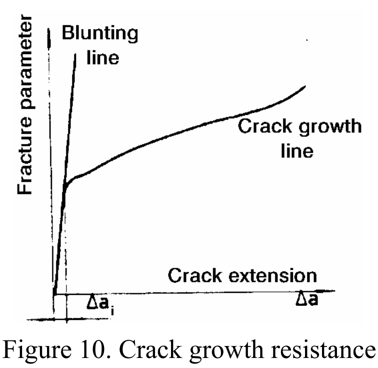

Figure 10. Crack growth resistance curve (R curve)

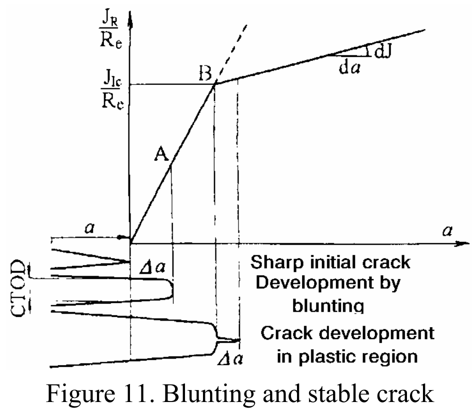

Figure 11. Blunting and stable crack growth processes, marked on R curve

When material blunting capacity is exhausted, crack starts to grow in a stable manner, so this value is accepted as critical for crack initiation, Δa_i in Fig. 11, being a measure of fracture toughness. In order to determine its position as accurate as possible, according to standard procedure, a regression line is drawn, replacing the R curve in defined segment. Point B as the intersection of regression and blunting lines defines critical *J* integral value as a material property, enabling determination of plane strain fracture toughness measure.

4. TESTING EQUIPMENT

In fracture mechanics parameters testing the load is measured, together with crack opening displacements and/or load line displacement in some testing methods. The first experiments were performed on tensile panels with through-crack and on pre-cracked three point bend specimens (single edge notch–SEN). A three point bend specimen is presented in Fig. 12 as positioned on supports of the testing machine.

The testing machine must be equipped with automotive device for load recording. Specimen holders have to assure minimum wear. Modern machines are designed in closed loop that enables load, displacement, or strain control and automotive recording of load, load line displacement, and crack opening displacement. The loading rate is limited to 0.55–2.75 MPa√m/s. Crack opening displacement clip gauge design is recommended in standards. Recommended design comprises strain gauges of 500 ohm in Wheatstone bridge. It can be positioned on knives, joined to the specimen, or on machined holders (Fig. 13). Other clip gauge designs are also applicable, but strict linearity is required.

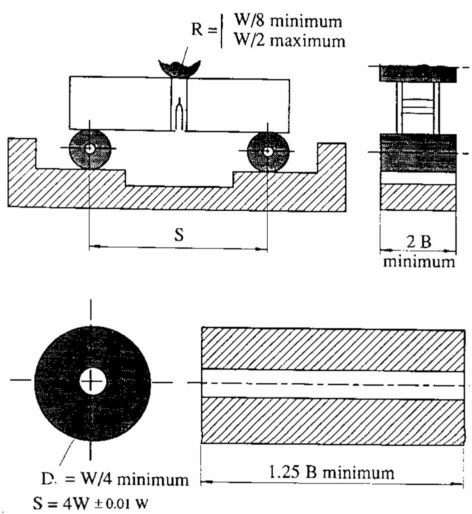

Figure 12. Three point bend specimen (single edge notch–SEN), positioned on supports of the testing machine

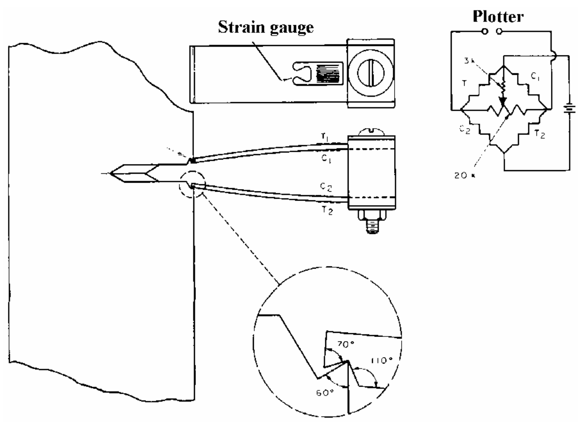

Figure 13. Recommended crack opening displacement clip gauge with Wheatstone bridge and details of positioning on holders, performed on a specimen

5. SPECIMENS FOR FRACTURE TESTING

Strict requirements for specimen shapes and manufacturing are specified in standards.

5.1. Marking of samples and specimens

Series of different pre-cracked specimens are defined, marked as presented in Fig. 14. A consistent and uniform specimen mark includes:
– mark for specimen shape;
– mark for acting load, in small brackets, behind the specimen shape mark;
– mark for crack direction, also in small brackets, which follows loading mark (Fig. 15).

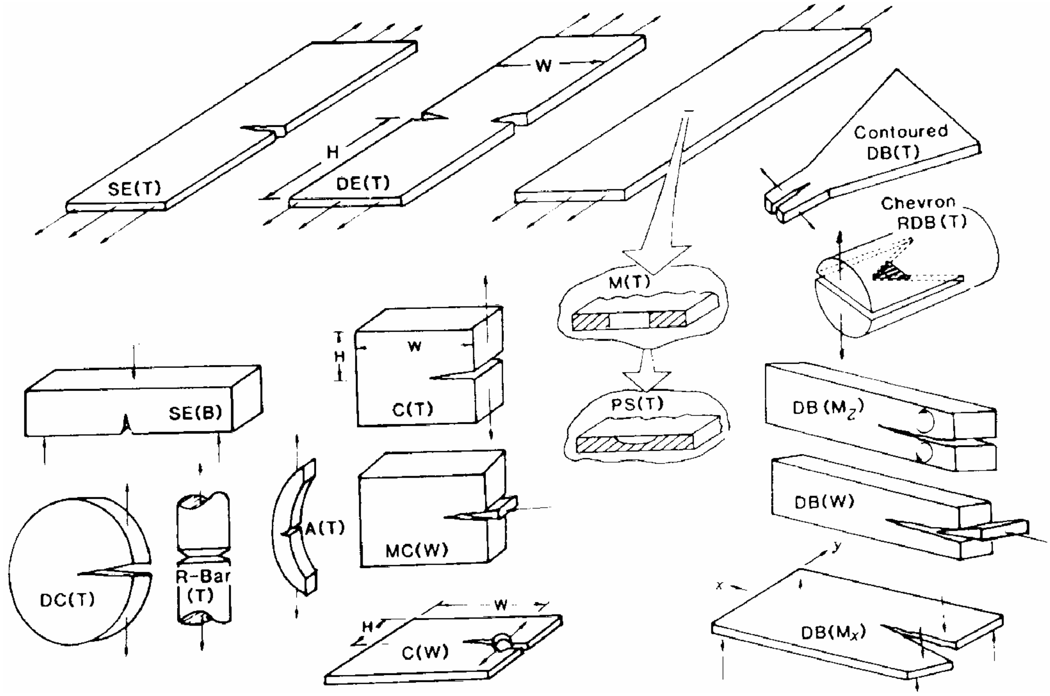

Figure 14. Basic fracture mechanics specimen shapes and their marks

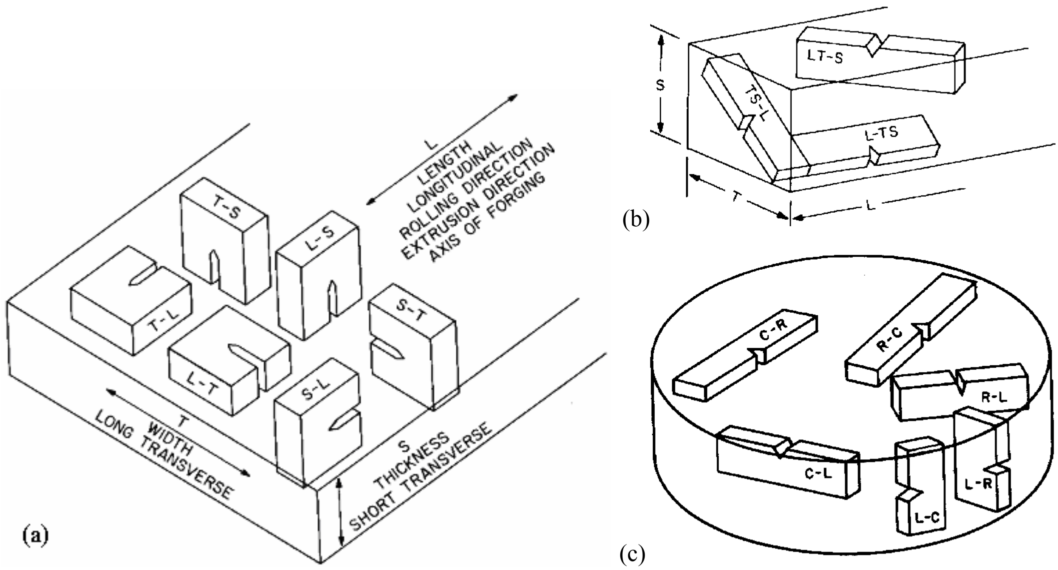

Figure 15. Marking of cracked specimen position in a material of rectangular and circular cross-section: a) specimen (and crack) position coinciding with main material directions; b) specimen inclined to main material directions; c) specimen from the circular cross-section material (L–direction of grain elongation; C–circumferential or tangential direction; R–radial direction)

On a parallelepiped shaped specimen, side surfaces are the sides perpendicular to the crack front, while the edge surfaces are all other surfaces (sides).

Different specimens, introduced by standards so far, contain marks of one, two, or three capital letters (Fig. 14). Therefore, the marks used are:

M – specimen with a central through-crack (for tension);

DE – specimen (for tension), cracked on both sides;
SE – specimen cracked on one side (*H/W* > 0.6);
C – compact version of the SE specimen (*H/W* = 0.6); i.e. MC for 0.3 < *H/W* < 0.6
DC – compact disc-shaped specimen;
A – arc-shaped specimen;
DB – double beam type specimen;
RDB – round double beam type specimen;
R – BAR – bar-shaped specimen;
PS – specimen with a central surface crack (for tension);
Chevron RDB – round specimen with a chevron type notch.

When the above mentioned marks are used, it is understood that a fatigue crack has been done on the specimen. If the specimen is made only with the notch, without the crack, then the mark "with notch" is added to the specimen mark.

The type of loading is marked by a letter in small brackets, added just behind the shape mark. The following marks are used: (T)–tension; (B)–bending; (M_x)–torsion moment around the *x* axis; (W)–opening by wedge; (W_b)–opening by screw.

The material is used in structures in different directions and the load will produce different crack behaviour because of anisotropy, depending on the direction of mechanical processing or grain direction. This has to be taken into account in specimen manufacture by determining the material delivery condition (rolled and double rolled plate, forging, drawn or rolled bar). For rectangular cross-section of a material with the anisotropy (plate, band, drawn, and rolled products, forgings, with asymmetric grain direction), for specimen positions coinciding to the main directions, inclined specimen positions, and for circular cross-section products, the marking system is shown in Fig. 15.

Capital letters are applied for direction marking: L–direction of the principal (main) deformation (maximum grain flow), (rolling direction for plates and bands, particular directions for forging); T–direction of least deformation; S–third orthogonal direction.

When specimen and crack position is marked with two letters, the first letter indicates the direction perpendicular to the crack plane, and the other letter indicates the direction of expected crack development (Fig. 15a). For marking specimens with inclined cracks, three letters are used. In that case, L–TS shows that the crack is perpendicular to the main direction L and that its development is expected between directions T and S (Fig. 15b). Mark TS–L shows that the crack plane is perpendicular to an intermediate orientation, between directions T and S and that crack development is expected in direction L.

The marking of specimen and crack position for material of circular cross-section, shown in Fig. 15c, presents the main deformation in the longitudinal direction. So, the letters used are: L–for the direction of grain elongation; R–for radial direction; C–for the circumferential or tangential direction.

5.2. Terms defining the crack

For standard testing, the most common used specimens are those with a through-crack, e.g. compact tension specimen C(T) or specimen cracked on one side for bending SE(B). Therefore, the given definitions (Fig. 16) are related to this crack type but are used for other types, when possible. The surface crack is used only for tensile panel (ASTM 740). Embedded cracks cannot be made under controlled process, therefore are not suitable for standard testing; however, they are often present in real structural components.

A real crack is, according to JUS C.A4.083, a cavity in a body, limited by two facing surfaces, which are at a distance much smaller than crack dimensions. Real crack surfaces are uneven and, depending on their initiation and growth, they can have larger or smaller roughness. Such a crack is not suitable for analysis, so the term “ideal crack” is introduced, defined as a mathematical crack. In the unloaded state it has two separated, smooth and overlapped facing surfaces in the same plane (the crack plane) xOz (Fig. 16a), connected at the smooth line–the crack front. The front of an ideal through-crack is a straight line, or semi-ellipse or ellipse of surface- and embedded cracks, respectively. In the loaded specimen additional crack elements will appear (Fig. 16b). Cracks defined in this way enable mathematical analysis of fracture mechanics parameters.

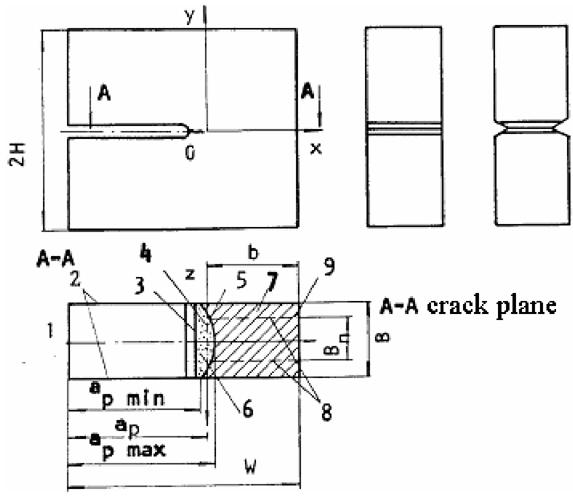

Figure 16a. Elements of an ideal through-crack in a flat specimen: 1–front crack surface (front plane); 2–side surfaces of specimen; 3–front of notch; 4–front of ideal crack; 5–front of real crack; 6–crack plane; 7–specimen crack plane cross-section; 8–front of side notch; 9–back specimen surface

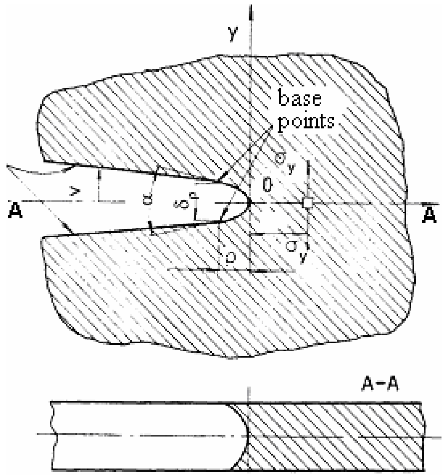

Figure 16b. Additional crack elements of flat specimens under loading effect: base points indicate fatigue crack tip before fracture testing; ρ–radius of blunted crack tip; δ_p–crack tip opening displacement; α–crack surface angle; v–crack opening displacement; σ_y–tensile stress component

The most important element of the through-crack is its length, a (Fig. 16a), as the linear measure in the main crack growth direction. In surface fracture, the depth, i.e. smaller semi-axis of the ellipse is a, while the longer semi-axis is c, and the same marking system is accepted for embedded cracks (Fig. 5).

During analysis the difference between physical, a_p, and effective crack length, a_e, should be made. Physical crack length is the distance between the referent plane on a specimen and corresponding crack front (Fig. 16a). Considering that the front of an ideal crack is curved, the average value of more measures along the crack front is taken for physical crack length. To obtain effective crack length, the quantity r_Y is added to physical crack length, which defines the effect of plastic zone ahead of the crack tip. It is practically impossible to measure the plastic-deformed zone size, therefore its influence is shown by increasing the radius ρ of crack tip blunting.

Initial crack length, a_o, is the crack length before the testing; a_{po} is the initial length of a physical crack. Crack growth, Δa, is the difference of actual and initial crack lengths. Normalized crack size, a/W, is the ratio of crack length, a, and specimen width, W. For the surface crack, crack entail is the ratio of crack depth, a, and specimen thickness, B.

6. SPECIMEN NOMINAL STRESS AND EFFECTIVE MATERIAL FLOW STRESS

It is necessary to determine the nominal stress in the smallest specimen cross-section for examination of cracked or notched specimen fracture, neglecting stress concentration and gradient, involved by shape geometry.

During pure tension by force P in specimens M(T), DE(T), PS(T), R-BAR, of cross-section A_N, nominal stress σ_N is introduced

$$\sigma_N = \frac{P}{A_N} \tag{9}$$

The area of rectangular cross-section is equal to:

$$A_N = B(W - a)$$

where B is specimen thickness, W is the width, a is crack or notch length, so $(W - a)$ is the remaining ligament.

For circular cross-section in a crack plane of R–BAR specimen, the smallest diameter is d, therefore the cross-section area is:

$$A_N = \frac{\pi d^2}{4}$$

Pure bending moment M occurs in SE(B) specimens, and the nominal stress is:

$$\sigma_N = \frac{6M}{B(W - a)^2} \tag{10}$$

In compact C(T) specimen, the stress is composed of bending and tensile stress, so the nominal stress is:

$$\sigma_N = \frac{2P(2W + a)}{B(W - a)^2} \tag{11}$$

Now the characteristic values of nominal stress can be defined:

– sharp-notched stress, σ_s, largest nominal stress (in the smallest cross section area of the specimen), which can be transferred by a specimen with notch; this value depends on the shape of the specimen and notch, since the smallest cross-section and elastic stress concentration also depend on it;
– cracked stress, σ_c, largest nominal stress (in the smallest cross-section area of specimen), which can be transferred by a cracked specimen;
– residual stress, σ_r, represents the stress at the time of fracture in a cross-section away from the crack plane, which is determined by material resistance equations.

Effective yield stress, σ_Y, is an accepted flow stress value in the uniaxial tensile test of standard smooth specimen. In the result analysis of fracture mechanics testing it can be the conventional yield stress, $R_{p0,2}$, or flow (strain hardening) stress, σ_Y, defined as an average of yield strength, R_p, and ultimate tensile strength, R_m:

$$\sigma_Y = \frac{R_p + R_m}{2} \tag{12}$$

6.1. Typical specimen size, configuration and preparation

Two specimen configurations are most popular in fracture mechanics testing: compact tension specimen, C(T), and single edge-notched bend specimen, SE(B), presented in Fig. 14, due to material economy and convenient preparation. Therefore, they will be presented here as typical. The choice between the bend and compact specimen is based on:

– The amount of material available (the bend takes more).
– Machining capabilities (the compact has more detail and costs more to machine).
– The loading equipment available for testing.

Proportional dimension of C(T) specimen and tolerance are presented in Fig. 17, for two options: straight (a) and stepped notched (b). Proportional dimensions and tolerance for a rectangular section bend specimen SE(B) are presented in Fig. 18.

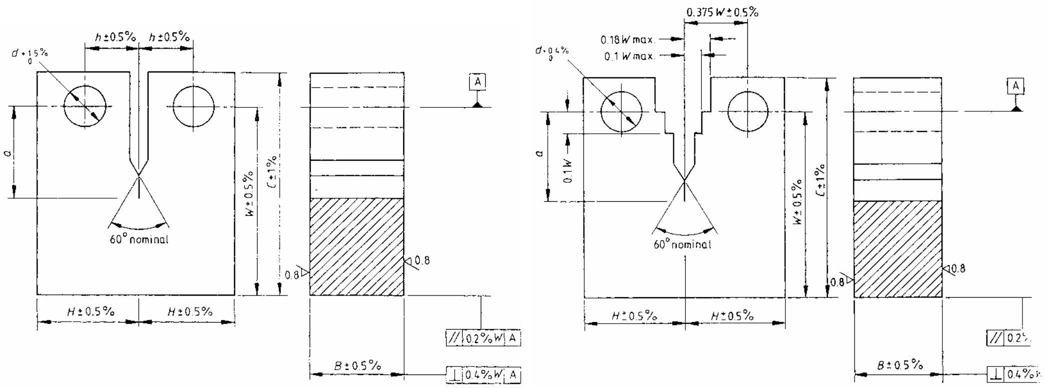

a. straight notch specimen b. stepped notch specimen

Figure 17. Proportional dimensions for compact tension specimen: B–thickness; W–effective width ($W = 2B$); total width, $C = 1.25W$ min; half height, $H = 0.6W$; hole diameter, $d = 0.25W$; half distance between holes, $h = 0.275W$; crack length, $a = (0.45$ to $0.55)W$, surface finish is in μm

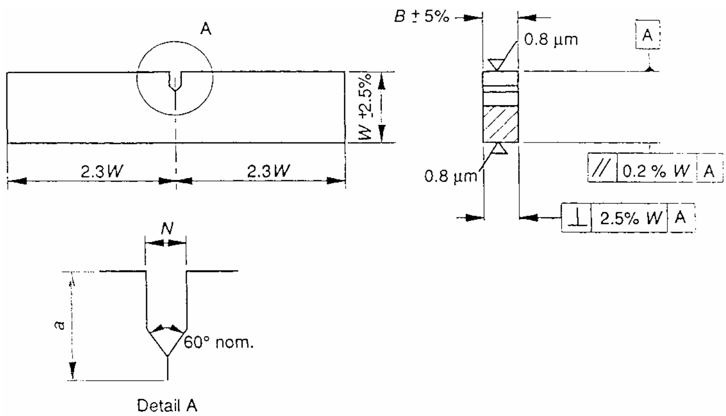

Figure 18. Proportional dimensions and tolerance for a rectangular section bend specimen: B–thickness; width, $W = 2B$; and crack length, $a = (0.45$ to $0.55)W$; surface finish is in μm

In certain cases, it may be desirable to use specimens of W/B ratios other than 2: for single-edge bend specimen $1 \leq W/B \leq 4$, and for compact specimen $2 \leq W/B \leq 4$; any thickness can be used as long as qualification requirements are met.

For valid results of plane strain fracture toughness testing according to standard, it is necessary that specimen thickness B and crack length a, are greater than the value obtained from the equations:

$$B \geq 2.5\left(\frac{K_{Ic}}{\sigma_Y}\right)^2 \quad a \geq 2.5\left(\frac{K_{Ic}}{\sigma_Y}\right)^2 \tag{13}$$

The choice of the starting specimen size is based on calculated value K_{Ic}, as its over-estimating is recommended, e.g. using factor 4 instead of 2.5 in Eq. (13). When the adequate K_{Ic} value is obtained with such a specimen, the next tests can use smaller specimens, taking into account that Eq. (13) is always satisfied. As an alternative to the criteria (13), data from Table 1 can be used to start assessment of the specimen size.

Table 1. Recommended specimen dimensions

Ratio $R_{p0.2}/E$ above		0.0050	0.0057	0.0062	0.0065	0.0068	0.0071	0.0075	0.0080	0.0085	0.0100
below	0.0050	0.0057	0.0062	0.0065	0.0068	0.0071	0.0075	0.0080	0.0085	0.0100	>
Recommended value of a, B, mm	100	75	63	50	44	38	32	25	20	12.5	6.5

For determining J_{Ic}, the measure of fracture toughness, C(T) and SE(B) specimens are recommended. The requirement, corresponding to Eq. (11), in this case is given as:

$$B \geq 25\frac{J_{Ic}}{\sigma_Y} \qquad b_o = W - a_o \geq 25\frac{J_{Ic}}{\sigma_Y} \tag{14}$$

Every thickness B is acceptable, if it fulfils condition (14), which allows much smaller dimensions compared to condition (13), which enables determining a measure of fracture toughness for tougher materials, too.

The dimensions of other specimen types can be determined on the basis of accepted B value, and the notch is made so that a specimen has a ratio a/W between 0.45 and 0.55. For final machining, 0.8 mm should be left, unless determined otherwise because of the available material (does not relate to the notch).

All specimens shall be precracked in fatigue. Experience has shown that it is impractical to obtain a reproducibly sharp, narrow machined notch which simulates a natural crack well enough to provide a satisfactory fracture toughness test result. The most effective artifice for this purpose is a narrow notch from which extends a comparatively short fatigue crack (precrack). It is produced by cyclically loading the notched specimen for a number of cycles, usually between 10^4 and 10^6, depending on specimen size, notch preparation, and stress intensity level. The dimensions of the notch and precrack, and the sharpness of the precrack shall meet certain conditions that can be readily met with most engineering materials since the fatigue cracking process can be controlled when careful attention is given to known contributory factors. However, there are some materials that are too brittle to be fatigue-cracked since they fracture as soon as the fatigue crack initiates; these are outside the scope of present test methods.

Three forms of fatigue crack starter notches are shown in Fig. 19. To facilitate fatigue cracking at low stress intensity levels, the root radius for a straight-through slot terminating in a V-notch should be 0.08 mm or less. If a chevron form of notch is used, the root radius may be 0.25 mm or less. In case of a slot, tipped with a hole, it will be necessary to provide a sharp stress raiser at the end of the hole.

The crack length (total length of the crack starter configuration plus the fatigue crack) shall be between 0.45 and 0.70W for J integral and δ determination, but is restricted to the range from 0.45 to 0.55 for K_{Ic} determination. For a straight-through crack starter terminating in a V-notch (Fig. 19), the length of the fatigue crack on each surface of the specimen shall not be less than 2.5%W or 1.3 mm minimum, and for a crack starter tipped with a drilled hole (Fig. 19), the fatigue crack extension from the stress raiser tipping the hole shall not be less than 0.5D or 1.3 mm minimum on both surfaces of the specimen, where D is the diameter of the hole. For a chevron notch crack starter (Fig. 19), the fatigue crack shall emerge from the chevron on both surfaces of the specimen.

The equipment for fatigue cracking should be such that stress distribution is uniform through specimen thickness; otherwise the crack will not grow uniformly. The stress distribution should also be symmetrical about the plane of the prospective crack; otherwise the crack may deviate from that plane and the test result can be significantly affected. The K calibration for the specimen, if it is different from the one given in this test method, shall be known with an uncertainty of less than 5%. Fixtures used for precracking should be machined with the same tolerances as those used for testing.

The fatigue precracking shall be conducted with the specimen fully heat-treated to the condition in which it is to be tested. No intermediate treatments between precracking and testing are allowed. The combination of starter notch and fatigue precrack shall conform to the requirements shown in Fig. 20.

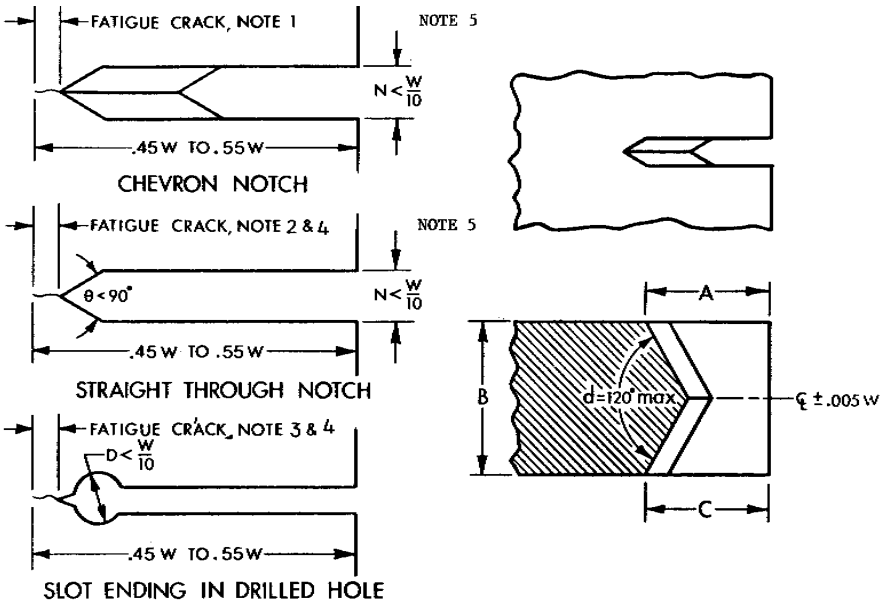

(a) Starter Notches and Fatigue Cracks (b) Detail of Chevron Notch

Figure 19. Fatigue crack starter notch configuration

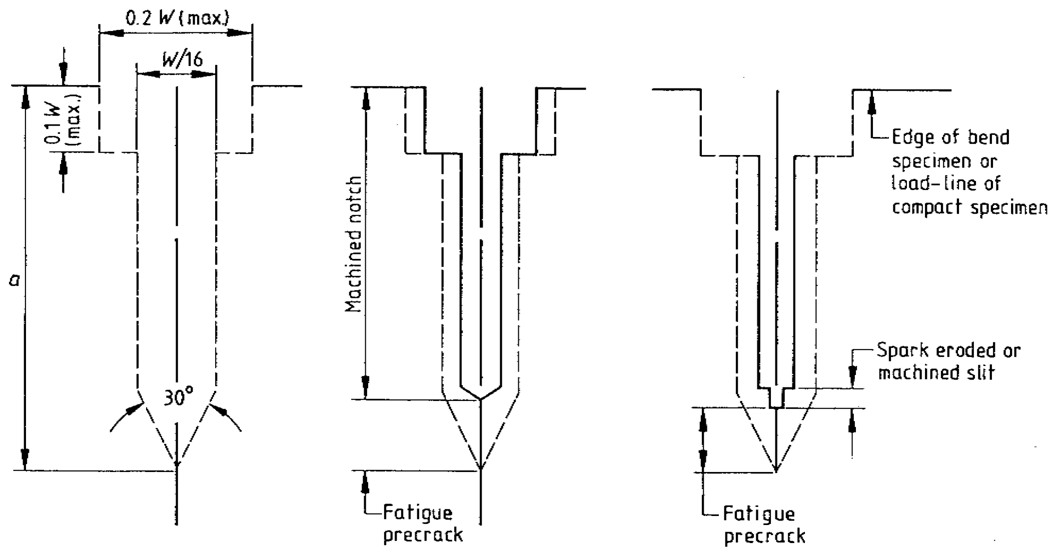

(a) Envelope (b) Notch geometries

Figure 20. Envelope of fatigue crack and crack starter notches

Allowable fatigue load values are based on the load P_f. There are several ways of promoting early crack initiation: (1) by providing a very sharp notch tip, (2) by using a chevron notch (Fig. 19), (3) by statically preloading the specimen in such a way that the notch tip is compressed in a direction normal to the intended crack plane (to a load not to exceed P_f), and (4) by using a negative fatigue load ratio; for a given maximum fatigue load, the more negative the load ratio, the earlier crack initiation is likely to occur. The peak compressive load shall not exceed P_f.

Fatigue precracking can be conducted under either load or displacement control. If the load cycle is maintained constant, the maximum K and the K range will increase with crack length; if the displacement cycle is maintained constant, the reverse will happen. The initial value of maximum fatigue load should be less than P_f. The specimen shall be accurately located in the loading fixture. Fatigue cycling is then begun, usually with a sinusoidal waveform and near to the highest practical frequency. There is no known marked frequency effect on fatigue precrack formation up to at least 100 Hz in the absence of adverse environments. The specimen should be carefully monitored until crack initiation is observed on one side. If crack initiation is not observed on the other side before appreciable growth is observed on the first, then fatigue cycling should be stopped to try to determine the cause and find a remedy for unsymmetrical behaviour. Sometimes, simply turning the specimen around in the fixture will solve the problem. The length of the fatigue precrack from the machined notch shall not be less than 5% of the total crack size, a, and not less than 1.3 mm. For the final 50% of fatigue precrack extension or 1.3 mm, whichever is less, the maximum load shall be no larger than P_f, a load such that the ratio of maximum stress intensity factor to Young's modulus is equal to or less than 0.0002 $m^{1/2}$ or 70% of the maximum load achieved during the test, whichever is less. The accuracy of these maximum load values shall be known within 5%.

Several important effects connected with the specimen should be mentioned. The first refers to material strength. It is clear from Eq. (11) that the required specimen thickness for plane strain established in tests is reversely proportional to the square of K_I/σ_Y. Therefore, the required specimen thickness is possible to obtain only if the tested material is of very high strength, e.g. steel with yield stress above 1000 MPa. For common structural steels, with yield stress up to 500 MPa, large thickness of specimen is required for valid plane strain fracture toughness testing, e.g. for steel S355, with yield stress 355 MPa, the specimen thickness should be 200 mm. Taking into account the ratio of specimen dimensions, it is clear that this kind of test is practically unfeasible. It can be concluded that standards for determining plane strain fracture toughness (ASTM E399, BS 5447, and JUS C.A4.084) are applicable on only a small class of materials with high strength level, i.e. only in the area of linear elastic fracture mechanic (LEFM). By introducing parameters of elastic-plastic fracture mechanics (EPFM), crack opening and J integral, the application area of fracture mechanics is significantly expanded and covers materials with low strength, too, interesting for general constructions, for which the testing result analysis determines the competent fracture mechanics parameter. Therefore, it is natural that new fracture testing standards are generalized, e.g. ASTM E 1820, BS 7448, EFAM GTP 94.

The second effect is referred to the shape and dimensions of the specimen. Nowadays generalized standards accept the application of only two specimen types, SE(B) and C(T) and there is no difference in requirements when testing materials have different strength. For industrial needs it is sufficient to use only these two specimen types. Structural integrity analysis on today's level of design and exploitation, especially for life assessment, can demand the application of other specimen types.

The sharpness of the notch and the crack is prerequisite for simulation of real crack in specimen. Plane strain condition is reflected to specimen thickness and to large stress concentration, which can be achieved only on the tip of a very sharp, fatigue crack. For a high strength material, which behaves as linear elastic, a sufficient stress concentration can be also achieved by a sharp notch (V notch on a Charpy specimen or notch made by electrical discharging). In that case, the fatigue crack may not be necessary to obtain valid testing for determining plane strain fracture toughness.

7. TESTING PROCEDURES FOR SPECIMENS CONTAINING CRACK

Standard recommendation is that three specimens should be tested under the same conditions. The ASTM E 1737 standard does not specify a number of specimens for the successive unloading method, but the older E 813 standard specifies the testing of at least five specimens under the same conditions.

Requirements for measuring dimensions are defined, where the crack length can be measured after the test, on a fractured specimen.

7.1. Typical diagrams obtained by pre-cracked specimen testing

For easier testing evaluation, the standards provide basic diagram forms, which can be obtained during the testing of fracture mechanics parameters. The six typical diagrams load vs. displacement (crack opening or load line), defined in BS 7448, are given in Fig. 21. First three diagrams, (1), (2), (3), because of total or most linear dependence of force F and crack opening V (i.e. load line displacement q) can produce a valid plane strain fracture toughness result K_{Ic}. Diagrams (4), (5), (6) correspond to the highest values of elastic-plastic fracture toughness (CTOD or J).

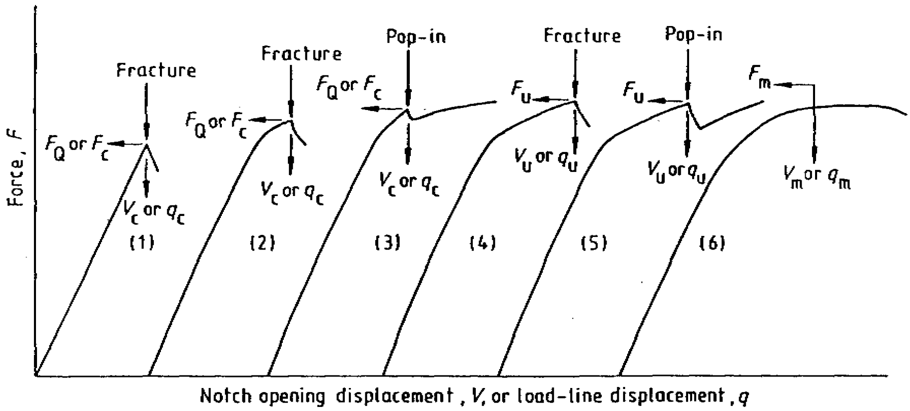

Figure 21. Typical diagrams for fracture toughness testing according to BS 7448

The characteristic of plane strain fracture toughness is brittle material behaviour, so the appropriate load for calculation, F_Q, is determined according to diagrams given in Fig. 22. First, the secant line is drawn, whose slope determined by quantity d, 5% lesser than the starting slope of the $F–V$ diagram, i.e. only 4% lesser on the $F–q$ diagram for bend specimens. Load F_Q is the highest load recorded before F_d for type I and II diagrams, and corresponds to the force F_d for a type III diagram. If the F_{max}/F_Q ratio is lower than 1.1, the K_Q is calculated, competent to assess plane strain fracture toughness. If that ratio is greater than 1.1, CTOD or J should be determined as a fracture mechanics parameter, as for type (4), (5), and (6) diagrams, shown in Fig. 21.

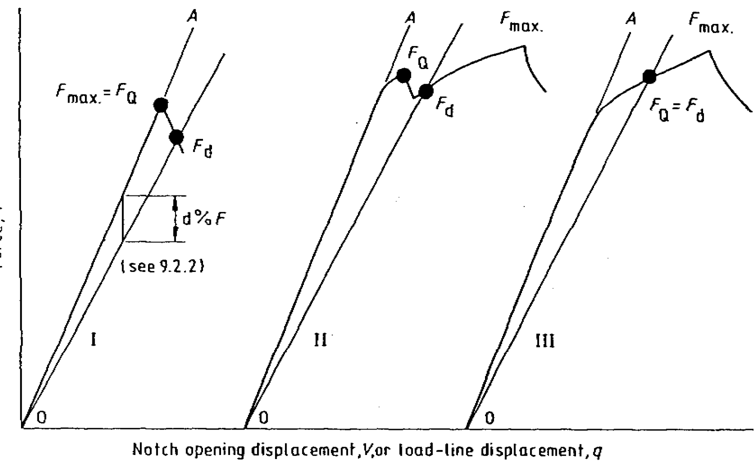

Figure 22. Determination of a appropriate load for calculation of plane strain fracture toughness

On diagrams in Figs. 21 and 22, the crack opening, i.e. notch opening displacement V or load-line displacement q are recorded on x axes. Subscript c (in V_c, q_c) indicates brittle fracture or pop-in if Δa is lesser than 0.2 mm. Subscript m (V_m, q_m) indicates that maximum load level is achieved for the first time for general yielding. Subscript p indicates the plastic component, which corresponds to F_c, F_u or F_m (Fig. 23). Subscript u indicates brittle fracture or pop-in for Δa greater than or equal to 0.2 mm. The same subscripts are also used to indicate appropriate crack-tip opening values CTOD (δ), and the J integral.

Calculation of an appropriate crack opening value δ requires determining appropriate load F and opening displacement V values. For diagrams (1) through (5) in Fig. 21 these values are (F_c, V_c) or (F_u, V_u), depending on whether Δa is lesser (subscript c), or greater, or equal to (subscript u) 0.2 mm, and correspond to:

- fracture before pop-in;
- first major fracture pop-in, or the load before reaching the maximum level, followed by a force reduced by at least 5%;
- the fracture, when all greater pop-in values give a value d less than 5%.

For type (6) diagram, (F_m, V_m) values are determined, corresponding to the maximum achieved load level, if the fracture or pop-in, which produces d value greater than 5% do not appear before reaching maximum load.

The plastic displacement component V_p is determined graphically (Fig. 23) or analytically, based on the elastic compliance, by subtracting the elastic component V_e from total displacement V.

Proper (F, q) values for J integral calculation (Fig. 24) are determined in a similar way, and considering bend specimens, the value d is 4%. The work of plastic component U_p should also be determined by measuring the area under the F–q dependence curve, directly from the diagram, by computer, by numerical integration, or combining numeric integration with elastic compliance, which means subtracting the elastic component U_e from the total area U. Except for the determination of single J integral values, its value can be used for determining the resistance curve, which involves a larger number of points in J integral and crack growth Δa diagram. The initial part of the resistance curve, up to crack growth of 2 mm, is also used for determining critical value J_{Ic} as a measure of fracture toughness. For this purpose, the ASTM E 1737 standard specifies a testing method of one specimen with the use of elastic compliance, by successive unloading, and monitoring crack opening V change, and the load-line displacement q with the increase of force F. An additional limitation in this test refers to minimal unloading force, chosen so that the force range is not less than half the force for fatigue F_M or 50% of the applied force F (lesser of these two quantities). In order to compare the actual crack length, the starting elastic compliance should be determined at a force chosen between 50% and 100% of maximum fatigue force. Decrease in successive unloading line slope corresponds to the increase of crack length, i.e. to the reduced specimen compliance. However, monitoring of crack growth by other means is also acceptable, like potential drop measurement during testing. In that case only the force vs. load-line displacement plot is used, from which the released energy can be determined.

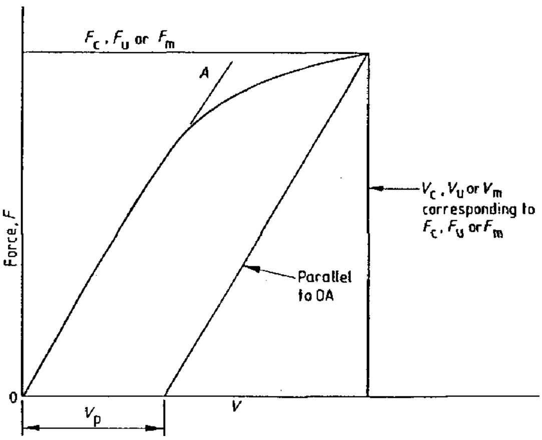

Figure 23. Determination of load and displacement for calculating CTOD

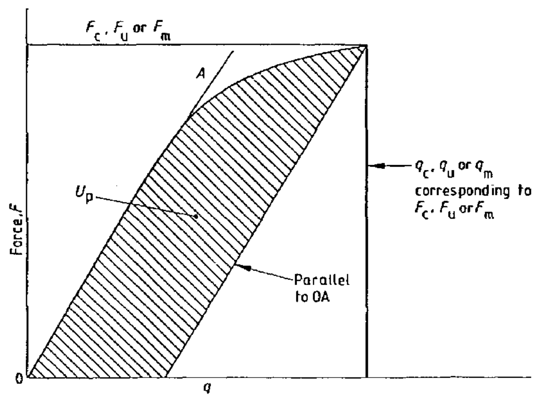

Figure 24. Determination of load and load-line displacement for J integral calculation

8. ANALYSIS OF TEST DATA

European and British standards for fracture mechanics testing have united existing standards for individual fracture mechanic parameters testing. Therefore, before starting the tests, proper fracture mechanics parameters should be assessed, in other words, one should chose between the stress intensity factor, K, the J integral, and crack tip opening displacement, δ. For unstable fracture, the parameters are measured at the point instability or near it. For stable crack growth, it is necessary to determine the resistance curve (the R curve), i.e. the change of J or δ with respect to crack growth Δa. The European standard for determining fracture toughness ESIS P2-92 specifies only the use of single edge notch bend (SEN(B)), and compact tensile (C(T)) specimens.

8.1. Selection of proper fracture mechanics parameter

It is impossible, prior to testing, to assess whether the specimen will behave in a stable or unstable manner, and the ideal diagram force–displacement in Fig. 25 determines which fracture mechanics parameter should be measured, as the plot form depends on material and dimensions. The testing temperature also affects the selection of proper fracture mechanics parameters when ferrite steels are tested, since the plastic to brittle transition of these steels at low temperatures (nil ductility transition temperature) is considered, as shown in Fig. 26.

In Figs. 25 and 26, the subscript “0.2” refers to blunting and crack growth of 0.2 mm, and “0.2/BL” refers to crack growth after blunting at the crack tip; subscript “5” shows that a special clip gauge for δ_5 has been used.

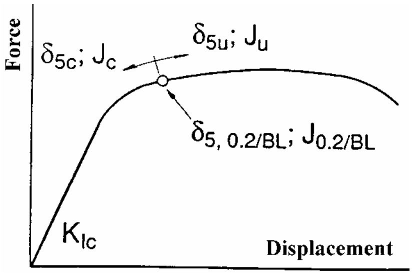

Figure 25. Selection of proper fracture mechanics parameter according to GKSS (EFAM GTP 94)

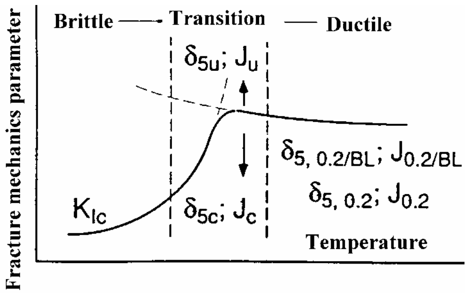

Figure 26. Effect of temperature on the selection of proper fracture mechanics parameter

8.2. Procedure with the specimen after testing

Except force and displacement data, the calculation of fracture mechanics parameters requires crack data: initial fatigue pre-crack length, stretch zone (blunting), and crack growth (Fig. 27). These values can be determined after testing and final specimen fracture. If unstable fracture has occurred while testing, i.e. if the specimen was broken during the test, initial crack length and stable crack growth are measured.

The final crack front is marked by additional fatigue of the specimen with the ratio minimum/maximum load greater than 0.6 and a reduced force compared to the final force in testing. For steel specimens, heating in a furnace at 300°C can be used for tinting.

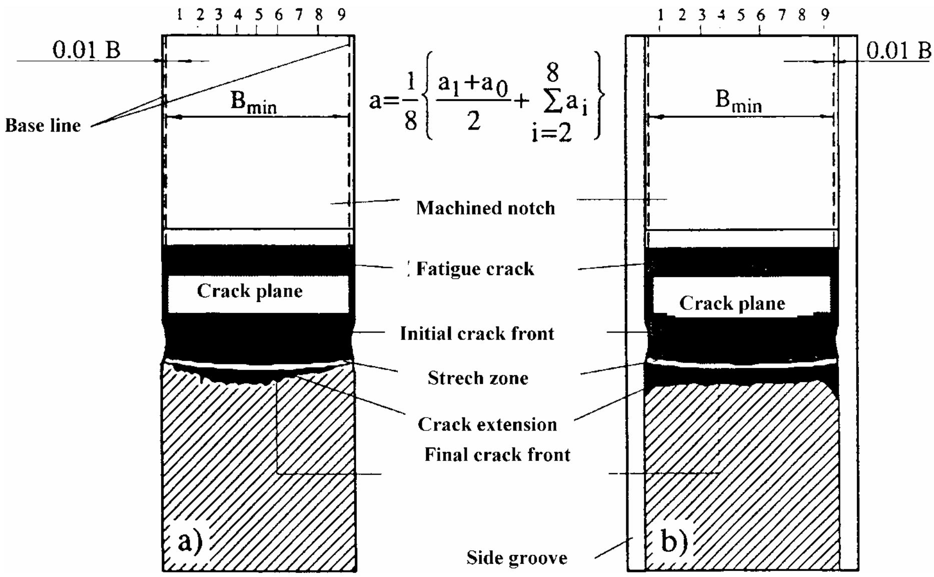

Figure 27. Definition of fracture characteristics for SEN(B) specimen:
a) specimens without side grooves; b) specimens with side grooves

The most accurate crack measuring is when the crack plane surface area is divided by specimen width. It is enough to measure the crack length in 9 equally placed positions (Fig. 27). Initial crack length a_o of SEN(B) specimen is the distance from the specimen surface to the tip of the fatigue pre-crack, while for a C(T) specimen it is the distance from the holder axis to the tip of the fatigue pre-crack. Crack length is calculated as the sum of average measurement at points 1 and 9 and the average of the remaining seven points (Fig. 27).

The test report should include information of any single value scattered for more than ±10% of the average value, because this can affect the result accuracy. With the same accuracy, the distance from notch tip to the fatigue pre-crack tip should be measured. The report should include if it is less than $0.05a_o$ or 1.5 mm. It is recommended to measure crack growth during testing, Δa, as the difference between the front of the final- and initial crack lengths with 0.05 mm accuracy. Also, determine the greatest and lowest crack growth in points 1–9 (Fig. 27), and include if the difference is greater than 20% compared to the average crack extension Δa, or greater than 0.15 mm. Visual inspection should determine if regions of arrested unstable crack growth are present on the crack surface, and if they are, also include in report.

9. CALCULATION OF FRACTURE MECHANICS PARAMETERS AND REPORT

For calculating selected fracture mechanics parameters (Figs. 25 and 26), data of specimen dimensions (B, W, C-W, z), initial crack length a_o, yield strength $R_{p0.2}$ at testing temperature, and processed data from force–displacement plots (Figs. 21 to 24) are necessary.

It is impossible to determine K_{Ic} for fracture after elastic-plastic deformation, but it is possible to determine critical CTOD or critical J integral (J_{Ic}). Data used to determine K_{Ic} can be taken from the F–V or F–q plots, and from F–V plots for CTOD. The F–q plot can be used for determining J integral, while the F–V diagram can be used for determining crack growth. In case of compact specimens C(T) with stepped notch, load-line displacement q and crack opening displacement are measured at the same position, therefore are equal, and those plots can be used to determine CTOD and J integral. Pop-ins, expressed by force drop (vertical axes) and displacement (horizontal axes) that are less than 1% are neglected. The significance of greater pop-in values is described in BS 7448.

9.1. Calculation of plane strain fracture toughness K_{Ic}

For plane strain fracture toughness calculation, K_{Ic}, it is necessary to analyze the testing diagram, calculate the previous result, K_Q, and check if the obtained result meets dimension requirements of the specimen, regarding the material yield strength $R_{p0.2}$.

Results are interpreted according to Fig. 21. The secant line OF_d is drawn from the origin with the slope less than the tangent OA of the initial part of the plot. This slope is 5%, except for F–q specimen plot SEN(B), where it is 4%. For type I and II diagrams, F_Q is the highest force before F_d, for type III it corresponds to force F_d. If the calculated ratio F_{max}/F_Q is larger than 1.1, the result can be invalid for K_{Ic}, but if it is lesser than 1.1, K_Q should be determined.

The formula for the SEN(B) specimen is:

$$K_Q = \frac{F_Q S}{BW^{1.5}} f\left(\frac{a_o}{W}\right) \tag{15}$$

where S is the support span; B–thickness; W–specimen width; and $f(a_o/W)$ is a function

$$f\left(\frac{a_o}{W}\right) = \frac{3\left(\frac{a_o}{W}\right)^{0.5}\left[1.99-\left(\frac{a_o}{W}\right)\left(1-\frac{a_o}{W}\right)\left(2.15-\frac{3.93a_o}{W}+\frac{2.7a_o^2}{W^2}\right)\right]}{2\left(1+\frac{2a_o}{W}\right)\left(1-\frac{a_o}{W}\right)^{1.5}} \tag{16}$$

Equations used for compact tension specimens C(T) are:

$$K_Q = \frac{F_Q}{BW^{0.5}} f\left(\frac{a_o}{W}\right) \tag{17}$$

$$f\left(\frac{a_o}{W}\right) = \frac{\left(2+\frac{a_o}{W}\right)\left(0.886+4.64\frac{a_o}{W}-13.32\frac{a_o^2}{W^2}+14.72\frac{a_o^3}{W^3}-5.6\frac{a_o^4}{W^4}\right)}{\left(1-\frac{a_o}{W}\right)^{1.5}} \tag{18}$$

Values of $f(a_o/W)$ are given in standards by tables for easier calculation of K_Q.

Now the value $2.5(K_Q/R_{p0.2})^2$ is calculated according to Eq. (13). If it is lesser than crack length a_o, thickness B, and ligament $W-a$, and if other standard conditions are fulfilled, this quantity is the plane strain fracture toughness, i.e. $K_Q = K_{\mathrm{Ic}}$. If this is not the case, the report can only contain the value of K_Q. The obtained results can be further used for eventual determination of CTOD or J integral.

9.2. Crack opening CTOD calculation

All six types of force–displacement plots (Fig. 21) can be used for determining CTOD (δ). Data required for F_c, V_c, i.e. F_u, V_u, are determined according to Fig. 21 with the Δa value for a plot without significant pop-in, and for the first major pop-in before fracture, types (3) and (5) in Fig. 21, or at the first maximum force level for which force drop is 5% or greater, or for fracture, when all previous pop-in values are less than 5%. Values F_m, V_m, are determined for plots type (6) from Fig. 21. The above mentioned plot values are necessary for calculating specimen thickness B, its width W, value $C-W$ for compact specimens, and distance of the knife edge, and initial crack length a_o.

The equation used for SEN(B) specimen is:

$$\delta = \left[\frac{FS}{BW^{0.5}} f\left(\frac{a_o}{W}\right)\right]^2 \frac{(1-\nu^2)}{2R_{p0.2}E} + \frac{0.4(W-a_o)V_p}{0.4W+0.6a_o+z} \tag{19}$$

The equation for the C(T) specimen is:

$$\delta = \left[\frac{FS}{BW^{0.5}} f\left(\frac{a_o}{W}\right)\right]^2 \frac{(1-\nu^2)}{2R_{p0.2}E} + \frac{0.46(W-a_o)V_p}{0.46W+0.5a_o+(C-W)+z} \tag{20}$$

and with stepped notch the equation is:

$$\delta = \left[\frac{FS}{BW^{0.5}} f\left(\frac{a_o}{W}\right)\right]^2 \frac{(1-\nu^2)}{2R_{p0.2}E} + \frac{0.46(W-a_o)V_p}{0.46W+0.54a_o+z} \tag{21}$$

9.3. *J* integral calculation

All six diagram types can be used for this calculation too. The method for determining quantities F_c, q_c, F_u, q_u, i.e. F_m, q_m is the same as for CTOD, except that opening displacement V is replaced by load-line displacement q. Released energy of plastic deformation U_p is determined according to Fig. 24, as already explained.

With defined specimen data and plot, the J integral is calculated for SEN(B) specimen from the equation:

$$J = \left[\frac{FS}{BW^{1.5}} f\left(\frac{a_o}{W}\right)\right]^2 \frac{(1-\nu^2)}{E} + \frac{2U_p}{B(W-a_o)} \tag{22}$$

and for C(T) specimens:

$$J=\left[\frac{FS}{BW^{0.5}}f\left(\frac{a_o}{W}\right)\right]^2\frac{(1-\nu^2)}{E}+\frac{\eta_p U_p}{B(W-a_o)} \tag{23}$$

where the coefficient η_p is specified according to standard ASTM 1737 as:

$$\eta_p=2+0.522\left(1-\frac{a_o}{W}\right) \tag{24}$$

9.4. Data validity check

Results of specimen preparation and testing should be continually checked to eventually stop invalid testing in its earliest stage.

Before fatigue loading it is necessary to check if specimen dimensions are in accordance with specified limits.

Before carrying out the fracture test it is necessary to check if:

– the minimum crack length on the side of the specimen is at least $0.45W$;
– the fatigue crack on both sides of the specimen is 1.5 mm or $0.025W$ greater than the machined notch length, whichever is greater;
– the difference of crack lengths on both sides did not exceed 15% of average length of these two measurements;
– the fatigue crack is located in the appropriate envelope on both surfaces, according to standard.

After the test on specimen fracture, check that:

– multi-plane fatigue precracking and fracture is not present at the fatigue precrack front;
– the average crack length a_o is between $0.45W$ and $0.55W$;
– the crack length in any two measuring points does not differ by more than 10% of a_o;
– no part of the fatigue crack is closer to the notch than 1.3 mm or $0.025W$, whichever is larger.

Also, the following conditions should be fulfilled:

– when manually analysing the force versus displacement record, the initial slope should be between 0.85 and 1.5;
– stress intensity factor for fatigue K_f must be within the specified limits;
– the fatigue ratio R must not exceed 0.1.

9.5. Test report

The test report should contain:

– title and number of the standard according to which testing has been performed;
– identity of the test specimen;
– identity and form of the material tested (e.g. forging, plate, casting), and its condition;
– the geometry and main dimensions of the specimen tested;
– if the specimen has normal or reduced dimensions;
– crack plane orientation;
– fatigue precracking details, including the final force F_f and R values;
– tensile strength R_m and yield strength $R_{p0.2}$ of the specimen material at temperature of fatigue precracking;
– the span S used in a three-point bend test, if applicable;
– the knife edge thickness z, if applicable for opening displacement measurement;
– the rate of increase in starting stress intensity factor K;

– force F versus notch opening displacement V record, and/or force F versus load-line displacement q record;
– temperature T during testing;
– yield strength $R_{p0.2}$ of the specimen material at testing temperature;
– a diagram of the fracture surface showing crack length a_o and the shape and size of the fatigue precrack, the extent of stable crack extension Δa, and any evidence of arrested brittle crack extension associated with pop-in behaviour, or any other unusual features of the fracture surface;
– the value of plane strain fracture toughness K_{Ic} or corresponding quantity K_Q for invalid testing, including the F_{max}/F_Q ratio;
– value and type of CTOD;
– value and type of J (J_c, J_u, J_m);
– details of any of the above items that fail to meet validity requirements in the stated clauses, and thereby result in an invalid determination of fracture toughness according to this method.

REFERENCES

1. Irwin, G.R., *Fracture*, in Handbuch der Physic VI, Springerverlag. (1958)
2. Knott, J.F, *Fundamentals of Fracture Mechanics*, Butterworth's, London. (1973)
3. Pellini, W.S., *Evaluation of Principles for Fracture Safe Design of Steel Structures*, NRL 6957, U.S. Naval Research Laboratory, Washington. (1969)
4. ASTM E399-83: Standard Test Method for Plane-Strain Fracture Toughness of Metallic Materials, Annual Book of ASTM Standards 1986, Vol. 03.01.
5. BS 7448-Part 1:1991, "Fracture mechanics toughness tests - Methods for determination of K_{Ic}, critical CTOD and critical J values of metallic materials"

STATIC AND IMPACT TESTING

Vencislav Grabulov, Military Technical Institute, Belgrade, Serbia & Montenegro

1. THE TENSILE TEST

1.1. Engineering stress-strain curve

Basic design information regarding strength and ductility of structural materials is provided by the engineering tensile test, widely used also as an acceptance test for the specification of materials. In this test, the specimen is subjected to a continually increasing uniaxial tensile force while simultaneous monitoring specimen elongation [1]. An engineering stress-strain curve is constructed from load-elongation measurements (Fig. 1). Significant points on the engineering stress-strain curve are shown in Fig. 2 and Fig. 3. The stress used in this stress-strain curve is the average longitudinal stress in the specimen, obtained by dividing the load P by the original specimen cross section area A_o.

$$S = \frac{P}{A_o} \tag{1}$$

The strain in the engineering stress-strain curve is the average linear strain, obtained by dividing the elongation of the specimen gauge length, δ, by its original length L_o.

$$e = \frac{\delta}{L_o} = \frac{\Delta L}{L_o} = \frac{L - L_o}{L_o} \tag{2}$$

Since both the stress and the strain are obtained by dividing the load and elongation by constant factors, the load-elongation curve will have the same shape as the engineering stress-strain curve. The two curves are frequently used interchangeably.

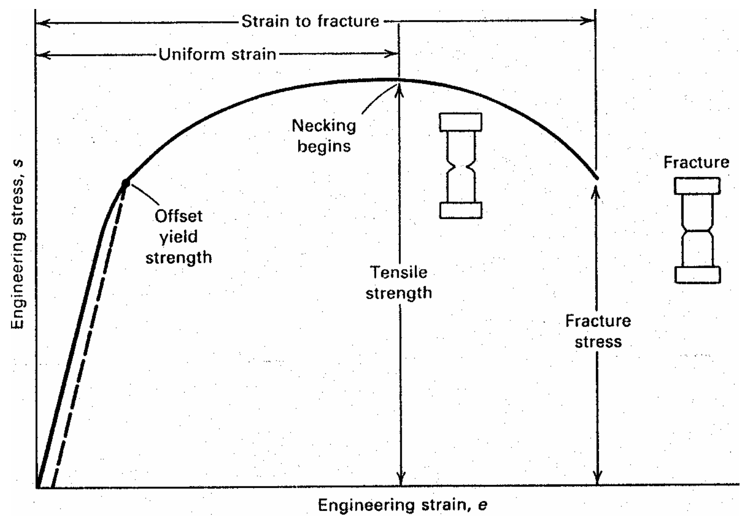

Figure 1. Engineering stress-strain curve

The shape of the curve and magnitudes of stress and strain of the material will depend on its composition, heat treatment, prior history of plastic deformation, and the strain rate, temperature, and state of stress imposed during testing. The basic parameters used to describe the stress-strain curve of a metal are the tensile strength S_{max}, yield strength or yield point (A or B), percent elongation, and reduction of area. The first two are strength parameters; the last two indicate ductility.

The general shape of the engineering stress-strain curve (Fig. 1) requires further explanation. In the elastic region stress is linearly proportional to strain. When the load exceeds a value corresponding to the yield strength, the specimen undergoes gross plastic deformation. It is permanently deformed if the load is released to zero. The stress producing continued plastic deformation increases with increasing plastic strain, i.e., the metal strain-hardens. The volume of the specimen remains constant during plastic deformation, $AL = A_oL_o$, and as the specimen elongates, it decreases uniformly along the gauge length in cross-section area. Initially, strain hardening more than compensates for this decrease in area and the engineering stress (proportional to load P) continues to rise with increasing strain. Eventually a point is reached where the decrease in specimen cross-sectional area is greater than the increase in deformation load, arising from strain hardening. This condition will be reached first at some point in the specimen that is slightly weaker than the rest. All further plastic deformation is concentrated in this region, and the specimen begins to neck or thin down locally. Because the cross-section area is now decreasing more rapidly than the deformation load is increased by strain hardening, the actual load required to deform the specimen falls and the engineering stress according to Eq. (1), likewise, continues to decrease until fracture occurs.

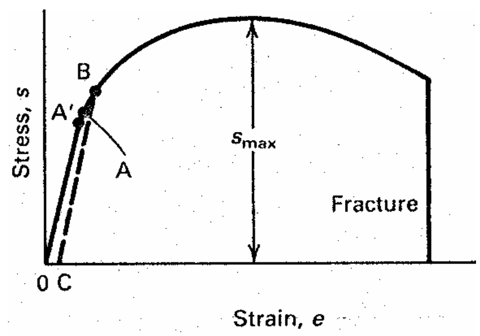

Figure 2. Typical tensile stress-strain curve for ductile metal, indicating yielding criteria in points A and B

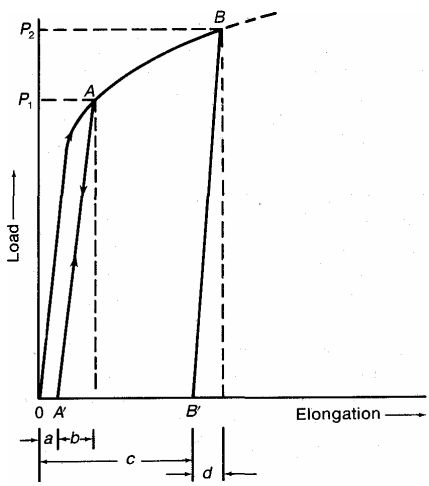

Figure 3. Loading and unloading curves showing elastic recoverable strain and plastic deformation

Consider a tensile specimen that has been loaded in excess of the yield stress and then the load is removed (Fig. 3). The loading follows the path 0-A-A'. Note that the slope of the unloading curve A-A' is parallel to the elastic modulus on loading.

The recoverable elastic strain while unloading is $b = S_1/E = (P_1/A_o)/E$ (E stands for elasticity modulus). The permanent plastic deformation is the onset a in Fig. 3. Note that elastic deformation is always present in the tensile specimen when it is loaded. If the specimen were loaded and unloaded along the path 0-A-B-B', the elastic strain would be greater than on loading to P_1, since $P_2 > P_1$, but the elastic deformation (d) would be less than the plastic deformation (c).

1.1.1. Tensile strength

The tensile strength, or ultimate tensile strength (UTS), is the maximum load divided by the original cross-sectional area of the specimen

$$S_u = \frac{P_{\max}}{A_o} \tag{3}$$

The tensile strength is the value most often quoted from the results of a tensile test; yet in reality it is a value of little fundamental significance for the strength of a metal. For ductile metals the tensile strength should be regarded as a measure of the maximum load which a metal can withstand under the very restrictive conditions of uniaxial loading. For many years it was customary to base the strength of parts on the tensile strength, suitably reduced by a safety factor. The current trend is in the more rational approach of basing the static design of ductile metals on yield strength. Because tensile strength is easy to determine and is quite a reproducible property, it is useful for purposes of specifications and for product quality control. Many empirical correlations between tensile strength and properties such as hardness and fatigue strength are often quite useful. For brittle materials, the tensile strength is a valid criterion for design.

1.1.2. Measures of yielding

The stress at which the onset of plastic deformation or yielding is observed depends on the sensitivity of strain measurements. In most materials there is a gradual transition from elastic to plastic behaviour, and the point at which plastic deformation begins is hard to define with precision. Various criteria for the initiation of yielding are used depending on the sensitivity of strain measurements and the intended use of the data.

1. True elastic limit based on microstrain measurements of the order of 2×10^{-6} mm/mm. This elastic limit is of very low value.
2. Proportional limit is the highest stress at which stress is directly proportional to strain. It is defined at deviation from the straight-line portion of the stress-strain curve.
3. The elastic limit is the greatest stress the material can withstand without any measurable permanent strain remaining on the complete release of load. With the sensitivity of strain usually employed in engineering studies (10^{-4} mm/mm), the elastic limit is greater than the proportional limit. Determination of the elastic limit requires a tedious incremental loading-unloading test procedure.
4. The yield strength is the stress required to produce a small specified amount of plastic deformation. The usual definition of this property is the offset yield strength determined by the stress corresponding to the intersection of the stress-strain curve and a line parallel to the elastic part of the curve offset by a specified strain (Fig. 1), usually specified as a strain of 0.2 percent (e = 0.002).

$$S_o = \frac{P_{(\text{strain offset}=0.02)}}{A_o} \tag{4}$$

A good way of viewing the offset yield strength is after the specimen is loaded to its 0.2% offset yield strength and thus unloaded, whence it becomes 0.2% longer than before the test. The yield strength obtained by an offset method is commonly used in design.

1.1.3. Measures of ductility

Ductility is a qualitative, subjective property of a material. In general, measurements of ductility are of interest in three ways [2]:

1. To indicate the extent to which a metal can be deformed without fracture in metal-working operations such as rolling and extrusion.
2. An indication to the designer, in a general way, of the ability of the metal to flow plastically before fracture. A high ductility indicates that the material is likely to deform locally without fracture.

The conventional measures of ductility obtained from tensile tests are the engineering strain at fracture e_f (usually called the elongation) and the reduction of area at fracture q. Both properties, usually expressed in percentage, are obtained after fracture, by joining the specimen back together and taking measurements of L_f and A_f

$$e_f = \frac{L_f - L_o}{L_o} \tag{5}$$

$$q = \frac{A_o - A_f}{A_o} \tag{6}$$

Since plastic deformation will be concentrated in the necked region of the tensile specimen, the value of e_f will depend on the gauge length L_o over which the measurement is taken. The smaller the gauge length, the greater will be the contribution to the overall elongation from the necked region, and the higher will be the value of e_f.

The reduction of area does not suffer from this difficulty. Reduction of area values can be converted into an equivalent zero-gauge-length elongation e_f. According to the volume constancy relationship for plastic deformation, $AL = A_oL_o$, one can obtain

$$\frac{L}{L_o} = \frac{A}{A_o} = \frac{1}{1-q}, \quad e_o = \frac{L - L_o}{L_o} = \frac{A_o}{A} - 1 = \frac{1}{1-q} - 1 = \frac{q}{1-q} \tag{7}$$

This represents the elongation based on a very short gauge length near the fracture.

Since the engineering stress-strain curve is often quite flat in the vicinity of necking, it may be difficult to establish the strain at maximum load without ambiguity.

1.1.4. Modulus of elasticity

The slope of the initial linear portion of the stress-strain curve is the modulus of elasticity, or the Young's modulus. The modulus of elasticity is a measure of stiffness of the material, for computing deflections of beams and other members. However, an increase in temperature decreases the modulus of elasticity. Typical values at different temperatures are given in Table 1, [3].

Table 1. Typical values of modulus of elasticity at different temperatures

Material	Modulus of elasticity E, $\times 10^3$ MPa				
	20°C	205°C	425°C	540°C	650°C
Carbon steel	207	186.3	155.25	134.5	124.2
Austenitic stainless steel	193	176	159	155	145
Titanium alloys	113.7	96.5	73.7	69.6	
Aluminium alloys	72.4	62	53.8		

1.1.5. Resilience

The ability of a material to absorb energy when deformed elastically and to return it when unloaded is called resilience. This is usually measured by the modulus of resilience, which is the strain energy per unit volume required to stress the material from zero stress to yield stress S_o. The strain energy per unit volume for uniaxial tension is $U_o = \frac{1}{2} S_x e_x$, and from the above definition the modulus of resilience U_R is

$$U_R = \frac{1}{2} S_o e_x = \frac{1}{2} S_o \frac{S_o}{E} = \frac{S_o^2}{E} \tag{8}$$

This equation indicates that the ideal material for resisting energy loads in applications where the material must not undergo permanent distortion, such are mechanical springs, is the one having a high yield stress and a low modulus of elasticity.

1.1.6. Toughness

The toughness of a material is its ability to absorb energy in the plastic range. The ability to withstand occasional stresses above yield stress without fracturing is particularly desirable in parts such are freight-car couplings, gears, chains, and crane hooks. Toughness is a commonly used concept which is difficult to pin down and define. One way of looking at toughness is to consider that it is the total area under the stress-strain curve. This area is an indication of the amount of work per unit volume which can be done on the material without causing it to rupture. Figure 4 shows stress-strain curves for high and low-toughness materials. The high-carbon spring steel has higher yield- and tensile strengths than the medium-carbon structural steel. However, the structural steel is more ductile and has a greater total elongation. The total area under the stress-strain curve is greater for the structural steel, and therefore it is a tougher material. This illustrates that toughness is a parameter which comprises both strength and ductility. The crosshatched regions in Fig. 4 indicate the modulus of resilience for each steel. Because of its higher yield strength, the spring steel has greater resilience.

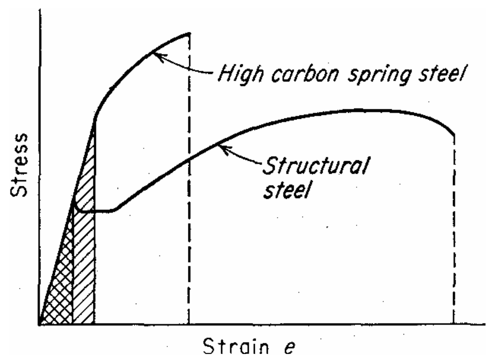

Figure 4. Comparison of stress-strain curves for high-and low-toughness materials

The area under the stress-strain curve can be approximated in different ways. For ductile metals which have a stress-strain curve like that of the structural steel (Fig. 4), the area under the curve can be approximated by either of the following equations:

$$U \approx S_u e_f \tag{9}$$

$$\text{or } U_T = \frac{S_o + S_u}{2} e_f \tag{10}$$

For brittle materials the stress-strain curve is sometimes assumed to be parabolic, and the area under the curve is given by approximation

$$U_T \approx \frac{2}{3} S_u e_f \tag{11}$$

1.2. True-stress – true-strain curve

The engineering stress-strain curve does not give a true indication of deformation characteristics of a metal because it is based entirely on original dimensions of the specimen, and these dimensions change continuously during the test. Also, ductile metal pulled in tension becomes unstable and necks down during the course of the test. Since the cross-section area of the specimen decreases rapidly at this stage in the test, the load required to continue deformation falls off. The average stress based on original area decreases likewise, and this produces the fall-off in the stress-strain curve beyond the point of maximum load. Actually, the metal continues to strain-harden all the way up to fracture, so that stress required to produce further deformation should also increase. If true stress is used, based on the actual cross-section area of the specimen, it is found that the stress-strain curve increases continuously up to fracture. If the strain is measured also instantaneously, the curve which is obtained is known as a true-stress–true-strain curve, or a flow curve. Any point on the flow curve can be considered as the yield stress for a metal strained in tension by the amount shown off the curve. Thus, if the load is removed at this point and then reapplied, the material will behave elastically throughout the entire range of reloading. Figure 5a shows the flow curve for a rigid, perfectly plastic material. For this idealized material, a tensile specimen is completely rigid (zero elastic strain) until axial stress equals σ_o, whereupon the material flows plastically at a constant flow stress (zero strain hardening). This type of behaviour is approached by a ductile metal which is in a highly cold worked condition. Figure 5b illustrates the flow curve for a perfectly plastic material with an elastic region. This behaviour is approached by a material such as plain carbon steel which has a pronounced yield-point elongation. A more realistic approach is to approximate the flow curve by two straight lines corresponding to the elastic and plastic regions (Fig. 5c).

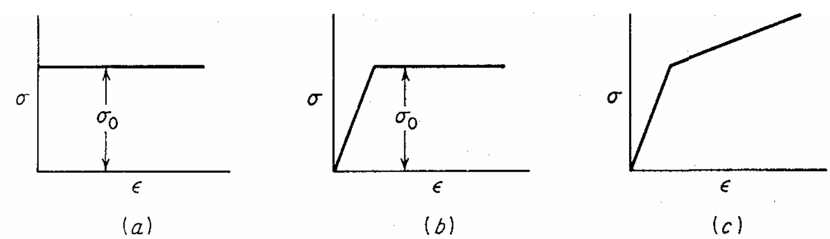

Figure 5. Idealized flow curves: (a) Rigid ideal plastic material; (b) Ideal plastic material with elastic region; (c) Piecewise linear (strain-hardening) material

The true stress σ is expressed in terms of engineering stress S by

$$\sigma = \frac{P}{A_o}(e+1) = S(e+1) \tag{12}$$

The derivation of Eq. (12) assumes both constancy of volume and a homogeneous distribution of strain along the gauge length of the tensile specimen, and should only be used until the onset of necking. Beyond maximum load the true stress should be determined from actual measurements of load P and cross-section area A.

$$\sigma = \frac{P}{A} \tag{13}$$

The true strain ε may be determined from the engineering or conventional strain e by

$$\varepsilon = \ln(e+1) \tag{14}$$

This equation is applicable only to the onset of necking. Beyond maximum load the true strain should be based on actual area or diameter measurements.

$$\varepsilon = \ln\frac{A_o}{A} = \ln\frac{(\pi/4)D_o^2}{(\pi/4)D^2} = 2\ln\frac{D_o}{D} \tag{15}$$

In Fig. 6, the true-stress–true-strain curve is compared with its corresponding engineering stress–strain curve. (Because of relatively large plastic strains, the elastic region has been compressed into the y axis). In agreement with Eqs. (2) and (4), the true-stress–true-strain curve is always to the left of the engineering curve until the maximum load is reached. Beyond maximum load, the high localized strains in the necked region, Eq. (15), exceed the engineering strain calculated from Eq. (2). Some flow curves are linear from maximum load to fracture, in other cases its slope continuously decreases up to fracture.

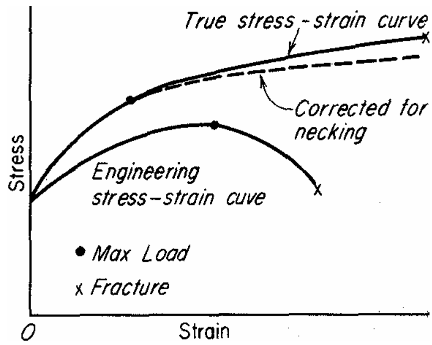

Figure 6. Comparison of engineering and true stress–strain curves

The formation of a necked region or mild notch introduces triaxial stresses which make it difficult to determine accurately the longitudinal tensile stress to fracture.

1.2.1. True stress at maximum load

The true stress at maximum load corresponds to the true tensile strength. For most materials necking begins at maximum load at a value of strain where the true stress equals the slope of the flow curve. Let σ_u and ε_u denote true stress and true strain at maximum load when the cross-sectional area of the specimen is A_u. The ultimate tensile strength is given by $S_u = P_{\max}/A_o$ and since $\sigma_u = P_{\max}/A_u$ and $\varepsilon_u = \ln(A_o/A_u)$, eliminating $P_{\max}$ yields,

$$\sigma_u = S_u\frac{A_o}{A_u}, \quad \sigma_u = S_u e^{\varepsilon_u} \tag{16}$$

1.2.2. True fracture stress

The true fracture stress is the load at fracture divided by the cross-section area at fracture. This stress should be corrected for the triaxial state of stress existing in the tensile specimen at fracture.

1.2.3. True fracture strain

The true fracture strain ε_f is the true strain based on the original area A_o and the area after fracture A_f,

$$\varepsilon_f = \ln\frac{A_o}{A_f} \tag{17}$$

This parameter represents the maximum true strain that the material can withstand before fracture and is analogous to the total strain to fracture of the engineering stress-strain curve. Since Eq. (14) is not valid beyond the onset of necking, it is not possible to calculate ε_f from measured values of e_f. However, for cylindrical tensile specimens the reduction of area q is related to the true fracture strain by the relationship

$$\varepsilon_f = \ln\frac{1}{1-q} \tag{18}$$

1.2.4. True uniform strain

The true uniform strain ε_u is the true strain based only on the strain up to maximum load. It may be calculated from either the specimen cross-section area A_u or the gauge length L_u at maximum load. Equation (14) may be used to convert conventional uniform strain to true uniform strain,

$$\varepsilon_u = \ln\frac{A_o}{A_u} \tag{19}$$

1.2.5. True local necking strain

The local necking strain ε_n is the strain required to deform the specimen from maximum load to fracture,

$$\varepsilon_n = \ln\frac{A_u}{A_f} \tag{20}$$

The flow curve of many metals in the region of uniform plastic deformation can be expressed by the simple power curve relation

$$\sigma = K\varepsilon^n \tag{21}$$

where n is the strain-hardening exponent and K is the strength coefficient. The strain-hardening exponent [3] may have values from $n = 0$ (perfectly plastic solid) to $n = 1$ (elastic solid) (Fig. 8). For most metals n has values between 0.10 and 0.50 (Tab. 2). A log-log plot of true stress and true strain up to maximum load will result in a straightline if Eq. (21) is satisfied by the data (Fig. 7). The linear slope of this line is n, and K corresponds to the true stress at $\varepsilon = 1.0$ (for area reduction $q = 0.63$).

It is important to note that the rate of strain hardening $d\sigma/d\varepsilon$, is not identical with the strain-hardening exponent. From the definition of n it follows

$$n = \frac{d(\log\sigma)}{d(\log\varepsilon)} = \frac{d(\ln\sigma)}{d(\ln\varepsilon)} = \frac{\varepsilon}{\sigma}\frac{d\sigma}{d\varepsilon} \quad \text{or} \quad \frac{d\sigma}{d\varepsilon} = n\frac{\sigma}{\varepsilon} \tag{22}$$

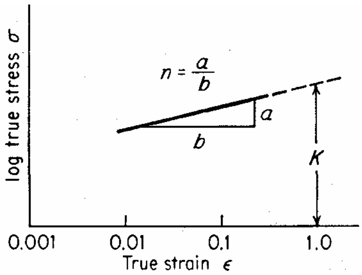

Figure 7. Log-log plot of true stress-strain curve

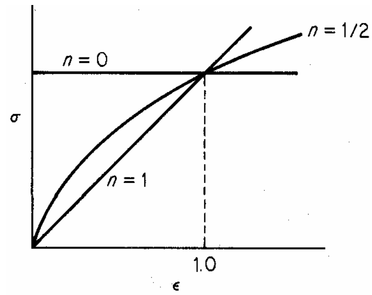

Figure 8. Various forms of power curve $\sigma = K\varepsilon^n$

Table 2. Values for *n* and *K* for metals at room temperature [4]

Metal	Condition	*n*	*K*, MPa
0.05% C steel	Annealed	0.26	530
SAE 4340 steel	Annealed	0.15	641
0.6% C steel	Quenched and tempered 575°C	0.10	1572
0.6% C steel	Quenched and tempered 740°C	0.19	1227
70/30 brass	Annealed	0.49	896

2. IMPACT TESTING

During World War II a great deal of attention was directed to the brittle failure of welded Liberty ships and T-2 tankers [4]. Some of these ships broke completely in two, while, in other instances, the fracture did not completely disable the ship. Most of the failure occurred during the winter. Failures occurred both when the ships were in heavy seas and when they were anchored at dock. A broad research program was undertaken to find the causes of these failures and to prescribe the remedies for their future prevention. This calamity focused attention on the fact that normally ductile mild steel can become brittle under certain conditions. In addition to research designed to find answers to this problem, other research was aimed at gaining a better understanding of the mechanism of brittle fracture and fracture in general. While the brittle failure of ships focused great attention to brittle failure in mild steel, it is important to understand that this is not the only application where brittle fracture is a problem. Catastrophic failures in pressure vessels, tanks, pipelines, and bridges have been documented [5], since the year 1886.

Three basic factors contribute to a brittle-cleavage type of fracture. They are (1) a triaxial state of stress, (2) a low temperature, and (3) a high strain rate or rapid rate of loading. All three of these factors do not have to be present at the same time to produce brittle fracture. A triaxial state of stress, such existing at a notch, and low temperature are responsible for most service failures of the brittle type. However, since these effects are accentuated at a high rate of loading, many types of impact tests have been used to determine the susceptibility of materials to brittle behaviour. Steels which have identical properties when tested in tension or torsion at slow strain rates can show pronounced differences in their tendency for brittle fracture when tested in a notched-impact test.

Since the ship failures occurred primarily in structures of welded construction, it was considered for a time that this method of fabrication was not suitable for service where brittle fracture might be encountered. A great deal of research has since demonstrated that welding, *per se*, is not inferior in this respect to other types of construction. However, strict quality control is needed to prevent weld defects which can act as stress raisers or notches. New electrodes have been developed for a weld with better properties than the mild-steel plate. The design of a welded structure is more critical than the design of an equivalent riveted structure. It is important to eliminate stress raisers and reduce rigidity.

2.1. Notched-bar impact tests

Various types of notched-bar impact tests are used to determine the tendency of a material to behave in a brittle manner. The results obtained from notched-bar tests are not convenient for design, since it is not possible to measure the components of the triaxial stress condition at the notch. Furthermore, there is no general agreement on the interpretation or significance of results obtained with this type of test.

Nowadays, Charpy specimen of a square cross section (10×10 mm) containing 2 mm deep 45° V notch, with a 0.25 mm root radius, is generaly accepted. The specimen is supported as a beam in a horizontal position and loaded behind the notch by the impact of a heavy swinging pendulum (Fig. 9) with the impact velocity of approximately 5 m/s. The specimen is forced to bend and fracture at a high strain rate on the order of 10^3 s^{-1}.

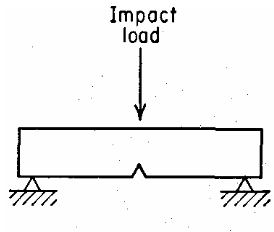

Figure 9. Sketch showing method of loading in Charpy impact test

Plastic constraint at the notch produces a triaxial state of stress. The maximum plastic stress concentration is given by

$$K_\sigma = \left(1 + \frac{\pi}{2} - \frac{\omega}{2}\right) \tag{23}$$

where ω is the included flank angle of the notch. The relative values of the three principal stresses depend strongly on the dimensions of the bar and the details of the notch. The standard Charpy V specimen is thick enough to ensure a high degree of plane-strain and triaxiality across almost all of the notched cross section, and provides a severe condition for brittle fracture. Therefore, nonstandard specimens should be used with great care.

The principal measurement from the impact test is the energy absorbed in fracturing the specimen. After breaking the test bar, the pendulum rebounds to a height which decreases as the energy absorbed in fracture increases. The energy absorbed for fracture, in joules (J), often designated Cv, is read directly from a calibrated dial on the impact tester. Sometimes impact test results are expressed in energy absorbed per unit cross-sectional area of the specimen (notch or impact toughness). Fracture energy measured by the Charpy test is only a relative energy and cannot be used directly in design equations.

Another common result obtained from the Charpy test is based on examination of the fracture surface. The fracture is fibrous (shear fracture), granular (cleavage fracture), or a mixture of both. These different modes of failure are readily distinguishable even without magnification. The flat facets of cleavage fracture provide a high reflectivity and bright appearance, while the dimpled surface of a ductile fibrous fracture provides a light-absorptive surface and dull appearance. Usually an estimate is made of the percentage of the fracture surface that is cleavage (or fibrous) fracture. Figure 10 shows how the fracture appearance changes from 100 percent flat cleavage (left) to 100 percent fibrous fracture (right) as the test temperature is increased. The fibrous fracture appears first around the outer surface of the specimen (shear lip) where the triaxial constraint is the least. Gradual decrease in the granular region and increase in lateral contraction at the notch with increasing temperature is visible. Sometimes in the Charpy test the ductility is measured as indicated by the percent contraction of the specimen at the notch.

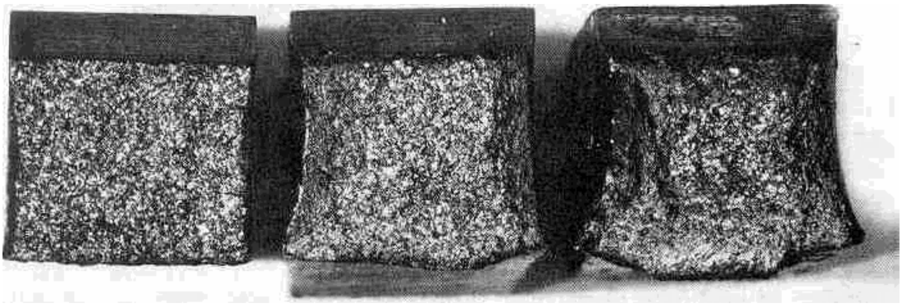

Figure 10. Fracture surfaces of Charpy specimens of mild steel, tested at different temperatures: 5°C (left); 38°C (center); 100°C (right)

The notched-bar impact test is most meaningful when conducted over a range of temperature so that the temperature for ductile-to-brittle transition can be determined. Figure 11 illustrates the type of curves. The energy absorbed decreases with decreasing temperature but for most cases the decrease is not sharp at a certain temperature, and it is difficult to determine accurately the transition temperature. In selecting a material from the standpoint of impact toughness or tendency to brittle failure, the important factor is the transition temperature. Steel A (Fig. 11) shows higher impact toughness at room temperature; yet its transition temperature is higher than that of steel B. The material with the lowest transition temperature is to be preferred.

Notched-bar impact tests are subject to considerable scatter, particularly in the region of the transition temperature [5]. Most of this scatter is due to local variations in the properties of the steel, but also notch shape and depth are critical variables, which can not be perfectly reproduced. Proper placement of the specimen in the anvil is also important.

The principal advantage of the Charpy V-notch impact test is that it is a simple test that utilizes a cheap, small specimen. Tests can readily be carried out over a range of subambient temperatures. Moreover, the design of the test specimen is well suited for measuring differences in notch toughness in low-strength materials such as structural steels. The test is used for comparing the influence of alloy studies and heat treatment on notch toughness. It frequently is used for quality control and material acceptance. The chief difficulty is that the results of the Charpy test are not directly applicable in design.

2.2. Instrumented Charpy test

The conventional Charpy test measures the total energy absorbed in fracturing the specimen. Additional information can be obtained if the impact tester is instrumented to provide a load-time history of the specimen during the test [6]. Figure 12 shows an idealized load-time curve for an instrumented Charpy test. With this kind of record it is possible to determine the energy required for initiating fracture (crack) and the energy required for propagating fracture. It also yields information on the load for general yielding, the maximum load, and the fracture load.

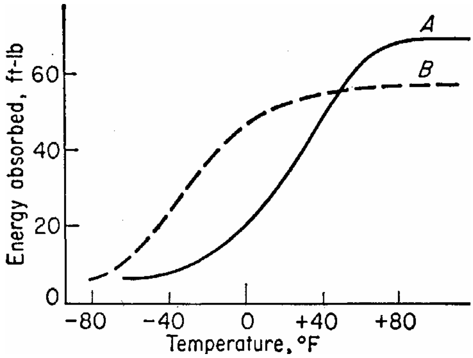

Figure 11. Transition-temperature curves for two steels

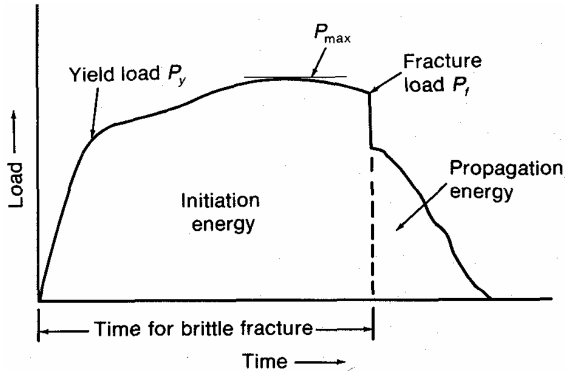

Figure 12. Load-time history for an instrumented Charpy test

If the velocity of the impact pendulum is assumed constant throughout the test then

$$E' = v_o \int_0^t P dt \tag{24}$$

where v_o is initial pendulum velocity, P is instantaneous load and t is time.

However, the assumption of a constant pendulum velocity v is not valid, since v decreases in proportion to the load on the specimen. It is usually assumed that [7]

$$E_t = E'(1-\alpha) \tag{25}$$

where E_t is the total fracture energy, $\alpha = E'/4E_o$, and E_o is the initial energy of pendulum.

Because the root of the notch in a Charpy specimen is not as sharp as in fracture mechanics tests with precracked specimens, there has been a trend toward using standard Charpy specimens which are precracked by the introduction of a fatigue crack at the tip of the V notch. These precracked specimens have been used in the instrumented Charpy test to measure dynamic fracture toughness values (K_{Id}).

The results of Charpy test can be used in design for material selection, appreciating the material behaviour described in next figures. The area under diagram (Fig. 12) is proportional to absorbed energy. Different shapes of diagram for the same absorbed energy are presented in Fig. 13. The material requires higher load in diagram (a) than in diagram (b), but for the same energy the fracture time is greater in case (b) than in case (a) indicating possible different material behaviour in loaded structure. Material (a) is convenient for impact loading (e.g. an armor protection), material (b) is recommended for pressurized equipment (e.g. pressure vessel). For the same load level the ratio between energy for crack initiation and its propagation can be quite different, e.g. 20:80 for case (c) and 80:20 for case (d). Without a deep analysis, it can be noticed that higher crack propogation energy is convenient for welded joint, having in mind that crack-like defects can not be excluded in welded structures. This also indicates that Charpy test results can be taken as an additional criterion of material weldability.

Shape of diagrams, in addition to absorbed energy values obtained in instrumented testing, defines material behaviour during fracture at different temperatures, primarily low temperatures, is in an idealized form presented in Fig. 14.

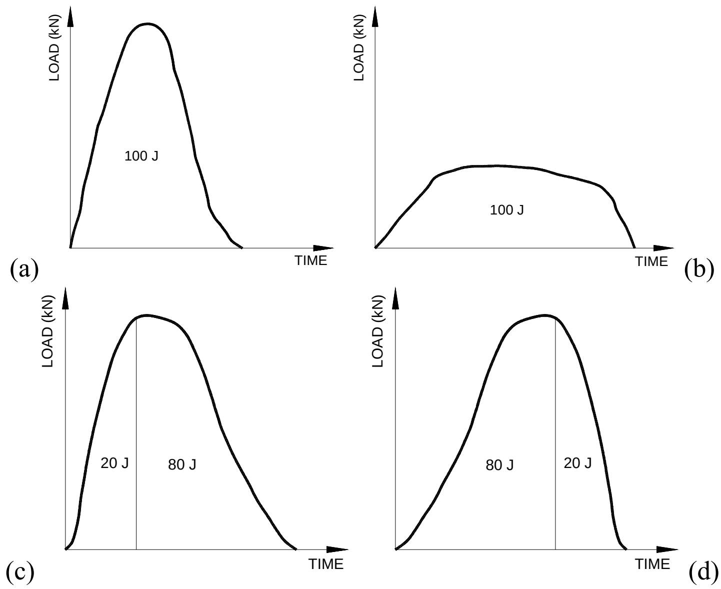

Figure 13. Different shapes of Charpy test diagrams for same absobred energy (100 J)

Both tested materials are of the same absorbed energy in temperature interval –140°C to +20°C, having the same ratio of crack initiation to crack propagation energy at room temperature (Fig. 14). However, this ratio is different for the same total absorbed energy. Crack initiation energy is always lower compared to crack propagation energy in case (a), whereas this relation is changed in case (b). This behaviour has to be appreciated when evaluating the use of material at low temperature and at high load rates.

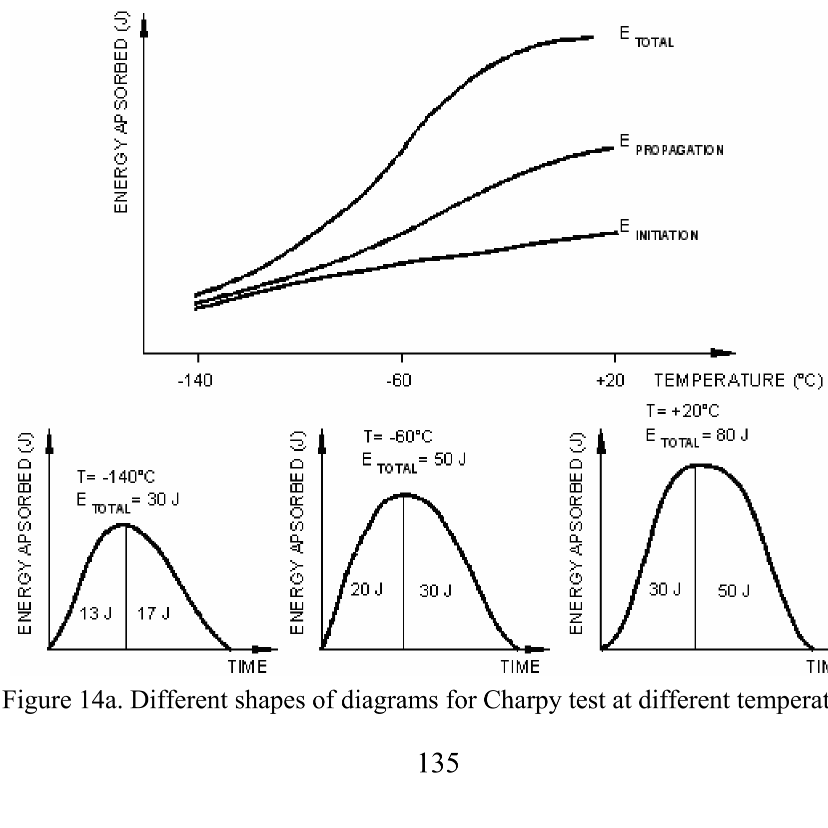

Figure 14a. Different shapes of diagrams for Charpy test at different temperatures

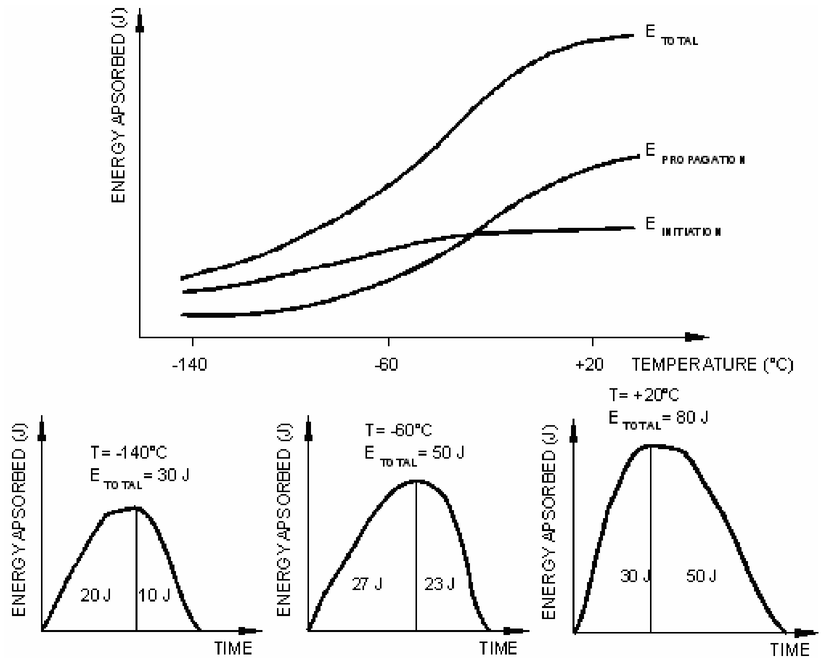

Figure 14b. Different shapes of diagrams for Charpy test at different temperatures

2.3. Instrumented impact test results at different temperatures

The significance of impact testing is illustrated by test results for two high strength steels presented in Fig. 15. Chemical composition is given in Table 3, and tensile properties in Table 4. The difference in strength and ductility is not expressed in the same level as the case with impact toughness properties. Steel A, with low carbon content, exhibited high impact energy at low temperatures (down to –100°C) for crack propagation and also crack initation [8]. However, there is a significant effect of rolling direction. For steel B, with 0.3% C, the impact energy is low, and nil ductility transition temperature can be determined (between –40°C and –60°C).

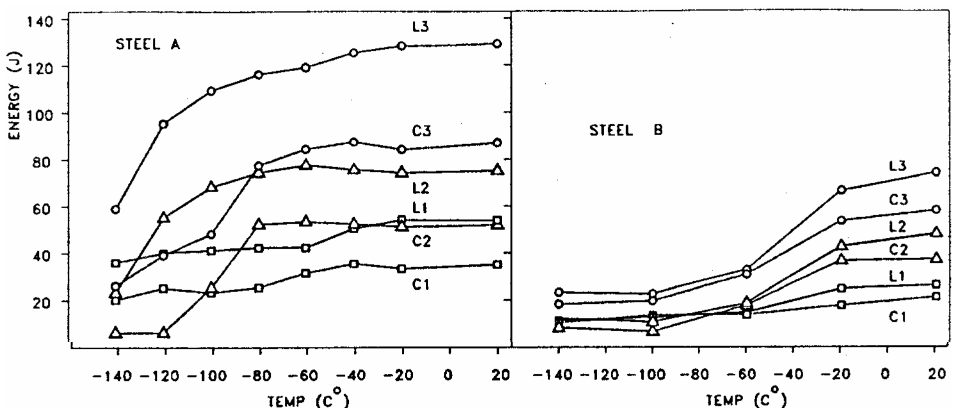

Figure 15. Instrumented impact test results obtained with Charpy V specimen for steels A and B
L–notch in cross-rolling direction; C–notch in rolling direction
1–crack initiation energy, 2–crack propagation energy, 3–total energy

Table 3. Chemical composition (wt%) of tested steels

Steel	C	Si	Mn	P	S	Cr	Ni	Mo	V	Al
A	0.1	0.27	0.35	0.014	0.012	1.11	2.65	0.26	0.1	0.05
B	0.3	0.28	0.73	0.02	0.008	2.05	1.87	0.3	-	-

Table 4. Tensile properties of tested steels

	Yield strength	Ultimate tensile strength	Elongation	Reduction of cross section area
Steel	YS, MPa	UTS, MPa	A, %	Z, %
A	780	825	18	68
B	940	1015	16.7	58.2

3. HIGH RATE IMPACT TEST

Probably the chief deficiency of the Charpy impact test is that the small specimen is not always a realistic model of the actual situation. Not only does the small specimen lead to considerable scatter, but a specimen with thickness of 10 mm cannot provide the same constraint as would be found in a structure with much greater thickness. The situation that can result is shown in Fig. 16. At a particular service temperature the standard Charpy specimen shows a high shelf energy, while actually the same material in a thick-section structure has low toughness at the same temperature. The most logical approach to this problem is the development of tests that are capable of handling specimens of extended thickness (e.g. explosion bulge test, drop weight test).

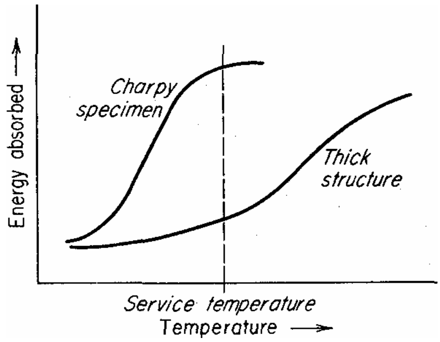

Figure 16. Effect of section thickness on transition-temperature curves

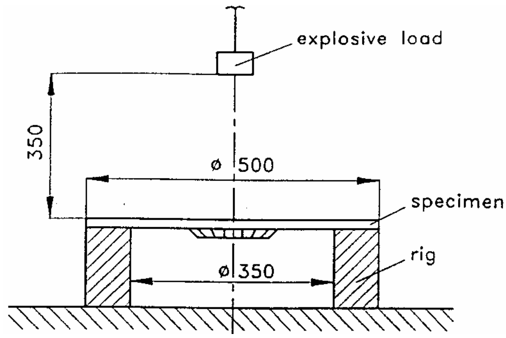

Figure 17. Explosion bulge test: disposition and principal dimensions

3.1. Exposion bulge test

The basic need for large specimens resulted from the inability to produce fracture in small laboratory specimens at stresses below gross yield stress, whereas brittle fractures in ship structures occur at service temperatures at elastic stress levels, as experienced with Liberty ships. The development of such tests and their rational method of analysis has been chiefly the work of Pellini [9] and his co-workers at the Naval Research Laboratory. Disposition and principal dimensions in the explosion bulge test are presented in Fig. 17.

The explosion bulge test, developed in the U.S. Naval Research Laboratory (NRL) to study the problem of brittle fracture in structural steels used in welded ship hulls, is presented in Fig. 18. Die support (rig) with the base allows bulging of properly positioned test plate (specimen). Cast explosive charge of specified mass and power should be applied at properly determined distance, obtained by cardboard box over the test plate.

Test assembly during shot is presented on the right. High rate of explosion loading contributes to brittle fracture of test plate.

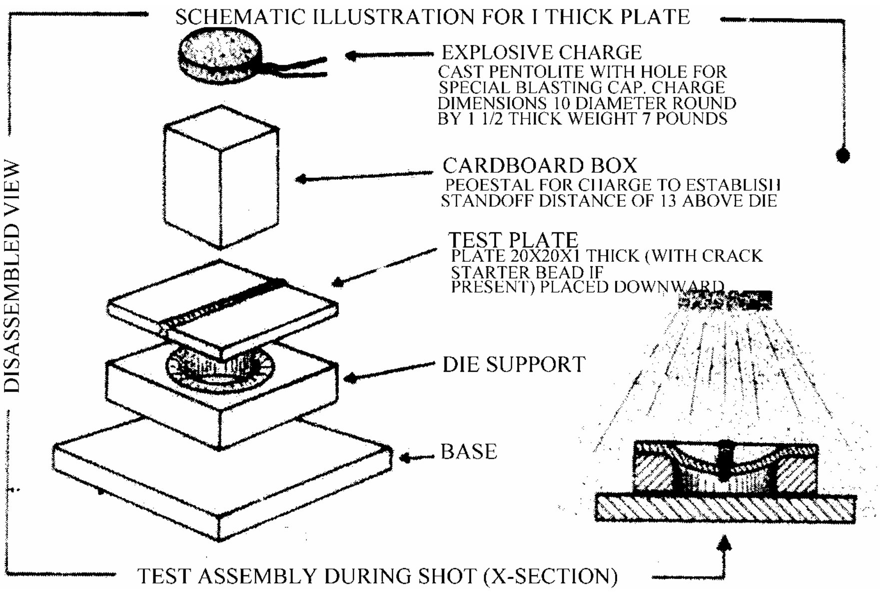

Figure 18. Explosion bulge test, developed in the U.S. Naval Research Laboratory (NRL)

In addition to fast fracture by explosion shot, a unique "crack-starter" can contribute to brittle fracture condition. In the first development [10] of explosion bulge tests the test plate was supplied with brittle weld bead deposited on the surface of 25 mm steel plate, sized 500×500 mm. The latter feature is a short bead of very hard brittle weld metal which is notched in a manner to insure the initiation of a cleavage crack as soon as the base metal is subjected to any bending. The specimen, with the welded short bead face down is placed upon the circular supporting die and a standardized charge of explosive is detonated at the fixed position above the specimen. During the extremely rapid loading, the brittle weld bead introduces small natural cracks in the test plate (similar to a crack in weld), initiating cleavage cracks at the root of the notch and transferring them to the base metal as running cracks. The behaviour of the test plate depends upon the ability of the base metal to arrest the running crack and to deform while permitting only high-energy absorbing, shear-type fracture to propagate. If the steel is not capable of arresting the running crack, the plate develops many cleavage fractures and breaks flat; that is, little plastic forming occurs downward into the die cavity. Tests can be carried out over a range of temperatures and then the appearance of the fracture determines the transition temperatures (Fig. 19). Below the NDT the fracture is a flat (elastic) fracture running completely to the edges of the test plate. Above the nil ductility temperature a plastic bulge forms in the center of the plate, but the fracture is still a flat elastic fracture out to the plate edge. At a still higher temperature the fracture does not propagate outside of the bulged region. The temperature at which elastic fracture no longer propagates to the edge of the plate is called the fracture transition elastic (FTE). The FTE marks the highest temperature of fracture propagation by purely elastic stresses. At yet higher temperature the extensive plasticity results in a helmet-type bulge. The temperature above which this fully ductile tearing occurs is the fracture transition plastic (FTP).

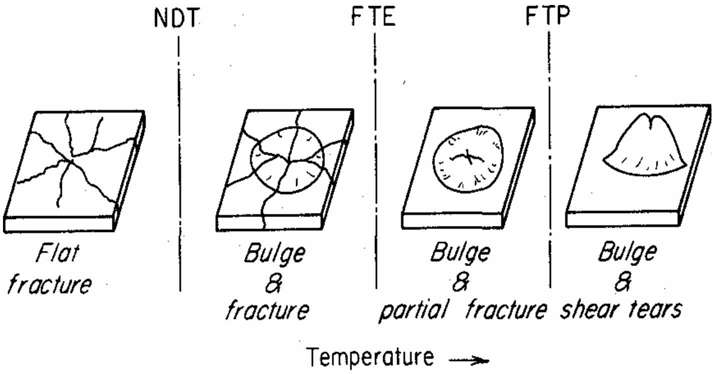

Figure 19. Fracture appearance vs. temperature for explosion–crack-starter test
NDT–Nil Ductility Transition; FTE–Fracture Transition Elastic; FTP–Fracture transition plastic

In this way welded joint specimens could also be tested (Fig. 20).

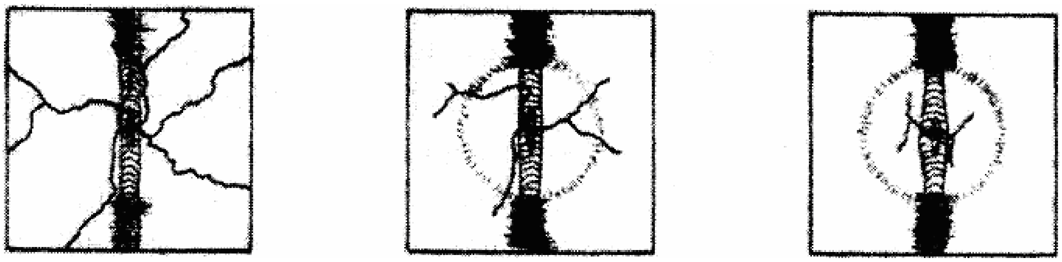

Figure 20. Fracture appearance vs. temperature for explosion–crack-starter test of welded joint specimens. Crack starter of very hard weld metal short bead in the middle and circular trace of supporting die are visible.
Left: Nil ductility temperature flat break. Brittle fractures extend to edge of plate
Middle: Fracture transition elastic. Fractures are arrested in elastically loaded die-supported region
Right: Fracture transition plastic. Fractures are arrested in plastically loaded (bulged) region

The explosive charge capacity was selected for loading the specimen to insure a continuing store of energy to feed the propagating cracks. In essence, the gas pressure was maintained for sufficient duration so that stress unloading could not occur during cracking. The final feature of the explosion bulge test is to have a series of specimens heated or cooled to progressive temperatures over a range that encompasses expected fracture transition points (Fig. 19). Welded joint (and unwelded) test plates are notched in the bead of brittle weld metal to provide small flaw and are subjected to repeated shots. Weld reinforcement on face is ground flush at end to permit notch depth developement without visible intimate contact with supporting die. Below nil ductility temperature, the test plates show no deformation because the weld crack is accepted by the base metal (starting in the heat-affected zone) as a brittle running fracture, and is unable to resist its propagation by cleavage fracture. Above this transition temperature range, the brittle weld crack is arrested. Energy from the explosive charges is effectively utilized by the plate, by successive bulging into the die. Plate thickness in bulge is measured after each shot.

The explosion bulge test makes use of a large plate specimen that incorporates novel features in its preparation and testing procedure. However, the application of explosion in the test introduced inconveniences and a new loading type had been proposed.

3.1.1. Explosion bulge test results

As an illustration, the results of explosion bulge test with the plates (BM) of steels A and B (Tables 3 and 4) are presented in Fig. 21, [8]. After each shot, the reduction of thickness ΔR and bulge extension B were measured. Again the effect of rolling direction of steel A is significant, and steel B exhibited linear behaviour.

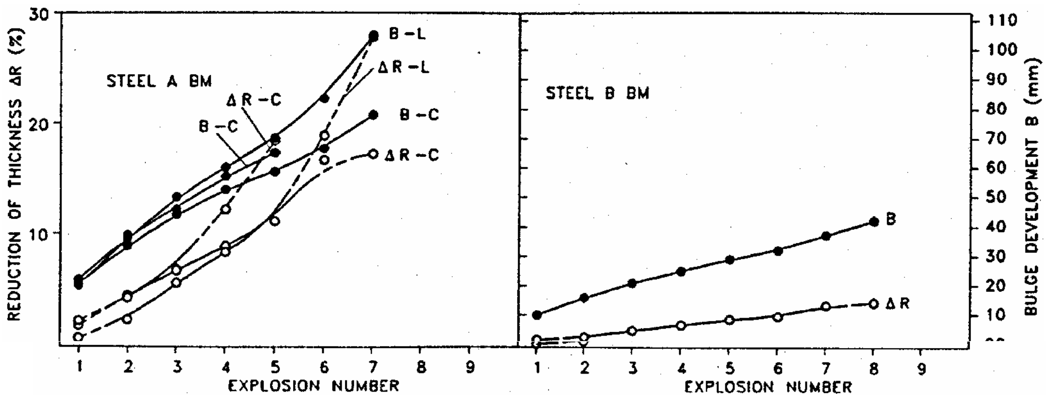

Figure 21. Typical results of explosion bulge test for steels A and B, expresed by reduction of thickness ΔR and bulge development B vs. number of explosions
L–notch in hard bead in cross-rolling direction; C–notch in rolling direction

3.2. DROP WEIGHT TEST

Experience gathered with the explosion bulge test in NRL has led to the development of drop-weight test, intended to avoid the explosion. The energy for DWT is obtained from potential energy of falling mass (weight). Due to significant weight of the tup and height of device, much more energy can be obtained compared to Charpy pendulum.

The drop weight test (DWT) was developed [11] specifically for the determination of the NDT temperature on full thickness plates (Fig. 22). The simplicity of the drop-weight specimen, the apparatus for applying load and the interpretation of results, contributed to wide use of this test. The stress applied to the specimen during the impact loading is limited to the yield point by a stopping block attached to the anvil below the specimen (Fig. 23). This is the practical device for evaluating the ability of the steel to withstand yield point loading in the presence of a small flaw.

The specimens may be oxygen-cut from a parent plate and additonally machined. When thinner specimens are prepared from a very thick plate, the original tolled surface is to be employed on the welded (tension) face of the specimen. Since the specimen is a wide beam loaded in three-point bending, this restriction limits the stress on the tension face of the plate to a value that does not exceed yield stress. A short bead of brittle weld metal, taken from explosion bulge test, is deposited on the plate surface, 15 to 25 mm thick, typically sized 80×350 mm (Fig. 24). Although intended primarily for the testing plate, a welded specimen can have the crack-starter notch located over the weld metal or heat-affected zone, as illustrated in specimen B. As shown in C, weld bead of special electrode ϕ5 mm is manually deposited by process in two increments, starting at ends and overlapping in area which will be notched by abrasive disk. When the tup strikes the back of the specimen, very earliest bending generates a sharp cleavage crack, which initiates in the root of the weld notch and runs to the weld fusion line. As bending continues and the imposed stress in the outer fibers rises to the yield point, the steel either (1) accepts initiation of a cleavage crack which “runs” completely through the section and results in a broken specimen (Fig. 25), or (2) initiation of cleavage fracture is resisted and the specimen bends the small, additional amount permitted by the anvil stop, without complete fracturing. The specimen, before testing cooled in a bath to the requested temperature, is supported as a simple beam. The brittle weld bead is fractured at near yield-stress levels as a result of dynamic loading from a falling weight. If the starter-crack propagates across the width of the plate on the tension surface to the edges, the test temperature is below the NDT. Complete separation on the compression side of the specimen is not required. The NDT is the highest temperature at which a nil ductility break is produced. The test is quite reproducible and NDT temperature in this test can be determined to the nearest – 12°C.

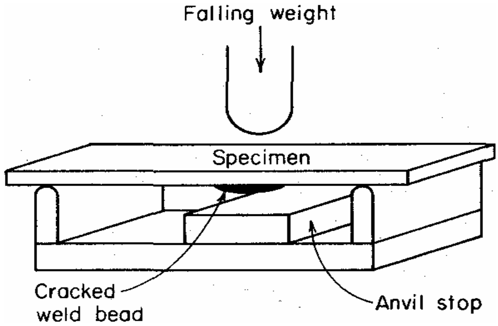

Figure 22. Drop weight test configuration

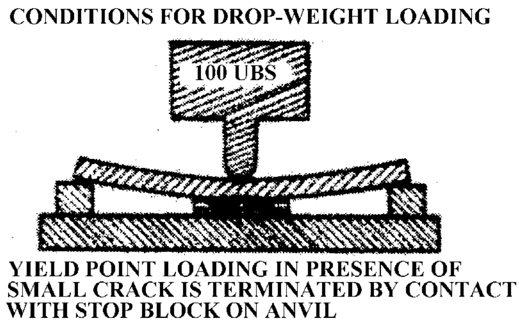

Figure 23. The anvil stop

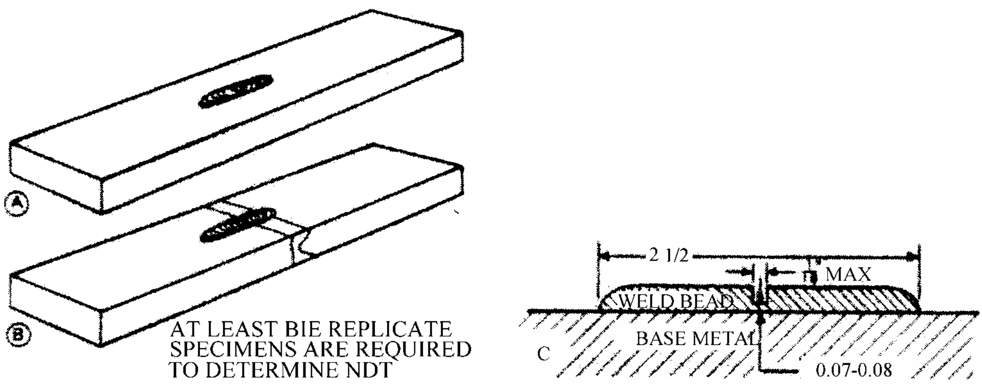

Figure 24. Drop weight test specimen

3.2.1. Determination of nil-ductility temperature from tested specimens

Figure 25 provides essential details of the bead-on-plate specimen with the “crack-starter” weld, and the procedure which is employed to test a series of specimens over a range of progressive temperatures to determine the NDT for steel. The drop-weight test was devised for testing relatively heavy structural sections, and is not recommended for base metal pieces less than 12.5 mm thick. A complete description of the standard method for conducting the NRL Drop-Weight Test is presented in ASTM E 208.

A specimen is considered broken if fracture on tension surface extends to one or both edges. Duplicate no-break performance is required 10°C above NDT. NDT for steel in specimens in Fig. 25 is 0°C.

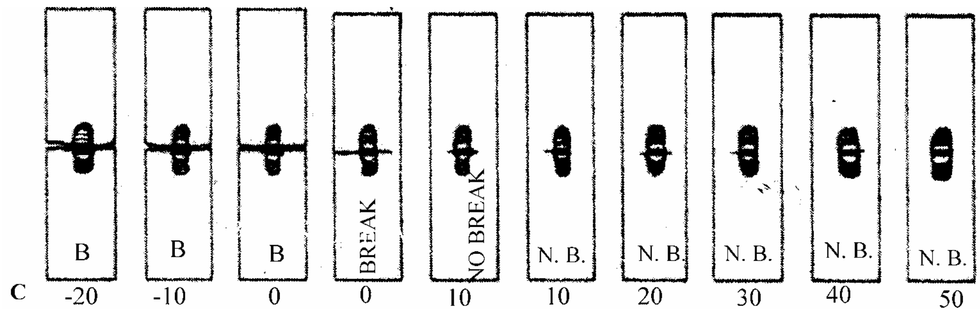

Figure 25. Results of drop-weight test for determination of nil-ductility transition temperature

3.3. Dynamic tear test (DT)

The dynamic tear test (DT) is an extended version of drop weight test, in effect a giant Charpy test (Fig. 26). While specimens are usually 15 and 25 mm thick, DT tests have been made on specimens up to 300 mm thick. The notch is an electron-beam weld which is embrittled metallurgically by alloying (Ti is added to produce a brittle Fe–Ti alloy). The narrow weld is fractured easily, providing a reproducible sharp crack. As in the Charpy test, specimens are fractured over a range of temperature in a pendulum-type machine and the energy absorbed in fracture is measured. However, while the maximum energy capacity of a standard Charpy impact tester is 325 J, the pendulum tester used with the DT test has a capacity of 13 550 J.

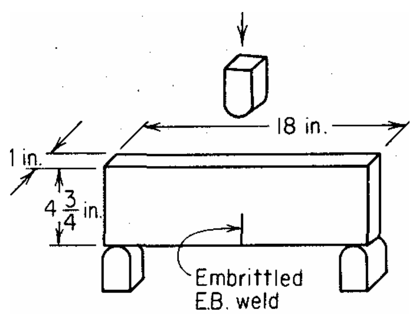

Figure 26. Dynamic drop-weight tear test

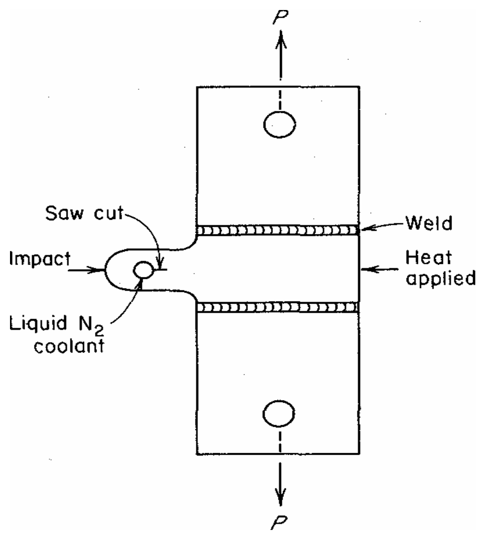

Figure 27. Robertson crack-arrest test

3.4. Robertson crack-arrest test

Another important type of test is the crack-arrest test [12], which provides a relationship between the stress level and the ability of the material to arrest a rapidly propagating crack. Figure 27 illustrates the Robertson crack-arrest test. A uniform elastic tensile stress is applied to a plate specimen 150 mm wide. A rapidly moving brittle fracture is initiated by impact loading at a starter crack on the cold side of the specimen. The crack propagates up a temperature gradient toward the hot side. The point across the specimen width at which the temperature is high enough to give sufficient ductility to blunt the crack is called the crack-arrest temperature (CAT). In an alternative form of the test, the temperature across the specimen is constant and tests are carried out with successive specimens at increasing temperature until the CAT is reached. Crack-arrest tests on mild steel below NDT show that the CAT is independent of temperature but the stress level for crack arrest is very low. If the stress is greater than 35 to 55 MPa, brittle fracture will occur. Obviously, this stress level is too low for practical engineering design, so that steels cannot be used below the NDT. While crack-arrest tests are among the most quantitative of brittle-fracture tests, they are not used extensively because they require large testing machines and large specimens.

4. FRACTURE ANALYSIS DIAGRAM

Nil-ductility transition temperature as determined by the drop weight test is regarded the most important reference point on the fracture analysis diagram because of the simplicity with which it is determined, and because a steel is characterized by a single NDT. Fracture analysis system introduces considerable promise for guiding engineering design and selection of steel for fracture-safe weldments and structures.

More detailed consideration is necessary before use of transition points in engineering design through the fracture analysis diagram, through reference to basic properties of the tension test. The sub-ambient temperature dependences of yield strength σ_o and ultimate tensile strength σ_u in a bcc metal are shown in Fig. 27. For an unnotched specimen without flaws, the material is ductile until a very low temperature, point A, where $\sigma_o = \sigma_u$. Point A represents the NDT temperature for a flaw-free material. The curve BCD represents the fracture strength of a specimen containing a small flaw ($a < 0.1$ mm). The temperature corresponding to point C is the highest temperature at which the fracture strength $\sigma_f \gg \sigma_o$. Point C represents the NDT for a specimen with a small crack or flaw. The presence of a small flaw raises the NDT of a steel by about 90°C.

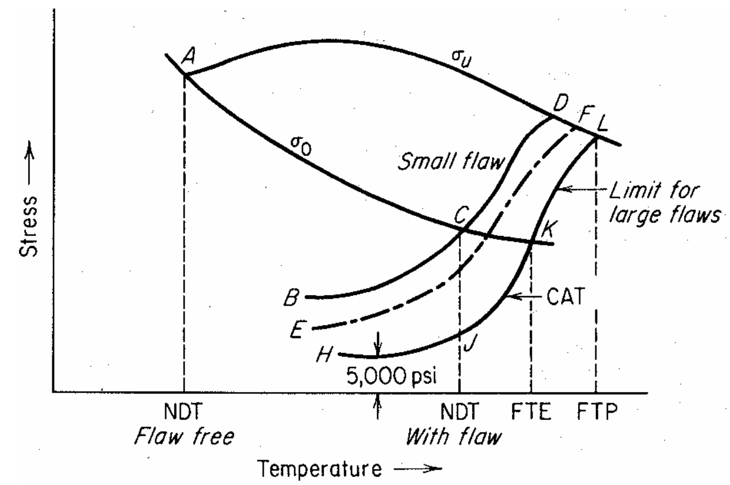

Figure 27. Temperature dependence of yield strength (σ_o), tensile strength (σ_u), and fracture strength for a steel containing flaws of different sizes

Increasing the flaw size decreases the fracture stress curve, as in curve EF, until with increasing flaw size a limiting curve of fracture stress HJKL is reached. Below the NDT, the limiting safe stress is 35 to 55 MPa. Above NDT the stress required for unstable propagation of a long flaw (JKL) rises sharply with increasing temperature. This is the crack-arrest temperature curve (CAT). The CAT defines the highest temperature at which unstable crack propagation can occur at any stress level. Fracture will not occur for any point to the right of the CAT curve.

The temperature above which elastic stresses cannot propagate a crack is the fracture transition elastic (FTE). This is defined by the temperature when the CAT curve crosses the yield-strength curve (point K). The fracture transition plastic (FTP) is the temperature where the CAT curve crosses the tensile-strength curve (point L). Above this temperature the material behaves as if it were flaw-free, for any crack, no matter how large, cannot propagate as an unstable fracture.

Data obtained from the DWT and other large-scale fracture tests have been assembled by Pellini and co-workers [13] into a useful design procedure called the fracture analysis diagram (FAD). The NDT as determined by the DWT provides a key data point to start construction of the fracture analysis diagram and transition temperature features of steels (Fig. 28). For mild steel below NDT the CAT curve is flat. A stress level in excess of 35 to 55 MPa causes brittle fracture, regardless of the size of the initial flaw. Extensive correlation between NDT and Robertson CAT tests for a variety of structural steels have shown that the CAT curve bears a fixed relationship to the NDT temperature. Thus, the NDT –1°C provides a conservative estimate of the CAT curve at stress of $\sigma_o/2$, NDT +15°C provides an estimate of the CAT at $\sigma = \sigma_o$, and, the FTE and NDT +50°C provides an estimate of the FTP. So, once NDT for structural steels is determined, the entire scope of the CAT curve can be established well enough for engineering design.

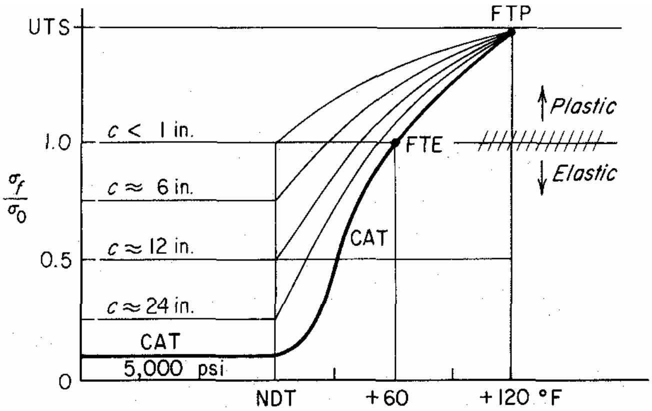

Figure 28. Fracture-analysis diagram showing influence of various initial flaw sizes [13]

The curve that has been traced out in Fig. 28 represents the worse possible case for large flaws in excess of 600 mm. One can imagine a spectrum of curves translated upward and to the left for smaller, less severe flaws. Correlation with service failures and other tests has allowed the approximate determination of curves for a variety of initial flaw sizes. Thus, the FAD provides a generalized relationship of flaw size, stress, and temperature for low-carbon structural steels of the type used in ship construction.

The fracture analysis diagram can be used in several ways for design. One simple approach would be to use the FAD to select a steel which had an FTE that was lower than the lowest expected service temperature. With this criterion the worst expected flaw would not propagate so long as the stress remained elastic. Since the assumption of elastic behaviour is basic in structural design, this design philosophy would be tantamount to being able to ignore the presence of flaws and brittle fracture. However, this procedure may prove to be too expensive and overconservative. A slightly less conservative design against brittle fracture, but still a practical approach, would be to design on the basis of an allowable stress level not exceeding $\sigma_o/2$. From Fig. 28 is visible that any crack will not propagate under this stress so long as the temperature is not below NDT –1°C.

Typical fracture analysis diagram for steel A from Tables 3 and 4 is designed, based on NDT temperature as determined in drop-weight test (Fig. 29).

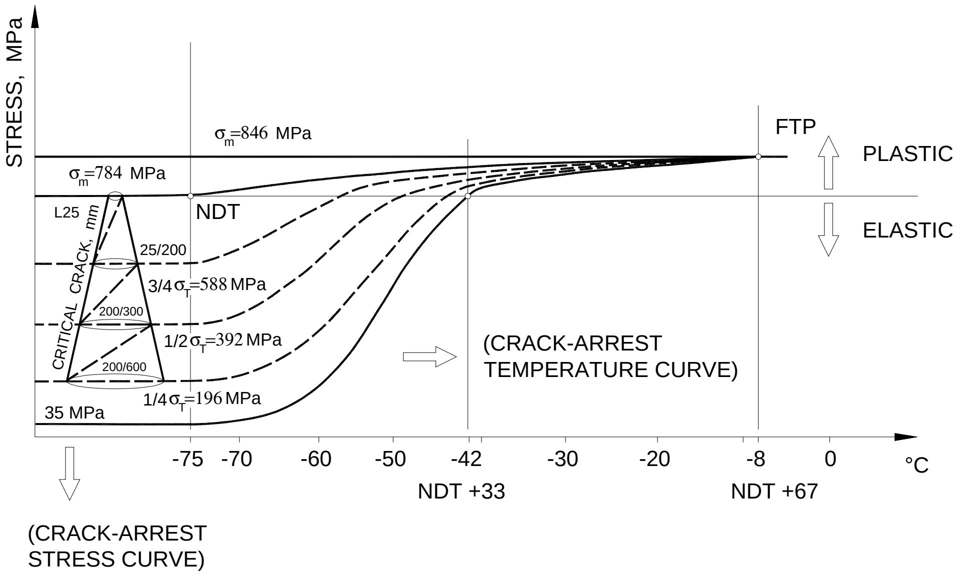

Figure 29. Fracture analysis diagram for steel A (Tables 3 and 4) [8]

The dynamic tear test (DT) can also be used to construct the FAD as presented in Fig. 30, using NDT as base (dashed line).

Below the NDT the fracture is brittle and has a flat, featureless surface devoid of any shear lips. At temperatures above NDT there is a sharp rise in energy for fracture and the fracture surfaces begin to develop shear lips. The shear lips become progressively more prominent as the temperature is increased to the FTE. Above FTE the fracture is ductile, void coalescence-type fracture. The fracture surface is a fibrous slant fracture. The upper shelf of energy represents the FTP. The lower half of the DT energy curve traces the temperature course of the CAT curve from NDT to FTE.

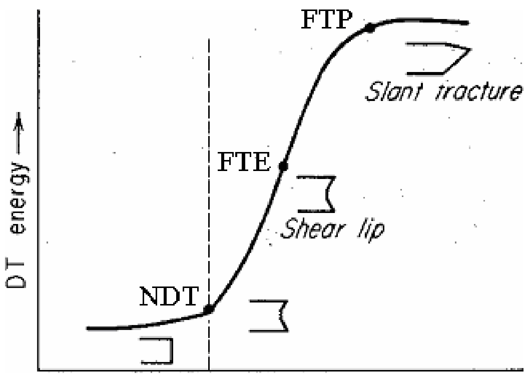

Figure 30. Application of DT test results for fracture analysis diagram design

The DT test is a highly versatile test because it is equally useful with low-strength ductile materials which show a high upper energy shelf and with high-strength low-toughness materials which have a low value of upper shelf energy. The large size of the DT specimen provides a high degree of triaxial constraint and results in a minimum of scatter. Extensive correlations are being developed between DT results and fracture toughness and Cv test data.

REFERENCES

1. Standard Methods of Tension Testing of Metallic Materials, ASTM Designation E8-69, "Annual Book of ASTM Standards," American Society for Testing and Materials, Philadelphia.
2. Dieter, G.E., *Introduction to Ductility, in: "Ductility,"* American Society for Metals, Metals Park, Ohio. (1968)
3. Standard Method of Test for Young's Modulus at Room Temperature, ASTM Elll-61, op. cit., pp. 409-413.
4. Williams, M.L., *Analysis of Brittle Behavior in Ship Plates*, Symposium on Effect of Temperature on the Brittle Behavior of Metals with Particular Reference to Low Temperatures, ASTM Spec. Tech. Publ., 158, pp. 11-44. (1954)
5. Shank, M.E., *A Critical Survey of Brittle Failure in Carbon Plate Steel Structures Other than Ships*, ASTM Spec. Tech. Publ., 158, pp. 45-110. (1954)
6. Fahey, N.H., *Impact Testing of Metals*, ASTM Spec. Tech. Publ., 466, pp. 76-92. (1970)
7. Augland, B., Brit. Weld. J., Vol. 9, p. 434. (1962)
8. Grabulov, V., *Prilog definisanju uticaja hemijskog sastava i debljine lima na pojavu prskotina u zavarenim spojevima čelika NIONIKRAL-70* (A contribution to determine the effect of chemical composition and plate thickness on crack occurrence in welded joints of NIONIKRAL-70 steel), Master degree theses, Faculty of Technology and Metallurgy, Belgrade. (1986)
9. Pellini, W.S., Weld. J., Vol. 50, pp. 915-1095, 147s-162s. (1971)
10. Puzak, P.P., Shuster, M.E., Pellini, W.S., Weld. J., Vol. 33, p. 481s. (1954)
11. Puzak, P.P., Pellini, W.S., NRL Rept. 5831, Aug. 21, 1962; ASTM Standards, pt. 31, pp. 582-601, Designation E208-69. (1969)
12. Robertson, T.S., Engineering, Vol. 172, pp. 445-448; J. Iron Steel Inst. London, vol. 175, p. 361. (1953)
13. Pellini, W.S., Puzak, P.P., NRL Rept. 5920, Mar. 15, 1963, and Trans. ASME, Ser. A: J. Eng. Power, vol. 86, pp. 429-443. (1964)

FRACTOGRAPHIC ANALYSIS

Katarina Gerić, Faculty of Technical Sciences, Novi Sad, Serbia and Montenegro

1. FAILURE ANALYSIS

Failure analysis and prevention have important roles in all engineering disciplines. It is necessary that the cause of failure is determined so that its occurrence can be prevented and the performance of the device, component or structure, improved. Failures of metallic components and systems can be the outcomes of design, materials selection, heat treatment, service application, welding, plating, and manufacturing. Considering that engineering failures can be very costly both in terms of human suffering and economic losses, it is necessary that failure analysis is taken seriously.

The most common forms of material failures are fracture, corrosion, wear, and deformation. Before the actual failure mode can be determined, however, a failure analysis must be performed. In order to analyse a failure, circumstance analysis is required followed by chemical analysis, mechanical properties and microstructural analysis. Fractographic analysis, Fig. 1, often has the most dominant role in analysis of failure of metal parts and constructions, [1].

Fractography is the science of examining fracture surfaces so as to understand the process and causes of failure (it often becomes very important in litigation over responsibility for failures). One of the objectives of fractography is to clarify the influence of different microstructures on failure.

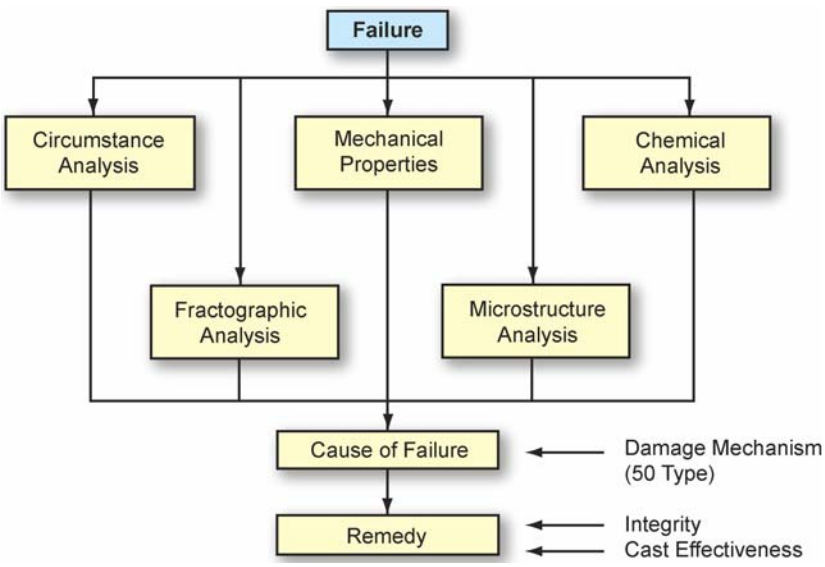

Figure 1. Studies required for failure analysis

Visual inspection of the fractured surface is usually the first step of an investigation of a failed component. The goal of this step is to locate the origin of the fracture. This step also lays the foundation for work to be done in microexamination, using a stereomicroscope with good lighting, if possible. One should check the condition of the surface in order to be able to prepare it for microexamination. Secondary cracks often have a surface that is not contaminated and can lend clues to the cause of failure. These might make good subjects for later microexamination. It is important to look for other characteristics that might have a bearing on the part's failure. These include case hardening regions, welds, surface coatings and existing imperfections.

2. FRACTURE SPECIMEN PREPARATION

When there is nothing left to do on the scene, it is time to move the analysis into the laboratory. There are several things to remember as one prepares to remove the broken components and transport them:

- Select any pieces that might provide clues, even if they themselves are not broken. If the device is small enough, bring the whole thing back to the laboratory.
- Never join the two fractured surfaces back together. Fractured surfaces are very delicate and important clues may be lost if these surfaces are disturbed.
- Never touch any surface with your fingers. Human skin has oils that can contaminate the fractured surface.
- Extreme care should be taken when samples are shipped or transported to the laboratory. The sample can be wrapped in paper or tape, so long as these don't contaminate the surface. Excess padding should be used so the samples are not damaged in transit. The entire sample should be stored in a plastic bag with a desiccant, a vacuum storage vessel, or a desiccator.

If this is not feasible, then the fractured surface needs to be protected with a surface coating to prevent corrosion. This coating should not react with the fractured surface chemically and should protect it from the environment and be easily removable. One could use a clear acrylic lacquer or cellulose acetate replicating tape.

Usually, cleaning of the fracture is required, particularly when electron-microscope examinations are to be made. Cleaning is for the purpose of removing protective coatings, corrosion products, and loose deposits such as dust, which may obscure part of the fracture or make interpretation difficult. Prior to cleaning, however, consideration should be given to the possibility that the deposits on the fracture surface can yield important information regarding the cause or progress of the fracture.

When the primary fracture has been damaged or corroded to a degree that prevents it from providing much information, it is desirable to open any secondary cracks to expose their fracture surfaces for examination and study. These cracks may provide more information than the primary fracture. If rather tightly closed, they may have been protected from corrosive conditions, and if they have existed for a shorter time than the primary fracture, they may have corroded less. Also, primary cracks that have not propagated to total fracture may have to be opened.

It is desirable to be able to distinguish between a fractured surface produced during opening and the surface produced by primary or secondary cracking. This can be accomplished by making sure that a different fracture mechanism is active in making the new break, such as by performing the opening operation at a very low temperature.

Microfractographic examination is carried out with naked eye or by using a scanning microscope (SEM) with a low magnification. Scanning electron microscopy is used as an addition to macrofractographic examination – purpose of it being to reveal the mechanism of fracture and the connection between material microstructure and the micromechanism of fracture. At low magnification, the feature in scanning-electron-microscope fractograph strongly resembles the aspects of the fracture, apparent to the naked eye; but at high magnifications, more detail is visible and needs to be categorized and described if the fractograph is to be related to the micromechanisms of fracture that were active. A metallographic analyst needs to carry out an investigation in this way in order to determine the mechanism of fracture, based on the appearance of failure surfaces and on the microstructure of broken parts.

3. CRACK ANALYSIS IN THE WELDED JOINT

The strength of material can be reduced by error during manufacture (welding, heat treatment), or by service effect (temperature, corrosion). Damage can be expected as a result of the reduced strength properties of the material, rather than higher loads.

Different types of cracks detected during service can be divided into manufacturing and service cracks, according to the time of crack formation, Fig 2.

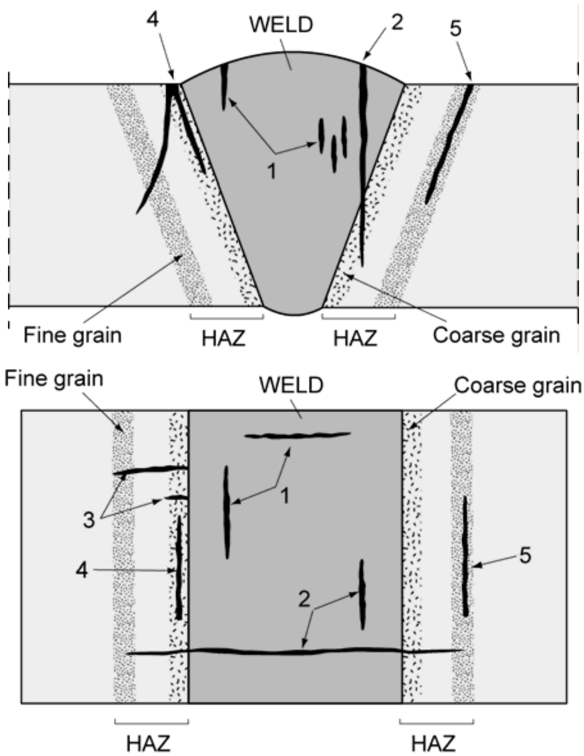

Figure 2. Schematic diagram of different crack locations in the weld region (manufacturing cracks, hot cracks-1, 4; cold cracks-1, 3; relaxation cracks-3, 4; service crack-2, overload and fatigue fracture, creep cracks)

The purpose of this part of the lecture is to determine the mechanisms of failure based on appearance of the fractured surface and the microstructure of the heat affected zone (HAZ) of high strength steel welded joints.

Spherical storage tanks for liquefied ammonia of 95 m^3 volume were composed of sections whose parts had been welded by the automatic submerged arc welding process. High strength steel of 13 mm thickness is chosen for the spherical storage tanks. The chemical composition of the fine grained, high strength, vanadium micro alloyed steel, St.E 500, and its mechanical properties are shown in Tables 1 and 2.

Table 1. Chemical composition, wt. %

C	Si	Mn	P	S	Al	Cu	Cr	Ni	Mo	V
0.20	0.51	1.42	0.020	0.010	0.018	0.035	0.018	0.574	0.017	0.180

Table 2. Mechanical properties

Yield strength	Tensile strength	Elongation	Charpy energy	Hardness
MPa	MPa	%	J	HV5
490	720	17.0	130.2	262

During welded joint testing, a vast number of macroscopic cracks had been detected. The first step was to take samples with the cracked material, positioned in liquid and gas phases of the sphere. In the next step, the small "boat" type specimens from meridian and equatorial welds were prepared, Fig 3. The crack, several centimetres long, was discovered in the equatorial weld, propagating in the heat affected zone, Fig. 4. Fractographic analysis was difficult due to corrosion of the fractured surface, and it was impossible to make reliable conclusions about the cause of failure.

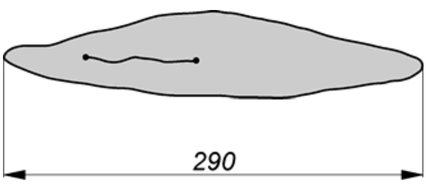

Figure 3. Small "boat" type specimen with crack

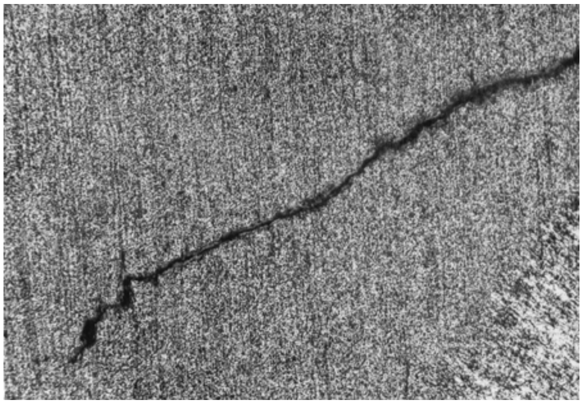

Figure 4. Crack propagation in HAZ

3.1. Fracture analysis of the heat-affected-zone

For better and easier examination of the cause of welded joint failure, simulated welding on the same steel was performed. The microstructure of different temperature regions in HAZ had been simulated on the Smitweld LS1402 device. The samples, 60 mm long, 11 mm wide, and 11 mm thick, had been exposed to different temperatures: 1350°C – corresponding to coarse grain formation; 1100°C – fine grain formation; 950°C – fine grain region above A_{c3} temperature – austenite-ferrite transformation; and 850°C – partial transformation of austenite, between temperatures A_{c1} and A_{c3}. The cooling time from 800°C to 500°C of 15 s was constant, selected as typical for tested steel welding. Impact testing was performed with Charpy specimens (10×10×55 mm) with a 2 mm V notch depth. The fractured surface of Charpy specimens was analysed by scanning electron microscopy, JEOL35, [2].

Regions corresponding to different simulation temperatures are shown in a welded joint scheme (Fig. 5). Macroexamination reveals principal fracture characteristics. The fracture has a flat surface, without traces of deformation. Plastic deformation of the specimen is spotted only by simulation at 850°C, Fig. 5d.

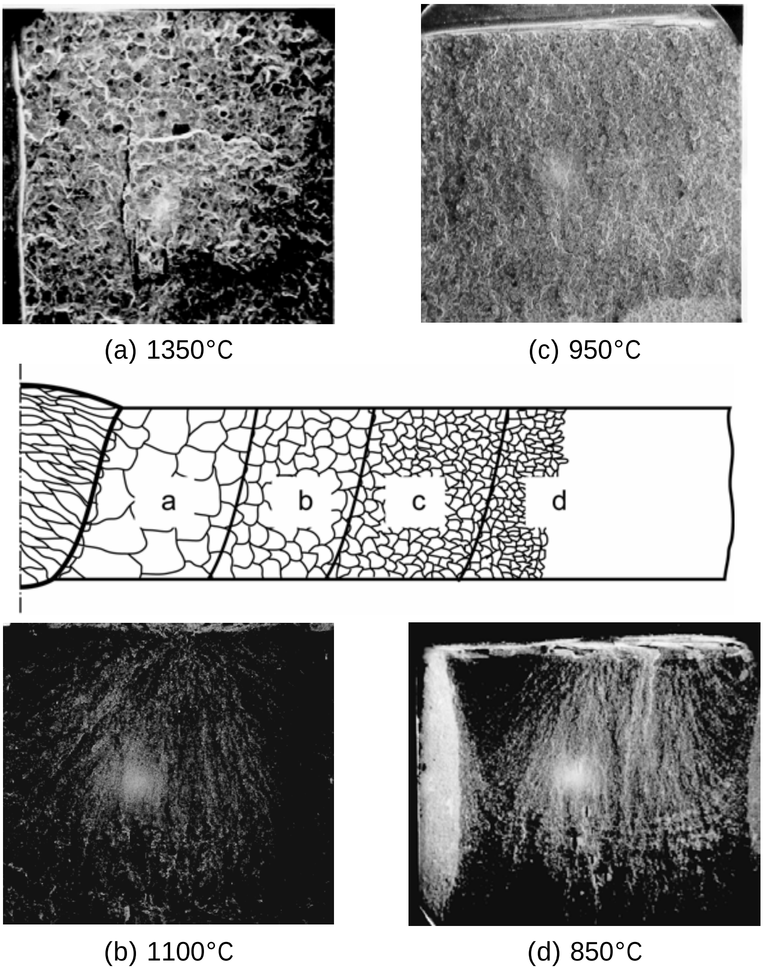

Figure 5. Scheme of welded joint and heat affected zone with macrofractographs of specimens simulated a) 1350°C, b) 1100°C, c) 950°C d) 850°C (10×)

For the specimen simulated at 1350°C, micrographic analysis shows very brittle fracture because of large austenitic grains in coarse grain HAZ region. The cleavage facets are up to 0.1 mm, similar in magnitude to the grain size, with noticeable river patterns, Fig. 6.

Brittle fractures are generally characterized by flat surfaces, absorbing little energy. The presence of many flat facets, where the crack tips moved without significant distortion of the material is noticeable.

Transgranular cleavage occurs at well-defined planes in the crystal. The plane of fracture is one of the {100} planes in most body-centred-cubic metals. Cleavage results from high stress along three axes with a high rate of deformation and at low temperatures. Characteristics of cleavage are cleavage steps, feather markings, herringbone structure, tongues and microtwins, Wallner lines and quasi-cleavage. A cleavage step is a step on a cleavage facet joining two parallel cleavage fractures. Feather markings are very fine, fan-like markings on a cleavage fracture. Tongues and microtwin tongues are fine slivers of metal on cleavage facets which form from cleavage across microtwins that, in turn, are formed by plastic deformation at the tip of the main crack. Wallner lines are distinct “V” shaped by pattern intersection of two groups of parallel cleavage steps, primarily found in brittle materials.

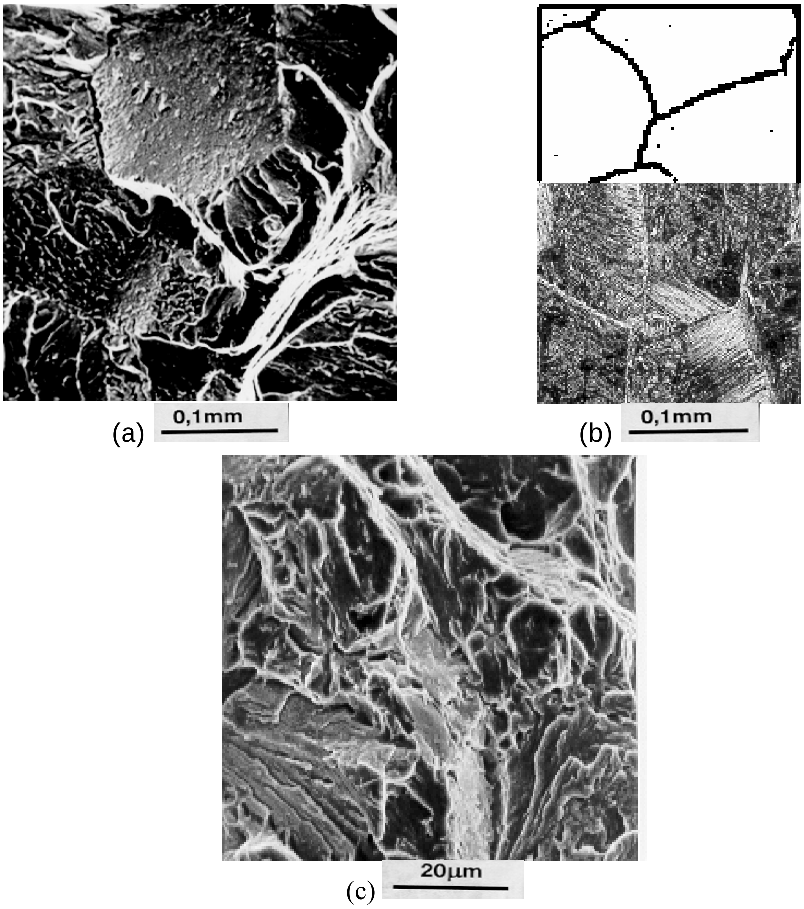

Figure 6. Fractography of specimen simulated at 1350°C: a) flat cleavage faces; b) microstructure and grain size; c) magnified flat cleavage faces

Specimens simulated at 1100°C also have a brittle fracture surface, but with smaller cleavage faces, Fig. 7.

Specimens simulated at 950°C have a brittle fracture surface, but with smaller cleavage faces, and framed with ductile fracture, Fig. 8. It is typical quasi-cleavage, a fracture mode resembling cleavage because of its planar facets, but the fracture facets are not specific well-defined planes. Quasi-cleavage fractures resulting from microvoid coalescence and from cleavage are relatively easy to identify, and the mechanisms of separation are well understood. Many high-strength engineering metals fracture by quasi-cleavage, which is a mixed mechanism involving both microvoid coalescence and cleavage. There is no apparent boundary between a cleavage facet (C) and bordering dimpled area (D), Fig. 8. Schematic presentation of quasi-cleavage is given in Fig. 9, [3].

The mechanism of quasi-cleavage is not well understood, but it can be identified by its fracture features. However, the occurrence of quasi-cleavage is common, and its appearance is usually distinguished by the following:

- Fracture by quasi-cleavage appears to be initiated within facet boundaries. This is in contrast to fracture by cleavage, which is usually initiated from one edge of the region being cleaved.
- Cleavage steps in quasi-cleavage appear to blend directly into tear ridges of the adjacent dimpled areas.

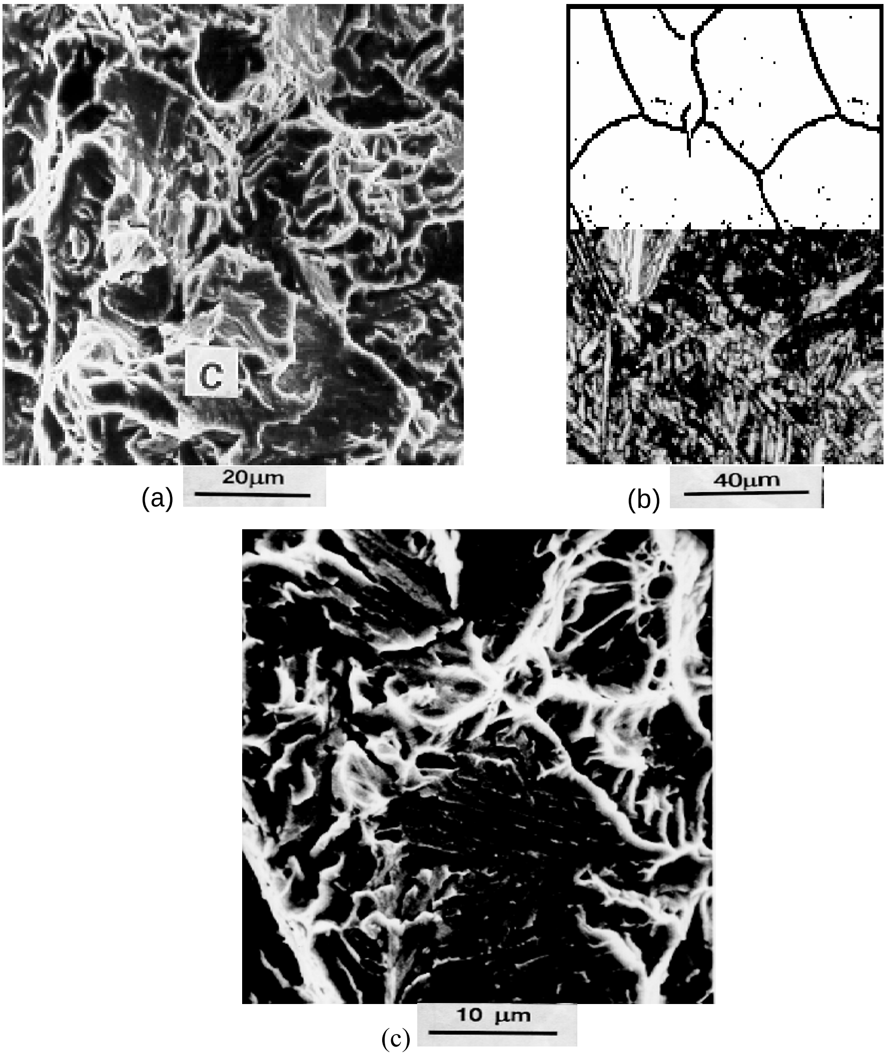

Figure 7. Fractography of specimen simulated at 1100°C: a) cleavage fracture (C); b) microstructure and grain size; c) highly magnified cleavage faces (C)

In quenched-and-tempered steels, small ill-defined cleavage facets, usually initiated at precipitated carbide particles, are connected by tear ridges and shallow dimples.

When tested under embrittling conditions, e.g. imposed by corrosive mediums or tri-axial stress, quasi-cleavage can occur in metals that normally are not known to have active cleavage planes. One explanation is that facets exhibiting quasi-cleavage features fractured ahead of the moving crack front; and then, as the stress increased, the cleavage facet extended by tearing into the matrix around it by microvoid coalescence.

For specimens simulated at 850°C, fracture surface is ductile in the vicinity of notch, Fig. 10b, and brittle, Fig. 10a. Small cleavage faces are in the order of 0.01 mm.

Ductile fractures absorb much more energy. The classic dimple rupture fracture is produced as intersecting dislocations produce voids in the material, which grow to become the dimples seen on the fracture surface. The material is torn apart with considerable deformation and high toughness.

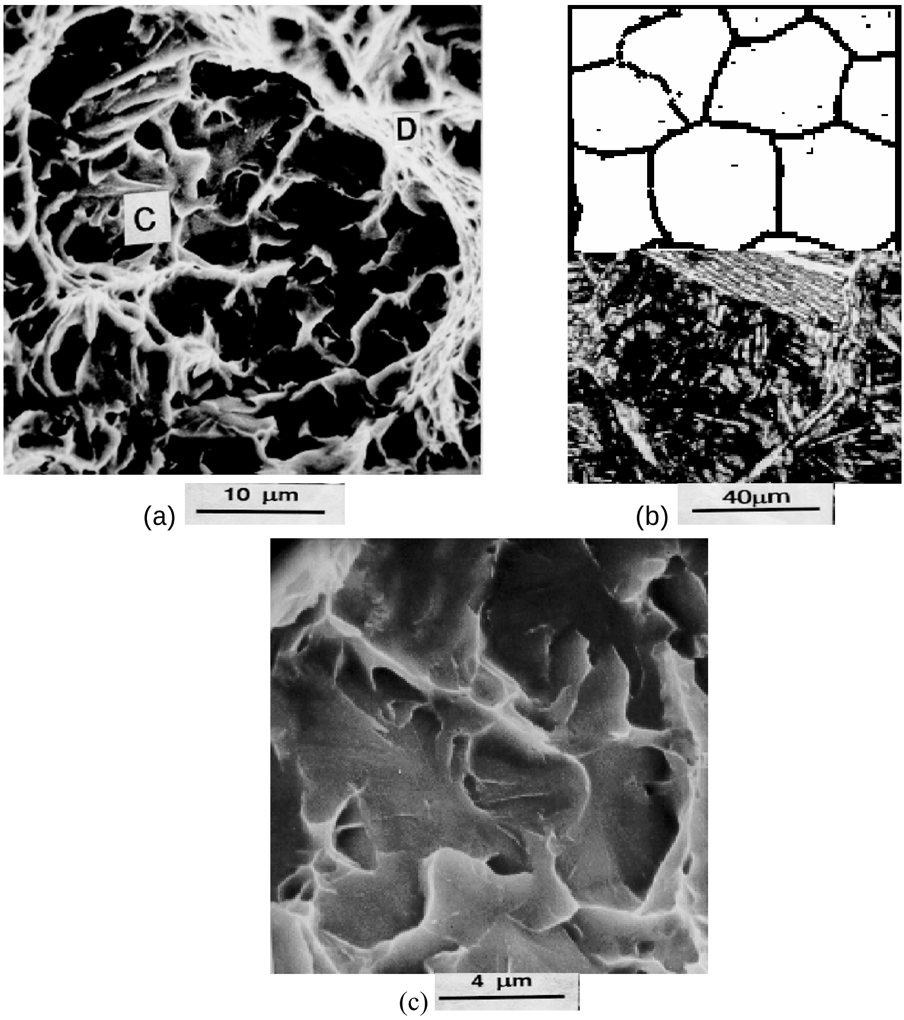

Figure 8. Fractography of specimen simulated at 950°C: a) cleavage fracture (C), framed by ductile parts (D); b) microstructure and grain size; c) highly magnified quasi-cleavage (C)

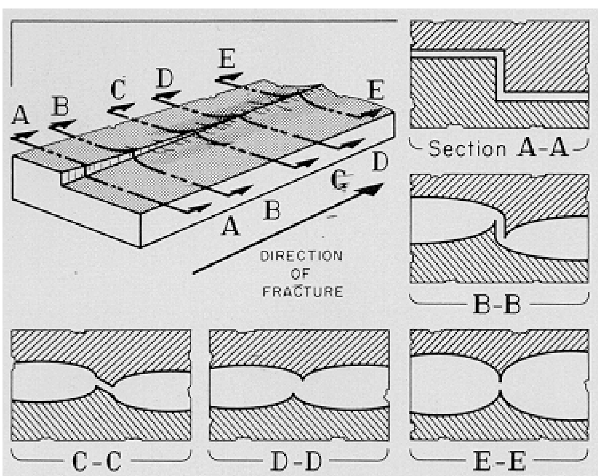

Figure 9. Schematic representation of quasi-cleavage

Microvoid coalescence, or dimple fracture, usually occurs under single load or tearing. This is shown by depressions in the microstructure called dimples, which occur from microvoid emergence in places of high local plastic deformation. Under increased strain, microvoids grow and coalesce until rupture occurs, thus dimple rupture. Dimple size and shape depend on the type of loading and extent of microvoid emergence. When a material is put under uniaxial tensile loading, equiaxed dimples with complete rims appear. Under a tear loading the dimples are elongated, the rims of the dimples are not complete and the dimples are in the same direction as the loading. Shear loading has the same features as tear loading except the dimples are in opposite directions. Oval dimples occur when a large void intersects a smaller subsurface void, the dimples form an oval shape and exhibit complete rims. A serpentine glide is an interwoven pattern of glide plane decohesion steps. Ripples are partially smoothed out areas of serpentine glide. A stretched area is a flat featureless area resulting from further straining of a ripple pattern. Intergranular dimple rupture occurs along grain boundaries due to nucleation and coalescence of voids at grain boundaries.

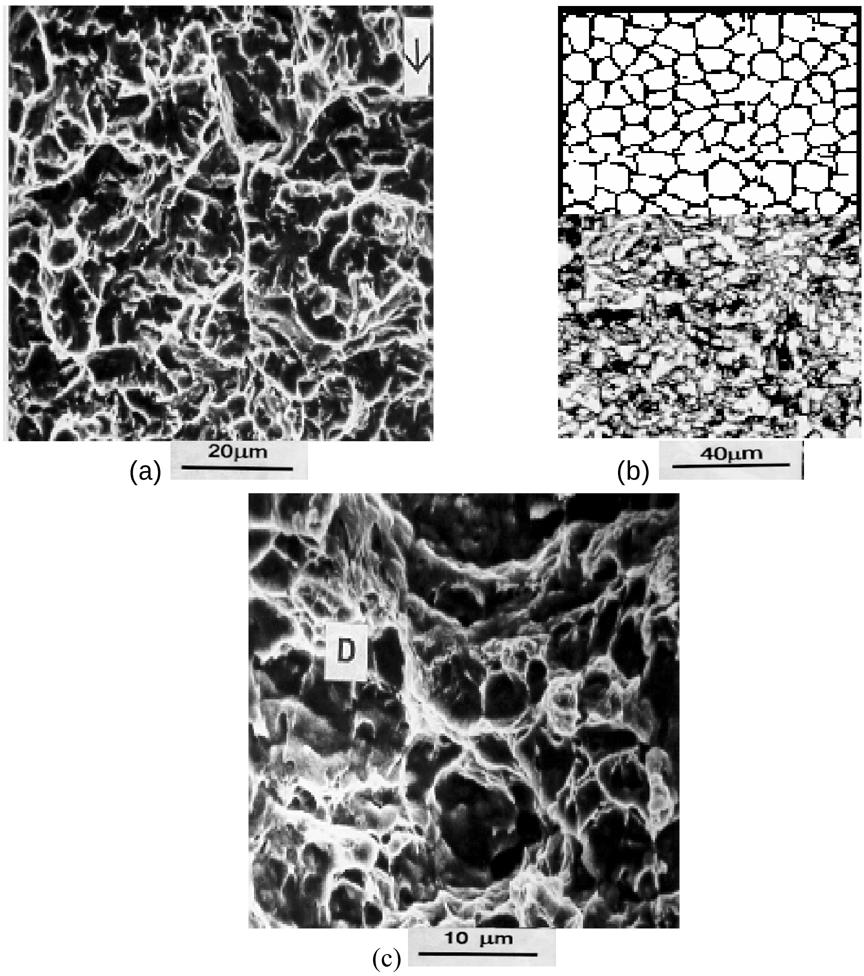

Figure 10. Fractography of a specimen simulated at 850°C: a) cleavage fracture; b) microstructure and grain size; c) ductile fracture (D)

Microvoid coalescence produces a dimpled appearance on the fracture surface. The dimple feature is found most often when a metal has been subjected to a single load to fracture, or in areas where a tearing type of fracture has occurred.

Microvoids usually initiate during plastic flow at inclusions, undissolved second phase particles (such as carbides), grain boundaries, cleavage planes, or at any site where a discontinuity concentrates the plastic flow. Separation at the site of microvoid initiation can occur across a second-phase particle or at a particle-matrix interface. As the plastic strain increases, the existing microvoids grow, new microvoids are initiated, and eventually the enlarged microvoids grow into close enough proximity so that the thin ridges, or membranes, separating them, rupture and fracture occurs. The resultant fracture surfaces have numerous cuplike depressions or "dimples".

Until recently, dimples have been classically divided into three groups: equiaxed dimples, shear dimples, and tear dimples. Schematic diagrams illustrating how these are conventionally formed are shown in Fig. 11. Equiaxed dimples do not always appear exactly equiaxed in SEM fractographs, because tilt angles of 30° to 45° are often used to provide good contrast, and therefore the dimples may appear slightly distorted. However, the shear-lip zone of a Charpy impact, tensile-test, or fracture-toughness specimen will display a well-defined network of oval dimples elongated in the same direction – the direction of shear. With shear dimples, it is quite difficult to identify the site of microvoid initiation, because the carbide particle or inclusion responsible may be hidden below the surface, which may have been rubbed or flattened out by shear displacement during fracture.

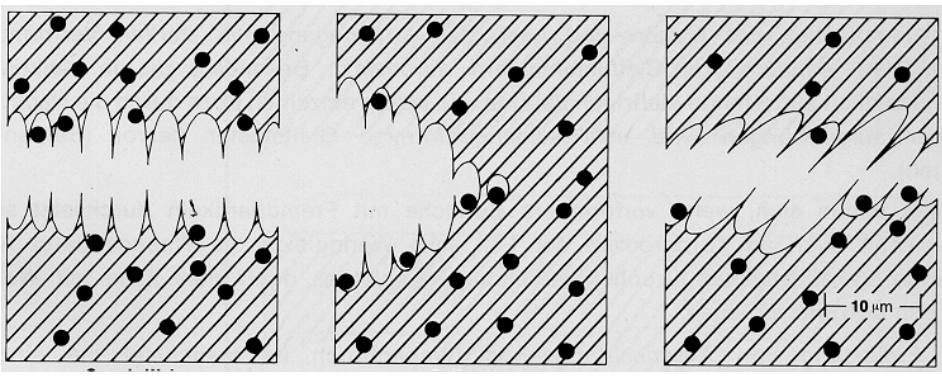

Figure 11. Schemes of the dimple shape

Tear dimples are formed by non-axial stress conditions, such as those that exist in precracked plane strain fracture toughness specimens and in drop-weight tear test specimens. Non-axial stress conditions are found also in the test where a wedge is forced into a notch. The elongated microvoids that become tear dimples are formed in a narrow band just ahead of a well-developed crack front, e.g. the tip of a fatigue crack.

4. FRACTURE INITIATION

During reheating in multipass welding of microalloyed high strength steels, a martensite–austenite microconstituent with very low ductility can occur, being formed in the coarse grain region. This is the reason of initiation of brittle fracture on martensite islands [4, 5]. SEM and TEM analyses of second phase particles reveal the nature of this phase to be mainly M–A constituent (high carbon martensite with some retained austenite, Fig. 12a and b.

Close examination of the initiation area reveals that initiation occurs at the point between two closely spaced particles, Fig. 13. Energy dispersive X-ray analysis (EDX) on the particles indicated that there was no inclusion. To identify these particles, the fracture surfaces were etched and re-examined in the SEM. Figure 14 shows matching facets after etching. The particles have the smooth and blocky appearance characteristics of M–A constituent and lie on a prior austenite grain boundary. Failure initiation has therefore occurred from between two M–A particles, in close proximity, located at the prior austenitic grain boundary.

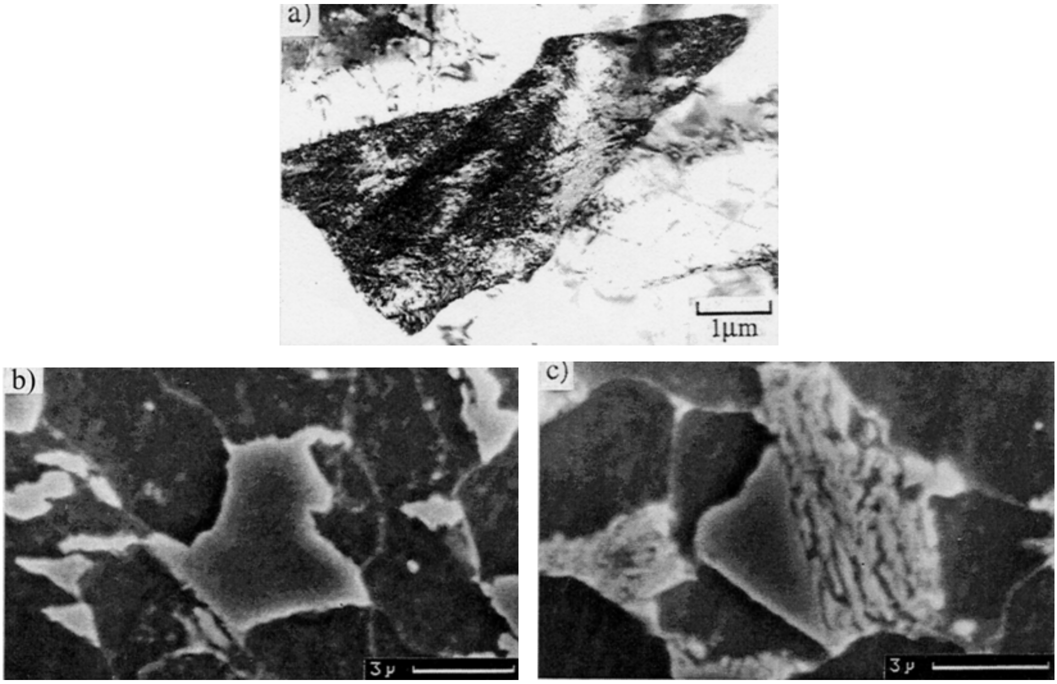

Figure 12. Second phase particles in the intercritically reheating coarse grain region microstructure: TEM and SEM micrograph of an M–A particle

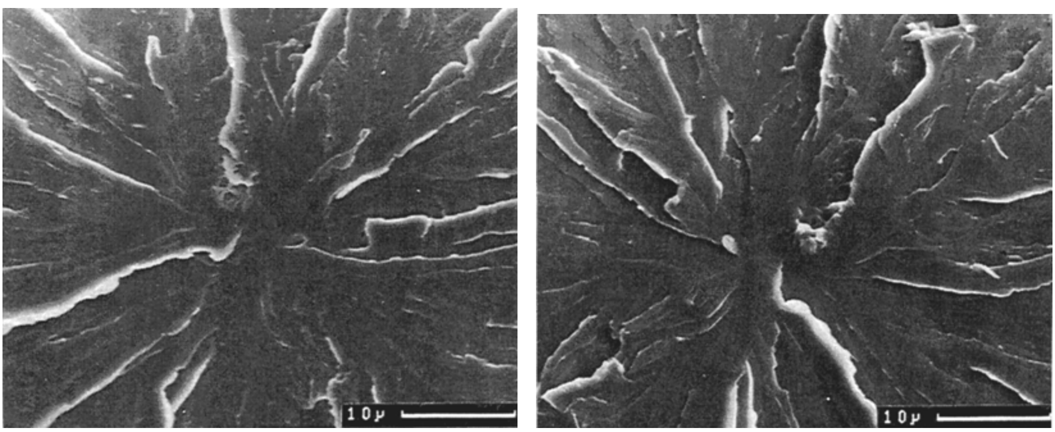

Figure 13. SEM micrographs of matching facets showing the initiation site for the intercritically reheating coarse grain structure

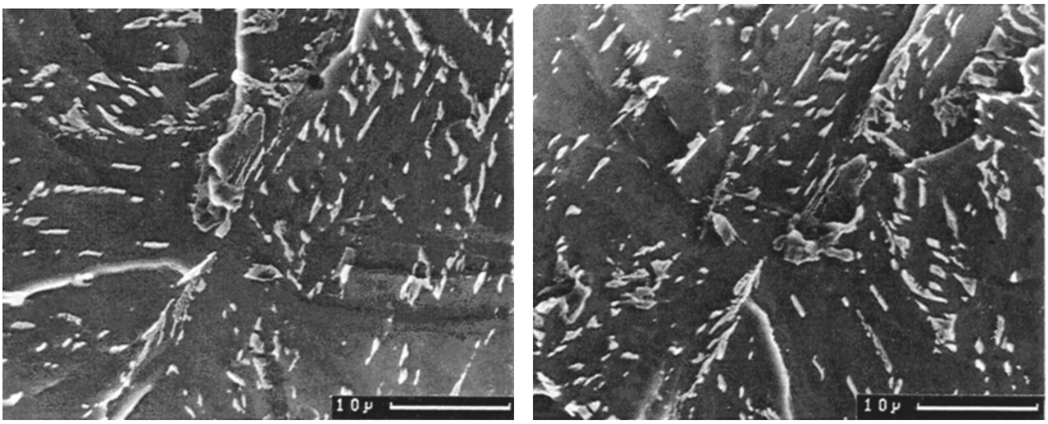

Figure 14. SEM micrographs of etched matching facets showing the initiation site for the intercritically reheating coarse grain structure

CONCLUSION

Using fractography analysis, it is possible to determine the cause of failure based on failure surface appearance. Difference in microstructural characteristics of high strength steel welded joints is an important factor influencing the failure mechanism. Different mechanisms of crack propagation, transcrystal cleavage, quasi-cleavage, ductile micro-void coalescence are a result of heterogeneous microstructure in HAZ. In high strength steel, cleavage fracture can be a major problem which has caused catastrophic fracture in the past, and information about fracture mechanisms are very helpful. The better understanding of micro-mechanisms of fracture can help to minimize the risk of failure. Upon determining the cause of failure, corrective actions can be applied and appropriate recommendations to solve the problem can be defined.

REFERENCES

1. Blačić, I., Grabulov, V., Veljanovski, B.: Fracture analysis and fractography, IBR, pp. 217-221. (1998)
2. Gerić, K.: *Crack initiation and propagation in HSLA welded joint*, Doctoral thesis, in Serbian. (1997)
3. ASM Metals Handbook, 9th Ed., Vol.1, ASM (1987)
4. Kim, B.C., Lee, S., Kim, N.J., Lee, D.Z.: *Microstructure and local brittle zone phenomena in high strength low alloy steel welds*, Met. Trans., Vol. 22A, pp. 139-149. (1991)
5. Davis, C.L., King, J.E., *Toughness comparison between the intercritically reheated coarse grained HAZ of two HSLA steels*, ICF 8, Kiev. (1993)

FRACTURE CASE STUDIES – BASIC PRINCIPLE

Petar Agatonovic, Germany

INTRODUCTION

The introductory short story is representative for the related developments and general importance of fracture mechanics application in the scope of structural integrity.

During pull-up at Air Force Base, Nevada, December 1969, an F111A (Fig. 1) experienced catastrophic failure of the left wing, causing the destruction of the aircraft and the death of the pilot. The failure initiated at a pre-existing manufacturing flaw due to a forging fold in a critical wing pivot fitting in the high strength D6AC steel forging. The flaw had passed undetected through inspections and grew to critical size when the airplane had accumulated only 105 flying hours, although the fatigue life was estimated to be about 10,000 flight hours.

Figure 1. F111 aircraft

The F111 had been based on the *safe life design philosophy*, developed after the war years in an effort to take into account cyclic stresses that lead to fatigue of airframes. The approach is similar to the conventional engineering method of stress allowable, based on the maximum stress that can be permitted in a material for a given design condition to prevent failure. Materials allowable were obtained through a testing program. Additionally, the safe life approach involves rigorous fatigue testing of a full, representative airframe assembly for 40 000 hours ensuring a safe life of 10 000 hours. The safety factor of four was to take into account unknowns, assumptions and variables applicable to the fleet as a whole. Unfortunately, while this approach proves the overall airframe design for a certain safe fatigue life, it does not take into account the effect of a single trivial defect, nowhere to be found by non-destructive inspection (NDI), introduced in a particular airframe at manufacture. Thus, the overall design may be acceptable respective requirement, but unforeseen small random flaws can undermine this and cause failures, well below the safe life, as it had occurred.

Regularly, the value of allowable stress has to be defined with a given probability. For this, it is necessary to consider how the safety factor and the reliability interact. In the deterministic approach the *Safety Factor* is the ratio of material strength and the stress caused by the limit load. In the probabilistic approach this factor is the ratio of the mean or average values of both parameters (“central safety factor”) or connected to any value of probability, Fig. 2. The resulting values will be then very different in dependence of the proposed reliability. Of interest is that for a particular part the actual safety factor, as the combination of actual stress and strength, is not known. We know that in case of a central safety factor, 50% of all parts have the safety factor above this value, and 50% are with a safety factor below this value. But we do not know how to classify this particular part. It is really possible that the safety factor for a particular part is below 1 and that this part will prematurely fail (shaded area in Fig. 2). This usually results in the conservative selection of the safety factor, so to allow for the allowable stress to be at the “minimum” of expected values. According to the MIL-Handbook, for example, *A-basis allowable* values correspond to the value for which at least 99% of the population have to survive (with a confidence level of 95%). Also in this case the particular component may be, as based on actual stress and strength combination, far above the allowable (if it belongs to the 99% group) or below (belonging to the 1% group).

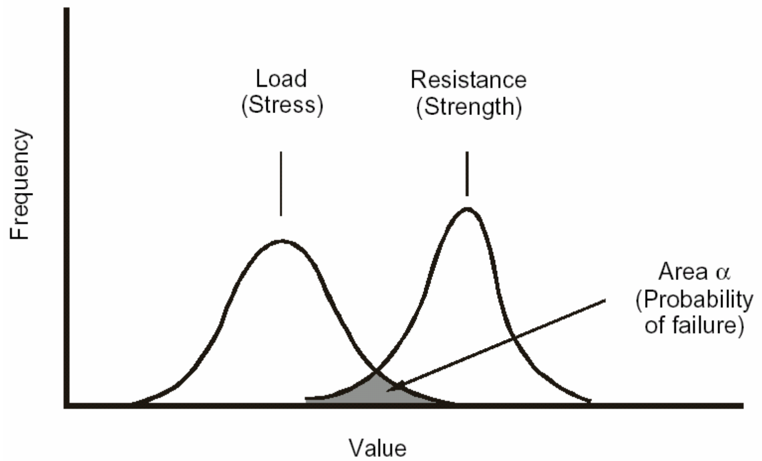

Figure 2. Statistical relationship of the safety

In spite of this, probabilistic methods were used for calibration of safety factors in standards and structural codes. The basic concept for reliability analysis is that resistance and load factors are statistical quantities with a central tendency (mean), dispersion about the mean (variance) and some form of distribution. This was real progress compared to pure empirical or estimated safety factors.

1. HOW FRACTURE MECHANICS CHANGE ENGINEERING APPROACH

The knowledge of component life expectancy (warranty life) is needed from the outset (“zero” time). For this purpose, the usual fatigue-life analysis has to determine life of unflawed structures using nominal values of fatigue-life characteristics. This so-called safe-life approach predicts a replacement time for machine components. Once a component reaches this replacement time, its safe-life is considered to be spent and the component is retired, whether or not any fatigue cracks are present.

As already discussed, there were two significant problems, if only this method is used: the safety of a structure was not assured if it contained a manufacturing or maintenance induced defect, and retirement time do not correspond to the available life capacity of the actual component. In addition, due to the first problem, to assure safety, the selected safety factor was too conservative (with many components fit-for-service prematurely retired). This can be avoided by the inspection of actual part and, when cracks are identified, determining the fitness for continued operation by fracture mechanics approach. Fracture mechanics provides methods, evaluating the structural integrity of defective components, and demonstrating whether they are capable of continued, safe operation. Consequently, the meaning of safe life is changed: a *fracture mechanics safe-life* analysis has to be conducted under the assumption of pre-existing initial flaws or cracks in the considered structure. In particular, this analysis shall show if the structure with the flaws placed in the most unfavourable location with respect to the applied stress and material properties, of sizes assumed or classified by the non-destructive inspection sensitivity and acted upon by the spectra of expected service loads and environments, will meet the safe-life requirement. The loading spectra, stress level, fracture toughness and crack growth rate of the parent material and weldments, and suitable to temperature and environment expected in service, shall be taken into consideration. The component has a *safe life* if it can be shown that the assumed or detected greatest defect in it will not grow to such an extent that the minimum specified performance (limit-load capability, no-leakage) is no longer assured within a safe life interval up to the next scheduled inspection or the maximum sustained stress-intensity factor $K_{\max}$, nor will exceed the stress corrosion threshold intensity factor K_{ISCC}.

Another damage-tolerance category is called *fail-safe* in which the structure is designed with sufficient redundancy to ensure that failure of one structural component does not cause failure of the entire structure. A structure is fail-safe if it is shown, by analysis or test, that as a result of structural redundancy, the structure remaining after failure of any element of the structure can sustain the new higher loads (with a safety factor reduced to 1…1.15), without losing limit-specified performance. Furthermore, an element failure shall not release any part or fragment that may result in a catastrophic or critical event. Hence, the goal of the fail-safe philosophy is to design multiple load path structures such, that if an individual element should fail, the remaining elements would have sufficient strength and remnant life to carry additional loads due from the failed element until the damage is detected through scheduled maintenance inspections. This necessitates periodic crack inspection of the structure. Fail-safe design can be useful only if it is supplemented by careful, regular inspection, followed by timely maintenance when required.

However, this method also does not consider the initiation and growth of small cracks and their possible linking up (e.g. at fasteners holes) and that the structure will eventually encounter loading above the strength provided in the remaining structure. As a result, the loss of several fail-safe aircrafts in the mid 1970s emphasized the need to locate cracks and repair damage before failure occurred. This situation leads to the solution called *Damage Tolerance Approach*. Based upon fracture mechanics, the damage tolerance approach redefined the basis for analysing fatigue cracks in different structures. The basic requirement is to detect cracks in all structural components, before they propagate to structural failure. By establishing inspection intervals for these components, based on the necessary time for a crack to grow from an initial, detectable size to critical crack size, the objective of the damage tolerance approach is realized. Therefore, a structure is considered to be damage tolerant if the amount of general damage and/or the size and distribution of local defects expected during period of operation until the next inspection do not lead to structural degradation below limit-specified performance.

Before component inspection intervals can be established, its usage profile must be defined for each location. Using crack growth equations, the stress spectrum is combined with material properties data and stress intensity factor solutions to determine the number of cycles or flight hours to failure. The result is usually divided by a factor of two to arrive at the inspection interval, and to ensure that, should a crack develop in a principal structural component, it will be inspected at least once before the crack propagates to failure. Since fracture mechanics provides a more precise characterization of crack behaviour, the large scatter factors typical for fatigue are not required. Damage tolerance approach allows reduced design safety factors, in addition to economic benefits. Components are replaced only if a crack of significant size is detected in inspection, unlike in the safe-life approach where components are retired whether or not they are damaged.

1.1. Economic aspects of fracture mechanics approach

Industrial competitiveness requires more efficiency of existing process plants in terms of their costs, downtime, production efficiency and quality. Industries rely on their plant *operating efficiently and uninterrupted* during production. Consequently, both users and vendors have been studying methods of extending the useful life of components beyond the lives of similar equipment subject to certain field problems, or beyond the normally specified design life. A number of *degradation mechanisms* which, when left unmonitored and without preventative-remedial measures being taken in plant design, often lead to failure. The *failure of plant* results not only in loss of production, of income, and for cost of unscheduled repairs, but all too often in injury and fatalities. However, the practice of replacing life-limited components at first signs of field problems in nominally similar equipment or at the end of their predicted lives can result in an unnecessary and large expense to the user. Vendors, users, regulatory agencies responsible for structural integrity are aware that there can be significant systematic errors, such as in estimates of loads, duty cycles, or stress, and statistical errors, such as fatigue life scatter, associated with initial estimates of life. Manufacturers can compensate these uncertainties by specifying conservative design life values or conservative field replacement/repair schemes.

Thus, barring large non-conservative design, fabrication, or logistics errors, the vast majority of a component population has the capability to exceed the initially predicted life without catastrophic failure. Studies indicate that a full 80% of parts replaced at calculated safe life limits have at least a full order of magnitude of remaining fatigue life. Therefore, in the current budgetary environment, field equipment is often used *beyond its design life*, demonstrating that the economic life in most cases exceeds the design life. To avoid large cost of replacing critical parts as they reach their safe-life limits or based on Retirement-By-Time basis a *Retirement-For-Cause* (RFC) program has become a cost-effective, yet safe alternative by which life-limited components are retired from service because of measurable fatigue, creep, corrosion, or wear damage, rather than because of subjective interpretations of problems with similar equipment, or because a calculated design life has expired. The RFC procedure can be an effective method for more fully utilizing the useful life of expensive components and therefore, have significant impact on the conservation of natural and capital resources.

Retirement-for-cause involves adequate periodic non-destructive evaluation (Fig. 3) to assess the damage state of components (whether or not detectable cracks exist). Those components with no detectable cracks are returned to service. This approach allows parts with low life to be detected and discarded before they can cause an incident, and parts with high life to be used to their full potential. Basic to an RFC program is the calculation of crack-growth rates under the expected service loads (mechanical and thermal). The results are used to define *safe-use intervals* between required non-destructive inspections.

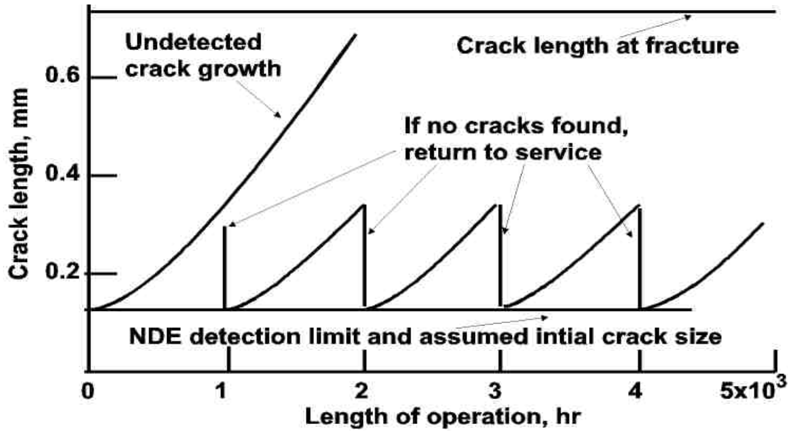

Figure 3. Schematic presentation of RFC procedure

1.2. Relevant aspects of fracture mechanics evaluation

Fracture mechanics is the science of why components or structures fail, enabling the structural integrity assessment. The conventional Linear Elastic Fracture Mechanics (LEFM) uses single parameter to represent structure resistance against failure, as K_{Ic}, K_c, COD, and J_c, being developed based on the Irwin solution for *strain energy release rate G*, necessary for crack extension. These methods assume outside of the crack tip only elastic deformations and defined parameters are interdependent and exchangeable. Corresponding critical values should be a material characteristic and independent on size or geometry, but this is true only for pure elasticity. Under normal conditions, critical values are more or less dependent on size and geometry.

However, the increase in fracture resistance under conditions of stabile crack extension shows that the distinct limiting parameters of the material are not valid in this case and the solution based on their application could lead to large scatter. For many materials and loading conditions, and/or specimen geometry, the assessment based on this simple solution could be very pessimistic and can lead to unnecessary replacement and shutdowns, with larger cost and inconveniency. Cracks in the real structure are seldom highly constrained, and the failure, predicted by LEFM as unstable crack extension of high speed (in its most dangerous form) is seldom in practice. More often, the breakdown of the structure is accompanied with plastic deformations and slow crack growth, characterized as ductile failure. But if plastic deformation is restricted, due to the high constraint, the resistance increase could not act and the material fails at critical stress intensity K_{Ic}, corresponding to plane strain conditions.

Today, the crack driving force is generally represented by *J*–integral, which relies on plasticity and crack increase in the scope of Elastic-Plastic Fracture Mechanics (EPFM). In this case, the part of energy is spent in plastic deformation and the stress stage in the changed section, according to plasticity, so exact evaluation is only possible if both contributions are considered.

Starting from both extreme conditions, e.g. LEFM and EPFM, the methods have been developed that combine the relevant criteria for pure brittle (elastic) and pure plastic failure in the form of the Fracture Assessment Diagram (FAD). Because of complex behaviour in all practical cases, which are, as a rule, between these limiting cases, the solutions are only possible that are based on interpolation or some approximation. Consequently, the classical form of FAD has been based on interpolation between two independent solutions: for failure due to the crack, based on LEFM, and failure due to the plastic collapse in the critical section, which can be predicted on the basis of plastic analysis. It is not difficult to recognize that this method has nothing to do with elastic-plastic fracture mechanics. In addition, evaluation of collapse introduces additional complexity in the solutions. According to the most known procedure R6, the collapse is not represented by unified material property and the geometry consideration is connected to different solutions in dependence of geometry and loading conditions with the consequence that in case of real geometry accurate evaluation could be unsafe.

For typical engineering materials with average ductility, the effect of the crack-like defect should not be forgotten and conditions for pure collapse do not appear. Starting from this presupposition, the new method has been developed by the author, and is based on approximation of stress-strain conditions (plasticity) in the net section weakened by the crack (geometry), and is successfully applied in the design of the ARIANE 5 rocket case and verified on two different materials.

The basic LEFM relationship can be presented as the product of two stress intensity factors: a conventional factor for stress, and one for strain (stress divided by E–modulus)

$$J = K_{\sigma} K_{\varepsilon} \tag{1}$$

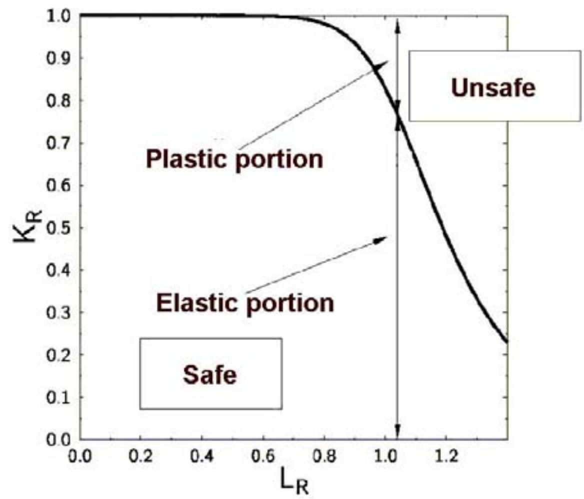

Figure 4. Fracture Assessment Diagram (FAD) based on stress-strain approximation solution

To consider net section (as usual in case of fatigue) both solution for K must be scaled by the ration of net section and remote, full section area. The stress intensity factor is calculated using reference elastic-plastic strain in the net section, which for engineering stress-strain curve with the constants B_F and n is:

$$\varepsilon = B_F \sigma^n \tag{2}$$

Based on this solution, J–integral change depending on load level and the corresponding FAD are constructed (Fig. 4) using:

$$K_r = \sqrt{\frac{L_r \sigma_T}{E \varepsilon_{ref}}} \tag{3}$$

The FAD-curve shows that up to the 70% of yield strength in section with the crack the available material plasticity is, based on crack tip blunting, sufficient to hold the fracture toughness or crack resistance of material unchanged. Beyond this level the plasticity is spent on global deformation, resulting in reduction of residual strength. The typical R-6 Option 2 solution is more conservative, predicting the fracture toughness reduction from the beginning, opposing the experimental evidence. Independent of the selected methods and procedures for purposes of structural integrity determination (damage tolerance, retirement-for-cause), detailed stress analysis and comprehensive fracture mechanics analysis of residual strength and life have to be conducted. To this end, different relevant aspects have to be considered.

1.2.1. Stress analysis aspects

An analysis to determine stresses, resulting from combined effects of force, internal pressure and associated thermal gradient, is usually performed using finite elements calculation. This kind of analysis will usually assume no crack-like defects in the structure. For an efficient and accurate analysis, the complex operational environment requires that all important structural phenomena are well understood and fully considered within the geometrical and physical model. Typical step-by-step analysis procedure, based on building blocks, is the most adequate (Fig. 5). Well-executed finite element analysis can result in saving money, time, and effort within the design process. The sense of exact calculation, probabilistic consideration, and damage tolerance design is to reduce safety factors, or in better use of available potential. On the other hand, a very exact calculation has no sense if the safety factors are unchanged, being the case if the selected safety factors are purely empirical and not based on analysis and verifying experimental results.

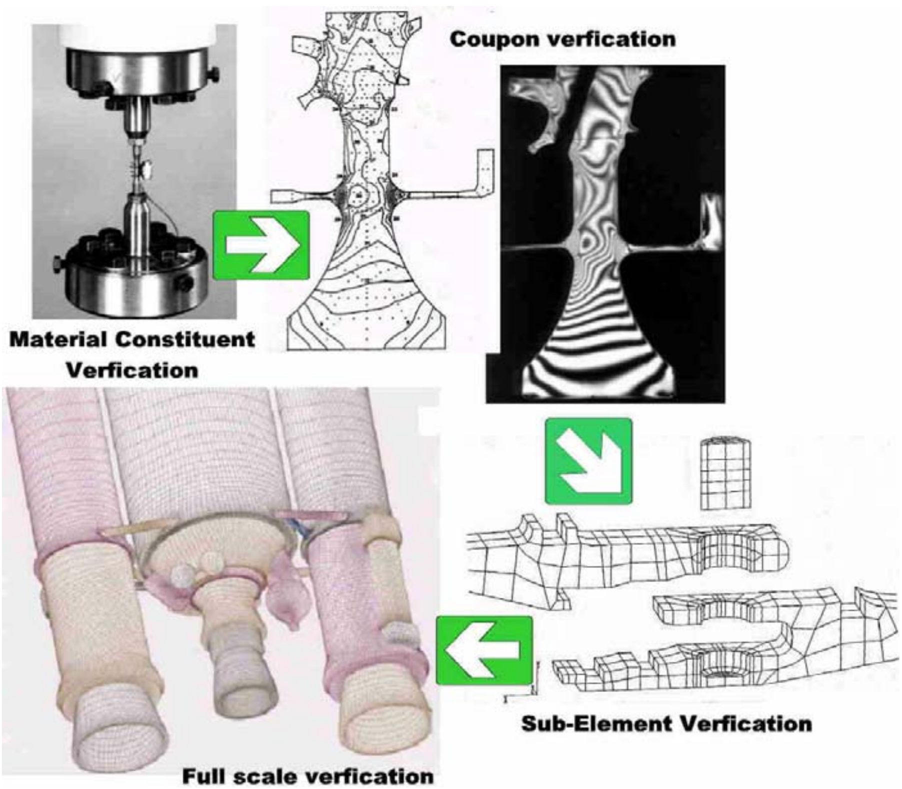

Figure 5. Building block verification strategy

1.2.2. Material property aspects

The integrity assessment of a cracked structure by conventional fracture mechanics is based on a single parameter, supposing that it uniquely characterizes the material fracture resistance. Under two-dimensional conditions (through crack defects) the parameter K_{Ic}, as the stress-intensity value at the crack tip for unstable crack growth, is the fracture toughness for plane strain conditions, and is an inherent material property, while resistance to the onset of ductile fracture is characterized by a critical value of the *J*–integral, J_{Ic}. Because the micro-mechanisms of fracture require attainment of the critical condition, described in terms of stress or strain, different values of applied crack driving force may be required to cause fracture in different structures. These interrelated effects of geometry and loading mode on near-tip stresses or strains, and fracture toughness, are referred as size effects. Early fracture mechanics research addressed size effects to establish size and deformation limits below which the geometry independence of fracture toughness is assured and a single parameter describes uniquely and completely stresses and strains near the crack tip. This enabled application of conventional single parameter fracture mechanics approximation to assess the fracture integrity of structures irrespective of the micro-scale fracture mechanism. Testing standards, which govern the measurement of K_{Ic} and J_{Ic}, require sufficient specimen thickness to produce predominantly plane strain conditions and sufficient crack depth to position the crack tip in a highly constrained field. The requirements of the testing standards guarantee that K_{Ic} and J_{Ic} are lower bound, geometry independent measures of fracture toughness.

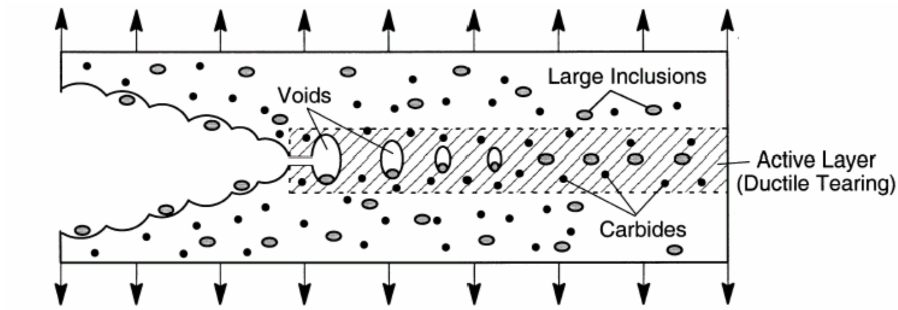

Figure 6. Ductile tearing by hole growth and coalescence

Stress fields at the crack tip can be divided into hydrostatic and shear components. Yielding of the material and the crack-tip blunting that post-yield plastic deformation can produce, are governed by the shear component of the stress field. Tensile hydrostatic stresses contribute directly to the opening-mode tensile stresses but do not influence yielding or crack-tip blunting. It follows that fracture toughness will be directly influenced by an increase in the hydrostatic component of the crack-tip stress field, because of reduced crack-tip blunting, which increases the crack-tip strain concentration. *Crack-tip constraint* is used to describe conditions influencing the hydrostatic component of the crack-tip stress field, exhibiting strong effect on apparent fracture toughness, being influenced by flaw depth and geometry, material properties, and loading conditions.

As it is already known, as a test specimen or structure containing a crack is loaded, it passes through a number of different regimes wherein different theories can be used to accurately link descriptors of macro scale loading to the onset and growth of fracture on the micro scale. So long as the crack-tip plastic zone is infinitesimal compared to all other characteristic lengths, and is embedded within a linear-elastic field, small scale yielding

(SSY) conditions exist. Under SSY, the single parameters can be used to relate uniquely crack-tip deformation conditions and remote loading. However, as the level of applied loading increases, the in-plane plastic flow produced by gross deformation of the specimen or structure is impinged upon local crack tip fields. This relaxes the kinematics constraint against further plastic flow at the crack tip. Once global and local plastic fields interact, the crack tip stresses and strains no longer increase in proportion to one another with amplitude governed by a single parameter. At these high deformation levels, equivalence of single-parameter characterizations of the fracture driving force (i.e. K, J, δ) between different cracked geometries, does not ensure identical crack-tip stress and strain fields.

Several two-parameter methodologies have been introduced to quantify the effects of specimen geometry and loading conditions on crack-tip constraint. All of the various constraint models share a common goal: to significantly extend the validity range of the single parameter, thereby facilitating accurate prediction and assessment of the conditions leading to fracture. The two-parameter methodologies were formulated by augmenting J (or K) with a second parameter (T, Q) to describe the near-tip fields in finite bodies under general loading conditions. It has been demonstrated that the T–stress has a significant effect on the shape and size of the crack-tip plastic zone. For the condition $T = 0$, the J–parameter uniquely characterizes the level of deformation and stress triaxiality over micro structurally significant distances ahead of the crack tip. T–negative values produce a substantial reduction in stress triaxiality with no corresponding changes in the J parameter, indicating a loss of constraint and of J dominance. Correcting for constraint effects can significantly reduce scatter of fracture toughness data, obtained with specimens tested uniaxially in the transition region. However, recent investigations showed that the J–T approach does not provide a consistent trend in estimating the stress triaxiality in some specimen geometries and that the T–stress is undefined under fully yielded conditions. Therefore, the new model introduced a correlative approach, based on the two-parameter J–Q description of the crack tip fields in which the J–integral sets the scale of deformation at the crack tip, and in which the hydrostatic stress parameter, Q, quantifies the level of near-tip stress triaxiality (relative to SSY conditions) over distances that are approximately $1 < r/(J/\sigma_0) < 5$ ahead of the crack tip.

Due to all these difficulties and uncertainties, a more pragmatic engineering approach for fracture integrity assessment of cracked structures has been advocated for long. This approach requires that constraint in the test specimen best approximates the structure (by matching thickness and crack depth between specimen and structure) providing an appropriate toughness for use in structural integrity assessment. Experimental studies show that use of geometry dependent fracture toughness value allows more accurate prediction of the fracture performance of structures than it is possible by using conventional fracture mechanics. However, the task of characterizing fracture toughness becomes more complex as testing of non-standard specimens is required, and different fracture toughness data are needed for each geometry of interest.

Most real engineering components do not contain such big inherent defects as those in different laboratory investigations, and material characterisation and failure usually begins from a crack initiated on a surface and contained within a single grain of the material (short cracks). So a further difficulty associated with predicting structural integrity is that actual cracks found in real structures are three dimensional, whereas fracture mechanics methods using characterization parameters as K_{Ic}, J_{Ic}, COD are derived from two-dimensional assumptions. FE–investigations of surface cracks showed that the effect of plasticity is twofold: an increase of the J integral and a loss of the plane strain constraint at the free surface. This leads to redistribution of the J–integral compared to the linear elastic K–solution. As a consequence, linear elastic solutions cannot be simply scaled to a yielding situation, and a fracture criterion, based on this would not be accurate. Considering this, the K_{Ie} has been proposed, determined on surface crack specimens.

1.2.2. Crack growth aspects

One of the most important contributions of fracture mechanics to structural integrity is the application in the study of crack growth. For technical materials, fatigue crack propagation has been shown as crack extension during every load cycle by corresponding striation development. The origin of striation is based on the plastic blunting process of the fatigue crack in each cycle. The example in Fig. 7 may help understand the concept of growing fatigue crack as related to *da/dN* values, presented by electron microscopic fractography of a fatigue fracture surface. The number on the left indicates the number of cycles (striation) at each stress level.

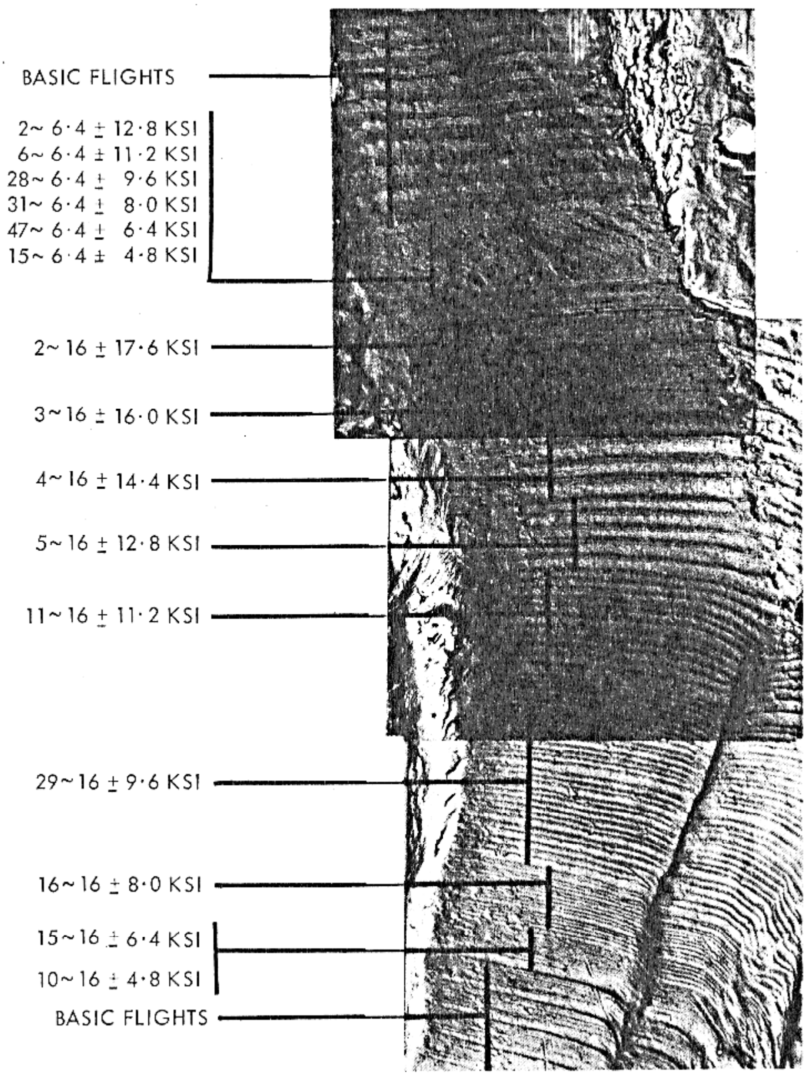

Figure 7. Fractographic view by electron microscope of a fatigue fracture surface

Since crack extension implies decohesion in the material in which a fracture mechanism of fatigue crack growth is operating. The mechanism details on an atomic level are actually unknown, but on a larger scale, several observations have been made:

- Crack propagation in several metals follows a transcrystalline path.
- Crack propagation occurs along slip planes only in the nucleation period. After crack forming, cracks usually grow in a macroscopic plane perpendicular to the main principal stress, at least as long as the crack growth rate is low (tensile mode fracture). The flat fracture mode is usually associated with plane strain conditions.
- At faster crack growth the growth direction remains perpendicular to the maximum principal stress, but the plane of fatigue fracture begins to translate to a slant plane stress fracture mode, at an angle of 45° with that stress (tearing fracture). In sheet materials this leads to shear lips (single or double) as shown in Fig. 8.

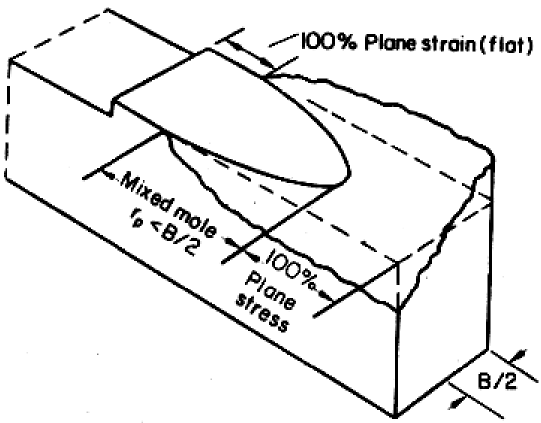

Figure 8. Crack rotation after extension

The mode in which a fatigue crack propagates is of significance to fatigue crack growth predicting capability. The fracture mechanics analysis of cracks is fairly well established in case of small-scale plasticity, constant amplitude, sufficiently large crack size and uniaxial loading. If crack growth is studied experimentally, a plot of da/dN vs. ΔK will have a shape as shown in Fig. 9. From this plot, these conditions are valid for crack growth in region B. In this region the so-called Paris law can be written as

$$\frac{da}{dN} = C\Delta K^m \tag{4}$$

where C and m are material parameters. This equation does not include any influence of previous loading history and there is no influence of the R-ratio.

On the right part of the curve, the above relationship is extended to take into account plastic deformation with the J–integral, i.e. the crack growth rate can be approximated as:

$$\frac{da}{dN} = C\Delta J^p \tag{5}$$

where ΔJ could be approximated by $\Delta K_\sigma \Delta K_\varepsilon$, i.e.

$$\frac{da}{dN} = C\left(\Delta K_\sigma \Delta K_\varepsilon\right)^p \tag{6}$$

In this way the effect of the specimen geometry or yielding of the residual net section could be also excluded and the linear shape of the curve prolonged. Note that the crack growth life is much less sensitive to the choice of critical crack size (which is generally based on extreme load), and also to crack growth in the area approaching K_C.

Before dealing specifically with the applied knowledge of fatigue crack-growth to life calculation of components, it is important to indicate the factors that may influence fatigue crack propagation.

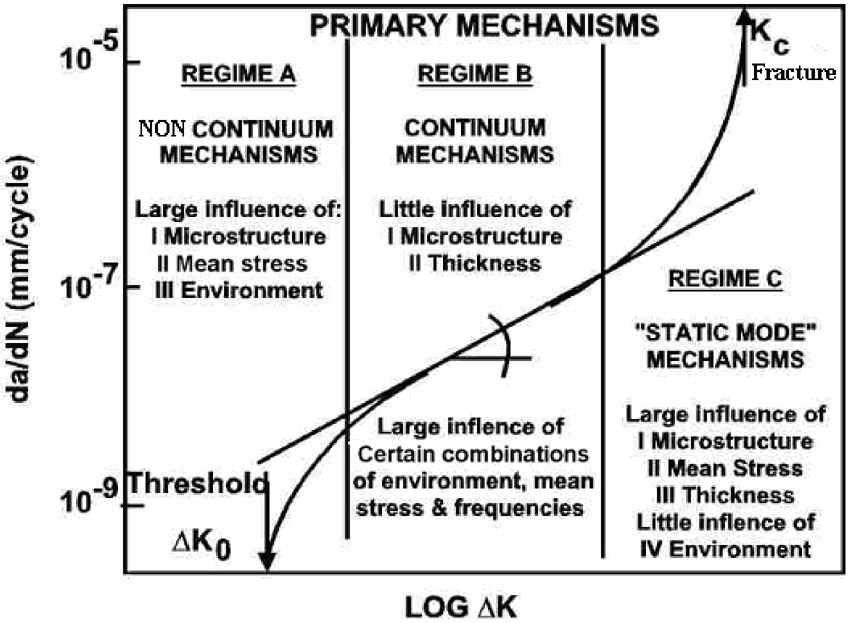

Figure 9. Three regime of fatigue crack propagation (schematic)

On the left end of the curve, the fatigue crack growth threshold is the theoretical value of ΔK at which da/dN approaches zero. However, relationships in this regime (A) are more complicated. A simple explanation would be that if the stress intensity range does not exceed ΔK_{th}, there would be no propagation of existing cracks. However this is only valid if the crack does not close, so that the stress intensity is $\Delta K = K_{max} - K_{min}$. But if the crack closes at some $K = K_{op} > K_{min}$ (K_{op} is not a material parameter or constant and depends on the type and history of loading) this relationship is no more valid and the stress intensity range causing crack growth reduces to an effective value

$$\Delta K_{eff} = K_{\max} - K_{op} \tag{7}$$

The phenomenon of fatigue crack closure is considered to have significant influence in fatigue crack growth propagation, hence it is the major implication in accurate life prediction. Observation and explanation of crack-closure behaviour revolutionized damage tolerance analyses and rationally explain many crack-growth characteristics (retardation and acceleration). Although a flood of experimental, analytical and numerical investigations of fatigue crack closure are reported in literature, there are still significant controversies in understanding fatigue crack closure. Nevertheless, the crack-closure concept put crack-propagation theories on a firm foundation and allowed development of practical life-prediction methods for variable-amplitude and spectrum loading, as experienced by components and structures.

The mechanism of closure is manifold (Fig. 10). At first, it was considered to arise from the fact that during fatigue crack growth, the material is plastically strained at the crack tip, and due to the restraint of surrounding elastic material on this residual stretch, some closure of crack surfaces occurs at positive loads during the fatigue cycle. This concept, termed *plasticity-induced crack closure*, has proved to be extremely effective in explaining, at least qualitatively, many aspects of fatigue crack propagation behaviour including the influence of load ratio, the role of variable amplitude loading, and so forth. However, under plane strain conditions, closure could not be explained in this way. So another mechanism, based on the role of crack flank corrosion deposits and fracture surface roughness or morphology has been proposed. *Roughness-induced crack closure* is especially significant in the threshold regime and the K_{max} sensitivity model captures closure caused by plasticity or crack-tip stretching closure not detected by compliance measurements is more influential in the Paris regime.

Due to relatively small differences, it is experimentally difficult to confirm existence of closure and quantitatively correlate with observed fatigue behaviour. Some may argue over this, because true effects of closure are negligible, but another problem may lie with inherent difficulties in measurements.

However, the actual mechanism of crack growth threshold is not entirely due to crack closure, but also depends on the microstructure. Therefore on top of this mechanical threshold, there is also a microstructural threshold, where the small crack (ranging in size from less than one to few grain diameters) can be arrested due to interaction with grain boundaries.

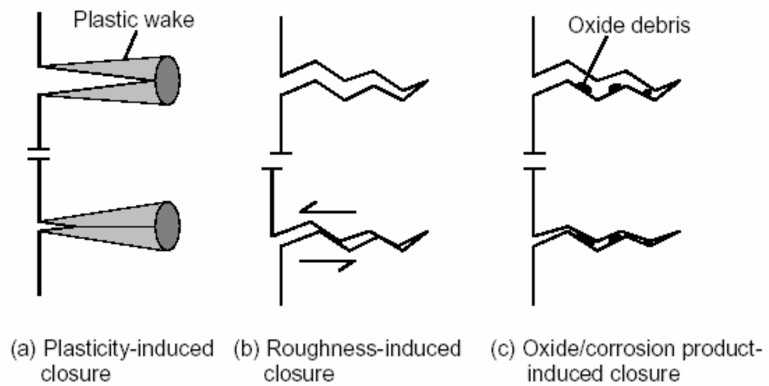

Figure 10. Various forms of fatigue crack closure mechanisms

Depending on the loading sequence, crack growth can be accelerated or decelerated, what is known as load interaction or load sequence effects. More specifically, crack growth deceleration is known as retardation. Two kinds of ideas persist in literature regarding causes of the load interaction effect: based on plasticity-induced crack closure, and based on the plastic zone ahead of the crack tip. In general, history effects can be rather pronounced in variable amplitude loading if the rate of stress intensity (*dK/da*) is low or the variable amplitude loading is not confined to single overloads. In the latter case, there are of course marked history effects, as long as the crack is propagating within the plastic zone stemming from the overload. Luckily, simple fatigue laws, not taking retardation effect into account, are usually conservative.

The fatigue crack growth threshold, defining crack growth rate as either very slow or nonexistent, has been commonly determined with standardized load reduction methods, where the maximum and minimum load applied to a cracked specimen are reduced so that the load ratio, *R*, remains constant. Experimental results suggest that this test procedure develops remote crack closure, i.e. crack face contact far behind the crack tip. Larger plastic strains are produced along the crack wake at high loads early in the test than at subsequent lower loads near threshold. This plastic wake, or history, can affect the crack driving mechanisms and generate artificially high threshold values when compared to steady-state data. This level of non-conservatism varies significantly from material to material and has generated a database of artificially high thresholds that do not accurately represent the material response of cracks growing under increasing *K*.

In the case of fatigue crack growth thresholds, where the threshold is traditionally considered as a safe value, where no crack growth occurs, accurate representation of the material behaviour and subsequent component fatigue life is crucial. Generally, for small magnitudes of ΔK the crack propagation is difficult to predict. It is very dependent on microstructure (grain size) and material flow properties, and the growth may experience arrest. However, it is rather difficult to predict in which manner, since finer grains will lead to a closer spacing of grain boundaries, through which the crack has to spread. To consider different effects at the place of simple Paris law, more complex generalized relationship of NASA/Flagro could be used:

$$\frac{da}{dN} = \frac{C(1-f)^n \Delta K^n \left(1 - \dfrac{\Delta K_{th}}{\Delta K}\right)^p}{(1-R)^n \left(1 - \dfrac{\Delta K}{(1-R)K_c}\right)^q} \tag{8}$$

where *C*, *n*, *p* and *q* are empirical constants, and *f* a crack opening function.

In summary, a number of limitations to the concept of ΔK_{eff} exist:

- The equations for determining K_{op} are mostly empirical and only reliable to a particular regime.
- Fatigue data cannot give a unanimous estimation of K_{eff}.
- In reality, K_{op} is not constant and changes continually depending on previous history.

As stated, the application of LEFM is presumed by the plastic zone at the crack tip, which must be surrounded in the elastic volume and therefore should be small (typically less than $a/50$). Only under these conditions the elastic stress intensity factor *K* is sufficiently accurate in describing the crack tip stress-strain state. In case of very small cracks (shorter than some cracks are considered mechanically short) this is not possible. They are long enough for continuum theory to be applicable (i.e. the surrounding material to be considered homogenous), but the cracks do not behave as long cracks. They typically grow faster than long cracks, which experience similar ΔK–levels, as the plastic zone is significant, compared to the crack size. Also, the crack closure load is higher for small cracks (especially for low ΔK), which leads to a higher ΔK_{eff}–value than for corresponding long cracks.

Crack growth analysis may reveal the point of its origin. A crack is visible damage, but only as the final stage of a less dramatic cumulative process, even though this process may be shortened in different ways. In case of fatigue, the beginning state of damage happens in most cases without reasonable or visual manifestation. Up to the time at which damage achieves the level to be discovered by NDI methods, a large portion of available lifetime could be spent. The corresponding period includes complex processes, not only of the crack initiation within the material microstructure, but also the transition period of main crack formation which, after incubation, could be treated as a main form of damage, responsible for further development leading to failure. The engineering concept of crack initiation, based on rational simplification of complex relationships, is necessary for analysis of crack growth residual life by using fracture mechanics. For this purpose the crack at initiation level must be geometrically well defined and, before being selected among others, should have propagated up to the size to be really predominant.

From current understanding of physical phenomena associated with crack nucleation and growth, the total life to failure of a component is considered to comprise four phases (see Fig. 11):

- Crack nucleation or crack incubation up to the development of significant discontinuity in the material microstructure. Such a discontinuity, however, may be present from the beginning in the form of a natural defect.
- A period of crack growth very much dependent on local microstructural and geometrical (i.e. notches) conditions of a component, for cracks of grain size order, also known as the short crack growth period. In this stage the crack growth is discontinuous and, for instance, can be stopped by some microstructural barrier.
- Macroscopic crack growth which can be described with the aid of continuum fracture mechanics methods (LEFM or EPFM), i.e. ignoring local microstructural events (Stage II). The crack growth is continuous and can be correlated to the relevant long crack behaviour and corresponding material characteristics.
- A final stage (Stage III) with large scale inelastic straining and collapse, where fracture mechanics methods could be only fairly applicable, or unstable crack growth of the component.

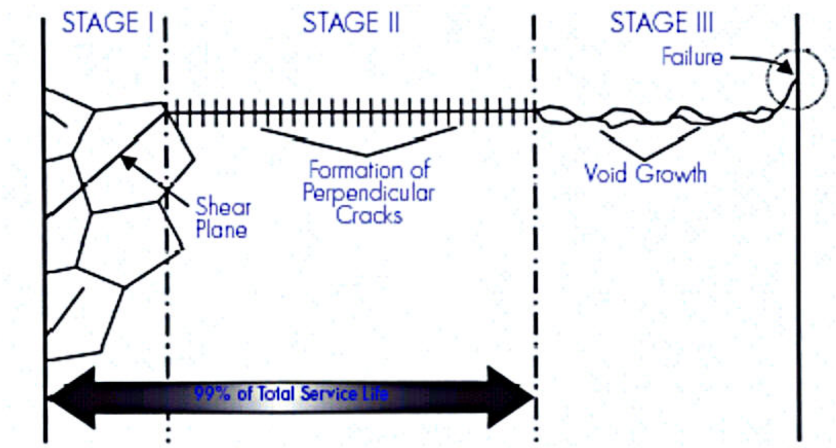

Figure 11. Stages of the Crack Propagation across a specimen

2. ENVIRONMENTAL EFFECT (CORROSION AND TEMPERATURE)

Stress corrosion cracking (SCC) caused by simultaneous action of tensile stress and corrosion is another slow crack growth mechanism which can be treated by LEFM, because applied stress intensity values are usually low in this cracking regime. If a susceptible material in service is placed in a corrosive environment under tension of sufficient magnitude, and the duration of service is sufficient to permit initiation and growth of cracks, failure will occur at lower stress than the material would normally be expected to withstand. Thus, one of the problems with SCC is that crack growth occurs at stress levels that are a small fraction of a given metal's normal tensile strength, and that rates increase very sharply with increase of K. Masked stress is more important than design stress, especially because stress corrosion is difficult to recognize and is a time-dependent process. Hence, if the combination of a likely defect size and the applied, or residual tensile stresses, causes the threshold for stress corrosion cracking (K_{ISCC}) to be exceeded, it is usually necessary to avoid the possibility of SCC. This is likely to require either a change in material, or surface protection.

Besides three basic ingredients of SCC process development, i.e. susceptible material, tensile stress, and corrosive environment, it is important to consider the following:

- in many applications producing SCC damage, slow strain rates are more essential than a stress level as they allow enough time for environmental action and disrupt formation of the protective interface (i.e. effectively act as a depassivating force),
- sources of strain rates can be steady, or cyclic applied loads, initial (residual) stresses, and the SCC damage process itself,
- commonly used metallic materials creep even at low temperatures and low stresses, and
- total creep may be negligible, but what is important from an SCC point of view are the associated slow strain rates over long periods.

In case of low temperature and low chemical concentration, SCC usually does not appear, even though the crack exists. On the other hand, the local corrosion pits are less dangerous than sharp cracks and may not produce crack initiation and growth.

The most important characteristic observed in SCC is the existence of a threshold stress-intensity K_{ISCC} for a given material in a given environment. Above this value, the controlling mechanical parameter in the sustained-stress crack growth is the stress-intensity factor K and the corresponding crack growth rate may be determined from the expression

$$\frac{da}{dt} = AK_{\max}^{q} \tag{9}$$

valid for conditions where $K_{\max}$ is a value between threshold stress intensity K_{ISCC} (below which there is no SCC crack growth) and fracture toughness K_{Ic}, for the specific environment. Combined effect of stress corrosion and cyclic stress can be approximated by linear sum of both effects (correcting the fatigue portion by cycle frequency):

$$\frac{da}{dt}_{total} = \frac{da}{dt}_{SCC} + f\,\frac{da}{dN}_{fatigue} \tag{10}$$

Thus, fatigue corrosion is a special case of stress corrosion caused by combined effects. Fracture of a metal part due to fatigue corrosion generally occurs at a stress far below the fatigue limit in laboratory air, even though the amount of corrosion is extremely small. For this reason, protection of all parts subject to alternating stress is particularly important wherever practical, even in environments that are only mildly corrosive.

The next important environment effect is based on temperature. Increase of temperature not only increases crack growth rate, but may also lead to new mechanisms of crack growth and damage development – creep. Under creep conditions, in case of uncracked material, damage growth is accompanied by incubation, growth, and coalescence of pores at grain boundaries within the material structure. They successively develop within the whole volume being exposed to the corresponding stress level, thus leading to development of a main crack.

Experimental results show that crack growth can be described by the relationship, which is based on the fracture mechanics parameter C^*:

$$\frac{da}{dt} = \beta C^{*\delta} \tag{11}$$

For materials with creep behaviour described by exponential laws,

$$\frac{d\varepsilon_c}{dt} = A\sigma_c^m \tag{12}$$

using *strain–strain rate* analogy with *J*–integral, this parameter can be estimated, based on the fully plastic solution, using the function h_1 (evaluated for different geometries [7]):

$$C^* = \alpha\varepsilon_o\sigma_o c h_1\left(\frac{a}{W}, n\right)\left(\frac{\sigma}{\sigma_o}\right)^{n+1} \tag{13}$$

which after substituting

$$\frac{\alpha\varepsilon_o}{\sigma_o} = A \;\rightarrow\; \text{or} \;\; \frac{\varepsilon}{\varepsilon_o} = \alpha\left(\frac{\sigma}{\sigma_o}\right)^n$$

has the following form

$$C^* = A c h_1\left(\frac{a}{W}, m\right)(\sigma_c)^{n+1} \tag{14}$$

The usual classification of damage development stages, based on crack initiation and growth, relative to the fatigue experience, here is further complicated by introducing creep mechanisms and their interaction with the fatigue processes. Creep deformation involves void nucleation and growth in the bulk of the material ahead of the crack tip. This combination of local crack growth and creep damage development throughout the material volume makes the separation and corresponding treatment of crack initiation and growth for purposes of creep-fatigue life assessment extremely difficult. Additionally, creep and environmentally induced internal damage in the region ahead of a crack tip, accelerate crack growth under cyclic effect. Because of this, in the high temperature range, the local event approach in service life analysis, i.e. crack initiation, has to be extended to a more general approach, based on *damage incubation* and considering both interacting processes of local crack development and early growth, as well as bulk damage. In most simple cases, assuming the existence of the main crack, the total crack growth per cycle can be assessed based on the superposition of both effects:

$$\frac{da}{dN} = \frac{da}{dn}_{fatigue} + \frac{1}{f}\frac{da}{dt}_{creep} \tag{15}$$

Finally, this short review concerning crack growth does not incorporate all of the possible effects. Under related conditions, additional considerations can be important and necessary, as mixed-mode loading, the influence of residual stresses, interaction between multiple cracks, variable amplitude loading, short crack behaviour and its interaction with the microstructure, stochastic aspects of fatigue crack initiation and early growth, and many others.

3. ASPECTS ON SYSTEM LEVEL

3.1. Data transfer, specimen and component relationships

Previously treated complex relationships concerning residual strength and lifetime evaluation strongly affect and have to be solved for practical purposes within the transferability. The term transferability here refers to the capability of reliable use of measurements and properties taken from simple test specimens, used for material characterization, for the prediction of large-scale structural components, i.e. covering the difference in geometry and loading conditions of laboratory specimens and large structures. The corresponding demonstration, especially concerning part-through surface crack behaviour, largely lacks in theory. It is obvious, based on previous discussions, that with respect to this the restrictions exist and must be considered. Transferability of results therefore is not an absolute characteristic but an approximation, which may be improved by systematic treatment of the problem.

Our investigation shows that the specimen with a surface crack gives most relevant loading conditions, in contrast to those experienced in real, especially pressurized structures. Since results of numerical and experimental verification tests are in full agreement with component-like test results, the transferability of results of the specimen with surface cracks to large structures were fully justified.

3.2. Importance of experimental verification

It is obvious that practical application of fracture mechanics parameters and concepts in structural integrity evaluation is connected to many uncertainties. Because of this, the achieved results are nearly always required to be proved and verified by experiments. The most useful direct method for verifying the design and life evaluation procedure is testing real components under real service conditions. Unfortunately, reasons not only of economic nature very often reject those possibilities. Although different tests are performed, it is unpractical to carry out long experiments to cover the service lifetime of components, which is usually over 20 or 30 years. Furthermore, unavoidable deviation, that must be tolerated, constrains direct transfer of achieved results to real conditions. Because of this, usually the experimental results should be numerically transferred or even extrapolated (by shorter tests) to the real conditions. To eliminate possible errors concerning test and analysis results it is very important to combine experimental and numerical methods so that these maximally support each other. Proper selection, concept, and adequate evaluation of test results are not possible without corresponding numerical analysis. Their main goals in this respect are:

- to accurately predict the behaviour of the structure in service conditions, as a presupposition of proper design, and in this way to reduce the necessity of expensive and time consuming additional tests, and
- to increase the total output of these tests by analysis and interpretation of test results.

Accelerated tests are performed by intensifying, in controlled conditions, one of the environmental parameters that cause actual aging or degradation mechanisms (e.g. fatigue, creep, cracking, wear, corrosion/oxidation, weathering). The results of accelerated test are only valid when the failure mechanism is identical to the one that occurs in the normal service environment. While intensifying a parameter may accelerate failure, the results have no applicability to actual service if they do not represent real conditions.

Accelerated testing consists of test methods that deliberately shorten (as measured) the life of the tested product or accelerate the degradation of the product performance. Based on this we can distinguish between two main types: *accelerated life test*, and *accelerated degradation test*. Accelerated degradation tests are in advantage compared to accelerated life tests in analysing performance before the material or the component fails and in determining residual life, with the knowledge enabling life extension. Extrapolating performance degradation for estimating when the failure level is reached is enabled by analysing degradation data. Such analysis is correct only if a good model for extrapolation of performance degradation, and a suitable performance failure, is established. A typical example of the accelerated degradation test is spinning of the disk withdrawn from service engines (leading-fleet engine). Based on residual life in the test, life extension of disks beyond their initial service life is performed. Another variant of accelerated degradation testing is damaging the product in a controllable way, i.e. by introducing artificial defects for the purposes of testing corresponding behaviour, or verification of inspection intervals. In many cases artificially introduced defects are provided by adequate components manufactured already with a defect. This kind of tests must not be carried out up to failure or to end-of-life if accurate measurements of crack extension are performed and methods exist for extrapolating further results.

The method of accelerated testing will depend on the material being examined, and on the environment and type of damage mechanism. In case of fatigue, the test parameters are stress or strain, frequency, and temperature. Use of increased cyclic loading frequency is perhaps the most suitable method for accelerated testing. In case of metallic materials, frequency independence is confined to elastic stress-controlled, high cycle fatigue, only. Generally, a 20% increase in loading level reduces the life cycle up to failure in fatigue testing for a third. For strain-controlled or low cycle fatigue tests, it is possible to increase strain range and accelerate failure. Again, this is valid as long as the failure mechanism is unchanged. It is worth pointing out that certain predictive models (such as the Coffin-Manson) may not be applicable for high strength materials. Also, materials other than metallic (ceramic) may not be tested by this method, as they are generally not strain-controlled.

Conditions become particularly complex if damage is dependent, not only from the number of cycles, but also from time under load. The simplest case in this respect is the monotonic loading where the damage is produced through creep effects (temperature). In this regime the parametric method is developed for purposes of interpolation and extrapolation of experimental results, based on the well-known Larson-Miller equation,

$$T(C + \ln t_r) = \frac{Q_c}{R} = F(\sigma) \tag{16}$$

Based on the relationships above, both creep deformation and creep damage behaviour can be, from an engineering point of view, adequately represented as a single two-dimensional $F(\sigma)$ master curve function of Time-Temperature parameter, as shown in Fig. 12, thus simplifying the analysis and the extrapolation of experimental data.

However, a more complex case is the combination of fatigue under high temperature conditions with time effect, leading to creep and oxidation. Reliable design of structures at highest temperatures is very difficult, because it is very different compared to room temperature application. Creep includes incubation and growth of pores in the bulk of materials (Fig. 13). Because of this, the combination of local crack growth from fatigue and damage development through creep (pores) in the whole volume makes the separation and corresponding treatment between crack initiation and crack growth for purposes of life assessment very difficult. Under conditions of load-temperature-time combination, temperature becomes the most important parameter that influences strain and damage development, both from fatigue and creep. To understand this, important investigations within of the BRITE Project have been conducted on typical alloy 800H materials at extremely high temperatures (850°C). Although austenitic steels, like the alloy used, exhibit excellent bulk oxidation resistance, grain boundary carbide precipitation takes place at this temperature. The precipitation phase is particularly sensitive to environmental degradation, so that oxygen diffusion along the grain boundary is much faster. Due to grain boundary oxidation, which penetrates deeper than surface oxidation, accelerated fatigue crack nucleation (or damage incubation) appears, and significant shortening is found in the lifetime of the cyclic dwell tests. The effect of the embrittled surface region and the rate of oxidation penetrating along grain boundaries (leading to accelerated crack initiation) have been considered for the correction (α) of the Strain Range Partitioning method:

$$\frac{1}{N_i} = \frac{f_{pp}}{N_{pp}}\alpha + \frac{f_{cp}}{N_{cp}} \tag{17}$$

using the Arrhenius type relationship with temperature dependence considered through typical activation energy constant Q:

$$\alpha = At^n e^{-\frac{Q}{RT}} \tag{18}$$

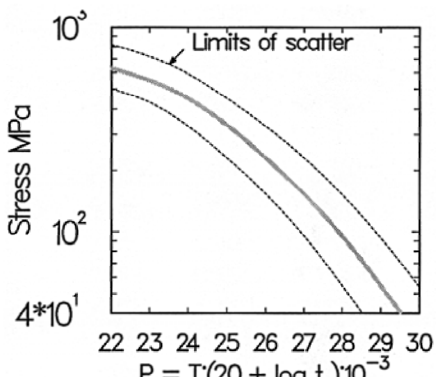

Figure 12. Results of creep test on IN738C

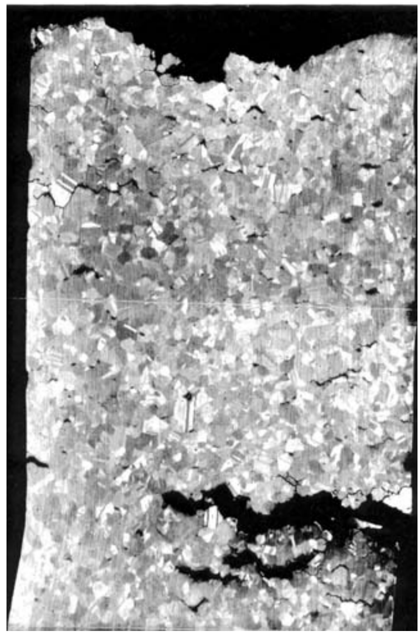

Figure 13. Damage development due to creep in balk of the specimen

By introducing the above time dependent correction in the Strain Range Partitioning equation, excellent results have been achieved in life prediction of cyclic dwell history tests in the relevant temperature range 750° to 850°C, for the given alloy. Additional evidence about the accuracy of the developed method has been accounted for by investigation, prediction, and comparison of available literature data for the alloy 800 H. The method produces very accurate results for all data included in the analysis, covering a number of different material lots, treatments, and testing conditions.

For practical application of the method, based on general time-temperature dependence as in Eqs. (17) and (18), the diagram in Fig. 14 has been developed, that shows the temperature and time dependence under creep-fatigue-oxidation conditions. The curves in the diagram for different α are nearly linear and parallel to each other. Assuming that the distance between is also the function of α, all curves may be represented by the general time-temperature function (or line) in the form

$$AT + \log t_r = F(\varepsilon_{\mathrm{IN}}, \alpha) \tag{19}$$

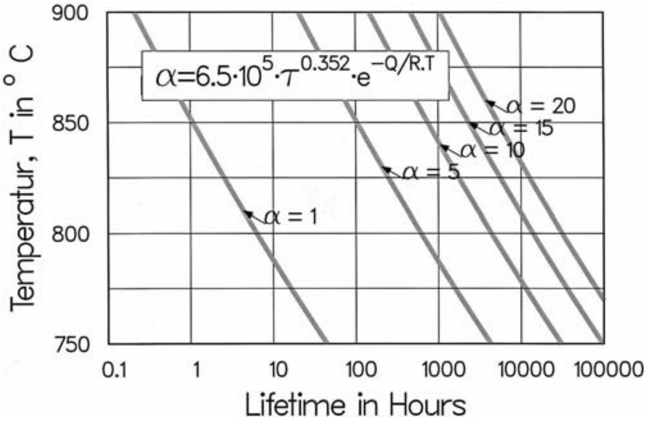

Figure 14. Time dependence for the creep-fatigue-oxidation interaction for IN 800H

This shows the possibility of reducing required total test time if the test temperature is increased compared to actual cases. According to the slope in Fig. 14, assuming equal inelastic strain range, the increase in test temperature for 60°C allows reduction in the necessary test duration from 10 000 hours to only 1000 hours, retaining the same oxidation damage effects. For testing purposes, the number of cycles may be adjusted to be unchanged, and the dwell time should be reduced according to the determined time reduction factor. Note that from different ways to accelerate the test performance, the increase in test temperature is less risky than an increase in load level or reduction of dwell time up to saturated relaxation. In the two latter cases the relevant mechanism of damage can be influenced or even rejected, where in case of increased temperature, this is a more seldom case and may be controlled, for example, in the range of validity of the activation energy parameter Q and exponent n. Therefore, in the combined load-temperature-time environment, the temperature becomes a major parameter accelerating damage development and may be very efficiently used to control or shorten the tests. Accordingly, the time-temperature substitution approach, as proposed based on the above results, can help to reduce the amount of experimental effort needed in the design of new components for operation in a high temperature environment and under creep-fatigue conditions, as well as to support their optimization and efficient redesign.

While the above relationships were developed and tested on only one austenitic steel, the behaviour of other high temperature materials is similar. For example, it has been observed in practice with steam headers that the oxidation potential of steam leads to forming of an oxidation layer, under steady state operating conditions. During this time the oxide grows with decreasing rate in time, i.e. with the increase of oxide thickness.

The change caused by decreasing of the bowl loading are accompanied with relatively rapid steam temperature reduction at the outlet, and this leads to the tensile stresses at the internal side of the header walls and nozzles. Tensile stresses are sufficient to break relatively brittle oxide layers. When the oxide layer is broken, metal is again subjected to steam and this allows accelerated oxidation all over again. This process is repeated in time and the header is subjected to oxidation mostly at the oxide layer with the longest crack, leading to formation of crack in ground materials and fatigue initiation.

3.3. Defect quantitative assessment

An important issue influencing integrity assessment is the accuracy and reliability of inspection techniques and procedures used to acquire flaw data. Although NDI is not in the scope of this paper, it must be pointed out due to great importance concerning structural integrity. Among typical fracture mechanics procedures, defect assessment is an integral part of any method. Defect quantitative technology is the basis for *safety estimation and management* of all components. Only with accurate quantities can we accurately evaluate the safety of structures with defects and make reasonable structural evaluation, whether it is safe for use, maintenance, or to be rejected. The size (length and depth), the location (surface, subclad, embedded), orientation (relationship of major and minor axes to loading) and frequency distribution will affect propensity towards initiation in an inspected event. Development of *intelligent NDT* technology, capable of quantitatively defining inspection results for purposes of further fracture mechanics analysis and decisions, has made possible to establish safety evaluation methods for components with defects.

Fabrication is seldom perfect, and thus good inspection is also required for failure avoidance. Components need to be designed so that they can be inspected, and an established inspection procedure accomplishes this to an adequate degree. However, quality cannot be inspected in an attempt to turn an inferior product into a superior one by upgrading it through inspection.

3.4. The impact of parameter accuracy and probabilistic consideration

Efforts on structural integrity must primarily be focused on first order parameters: the initial flaw assumption, load interaction models, crack growth rate data, and stress intensity factor (applied stress, boundary correction factor). The secondary parameters have less effect to accuracy of safe or residual life evaluation as, for example, yield stress, fracture toughness, and threshold stress intensity factor. Depending on the situation, the threshold values could also be very important.

As already stated, deterministic fracture analysis practice uses relatively large safety or scatter factors to account for many uncertainties or errors, such as: analytic model inconvenience, inaccuracy of stress intensity predictions, and the scatter of experimental crack growth data. Stochastic analysis methods extend the accepted deterministic methods by allowing (or forcing) the analyst to explicitly account for these uncertainties by treating them as random variables (or processes or fields), requiring to consider the parameters' likely range and distribution. However, both deterministic and stochastic analysis will suffer from, e.g. the same shortcomings of model inadequacy. The stochastic model has the advantage of addressing uncertainties, specifically using probability and statistical theory. Use of a stochastic approach and a reliability based design criteria can be beneficial in avoiding over- or under-conservatism that may result from the use of a deterministic safety factor approach.

4. PRACTICAL APPLICATION OF FRACTURE MECHANICS

4.1. Fracture–critical parts evaluation

Fracture control by damage-tolerance design has been firstly implemented in the development of commercial and military aircraft structures. According to the fracture control procedure, all parts have to be classified as fracture-critical or non-fracture-critical components. A *Fracture Critical Part* is defined as a part or assembly whose failure due to cracking could result in loss of life or loss of the structure. Unfortunately, the analyst in practice will never have all the necessary information and, in this respect, some compromise must always be made. Problem overcoming in this respect could be accomplished by a systematic procedure, which means approaching the solution in iterative steps leading to more and deeper access to the nature of the problem. Achieved positive level of information leading to solutions is valued in each iteration, as also the negative level, which exhibits additional data necessary to improve results or to make accurate selection among alternatives. Under ideal circumstances this may lead to the optimal solution – in the practical case to the best compromise or problem solved by an estimate, based on a combination of theoretical and empirical answers, and engineering judgment. These kinds of solutions are unavoidable and truly necessary in practice.

4.2. Strategies for structural integrity assurance

In demonstrating a possible practical solution it is necessary to recall the history of the F111 failure. The F111 aircraft were put in reserve due to early failures, and by looking at the solution of the problem, the experts used fracture mechanics (already available at the time). However, the F111 was designed and built – in effect, it was too late for the new design approach. There was also another problem: most of the primary structural steel members of concern were located in areas of limited accessibility, and the available NDI techniques could never reliably detect all flaws. What was needed was a global test or method, able to completely inspect all complex structures. There was only one viable option to fulfil these requirements – a low temperature cold proof test. The cold proof test enables evaluation of current structural integrity of the airframe in a global fashion, while permitting prediction of a period of safe life operation before another inspection or cold proof test is required. Clearly, proof loading does not change safety factor values and the overall probability of failure, but it changes the corresponding probability of failure in service (as failed components during proof tests do not enter service).

It is usual today for all pressure containing components to carry out the corresponding test under pressure at the start of service, to demonstrate structural integrity for operating conditions. The practice of *proof testing* prior to operational usage is a good design practice. The rationale behind this belief is that successful proof test provides increased assurance of component survival at a lower stress during operation and structural integrity is improved, because by proof test, critical components are removed from the in-service population with saved reliability of the surviving components. However, formal use of this test is not sufficient, in spite of all advantages, quantitative information concerning key parameters is not available, as for example: existence and size of cracks and defects, the total lifetime of safe use without risk of failure, necessary overload level and risk of failure during the test. The full benefit of this test, which is not only limited to the component loaded by pressure, can be only realized by applying fracture mechanics, since after successful testing, the safe condition during some period of use in future could be precisely specified and the preparation and execution of the test optimized. The principle of fracture mechanics procedure allowing effective proof testing is illustrated in Fig. 15.

The purpose of proof tests is to load the entire aircraft structure (or its components) to certain levels to check structural integrity and establish initial fictitious crack sizes associated with critical structural components for fatigue life analysis. For full performance, the proof load levels are usually slightly lower than the design limit load. If a previously undetected crack exists in a certain structural component that is larger than the critical crack size for proof load, that component will certainly fail during proof load tests. Thus, a catastrophic accident during service can be avoided. If the entire structure survives the proof load tests, then the critical stress of structural components has been subjected to a proof load tensile stress σ_o induced by the proof load P_o. If K_{Ic} denotes material fracture toughness, the maximum crack length a_o a structural component can carry under the proof load without failure, may be calculated using σ_∞^P. In reality, there may not be any cracks during proof tests; however, it is assumed that a fictitious crack of length a_o has been there at critical stress of structural components during proof load tests. In fact, a_o is the initial fictitious maximum defect size that could just survive the proof test overload, P_o without failure, calculated using fracture mechanics. For a_o evaluation it is necessary to take the upper value of fracture toughness, which gives conservative (lower) residual life evaluation. If σ_S is defined as the peak operational stress level (highest peak of stress cycles, but significantly lower than proof test load), the structural component can carry a crack of size a_S, which is much larger than a_o. It is the operational limit crack size toward which the initial crack a_o is allowed to grow after repeated operations. The difference $\Delta a = a_S - a_o$ is then the permitted increase in crack size for structural components in repeated operation. The remaining life is determined by subcritical crack growth in service, due to expected mechanisms (fatigue, environmental attack, and creep), up to a maximal tolerable size a_S,

$$N = \frac{\Delta a}{\sum \frac{da}{dn}} = \int_{a_o}^{a_S} \frac{dn}{da} \tag{20}$$

By adjusting the value P_o, hopefully one arrives at the value of a_o, which in combination with

$$\text{Test Factor } = \frac{P_o}{P_S} \tag{21}$$

guarantees that the required remaining life can be realized without incurring an unacceptable risk of failure during proof. This test is not very useful if probability of failure is high. In general, the evaluation of a_o is simpler than a_S, because conditions for the proof test are controlled and very well known, and also less complex than service conditions.

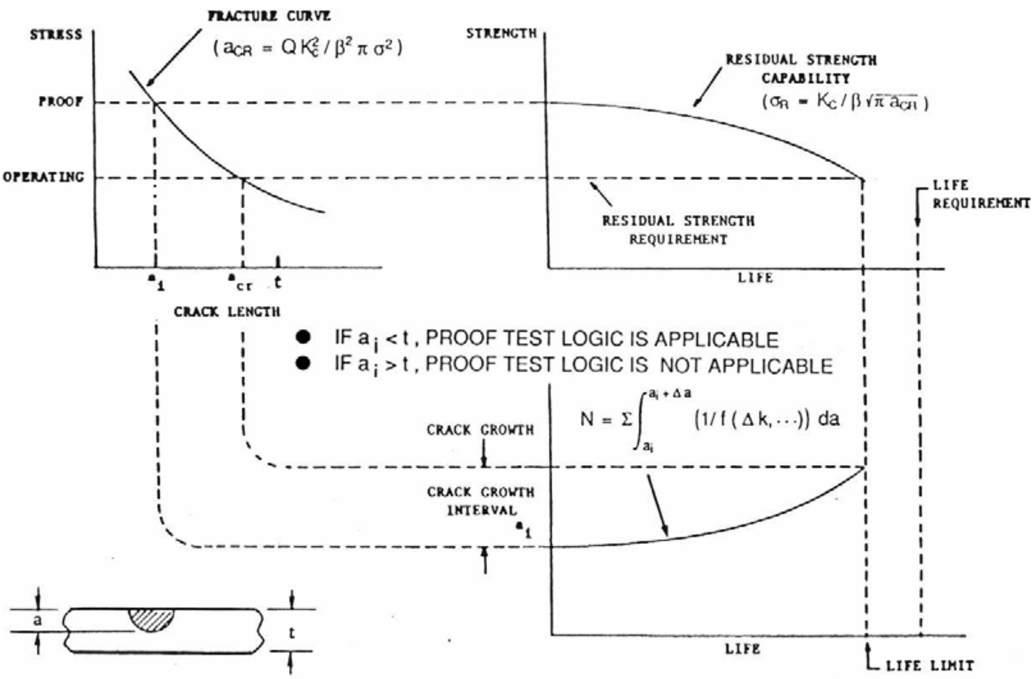

Figure 15. Proof test logic based on fracture mechanics

In the proof test, failure does not necessarily imply a catastrophic event, but refers to any indication that the component is not fit for service. For example, leakage between compartments in aerospace propulsion systems during operation could result in release of volatile liquids with catastrophic results. In this case, component wall penetration by a defect during proof loading would be classified as a failure, even if the flaw through wall remained stable during the test.

An important aspect of applying the proof test method is recognition that the defect of size a_o (a postulated defect whose size is calculated using a worst case scenario) may not actually exist in the component. Despite of this, a_o must not be a real crack; its application does not mean shortening of available life. With this approach only a certain period of service without risk is guaranteed, and with further life extension, after successful repeated proof testing in verifying the next applicability of the part, life extension is possible. Moreover, in this way the full real life capacity (above minimal design life), as a result of lifetime randomness, could be used. This means at the same time, the worst-case scenario is valid, only for purposes of first iteration of available life, only up to the next inspection and proof testing, when new life evaluation is carried out in the same way.

Based on the review of proof testing, different benefits arising from this testing may be given, as: increased structural reliability, manufacture and quality assurance, enhancement of NDI application, defect sizing and flaw screening in situations where NDI is not useable, residual stress reduction and verification of stress analysis. Benefit of proof testing is especially significant for quantitative flaw detection. With it, the introduction of a part in exploitation is possible with high probability that there are no cracks larger than the one evaluated by fracture mechanics. In addition, relative benefit is the reduced danger of the real crack or flaw, due to crack blunting under proof test overloading. Finally, the proof test enables stress measurement during the test for its quantification. This is very important, as an accurate prediction of stresses under service conditions is necessary for evaluation of fracture mechanics parameters and as a demonstration of structural reliability. Concerning this, the most important subject of proof test design, in addition to failure prevention due to excessive loading, is to avoid unnecessary component damage. Damage during testing can appear due to many reasons. For example, if the test is performed in conditions where material toughness is lower than in service conditions, cracks could be created (from overloading), which cannot originate under normal conditions. Frequent test failures are possible if the size a_o is small compared to typical defects introduced during manufacture. Therefore, although more severe conditions and the proof test number could lead to in-service reliability improvements for structures surviving this test, this can also have disadvantage of unnecessary increase in a number of test failures due to cracks which are smaller than a crack that could grow to critical size, capable of service failure. Here an optimum is necessary.

The design of proof testing is a serious task, which is only possible and based on detail design investigation, and on stressing and working conditions. In situations where more complex structures, as pressure vessel, are usually investigated by more complex methods (finite elements) in case of pipes, the approximate methods are often used, [11].

Under in-service conditions (loading, temperature, environment), a surface crack in a vessel can grow and this may lead to gradual wall penetration or bursting of the vessel. In case of wall penetration the internal medium is released, leading to pressure reduction and could be timely observed by inspection. Based on this, the fracture mechanics concept *Leak-Before-Break* (LBB) is developed, meaning that pressurized component failure will be signalled by a detectable leak and may be fully controlled. If the necessary presuppositions based on this criterion are fulfilled, the crack extension from any defect in components should always lead to through-wall cracking and leakage before component rupture can develop and could be discovered by inspection before the initiated through-crack gains size, which may initiate instable fracture.

In practical application, characterized by leakage preceding failure, the LBB must always have sufficient safety reserve in time between these two occurrences for remedial actions of leakage discovering, component unloading, and necessary repair, that has to be carried out with safety. If this is fulfilled, LBB can be used as a method to preclude bursting or rupture of the equipment. Consequently, the corresponding concept has important safety aspect relevance.

Component behaviour and relevant relationships can be presented in a simplified way in the so-called leak-before-break diagram (Fig. 16). Axes in the diagram are: relative crack depth a/t and critical surface crack half-length c/c_c. Line AB defines the place of crack growth initiation of a surface crack. The second vertical line with $c/c_c = 1$ separates the range of the through-wall crack below and above critical crack length and in this way, the area of safety. It can be seen, however, that part-through cracks of length higher than c_c may also be stable if their position is below the ligament failure line. But if these cracks grow further (Fig. 16, curve 1) due to fatigue or sustained crack growth, it will produce fracture, and the application of leak-before-break concept is not possible. In the second example (curve 2 in Fig. 16, arrow), the ligament line is first achieved and stable leakage may appear if the crack grows along the surface up to the size where crack opening is sufficient for leakage to be discovered before critical crack size is achieved. If the crack growth path position is very near to $c = c_c$ and its shape curved in the same direction (arrow 3), the conditions of catastrophic fracture may also be possible.

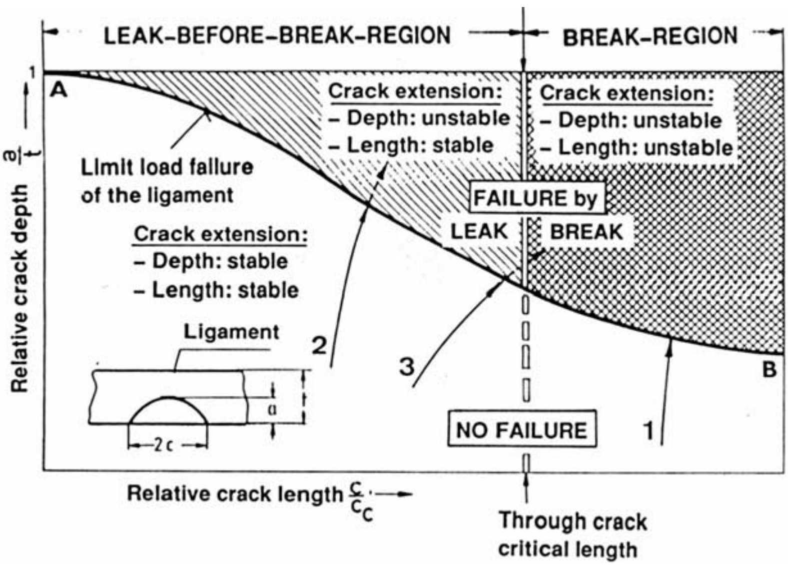

Figure 16. Scheme of the Leak-Before-Break procedure

It is clear that in case of leakage the fracture failure can be prevented only if pressure is reduced by leakage or if leakage is timely detected and the necessary action performed before unstable crack growth can develop. If there is anything that retards the leakage or its discovering, than LBB protection may partially or totally be missing. Generally, the leak-before-break criterion is not sufficient to guarantee fail-safe response of the structure for all possible conditions. Therefore, careful fracture mechanics analysis of the structure has to be performed and the results considered within the quality control programme.

Leakage and crack detection in tubing is often very complicated due to the large number of pipes and elbows that are additionally loaded by moments. In case of vessel loading, it is easier to define, and crack detection is simpler. In spite of this, LBB method is successfully applied in many cases. This is stimulated by realization of technical and economical advantages. For *leakage area* evaluation, all local loads and corresponding conditions have to be considered, which in case of high temperature also include creep. Crack opening under load can be estimated based on data [3] for the plate with a central crack. Pressure vessels with non-hazardous LBB failure mode may be also demonstrated by test, showing that an initial flaw of any flaw shape range of $0.05 < a/2c < 0.5$ will propagate through the thickness of the pressure vessel before becoming critical. The test may be conducted on samples that simulate the material (parent material, weld metal and heat-affected-zone – HAZ), and thickness of the pressure vessel, or on a pressure vessel representative of the hardware. Test specimens shall be pre-cracked and cycled through the design spectrum to demonstrate stable crack growth completely through wall thickness. A sufficient number of tests are to be conducted to establish that all areas (thickness) and stress fields will exhibit a leak-before-burst mode of failure.

Unit availability and effective utilization of inspection funds are two of the most important concerns within equipment life management. Operators are continually faced with decisions regarding component replacement and/or repair. For this purpose *fitness-for-service* assessment is a multidisciplinary engineering analysis of the structure to determine if it is fit for continued service until the end of a desired period of operation, such as until the next turnaround or planned shutdown. Fitness-for-purpose is the shorthand name for a concept which has emerged almost spontaneously in more than one country in response to the proliferation in recent years of powerful new methods of quality assessment, which are created through the efforts of scientists and engineers to provide a more certain prediction scenario. Main results of fitness-for-service assessment are decisions to run, alter, repair, or monitor the equipment, and guidance on inspection intervals. Different codes are developed for application of fitness-for-purposes. API 579 and BS 7910 are two mostly used procedures which are also regulator accepted. Worldwide survey of pressure system users shows that 53% use fitness-for-purpose assessments for purposes of determining residual life of damaged plant and ensuring safe operation beyond design life, and in some cases extending the inspection intervals. Assessed equipment are pressure vessels, process piping, shell and tube heat exchangers, boilers, and general structures, pumps, turbines, compressors. Application of these codes is very helpful to solve practical problems and they are important components in the fitness-for-purpose listing.

4.3. Remaining life assessment

Many safety-critical components in power plants are made of steels developed to resist deformation in the range 480–565°C with design stresses limited to 15–90 MPa to assure required life for given geometry, loading and material properties. Large scatter and different uncertainties are typical for all these parameters. Mechanical and thermal condition in service may not be completely defined and so-called nominal conditions are usually based on maximal loading during prescribed operating conditions, which are not applied during all the time. On the other hand, damages appearing as a result of frequent change of service conditions and in shutdowns are usually ignored. Material properties are considered, based on allowable levels, which are chosen, i.e. according to ASME code based on 80% of the lowest values of creep rupture strength for 100 000 hours (Fig. 17). This safety margin against the minimal properties of the distribution is necessary, as the long-time values are usually based on linear extrapolation of experimental short-time data. The experience with old power plants showed however, that the deterministic life evaluation, applying the worst case assumption, pile-up conservative assumptions leading to the pessimistic assessment, different to the actual situation and shortening the life time.

Typical creep results (Fig. 17) show that between allowable, minimal and mean values, significant life capacity exists compared to the design life, which is reached first. Although a large amount of reserve exists, in the particular case there are no quantitative data, and starting from the worst case assumption it will not be possible to use these capacities. Obviously, the solution of this problem, without negative effects on general safety and reliability of the equipment, is only possible using special methods to measure actual life consumption and remaining life capacity of parts in service and ruling out the corresponding random effect in this respect. Accordingly, from the design life calculation point of view, here is not a matter of correcting the errors in calculation and all strives of "improvement" in this respect will not be successful. However, the modern method of life design certainly considers the corresponding experiences with the introduction of life monitoring and equipment inspection, contributing in this way to the overall efficiency and reliability of equipment. Programmes for monitoring and life extension are now usual in power plants. The goal of these programmes is the increase of availability, efficiency and reliability of existing power plants by reassessing their structural integrity and the guarantee of safe and economical usage.

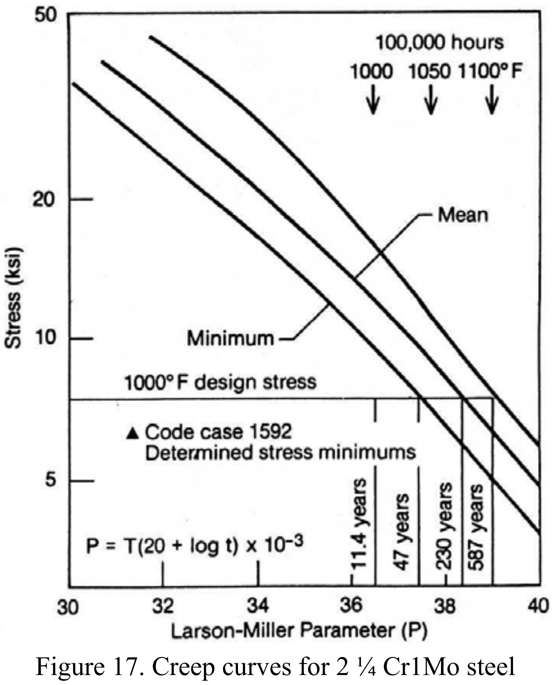

Figure 17. Creep curves for 2 ¼ Cr1Mo steel

For components with dominating creep life, the monitoring programme is relatively simple. Before the late 1980's, the traditional way to evaluate the condition of plant tubing was to remove tube samples and examine them in the laboratory for build-up of internal oxide, wall thinning, hardness and chemistry analysis. Hardness tests provided some guidance to (creep) strength of the material and the internal oxide scale provided an estimate of the operating temperature. The major drawback to this approach was that only a small number of tubes were sampled and it took time to get the information back to the maintenance personnel. Today, it is generally known that damage development under creep conditions is based on the behaviour of pores on grain boundaries. Based on systematic investigations, the correlation between creep damage development and life extension is found. Because the part of life linked to macro crack existence (tertial creep) takes only 20% of total life (Fig. 18), it is clear that the assessment based on pore estimation is relatively safe against unexpected rupture and failures.

The corresponding evaluation is based on the use of replicas. Metallographic replica technique is the NDI method applied to achieve metallographic material data for creep damage at the investigated location. A replica is in common sense a volume surface image and can be used to discover cracks, creep cavitations, porosity, inclusions, and other similar defects. The great advantage of the replica technique is that efficient preparation and collection of copies can be made on-site by skilled personnel and the evaluation can be done in the laboratory on powerful microscopes by qualified personnel.

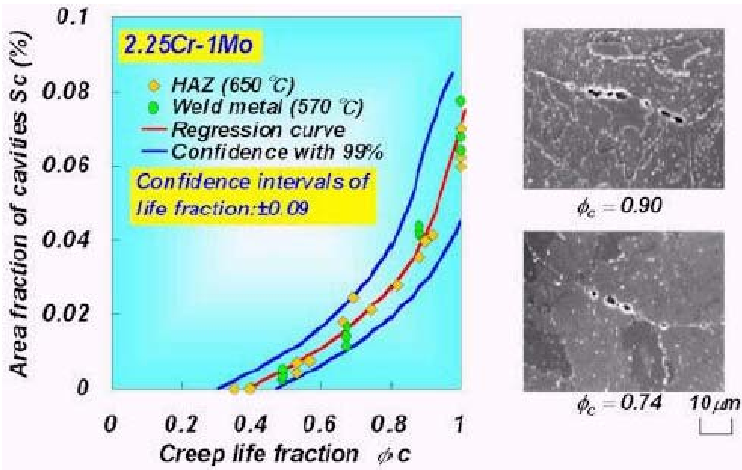

Figure 18. Relation between area fraction of cavities and life fraction

The creep damage measured by replicas is firstly classified according to Wedel-Neubauer [11], in 4 classes (Fig. 19), correlated to a schematic creep curve (Table 2). Recommendations have been produced for performing and evaluating replica inspection results, [2]. For example, the time for first in-service replica inspections is given as material dependent (Table 1), as well as the proposed maximum time to the next inspection. These recommendations apply in particular to the case where no earlier inspection data are available from exactly the same location, and where only parallel experience can be used as a guideline. This initial classification is extended (mean classes B and C) to allow more precise evaluation (RWTÜV, Nordtest). However, serious system error appears if the residual life time procedure, which is based on creep dominance, is applied for the condition of other kind of damage, for example fatigue.

Table 1. Recommendations for different materials

Material type	14 MoV 6.3	13 CrMo44	10 CrMo9 10	X20 CrMoV 12 1
Recommended maximum time in service (h) for first replica inspections. Welds and bends, service temperature ≤ 500°C	50 000	1 000 000	1 000 000	120 000

Table 2. Wedel-Neubauer classification

Damage class	Description	Approximate minimal life	Recommended action
	No pores are seen, but only spheroidized carbides are observed		Inspection recommended after six years
A	Microvoids isolated on grain boundaries	0.27	Monitor further development. Next inspection after three years.
B	Microvoids are distributed so that an alignment of damage boundaries (pore chains) normal to the maximum stress can be seen	0.46	Monitor. Inspection is needed after two years or less.
C	Coalescence of cavities causes separation of some grain boundaries (boundary microcracks)	0.65	Limited service until repair or replacement by a new component within six months.
D	Cracks many boundaries long	0.84	Immediate repair or retirement.

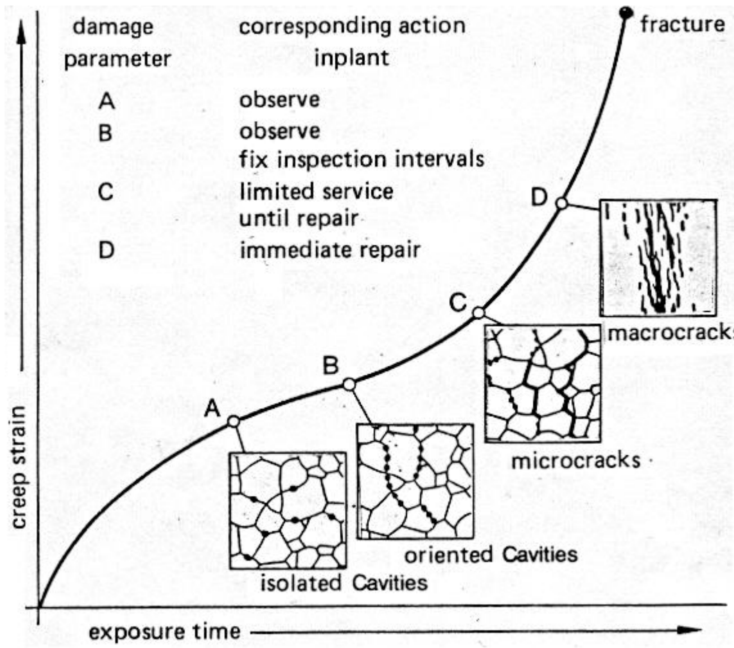

Figure 19. Creep damage classes as seen from the replicas

4.4. Treatment of welded structures

The problem of welded structures is so complex that it cannot be treated here in sufficient detail. However, due to vital importance for structural integrity, some very general remarks have to be made. Weldments are of major concern, especially for power plants, where nearly no parts are produced without welding. Considering the high loading and usual geometrical discontinuities of these joints, it is not surprising that welded joints are a frequent place of failure in structures. In fact, welded structures have special characteristics, some of which tend to make them more susceptible to cracking, and thus to more catastrophic fractures. For example, they are metallurgical composites with three typical areas in a continuous chain with different strength and toughness: parent material, weld metal, and heat-affected-zone (HAZ). Considering the transitions between parent and weld metal and the corresponding successive changes in properties and grain structure within the heat affected zone, further division can also be made. Yet another consideration is the fact that the composite welded structure is interconnected and discontinuities from one part of the structure can propagate by a number of mechanisms into other parts of the structure without interrupting interfaces. Generally, weldment behaviour regarding defects depends on difference in strength and toughness parameters between parent (base) and weld metal (matching effect). Crack behaviour regarding initiation, growth, and especially the capacity to arrest the growing crack, is of great importance for practical applications.

Welded engineering structures are normally designed for performance within the elastic stress range of the parent metal. Concerning the deformation behaviour, the yield strength mismatch does not affect deformation behaviour in the elastic loading range, i.e., as long as the applied stress is smaller than the lowest yield strength (parent or weld metal). Of course, the use of design stress, which is some fraction of yield strength, does not automatically mean that nowhere in the structure the design stress exceeds this level. As soon as yielding occurs in the weld or parent metal, yield strength mismatch is to be considered. From the design point of view, it is rational to require that a defected weld sustains applied nominal stresses of the parent metal yield strength level without yielding. Furthermore, the need for adequate plastic straining capacity of the welded joint as a whole can limit the use of undermatching weld metals. Consequently, as overmatching weldments permit more straining than undermatching ones, it is attractive to ensure weld metal yield strength overmatching because in this case the requirements concerning weld metal toughness may be reduced.

The distribution of plasticity throughout the panels also depends on the crack size and location. For large surface cracked panels, the crack size dominates the deformation and a mismatching effect (beneficial or detrimental) on the crack driving force is lost. Small surface cracks, when positioned in undermatched weld metal, significantly reduce ductility of the welded joint and substantially increase the applied crack driving force. However, this is not the case for cracks in HAZ.

Another important characteristic of many welded structures are residual stresses, and their effects are difficult to assess. Welding processes and different thermal expansions of clad/parent metal introduce residual stresses, which influence the effective initiation toughness for shallow flaws in the vessel wall. Their effects may be diminished by post-weld heat treatment, but not eliminated. The term – welding residual stresses – includes, in analogy to the manufacturing residual stresses, all residual stress states, which appear in various welding processes. Thereby, completely different source parameters acting together during welding can contribute to the weld residual stress state (Table 3). The basic mechanism of residual stress creation is the shrinking of high heated areas, hindered by the cooler, and less or even non-shrinking areas.

The constrained longitudinal shrink in single pass arc welding leads to residual stress distributions in the longitudinal and cross direction of the seam (y–axis) and along a vertical line (x–axis), as schematically shown in Fig. 20. The stresses in the length direction in the seam area and in the HAZ adjacent area are tensile stresses. These hold the balance to compressive stresses outside the seam mean position. In sufficiently large seam, tensile stresses in the length direction in the centre of the metal have a nearly constant level. At seam end they fall to zero. On the left in Fig. 20, based on the stress distribution along the seam, the distribution of transverse strains is schematically presented. They become zero at seam end, but increase toward the seam mean position. This means, as seen along seam length, that transverse strains are constrained and therefore, even when no outer forces or residual stresses restrict cross shrinking, in the direction crosswise to the seam residual stresses must also appear. The distribution of these stresses is also schematically given in Fig. 20. If no outer shrink constraint exists in the transverse direction, their amounts are overall smaller than stresses in the longitudinal direction. At long welds, the cross strain constraint goes in the area of the seam against zero and correspondingly the cross residual stresses at the same place approach zero.

Table 3. Possible causes for weldment residual stresses

<table>
<tr><td colspan="2">Non-homogeneity of</td></tr>
<tr><td>Shrinking processes</td><td>Transformation processes</td></tr>
<tr><td colspan="2"><u>Method procedure caused temperature differences:</u>
- across the seam: Between seam HAZ and base material
- in thickness direction: Between different layers
Between deposit and base metal
Between melt line and base metal</td></tr>
<tr><td>Shrinking residual stresses
through the difference in shrinking of differently heated zones</td><td>Transformation residual stresses
through the volume change in transformed zones only</td></tr>
<tr><td colspan="2">without (in principle) necessity of yielding, due to the outcome of the process only</td></tr>
<tr><td>Tensile residual stresses
in finally cooled zones</td><td>Compression residual stresses
in finally transformed zones</td></tr>
<tr><td colspan="2"><u>Temperature differences caused by cooling</u>
In the thickness direction: Surface cools down quicker than the kernel</td></tr>
<tr><td>Quenching residual stresses
through yielding due to constrain between surface and kernel</td><td>Transformation residual stresses
through yielding due to non-simultaneous transformation of surface and kernel</td></tr>
<tr><td colspan="2">By outcome of the process alone:</td></tr>
<tr><td>Compression residual stresses
in firstly cooled zones, i.e. on surface</td><td>Tensile residual stresses
in firstly transformed zones, i.e. at surface</td></tr>
</table>

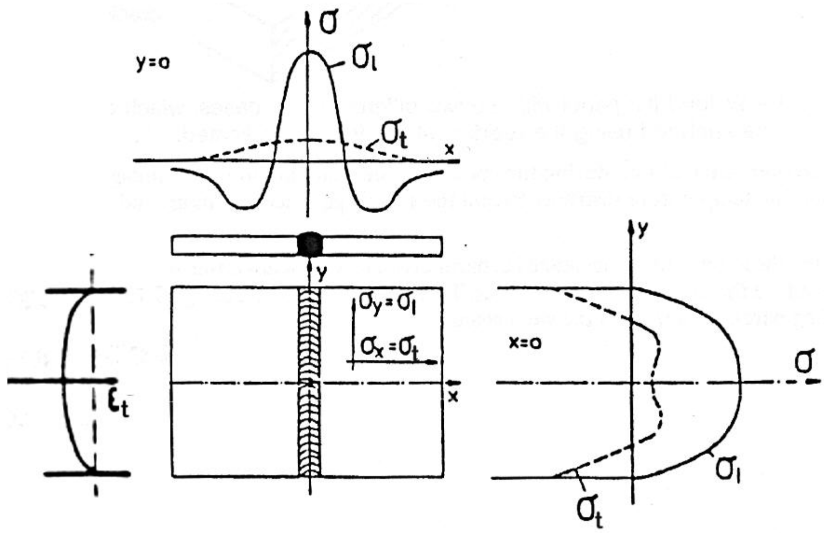

Figure 20. Longitudinal (σ_l) and transversal stress (σ_t) distribution in the welded plate

Residual stresses have an effect on crack growth, but due to residual stress redistribution this effect may be very complex. During service, residual stresses are subjected to change due to redistribution, relaxation, overloading, and similar. In case of residual stress ignorance in calculation, the results may be at the unsafe side.

The determination of fitness-for-service and the prediction of the impact of weld discontinuities on components are based on fracture mechanics. The three primary factors controlling fractures are: discontinuity size, material toughness, and applied stress. Knowing two of these three, engineers apply fracture mechanics to estimate the value of the third, to produce acceptable welds. However, actual methods for the evaluation of crack effects (crack propagation, failure) in the welded structures are mostly derived based on homogeneous materials, assuming cracks in materials with properties and microstructure that remain unchanged in the whole volume. In the case of weldments this is far from reality and for the purposes of adding predictability to welded components, additional investigations and developments are necessary. Recently, the SINTAP method for weld strength mismatched structures has been developed. It is based on two existing defect assessment approaches for welded structures – the modified R6 method and the ET-MM method. The consideration of Lüders strain allows more accurate consideration of strain capacity in the mismatched weldment.

CONCLUDING REMARKS

In the drive towards industrial competitiveness, it is vital that existing process plants become more efficient in terms of their cost, downtime, production efficiency and quality. Industries rely on plant operating efficiency and uninterruption during production. However, purely by design the plant suffers from a number of degradation mechanisms which, when unmonitored and without preventative – remedial measures being taken, often lead to failure. The failure of plant not only results in loss of production, loss of income and costly unscheduled repairs, but also all too often results in injury and loss of life.

Even so, the practice of replacing life-limited components at first signs of field problems in similar equipment or at the end of their predicted lives may result in an unnecessary and large expense to the user. Therefore, in the current budgetary environment, fielded equipment is often used beyond its design life. To avoid large costs of replacing critical rotating parts as they reach their design life limits, or, based on retirement-by-time basis, a retirement-for-cause procedure has been developed as a cost-effective, yet safe, alternative. The main products of retirement-for-cause assessment, based on fracture mechanics science explaining how and why the structure components fail, are a decision to run, alter, repair, monitor, or replace the equipment and a guidance on reliable inspection interval lay down for the equipment.

REFERENCES

1. Agatonović, P., *Development of residual strength evaluation tool based on stress-strain approximation*, International Journal of Fracture, 98, pp. 129-152.
2. Agatonović, P., *Procena integriteta i veka na osnovu analize podržane eksperimentima*, Sedma medj. letnja škola mehanike loma, Ed. S. Sedmak i A. Sedmak, Velika Plana, Jun 1997.
3. Agatonović, P., *Različite strategije u cilju odredjivanja garantovane preostale čvrstoće i veka*, Integritet i vek konstrukcija (2/2001), str. 75-89.
4. Redmond G., *From 'Safe Life' to Fracture Mechanics - F111 Aircraft Cold Temperature Proof Testing at RAAF Amberley*, NDTSL-DGTA, RAAF Base Amberley, QLD.
5. Kirk, M.T., *The second ASTM/ESIS symposium on constraint effects in fracture; an Overview*, Int. J. Press. Vess. & Piping, 64, pp. 259-275. (1995)

6. Ritchie, R.O., Suresh, S., *Some consideration on fatigue crack closure at near-threshold stress intensities due to fracture surface morphology*, Metallurgical transaction, Vol. 13A, May 1982, pp. 937-940.
7. Kumar, V. et al., *An Engineering Approach for Elastic-Plastic Fracture Analysis*, EPRI NP-1931, Palo Alto, CA.
8. Chell, G. et al, *Significant Issues in Proof testing: A Critical Appraisal*, NASA CR-4628, 1994.
9. Agatonović, P., Taylor, N., *Life Assessment Technology for Creep-Fatigue Situation Based on Damage Incubation*, Fracture Mechanics Application in Lifetime Estimation of Power Plant Components, 26-30 May 1989, Dubrovnik.
10. Agatonović, P., *Lifetime temperature dependence of components*, European Conference 'Life Assessment of Industrial Components and Structures', Cambridge, 30 Sept/1 Octob. 1993.
11. Neubauer, B., Wedel, U., *Restlife estimation of creeping components by means of replicas*, Advances in Life Prediction Methods, ASME 1983.
12. Viswanathan, R., *Life assessment of high temperature components – current concerns and research in the US*, 'Life Assessment of Industrial Components and Structures', Cambridge, 30 Sept/1 Octob. 1993.
13. Schwalbe, K.H., *Effect of weld metal mis-match on toughness requirements*, International Journal of Fracture, 56, pp. 257-277. (1992)

MALFUNCTIONING DURING SERVICE LIFE

Vera Šijački Žeravčić, Faculty of Mechanical Engineering, S&Mn
Gordana Bakić, Faculty of Mechanical Engineering, Belgrade
Miloš Djukić, Faculty of Mechanical Engineering, Belgrade
Biljana Andjelić, Technical Faculty, Čačak, University of Kragujevac, S&Mn
Dušan Milanović, "Vectram," Belgrade

INTRODUCTION

Systematic analysis of the number and duration of malfunctions and their causes, types, and consequences in a given plant can be carried out at different levels, starting from malfunction analysis of individual systems through analysis of components comprising the system, and finally the analysis of the parts of a single component. Accordingly, systematic malfunction analysis of a plant system can be defined at three different levels [1-3]:

- System level – malfunction analysis is carried out at the level of a particular system.
- Component level – malfunction analysis is carried out at the level of a particular component of the system under examination.
- Parts analysis – malfunction analysis is conducted at the level of parts of a system under examination.

Malfunctions [4-7] of thermal power plants (TPP) can be divided into three basic groups in respect to the effects produced:

- Functional malfunctioning whose end result is complete interruption of system performance within specific limits;
- Performance malfunctioning of a system that is manifested by reduced performance but remaining within the specified limits;
- Part malfunctioning that has no effect on the system functionality.

1. CLASSIFICATION OF MALFUNCTIONING CAUSES

Designers are often confronted with the requirement to minimize the possibility of a failure/fracture of different constructions. To comply with this requirement, it is essential to understand the basic mechanisms of fracture of materials under specific (service) conditions, as well as to understand the design principles applied to prevent fracture of a particular part in service. In general, fracture of engineering materials, particularly occurring in thermal power plants [8-10], is always undesirable, primarily because of following reasons: life-threatening possibility to personnel, direct economic loss, outages of unknown duration, and possible breakdown of plant availability.

However, even when causes of fracture and material behaviour under service life conditions are known, the use of preventive measures to avert the occurrence of fracture is rather difficult.

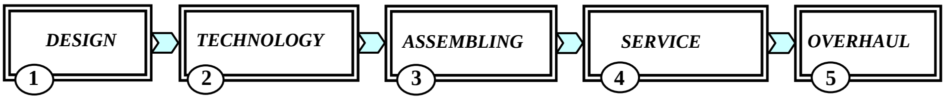

Figure 1. Fossil fuel power plant life cycle phases – possible flaw origins

The classification we have suggested, chronological and functional, comprises all possible flaws that may occur in a fossil fuel power plant, starting from its design phase, construction and exploitation, Fig. 1, Table 1 and 2 [3,5,7]. A certain number of flaws during exploitation can be relatively quickly detected, primarily those originating from design and construction nature. However, technological flaws in materials appear to be hidden which, even under normal service conditions, could be activated and depending on their size, cause small or considerable damage, or even fracture of a component.

Table 1. Chronological classification of flaws

Chronological classification of flaws	
Group of flaws	*Examples*
Design	Inadequate design Inadequate designed dimension of components Improper assumption of working condition Dimension deviation in built-in components from designed point
Technology	Deviation from designed/required chemical composition, microstructure, mechanical characteristic, number of inclusions ... Weld flaws Deviation of pre/post heat treatment and welding parameters from designed parameters Deviation from designed surface quality
Assembly	Mechanical surface damages due to transportation and assembly Improper assembling of components Improper assumption of working condition Assembling weld flaws
Service	Fatigue cracks, creep cracks due to deviation from working parameters Environmental induced cracks due to deviation of water treatment Components dimension deviation due to overloading (p, t)
Overhaul	Cracks initiated by residual stresses in weld after repair welding during overhaul Weld flaws Assembling flaw

For these reasons it is essential to determine the distribution of flaws according to their causes and time of their appearance during service life. However, despite that flaw analysis is essential when applying measures for improving the plant reliability, the analysis of flaw causes, if it ever is conducted, contains a number of shortcomings such are:

- often, it is not possible to determine the cause of a flaw,
- instead of a cause, a characteristic of the event is seen, for instance fatigue fracture, stress corrosion, etc.,
- practically in all cases of analysis of flaw/damage, the quantitative analysis of effects from different factors causing the damage is lacking.

Table 2. Functional classification of flaws

Functional classification of flaws	
Group of flaws	*Examples*
Overloading (High stress)	Fatigue cracks, creep cracks Cracks due to static loading Brittle cracks
Overloading (High stress) + + other causes	Cracks initiated by residual stresses Stress corrosion and corrosion fatigue cracks Brittle cracks due to material aging Thermal fatigue cracks
Corrosion attack	General corrosion Oxygen corrosion Intercrystalline corrosion Pitting corrosion Hydrogen corrosion
Corrosion attack + other causes	Fretting corrosion Cavitation erosion Flaws from category 2 stimulated by aggressive environment
High temperature	High temperature material aging Micro structural degradation Voids (creep) Scaling Residual stresses

2. METHODOLOGY FOR DETECTING CAUSES OF MALFUNCTIONING

Although there are a large number of methodologies for determining the causes of malfunctioning, there is very little difference between them. The methodology [11] we have applied contains all components of the root cause analyses. It is characterized by three distinct groups of activities:

- *Visual inspection with macro photography* of all parts that directly and indirectly contribute to fracture, preferably on-site and without any preparation. Visual inspection is the most important operation of preliminary examination of a damaged component. The human eye has extraordinary capabilities of detecting small changes in colour and texture of materials over a large surface area, more than any optical or electronic device. Visually noticeable characteristics of the damaged zone of a component, fracture features, and propagation directions of crack/macroscopic damage, provide useful information on the sequence of the process development and a possible cause of damage. It should be pointed out that there is no systematic analysis of the appearances and characteristic locations of the damages, for instance, on boilers due to inadequate attention given to this domain.
- *Examination of material properties for a given application.* In this phase of examination, it is essential to determine the material *chemical composition*. This analysis is often neglected or is carried out at the end, if and when there is a need for it. In other words, standard material chemical analysis provided by the supplier, is often taken as adequate and exact. Unfortunately, this is not always the case since it was found that analysis of not only deleterious elements, such as S and P, but also alloying elements shows considerable deviations. Therefore, the method we have applied is based on parallel determination of chemical analysis and other examinations. Sometime it is possible to determine causes of malfunctioning merely based on these examinations.

Following the chemical analysis, *mechanical properties* are determined while optical and scanning electron microscopes are used to characterize *micro structural properties* of the fracture surface. It should be pointed out that most complex examinations are those associated with material microstructure, since the material very often satisfies mechanical characteristic requirements but not microstructural as well, that may have a decisive influence on operational reliability.

- *Data collection from the service life history of a damaged part* in respect to, for instance, type of material, operational parameters such are: type of load, temperature and time, quality of the working environment, etc. On domestic thermal power stations, data is very often lacking since the information collected is partial (irregular data collection) or unreliable (based on the recollected memory of maintenance personnel) and thus using these data must be taken with great reserve. Once data collection is complete, detailed analysis is carried out leading to the synthesis of results obtained, that enable determination of the actual cause.

From the techno-economical point of view, the damage degree depends on the flawed plant component. Several examples of failures that have occurred on domestic thermal power plants during the last 10 years are a consequence of inadequate quality of the starting material that clearly indicates the need for flaw classification and strict control of the material to be used.

2.1. Some examples from PRACTICE

Example 1. DESIGN FLAWS
Equipment: *Boiler drum*

One of the most illustrative examples [12] of poor design is definitely submerged drum of TPP, 110 MW. According to the design, the drum, which is located under the economizer tubing system (water heater), should maintain the required water level with the use of corresponding valves. However, during exploitation it was demonstrated that this was impossible to achieve. The problems in boiler operations were detected in the early stages since individual tubes of the wall evaporator had a negative flow that, in some locations, had no water phase and were subjected to high thermal stresses.

It is clear that such operation has very quickly led to malfunction, spreading not only to the evaporator but also to other parts of the tubing system. Detailed analysis of causes for malfunctioning led to the conclusion that there were many types of damages on this tubing system but every analysis of the malfunction showed the same – clear connection with the submerged drum. Although several attempts to upgrade the design were carried out resulting only in partial improvement. The designed functionality, however, was never achieved. The selected examples show also other types of flaws.

Example 2. TECHNOLOGICAL FLAW
Equipment: *Steam turbine feed pump*
Failed part: *Second stage turbine blades*
Material: *X22CRMOV121 (DIN)*
Type of failure: *Fatigue corrosion*
Cause of failure: *Unbeneficial microstructure due to improper choice heat treatment parameter*

High content of alloying elements as well as complex processes taking place during the inappropriate thermomechanical treatment of high alloyed steels can cause unbeneficial microstructural characteristics during production – known as metallurgical instability. Metallurgical instability in these steels includes several complex processes such as carbide segregation in grain boundaries, inhomogeneous distribution of carbide particles, plenty of different non-metallic inclusions and appearance of large content of ferrite in the basic martensite structure. The most unbeneficial flaw is ferrite because of its low mechanical properties and relatively low corrosion resistance. Generally, these flaws cause decrease in mechanical properties and especially decrease corrosion and oxidation resistance of steel, which leads to the decrease of time to fracture.

The specimens for experimental investigation were cut from turbine blades, stators and rotors, Figs. 2–4, made of high-content chromium steel X22CrMoV121 (according to DIN standards), which fractured after less then half the predicted life time. These steels belong to the martensitic steel type, with 5% of maximal allowed δ-ferrite content and which are highly used for turbine blades. The comprehensive experimental investigation of microstructure and fracture features 32 different specimens tested by optical microscopy, scanning electron microscopy with energy-dispersive analyzer, all performed in the aim of determining microstructural variations, and their possible influence on fracture, corrosion, and oxidation resistance of blades [13-15].

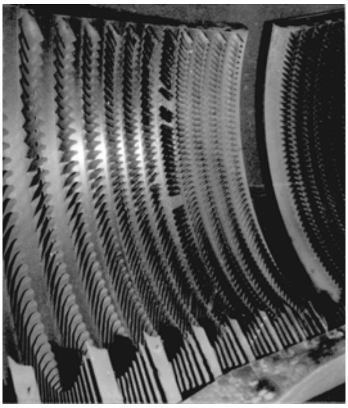
Figure 2. Failed stator blades


Figure 3. Failed rotors blades


Figure 4. Failed rotors blades

The basic microstructure of tested steels is martensite with carbides, separated in grain boundaries and within the grains, Figs. 5–6. In addition, an appearance of an extremely large amount of ferrite is detected. The various microstructural flaws already mentioned are presented on SEM micrographs: the striped carbides distribution; the inhomogeneous distribution of chromium and the related inhomogeneous distribution of carbides in different zones; very large carbides of chromium, separated in grain boundaries with decohesion in the particle–matrix interface; very long MnS inclusions passing through several grains; massive silicon inclusions are also revealed. A relatively large number of specimens have a martensitic–ferritic or pure ferritic structure with large chromium carbides in grain boundaries instead of the necessary structure of tempered martensite. Delaminations of microstructure are observed too, Figs. 7–12.

As illustrated on the last four figures, the corrosion pits, because of the complex stress distribution and cycling loading, have been the source of fatigue crack initiation, Figs. 13–16. The fracture scenario is presented in Fig. 17.

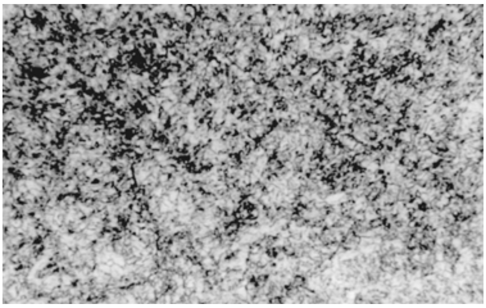

Figure 5. Proper microstructure – tempered martensite with carbides

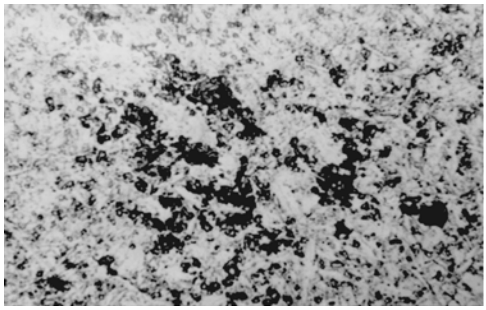

Figure 6. Improper microstructure – martensite with inhomogeneous carbide distribution

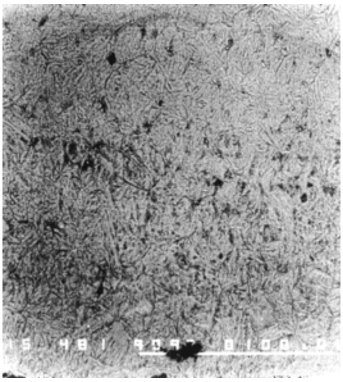

Figure 7. Fine grained martensite

Figure 8. Rough grained martensite

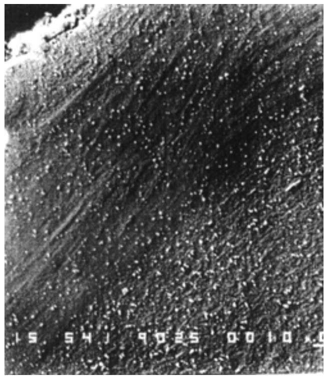

Figure 9. Inhomogeneous carbide distribution

Figure 10. Ferrite with carbide in grain boundaries

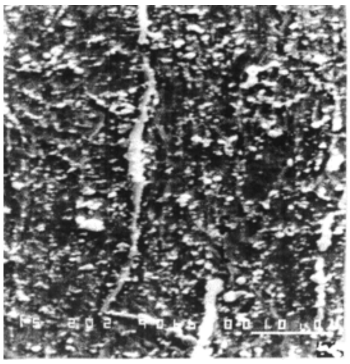

Figure 11. MnS inclusions with decohesion

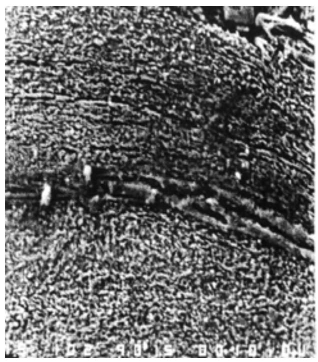

Figure 12. Delamination and MnS inclusions

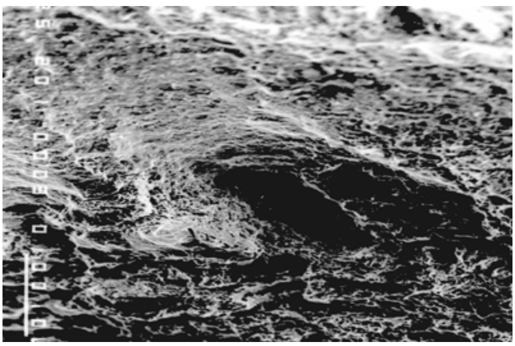

Figure 13. Initiation of fatigue crack on corrosion pits

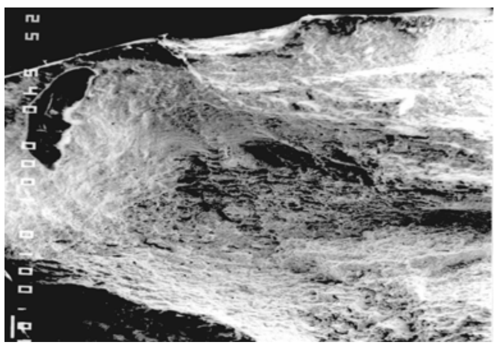

Figure 14. Fatigue – striation

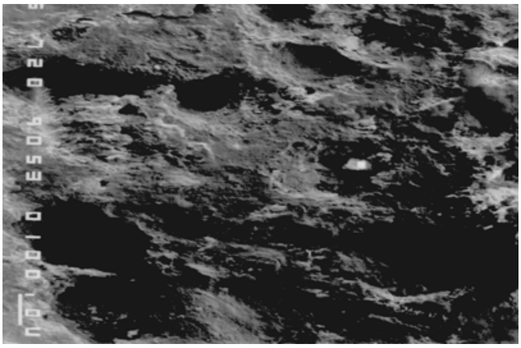

Figure 15. Corrosion pits and cavities

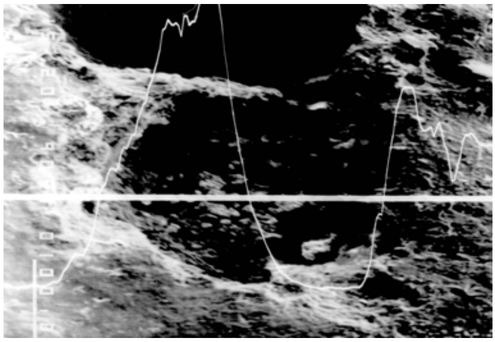

Figure 16. Cr – distribution in the corrosion pits

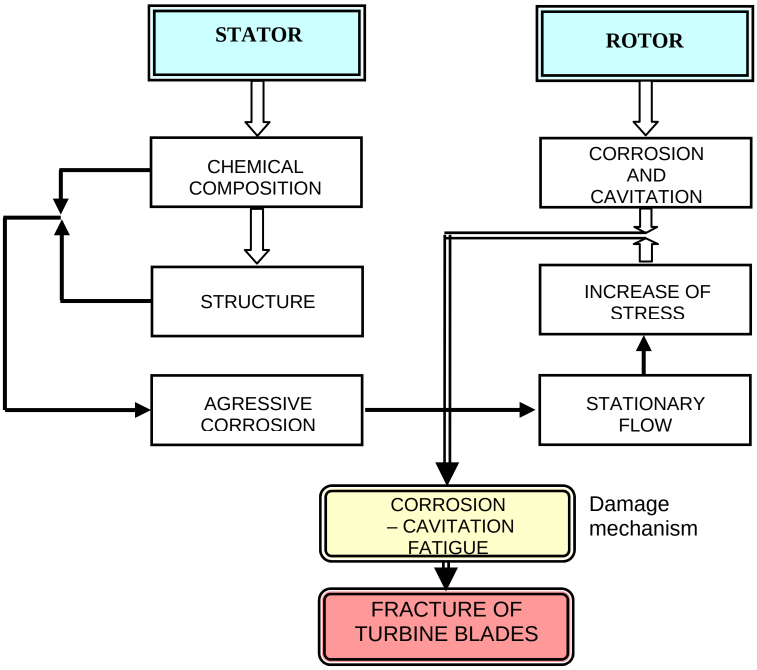

Figure 17. Scenario of failure

Example 3. ASSEMBLING FLAW
Equipment: *Thermal power plant, Unit 210 MW*
Failed part: *Down-comers tubes*
Material: *0.5Cr 0.5Mo 0.25V*
Type of failure: *Stress corrosion cracking*
Cause of failure: Sensitization in weld repair with austenitic electrode after prolonged service

Austenitic stainless steels are often used for welding or repair welding of dissimilar metal joints as a filler material. However, because of their coefficients of thermal expansion and low thermal conductivity, and high residual stresses and distortion being related to the same quantities of joined metals, many problems emerge during exploitation at elevated temperature. Basic structures of austenitic steels are simple and several transformation phases can be produced during welding that play a significant role in service behaviour. Extensive transformation may take place during component life if it is maintained at elevated temperature.

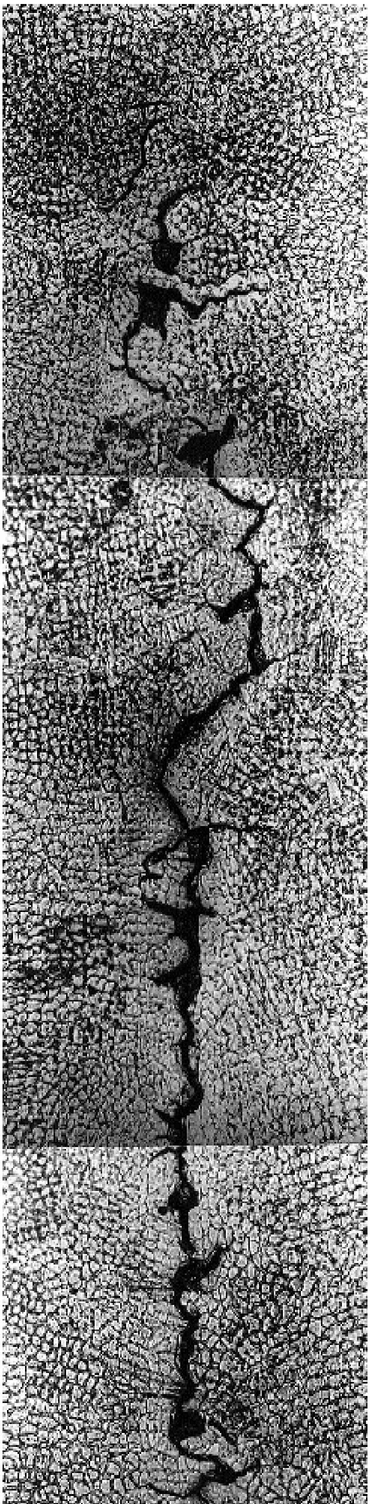

Figure 18. Austenitic weld zone. Branched stress corrosion cracks. Inclusions

Figure 19. Welding flaw in austenitic zone

Figure 20. Austenitic weld zone. Stress corrosion crack. Precipitated carbides in grain boundaries and zone without carbides in the vicinity of crack

Figure 21. SEM micrograph of austenitic-ferritic interface. Large crack, brittle intercrystalline fracture in austenitic zone. Complex silicate inclusions

The investigated joint was part of down-comer tubes assembled 20 years ago, in the 210 MW thermal power plant. The base materials of welded tubes are the low alloyed CrMoV steel. Electrodes, with chemical composition very close to the base material were used as a filler material. Because of observed flaws, the part of the welded joint was repaired but with an austenitic stainless steel electrode, with 12.5% Cr and 19.1 % Ni. Welded joints were 152 000 hours in exploitation at working temperature of 340°C and internal operating pressure of 16 MPa, prior to the onset of failure [16-19].

Failure originated in the boundary layer of the section, welded with austenitic and ferritic electrodes, and followed by crack propagation through ferrite filler material. Sensitization – meaning the decrease of chromium content in the area close to grain boundaries, below the level (< 12%), which provides corrosion stability. At the same time, chromium precipitates in the form of ($Cr_{23}C_6$) complex carbides in grain boundaries. As a result of this process, intercrystalline stress corrosion occurs with brittle fracture.

Branched stress corrosion cracks in the austenitic weld zone are shown in Figs. 18 to 20. Carbides that precipitated in grain boundaries and zones without carbides in the vicinity of the crack can also be noticed. In Fig. 21, a large brittle intercrystalline fracture crack is shown in the austenitic zone, and complex silicate inclusions.

Example 4. SERVICE FLAW
Equipment: *Thermal power plant, Unit 110 MW*
Failed part: *Water wall tubes*
Material: *Low carbon steel*
Type of failure: *Hydrogen damage*
Cause of failure: *Improper water lay up procedure (low pH)*

During exploitation of a fossil fuel power plant, significant failures on water wall tubes took place [20-23]. Water wall tubes (∅60×6) made of steel – 0,2C 0,5Mn 0,25Cr were operating at p = 15.5 MPa and t = 350°C.

Window type fracture with local wall thinning was observed on the water wall tube fireside, in the zone of maximal heat flux. The outer surface of specimens exhibited a general corrosion condition. Uneven scaling was visible on the inner surface of the tube fireside, especially downstream of the welded joint, and also on all outer tube surfaces. It was also observed that the weld joint in the damaged zone had backing rings (poor weld overlay, which penetrated to the inside surface), Fig. 22.

Chemical analysis of specimen showed that carbon content detected on inner surfaces is lower (0.23%C) then on the outer surfaces (0.25%C), which indicated a certain level of decarburization of the inner surface layer.

The undamaged areas of all tested samples have wall thickness as is designed (6 mm), but in damaged areas, a local diminishing of wall thickness is measured (2.9–5.75 mm). Hardness was measured in damaged as well as in undamaged areas of the specimens. The obtained results are in the range 141–184 HV30 and exceed the recommended value of ~145 HV for the material in normalized state. Increased hardness values could indicate on certain embrittlement of the material that was verified in mechanical tests. The yield strength, R_{eH} = 403 MPa, is significantly higher then the minimum design value R_{eH} = 216 MPa, and is very close to the designed minimal tensile strength R_m = 420 MPa. The obtained tensile strength value, R_m = 480 MPa, satisfies the recommendation. Deformation characteristics, expressed by elongation, A_5 = 13.2%, is much lower than the designed, A_{min} = 24% and indicates a significant decrease of material plasticity, i.e. significant embrittlement. The base structure is mostly ferritic while pearlite is mainly degraded or not present at all. Also, a distinctly striped structure with non-homogenous distribution of very fine elongated MnS inclusion was visible. However, a very characteristic microstructure with many discontinuous intergranular cracks, found in the failure area, indicates on hydrogen damaging, Figs. 23–24.

Figure 22. Macro photo of "window" type fracture with schematic view of the specimen

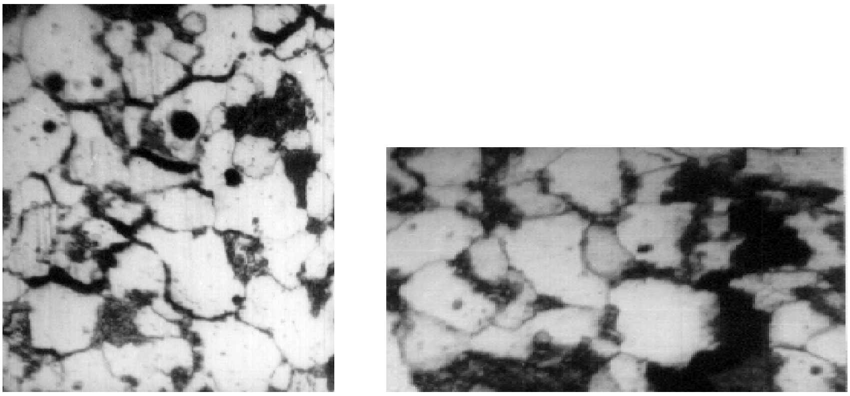

Figures 23 and 24. Cracks due to hydrogen damaging

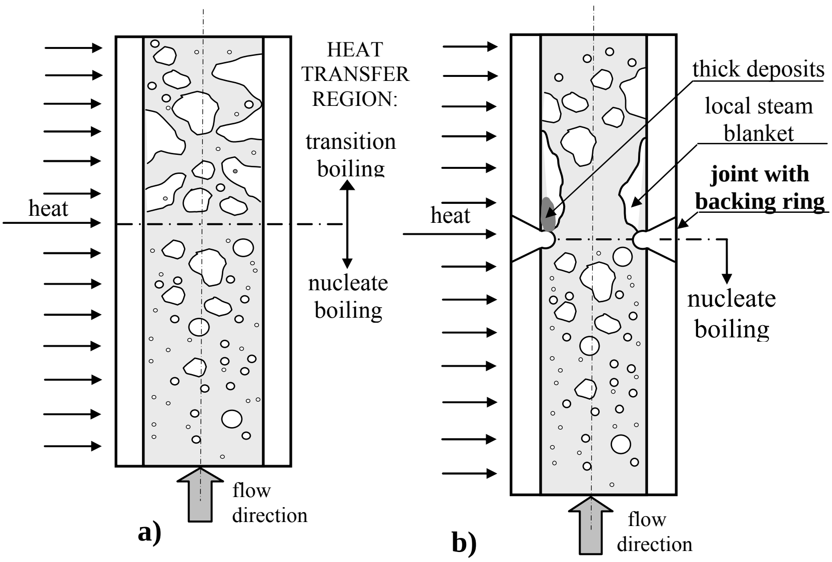

Figure 25. Flow patterns during: a) transition boiling, b) local steam blanket formation downstream flow disrupter

In this case, visually observed joints with backing ring act as local flow disrupters, which periodically caused formation of the steam blanket or the bubbling in the rinsed area (Fig. 25b). This process causes the deposition of dissolved or suspended solids just downstream of the flow disrupter. So, downstream of joint, thick deposit is formed as it is observed during visual examination. In the deposit area, the local pH value drops significantly due to the concentration of acidic content. It is very important to note that this process appeared at a moderate heat flux value, $q < 400$ kW/m^2, and is not necessarily connected, especially to the water wall tube zones, with local high heat fluxes.

When the normal operating condition in a tube is interrupted, local areas with deposit and elevated acidic concentration (locally low pH value) are formed, and the condition for hydrogen formation, as one of the corrosion products, are taking place.

Even a low decrease of water alkality may cause local damage of protective magnetite layer and as a consequence an intense diffusion of hydrogen into metal. Also, tube metal temperature fluctuations and presence of porous deposit on the water side intensify local diffusion of hydrogen. Window type fracture is characteristic for hydrogen damaging.

Example 5. SERVICE FLAW
Equipment: *Thermal power plant, Unit 110 MW*
Failed part: *Water wall tubes*
Material: *15Mo3 (DIN)*
Type of failure: *Corrosion damages*
Cause of failure: *Multiple corrosion mechanism*

In general, corrosion is an irreversible process of metal/material deterioration or destruction because of environmental activity. During this process material properties are decreasing and the material availability is being lost. The deterioration or destruction of metal incorporated into fossil fuel power plants may be provoked due to various causes: chemical, electrochemical, and mechanical [1,2,24-26]. Thus, a different principal type of corrosion as: chemical, electrochemical, erosion corrosion, and fretting corrosion, with specific damages, can generate. Corrosion processes on furnace water wall tubes, apart of their significantly different steam parameters (3.4–19.5 MPa, 240–360°C), have occurred in conditions of boiling regime. Therefore, it is necessary to observe the particular corrosion processes within the material (steel)–water–boiling system regime.

During the exploitation of the 110 MW power plant, significant corrosion damages on the furnace water wall panel (∅57×5), made of 15Mo3 steel, are detected. Some problems with the water wall tube rupture have appeared after prolonged steam boiler stagnation without proper protection. The samples for investigation were taken from three different zones per attitude (hopper zone and zone below burners, zone between burners and recirculation opening and the zone above recirculation opening) and per boiler sides. On the basis of performed tests, it is concluded that:

- all three furnace water wall zones are exposed to complex corrosion process development;
- steam-water corrosion is especially pronounced in the second zone above the burners and is followed by significant wall tube thinning, Figs. 26–29;
- dominant hydrogen damage followed by decrease in strength and plasticity characterize the first zone, which had included the area between the hopper and burners, Fig. 30;
- corrosion fatigue cracks, as one of environmentally enhanced damages, are the consequence of combined acting of corrosion and thermally induced stresses, Fig. 31.

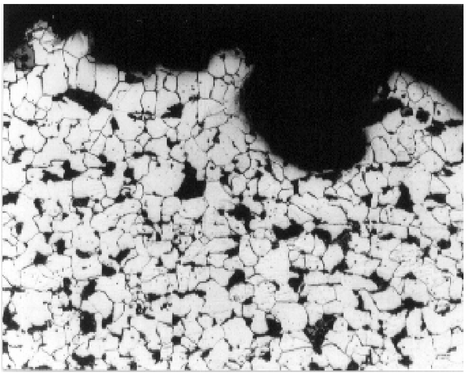

Figure 26. Corrosion damages, ×200

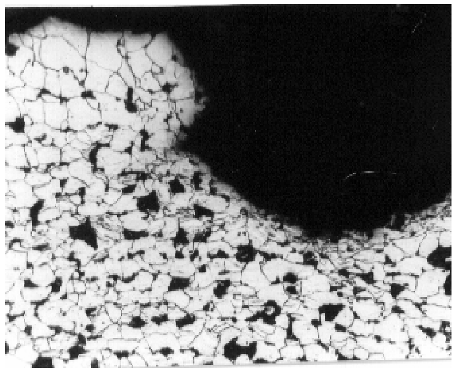

Figure 27. Corrosion damage, ×200

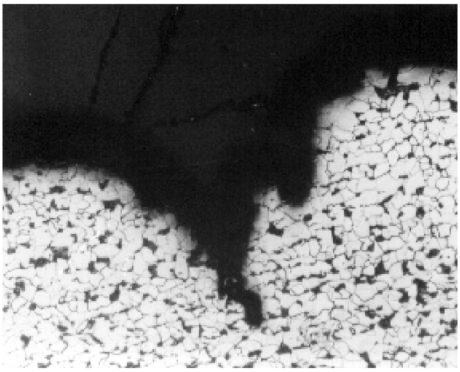

Figure 28. Corrosion damage with sharp tip, ×50

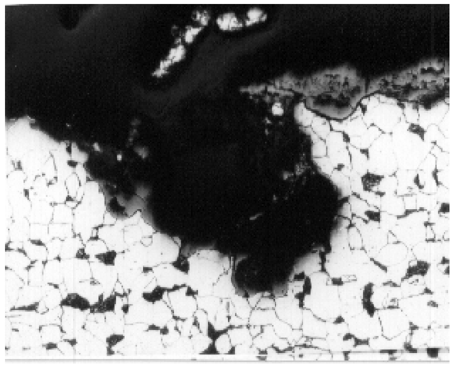

Figure 29. Corrosion damage. Oxide scale. Deposit. ×200

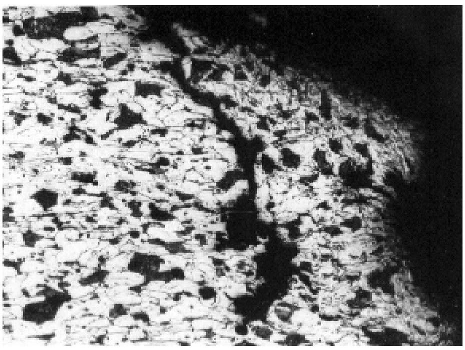

Figure 30. Hydrogen damage, ×100

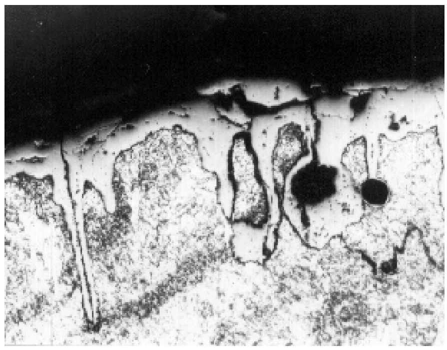

Figure 31. Corrosion fatigue, ×100

Example 6. Combined flows: design, technological, service
Equipment: *Main hot water pipeline*
Failed part: *Welded joints*
Material: *Low carbon steel*
Type of failure: *Leakage*
Cause of failure: *Multiple*

The problems detected during the exploitation of magistral piping [27,28], Fig. 32, were associated with the frequency of pipe leakage, especially in the vicinity of the welds but also on separate segments. The rate of frequency/number of malfunctioning increased significantly during the last 3 years of exploitation and has required frequent weld repairs,

Fig. 33. According to the design specification, magistral piping was made of seamed tubes, dimensions of ∅406×7 mm and covered with polyurethane. Detailed visual examination and extensive destructive testing showed that frequent leakage of piping is due to design flaws and also due to technological and service flaws. It was established that the piping built-in thickness (approximately 4.5–5.5 mm) is considerably lower from the designed value, and thus qualifies as a technological flaw.

Figure 32. Main hot water pipeline

Figure 33. Repaired weld area

Furthermore, the material used for the piping did not correspond to the required type, specified by design. Technological flaw was observed in the case of insulating material that severely degraded during exploitation, Fig. 34, due to the high metal temperature ($T = 130°C$) that has provoked the development of a very intensive corrosion attack on the metal. In addition, the spiral welds showed no typical flaw that could be characterized, not only as of design, but also as a technological-assembly flaw. As a result of poor positioning of electrodes during welding, an axial mutual displacement of the external to the inner weld has occurred, Fig. 35. The results of such a flaw are the increase of tensile stresses in the weld during exploitation and their non-uniform distribution. This affected initiation and propagation of cracks that appeared in large numbers in both heat-affected zones of the weld external and inner sides, Fig. 36. Inadequate preparation of the working fluid caused the separation of the deposits on the inner piping surface and development of pitting corrosion under the deposits.

This example clearly shows the additive effect of a number of flaws during the designing phase as well as due from assembling and exploitation. The final result is a significant loss in exploitation reliability of the main pipeline and a need for its replacement.

Figure 34. Damaged area due to leaking, wet insulation

Figure 35. Misaligned welds with crack in common HAZ

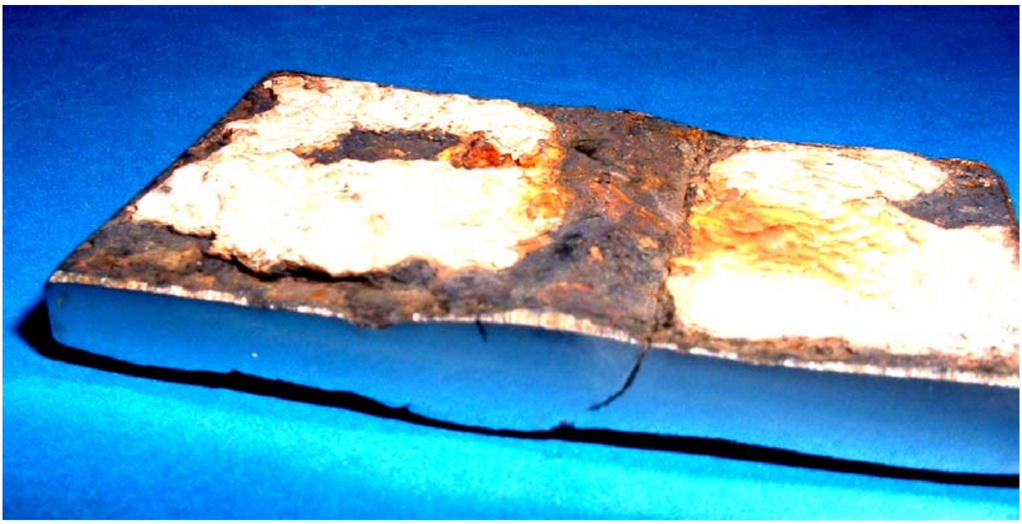

Figure 36. Penetrated crack in HAZ where leaking occurred

REFERENCES

1. *Corrosion in power generating equipment*, Proc. of 8th International Brown Bowery Symp. On power generating equipment, Baden, Switzerland. (1983)
2. Mars G. Fontana, *Corrosion engineering*, McGraw Hill International Editions. (1987)
3. Šijački Žeravčić, V., Bakić, G., Đukić, M., Anđelić, B., Milanović, D., *Model of outages classification and statistical computation applied to tube system of thermal power plants*, Preventivno Inženjerstvo, Vol. XI, No.2. (2003)
4. Kaplun, *Optimizacija nadežnosti energoustanovok*, Nauka. (1982)
5. Getman, Kozin, *Nerazrušajuščij kontrolj*, Moskva. (1997)

6. Smith, M., *Reliability-Centered Maintenance*, McGraw-Hill. Inc., New York. (1993)
7. Šijački Žeravčić, V., Anđelić, B., Bakić, G., Đukić, M., Milanović, D., Vlajčić, A., Maksimović, P., *Influence of material quality on TPP reliability*, Elektroprivreda, Vol. LV, br. 4, str. 64-71. (2002)
8. Šijački Žeravčić, V., Bakić, G., Marković, D., Milanović, D., Đukić, M., *RCM in Power Plant Practice Illustrated on Observation of Material Aging and Defining of Component Life Exhaustion,* Proc. of Int. Conf. POWER-GEN Middle East 2002, Abu Dhabi, UAE, paper No334. (2002)
9. Šijački Žeravčić, V., Bakić, G., Đukić, M., Anđelić, B., *Material quolity control of thermal power plant components from the reliable exploitation point of view*, Proc. on 10th Symp. PREVING 2002, Belgrade, pp. 314-319.
10. Šijački Žeravčić, V., Bakić, G., Milanović, D., Anđelić, B., Đukić, M., *General consideration about design solution influence on reliability of thermal power plants,* Proc. of 5th Inter. Symp. DQM 2002, Belgrade, pp. 56-65.
11. Šijački Žeravčić, V., Vujović, R., Milanović, D., Bakić, G., Đukić, M., *Preventive engineering necessarity of pressure vessels undergone to the severe exploitation conditions,* Procesna tehnika, Vol. XV, 3, pp. 266-271. (1999)
12. Šijački Žeravčić, V., Radović, M., Stamenić, Z., Bakić, G., Djukić, M., *Exploitation availibility estimation of furnace walls system of steam generator*, Unit 5, 100MW, TE Kolubara, Report, Faculty of Mechanical Engineering, University of Belgrade, p. 41. (1998)
13. Šijački Žeravčić, V., Marković, A., Radović, M., Stamenić, Z., Marinković, I., *Case study of turbine blades damages of secondary stage turbine feed pump*, Unit 2, TENT-B, Fac. of Mech. Eng., Belgrade, Report No 12-16-12.04/1995, p. 81. (1995)
14. Šijački Žeravčić, V., Radović, M., Stamenić, Z., Bakić, G., *The Influence of Microstructure Variations on Turbine Blades Fracture, Proc. of Conf. on Mat. Structure & Micromechanics of Fracture*, July 1-3, 1998, Brno, Czech Republic, p. 63.
15. Šijački Žeravčić, V., Kovačević, K., Radović, M., Marković, A., *Fracture features of broken turbine blades*, Proc. of 2nd Congress of Electron Microscopy, Belgrade, Serbia, pp.185-186. (1997)
16. Šijački Žeravčić, V., Milosavljević, A., Marković, A., Stamenić, Z., Milanović, D., *Study of catastrophic failure causes of downcomer tubes of "Nikola Tesla –A"*, Report, Fac. of Mech. Eng., Belgrade, p. 93. (1992)
17. Suutala, N., Takalo, T., Moisio, T., *Ferritic – Austenitic Solidification Mode In Austenitic Stainless Steel Welds*, Met. Trans. A, 11A, pp. 7-17. (1980)
18. Lee, J.B., Eberle, W., Somsak, J.A., *A New Test for Determining Intergranular Corrosion Properties of Stainless Steels*, ibid 17, pp. 19-27.
19. Šijački Žeravčić, V., Milosavljević, A., Marković, A., Stamenić, Z., Bratić, A., Milanović, D., *Microstructural characteristics of joints after repair welding with austenitic electrode after prolonged service*, Proc. of Inter. Symp. on Materials Ageing and Component Life Extension, Milan, Italy, pp. 723-732. (1995)
20. Šijački Žeravčić, V., Radović, M., Stamenić, Z., Bakić, G., Đukić M., *Failure analysis of furnace wall tubes, TE Pljevlja, 100 MW*, Report, Fac. of Mech. Eng., Belgrade, p. 52. (1997)
21. Šijački Žeravčić, V., Stamenić Z., Radović M., Bakić G., Đukić M., *Hydrogen embrittlement of the furnace wall tubes*, Proc. of Conf. on Mat. Structure & Micromechanics of Fracture, July 1-3, 1998, pp. 61 Brno, Czech Republic
22. Đukić, M., *Hydrogen damages of boiler furnace wall tube metal*, MSc thesis, Faculty of Mechanical Engineering, University of Belgrade. (2002)
23. Šijački Žeravčić, V., Đukić, M., Bakić, G., *Hydrogen embrittlement and long time overheating of the furnace wall tubes due to exploitation over critical-heat-flux*, Proc. of 3rd Conf. of Mac. Met. Union, Ohrid, FYR Macedonia. (2000)
24. Šijački Žeravčić, V., Voldemarov, A., Bakić, G., Đukić M., Anđelić, B., Milanović, D., *Residual Life Assessment of First Stage Steam Boiler Reheater Tubing System From the Corrosion*

Damages Point of View, Phisico Chemical Mechanics of Materials, special issue – Problems of Corrosion and Corosion Protections of Materials, No3, pp. 51-57. (2002)
25. Šijački Žeravčić, V., Bakić, G., Đukić, M., Milanović, D., *Review of Corrosion Damages of Water-Steam System of Domestic Fossil Fuel Plants in Regard to a Quality of Build-up Material*, Phisico Chemical Mechanics of Materials, special issue – Problems of Corrosion and Corosion Protections of Materials, No3, pp. 57-64. (2002)
26. Šijački Žeravčić, V., Bakić, G., Đukić, M., Milanović, D., Anđelić, B., *Case Study of Boiler Tubes Damages Coused by Different Corrosion Processes*, Proc. of Conf. METALURGIJA 2000, FYR Macedonia, pp. 63-68. (2000)
27. Šijački Žeravčić, V., Bakić, G., Đukić, M., Anđelić, B., *Study of material state, failure causes and further avaliability condition of pressurized magistral pipieline*, Kolubara cole mine – rafination, Vreoci, Report, Fac. of Mech. Eng., Belgrade, pp. 52. (2003)
28. Caleyo, F., Gonzalez, J.L., Hallen, J.M., *A study on the reliability assessment methodology for pipelines with active corrosion defects*, Pressure Vessels and Piping, 79, pp. 77-86. (2002)

FRACTURE TOUGHNESS OF METALS UNDER CYCLIC LOADING

V. T. Troshchenko, V. V. Pokrovskii, Pisarenko Institute of Problems of Strength, National Academy of Sciences of Ukraine, Kiev, Ukraine

INTRODUCTION

A study of fracture of various engineering components and structures has revealed that in most cases their fracture is due to material fatigue, which is known to be responsible for initiation and propagation of fatigue cracks in cyclic loading and such cracks ultimately lead to complete failure of a component.

The most dangerous fracture case is where a component completely fails with a fatigue crack of small size and final fracture is of brittle mode, thus hindering the detection of small cracks at an early stage of damage.

Figure 1 illustrates the temperature dependence of the ratio between the portion of the section occupied by a fatigue crack at the moment of fracture in high-cycle fatigue and the total section of a specimen, $\bar{F}$, for carbon and austenitic steels [1].

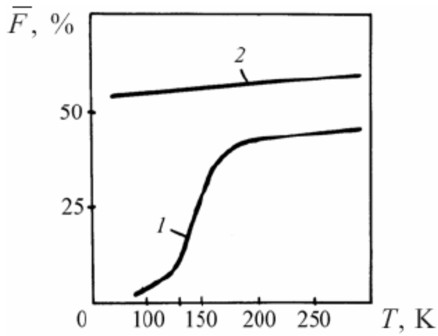

Figure 1. $\bar{F}$ as a function of temperature *T,* for a carbon steel (1) and an austenitic steel (2)

It is evident that in case of carbon steel at low temperature, which makes it brittle, final fracture can occur when a fatigue crack occupies only a few percent of the total section of the specimen.

Clearly, for materials prone to embrittlement, one can expect still further decrease in fatigue crack size limits in view of such factors as hydrogenation, radiation, and corrosive effects. At the same time, in the case of austenitic steels and aluminium alloys, which do not embrittle at low temperature [1], the area occupied by a fatigue crack prior to fracture scarcely decreases with lowering temperature.

A transition from stable fatigue crack propagation to final fracture is governed mainly by fatigue fracture toughness K_{fc}. This characteristic is defined as the highest value of the cycle stress intensity factor whereby the final fracture of a specimen with a fatigue crack occurs under conditions of cyclic loading [2].

It was mentioned in [3] that the concept of fatigue fracture toughness had been first introduced by Yokobori and Aizawa [4] in 1970. The works of Ivanova and Kudryashov

[5], Yarema and Kharish [6], and Kawasaki et al. [7] were among the first dedicated to fatigue fracture toughness of metals and alloys. Then, the subject was taken on by Satoh et al. [8], Clark [9], Kitsunai [10, 11], Sawaki et al. [12], Ando et al. [13] as well as other researchers [14-19]. At the Pisarenko Institute of Problems of Strength of the National Academy of Sciences of Ukraine, they started similar research in early 1970s [1,20-28].

The data obtained by various researchers demonstrated that fatigue fracture toughness of high strength steels, especially in low temperature tests, can be substantially lower (down to 50%) than that in static loading [7,21]. In this case, a transition from stable fatigue crack propagation to final fracture is accompanied by crack jumps whose size grows with increasing current values of stress intensity factors [11,23,27]. The models of transition from a stable fatigue crack propagation to the unstable one, which were proposed in [11,26], are based on the assumption that cyclic mode of loading causes damage to the material at the crack tip and thus is responsible for a decrease in fracture toughness.

Despite numerous works on fatigue fracture toughness of metals and alloys, the following issues have still to be clarified: How big is the difference between fracture toughness characteristics in static and cyclic loading, and for which materials and test conditions? What are the peculiarities of the stable-to-unstable transition of fatigue crack propagation? How do temperature, stress ratio, specimen dimensions, plastic prestraining, and damage of a material under cyclic loading and other factors affect the value of fatigue fracture toughness?

In the present work, we discuss the above-mentioned issues using results of investigations into the fatigue fracture toughness of metals and alloys, which have been obtained recently at the Pisarenko Institute of Problems of Strength of the National Academy of Sciences of Ukraine [29-50].

1. EXPERIMENTAL PROCEDURE AND MATERIALS

The experiments involved tensile testing of compact specimens, 7.5 to 150 mm in thickness on electrohydraulic machines of various capacities [51]. The machines were equipped with specimen cooling and heating systems that provided a test temperature T ranging from 77 to 623 K, [51]. The specimen preparation and crack growing procedures were in conformity with the accepted standards.

The fatigue crack development was observed with an optical system in stroboscopic light. In order to determine the crack front, we measured the fracture surface of a specimen. If necessary, the crack front was fixed by varying the load. In the general case, the formula for calculating the stress intensity factor (SIF) we used, had the averaged crack length. The fatigue crack growth rate (FCG) was calculated by dividing the crack length increment by the number of loading cycles in which the crack covered that distance. Thus, values of the crack growth rate *da/dN* and stress intensity factors obtained were related to the final crack size.

Cycling of specimens was performed at constant load in the loading frequency range, varying from 10 to 15 Hz. Brittle jumps of the crack were detected using acoustic emission signals, which also allowed measurement of crack growth rate during the brittle jumps, [36].

We calculated the stress intensity factors by the formula,

$$K_{\mathrm{I}} = \frac{P\sqrt{a}}{t\sqrt{w}} Y \tag{1}$$

$$Y = 29.6 - 185.5\left(\frac{a}{w}\right) + 655.7\left(\frac{a}{w}\right)^2 - 1017\left(\frac{a}{w}\right)^3 + 638\left(\frac{a}{w}\right)^4$$

where P is the load, a is the crack size, and t and w are the specimen thickness and width, respectively.

The plane strain conditions were determined by the criterion

$$t \geq 2.5\left(\frac{K_{\mathrm{I}}}{\sigma_{0.2}}\right)^2 \tag{2}$$

where $\sigma_{0.2}$ is the material yield stress.

The size of the plastic zone at the crack-tip in plane strain conditions was found by

$$2r_y = \frac{1}{3\pi}\left(\frac{K_{\mathrm{I}}}{\sigma_{0.2}}\right)^2 \tag{3}$$

We determined the dynamic fracture toughness ($K_{\mathrm{I}d}$) by the results of impact tests [31, 49,52] and by the crack arrest upon testing ($K_{\mathrm{I}a}$), [31,39,49]. More details of the experimental procedures can be found in the respective works referenced herein.

The studied materials were different heat-resistant steels (15Kh2MFA, 15Kh2MFAA, 15NMFA, 10KhMFT), used for manufacturing high pressure vessels, including those for nuclear reactors, subjected to various heat treatment conditions. Chemical analysis and heat treatment conditions for these steels are given elsewhere [30,37,38,40,49,50]. Also, our studies included high strength chrome-molybdenum steels [39], the ductile austenitic steel 08Kh18N10TN [35], and titanium alloys [53,54].

Mechanical properties of considered materials are summarized in Table 1.

Heat-resistant steel No. 2 has been subjected to a special heat treatment to simulate radiation embrittlement.

Steels referred as 1, 3, 5–7, which embrittle with decreasing temperature, were tested at low temperatures. Table 1 also lists the values of the ratio between ultimate strength σ_u and yield stress $\sigma_{0.2}$ for the tested materials. This ratio represents the plasticity margin and at the same time, the material's tendency to cyclic hardening or softening as follows from the reported findings [32,49,50,55]. The materials exhibited $\sigma_u/\sigma_{0.2} < 1.2$, qualifying as cyclically softening materials.

It is evident that heat resistant steels, referred as 1–3, 5, and chrome-molybdenum steels, referred as 6, 7, fall into the category of cyclically softening materials. Austenitic steel 8 qualifies as a cyclically hardening material, while titanium alloys, referred as 9 and 10, and heat resistant steel 4, are among cyclically stable materials. Steel 2, which was subjected to a special heat treatment, and high strength steels, referred as 6 and 7, exhibit the smallest plasticity margin. As a rule, this characteristic drops with decreasing test temperature.

Correlation between fracture toughness characteristics under static and cyclic loading, Table 2, gives the values of the stress intensity factor, calculated from maximum load, $K_Q^{\max}$, as a fracture toughness characteristic for considered materials. This characteristic is best comparable to the fatigue fracture toughness K_{fc}, determined from the maximum load in a cycle. In the case where plane strain conditions are fulfilled, we have $K_Q^{\max} \cong K_{\mathrm{I}c}$.

In the present work, we used the symbols $K_Q^{\max}$ and K_{fc}, whether or not the plane strain conditions in fracture were fulfilled. The fulfilment of these conditions was specified separately for each particular case. Table 2 gives also the values of stress intensity factors, which correspond to the onset of jump-like fatigue crack propagation, K_{fc}^1, and dynamic fracture toughness, K_{Id}. The sign "+" indicates that during the determination of static fracture toughness, plane strain conditions were attained.

Table 1. Mechanical properties of the materials under study

No	Material	T	$\sigma_{0.2}$	σ_u	$\sigma_u/\sigma_{0.2}$	δ	ψ
		K	MPa	MPa		%	%
1	Steel 15Kh2MFA (I)	77 183 213 243 293 623	1041 696 674 647 584 545	1115 805 783 752 700 611	1.070 1.160 1.130 1.160 1.200 1.120	18.6 24.1 23.0 20.4 21.0 14.7	31.1 72.1 72.8 74.2 74.6 70.3
2	Steel 15Kh2MFA (II)	77 183 293 373 473 623	1440 1160 1100 1040 956 880	1590 1250 1157 1109 1016 970	1.104 1.080 1.050 1.066 1.062 1.102	3.1 14.2 16.6 15.7 15.6 15.2	2.9 54.0 67.2 65.8 67.4 65.2
3	Steel 15KhMFAA	123 183 243 293	923 689 616 554	926 761 718 650	1.003 1.104 1.165 1.173	18.2 22.4 21.9 19.9	54.8 60.4 75.1 77.4
4	Steel 10KhMFT	293	422	622	1.470	21.9	73.1
5	Steel 15Kh2NMFA	77 183 213 243 293 623	1077 697 658 657 593 503	1111 790 766 756 707 569	1.030 1.130 1.164 1.150 1.192 1.130	12.5 23.5 21.0 18.2 19.6 13.4	17.1 66.6 68.0 66.3 69.5 69.2
6	Chrome-Molybdenum Steel (I)	77 153 183 213 243 293 623	1219 993 964 920 904 855 719	1250 1031 1004 970 943 902 791	1.025 1.038 1.041 1.054 1.043 1.055 1.100	21.2 19.7 20.7 20.8 19.9 20.3 13.6	54.1 68.4 68.1 69.1 69.7 71.5 58.8
7	Chrome-Molybdenum Steel (II)	4.2 77 123 158 213 293 623	1725 1502 1364 1286 1235 1161 959	1812 1519 1377 1318 1259 1191 1031	1.050 1.010 1.009 1.025 1.019 1.025 1.075	– 15.8 12.4 15.0 16.7 16.2 13.8	– 49.8 55.8 59.5 63.3 62.2 58.9
8	Steel 08Kh18N10TN	293	272.4	555.7	2.040	54.0	67.8
9	Titanium Alloy (Ti-6A1-4V)	293	847	958	1.130	10.7	30.3
10	Titanium Alloy (Ti-2A1-1.5V)	293	622	740	1.190	–	42.4

T – test temperature; $\sigma_{0.2}$ – yield stress; σ_u – ultimate tensile strength;
δ – elongation; ψ – contraction

Table 2. Fracture toughness characteristics

No	Material	T	$K_Q^{max}(K_{Ic})$	K_{fc}	K_{fc}/K_Q^{max}	PSC	K_{fc}^1	K_{Id}	K_{fc}/K_I
		K	MPa√m	MPa√m	–		MPa√m	MPa√m	–
1	Steel 15Kh2MFA (I)	93	57.0	–	–	+	–	–	–
		123	61.0	42.0	0.69	+	–	–	–
		183	78.0	39.2	0.50	+	34.0	60.0	0.65
		213	127.0	57.2	0.45	–	40.0	68.0	0.84
		243	138.0	113.0	0.82	–	90.0	113.0	1.00
		293	137.0	121.0	0.88	–	–	122.0	0.99
		623	–	121.0	–	–	–	–	–
2	Steel 15Kh2MFA (II)	77	54.0	–	–	+	–	–	–
		293	68.0	40.0	0.59	+	27.1	48.0	0.83
		363	–	41.0	–	+	29.1	–	–
		393	103.0	58.0	0.56	+	49.0	–	–
		433	185.0	157.0	0.85	–	–	–	–
		473	254.0	150.0	0.59	–	–	–	–
		623	178.0	126.0	0.71	–	–	–	–
3	Steel 15KhMFAA	123	40.6	33.7	0.83	+	28.5	–	–
		183	55.7	45.4	0.81	+	38.6	–	–
		243	146.0	115.0	0.78	–	–	–	–
		293	149.0	120.0	0.80	–	–	–	–
4	Steel 10KhMFT	293	61.3	62.0	1.01	–	–	–	–
5	Steel 15Kh2NMFA	183	63.1	40.4	0.64	+	37.9	54.0	0.75
		213	110.7	60.3	0.54	–	50.3	68.0	0.89
		243	106.0	72.4	0.68	–	–	86.0	0.84
		293	129.4	129.4	1.00	–	–	117.0	1.10
6	Chrome–Molybdenum Steel (I)	77	68.9	–	–	+	–	67.3*	–
		123	80.0	60.3	0.75	+	48.0	71.8*	0.83
		153	146.9	80.2	0.54	–	–	75.6*	1.06
		183	149.2	–	–	–	–	–	–
		293	129.7	–	–	–	–	–	–
7	Chrome–Molybdenum Steel (II)	77	49.5	–	–	+	–	46.4*	–
		123	55.1	41.4	0.75	+	36.0	46.2*	0.90
		153	79.2	60.5	0.76	+	–	71.0*	0.85
		183	112.7	–	–	+	–	–	–
		213	144.0	–	–	–	–	–	–
		293	146.7	–	–	–	–	–	–
8	Steel 08Kh18N10TN	293	101.8	104.2	1.03	–	–	–	–
9	Titanium Alloy (Ti–6A1–4V)	293	119.0	106.0	0.89	–	–	–	–
10	Titanium Alloy (Ti–2A1–1.5V)	293	134.0	102.0	0.76	–	–	–	–

K_Q^{max} – stress intensity factor for maximum load; K_{fc}^1 –stress intensity factor for jump-like fatigue crack propagation; T – test temperature; K_{fc} – fatigue fracture toughness**;** K_{Id} – dynamic fracture toughness, PSC – plane strain conditions according to criterion (2). Asterisks indicate fracture toughness values obtained at crack arrest.

The results given here were obtained in testing 25 mm thick specimens with the stress ratio in a cycle R = 0.1.

When analyzing experimental findings, one should take into account the probability that there may be some difference in the properties, including fracture toughness, of the same steels. This can be attributed to the fact that the test samples had to been taken from various batches and might slightly differ in properties.

Figure 2 compares the static and a fatigue fracture toughness characteristic of the considered materials, shown in coordinates $K_{fc}/K_Q^{\max}$–$K_Q^{\max}$. This figure presents more data than Table 2 because we additionally used the results for specimens: of various sizes [30,35,37]; tested at various stress ratios [29,33,35,40]; for plastically prestrained specimens [41-43]; specimens of titanium alloy with different content of nitrogen and oxygen impurities [53]; and specimens of steel 20L after various service periods [56]. The results of investigation of the influence of these factors on fatigue fracture toughness will be discussed in the next report.

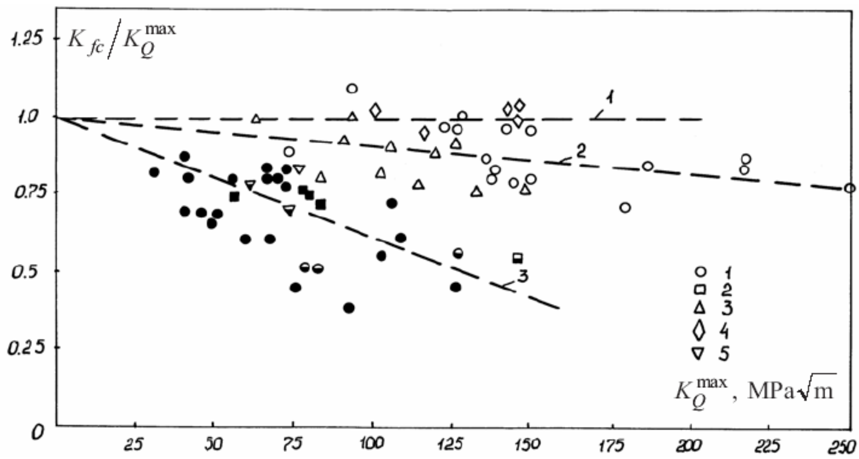

Figure 2. Comparison between fracture toughness characteristics under static and cyclic loading: (1) heat resistant steels; (2) chrome–molybdenum steels; (3) titanium alloys; (4) austenitic steel; (5) 20L steel. (Open and solid symbols indicate fulfilment or non-fulfilment of plane strain conditions, respectively; half-solid symbols correspond to the case where plane strain conditions were fulfilled in the K_{fc} determination and not fulfilled in the $K_Q^{\max}$ determination.)

Based on presented results (Fig. 2), we can conclude that fatigue fracture toughness of some steels may be considerably lower (up to 60%) than static fracture toughness. One should take this into account when estimating the limiting state of components with fatigue cracks.

The most significant decrease in fatigue fracture toughness is observed when final fracture of a specimen under cyclic loading occurs under plane strain conditions, irrespective of whether these conditions are attained by heat treatment of the material or by lowering the test temperature. Such considerable decrease of this characteristic takes place when plane strain conditions are fulfilled; in this case, the fracture toughness characteristics remain high.

All of the materials studied in the presented work, which exhibited a significant decrease in fatigue fracture toughness as compared with the static one, fall into the category of high strength cyclically softening steels, that are often used for manufacturing heavy duty components, designed for service under variable loading.

Distinctive features of deformation at the crack tip in cyclically softening steels [28] reveal that under cyclic loading in plane strain conditions, these steels exhibit an intensive localization of strains at the crack tip and a fracture mechanism changeover from slip bands shear to cleavage in the plane – perpendicular to the applied force.

In case of ductile fracture, the fatigue fracture toughness characteristics, which can be considered merely as conditional ones in this case, are equal to, or somewhat lower than static fracture toughness characteristics. Similar results were also reported by other scientists [49,50] for metals and alloys in a plastic state which, in most cases, belong to the category of cyclically hardening and cyclically stable materials.

The considerable scatter of experimental data can be attributed to high sensitivity of studied characteristics to the microstructure and properties of the material.

In view of results given in Fig. 2, the relationship between cyclic and static fracture toughness characteristics can be described as

$$K_{fc} \Big/ K_Q^{\max} = -bK_Q^{\max} \tag{4}$$

where *b* is the parameter representing the intensity of a decrease in fatigue fracture toughness with increasing $K_Q^{\max}$. According to the results (Fig. 2), the mean value of *b* is about $(4–5)\cdot10^{-3}$ in case of plane strain fracture and about $1\cdot10^{-3}$ in ductile fracture.

2. SPECIAL FEATURES OF THE TRANSITION FROM STABLE TO UNSTABLE FATIGUE CRACK PROPAGATION

Final fracture of a specimen with a fatigue crack may be preceded by brittle crack jumps [10,11,23,27]. Data from Table 2 show that jump-like crack propagation is observed in plane strain conditions or close to them. Stress intensity factor values of jump-like fatigue crack propagation K_{fc}^1 can be much lower than K_{fc} or $K_Q^{\max}$.

It was demonstrated [27,31,33] that brittle crack jumps are possible only if the stress intensity factor exceeds a certain value, that is typical for considered material. These values of the stress intensity factor are taken as K_{fc}.

Figure 3 compares K_{fc}^1 and K_{fc} values for studied materials. It is evident that K_{fc}^1 is approximately 20% lower than K_{fc}, and scattering of results is relatively small. It was found [46] that scatter in fatigue fracture toughness characteristics is considerably smaller than that in static fracture toughness characteristics. It follows from Fig. 3 that K_{fc}^1 can be predicted by the properly corrected relationship (4). In view of this, K_{fc}^1 can be considered as a characteristic, which governs the transition from stable to unstable fatigue crack propagation [11,27].

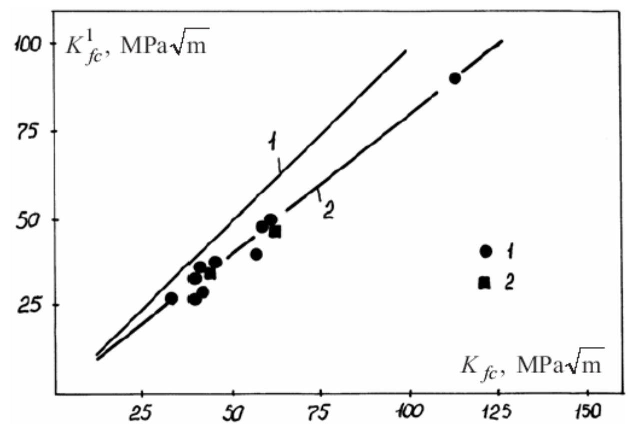

Figure 3. Comparison of K_{fc}^1 and K_{fc} for heat resistant (1) and chrome–molybdenum (2) steels

Figure 4 shows fatigue crack growth rate in coordinates $da/dN–K_{max}$ for heat resistant steels at room temperature and various stress ratios in a cycle $R = K_{\min}/K_{\max}$ [33]. As it is evident from Fig. 4 and Table 2, the first of these steels undergoes ductile fracture at room temperature, while the second one, which was specially heat treated, exhibits fracture under plane strain conditions. Specimens of steel 15Kh2MFA (I) fail completely at the first crack jump, whereas the final fracture of specimens of steel 15Kh2MFA (II) is preceded by several crack jumps.

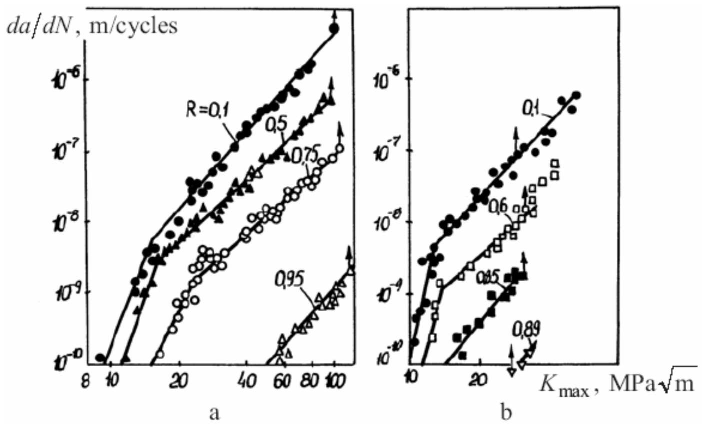

Figure 4. Fatigue crack growth rate vs. K_{max} for steels 15Kh2MFA (I) (a), and 15Kh2MFA (II) (b), at various cycle stress ratios. Symbols with arrows indicate onset of unstable (jump-like) fatigue crack propagation.

An increase in the stress ratio has an insignificant effect on K_{fc}^1 for both steels under study, but it leads to a considerable decrease in critical fatigue crack growth rate, whereby the transition from stable to unstable fatigue crack propagation occurs. In this context, at high stress ratios the risk of sudden brittle fracture of materials, similar to the embrittled steel 15Kh2MFA (II), rises dramatically because the process of unstable jump-like fatigue crack propagation can start in the near-threshold region immediately after crack initiation, and in this case, the crack size will be very small when the limiting state is reached.

Figure 5 shows a detailed illustration of the pattern of fatigue crack propagation in steel 15Kh2NMFA at 183 K, which precedes the final fracture of a specimen [27].

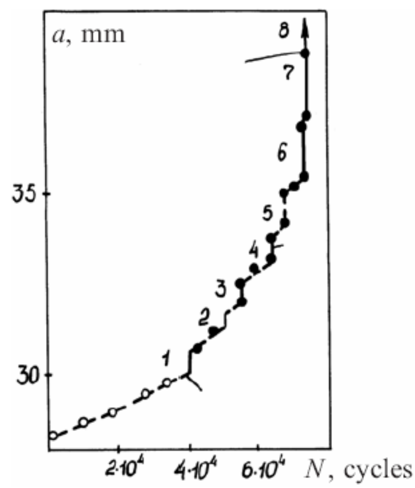

Figure 5. Fatigue crack growth kinetics for 15Kh2NMFA steel at 183 K; 1–8 crack jump number

The mechanism of unstable fatigue crack propagation in the embrittled heat resistant steel 2 (Table 1) at room temperature, considering the influence of the stress ratio and specimen dimensions, has been studied comprehensively, [37].

Figure 6 (a,b,c) shows dependences of the number of cycles in-between crack jumps, ΔN^i, the size of a brittle crack jump, $\Delta a_c^{\,i}$, and the dimensions of stable crack increment zones between jumps, Δa^i, on the stress intensity factor $K_{fc}^{\,i}$. Figure 6 (d) shows ΔN^i as a function of $(1 - R)K_{fc}^{\,i}$. The dashed line in Fig. 6b represents the dependence of the plastic zone size $2r_y$, as calculated by formula (3), on the respective stress intensity factors.

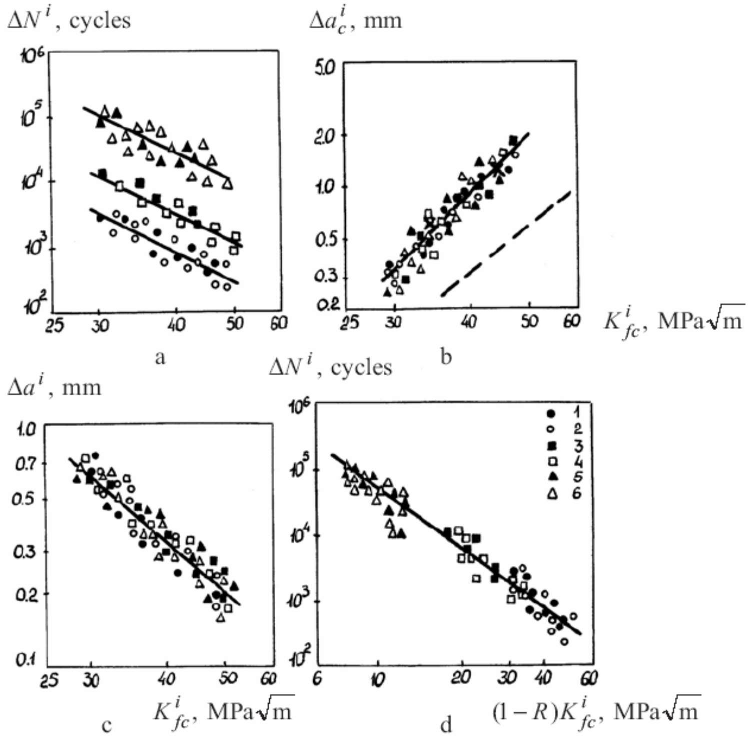

Figure 6. The functions $\Delta N^i - K_{fc}^{\,i}$ (a), $\Delta a_c^{\,i} - K_{fc}^{\,i}$ (b), $\Delta a^i - K_{fc}^{\,i}$ (c), $\Delta N^i - (1 - R)K_{fc}^{\,i}$ (d) for steel 15Kh2MFA (II), specimen thickness 25 mm (1, 3, 5) and 150 mm (2, 4, 6). (1, 2) R = 0.1; (3, 4) R = 0.35; (5, 6) R = 0.75

It is evident that the dimensions of brittle jumps and of stable crack propagation zones between such jumps are independent of the stress ratio and specimen size, and are uniquely determined by $K_{fc}^{\,i}$, i.e., by the maximum value of the stress intensity factor in a cycle wherein these jumps occur. At the same time, the number of cycles of stable crack propagation between jumps is determined by the stress intensity factor range $\Delta K_{fc}^{\,i} = (1 - R)K_{fc}^{\,i}$ (Fig. 6d). The dimensions of brittle jumps appreciably exceed the plastic zone size as calculated by formula (3).

Figure 7 compares the values of Δa_c and $2r_y$ calculated by formula (3) for chrome–molybdenum steels 6 and 7. In this case, the Δa_c value is also much higher than $2r_y$ [39].

It is demonstrated [31,49,50] that better agreement between the calculated and experimental data can be achieved if the cyclic proportionality limit $\sigma_p^{\,c}$ is used instead of yield stress $\sigma_{0.2}$ in formula (3). For cyclically softening materials, i.e., the category to which most of the materials under consideration belong to, this characteristic is substantially lower than yield stress $\sigma_{0.2}$.

In such a case, the value of $2r_y = a_c$ determines the size of the crack-tip zone, damaged in cyclic loading. The characteristics that govern the elastic–inelastic transition of material deformation behaviour under static and cyclic loading are compared in [32,49,50]. In view of the aforesaid, the function $a_c^i = f(K_{fc}^i)$ for plane strain conditions can be written as

$$a_c^i = \frac{1}{3\pi}\left(\frac{K_{fc}^i}{\sigma_p^c}\right)^2 \tag{5}$$

The calculation of a_c^i for steel 2, performed [37] using an experimental value of σ_p^c for this steel, revealed good agreement between calculated ("+" signs in Fig. 6b) and experimental data. The crack growth rate during crack jumps was studied using acoustic emission [36]. It was found that this characteristic reaches high values and can differ essentially for various materials.

Figure 8 shows the mean crack growth rate during a brittle jump, V_{cr}, as a function of jump length, Δa_c, for heat resistant steels 2 (at 293 K) and 5 (at 183 K).

In [11,26,31] attempts were made to construct a model of transition from stable to unstable fatigue crack propagation. The model proposed in [26,31] is based on the following assumptions:

- a material at the crack tip is damaged under cyclic loading and the value K_{fc}^i decreases with increasing number of loading cycles;
- local fracture (jump) at the crack tip does not lead to complete fracture of a specimen if the fracture toughness of the material outside the damage zone (considering crack growth rate during crack jumps) is higher than the value of the stress intensity factor in the crack as it leaves the damage zone;
- if the stress intensity factor in the crack, leaving the damaged zone, is higher than the fracture toughness of the material outside this zone, final fracture will occur.

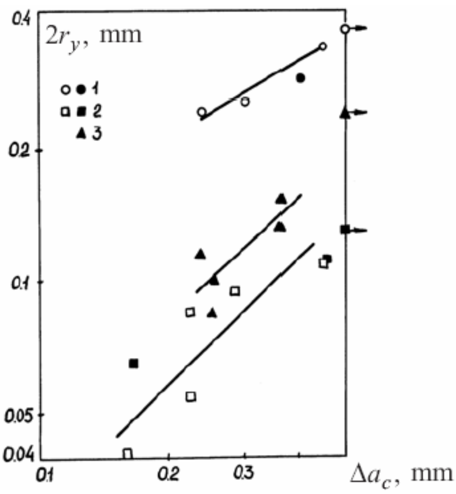

Figure 7. Relationship between $2r_y$ and Δa_c for chrome–molybdenum steels No. 6 at 123 K (1), No. 7 at 123 K (2), and 153 K (3). (Open and solid symbols correspond to crack jump inside a specimen and a crack reaching the side surfaces, in respect; symbols with arrows correspond to final fracture of specimen.)

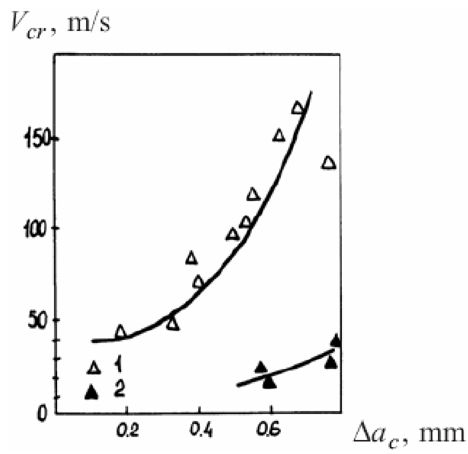

Figure 8. Dependence of mean crack growth rate during a jump on the jump length for steels 15Kh2MFA (II) (1) and 15Kh2NMFA (2)

Figure 9 presents a scheme of the transition from stable to unstable fatigue crack propagation, which corresponds to the considerations above. In this figure, $K_Q^{\max}$ is the static fracture toughness of an intact material; K_D is the fracture toughness of the material as the crack leaves the damaged zone allowing for crack growth rate. The value of K_D can differ from that of $K_Q^{\max}$ due to both the influence of crack growth rate and the change in properties of the material outside the local damaged zone, which occurs in the course of cyclic loading.

According to results given in Fig. 6d, the function $N = f(K_{fc}^{i})$, relating the number of loading cycles, prior to crack jump, to the stress intensity factor, can be presented as

$$N = A\left[(1-R)K_{fc}^{i}\right]^{n} \tag{6}$$

where A and n are constants.

When the function $N = f(K_{fc}^{i})$ corresponds to curve 1 in Fig. 9, the material will fail at the first crack jump, but when this function corresponds to curve 2, final fracture will be preceded by several crack jumps. In this case, the fatigue fracture toughness K_{fc} will fit the stress intensity factor value, which occurs at the last crack jump.

According to the scheme shown in Fig. 9, the quantity K_{fc} will be close to (somewhat below) K_D. If the difference between $K_Q^{\max}$ and K_D depends mainly on crack growth rate and fracture toughness in dynamic loading is lower than in static loading, then the fatigue fracture toughness K_{fc} is likely to be close to the dynamic fracture toughness $K_{\mathrm{I}d}$ of the material.

Figure 10 compares fracture toughness characteristics of heat resistant and chrome–molybdenum steels under cyclic and dynamic loading. One can see a good correlation between K_{fc} and $K_{\mathrm{I}d}$. This suggests that fatigue fracture toughness characteristics of materials, similar in properties to those studied herein, can be judged from dynamic fracture toughness characteristics and vice versa. Based on the model formulated above, other possible cases of the relationship between fracture toughness characteristics under static, dynamic, and cyclic loading have been discussed in [26,31].

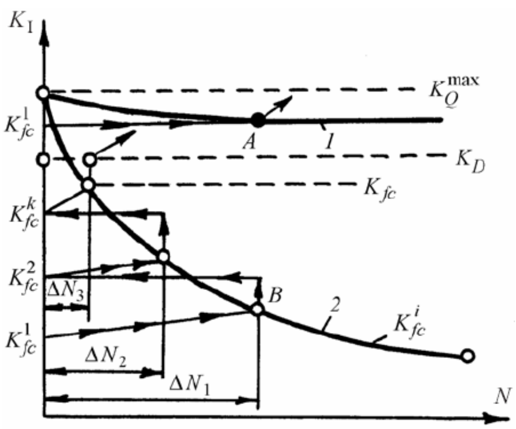

Figure 9. Schematic representation of unstable fatigue crack growth. (Points A and B correspond to crack jumps.)

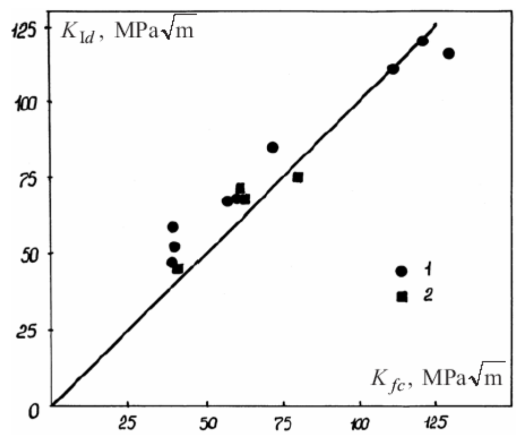

Figure 10. Comparison between fracture toughness characteristics of heat resistant (1) and chrome–molybdenum (2) steels under dynamic and cyclic loading

CONCLUSIONS

We have demonstrated that fatigue fracture toughness characteristics of steels in an embrittled state due to prior heat treatment or low test temperature can be considerably lower than static fracture toughness characteristics. This finding should be taken into account when formulating the limiting state conditions for cracked components.

The conditions for a transition from stable to unstable crack propagation have been studied in view of the influence of: test temperature, stress ratio in a cycle, and specimen dimensions. A model of unstable fatigue crack propagation and final fracture under cyclic loading has been substantiated.

REFERENCES

1. Troshchenko, V.T., Pokrovskii, V.V., *Investigation of the regularities in fatigue fracture of steels Kh18N10T, Kh16N6, and 15G2AFDps and aluminum alloy AMg6 at low temperatures*, Steels and Alloys for Cryogenic Engineering [in Russian], Naukova Dumka, Kiev, pp. 157-164. (1977)
2. *Methodical Recommendations. MR-95. Determination of Crack Growth Resistance (Fracture Toughness) Characteristics under Cyclic Loading* [in Russian], International Institute for Safety of Complex Engineering Systems, Moscow, pp. 83-180. (1995)
3. Ivanova, V.S., *A concept of fatigue fracture toughness*, Fatigue Fracture Toughness of Metals and Alloys [in Russian], Nauka, Moscow, pp. 5-19. (1981)
4. Yokobori, T., Aizawa, T., *A proposal for the concept of fatigue fracture toughness,* Rep. Res. Inst. Str. Fract. Mater., 6, pp. 19-23. (1970)
5. Ivanova, V.S., Kudryashov, V.G., *A method for determination of fracture toughness (K_{Ic}) from fatigue test results*, Probl. Prochn., No. 3, pp. 17-19. (1970)
6. Yarema, S.Ya., Kharish, E.L., *The function of duration of the crack development period under repeated impact reloading*, Probl. Prochn., No. 8, pp. 28-32. (1970)
7. Kawasaki, T., Nakanishi, S., Sawaki, Y., *Fracture toughness and fatigue crack propagation in high strength steel from room temperature to 180°C,* Eng. Fract. Mech., 7, pp. 465-472. (1975)
8. Satoh, K., Toyoda, M., Nayma, M., *Transition behaviors to cleavage fracture of low-toughness material with fatigue crack growth,* J. Zosen Kyokai Ronbunshu, 146, pp. 490-496. (1979)
9. Clark, W.G., *Some problems in the application of fracture mechanics*, ASTM STP 743, pp. 269- 287. (1980)
10. Kitsunai, Y., *Fractographic study of fatigue crack propagation at low temperature*, J. Soc. Mater. Sci. (Jap.), 34 (381), pp. 50-55. (1985)
11. Kitsunai, Y., *Ductile-brittle transition behavior of structural steel in fatigue crack growth under low temperature*, Trans. Jap. Soc. Mech. Eng., A52 (476), pp. 896-901. (1986)
12. Sawaki, Z., Tada, S., Hashimoto, S., Kawasaki, T., *Fatigue fracture toughness and crack propagation rate,* Int. J. Fract., 35, pp. 125-137. (1987)
13. Ando, K., Ogura, N., Nishioka, T., *Effect of grain size on fatigue fracture toughness and plastic zone size attending fatigue crack growth*, Proc. 2nd Int. Conf. on Mechanical Behavior of Materials, Boston, U.S.A., pp. 533-537. (1976)
14. Smolentsev, V.I., Kudryashov, V.G., *A procedure of comparing the K_{Ic} values obtained under static and cyclic loading*, Zavod. Lab., No. 6, pp. 734-738. (1972)
15. Kudryashov, V.G., *Fatigue fracture toughness K_{If}*, Fiz.-Khim. Mekh. Mater., No. 5, pp. 110-112. (1978)
16. Yarema, S.Ya., Ostash, O.P., *On fracture toughness of materials under cyclic loading*, Fiz.-Khim. Mekh. Mater., No. 5, pp. 112-114. (1978)
17. Ivanova, V.S., Maslov, L.I., Botvina, L.P., *Fractographic features and fracture toughness of steel under cyclic loading*, Probl. Prochn., No. 2, pp. 37-41. (1972)

18. Malkov, A., *The influence of hydrogen on fracture toughness and crack growth in titanium alloys*, Advances in Fracture Resistance in Materials, Vol. 2, Tata McGraw-Hill Publishing Company Ltd., New Delhi, pp. 613-619. (1996)
19. Roman, I., Ono, K., *Model for fracture toughness alteration due to cyclic loading*, Int. J. Fract., 19, pp. 67-80. (1992)
20. Troshchenko, V.T., Pokrovskii, V.V., *A study of mechanisms of fatigue and brittle fracture of steel 15G2AFDps at low temperature*, Probl. Prochn., No. 3, pp. 11-17. (1973)
21. Troshchenko, V.T., Pokrovskii, V.V., Prokopenko, A.V., *Investigation of the fracture toughness of constructional steels in cyclic loading*, Advances in Research on the Strength and Fracture of Materials, M. Taplin (Ed.), 3B, pp. 683-686. (1977)
22. Troshchenko, V.T., Prokopenko, A.V., Pokrovskii, V.V., *A study of fracture toughness characteristics under cyclic loading. Part 1*, Probl. Prochn., No. 2, pp. 8-15. (1978)
23. Troshchenko, V.T., Prokopenko, A.V., Pokrovskii, V.V., *A study of fracture toughness characteristics under cyclic loading. Part 2*, Probl. Prochn., No. 3, pp. 3-8. (1978)
24. Troshchenko, V.T., Pokrovskii, V.V., Prokopenko, A.V., *Cyclic loading and fracture toughness of steels*, Fatigue Eng. Mater. Struct., 1, No. 2, pp. 247-266. (1979)
25. Troshchenko, V.T., Pokrovskii, V.V., Skorenko, Yu.S. et al., *The influence of cyclic loading on crack growth resistance characteristics of steels. Part 1*, Probl. Prochn., No. 11, pp. 3-10 . (1980)
26. Troshchenko, V.T., Pokrovskii, V.V., *The influence of cyclic loading on crack growth resistance characteristics of steels. Part 2*, Probl. Prochn., No. 12, pp. 14-17. (1980)
27. Troshchenko, V.T., Yasnii, P.V., Pokrovskii, V.V., *Investigation of the regularities in unstable crack propagation under cyclic loading*, Probl. Prochn., No. 6, pp. 3-7. (1980)
28. Pokrovskii, V.V., *On prediction of the influence of load cycling on the brittle fracture resistance of cracked structural alloys*, Probl. Prochn., No. 9, pp. 35-41. (1981)
29. Troshchenko, V.T., Yasnii, P.V., Pokrovskii, V.V., Popov, A.A., *The influence of temperature and loading asymmetry on cyclic crack growth resistance of steel 15Kh2NMFA*, Probl. Prochn., No. 10, pp. 3-7. (1981)
30. Troshchenko, V.T., Yasnii, P.V., Pokrovskii, V.V. et al., *The effect of specimen dimensions on crack growth resistance of pressure-vessel heat-resistant steels*, Probl. Prochn., No. 10, pp. 3-11. (1982)
31. Troshchenko, V.T., Pokrovskii, V.V., *Fracture toughness of structural alloys under cyclic loading. Part 1*, Probl. Prochn., No. 6, pp. 3-9. (1983)
32. Troshchenko, V.T., Pokrovskii, V.V., *Fracture toughness of structural alloys under cyclic loading. Part 2*, Probl. Prochn., No. 6, pp. 10-15. (1983)
33. Troshchenko, V.T., Yasnii, P.V., Pokrovskii, V.V., *Prediction of the influence of loading cycle asymmetry on the fatigue fracture toughness of structural alloys*, Probl. Prochn., No. 11, pp. 30-35. (1985)
34. Troshchenko, V.T., Yasnii, P.V., Pokrovskii, V.V., *The influence of test temperature on crack growth resistance of heat-resistant structural steels*, Fiz.-Khim. Mekh. Mater., No. 1, pp. 98-106. (1986)
35. Pokrovskii, V.V., Kaplunenko, V.G., Zvezdin, Yu.I., Timofeev, B.T., *The effect of loading cycle asymmetry on cyclic crack growth resistance characteristics of heat-resistant steels*, Probl. Prochn., No. 11, pp. 8-13. (1987)
36. Yasnii, P.V., Pokrovskii, V.V., Strizhalo, V.A., Dobrovol’skii, Yu.V., *A study of the velocity of brittle crack jumps using an acoustic emission method*, Probl. Prochn., No. 11, pp. 32-36. (1987)
37. Troshchenko, V.T., Pokrovskii, V.V., Kaplunenko, V.G., Timofeev, B.T., *The influence of specimen dimensions and cycle asymmetry on the regularities of unstable crack propagation under cyclic loading*, Probl. Prochn., No. 3, pp. 8-12. (1987)
38. Pokrovskii, V.V., Tokarev, P.V., Yasnii, P.V. et al., *The effect of test temperature on crack growth resistance of pressure-vessel steels with various impurity content*, Probl. Prochn., No. 1, pp. 11-16. (1988)

39. Troshchenko, V.T., Pokrovskii, V.V., Yasnii, P.V. et al., *The influence of temperature on crack growth resistance characteristics of steel of various strength level*, Probl. Prochn., No. 9, pp. 8-13. (1988)
40. Troshchenko, V.T., Pokrovskii, V.V., Yarusevich, V.L. et al., *Investigation of the effect of temperature on crack growth resistance of steel and welded joint*, Probl. Prochn., No. 2, pp. 8-14. (1988)
41. Yasnii, P.V., Pokrovskii, V.V., Shtukaturova, A.S. et al., *A study of the influence of plastic prestraining on mechanical properties and microstructure of structural steel*, Probl. Prochn., No. 9, pp. 41-45. (1988)
42. Troshchenko, V.T., Pokrovskii, V.V., Yasnii, P.V. et al., *The effect of single plastic prestraining on crack growth resistance*, Probl. Prochn., No. 12, pp. 9-14. (1988)
43. Troshchenko, V.T., Pokrovskii, V.V., Yasnii, P.V. et al., *The influence of single plastic prestraining on brittle fracture resistance*, Fiz.-Khim. Mekh. Mater., No. 6, pp. 3-12. (1989)
44. Troshchenko, V.T., Yasnii, P.V., Tokarev, P.V., Timofeev, B.T., *The influence of cyclic plastic prestraining on crack growth resistance*, Probl. Prochn., No. 11, pp. 14-20. (1989)
45. Troshchenko, V.T., Pokrovskii, V.V., *Fatigue fracture toughness of steels*, Engineering Against Fatigue, Balkema, Rotterdam, pp. 269-276. (1999)
46. Troshchenko, V.T., Yasnii, P.V., Pokrovskii, V.V., Podkol'zin, V.Yu., *The problem of scatter in fracture toughness data*, Fatigue Fract. Eng. Mater. Struct., 16, No. 3, pp. 327-334. (1993)
47. Troshchenko, V.T., *Stable and Unstable Fatigue Crack Propagation in Metals*, Handbook of Fatigue Crack Propagation in Metallic Structures (Ed. A. Carpinteri), Elsevier (1994)
48. Troshchenko, V.T., Pokrovskii, V.V., Yasnii, P.V., *Unstable fatigue crack propagation and fatigue fracture toughness of steel*, Fatigue Fract. Eng. Mater. Struct., 17, No. 9, pp. 991-1001. (1994)
49. Troshchenko, V.T. (Ed.), *Cyclic Strains and Fatigue of Metals*, [in Russian], Vol. 2, Naukova Dumka, Kiev. (1985)
50. Troshchenko, V.T., Pokrovskii, V.V., Prokopenko, A.V., *Crack Growth Resistance of Metals under Cyclic Loading* [in Russian], Naukova Dumka, Kiev. (1987)
51. Troshchenko, V.T., Pokrovskii, V.V., Yasnii, P.V., Kaplunenko, V.G., *Limiting State of Metals with Cracks* [in Russian], Preprint, Institute of Problems of Strength of the Academy of Sciences of the Ukr.SSR, Kiev. (1988)
52. Prokopenko, A.V., Znachkovskii, O.Ya., Izarov, M.A., *On determination of fracture toughness characteristics in impact bending with oscillography*, Probl. Prochn., No. 7, pp. 47-51. (1978)
53. Troshchenko, V.T., Pokrovskii, V.V., Yarusevich, V.L. et al., *The influence of interstitial impurities on crack growth resistance of ductile titanium alloys*, Probl. Prochn., No. 8, pp. 23-36. (1991)
54. Pokrovskii, V.V., Yasnii, P.V., Yarusevich, V.L. et al., *A study of the crack growth resistance of a welded joint of VT6S titanium alloy*, Probl. Prochn., No. 3, pp. 37-40. (1988)
55. Tanaka, K., Nishijima, S., Matsuoka, S., *Low- and high-cycle fatigue properties of various steels specified in JIS for machine structural use*, Fatigue Fract. Eng. Mater. Struct., 4, No. 1, pp. 97-108. (1981)
56. Pokrovskii, V.V., Yasnii, P.V., Kostenko, N.A. et al., *The influence of accumulated operation time on crack growth resistance of the rolling stock freight car coupler carrier*, Probl. Prochn., No. 2, pp. 28-32. (1988)

FRACTURE TRANSFERABILITY PROBLEMS AND MESOFRACTURE

Guy Pluvinage, Laboratoire de Fiabilité Mécanique, ENIM-Université de Metz, France

INTRODUCTION

Scale effects were first mentioned by Leonardo da Vinci (1452-1519), who performed tensile tests in the following manner: a bucket was suspended from a beam on an iron wire (thread) the length of two "brasses" (3.248 m), Fig. 1. Fine sand flowing from a hopper filled this bucket through a narrow gap. When the total weight of sand plus the bucket overcame the load resistance of the iron thread, failure occurred and the bucket fell into a soil hole.

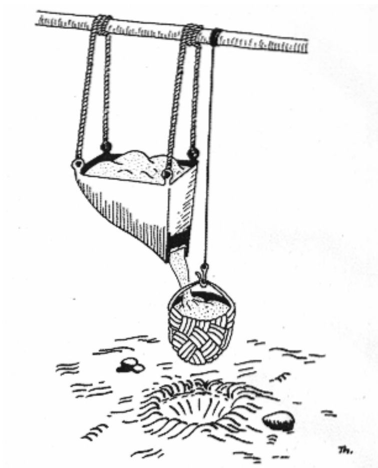

Figure 1. Description of device used by Leonardo daVinci for tensile tests on iron threads

The total weight and place of fracture were noted. The experiment was repeated with iron threads of decreasing length (one whole brasses length, half a length, quarter of length, etc…). Leonardo da Vinci noticed that fracture load increased with decreasing thread length and was the first who mentioned the phenomenon of scale effect, but provided no explanation.

Scale effects are one of the aspects of general problems of transferability. This word includes all the influence on mechanical properties, such as fracture toughness and fracture strength, of geometrical and mechanical parameters. More precisely, these parameters are generally, the size, width, ligament size, constraint, and notch effects. The main consequence of these effects is the fact that mechanical properties cannot be considered as intrinsic to material but depend on applied conditions. Consequently, the use of results obtained on small laboratory specimens to large structures remains problematic. This is a problem for engineering use, because it seems not appropriate to apply "one parameter" corrected eventually with empirical formulae.

This lecture presents the effects of size, ligament size, and notch radius on fracture toughness and fracture resistance, and the state of the art of scaling laws proposed in literature for overcoming these effects.

One promising way to take into account globally all these effects is mesofracture. This approach, as a developing part of mesomechanics is based on two principles: (a) fracture is basically a non-local approach; (b) stress gradient plays an essential role in the real state of stress. Consideration of transferability problem with a non-local approach requires defining an average value in a "mesovolume," called the fracture process volume. A particular method called the "volumetric method" is described. This concept, relatively new, supposes that the mechanical state of a structure can be examined in an individual specific volume, having a size greater than the microstructure unit and less than the size of the structure (meso = between). The stress state in each "mesovolume" depends on the stress state of adjacent volumes. All the theories emanating from material science and engineering developed in the last 30 years consist mainly of methods "micro/macro" and lead to mechanical properties that are intrinsic to the material and result from microstructural organisation. The mesovolume can be considered as the independent scale operator and can be the link between nano- and microstructures.

Transferability problems attracted new interest with development of nanostructure materials. Nanomaterials offer important possibilities for specific applications and modified the principles of material choice and design. In addition to amazing magnetic and optic properties, these materials exhibit a broad range of extraordinary mechanical properties such as superplasticity at low temperature, ultra high hardness and abrasiveness, high tensile and compressive strength, significant fracture and fatigue resistance.

The achieved development of such interesting materials has positioned the crucial question why mechanical properties are so different from the macro or micro level to nanometre dimensions. This problem, like the more general problem of scale effect, is not solved yet and represents a serious challenge to the development of nanomaterials and general knowledge in material sciences.

Large potential application is expected by the development of bi-materials. Multifunctional materials are based on the concept of enhanced bulk properties, or barrier and surface characteristics for higher performance. This is a typical example where the elementary volume is an addition of different materials or different macrostructures, and interactions will be in this case of major importance.

1. PHENOMELOGICAL ASPECTS OF SIZE EFFECTS

Phenomenological aspects of size effect will be presented on smooth and cracked specimens. For smooth specimens, they are studied according to the loading mode (tension, bending, torsion, and internal pressure). For cracked and notched specimens, the presentation is divided into brittle and ductile fracture.

1.1. Scale effects on yield stress for smooth specimens

1.1.1. Scale effects in tension

Richards [1] has performed a series of tests on smooth specimens of mild steel C 1020 with three diameters (3.175 mm, 12.7 mm, and 31.75 mm). He has plotted experimental results as upper yield stress versus volume, and found a strong scale effect associated with an increasing scatter for small specimens (Fig. 2). Analysing the results by the Weibull weakest link theory, he has found that yield stress σ_y is a power function of specimen volume,

$$\sigma_y = \frac{C_1}{V^{1/58}} \tag{1}$$

where C_1 is a constant, V is specimen volume, 58 corresponds to Weibull modulus value.

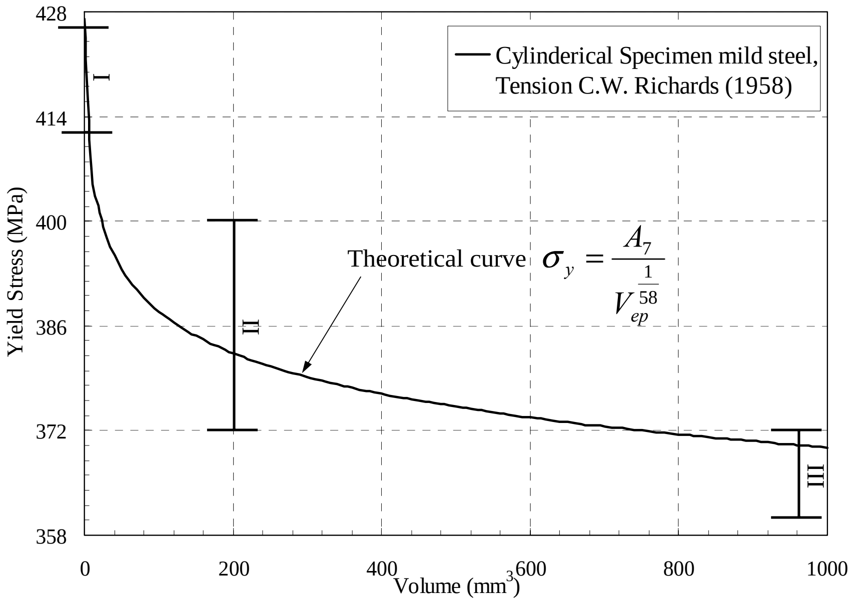

Figure 2. Scale effect in tension, experiments of Richards [1], explained by Weibull theory

1.1.2. Scale effects in bending

Richards [1] also performed a series of four point bending tests on a beam of mild steel C 1020. Beams of rectangular section had height W varying from 4.0 to 25.4 mm (scale factor 6.35). In these tests, span Se, thickness B and the distance between upper and lower actions e, are proportional to the height (Se = 11.6W, B = 0.5W, and e = 2.9W). Decreasing of yield stress in bending with scale factor is presented in Fig. 3.

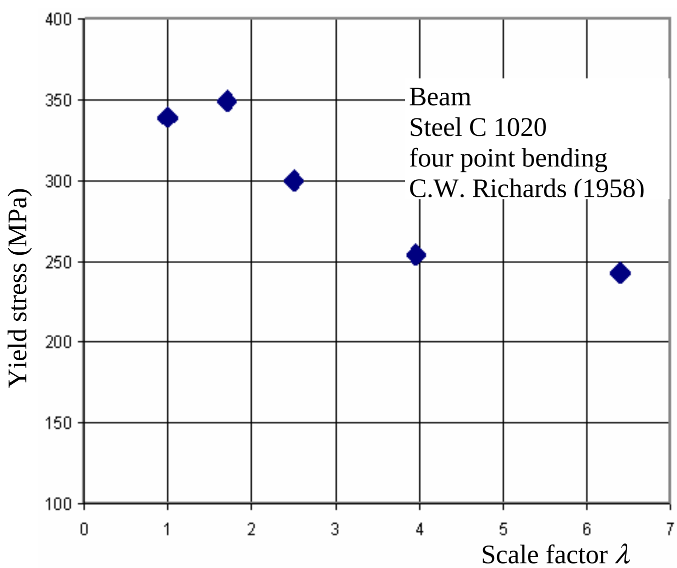

Figure 3. Scale effects in bending, experiments of Richards [1]

1.1.3. Scale effects in torsion

Morrison [2] made torsion tests on a cylindrical steel specimen with a diameter ranging from 2.56 to 25.4 mm (scale factor 9.83). Experimental results, presented as the ratio of yield stress in torsion and in tension vs. diameter (Fig. 4), exhibited a strong decrease. Malmberg [3] has explained this effect by volumetric method. He assumed that plastification occurs only when yield stress is reached in a layer of critical thickness.

Plasticity criterion can be written as:

$$\frac{1}{A_{ef}}\int_{r-d_{ef}}^{r} 2\pi r dr \le \tau_y \tag{2}$$

where r is the specimen radius and τ_y is the shear yield stress ($\tau_y = \sigma_y/\sqrt{3}$ according to von Mises; $\tau_y = \sigma_y/2$ according to Tresca) and A_{ef} the surface layer of thickness d_{ef}.

By integrating Eq. (2) one can get

$$\frac{1}{A_{ef}}\int_{r-d_{ef}}^{r} 2\pi r dr = \tau_{\max}\frac{\pi r^2}{A_{ef}}\frac{2}{3}\left[1-\left(1-\frac{d_{ef}}{r}\right)^3\right] \tag{3}$$

The apparent shear yield stress $\tau_{\max}$ is given by

$$\frac{\tau_{\max}}{\tau_y} = a^* \frac{3/2}{\left[1-\left(1-\dfrac{d_{ef}}{r}\right)^3\right]} \tag{4}$$

with $a^* = A_{ef}/\pi r^2$. Relation between shearing and tensile yield stress produces:

$$\frac{\tau_{\max}}{\sigma_y} = \frac{3\tau_y}{2\sigma_y}\frac{a^*}{\left[1-(1-a^*)^{3/2}\right]} \tag{5}$$

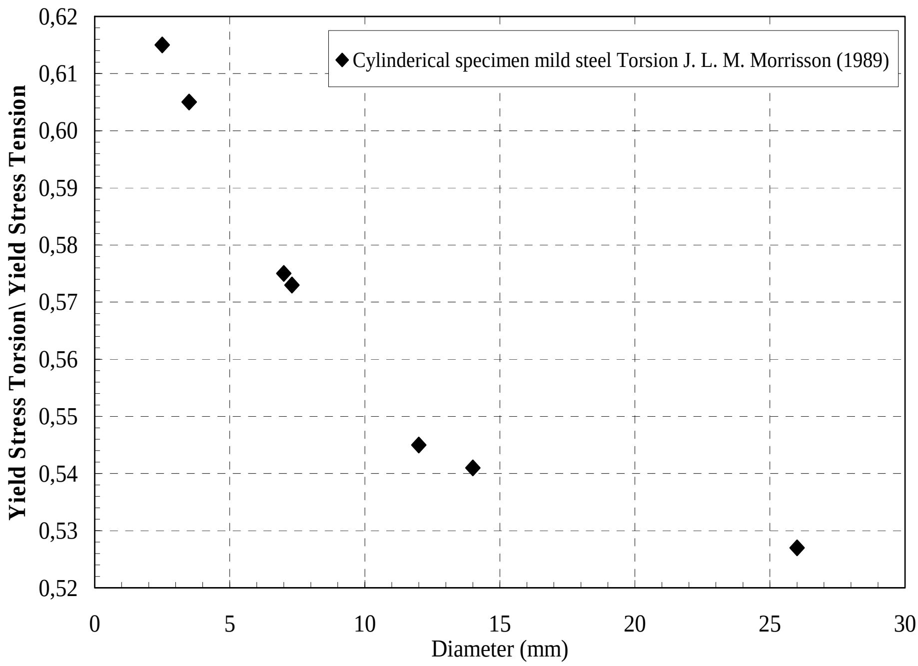

Figure 4. Scale effects in torsion, experiments performed by Morrison [2]

Using results from Morrison, Malmberg computed values of A_{ef} and d_{ef} (Table 1).

Table 1. Values of A_{ef} and d_{ef} computed by Malmberg from Morrison's results

	A_{ef} (mm^2)	d_{ef} (mm)
Von Mises	$1.3\cdot10^{-3}$	$15\cdot10^{-2}$
Tresca	$4.2\cdot10^{-3}$	$56\cdot10^{-3}$

1.1.4. Scale effects on tube submitted to internal pressure

Cook [4] has studied scale effect on yield stress of pipe under internal pressure. He used three types of mild steels (designated A, B and C) and pipes of 6 different diameters. Ratio of external and internal diameter was kept constant and equal to 3. Assuming that there is no scale effect in tension he has plotted pressure at yield stress over tensile yield stress versus internal pipe diameter. Noticeable scale effect Cook has attributed to the existence of a critical layer, in which plasticity occurs when yield stress is overcome.

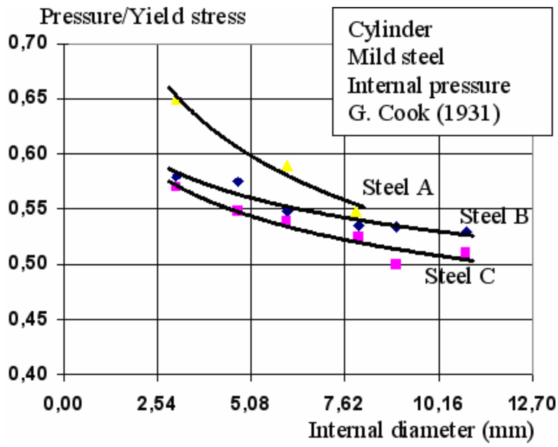

Figure 5. Scale effects in cylinder exposed to internal pressure, experiments by Cook [4]

1.2. Scale effect on fracture stress of smooth specimens

Chechulin [5] has made tests on 7 different Soviet steels with cylindrical specimens of diameters 1.5; 3; 6; 15 and 20 mm. He has found size effects on ultimate strength and fracture strain, but the size effect on the relative fracture area reduction Ψ is more pronounced (Fig. 6).

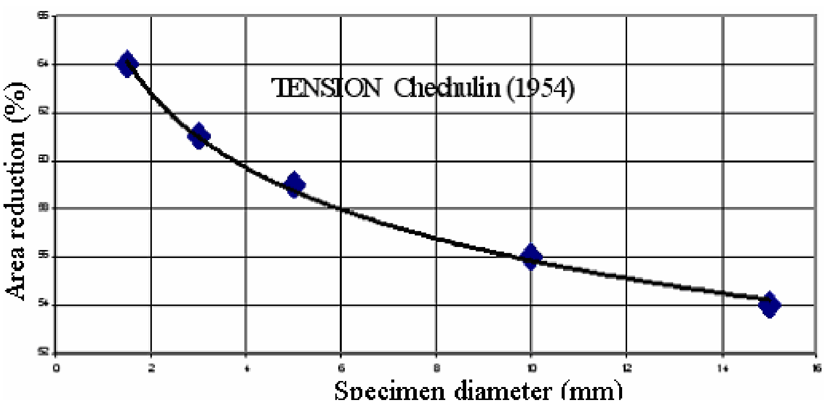

Figure 6. Scale effect on ductile fracture area. Experiments by Chechulin [5]

Matic, Kirby and Jolles [6] have noticed that necking at plastic instability is of similar geometrical evolution. If L_s is the length of the specimen necking and D the diameter, the following relationship can be established:

$$\frac{L_s}{D} = C_2 \tag{6}$$

where C_2 is a constant.

If L is the current length of the specimen, the elongation is given by:

$$\Delta L = \varepsilon L = \varepsilon_f (L - L_s) + \varepsilon_s L_s$$

where L_s is the length at necking, ε_s is the stress at necking and ε_f is the fracture strain. Rearranged, this equation obtains the form:

$$\varepsilon = \varepsilon_f - \frac{L}{L_s}(\varepsilon_s - \varepsilon_f) \tag{7}$$

$$\varepsilon = \varepsilon_f - \frac{DC_1}{L_s}(\varepsilon_s - \varepsilon_f) \tag{8}$$

$$\varepsilon = c_1 - c_2 \frac{\sqrt{S}}{L} \tag{9}$$

with $c_1 = \varepsilon_f$, and $c_2 = C_2\sqrt{4/\pi}(\varepsilon_s - \varepsilon_f)$.

The fact that it is necessary to keep for different specimens the ratio $\sqrt{S}/L$ constant has been introduced in some standards.

1.3. Scale effects for cracked or notched specimens

1.3.1. Scale effects for brittle fracture

Sinclair and Chambers [7] performed fracture tests on brittle materials in plane strain conditions (Fig. 7) and on ductile materials in plane stress conditions (Fig. 8) and found that the classical linear elastic fracture mechanics cannot predict fracture stress and is too conservative.

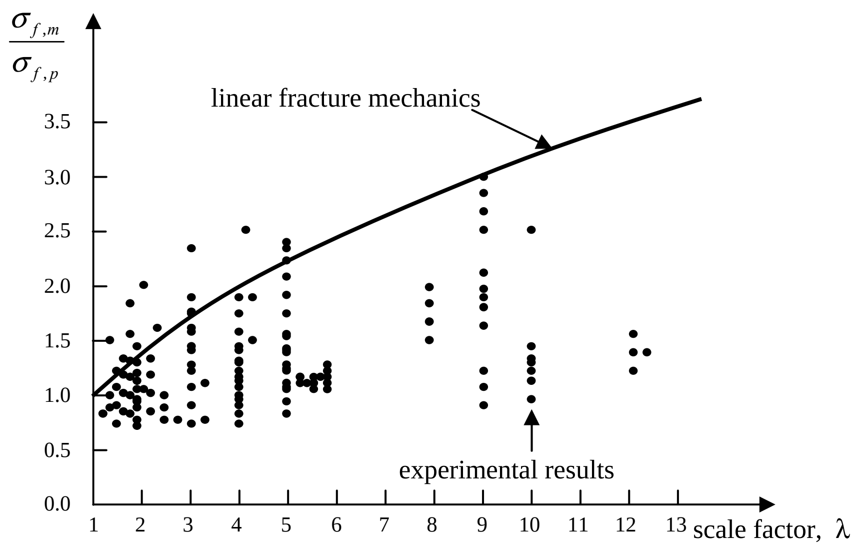

Figure 7. Scale effects on brittle fracture in plane strain.
Experiments by Sinclair and Chambers [7]

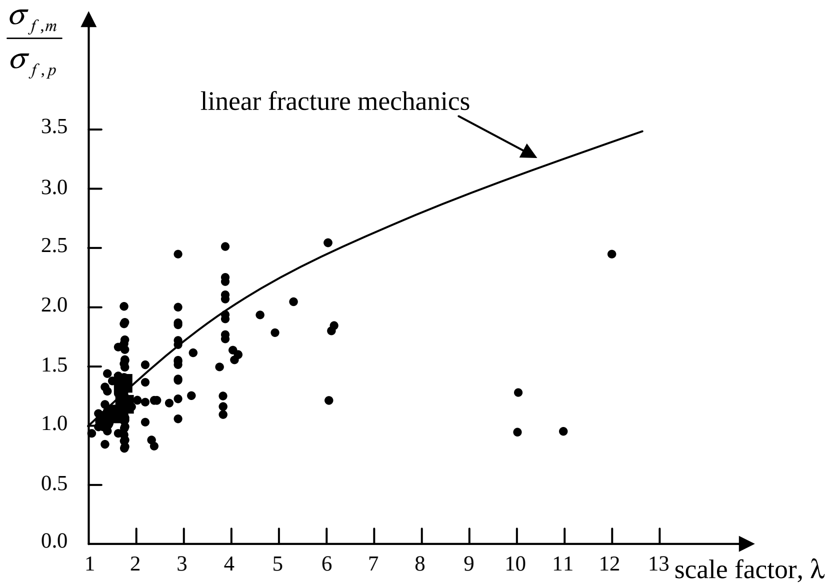

Figure 8. Scale effects on ductile fracture in plane stress.
Experiments by Sinclair and Chambers [7]

Let us consider two specimens geometrically identical: the smaller is the model "*m*", and the larger is the prototype "*p*". The ratio of their geometrical dimensions, including crack length is equal to the scale factor λ.

The fracture toughness K_{Ic} is given in each case by

$$K_{\mathrm{I}c} = \sigma^m_{g,c}\sqrt{\pi a}\, F_\sigma(a/W) \text{ and } K_{\mathrm{I}c} = \sigma^p_{g,c}\sqrt{\pi\lambda a}\, F_\sigma(\lambda a/\lambda W) \tag{10}$$

where $\sigma_{g,c}{}^m$ and $\sigma_{g,c}{}^p$ are the critical gross stress for model and prototype, respectively, a is the crack length and F_σ is a geometrical function.

Assuming that fracture toughness is an intrinsic property of the material, the ratio of critical gross stress is given by the following scaling law:

$$\frac{\sigma^m_{g,c}}{\sigma^p_{g,c}} = \sqrt{\lambda} \tag{11}$$

Similarly the scaling law based on critical strain is given by

$$\frac{\varepsilon^m_f}{\varepsilon^p_f} = \frac{1}{\sqrt{\lambda}} \tag{12}$$

For ductile materials the stress–strain behaviour is describe by Ramberg–Osgood law:

$$\varepsilon = \frac{\sigma}{E} + K'\frac{R_e}{E}\left(\frac{\sigma}{R_e}\right)^N \tag{13}$$

where R_e is yield stress, N is the strain hardening exponent, and K' constant.

Hutchinson [8], and Rice and Rosengreen [9] have proposed for this behaviour the following expression for stress and strain distribution:

$$\sigma_{ij} = r^{-\frac{1}{N+1}} K_{\mathrm{I}} \tilde{\sigma}_{ij}(\theta) \tag{14}$$

$$\varepsilon_{ij} = K' \frac{R_e}{E} \left(\frac{K_\mathrm{I}}{R_e} \right) r^{-\frac{1}{N+1}} \tilde{\varepsilon}_{ij}(\theta) \tag{15}$$

where $\tilde{\varepsilon}_{ij}(\theta)$ and $\tilde{\sigma}_{ij}(\theta)$ are angular functions and K_I is the stress intensity factor. These relationships lead to following scaling laws:

$$\frac{\sigma_{g,c}^m}{\sigma_{g,c}^p} = \lambda^{\frac{1}{N+1}} \tag{16}$$

$$\frac{\varepsilon_f^m}{\varepsilon_f^p} = \lambda^{\frac{N}{N+1}} \tag{17}$$

1.3.2. Scale effects for ductile fracture

Carassou et al. [10] have tested different notched tensile specimens of carbon–manganese steel at temperature 100°C, which exhibited failure in a ductile manner. They found a pronounced scale effect on fracture strain (Fig. 9).

Assuming the growth of cavities which are one of the ductile fracture mechanisms:

$$\frac{\sigma_{eq}^2}{\Phi^2} + 2 f_V q_1 \cosh\left(\frac{3}{2} \frac{q_2 \sigma_m}{\Phi} \right) - \left(1 + q_3 f_V^2\right) = 0 \tag{18}$$

and that fracture occurs at instability:

$$\frac{d\sigma_{eq}}{d\varepsilon_{eq}} = 0 \tag{19}$$

they computed the failure probability of elementary volume using Weibull Theory.

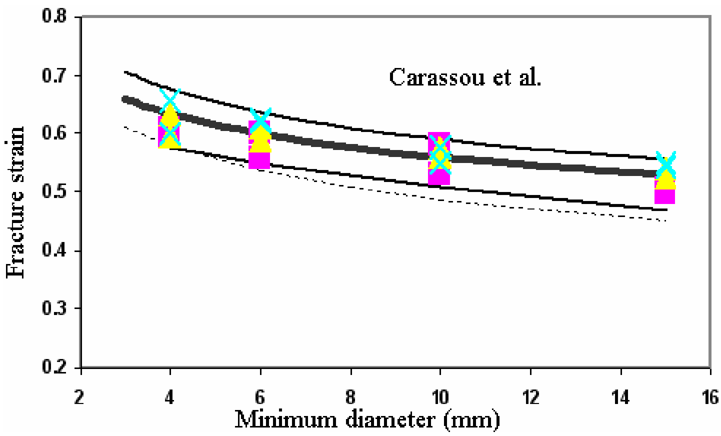

Figure 9. Scale effects on ductile fracture strain. Experiments by Carassou et al. [10]

1.4. Scale effects on ductile tearing

Devaux et al. [11] have performed tests on axisymmetric and CT specimens produced of steel A 508 Cl 3. Axisymmetric specimens have 3 diameters (5, 30 and 50 mm) with a precrack proportional to the diameter. Two thickness values (25 and 50 mm) of CT specimens were used. The J–Δa curves are drawn, and are close to each other. However, the $J_{0.2}$ value is smaller for smaller specimens and maximum critical opening displacement is greater for the larger specimen.

1.5. Scale effect on ductile to brittle transition

Malmberg et al. [3] have assumed that two failure modes are possible for a cracked specimen:

- plastic instability, which occurs under load F_{inst}
- rapid crack propagation at load F_{crack}.

For plastic instability no scale effect is taken into account and

$$\frac{\sigma_{inst}^{p}}{\sigma_{inst}^{m}} = 1 \tag{20}$$

where σ_{inst} has superscripts for the model "*m*" and the prototype "*p*", respectively.

In non-linear fracture mechanics the scaling law for the critical stress σ_{crack} is:

$$\frac{\sigma_{crack}^{p}}{\sigma_{crack}^{m}} = \lambda^{\frac{1}{n+1}} \tag{21}$$

where n is the strain hardening exponent. The transition of failure mode can be considered using the ratio

$$\frac{\left(\dfrac{P_{inst}}{P_{crack}}\right)_p}{\left(\dfrac{P_{inst}}{P_{crack}}\right)_m} = \lambda^{\frac{1}{n+1}} \tag{22}$$

Brittle to ductile transition can be described by the so-called brittleness number β:

$$\beta = \frac{\text{elastic energy}}{\text{fracture energy}} = \frac{\alpha' D^3 \left(\sigma_y^2 / E\right)}{\alpha'' D^3 \gamma} = \alpha''' \frac{D^2 \sigma_y^2}{\gamma}$$

where α', α'' and α''' are parameters characterizing structure geometry D, a term representing structure size, and σ_y is the yield stress. The brittleness number can be rewritten:

$$\beta = \frac{D}{c_f} \tag{23}$$

where c_f is a term proportional to plastic zone

$$c_f = \frac{E\gamma}{\sigma_y^2} \tag{24}$$

2. PROBABILISTIC APPROACH OF SIZE EFFECT

2.1. Probabilistic approach based on Weibull theory

This probabilistic approach is based on the weakest link theory of Weibull. From this theory, the fracture probability is given by

$$P_r(\sigma, V) = 1 - c\exp\left[-\frac{V}{V_o}\left\langle\frac{\sigma}{\sigma_o}\right\rangle^m\right] \tag{25}$$

where c is an integration constant, V_o is the elementary volume, and m is the Weibull modulus.

The average value of the fracture stress is given by:

$$\sigma_f = \int_{-\infty}^{\infty} \sigma dP_r(\sigma) \tag{26}$$

$$\sigma_f = \frac{Vm}{V_o \sigma_o^m} \int_{-\infty}^{\infty} \sigma^m \exp\left[-\frac{V}{V_o} \left\langle \frac{\sigma}{\sigma_o} \right\rangle^m \right] d\sigma = \sigma_o \Gamma\left(1 + \frac{1}{m}\right) \left(\frac{V}{V_o}\right)^{1/m} \tag{27}$$

where Γ is the symbol of the gamma function,

$$\Gamma(p) = \int_0^{\infty} u^{p-1} e^{-u} du\ , \text{ with } \ u = \frac{V}{V_o} \left\langle \frac{\sigma}{\sigma_o} \right\rangle^m \tag{28}$$

Considering two determined volumes V_1 and V_2, the respective average fracture stresses are given by the following relationship:

$$\sigma_f^1 = \left(\frac{V_2}{V_1}\right)^{1/m} \sigma_f^2 \tag{29}$$

Relationship (29) represents the scaling law according to the probabilistic approach.

In the case of a beam submitted to bending, integration of the Weibull function gives:

$$\int_V f_W \left[\sigma_{yy}(y) \right] dV = \frac{LB}{V_o} \left(\frac{2\sigma_b}{h\sigma_o} \right)^m \int_0^{h/2} y^m dy = \frac{V}{2(1+m)V_o} \left(\frac{\sigma_b}{h\sigma_o} \right)^m \tag{30}$$

where B is the thickness of the beam, h is the height, and σ_b is the bending stress. It can be found from (30) that:

$$\frac{\sigma_{f,b}}{\sigma_{f,t}} = \left[2(1+m)^{1/m} \right] \tag{31}$$

A similar relation can be established between torsion or another mode of loading. More generally we can write the Weibull scaling law:

$$\sigma_f^1 = \left(\frac{D_2}{D_1}\right)^{d_e/m} \sigma_f^2 \tag{32}$$

where d_e is the space dimension (1–uniaxial loading, 2–plane stress), D_1 and D_2 are characteristic dimensions of the structures.

2.2. Probabilistic approach can be based on cumulative distribution of defects

Carpinteri [12] has proposed a defect distribution law in the following form:

$$P(a) = 1 - \frac{c}{Na^N} \tag{33}$$

with $c = N(1 - P_o)a_o^N$ for $(1 < N < \infty)$, and a_o is a defect size greater than the average value. In this case the scaling law can be written as a power function of exponent α_N,

$$\frac{\sigma_f^p}{\sigma_f^m} = c\left(\frac{D}{D_o}\right)^{\alpha_N} \tag{34}$$

where D is a characteristic dimension of the structure, D_o is a normalization constant, the value $\alpha_N = \alpha(\gamma)/(N-1)^{\xi}$, where γ is the defect angle, and ξ is an exponent function of the defect density.

For an elastic-plastic material, according to the Ramberg-Osgood law, the exponent is:

$$\alpha_N = \frac{\alpha(\gamma)}{(n+1)(N-1)^{\xi}}$$

where n is the strain hardening exponent. Carpinteri [12] has verified this scaling law from tests performed with four-point bending by Sabnis and Mirza [13], Fig. 10.

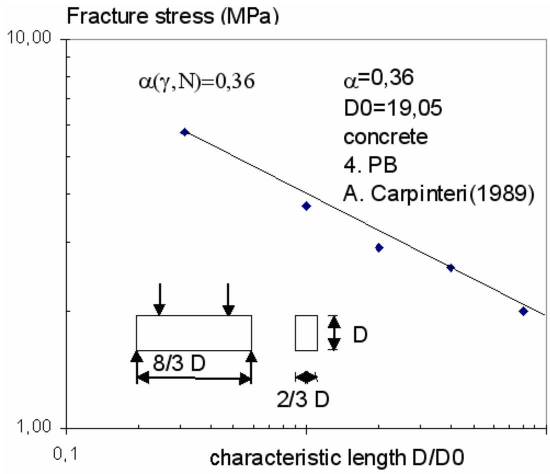

Figure 10. Scaling law by Carpinteri, based on defect distribution [12]. Experiments by Sabnis and Mirza [13]

3. FRACTAL APPROACH

3.1. Fractal character of fracture surfaces

Disorder character of a line, surface or volume can be characterized by the fractal dimension d_f. In Euclidian space, the length of a line is multiplied by a scale factor λ, the surface by λ^2, and the volume by λ^3. This means that in Euclidian space, the scale factor is elevated to the power d_e (d_e = 1 for a line, d_e = 2 for a surface, and d_e = 3 for a volume). In Euclidian space, the size is then given by:

$$Y_\lambda = \lambda^{d_e} * Y_1 \tag{35}$$

Extension in the fractal dimension leads to:

$$Y_\lambda = \lambda^{d_f} * Y_1 \tag{36}$$

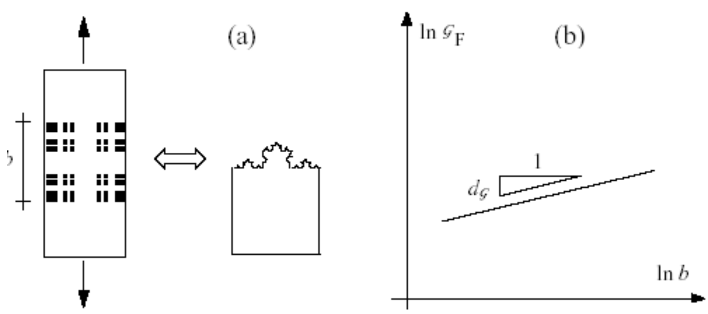

Figure11. Critical strain energy release rate versus size of element in a bi-logarithmic graph. The fractal dimension is the slope of the curve.

The fractal dimension d_f is equal to:

$$d_f = \phi + d_e \tag{37}$$

For a surface, d_f takes the value 2.5 for Brownian disorder, and 2 for Euclidian order.

In fractal space, fracture stress has the dimension [load*length]$^{-(2-\phi)}$. The fractal critical energy release rate has the dimensions [load*length]$^{-(2+\phi)}$.

3.2. Scale effect on strain energy release rate G_f

Carpinteri [14] assumed that the fractal fracture toughness G_f^* is size independent. For two geometrically similar specimens (model – small, and prototype – large):

$$G_f^* = \frac{U_{c,p}}{D_p^{2+\phi}} = \frac{U_{c,m}}{D_m^{2+\phi}} \tag{38}$$

Here, $U_{c,p}$ and $U_{c,m}$ are the work for fracture of the prototype and of the model, respectively; D_p and D_m characteristic dimensions of model and prototype, respectively. In Euclidian space, the fracture toughness is

$$G_f^p = \frac{U_{c,p}}{D_p^2}, \quad G_f^m = \frac{U_{c,m}}{D_m^2} \tag{39}$$

From the relationships (38) and (39) follows the scaling law:

$$G_f^p = G_f^m \left(\frac{D_p}{D_m}\right)^{\phi} \tag{40}$$

The exponent ϕ equals to 0.5 for small structures and to 0 for large structures. For any structure size, the scaling law is given by:

$$G_f^p = G_f^{\infty}\left(1 + \frac{L_{ch}}{D}\right)^{\phi} \tag{41}$$

where L_{ch} is a characteristic length that controls transition from fractal to Euclidian behaviour.

This law has been applied to experimental results from Kim et al. [15] on two types of concrete, of compression strength 20 MPa and 100 MPa (Fig. 12).

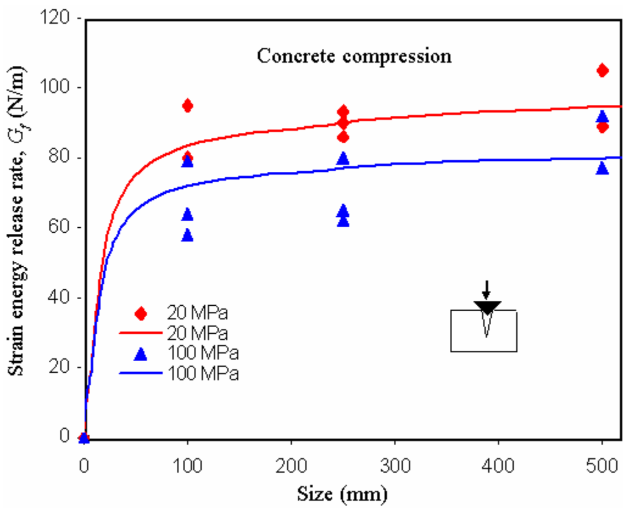

Figure12. Multifractal scaling law of critical strain energy release rate of Carpinteri [14], applied to experimental results of Kim et al. [15]

3.3. Scaling law on fracture stress

Similarly one can obtain a scaling law on fracture stress

$$\sigma_{c,p} = \sigma_{c,m} \left(\frac{D_p}{D_m} \right)^{-\phi} \tag{42}$$

Carpinteri [14] has derived a multifractal scaling law for the critical stress for any value of the scale factor

$$\sigma_c = \sigma_c^{\infty} \sqrt{\left(1 + \frac{L_{ch}}{D} \right)} \tag{43}$$

This scaling law has been applied on results obtained by Ferro in Fig. 13. Fracture stress on concrete specimens has been plotted versus ligament size.

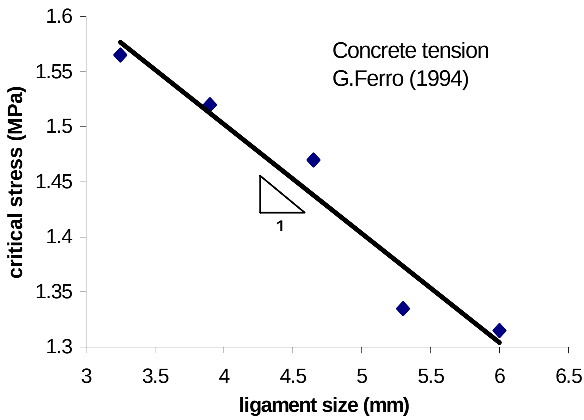

Figure 13. Multifractal scaling law of critical stress by Carpinteri [14], applied to experimental results of Ferro

4. ASYMPTOTIC METHOD

Bazant [16] has developed several scaling laws based on asymptotic and energetic approaches. The most important scaling law referred to the critical stress that is defined by two asymptotic behaviours: plastic collapse without scale effects and brittle fracture with maximum scale effects (Fig. 14). Bazant has recently [17] proposed a scaling law for fracture emanating from a defect on a smooth surface, and has also proposed an universal scaling law able to treat the two previous cases.

4.1. Asymptotic scaling law for critical stress of a cracked or notched structure

For a cracked structure the complementary energy stored is

$$\Pi^* = \frac{\sigma_g^2}{E'} BD^2 f(\eta, \eta_o, \eta_{ef}) \tag{44}$$

where Π^* is the complementary energy; B thickness; D representative dimension; σ_g gross stress; E the Young's modulus, $E' = E/(1 - \nu^2)$; η shape function ($\eta = a/D$, $\eta_o = a_o/D$, $\eta_c = a_c/D$, with a current initial crack length a_o. Also $\eta_c = c_f/D$, where c_f is a dimension characteristic of plastic zone size width,

$$\eta = \eta_o + \eta_c \tag{45}$$

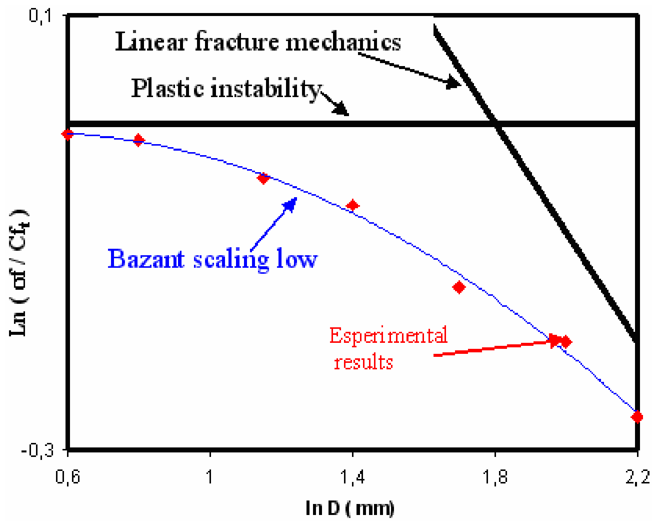

Figure 14. Asymptotic scaling law of Bazant [16] for two asymptotic behaviours: plastic collapse and brittle fracture

Fracture resistance of the material depends of the same geometrical parameters as the complementary energy:

$$R = G_c r(\eta, \eta_o, \eta_{ef}) \tag{46}$$

The criterion for crack propagation is given by:

$$G = \frac{1}{B}\left[\frac{\partial \Pi^*}{\partial a}\right] R \tag{47}$$

The strain energy release rate is equal to

$$G = \frac{\sigma_{g,c}^2}{E'} BDg(\eta, \eta_o, \eta_{ef}) = G_c r(\eta, \eta_o, \eta_{ef})$$

with $g(\eta, \eta_o, \eta_{ef}) = \dfrac{\partial f(\eta, \eta_o, \eta_{ef})}{\partial \eta}$ and $\sigma_{g,c}$ – the critical gross stress.

The critical load is defined by a condition of tangency of R and G curves:

$$\left[\frac{\partial G}{\partial \eta}\right]_{\sigma_{g,c}} = \left[\frac{\partial R}{\partial \eta}\right] \tag{48}$$

This condition can be rewritten as follows:

$$\frac{1}{G}\left[\frac{\partial G}{\partial \eta}\right]_{\sigma_{g,c}} = \frac{1}{R}\left[\frac{\partial R}{\partial \eta}\right] \tag{49}$$

The solution to this problem is the value reached by the non-dimensional crack length

$$\eta = \eta_m(\eta_o, \eta_c) \tag{50}$$

where η_m is the value of non-dimensional crack length at maximum load.

The critical stress $\sigma_{g,c}$ is given by:

$$\sigma_{g,c} = \sqrt{\frac{E' G_c}{Dh(\eta_o, \eta_m)}} \quad \text{with} \quad h(\eta_o, \eta_m) = \frac{g(\eta_o, \eta_c, \eta_m)}{r(\eta_o, \eta_c, \eta_m)}. \tag{51}$$

If the process zone is relatively small, the function $h(\eta_o,\eta_m,\eta_c)$ can be approximated by a Taylor series in the vicinity of the point $(\eta_o,0)$:

$$\sigma_{g,c} = \sqrt{\frac{E'G_c}{D}}\left[h(\eta_o,0) + \frac{\partial h(\eta_o,0)}{\partial\theta} + \frac{1}{2}\frac{\partial^2 h(\eta_o,0)}{\partial\theta^2}\left(\frac{c_f}{D}\right)^2 + \cdots\right] \tag{52}$$

By limiting to the linear term of the Taylor series:

$$\sigma_{g,c} = \sqrt{\frac{E'G_c}{h(\eta_o)c_f + h(\eta_o)D}} \tag{53}$$

This equation can be written in the following form:

$$\sigma_{g,c} = \frac{Cf_t}{\sqrt{1+\beta}} \tag{54}$$

with $\beta = \dfrac{D}{D_o}$, $D_o = c_f \dfrac{h'(\eta_o)}{h(\eta_o)}$, and $C = \sqrt{\dfrac{E'G_c}{h(\eta_o)c_f}}\dfrac{1}{f_t}$, where f_t represents the ultimate tensile strength.

When D tends to zero, Eq. (54) shows clearly a ductile asymptote, critical stress is given by Cf_t. When D tends to infinity, Eq. (54) exhibits a brittle asymptote and fracture is governed by linear elastic fracture mechanics with the critical gross stress

$$\sigma_{g,c} = \frac{Cf_t}{\sqrt{\beta}} \tag{55}$$

These two asymptotes intersect in point D_o characterizing brittle to ductile transition.

4.2. Scale effects with asymptotic approach for smooth specimens

By replacing $\eta_o = 0$ in Eq. (52) and limiting the series development to the quadratic term, one obtains a scaling law for a smooth structure. For $h(\eta_o,0) = h(0,0) = 0$ it follows:

$$\sigma_{g,c} = \sqrt{\frac{E'G_c}{h'(0)c_f + \frac{1}{2}h''(0)c_f^2 D^{-1}}} = \frac{f_t^\infty}{\sqrt{\left(1 - 2\frac{D_b}{D}\right)}} \tag{56}$$

with $f_t^\infty = \sqrt{\dfrac{E'G_c}{h'(0)c_f}}$, $D_b = \dfrac{\langle -h''(0)\rangle}{4h'(0)}\bar{c}_f$.

Macauley brackets have been introduced because $h''(0)$ can be negative. Introducing the factor κ takes into account that the fracture process zone is more important on a smooth surface than at the crack tip:

$$\bar{c}_f = \kappa c_f \tag{57}$$

In the case where $D_b/D << 1$, Eq. (56) is approximated by

$$\sigma_{g,c} = \frac{f_t^\infty}{\sqrt{\left(1 - 2\frac{D_b}{D}\right)}} \approx f_t^\infty\left(1 + \frac{D_b}{D + \varpi D_b}\right) \tag{58}$$

where ϖ is an empirical constant to limit critical gross stress value when $D \to 0$.

4.3. Universal scaling law with asymptotic approach

Using the first three terms of Eq. (52), Bazant has obtained a universal scaling law:

$$\sigma_{g,c} = \sigma_o \frac{1}{\sqrt{\left(1+\dfrac{D_b}{D_o}\right)}} \left\{ 1 + \frac{1}{\left[\left(1+\dfrac{D_b}{D+\varpi D_b}\right)\right]\left(1+\dfrac{D_b}{D_o}\right)} \right\} \tag{59}$$

with $\sigma_o = \sqrt{\dfrac{E' G_c}{h'(\eta_o) c_f}}$, $D_b = \dfrac{\langle -h''(\eta_o)\rangle}{4h'(\eta_o)} \bar{c}_f$, $D_o = \dfrac{c_f h'(\eta_o)}{h(\eta_o)}$, c_f is related to the facture volume at crack tip and $\bar{c}_f$ for a smooth surface.

5. CONSTRAINT TRANSFERABILITY PROBLEM IN FRACTURE TOUGHNESS

In addition to the size effect, the ligament size also influences fracture toughness. Figure 15 shows the influence of normalized notch length *a/W* (*a* is notch length and *W* is the width) on brittle to ductile transition, depending on temperature, as determined on precracked specimens of cast steel. For decreasing ligament size and increasing ratio *a/W*, the shift to higher temperatures is obvious [23]. Different master curves for nuclear waste container cast steel indicate clearly that transition temperature t_{DB} is shifted to higher value when the ligament size increases. In the transition regime, fracture toughness increases with decreasing ligament size (Fig. 16).

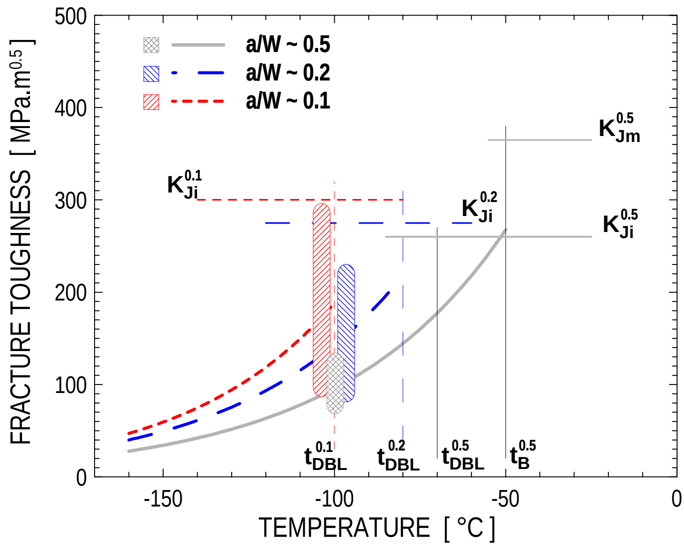

Figure 15. Influence of normalized notch length *a/W* on brittle to ductile transition depending on temperature, as determined on precracked specimens of cast steel

5.1. Constraint effect on stress distribution

The ligament size effect on fracture toughness expressed by the critical notch stress intensity factor can be explained by the lost constraint. This can be evaluated by distribution of tensile crack opening stress (Fig. 17): it is shifted to lower values when the ligament size decreases due to stress relaxation on the front/back free boundary. First estimation of this effect is made using a constraint factor *L*, defined as the ratio of maximum to yield stress:

$$L = \sigma_{max}/R_e \tag{60}$$

For a crack in a small scale yielding situation, this ratio is close to 3. It decreases with distance, non-dimensional $r\sigma_o/J$, and crack length.

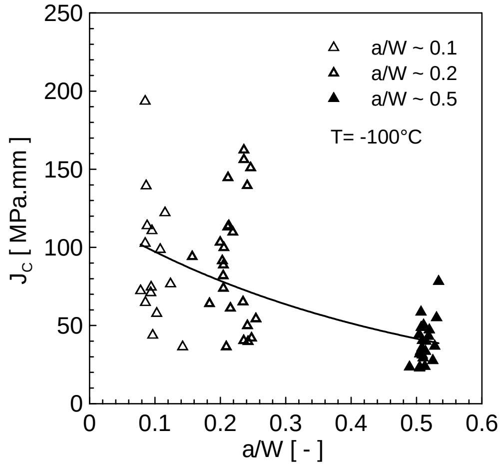

Figure 16. Influence of ligament size on fracture toughness J_c for nuclear waste container cast steel

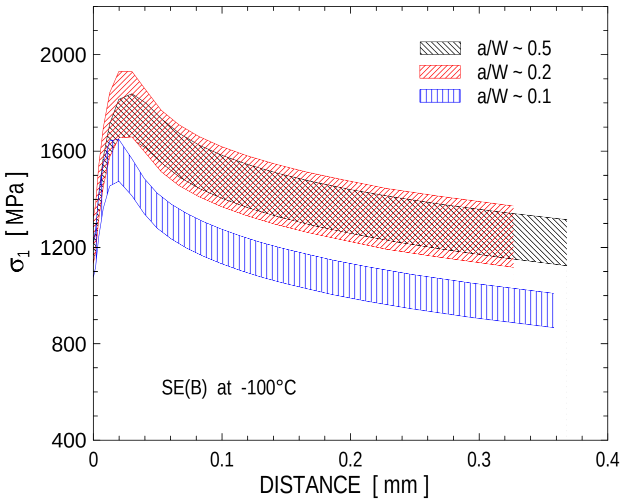

Figure17. Distribution of tensile opening stress along the distance for different ligament size

Loss of constraint has been defined in another way by Dodds et al. [18] by using the Q parameter. This parameter is defined as the difference between stress levels of given ligament size and at referential small scale yielding (SSY), and is divided by yield stress,

$$Q = \frac{\theta_{\sigma\sigma} - (\theta_{\sigma\sigma})_{ssy}}{R_e} \tag{61}$$

Due to the shape of stress distribution, a validity condition based on stress gradient is,

$$\operatorname{grad} Q = \frac{Q_{(1)} - Q_{(5)}}{4} \leq 0.1 \tag{62}$$

where $Q_{(1)}$ and $Q_{(5)}$ are values determined at non-dimensional distances 1 and 5, in respect.

5.2. Transferability method for constraint effects

Two transferability methods for constraint effect on fracture toughness obtained using one specimen geometry to other specimen geometry are proposed:

- Dodds method, [18];
- Koppenhoefer method, [19].

It is necessary for Dodds' method to compute Q value for each geometry and establish a relationship between Q value and fracture toughness. The relations presented in Fig. 18 allow transferability of fracture toughness by interpolation.

Koppenhoefer's method is based on statistical distribution of Weibull stress σ_w:

$$P_f(\sigma_w) = 1 - \exp\left[-\left(\frac{\sigma_w}{\sigma_{no}}\right)^m\right] \tag{63}$$

Fracture toughness distribution J_c is given by the following relationship:

$$P_f(J) = 1 - \exp\left[-\left(\frac{J}{J_{no}}\right)^\alpha\right] \tag{64}$$

where $\alpha = 2$ for small scale yielding. This leads to:

$$\left(\frac{J}{J_{no}}\right)^\alpha = \left(\frac{\sigma_w}{\sigma_{no}}\right)^{mw} \tag{65}$$

Figure 19 shows effect of geometry on failure distribution.

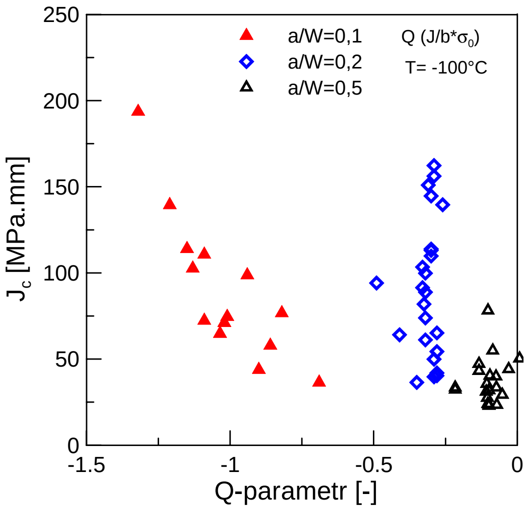

Figure 18. Dependence of fracture toughness J_c on Q parameter, proposed by Dodds

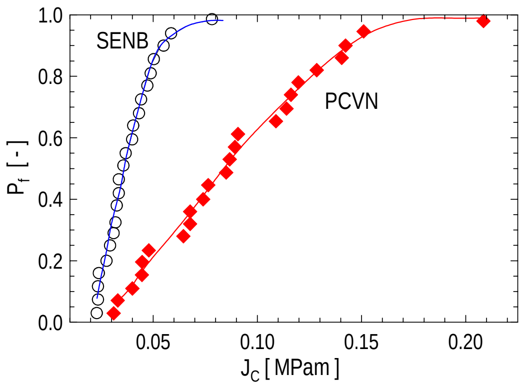

Figure 19. Fracture toughness probability distribution for bending (SENB) and Charpy specimens

The Koppenhoefer method proposes to establish Weibull constraint curves depending on normalized toughness $J/b\sigma_o$ for different situations and to recalculate for the same fracture in two operations, since Weibull's modulus and toughness change simultaneously (Fig. 20).

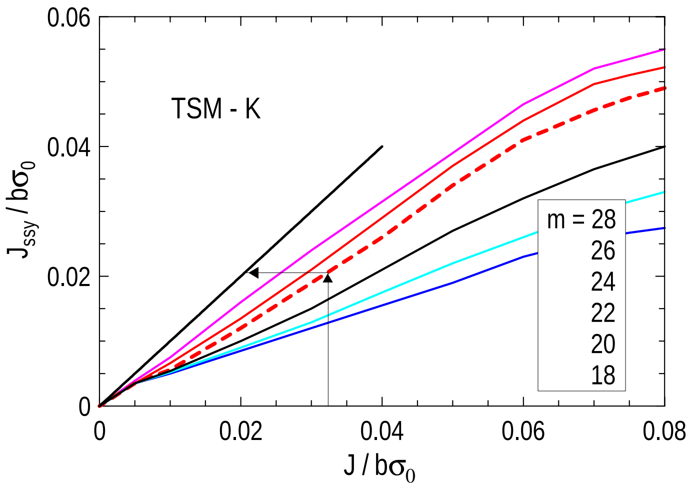

Figure 20. Transferability curve for nuclear waste container cast steel, obtained by the Koppenhoefer method

6. NOTCH EFFECTS ON FRACTURE TOUGHNESS

6.1. Scaling law for notch with different opening angle

Relationships between the applied gross stress or load and the stress intensity factor K^*_{I} for a specimen having a crack (sharp notch of infinite acuity) can be found. Solutions can also be found for a plate in tension with a crack (sharp notch of infinite acuity) and for a three point bend specimen with a notch of infinite acuity (Figs. 21a and b).

For the first case:

$$K_{\mathrm{I}}^{*}(\psi) = \sigma_g W^{\alpha} F_{\sigma}\left(\frac{a}{W}\right) \tag{66}$$

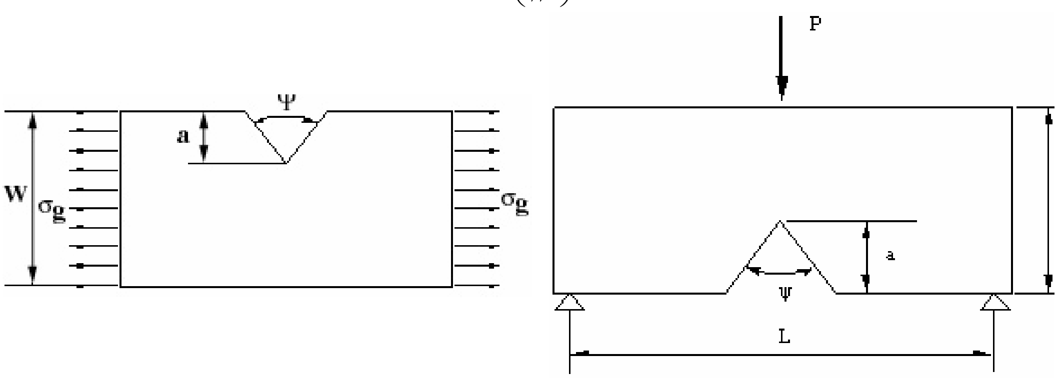

Figure 21a. Scheme for determination of stress intensity factor of cracked plate in tension (notch of infinite acuity, $\rho = 0$), Eq. (66)

Figure 21b. Scheme for determination of stress intensity factor for cracked three point bend specimen (notch of infinite acuity) Eq. (68)

Due to similarity, from the Buckingham theory, when $\psi \to \pi$, $\alpha \to 0$, one can obtain:

$$F_{\sigma}\left(\frac{a}{W}\right) = \frac{1}{1-(a/W)} \tag{67}$$

For cracked three point bend specimen:

$$K_{\mathrm{I}}^{*}(\psi) = \frac{PL}{BW^{2-\alpha}} F_{\sigma}\left(\frac{a}{W}, \psi\right) \tag{68}$$

where L is the span, B is the thickness, and W is the width of specimen. The geometrical correction function can be expressed as the product of two functions, $c(\psi)$ and $g(a/W)$ of separate parameters ψ and a/W.

$$F_{\sigma}\left(\frac{a}{W}, \psi\right) \cong c(\psi) g\left(\frac{a}{W}\right) \tag{69}$$

Function $c(\psi)$ exhibits two extreme values $c(0) = 0.5$ and $c(\pi) = 1$ and can be approximated by the following relationship (where β is an unknown exponent):

$$c(\psi) \cong \frac{1}{2}\left[1 + \left(\frac{\psi}{\pi}\right)^{\beta}\right] \tag{70}$$

For a notch with an opening angle Ψ, the scaling law (Fig. 22) can be written as:

$$\ln \sigma_f = g(K_{\mathrm{I}c}^{*}, a/W) - \alpha(\psi) \ln W \tag{71}$$

where g is a function of geometry; α varies from 0.5 (crack, $\Psi = 0$) to 0 (smooth specimen, $\Psi = \pi$).

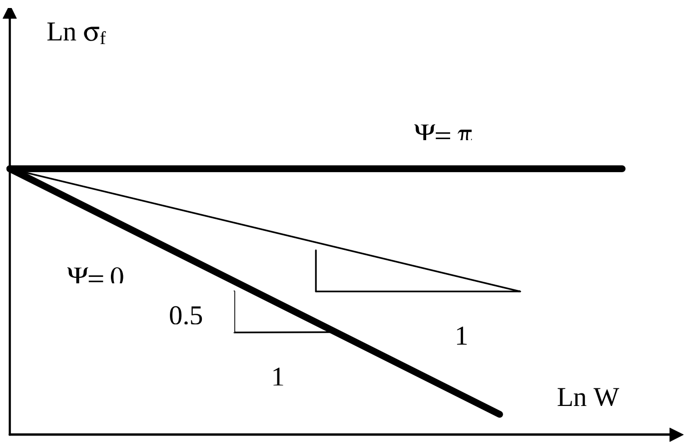

Figure 22. Scaling law for a notch with opening angle Ψ

6.2. Transferability problems for notch effects

Notch radius has an important effect on fracture toughness, as presented in Fig. 23. The fracture toughness defined as the critical notch stress intensity factor is plotted versus temperature. One can notice a shift of the transition temperature when decreasing notch radius. The change of fracture toughness can be described by the transferability parameter Q^* or Q.

This transferability parameter Q^* is defined according to the relationship (72), where b is ligament size, and α is the exponent of the pseudo singularity of the stress distribution.

$$Q^*(T) = \frac{K^{c}_{\rho(a/W=0.5)}(T)}{R_e(T) b^{\alpha}_{(a/W=0.5)}} - \frac{K^{c}_{\rho(a/W=0.1)}(T)}{R_e(T) b^{\alpha}_{(a/W=0.1)}} \tag{72}$$

The dependence of Q^* with temperature is plotted in Fig. 24.

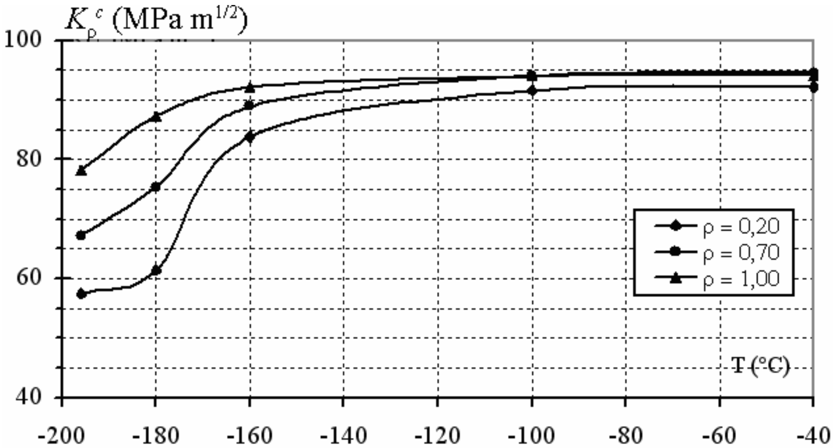

Figure 23. The effect of notch radius on transition temperature (nuclear waste container cast steel)

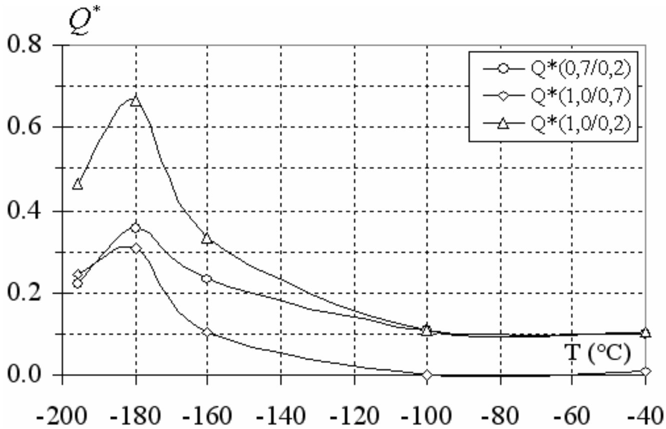

Figure 24. Dependence of transferability parameter Q^* with temperature (nuclear waste container cast steel)

7. MESOFRACTURE

7.1. Basis of mesofracture

Mesofracture, a promising part of mesomechanics, is based on two principles:

- Fracture is basically a non-local approach.
- Stress gradient plays an essential role in the real state of stress.

Considering the transferability problem with as a non local approach means that it is necessary to define an average value in a mesovolume called the fracture process volume. Several definitions of this fracture process volume can be found in literature. It seems that the size is not connected to the material microstructure but depends on geometry and on the loading mode. This volume is generally one order of magnitude to microstructure and typically a volume at mesoscale. It is considered as the high stressed region with different limit (for example 10% of maximum stress decrease).

In this fracture process, volume or effective volume V_{ef}, the effective strain or stress can be defined as the average of the weighted distribution. In order to take into account the essential role of stress gradient, stress distribution is weighted by the weight function ϕ. Following this, effective strain and stress are defined as follows:

$$\varepsilon_{ef} = \frac{1}{V_{ef}} \int_V \phi(x-s)\varepsilon(s)dV_{ef}(s)$$
$$\sigma_{ef} = \frac{1}{V_{ef}} \int_V \phi(x-s)\sigma(s)dV_{ef}(s) \tag{73}$$

where $\varepsilon(s)$ or $\sigma(s)$ are the stress or strain in one point, V_{ef} is the effective volume, and ϕ a weight function. Several kinds of weight functions can be used and have following forms:

$$\phi = (1 - r\chi) \tag{74}$$

$$\phi = \left(e^{r\chi/2}\right) \tag{75}$$

$$\phi = \left[1 - \left(\frac{r}{C_4 X_{ef}}\right)^2\right]^2 \quad \text{(“bell” function)} \tag{76}$$

where r is the distance, and χ is the relative stress gradient defined as:

$$\chi = \frac{1}{\sigma_{yy}} \frac{d\sigma_{yy}}{dr} \tag{77}$$

and C_4 is a constant, X_{ef} is the effective distance characteristic of the zone over which stress or strain is averaged.

7.2. Volumetric method for mesofracture [20]

It is assumed, according to the mesofracture principle that the fracture process requires a physical volume. This assumption is supported by the fact that fracture resistance is affected by loading mode, structural geometry, and the scale effect. By using the value of the “hot spot stress” i.e. the maximum stress value, it is not possible to explain the influence of these parameters on the fracture resistance.

It is necessary to take into account the stress value and the stress gradient in all neighbouring points within the fracture process volume. This volume is assumed to be quasi-cylindrical by analogy with a notch plastic zone of similar shape. The diameter of this cylinder is called the “effective distance”. By computing the average value of stress within this zone, the fracture stress can be estimated. This leads to a local fracture stress criterion based on two parameters: the effective distance X_{ef} and the effective stress σ_{ef}. The graphical representation of this local fracture stress criterion is given in Fig. 25, where the stress normal to the notch plane is plotted against the distance ahead of notch.

For the determination of X_{ef}, the graphical procedure is used. It has been observed that the effective distance is related to the minimum value of the relative stress gradient χ.

This distance corresponds to the beginning of the pseudo stress singularity. Its definition as the distance of minimum relative stress gradient is indicated in Fig. 25.

Charpy V notch specimens made of CrMoV steel (yield stress of 771 MPa) were tested statically in bending at one selected temperature in the lower shelf region. The tensile stress distribution at the notch was calculated using a FEM for elastic–plastic analysis of 2D model in plane strain conditions. The effective distance X_{ef} was determined using normal stress distributions below the notch root, plotted in bi-logarithmic axes. The relative stress gradient (see Eq. 78), plotted on the same graph, allows to obtain an effective distance precise value (Fig. 26). For a fracture load of 131 kN, the effective distance was 0.380 mm. The effective stress is defined as the average of the weighted stress inside the fracture process zone:

$$\sigma_{ef} = \frac{1}{X_{ef}} \int_0^{X_{ef}} \sigma_{ij} dx \tag{78}$$

For this material the mean value of the effective stress is 1223 MPa, which can be compared to the average maximum local stress at fracture, σ_{max} = 1310 MPa.

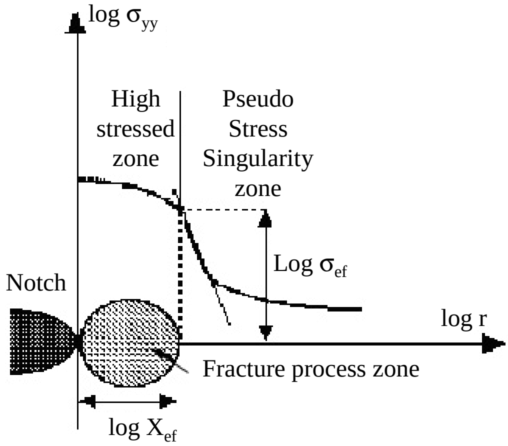

Figure 25. Schematic presentation of a local stress criterion for fracture emanating from notches

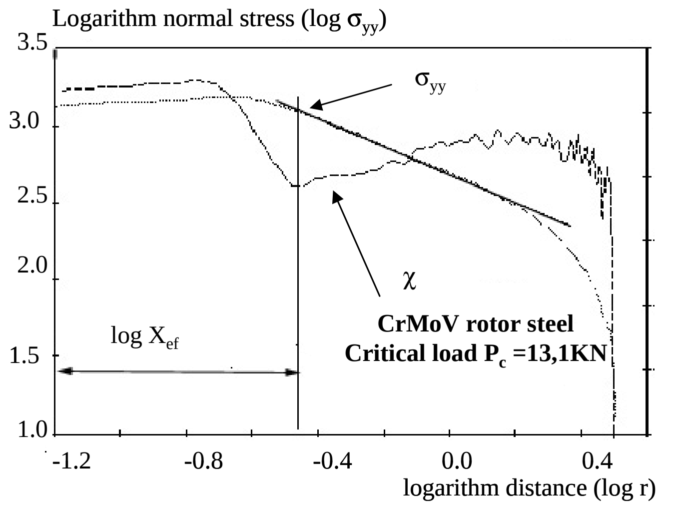

Figure 26. Notch root stress distribution at notch root together with the relative stress gradient versus distance from the notch tip for a fine carbide CrMoV rotor steel

8. GRADIENT APPROACH

Aifantis [21] proposed to modify the plastic flow rule by including the plastic strain Laplacian:

$$f = \sigma_{eq} - \left(\Phi(\varepsilon_{pl,eq}) - c\nabla^2 \varepsilon_{pl,eq}\right) = 0 \tag{79}$$

where σ_{eq} is the von Mises equivalent stress and $\varepsilon_{pl,eq}$ is the plastic equivalent strain,

$$\bar{\varepsilon}_{pl,eq} = \frac{1}{l_c} \int_{-\infty}^{\infty} \alpha(u) \varepsilon_{pl,eq}(x+u) du \quad \text{and} \quad u = s - x \tag{80}$$

Assuming that $\varepsilon_{pl,eq}$ varies slowly, $\varepsilon_{pl,eq}(x+u)$ can be approximated by a Taylor series:

$$\bar{\varepsilon}_{pl,eq} = \varepsilon_{pl,eq}(x) + \frac{\partial \varepsilon_{pl,eq}}{\partial x}(x) l_c \mu_1 + \frac{\partial^2 \varepsilon_{pl,eq}}{\partial x^2}(x) l_c^2 \mu_2 + \cdots + \frac{\partial^n \varepsilon_{pl,eq}}{\partial x^n}(x) l_c^n \mu_n \tag{81}$$

with $\mu_i = \int_{-\infty}^{\infty} \alpha(s) \frac{s^n}{l_c^n + 1} ds$; $\alpha(s)$ is an even function; μ_i values are zero for odd values of i.
By limiting Taylor series development to two terms, it reduces to:

$$\bar{\varepsilon}_{pl,eq} \approx \varepsilon_{pl,eq}(x) + \frac{\partial \varepsilon_{pl,eq}}{\partial x}(x) l_c \mu_1 + \frac{\partial^2 \varepsilon_{pl,eq}}{\partial x^2}(x) l_c^2 \mu_2 \tag{82}$$

Malmberg [22] has used a local approach based on strain gradient to explain the evolution of yield shearing stress in torsion:

$$\tau = G\gamma = G\varphi r \tag{83}$$

where: G – shearing modulus, γ – shear strain, r – specimen radius, ϕ – rotation angle.

In the plastic region, plastic flow rule includes gradient terms:

$$\tau = \tau_y - c_1 \nabla \gamma - c_2 \nabla^2 \gamma = \tau_y - c_1 \varphi - c_2 \frac{\varphi}{r} \tag{84}$$

where τ_y is the shear yield stress, and c_1 and c_2 are constants. The boundary between the elastic and plastic region is defined by:

$$r = r_y ; \quad \tau = \tau_y \tag{85}$$

$$\tau_{y,ap} = G\varphi r_y = \tau_y - c_1 \varphi - c_2 \frac{\varphi}{r_y} \tag{86}$$

where $\tau_{y,ap}$ is the apparent yield stress, and r_y the radius of the elastic boundary. Apparent yield stress is obtained when $r_y = r^*$, where r^* is the specimen radius.

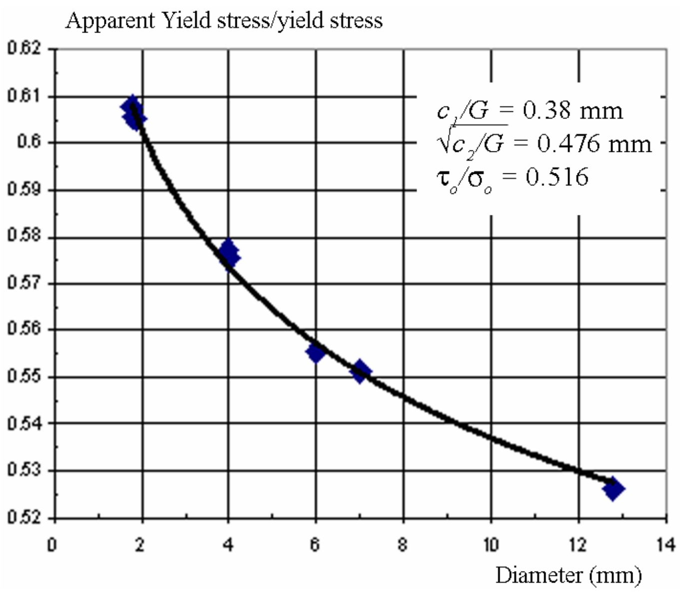

Figure 27. The applications of Malmberg's model [22] to Morrison results

The scaling law on shearing yield stress can be written as:

$$\tau_{y,ap} = \frac{\tau_y}{\left(1 + \frac{(c_2/G) + (c_2/G) r^*}{r^{*2}}\right)} \tag{87}$$

Figure 27 shows applications of Malmberg's model [22] to Morrison results.

CONCLUSION

In Table 2 the different scaling laws presented in this lecture are summarized.

Table 2. Summary of the described scaling laws

Scaling laws	Author	Formulae
Probabilistic approach	Weibull	$\sigma_f^1 = \left(\frac{D_2}{D_1}\right)^{de/m} \sigma_f^2$
Fractal approach	Carpinteri [14]	$G_f^p = G_f^\infty \left(1 + \frac{L_{ch}}{D}\right)^\phi$
Asymptotic methods	Bazant [16]	$\sigma_{g,c} = \frac{Cf_t}{\sqrt{1+\beta}}$
Scaling law for notches	Carpinteri [14]	$\ln \sigma_f = g(K_{Ic}^*, a/W) - \alpha(\psi) \ln W$

For transferability problems a promising way is mesofracture which assumes existence of an effective volume V_{ef}. In this volume the effective strain or stress can be defined as the average of the weighted distribution.

Finally in 16th century, Galileo Galilei said "from the small to the big is not so simple". This sentence is always actual.

REFERENCES

1. Richards, C.W., *Effect of size on the yielding of mild steel*, Proc. Am. Soc. Testing Mat., Vol. 58, pp. 995-970. (1958)
2. Morrisson, J.L.M., *The yield of mild steel with particular reference of the effect of size of specimen*, Proc. of the Inst. of Mech. Eng., 142, 1, pp. 193-223. (1939)
3. Malmberg, T., Tsagrakis, I., Eleftheriadis, E., Aifantis, E.C., *On the plasticity approach to size effects. Part 1/Reviews*, Forschungszentrum Karlsruhe, Scientific Report FZKA 6321. (1999)
4. Cook, G., *The yield point and initial stages of plastic strain in mild steel subjected to uniform and non-uniformstress distributions*, Phil. Trans. Roy. Soc., A, Vol. 23, pp. 103-147. (1931)
5. Chechulin, B.B., *Influence of specimen size on the characteristic mechanical value of plastic fracture*, (in Russian), Zhur. Tekh. Fiz., 24, pp. 1093-1100. (1954)
6. Matic, P., Kirby, G.C., Jolles, M.I., *The relation of tensile specimen size and geometry effects to unique constitutive parameters for ductile materials*, Proc. Roy. Soc., London, A 417, pp. 309-333. (1988)
7. Sinclair, G.B., Chambers, A.E., *Strength size effects and fracture mechanics: what does the physical evidence say?*, Engineering Fracture Mechanics, Vol 26, N°2, pp. 279-310. (1987)
8. Hutchinson, J.W., *Singular behaviour at the end of a tensile crack in hardening material*, J. Mech. Phys. Solids, Vol.16, pp. 13-31. (1968)
9. Rice, J.R., Rosengreen, G.F., *Plane strain deformation near a crack tip in a power law hardening material*, J. Mech. Phys. Solids, Vol.16, pp. 1-12. (1968)
10. Carassou, S., Soilleux, M., Marini, B., *Probabilistic modelling of the size effect on ductility of a C-Mn steel*, Journal de physique IV, pp. 63-70. (1998)

11. Devaux, J.C., Rousselier, G., Mudry, F., Pineau, A., *An experimental program for the validation of local ductile fracture criteria using axisymmetricallly cracked bars and compact tension specimens*, Engineering Fracture Mechanics, Vol. 21, N°2, pp. 273-283. (1985)
12. Carpinteri, A., *Decrease of apparent tensile and bending strength with specimen size: Two different explanations based on fracture mechanics*, International Journal of Solids and Structures, Vol. 25, N°4, pp. 407-429. (1989)
13. Sabnis, G.M., Mirza, S.M., *Size effects in models concretes*, J. Struct, Div. ASCE, Vol. 105, pp. 1007-1020. (1979)
14. Carpinteri, A., *Scaling laws and renormalisation groups for strength and toughness of disordered materials*, Int. J. Solids Structures, 31, N°3, pp. 291-302. (1994)
15. Kim, J.K., Mishashi, H., Kirikoshi, K., Narita, T., Proccedings of the first International Conference on Fracture Mechanics of Concrete Structures, FRAMCOSI, Breckenridge, pp. 561-566. (1992)
16. Bazant, Z.P., *Size effect in blunt fracture: Concrete, rock, metal*, Journal of Engineering Mechanics - ASCE , Vol 10, pp. 518-535. (1984)
17. Bazant, Z.P., *Scaling law of quasi brittle fracture asymptotic analysis*, International Journal of Fracture, 83, pp. 19-40. (1997)
18. Dodds, R., Ruggier, C., Koppenhoefer, K., *3D Constraint effects on models for transferability of cleavage fracture toughness*, ASTM 1321, pp. 179-197. (1997)
19. Koppenhoefer, K., Dodds, R., *Constraint effects on fracture toughness of impact loaded precracked Charpy specimens*, International Journal of fracture, pp. 101-133. (1993)
20. Pluvinage, G., *Application of notch fracture mechanics to fracture emanating from stress concentrations*, Nuclear Engineering, N°185, pp. 173-184. (1998)
21. Aifantis, E.C., *The physics of plastic deformation*, International Journal of Plasticity, Vol. 3, pp. 212-247. (1987)
22. Malmberg, T., Minutes of the task 5 group meeting, Joint research centre, EU project. FI4S-CT96-0024. (1998)
23. Dlouhy, I., Holzmann, M., Chlup, Z., *Fracture resistance of cast ferritic C.Mn steel for Container of spent Nuclear fuel*, Transferability of fracture Mechanical Characteristics, Ed. Dlouhy, Nato Sciences Series, pp. 47-64. (2001)

APPLICATION OF FRACTURE MECHANICS IN NUCLEAR INDUSTRY

Stefan Vodenicharov, IMS-BAS, Bulgaria

Energy resources of our planet have decreased by half since 1960. At the same time the continuous growth of population and development of technologies demand greater and greater energy consumption which leads to continuous exhausting of oil, coal, and natural gas resources. The only possibility to satisfy the energy needs of mankind and to increase its prosperity is to use nuclear energy. The dependence of the well being of mankind on energy consumption per capita is proved by statistical data available from USA, Finland, Germany, Poland, Russia, Ukraine, and some other countries.

The reactor pressure vessel (RPV) is the main part of a nuclear power installation and its integrity is of crucial importance for safe exploitation of nuclear power plant (NPP).

The WWER RPVs work under high neutron flux irradiation at pressures from 10 MPa to 14 MPa and temperatures from 270°C to 290°C. Aging of RPV metal is running due to neutron irradiation, thermal influence, corrosion, and low-cycle fatigue. The critical zones in WWER-440 and WWER-1000 are the shells and the welds around the core zone.

Radiation defects are forming in the crystal lattice of RPV metal during irradiation, which leads to metal strengthening (increase of yield strength, ultimate strength, microhardness, and hardness) and the increase in embrittlement transition temperature. For example, after irradiation of the RPV steel, the yield strength at 100°C increases for 320 MPa and the ultimate strength for 360 MPa (Fig. 1).

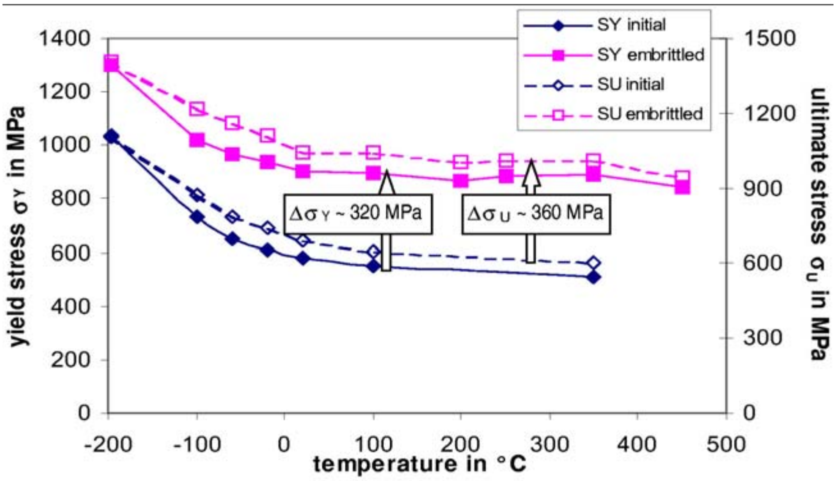

Figure 1. Increase of steel strength by irradiation

The absorbed energy for crack propagation decreases with the increase of neutron fluence (Fig. 2). For example, the absorbed fracture energy for propagation of a crack to length 4 mm in a non-irradiated specimen is 290 kJ/m^2. After neutron irradiation to fluence 8.10^{23} n/m^2, the absorbed energy decreases to 220 kJ/m^2 and after irradiation to fluence 5.10^{24} n/m^2, down to 165 kJ/m^2.

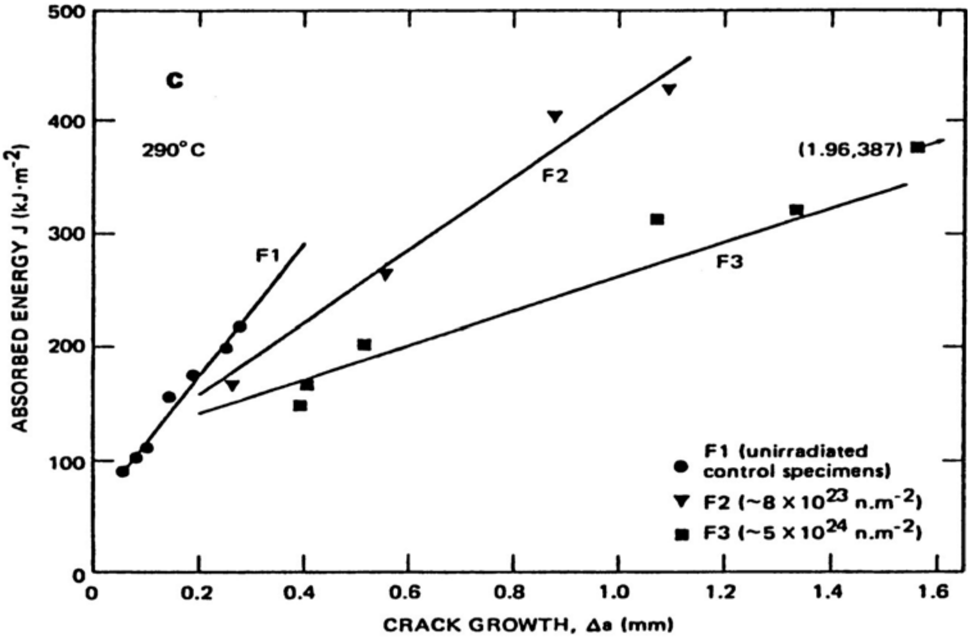

Figure 2. Crack growth vs. absorbed energy for different neutron fluences

After neutron irradiation the temperature dependency of impact fracture energy of RPV metal is shifted to higher temperature, the transition temperature *Tk* increases, the upper shelf energy and the slope of transition zone of Charpy curve decrease (Fig. 3).

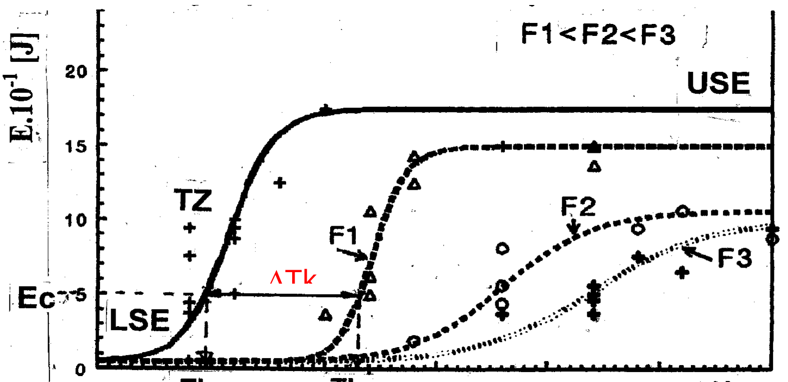

Figure 3. The effect of neutron irradiation of RPV metal on Charpy impact energy, transition temperature *Tk*, upper shelf energy, and the slope of transition zone

The critical temperature of embrittlement of RPV metal after neutron irradiation could be presented as:

$$T\kappa = Tko + \Delta T,$$

where *Tko* is transition the temperature in non-irradiated state and ΔT is the shift of transition temperature due to neutron irradiation.

The shift of transition temperature ΔT depends on neutron fluence *F*, metal composition (P, Cu, Ni), heat treatment, and irradiation temperature *Tirr*.

The criterion for RPV safe operation is $T\kappa < T\kappa^a$, where Tk^a is the maximum allowable transition temperature, determined by PTS analysis and fracture mechanics calculations.

Two methods are used for Tk determination: three-point bend impact testing of surveillance specimens, or calculation by empirical equation. Different equations for Tk dependency on fluence and impurity concentration are accepted in different standards:

Russian standard:

$\Delta Tk = Af \cdot (F/10^{18})^{0.333}$

WWER-440	Af (WM) = 800 (P% + 0.07Cu%)
$Tirr \Rightarrow 270$°C	Af (BM) = 1100P% – 2
WWER-1000	Af (WM) = 20
$Tirr \Rightarrow 290$°C	Af (BM) = 23

where:

Af is the chemical coefficient;

F [n/cm^2] is the neutron fluence ($E > 0.5$ MeV);

P%, Cu% are concentrations of P and Cu.

French standard RCM:

$\Delta T = CF \cdot f^{0.35}$

$CF = [8 + (24 + 1537(\mathrm{P} - 0.008) + 238(\mathrm{Cu} - 0.08) + 191\mathrm{Ni}^2\mathrm{Cu})]$

$F = F/10^{19}$ n/cm^2 ($E > 1$ MeV), $Tirr \Rightarrow 290$°C

USA standard – Regulatory commission 1.99:

Edition 1

$\Delta Tk = [40 + 1000(\mathrm{Cu\%} - 0.08) + 5000(\mathrm{P\%} - 0.008)](F/10^{19})^{0.5}$

F [n/cm^2] ($E > 1$ MeV)

Edition 2

$\Delta T\kappa = CF \cdot f^{[\,0.28 - 0.10\log f]}$

$CF = (-10 + 470\mathrm{Cu\%} + 350\mathrm{Cu\%Ni\%})$

where:

$f = F/10^{19}$ [n/cm^2] ($E > 1$ MeV), $Tirr \Rightarrow 277 - 310$°C;

Cu% $\Rightarrow$ 0.01–0.04%; Ni% $\Rightarrow$ 0–1.2%; P% < 0.024%.

The morphology of fracture surfaces of Charpy specimens tested at upper shelf temperature, transition zone, and low shelf of Charpy curve is different (Fig. 4). At the upper shelf, the fracture surface is characterized by elements of ductile fracture. At the transition temperature, a central zone of brittle fracture appears. The relative part of brittle fractured zone increases with decreasing temperature. The elements of ductile fracture disappear completely at low shelf temperature.

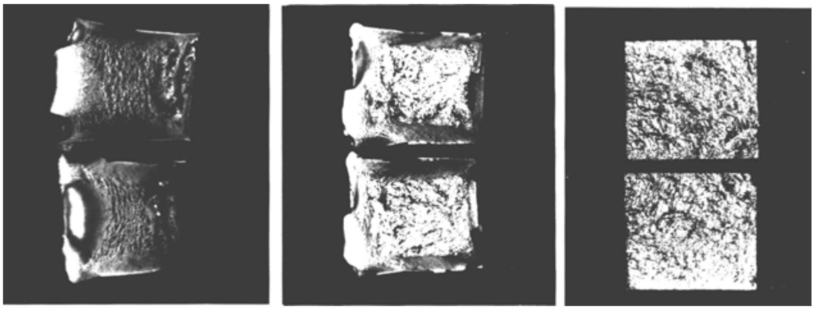

Figure 4. Fracture surface of Charpy specimens: ductile fracture at upper shelf (left); brittle fracture of central part in transition regime (middle); and brittle fracture at lower shelf (right)

A Surveillance program for monitoring the RPV metal embrittlement is foreseen for assuring safe exploitation of each power unit. This program includes irradiation of surveillance specimens at conditions corresponding to RPV wall condition and periodical testing of irradiated specimens in order to determine the current status of RPV metal. A container with two surveillance specimens is demonstrated in Fig. 5.

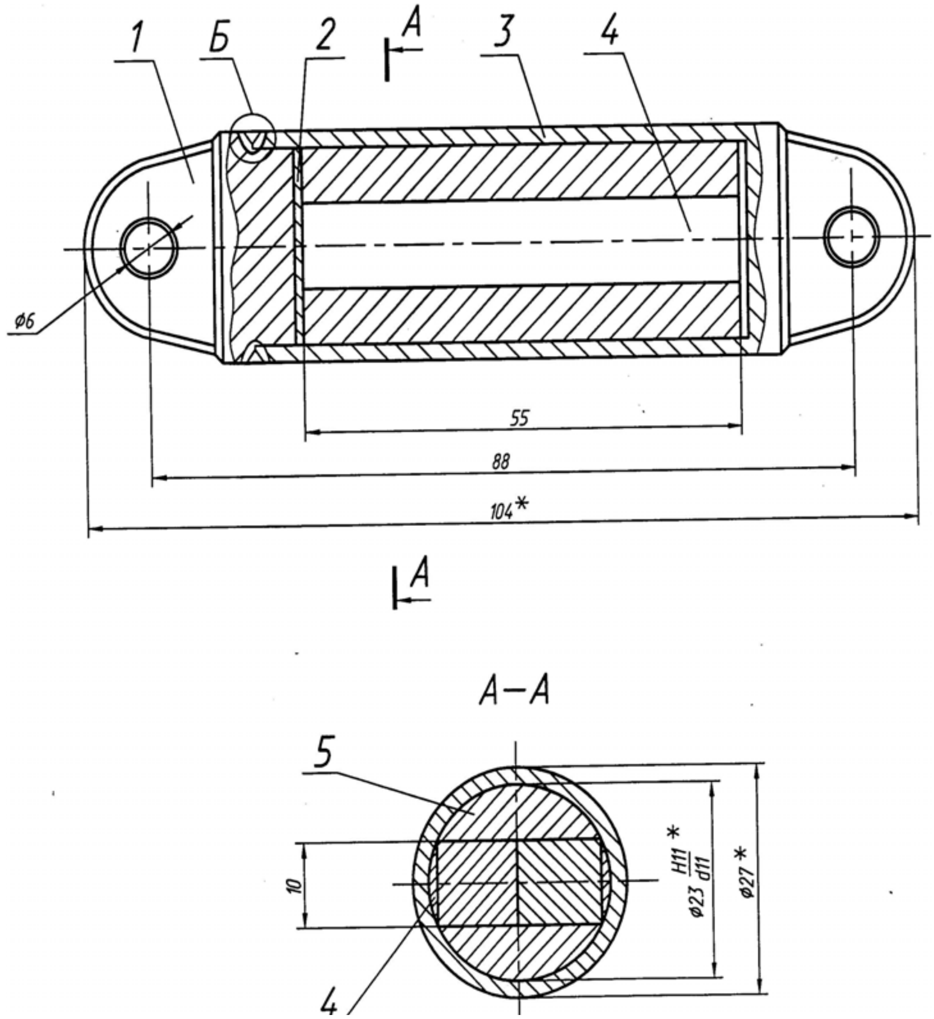

Figure 5. Container with two surveillance specimens

In order to overcome some deficiencies of the standard Surveillance program of WWER-1000 RPV, a model standard assembly is manufactured in IMS (Fig. 6). The main tasks of the investigation are:

– Determination of irradiation temperature on surveillance specimens.
– Precise determination of the neutron field on surveillance specimens.

Charpy specimens, manufactured from 15X2HMFAA. steel, are exposed to irradiation in the assembly.

Temperature monitors of low melting eutectic alloys are used for measuring the irradiation temperature. The set of temperature monitors covers the temperature range from 288°C to 300°C. The monitors are inserted in a central hole drilled in the top of surveillance specimens. Sets of neutron monitors of type Fe, Cu, Nb are provided for precise determination of neutron field in each irradiation capsule. The neutron monitor sets are located in the notch zone of the specimens and in the aluminium filler.

The assembly was irradiated during one fuel cycle. The examination of temperature monitors showed that the irradiation temperature is lower than 302°C. The measurement data of neutron monitor activities proved that the accuracy of methods and programs used for neutron fluence estimation is better than 15 relative percents. It was established also that the neutron field on the standard assembly is highly inhomogeneous and the difference between fluence value on different specimens from the same assembly row reaches 1.6 times.

Figure 6. The IMS model of assembly for standard Surveillance program of WWER-1000 RPV

The performance of reliable fracture mechanics safety analysis is necessary for assuring safe operation of NPP energy units. The following activities should be fulfilled for this purpose:

- Evaluation of the current status of selected critical components, systems and equipment of the units, taking into account the operating experience and actual accidents.
- Systems and components analysis based on material properties, mechanical loads, stresses and environment.
- Assessment of aging processes (neutron embrittlement, thermal aging, corrosion, fatigue, wear).
- Optimization of inspection and on-line monitoring programmes for materials aging.
- Definition of preventive measures, additional inspections, repair and replacement work.
- Determination of the safety margin of plant operation based on actual loading and material properties.

CORROSION AND STRESS CORROSION CRACKING

Dragutin Dražić, Serbian Academy of Science and Arts and Centre for Electrochemistry
Bore Jegdić, Military Technical Institute, Belgrade, Serbia and Montenegro

INTRODUCTION

Stress-corrosion cracking (SCC) is a phenomenon in which time-dependent crack growth occurs when necessary electrochemical, mechanical, and metallurgical conditions (Fig. 1) are fulfilled. When hydrogen is generated as a product of the corrosion reaction, crack growth can occur due to local hydrogen embrittlement process. Corrosion fatigue is a related process in which the load is cyclic rather than static, as in stress-corrosion cracking. A common feature of these processes is subcritical crack growth to a size at which catastrophic failure occurs. A second common feature of these processes is that these mechanisms are localised in the crack tip region. Such processes are major cause of service failures.

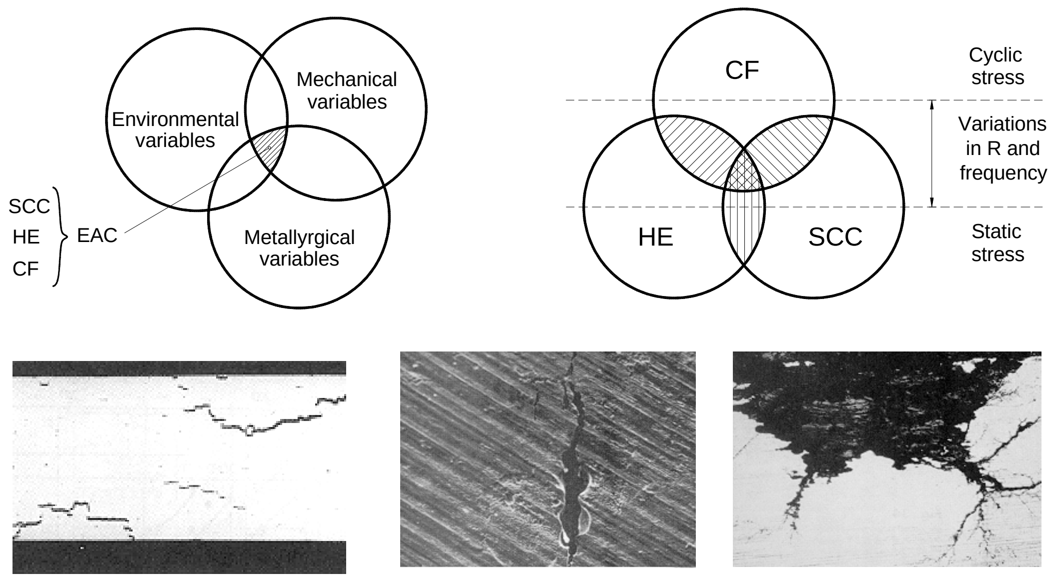

Stepwise cracking of low-strength pipeline steel exposed to H_2S

SCC initiation from a pit (front view)

SCC initiation from a pit (cross section view)

Figure 1. Necessary conditions for Stress Corrosion Cracking (SCC), Hydrogen Embrittlement (HE) and Corrosion Fatigue (CF) [1]

Environment that cause SCC

Environments that cause SCC are usually aqueous, and can be either condensed layers of moisture or bulk solutions. This failure is frequently a result of specific chemical species (ions) in the environment. For example, in alpha brass SCC traditionally referred as season cracking, is usually due from the presence of ammonia in the environment, and where chloride ions cause cracking in stainless steels and aluminium alloys. Also, an environment causing SCC in one alloy may not cause it another one. In general, SCC is frequently observed in metal/environment combinations that result in the formation of a film on the metal surface. These films may be passivating layers, tarnish films, or dealloyed layers. In many cases these films reduce the rate of general or uniform corrosion. As a result SCC is of greatest concern in corrosion-resistant alloys exposed to aggressive aqueous environments (Fig. 2).

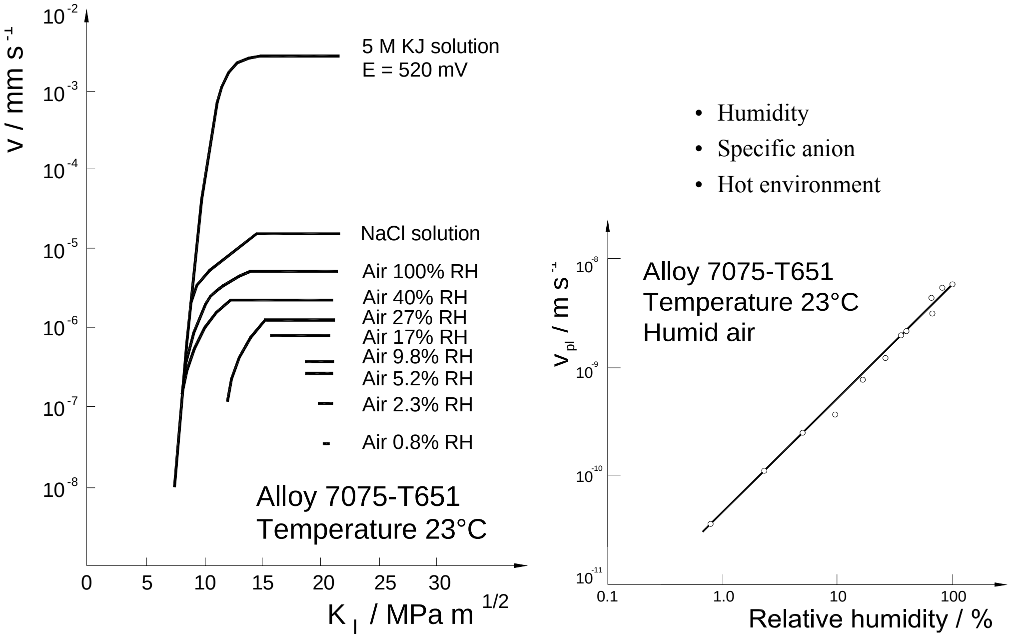

The environment effects by:

- Chemical reactions (independent on potential), e. g.:
  $FeO + 2Cl^- + H_2O = Fe^{2+} + 2Cl^- + 2OH^-$ (passive film destruction)
  $Fe + 2H_2O = Fe^{2+} + H_2 + 2OH^-$ (chemical dissolution)
- Electrochemical reactions (potential dependent rates), e.g.:
  $Fe = Fe^{2+} + 2e^-$ (anodic dissolution–oxidation)
  $2H^+ + 2e^- = H_2$ (cathodic H_2 evolution–reduction)

Figure 2. Environments that can cause stress corrosion and stress corrosion cracking, *v*–crack propagation rate; K_I–stress intensity factor [2]

Initiation of SCC

SCC is frequently initiated at pre-existing crack-like defects or at corrosion–induced surface features, as pits or intergranular corrosion (Fig. 3). The pits can be formed during cleaning operations or exposure to the service environment, for example: at inclusions that disturb the homogeneity of the surface, or by breakdown of the protective film in the presence of halogen ions. In electrochemical terms, pits are formed when the metal potential exceeds the pitting potential. The transition between pitting and SCC depends on the same parameters that control the SCC, that is, the electrochemistry of the base of the pit, metal composition, and stress and strain rate at the base of the pit. Fracture mechanics implies that the structure already contains a crack or a crack-like flaw. Except for the case of gaseous hydrogen induced SCC all other environmentally induced SCC are at least initiated by electrochemical processes, while the growth of crack tips are also controlled by electrochemical reactions. Therefore, electrochemical processes are of great importance in the analysis and evaluation of the possibilities and forecasting possible stress corrosion and fatigue corrosion failures.

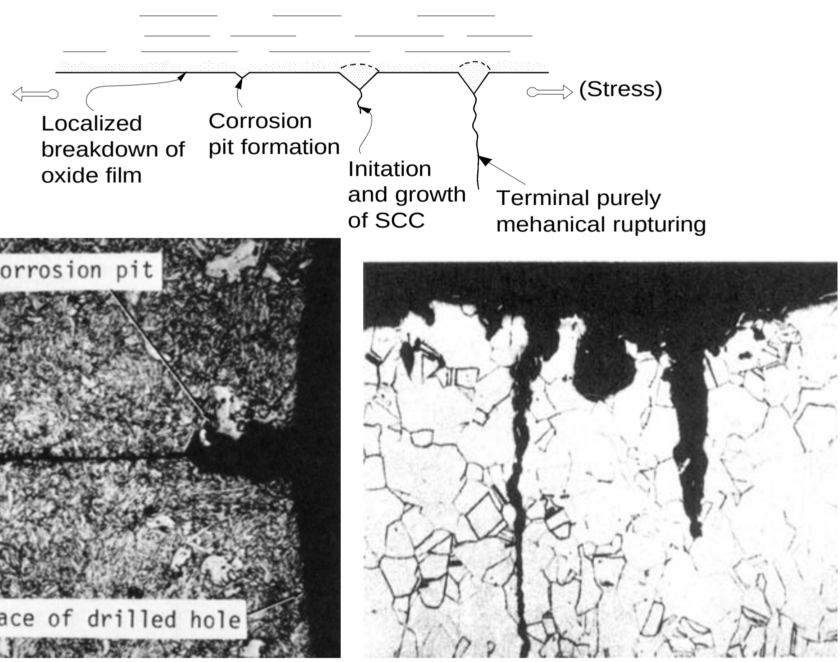

Stainless steel: fatigue crack initiated at the pit bottom

Typical fatigue crack in a copper alloy

Figure 3. Development of a pit into a crack

1. BASIC ELECTROCHEMISTRY OF CORROSION

Electrochemical reactions differ from ordinary chemical reactions in that the one of the reactants participating in the reaction are free electrons, so that an electrochemical reaction is always an oxidation or reducing process, depending weather reactants are loosing or accepting electrons. Electrochemical reactions are usually occurring on the surface of metals in contact with a solution containing some ionic species (e.g. salts or acids) usually called electrolytes. Electronically conducting metal serves as a donor or acceptor of free electrons, depending on the conditions at the metal/electrolyte boundary, and, even more important, on the possible electric contact of metal under study with some other metal in the same electrolyte. Such a case is shown schematically in Fig. 4 (left side) and represents an electrochemical cell. In this case, this is a cell consisting of a Zn electrode immersed in the solution of Zn^{2+} ions coupled with a Pt electrode immersed in the solution containing H^+ ions, e.g. any acid, and a porous separator. Electrochemical reactions occurring in such a cell are indicated in Fig. 4 as two reactions occurring separately at two electrodes (Eq. 1–3). Platinum as a noble metal in such a cell does not participate in the reaction but serves only as the free electron donor or acceptor.

If the voltmeter, which in this case shows voltage of 0.763 V, with the negative pole at the Zn electrode (it is assumed that this voltmeter consumes negligible current for its action) and corresponds to the no-current flow equilibrium state of the electrochemical cell, is replaced by a current consumer, e.g. a resistor, or even bridged, the existing voltage drop will cause flow of electrons through the wire and bring electrons leaving Zn to Pt electrode, and consequently provoke reactions (1) and (2) occurring in the direction from left to right. If not stopped, this process will go on until all metallic Zn is consumed. Basically this is what is happening when we use common zinc–metal hydride batteries, but also when we put a piece of zinc in acid and it dissolves in the solution by direct electrochemical corrosion. If we add reaction (1) to reaction (2) we obtain reaction (3) (Fig. 4), which represents overall processes as a single chemical reaction of the redox type, but the mechanism of this reaction is, as documented previously, electrochemical in nature, and follows the laws of electrochemical kinetics. Therefore for good understanding and control of such processes the knowledge of electrochemical kinetics of all electrochemical processes participating in corrosion processes is necessary.

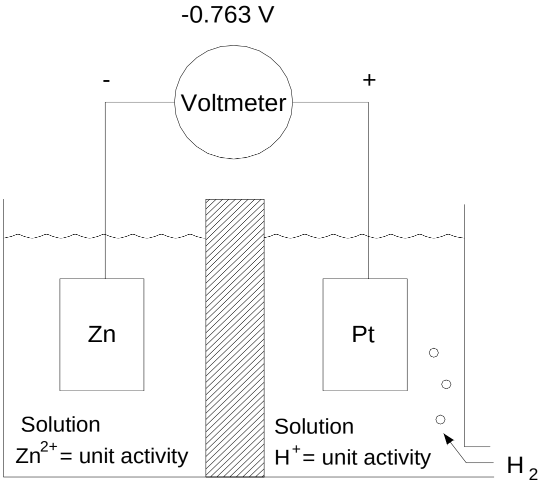

$$Zn = Zn^{2+} + 2e^{-} \quad (1)$$

$$2H^{+} + 2e^{-} = H_2 \quad (2)$$

$$Zn + 2H^{+} = Zn^{2+} + H_2 \quad (3)$$

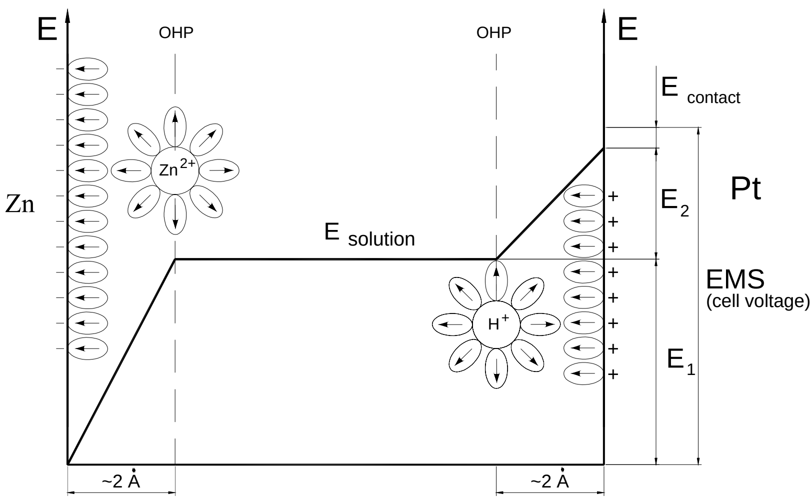

- Galvanic corrosion (macro cell)
- Local corrosion (micro cell)
- Uniform corrosion (both reactions at the same surface)

Figure 4. Electrochemical cell at equilibrium (no current flow) [3]

Since electrified ions in the electrolyte, water dipoles, and free electrons in the metal are electrically influenced by each other, a very thin electrochemical double layer of a few angstroms in thickness forms at metal/electrolyte boundaries (Fig. 4, below). The imaginary plane of the closest approach of hydrated ions to the metal surface is called the outer Helmholz plane (OHP), and between it and the metal surface the electric field has the strength of ca. 10 000 000 V/cm. Voltage drops at each double layer, including the outer voltage drop at the eventual contact of different metals in the measuring circuit, cumulatively form the total cell voltage accessible to measurement.

Gibbs energies of individual electrochemical reactions differ, and according to their values and sign, the equilibrium of these reactions is shifted more to the left or to the right. Their electrochemical reactivity can be easily compared by measuring the cell voltages if different metals replacing Zn were used in a cell as presented in Fig. 4. When tabulated, these voltages form the well known Volta or electrode potential scale (Fig. 5).

ELECTRODE POTENTIAL SCALE

$Au^{3+} + 3e^- = Au$	1.500
$O_2 + 4H^+ + 4e^- = 2H_2O$	1.229
$Pd^{2+} + 2e^- = Pd$	0.987
$Hg^{2+} + 2e^- = Hg$	0.854
$Ag^+ + e^- = Ag$	0.800
$Hg_2^{2+} + 2e^- = 2Hg$	0.789
$Cu^+ + e^- = Cu$	0.521
$Cu^{2+} + 2e^- = Cu$	0.337
$2H^+ + 2e^- = H_2$	0.000
$Pb^{2+} + 2e^- = Pb$	–0.126
$Sn^{2+} + 2e^- = Sn$	–0.136
$Ni^{2+} + 2e^- = Ni$	–0.250
$Co^{2+} + 2e^- = Co$	–0.277
$Cd^{2+} + 2e^- = Cd$	–0.403
$Fe^{2+} + 2e^- = Fe$	–0.440
$Cr^{3+} + 3e^- = Cr$	–0.740
$Cr^{2+} + 2e^- = Cr$	–0.910
$Zn^{2+} + 2e^- = Zn$	–0.763
$Mn^{2+} + 2e^- = Mn$	–1.180
$Ti^{2+} + 2e^- = Ti$	–1.630
$Al^{3+} + 3e^- = Al$	–1.660
$Mg^{2+} + 2e^- = Mg$	–2.370
$Na^+ + e^- = Na$	–2.710
$Ca^{2+} + 2e^- = Ca$	–2.870
$K^+ + e^- = K$	–2.930
$Li^+ + e^- = Li$	–3.050

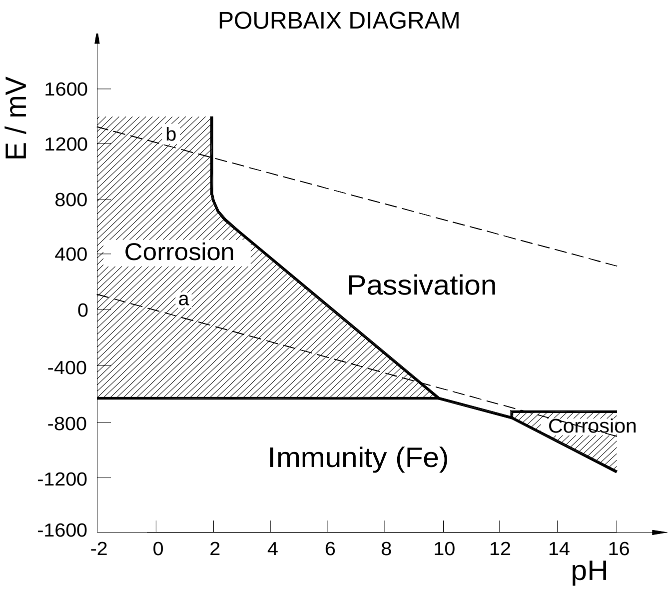

(a) $2H^+ + 2e^- = H_2$
(b) $O_2 + 4H^+ + 4e^- = 2H_2O$

Figure 5. Volta electrochemical scale and a Pourbaix diagram for iron [4]

Since it is not physically possible to measure the absolute voltage drop of a single double layer (as soon as the wire of the measuring voltmeter is introduced in the electrolyte, it forms a new electrochemical cell with at least two electrodes, i.e. double layers) an electrochemical convention is adopted – that the voltage drops between the measured metal and a Pt electrode in a H^+ containing electrolyte and presence of gaseous hydrogen is named the electrode potential against a standard hydrogen electrode (SHE), as a conventionally accepted zero at the so-called hydrogen potential scale. As shown by numbers in the Volta potential scale, different electrochemical cells can be formed by combining two different reactions to form a cell, in which when short-circuited, the most electronegative reaction will be anodic, i.e. metal dissolves or corrodes, while the most electropositive reaction consumes electrons and behaves as the so-called cathode. This table shows that any electrode process, being more electropositive than the potential of a metal under consideration, can cause electrochemical corrosion of this metal. This, for example, is the case of Zn in acidic solution; Fe or Cd in acidic solution; but not Cu in the same solution. If however, one allows access of oxygen to a Cu surface, reduction of O_2 will be a cathodic reaction with electron consumption, and a cell with a voltage drop of 0.892 V will be formed, with intensive Cu dissolution if the cell is short-circuited. Any other combination of electrochemical reactions will have the same behaviour. It is a well known example from the British naval history, from the beginning of the 19th century, when copper plates on war ships were fixed with iron nails. After short times due to the Cu–Fe corrosion cell action, nails corroded and all the copper plates finished in the sea.

Electrode potentials can be represented by the well known Nernst equation

$$E = E^\circ - (RT/nF)\ \ln([R_1][R_2][R_i]/[Ox_1][Ox_2][Ox_j]) \tag{4}$$

where E^o is the standard electrode potential from the Volta potential scale for the specific electrode reaction, n is the number of exchanged electrons in the electrochemical reaction, while squared parentheses represent concentrations of substances R_1, R_2, etc., on the reduced side in the electrochemical reaction and Ox_1, Ox_2, etc., on the oxidized side. If some of the species participating in the reaction has stoichiometric number (showing how many particles participate in the reaction) $v > 1$, the corresponding concentration term should be raised to the power of v. For example, for the reduction of O_2 (Fig. 5, Volta Table) the Nernst equation should be written as:

$$E(O_2) = E^\circ(O_2) - (RT/4F)\cdot\ln([H_2O]_2/[O_2][H^+]_4) \tag{5}$$

Using the convention that concentrations (or more precisely activities) of pure substances under standard conditions are equal to unity, i.e., in water solutions $[H_2O] = 1$ and $[O_2] = 1$, and the corresponding numerical values for the gas constant R, standard temperature T and Faraday's constant F, as well as the standard electrode potential for oxygen reduction from the Volta Table, +1.229 V, and converting ln into log, one obtains

$$E(O_2) = 1.229 + 0.059\cdot\log[H^+] \tag{6}$$

showing that potential for oxygen reduction, Eq. (12) depends on pH ($pH = -\log\ [H^+]$). This dependence is shown by a dashed line (b) in the Pourbaix diagram for Fe (Fig. 5), presenting the electrode potentials for Fe as a function of pH. A similar equation can be obtained for the hydrogen evolution reaction, Eq. (2), in Fig. 4.

$$E(H_2) = 0.059\cdot\log[H^+] \tag{7}$$

which differs from Eq. (5) in the values of the standard electrode potentials (note that in Volta Table $E^\circ(H_2) = 0.000$ V). Full lines in the Pourbaix diagram represent the separation of the region of thermodynamic stability of various forms in which Fe can exist as a function of potential and pH, bearing in mind that at higher pH values of the solution, solid iron oxides or hydroxides, are stable forms. In fact they are the main constituents of what is commonly known as iron rust. They are stable in the region indicating Passivation, i.e., metallic iron is in a so-called passive state in which the surface is covered with a thin layer of iron oxide 2–5 nm thick, and represents a state of fairly good corrosion stability. Shaded regions represent conditions when soluble Fe^{2+} ions are stable in acidic solutions ($pH < 7$), or $HFeOO^-$ soluble species are stable in ionic form in excess of alkalies ($pH > 12$). In the absence of oxygen, if conditions are such that the Fe electrode has the potential in shaded areas between the full line representing stable Fe (Immunity) and the dashed line (a) representing hydrogen evolution reaction, iron will spontaneously corrode with gaseous hydrogen evolution,

$$Fe = Fe^{2+} + 2e^- \tag{8}$$
$$2H^+ + 2e^- = H_2 \tag{9}$$
$$Fe + 2H^+ = Fe^{2+} + H_2 \tag{10}$$

Reaction (10) represents the overall corrosion reaction with hydrogen evolution, caused by the action of acid H^+ ions. Its electrochemical nature is represented by electrochemical reactions (8) and (9), and its rate will depend exclusively on the individual rates of these reactions. In other words, the rate of corrosion is determined by electrochemical kinetics of these reactions.

Corrosion can be caused also by electrochemical reduction of oxygen, if present, and it can be represented by corresponding electrochemical reactions (12). By summing electrochemical reactions, overall corrosion reaction (13) caused by oxygen can be written:

$$Fe = Fe^{2+} + 2e^- \tag{11}$$
$$O_2 + 4H^+ + 2e^- = 2H_2O \tag{12}$$
$$Fe + O_2 + 4H^+ = Fe^{2+} + 2H_2O \tag{13}$$

It should be pointed out that the necessary condition for the reaction which can provoke corrosion is to have the potential dependence according to the corresponding Nernst equation in the potential range more positive than the solid line dividing Immunity and Corrosion regions. This could be any other electrochemical reaction with corresponding Nernst potential in that region. For example, reduction of Fe^{3+} ions to Fe^{2+}, or Cu^{2+} to metallic Cu (so-called cementation process). It should be, however, always borne in mind that the Nernst equation and its application, Pourbaix diagrams, represent the equilibrium, i.e. thermodynamic data, indicating only the thermodynamic possibility that corrosion processes can occur. In other words, thermodynamics is only the necessary condition which has to be satisfied. It does not say in what time interval it will happen, i.e. it does not say anything about the reaction, i.e. corrosion rates.

As it will be shown later, by proper control of electrode potential, or addition of corrosion inhibitors in the solution, the rate of these reactions can be considerably decreased, and consequently the overall corrosion is decreased or even practically eliminated. Needless to say is as with other chemical reactions, the addition of reaction activators (i.e. catalysts) considerably accelerates corrosion, causing sometimes catastrophic results.

Electrochemical reaction rates are controlled by electrochemical kinetics. In a simplified form it can be quantitatively represented by Tafel equations (Fig. 6) when electrochemical processes are controlled by the exchange of electrons with the reacting particles inside double layers. As presented for the case of a zinc electrode, decrease of the double layer potential difference, i.e. shifts of the electrode potential in the positive direction accelerates the electrode reaction of metal dissolution (anodic reaction), while the increase of potential difference, i.e. shifts of the electrode potential in negative direction accelerates the electrode reaction of metal deposition (cathodic reaction). Tafel equations correlate the electrode potential, in fact the double layer potential difference (Fig. 6) with the logarithm of reaction rate, i.e. current density ($\log i$), while specific characteristics of each metal are expressed by numerical values of the Tafel constant a and Tafel slope b. Current density in the Tafel equation is usually related to the geometrical surface area of the electrode surface of 1 cm^2, assuming that the surface is bare. If the surface is blocked by some inactive substance not participating in the reaction (e.g. oxide, adsorbed organic molecules, etc.) with the degree of coverage θ, often termed as reaction inhibitors, the active metal surface is a part of unblocked surface $(1 - \theta)$, by which one should multiply the reaction current density to obtain the real effective current, i.e. $i(1 - \theta)$. So by proper use of reaction inhibitors (cathodic, anodic, or with double action) the corrosion rates can be considerably decreased and kept under control. But note that if thermodynamic data show corrosion processes are possible, corrosion cannot be stopped totally, because that would ask for inhibitor coverage of 100%, i.e. $\theta = 1$, which is impossible to be accomplished in real systems.

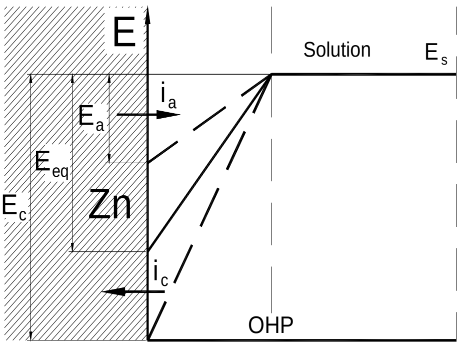

TAFEL EQUATIONS:
$\log i_a = a_1 + b_1 \cdot \log E_a$
$\log i_c = a_2 + b_2 \cdot \log E_c$
$Zn = Zn^{2+} + 2e^-$ (anodic)
$Zn^{2+} + 2e^- = Zn$ (equilibrium)
$Zn^{2+} + 2e^- = Zn$ (cathodic, high c_{Zn2+})
$2H^+ + 2e^- = H_2$ (cathodic, high c_{H+})

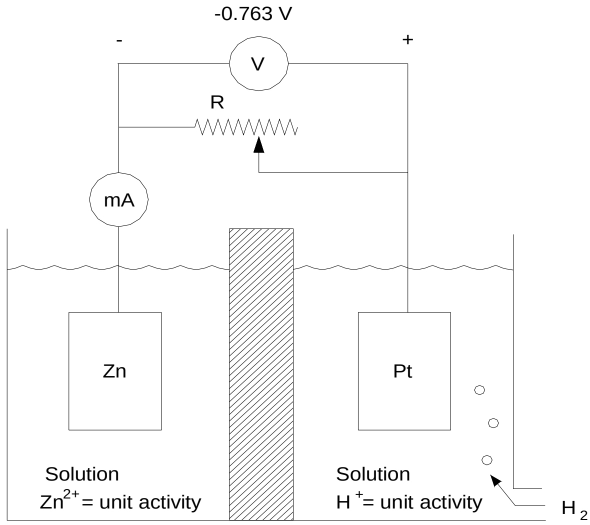

Figure 6. Effect of polarization of an electrode from an external power source [5]

Figure 7 graphically presents Tafel lines for a hypothetical corrosion process with a single cathodic and anodic electrochemical reaction in which i_o is the so-called exchange current density, and is a main constituent of a Tafel constant a. When the numerical value of a is larger, so is the exchange current density, and that means that the Tafel line for the corresponding process will be shifted to the right in the diagram. The opposite happens if the exchange current density is smaller.

On the right hand side of Fig. 7 the same Tafel lines of individual electrochemical processes are plotted together in a form which can be experimentally obtained for a corroding metal. Namely, the corrosion process spontaneously occurs when partial individual electrochemical reactions having opposite signs are numerically equal. This happens when they intersect in a diagram of individual partial currents (left hand side in Fig. 7), indicating equivalence of partial anodic reaction (dissolution) and cathodic reaction (e.g. hydrogen evolution – the O in Fig. 7, which may be any substance in its oxidized form, H^+, O_2, Fe^{3+}, etc., and can be electrochemically reduced to its stable R form). In this situation one cannot detect any external current, even though one can use this intersection point to express the effective corrosion rate as the value of equivalent corrosion density, $\log i_{corr}$ which is equal to current density of metal dissolution at this potential. Therefore the potential of this intersection point is named corrosion potential, E_{corr}. Experimentally, one can determine the corrosion rate, i.e. $\log i_{corr}$, from the intersection of measured cathodic and anodic Tafel lines, or by extrapolating one of them to separately determined corrosion potential, E_{corr}. This is the basis of many commercially available electronic devices for determining corrosion rates which are used in laboratories and for field operation, even for automatic monitoring of corrosion rates for ships, docks, pipelines, bridges.

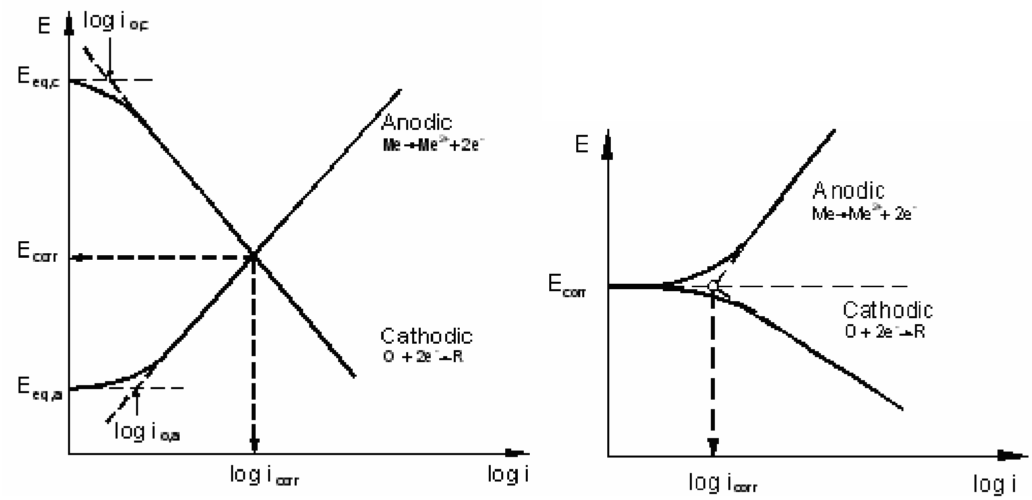

Tafel plots for corrosion processes:
Anodic current: $\log i_a = a_1 + b_1 \cdot \log E_a$
Cathodic current: $\log i_c = a_2 + b_2 \cdot \log E_c$

Tafel plots for corroding metal:
$i = i_a + i_c$
at E_{corr}: $i = 0$; $i_a = i_c = i_{corr}$

Figure 7. Partial polarization curves (Tafel lines) for individually occurring electrochemical reactions on a corroding metal (left). Experimentally measurable Tafel lines for a corroding metal (right)

Most commercially used metals, especially their alloys, have a property that in a broader span of potentials on the positive side exhibit the phenomenon of passivity. In fact at some values of anodic polarization, an oxide layer forms at the surface with coverage close to unity ($\theta \to 1$) or even equal to 1, but with its own electrochemical activity at a very reduced level (very small i_o).

Characteristics of most anodic polarization curves for easy passivating metals (e.g. Fe, Ni, Cr) are the appearance of a passivation peak (Fig. 8, left) at a certain anodic current density i_{pp}, and passivation potential E_{pp}, when the passivating anodic current i_{pp} suddenly drops to very small currents i_{p} (a few micro amperes). If the potential of metal can be in some way kept in the passivation region, corrosion of metal would be practically eliminated. This is illustrated by the diagram on the right, schematically representing the anodic polarization curve for an easy passivating metal and partial cathodic polarization curves for three cathodic processes having different equilibrium potentials (Volta scale, see Fig. 5). If, for example, reaction 1 is a hydrogen evolution reaction, Tafel line 1 will intersect the anodic polarization curve in the region of active anodic dissolution of metal, i.e. before the passivation peak, thus the corrosion diagram, as often termed, looks as the diagram on the left in Fig. 8. To passivate such a metal, one has to shift the electrode potential to the passive potential range, e.g. potentiostatically, and then passivate the metal. This approach is used in a so-called anodic corrosion protection method. However, as in Fig. 8, this potential should be carefully controlled, since some metals (Fe, Cr) exist in several valence states at more positive potentials and lose the primary passive layer and reach the so-called transpassive region in which they can be again anodically dissolved in a form of soluble higher valence ions. If these ions can form another oxide layer, a secondary passivity is reached, and at more positive potentials oxygen evolution starts.

Passivation can be achieved also, in a more simple way by introducing oxygen (or air) into the electrolyte when electrochemical oxygen reduction reaction (reaction *b* in Fig. 5) with its Tafel line 3 intersects the anodic polarization curve in the region of anodic passivity. In this case the metal will obtain the value of corrosion potential of intersection point, and also the corrosion current density will be equal to the passive current i_p. This is why many metals and alloys, when used in open systems (i.e. in contact with air) behave as passive. However, if the concentration of oxygen decreases for some reason, Tafel line will shift to the left (Fig. 8, right) and eventually reach the situation marked with 2. In this case, the intersection of polarization curves is in position 2 when corrosion current density is rather large. Hence, in order to be able to control corrosion rates, experimentally determined polarization (or corrosion) diagrams for each situation considered have to be known. Otherwise, one can make the situation even worse by mistake.

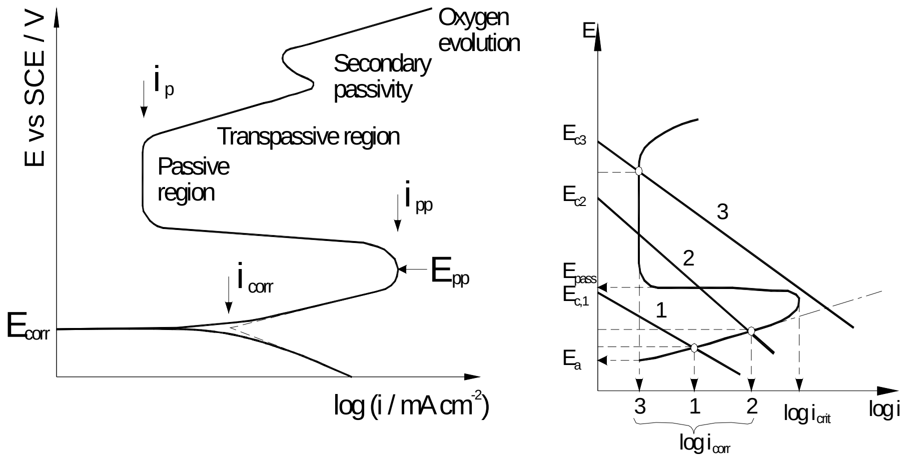

Figure 8. Polarization curves for metals or alloys which passivate at positive potentials [6]

2. PASSIVITY AND PITTING

It was mentioned earlier that very often bottoms of pits are positions from which cracks start developing when the material is exposed to constant or frequency dependent stresses. Pitting appears when the passive layer for some reason breaks at some places, exposing bare metal surface to the electrochemical anodic dissolution. In other words, while the passive surface behaves as the case 3 in Fig. 8 (right), the bottom of the pit, not being protected by oxide layer, or because of the lack of oxidizing agent in the pit, obtains electrochemical characteristics represented by case 2 or even 1. That means that metal dissolves very actively and the depth of the pit increases. A certain number of developed pits can stop growing if the rate of transport of oxygen or oxide growth is able to heal the compactness of passive layer even inside the pit, and in such a way stop further pit growth. Depending on the conditions, pitting can create a number of rather serious damages on pipeline walls, reservoirs, steam boilers, etc.

The most important conditions for the start of pitting are; (*i*) chemical and structural properties of the metal or alloy, (*ii*) pitting potential, E_{pit}, and (*iii*) the most important, presence of chloride ions in the electrolyte. The effects of these factors are depicted in Fig. 9. The diagram on the left shows the effect of chromium concentration in the alloy, showing why low Cr concentration alloys are sensitive to active corrosion. The intersection of anodic and cathodic Tafel lines are in the range of *active anodic dissolution* while for case 3, the intersection is in the *passive* range, i.e. the alloy behaves as passive (this is due to the formation of a passive chromium oxide layer at the surface). Diagram on the right shows the effect of chloride ions on the behaviour of stainless steel. Both alloys are selfpassivating in the presence of oxygen and their polarization diagrams correspond to case 3 on the diagram (left side), i.e. the open circuit potential is in the passive potential range with very low corrosion rate. Hastelloy passive layer is resistant to the action of chloride ions and anodic current starts increasing at the potential of about 0.6 V (versus saturated calomel electrode – SCE). This corresponds thermodynamically to the potential of the start of oxygen evolution in neutral NaCl solution (pH ~ 7). In other words, passivity is protected up to very high anodic potentials. However, stainless steel is sensitive to the presence of chloride ions, and at potential of cca. 0.0 V (vs. SCE) anodic current suddenly increases. It is the result of intensive pit formation and anodic metal dissolution inside pits. This potential value is called pitting potential, E_{pit}, and is a function of: material type and composition; thermal treatment; and solution composition. Note that in the absence of chloride ions, e.g. in sulphate solutions, polarization curve for stainless steel would be similar to the curve for Hastelloy.

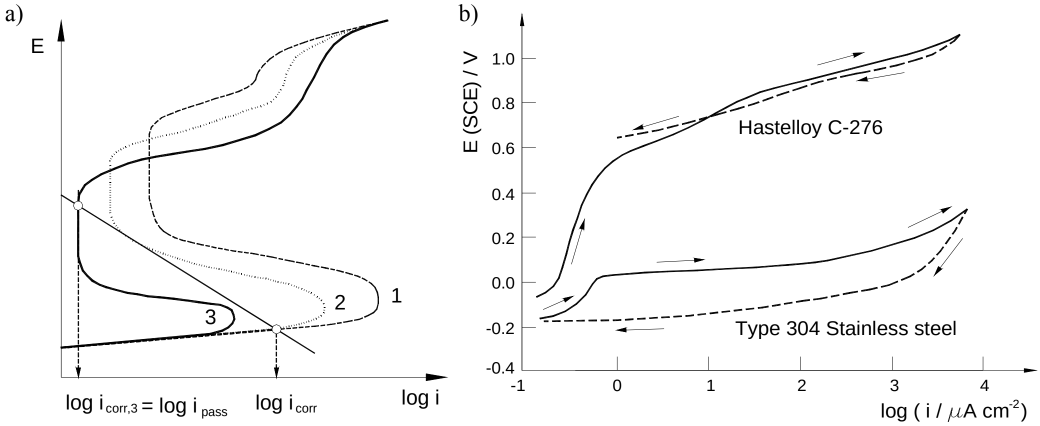

Figure 9. a) Schematic polarization curves for stainless steel: (1) 3% Cr (2) 10% Cr (3) 14% Cr. Straight line is cathodic current for O_2 reduction. b) Polarization curves for Hastelloy C–276 and stainless steel 304 in 3.5% NaCl [6]

2.1. Pit growth mechanism

The most important point in the theory of pit growth is a formation of a corrosion cell between the passive surface, which has electronic conductivity enabling cathodic reaction of oxygen reduction to H_2O in acidic, or OH^- ions in neutral and alkaline solutions (i.e. when pH > 5), and active anodic dissolution of metal at the bottom of the pit, which is not passive because of the presence of Cl^- ions, i.e. anodically dissolves at high rate (Fig. 10). When they accumulate in the void, the hydrolysis of formed metal ions with water molecules forms metal hydroxides and H^+ ions. By this reaction pH can decrease to 2–3 at the pit bottom, but not less. The difference between cathodic potential at the passive surface and active anodic dissolution potential at the pit bottom is compensated by ohmic potential drop in the electrolyte inside the pit. This potential difference is not larger than 200 mV, according to experimentally obtained data [7].

3. MECHANISMS OF STRESS CORROSION CRACKING (SCC) AND CORROSION FATIGUE CRACKING (CFC)

According to present views, fast progressing of crack tips leading to cracking of stressed materials (SCC and CFC) can be explained depending on the kind of metal or alloy, by two different mechanisms, anodic dissolution model, and hydrogen embrittlement model (Figs. 11 and 12).

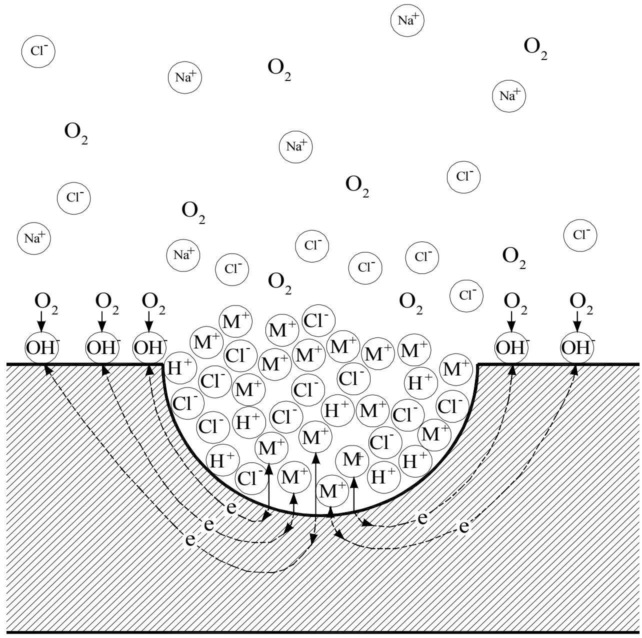

Micro cell action in pit growth:
- Oxygen reduction at adjacent surfaces (cathodic process)
- Metal dissolution at the pit bottom (anodic process)

Figure 10. Schematic representation of the pit growth mechanism [8]

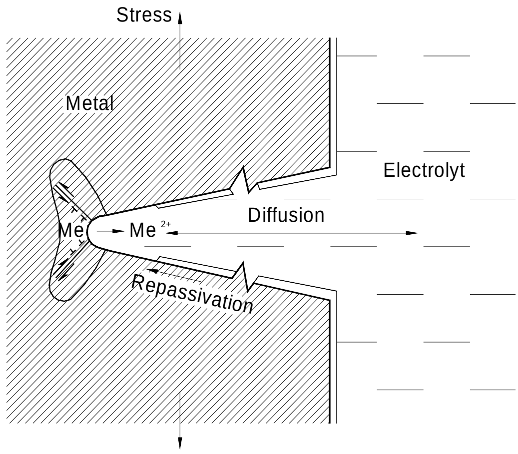

- Active crack tip and passive crack walls
- Rupture protective surface film by emerging dislocations (slip steps)
- Rapid anodic bare metal dissolution on the crack tip (i_a): $v = \frac{M}{z \cdot F \cdot \rho} \cdot i_a$
- Slip planar (stacking–fault energy, precipitate type, etc.)
- Transgranular SCC austenitic stainless steels

Figure 11. Anodic dissolution model of crack propagation [10]

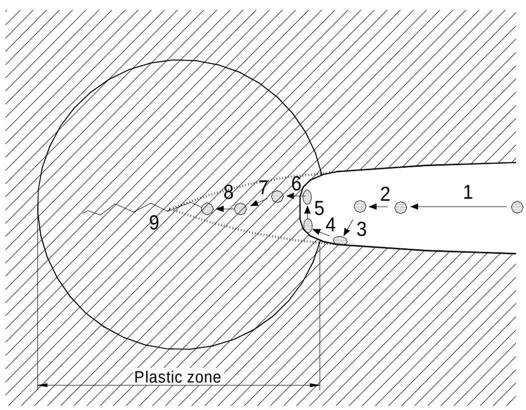

(1) mass transport along the crack to or away from the crack tip
(2) reactions in the solution near the crack
(3) surface adsorption at or near the crack tip
(4) surface diffusion
(5) surface reactions
(6) absorption into the bulk metal
(7) bulk diffusion to the plastic zone ahead of the advancing crack
(8) chemical reactions in the bulk
(9) rate of interatomic bond rupture

Figure 12. Hydrogen embrittlement model of stress corrosion crack propagation [11]

Anodic dissolution model is essentially the same as the pit growth mechanism, except that the rate of anodic reaction is increased because the stressed metal at the tip dissolves at much higher rate than normally since newly formed surfaces dissolve up to 10 times faster than normally [9].

Hydrogen embrittlement model is based on the fact that most ferrous metals can absorb considerable amounts of hydrogen and because of changes in the lattice structure, they become brittle. Because of increased stress concentration around the tip, brittle metal structure cannot sustain the stresses, and the crack continues to propagate. Processes involved here are illustrated in Fig. 12.

The most important point in this mechanism is the presence of hydrogen at the tip of a crack and its fast penetration into the bulk of the metal in front of the tip. However, this model has one difficulty. Normal electrochemistry cannot explain where this hydrogen is coming from. According to ideas involved in this model, crack tip dissolves anodically in the same manner as in the anodic dissolution model, but simultaneously evolving hydrogen accelerates tip propagation by the embrittlement action. This model is supported by a large number of independent experimental data concerning the increase of absorbed hydrogen concentration in the vicinity of the tip, increase of brittleness, etc. The problem is that the model, as mentioned above, cannot explain how anodic reaction at the crack tip produces hydrogen. If the crack is considered similarly to the case of pit growth, as a corrosion cell with cathodic reaction at the outside passivated surface, and anodic dissolution reaction at the tip of a crack, then from a simple corrosion diagram (Fig. 7) it is concluded that during anodic polarization cathodic reaction, i.e. hydrogen evolution is suppressed almost completely (note the logarithmic scale on the horizontal axis).

There is experimental evidence that hydrogen bubbles evolve from pits and cracks, and can be collected and analyzed as hydrogen. Also, potentials inside pits and cracks were measured, and also the pH at their bottoms. Figure 13 illustrates results obtained by Seys et al. [7] in a form of a Pourbaix diagram for Fe, presenting point 1 as the condition of a passive stainless steel and points 2 and 3 representing the variation of pH at the bottom of a pit and more importantly, potential at the bottom. An important point is that their potential is *more positive* than the reversible potential of the hydrogen evolution reaction (lower dashed line in the diagram), meaning that thermodynamics of the hydrogen evolution reaction forbids appearance of gaseous hydrogen at this potential. Hence, an important question arises. How is this hydrogen formed, that is so important for propagation of cracks?

Arguments in literature say that hydrogen in the metal is introduced already during manufacturing, and is really possible. However, as shown in Fig. 13b, even after removal of hydrogen absorbed during the manufacturing process, after leaving such material in contact with electrolyte, the fracture time returns to its initial value, indicating that hydrogen does not originate from the manufacturing process but forms during pitting and crack propagation. Hence, the question of hydrogen origin, causing fast propagation of stress corrosion cracks has still no acceptable answer.

An answer to this question, according to the experience of our co-author in the studies of electrochemistry of aluminium, stainless steels, and chromium [12-14], points that besides electrochemical processes of metal dissolution, represented by Eqs. (8–10), a parallel chemical process, as suggested earlier by Kolotyrkin et al. [15,16], occurs in a reaction with water molecules from the electrolyte, represented by an overall equation:

$$Fe + 2H_2O = Fe^{2+} + H_2 + 2OH^- \quad (14)$$

In this reaction there are no electrons involved, therefore it *is not* electrochemical and *does not depend* on electrode potential. Therefore it can occur at any potential outside or inside a pit or a crack and supply hydrogen which, either escapes as bubbles from pits or cracks, or penetrates inside the metal in front of a crack tip making it brittle. This is supported by the fact presented in Fig. 2 (right), that even the presence of humidity in the atmosphere can cause susceptibility to SCC proportional to the value of relative humidity, i.e. the amount of capillary condensed water.

a)

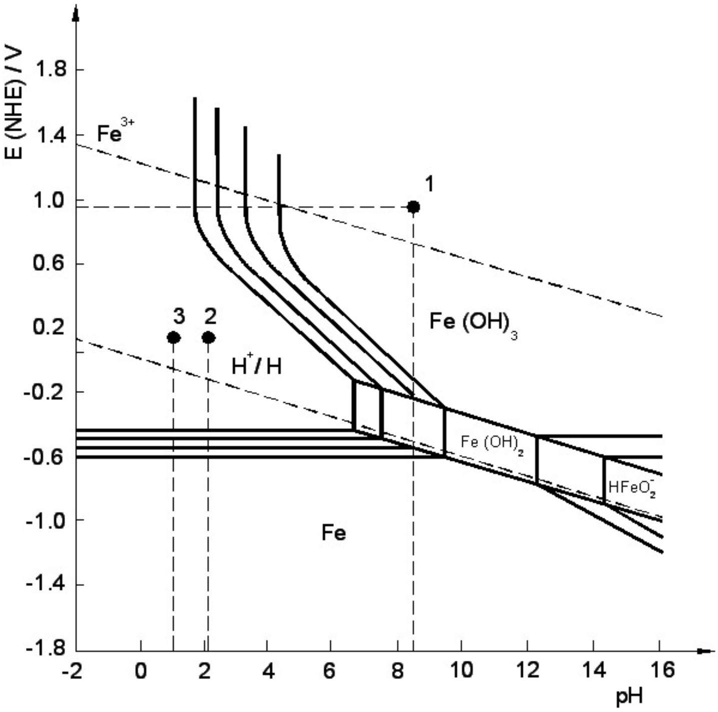

b)

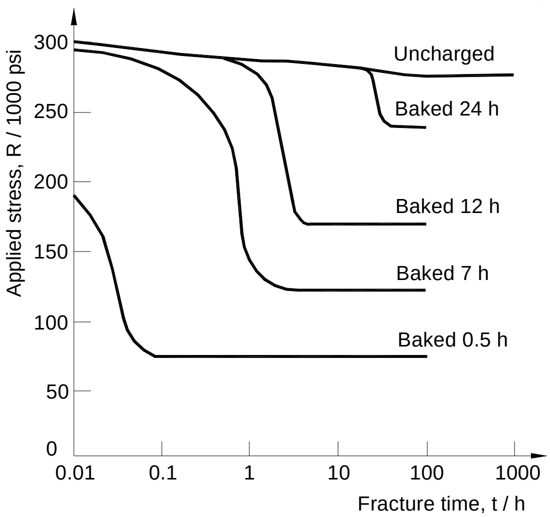

Figure 13. a) Pourbaix diagram for Fe with experimentally obtained data for the potential of stainless steel in 0.1 M $KHCO_3$ + 0.1 M KCl solution (pH 8.4). Point 1 measured at the outside surface. Points between 2 and 3 measured at the bottom of a pit [7]. b) Effect of the removal of absorbed hydrogen on fracture time of AISI 4340 alloy steel [30]

4. STRESS–CORROSION TESTING

Testing of SCC can be performed using specimens without a crack (smooth specimens), or using precracked (fracture mechanics) specimens. Stress corrosion testing can also be conducted by slowly increasing the load or strain of smooth or precracked specimens in a corrosive environment.

4.1. Tests on statically loaded smooth specimens

Tests on statically loaded smooth specimens are usually conducted at various fixed stress levels and time to failure of specimens in the environment is measured. The threshold stress R_{th} is determined when time to failure approaches infinity, Fig. 14. These experiments can be used to determine the maximum stress that can be applied in service without SCC failure, or to evaluate the influence of metallurgical and environmental changes on SCC [11].

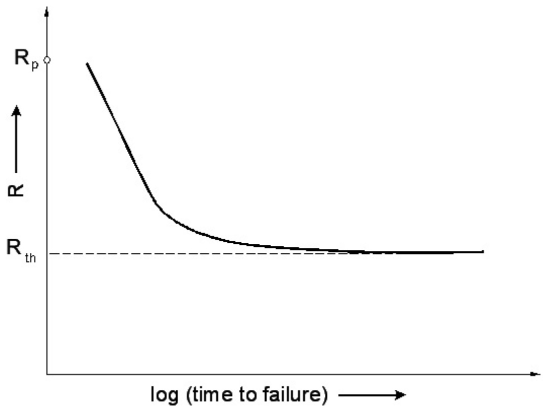

- Threshold stress R_{th} (maximum stress without SCC failure).
- Evaluate influence of metallurgical and environmental changes.

Figure 14. Scheme of typical results obtained by statically loaded smooth samples

4.2. Slow strain rate testing (SSRT)

Stress corrosion tests can also be conducted by slowly increasing load or strain on specimens in corrosive environment. These tests, developed by Parkins, are called slow-strain-rate tests (SSRT). The most significant variable in slow strain rate testing is the magnitude of strain rate. If the strain rate is too high, ductile fracture will occur before necessary corrosion reactions can take place. Relatively low strain rates must be used, but at too low a strain rate, corrosion may be prevented because of repassivation or film repair so that the necessary reactions of bare metal cannot be sustained, and SCC may not occur (Fig. 15a, alloy B). The repassivation reaction observed at very low strain rates and that prevents formation of anodic SCC does not occur when cracking is the result of embrittlement by corrosion product hydrogen (Fig. 15a, alloy A). This mechanistic difference can be used to distinguish between anodic SCC and cathodic SCC (hydrogen embrittlement) [17].

For the chosen strain rate, the ratio between the ductility to failure in a corrosive environment and the ductility to failure in an inert environment is the measure of material susceptibility to SCC (Fig. 15b gives an example for this). Frequently, this type of test is used to evaluate the influence of metallurgical and environmental variables on SCC resistance of tested materials. This type of experiment yields rapid comparisons of materials according to their SCC resistance in environment of interest, but the application of these data to the prediction of actual in-service lifetime is difficult. Recent work, however, has shown that average stress corrosion crack propagation rate and threshold stress can be obtained with modified techniques combined with microscopy [17]. For example, average stress corrosion crack growth rate can be determined from the depth of the largest crack measured on fracture surfaces of specimens, divided by the time of testing. In this procedure, SC crack is assumed to be initiated at the start of test, which is not always true. On the other hand, fracture mechanics implies that the structure already contains a crack or a crack-like flaw.

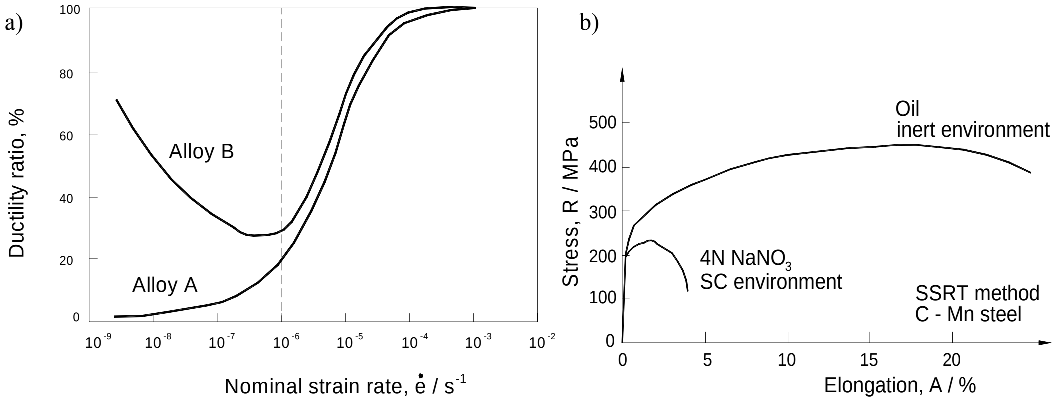

Figure 15. a) Scheme of typical ductility vs. strain rate behaviour of two different types of alloys tested by SSRT. b) Nominal stress vs. elongation curve for C–Mn steel, obtained by SSRT [17]

4.3. Fracture mechanics SCC test methods

Evaluation of SCC by mechanically precracked (fracture mechanics) specimens are usually conducted with either a constant applied load (Fig. 16a), or with fixed crack opening displacement COD, and the actual rate of crack propagation $v = da/dt$ is measured (Fig. 16b). The magnitude of stress distribution at the crack tip (the mechanical driving force for crack propagation) is quantified by the stress intensity factor K_I (in the scope linear elastic fracture mechanics LEFM) for specific crack and loading geometry. As a result, the crack propagation rate, logda/dt is plotted versus K_I. These tests can be made such that K_I, increased with crack length (at constant or gradually rising applied load), decreases with increasing crack length (constant crack opening displacement COD), or is approximately constant as the crack length changes (special tapered samples) [11].

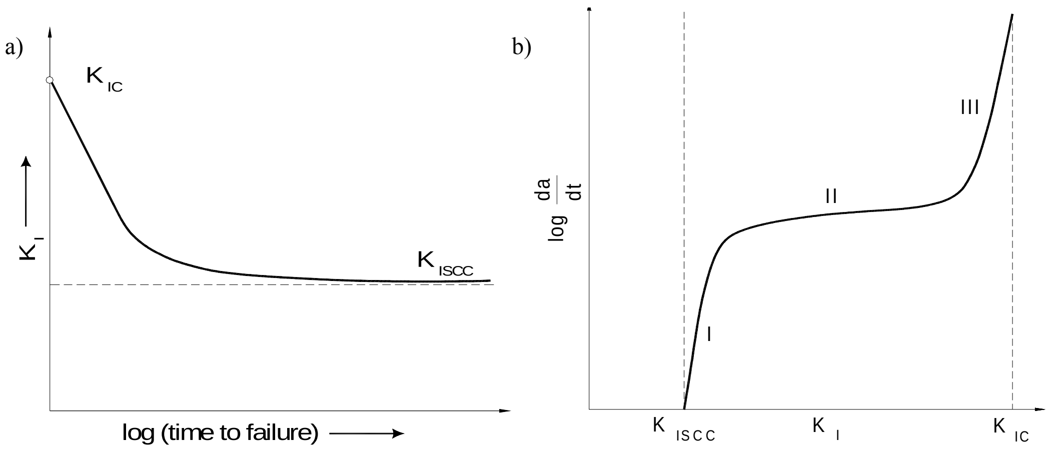

Figure 16. Scheme of SCC results obtained by: a) constant load and
b) constant displacement (COD) fracture mechanic test method

In order to monitor SC crack propagation, specimens of large length must be applied. Most convenient are DCB and T–WOL specimens. The specimen thickness must be higher than a minimum value should be fulfilled, providing the basic fracture mechanics requirement for plain strain conditions at the crack tip. In cases of COD methodology on DCB specimens, they are stressed by bolts and exposed to effects of the SC environment. Monitoring of crack length is performed until the moment of significantly low crack propagation growth. After testing, the specimens are mechanically fractured (separated) and the initial mechanical crack length is measured on the fractured surface, as well as the total length of the mechanical and stress corrosion crack at the moment of SC crack arrest. On the basis of values of mechanical crack lengths a_c and corresponding COD values, the fracture toughness K_{Ic} of the tested materials is determined by inserting these values into the fracture mechanics equation for DCB specimens (ASTM G 168):

$$K_{\mathrm{I}} = \frac{\sqrt{3}EV_{LL}}{4\sqrt{H}\left(\dfrac{a}{H}+0.673\right)^2} \tag{15}$$

where: H is specimen half length; V_{LL}–load line crack opening displacement, a–crack length; and E–Young's modulus.

The calculated stress intensity values K_{Ic} are the initial values of K_{I} for further SCC testing. (Almost an identical procedure of fracture toughness K_{Ic} determination and further SCC testing on DCB specimens is suggested by Speidel [18]). In an analogous way, the value of stress intensity factor at crack arrest, K_{ISCC}, is determined. The crack length data are incorporated into the diagram, showing the dependence of crack length and testing time in corrosive environment and used later for calculation of crack propagation rate da/dt, and for corresponding K_{I} values (as shown in Fig. 16b).

In recent years, the concept of elastic plastic fracture mechanics (EPFM) approach has been applied in determining threshold value J-integral (J_{ISCC}), critical value of crack tip opening displacement δ_{ISCC}, and crack propagation rate, during stress-corrosion cracking. The value K_{ISCC} can be calculated from J_{ISCC} values by applying an identical expression such as the relation between K_{Ic} and J_{Ic}. Using the EPFM value, the stress-corrosion propagation rate is also obtained from data of the "breaking-load stress-corrosion test" on smooth specimens [17].

No crack propagation is observed below the value of threshold stress intensity level K_{ISCC} (Fig. 16a and 16b). This level presumably corresponds to the stress level for the synergetic interaction of alloys with the environment. There are numerous physical processes that may be associated with threshold stress intensity factor K_{ISCC}, including a fracture strain for a "slip-dissolution mechanism," or a critical crack opening displacement COD for transport of species in the crack. At low stress intensity levels (but higher than K_{ISCC}), crack propagation rate increases rapidly with the stress intensity factor (stage I). At intermediate stress intensity levels, the crack propagation rate approaches some constant velocity that is independent of the mechanical driving force K_{I} (stage II). This rate of the plateau v_{pl} is a characteristic of alloy-environment combinations and is the result of the rate limiting environmental processes such as mass transport of environmental species, or by processes such as electrochemical (or chemical) reaction kinetics on the crack tip, or the hydrogen diffusion rate through metal from the crack tip to the location of the maximum three-axial stress state, where fracture actually occurs. In stage III the crack propagation rate exceeds the plateau velocity as K_{I} approaches critical stress intensity level for mechanical fracture in an inert environment, K_{Ic} [11].

The SC crack growth rate at the first stage of the kinetic diagram log$v$–K_I can be written in the following form [19]

$$v_I = C_I \exp(mK_I) \tag{16}$$

where constants C_I and m do not depend on K_I, but on the tested material and corrosive environment, and can be experimentally determined.

The SC crack growth rate at the plateau v_{pl} can be expressed by the following, [19]:

$$v_{pl} = C_{II} \exp\left(-\frac{E_a}{RT}\right) \tag{17}$$

where E_a is the activation energy of some of previously mentioned (or other) processes which control the crack rate at the plateau, R is the universal gas constant, T is the temperature in K, and C_{II} is the constant depending on the metal/environment relation and can be experimentally determined.

5. EFFECT OF METAL COMPOSITION AND MICROSTRUCTURE AT SCC

In some cases, composition and structure of alloys have great influence on the process of SCC. For example, in alpha brass SCC occurs in ammonia if the content of zinc is higher that about 15%. Grain size and residual stress also have a significant influence.

In contrast to brasses, the metallurgical structure plays a dominant role in determining susceptibility to SCC of high-strength aluminium alloys in presence of tensile stresses and moist chloride-containing environments [18,20,24]. Under given conditions, these alloys vary from highly susceptible to practically immune to intergranular stress-corrosion cracking. Microstructures formed by heat treatment determine such behaviour of alloys. The effect of heat treatment on SCC susceptibility of high-strength precipitation hardening Al-Zn-Mg-(Cu) alloys is as follows: under solution-heat treated and quenched conditions, these alloys are very resistant to SCC, but of course, too weak to be used under these conditions. On ageing, these alloys become progressively stronger, but also increasingly susceptible to stress corrosion. Maximum stress corrosion susceptibility is observed under intermediate-strength underaged conditions; but after that, alloys become increasingly more resistant to SCC. Thus, the high strength peak-aged condition is moderately susceptible to stress corrosion, while the intermediate-strength over-aged condition is relatively resistant. Therefore, in practice there is a choice between maximum strength alloys with moderate SCC susceptibility and somewhat lower strength alloys with little SCC susceptibility. In addition, two-step precipitated hardening gives high SCC resistance with relatively little lost in strength (Fig. 17).

In high-strength low-alloy quenched and tempered steels, SCC occurs in the presence of moisture or bulk aqueous environment, particularly containing H_2S. The crack path is usually intergranular with respect to prior austenite boundaries. The major metallurgical variable in this instance is the strength level; the stronger the steel, the greater is its susceptibility. However, at constant strength level, steels with martensitic structures are considerably more susceptible to SCC than steels with bainitic structures [22], Fig. 18.

In practice, by far the most common case of SCC is that occurring when austenitic stainless steels are simultaneously exposed to tensile stresses and hot, aqueous chloride-containing environments. In this case, the major variable is alloy composition and structure; virtually, all austenitic stainless steels are more or less susceptible to SCC in this environment, while ferritic and ferritic/austenitic stainless steels are highly resistant or immune, Fig. 19.

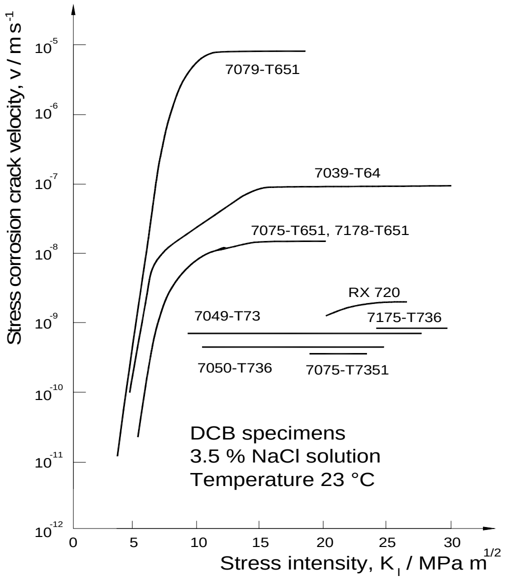

- Humid air and aqueous chloride solutions
- Intergranular SC failure
- Heat treatment:
  - peak–aged conditions – high strength but high SCC susceptibility
  - over–aged conditions – intermediate strength but higher SCC resistance
  - two–step precipitation hardening – high SCC resistance and little loss of strength.

Figure 17. SCC characteristics of several high-strength aluminium alloys [18]

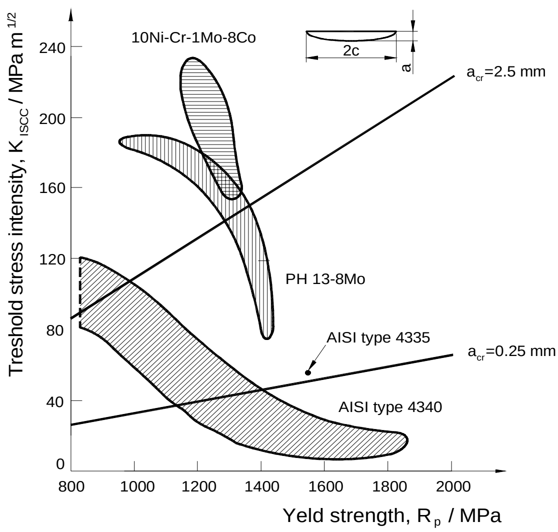

- Humid air, aqueous electrolytes, particularly containing H_2S
- Intergranular SCC (along prior austenite boundaries)
- Strength level: stronger steel, greater is its susceptibility
- Constant strength level: martensitic structures–more susceptible than bainitic structures
- Alloy composition influence at lower strength levels

Figure 18. SCC characteristics of several high-strength low-alloy steels [17]

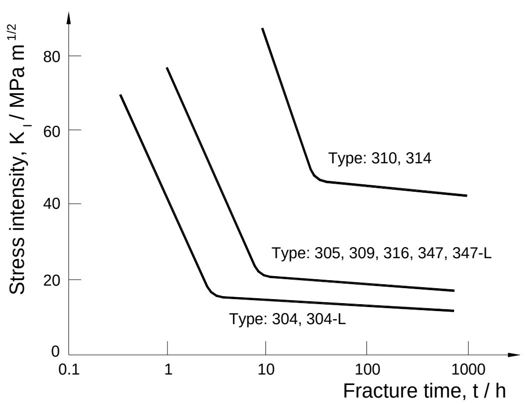

- Hot, chloride solution
- Intergranular and/or transgranular SCC failure
- All austenitic stainless steels more or less susceptible to SCC
- Ferritic and ferritic/austenitic stainless steels are highly resistant

Figure 19. SCC characteristics of several austenitic stainless steels [22]

6. FRACTOGRAPHY OF SCC

A SC crack is practically always a brittle fracture, even in cases of ductile metals. The final fracture zone is usually caused by tensile overload and may show macro/microscopic ductility. Fatigue failures also occur without evidence of ductility, but fractured surfaces are usually smoother than those associated with SCC, [23].

Stress corrosion cracking occurs as intergranular and/or transgranular fracture. SCC is usually intergranular in aluminium alloys, alpha-brass, and high-strength steels. Cracking is primarily transgranular in chloride SCC of austenitic stainless steels [23].

7. DEFECT-TOLERANT DESIGNING CALCULATION

Experimental results obtained by fracture mechanics analysis, such as fracture toughness K_{Ic}, fatigue crack propagation threshold value ΔK_{th}, and fatigue crack propagation rate *da/dN* are widely applied in practice for design, material selection, and failure analysis. These procedures are explained in detail in literature [25-29].

It is possible to use laboratory fracture mechanics results of SCC for predicting the behaviour of a detected crack, i.e. if it starts to grow under given conditions and for lifetime calculation [19].

When safety requirements are severe (or the stress corrosion crack propagation rate is high, for example in high-strength steels), crack propagation is not permitted and the applied stress intensity factor must be less than the threshold stress intensity factor for SCC, $K_I < K_{ISCC}$. Critical (maximum) stress-corrosion crack depth (a_{CSCC}), which can be allowed in engineering structures, can be calculated from parameters K_{ISCC}, $R_{p0.2}$ and the geometric factor Y. This critical crack depth is also very useful for comparing alloys for application in a given environment.

When safety requirements are less severe, or when the presence of a crack gradually (slowly) extending with time, $K_{ISCC} < K_I < K_{Ic}$ is allowed, then calculation of engineering structure life-time is performed. This is obtained by using experimental data for stress corrosion crack growth rate (from kinetic diagrams log$v$–K_I) obtained in an environment similar as in service, determining the depth of the existing crack in a structure a_o (using non-destructive evaluation method–NDE) and calculating critical crack depth for mechanical fracture a_c (from parameters K_{Ic}, $R_{p0.2}$, and the geometric factor Y). The total lifetime expression is obtained as the solution of the integral:

$$t_f = \int \frac{1}{v_{SCC}} dt$$

in boundaries from a_o to a_c (or a_T – tolerable crack length).

Experimentally obtained SCC data can be applied for predicting crack behaviour in the structure exposed to simultaneous effects of tensile stress and corrosive environment, and also for calculating lifetime of a structure. The critical crack length for fracture in an inert, a_c, as well as in SC environment, a_{CSCC}, can be calculated by the following equation

$$a_c = \frac{1}{\pi}\left(\frac{K_I}{R_{app}Y}\right)^2 \tag{18}$$

where K_I can be the fracture toughness of the tested material, K_{Ic}, or the threshold stress intensity factor K_{ISCC}, R_{app} is the applied stress, and Y is the geometrical factor for the given structural configuration and crack geometry.

If the initial crack length a_o in the structure, determined by some non-destructive evaluation NDE methods, is longer than the critical value a_{CSCC}, this crack will grow by time. The final crack length can be critical a_c when failure occurs, or it can be tolerable a_T, i.e. lower than the critical value, depending on the “safety factor”.

The residual lifetime of a structure can be calculated in the following way. Similarly to parallel processes where the slowest process controls the overall process rate, the same approach can be used here

$$\frac{1}{v_T} = \frac{1}{v_\mathrm{I}} + \frac{1}{v_{pl}} \tag{19}$$

where v_I and v_{pl} are the SC crack growth rates in the first stage and in the second stage (plateau of velocity), in respect, while the effect of the third SC crack growth rate stage is neglected (due to high SC crack growth rate in that stage when K_I approaches $K_{\mathrm{I}c}$).

The total SC crack growth rate v_T from the previous equation (19) is

$$v_T = \left(\frac{da}{dt}\right)_T = \frac{v_\mathrm{I} v_{pl}}{v_\mathrm{I} + v_{pl}} \tag{20}$$

Assuming that, for sake of simplification, the temperature remains constant during exploitation, the SC crack growth rate at the plateau is also constant, and because SCC usually occurs at constant applied stress R_{app}, then mK_I in Eq. (16) can be written as $D\sqrt{a}$ (where D is constant and equals $mYR_{app}\sqrt{\pi}$, supposing that the geometrical factor Y is constant). If Y is not constant, which is generally the case, its change has to be taken into account. The same applies to changes in the environment, temperature, and stress. By incorporating the values v_{pl} and v_I into Eq. (20), the total lifetime expression is obtained, as the solution of the integral calculated in boundaries a_o to a_c (or a_T):

$$t_f = \frac{a_c - a_o}{v_{pl}} - \frac{2}{C_\mathrm{I} D^2 \ln^2 10}\left[\frac{D\ln 10\sqrt{a_c}+1}{10^{D\sqrt{a_c}}} - \frac{D\ln 10\sqrt{a_o}+1}{10^{D\sqrt{a_o}}}\right] \tag{21}$$

If the calculated lifetime is very short, it is necessary to consider other possibilities to decrease effects of SC environment. One of the possibilities is to reduce the applied stress to the value when the crack stops to propagate (i.e. when K_I is lower than $K_{\mathrm{I}SCC}$). The other possibility is to apply heat treatment that provides higher SCC resistance, or to choose other material with high resistance to SCC, as well as to apply cathodic (or anodic) protection, corresponding inhibitors, organic or inorganic coatings. This possibility will not be discussed in this paper.

CONCLUSIONS

- Environment has great influence on stress corrosion and corrosion fatigue and rates of stress corrosion cracking and corrosion fatigue cracking. In most cases the influence of the environment on stress corrosion or on corrosion fatigue is electrochemical or chemical, or both.
- Most often pitting is the precursor of stress corrosion cracking or corrosion fatigue cracking.
- Understanding of the mechanism of stress corrosion can lead to better improvement of metallurgical properties of materials, methods of protecting material from the action of the environment, and rational methods of designing structures.

REFERENCES

1. Sprowls, D.O., *Evaluation of Corrosion Fatigue*, Corrosion, Metal Handbook, Vol.13, 9th Ed. ASM, Ohio, p. 291. (1997)
2. Speidel, M.O., *Hydrogen Embrittlement and Stress-Corrosion Cracking of Aluminum Alloys*, Hydrogen Embrittlement and Stress-Corrosion Cracking, Ed., R. Gibela and R.F. Hehemann, ASM, Ohio, p. 271. (1986)
3. Bockris, J.O'M., Dražić, D.M., *Electrochemical Science*, Francis & Taylor, London. (1972)
4. Pourbaix, Atlas of Electrochemical Equilibria in Aqueous Solutions, Pergamon Press, New York, p. 226. (1966)
5. Despić, A.R., Dražić, D.M., Tatić, O., *Osnovi elektrohemije*, Naučna knjiga, Beograd. (1971)
6. Scully, J.R., *Electrochemical Methods of Corrosion Testing*, Corrosion, Metal Handbook, Vol. 13, 9th Ed., ASM, Ohio, p. 212. (1997)
7. Seys, A.A., Brabers, M.J., Van Haute, A.A., Corrosion 30, p. 47. (1974)
8. Dexter, S.C., *Localized Corrosion*, Corrosion, Metal Handbook Vol. 13, 9th Ed. ASM, Ohio, p. 104. (1997)
9. Dražić, V.J., Dražić, D.M., J. Serb. Chem. Soc., 60, p. 699. (1995)
10. Kaesche, H., *Die Korrosion der Metalle*, Physicalisch–chemische Prinzipien un actuelle Probleme, Berlin–Heiindelberg–New York. (1979)
11. Jones, R.H., *Stress Corrosion Cracking*, Corrosion, Metal Handbook, Vol. 13, 9th Ed. ASM, Ohio, p. 145. (1997)
12. Dražić, D.M., Popić, J.P., J. Appl. Electrochem., 29, p. 43. (1999)
13. Dražić, D.M., Popić, J.P., Russ. J. Electrochem., 36, p. 1182. (2000)
14. Dražić, D.M., Popić, J.P., J. Serb. Chem. Soc., 67, p. 777. (2002)
15. Kolotyrkin, Ya.M., Florianovich, G.M., Elektrokhimiya 9, p. 988. (1973)
16. Florianovich, G.M., Russ. J. Electrochem., 36, p. 1037. (2000)
17. Sprowls, D.O., *Evaluation of Stress-Corrosion Cracking*, Stress–Corrosion Cracking, Ed. R.H. Jones, ASM, Ohio, p. 363. (1993)
18. Speidel, M.O., Metall. Trans. A, 6A, p. 631. (1975)
19. Ritchie, R.O., *Environmentally assisted sub-critical crack growth*, University of California, lecture manuscript.
20. Procter, R.P.M., *Effect of Metallurgical Structure on Corrosion*, Corrosion, Ed. L.L. Shreir, London, p. 1:33. (1976)
21. Marsh, P.G., Gerberics, W., *Stress-Corrosion Cracking of High-Strength Steels (Yield Strengths Greater than 1240 MPa)*, Chapter 3, Stress-Corrosion Cracking, Ed. R.H. Jones, ASM, Ohio, p. 41. (1993)
22. Brown, B.F., *Stress-Corrosion Cracking Control Measures*, NACE, NBS monograph, Houston, p. 55. (1977)
23. Staford, S.W., Mueler, W.H., *Failure Analysis of Stress-Corrosion Cracking*, Chapter 18, Stress-Corrosion Cracking, Ed. R.H. Jones, ASM, Ohio, p. 417. (1993)
24. Davis, J.R., *Corrosion of Aluminum and Aluminum Alloys*, ASM, Ohio. (1999)
25. Gerberich, W.W., Gundersen, A.W., *Design, Materials Selection and Fracture Analysis*, Chapter 9, Application of Fracture Mechanics for Selection of Metallic Structural Materials, Ed. J.E. Campbell, W.W. Gerberich and J.H. Underwood, ASM, Ohio, p. 311. (1982)
26. Hertzberg, R.W., Deformation and Fracture Mechanics of Engineering Materials, J. Wans Sons, New York. (1983)
27. Drobnjak, Dj., *Mehanika loma i odabrani zadaci iz mehanike loma (Fracture Mechanics and Chosen Problems from Fracture Mechanics*), Physics of Fractures, (material for MS studies), Beograd. (1990)
28. Failure Analysis and Prevention, Metals Handbook, Vol. 11, 9th Ed. ASM, Ohio. (1997)
29. Fatigue and Fracture, Metals Handbook, Vol. 19, 9th Ed., ASM. (1997)
30. McEvily, A.J., *Atlas of Stress-Corrosion and Corrosion Fatigue Curves*, ASM, Ohio, p.78. (1990)

STRESS ANALYSIS FOR STRUCTURAL INTEGRITY ASSESSMENT

Taško Maneski, Faculty of Mechanical Engineering, Belgrade, S&Mn

1. DIAGNOSTICS OF STRUCTURAL BEHAVIOUR

Diagnostical treatment of the behaviour of structures is based on computer modelling and structural analysis, performed by a finite element numerical method "KOMIPS" used throughout static, dynamic, and thermal calculation of the structural elements.

KOMIPS allows modelling and complex calculation of real strain and stress, defining structural element real behaviour, reliable forecast of construction response to service loading according to the decisional data (operating regime, repair, reconstruction, retrofitting, optimizing, evaluation of the selected solution type of construction), prediction of critical elements or structural failure, service life assessment and reliable operation. Improvement of structural performance, which can be reached by this approach allows extension of structural service life and increases reliability.

In-service problems of components mainly originate from badly designed geometry. Very often they result from insufficient material resistance and welded joints.

Very low application costs and high level of obtained results have made this method unavoidable in engineering structural analysis. The system KOMIPS has specific calculations for a closer view on structural behaviour. Load distribution, membrane and bending stresses, deformation energy, together with potential and kinetic energy allow very efficient structural performance diagnostics on designed or performing structures. Requirements for satisfactory structural performance in service are: significant difference between the highest operating and yield stress, regular strain and energy distribution, low stress concentration, high crack resistance of material, good response to dynamic impulse load, high first frequency and sufficient distance between frequencies, smaller dynamic reinforcement (increasing) factor.

1.1. Loading distribution

Loading distribution and its transfer through the structure from loading point to the support is the basis of structural performance. In fact, loading lines pass through minimal resistance regions within the material.

1.2. Distribution of stresses (membrane and bending, normal and tangential)

In finite plate elements and beams this application finds weak points (high bending stress) and strong points (only acting membrane and normal stresses), and also points with low stress level. It may also show which modifications should be carried out in order to minimize negative bending effect and achieve better loading distribution.

1.3. Strain energy distribution

Strain energy distribution according to element groups (structural parts) effectively shows the loading transfer throughout structural parts and defines sensitivity to possible modifications.

The equilibrium equation for potential energy and external forces is calculated by multiplying the basic static equation from left with the transposed deformation vector $\{\delta\}^{\mathrm{T}}[K]\{\delta\} = \{\delta\}^{\mathrm{T}}\{F\} \equiv E_d$.

Strain energy for finite element is: $e_d = \{\delta_{sr}\}_e^{\mathrm{T}}[\bar{k}_{rs}]_e\{\delta_{sr}\}_e$, where $\{\delta_{sr}\}_e$ – belongs to global strain vector, and $[\bar{k}_{rs}]_e$ belongs to global element stiffness "e".

1.4. Kinetic and potential energy distribution on main oscillating forms

Kinetic and potential energy distribution on main oscillating forms defines performance more precisely. By multiplying the dynamic equation from the left with the transposed eigenvector matrix, the equilibrium of potential and kinetic energy is $[\mu]^{\mathrm{T}}[K][\mu] = [\mu]^{\mathrm{T}}[M][\mu]\{\lambda\}$.

The kinetic e_k^r and potential energy e_p^r for finite element "e" and for the whole structure E^r for the r^{th}–main form are given as:

$$e_k^r = \omega_r^2 \{\mu_{sr}\}_e^{\mathrm{T}} [m]_e \{\mu_{sr}\}_e, \quad e_p^r = \{\mu_{sr}\}_e^{\mathrm{T}} \left[\overline{k_{rs}}\right]_e \{\mu_{sr}\}_e,$$

$$E^r = E_k^r = E_p^r = \omega_r^2 \{\mu_r\}^{\mathrm{T}} [M]\{\mu_r\} = \{\mu_r\}^{\mathrm{T}} [K]\{\mu_r\}$$

where: ω_r is the r–natural frequency, $\{\mu_r\}$ is the r–eigenvector, and $\{\mu_{sr}\}_e$ belongs to the r–eigenvector element. The relative change in squared r–natural frequency (by re-analisys, without repeated calculation) is given as: $\dfrac{\Delta\omega_r^2}{\omega_r^2} = \dfrac{\alpha_e e_p^r - \beta_e e_k^r}{E^r}$, where α_e, β_e define the modification of element e.

1.5. Decision parameters

High-quality parameters resulting from analysis of condition and performance diagnostics are effectively used in following activities: design; manufacture or purchase of structure; reconstruction or structure overhauling; facility revitalization, for correct and precise decision making.

1.6. Structural failure

Crack initiation and growth are in-service problems of numerous structures. Classical linear elastic fracture mechanics solves this problem by comparison of crack driving force and material crack resistance in structure. Crack analysis in real structure has to include plastic analysis, involving J integral and crack opening dicplacement (COD).

For this approach it is necessary to locate points on the structure where crack-like defects can appear "conditionally". Crack (defect) existence must not significantly effect element carrying capacity, and its growth must be limited.

The calculation methods for cracked structure performance are as follows:

- Modelling and calculation of entire structure with and without crack-like defect.
- Performance diagnostics of entire structure with and without crack-like defect.
- Calculation of structural element with crack.
- Calculation models for different crack dimension and positions.
- Performance diagnostics of structural element with crack-like defect.

Performance diagnostics of cracked elements (compliance) in a cracked structure includes evaluating influence of crack position and size (a) on following characteristics:

- deformation change (maximal deformation; maximal crack extension a; maximal crack opening displacement–COD, and crack tip opening displacement–CTOD),
- incremental advance of the element compliance (dC/da),

- stress change (σ_{eq}, σ_x, σ_y, τ_{xy}) and distribution in elements,
- stress ratio change (σ/τ and $\sigma/\tau_{mem}/\sigma/\tau_{bend}$),
- strain energy change E_d,
- strain energy increment (dE_d/da),
- strain energy distribution in zones,
- strain energy on crack tip element, and
- product σ_y*CTOD.

The stress value can be normalized, that is divided by yield stress (σ/R_{eH}). Crack size can be normalized by element width.

1.7. Life time estimation

Remaining structural life is estimated according to structural behaviour. Remaining strength and service life of a structure with a real or simulated crack is evaluated from the behaviour, taking into account the crack size and location, or the crack driving force, and comparing to material crack growth resistance.

2. REVITALIZATION OF THE STRUCTURE (RETROFIT)

Rehabilitation, reconstruction, or revitalization should be performed only when the structure shows a localized low level of performance. In case of poor global performance, the structure should be replaced. Such structures should be reconstructed in a suitable way to eliminate bad performance.

Reconstruction and revitalization mainly include changes in geometry and necessary analyses of material properties, particularly welded joints. Revitalization of the structure means reconstruction aimed at life extension.

3. EXAMPLES

Many real problems in practice have been considered by applying the described methods, and some of them are presented.

3.1. Analysis of cracked plate

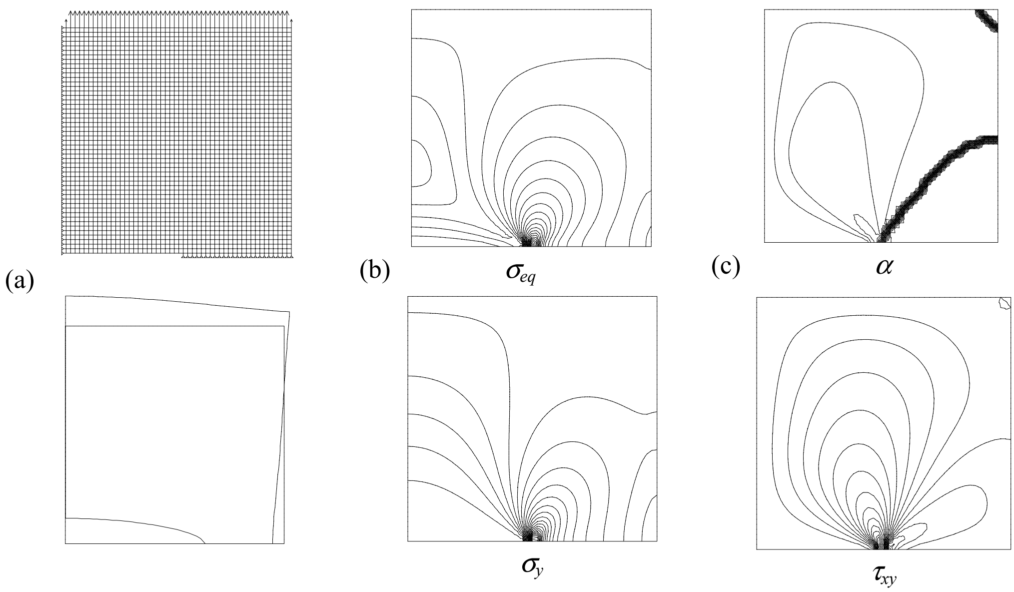

Figure 1. Model of the quarter of plate with 25 mm crack length (a) and distribution of stress field components (b, c)

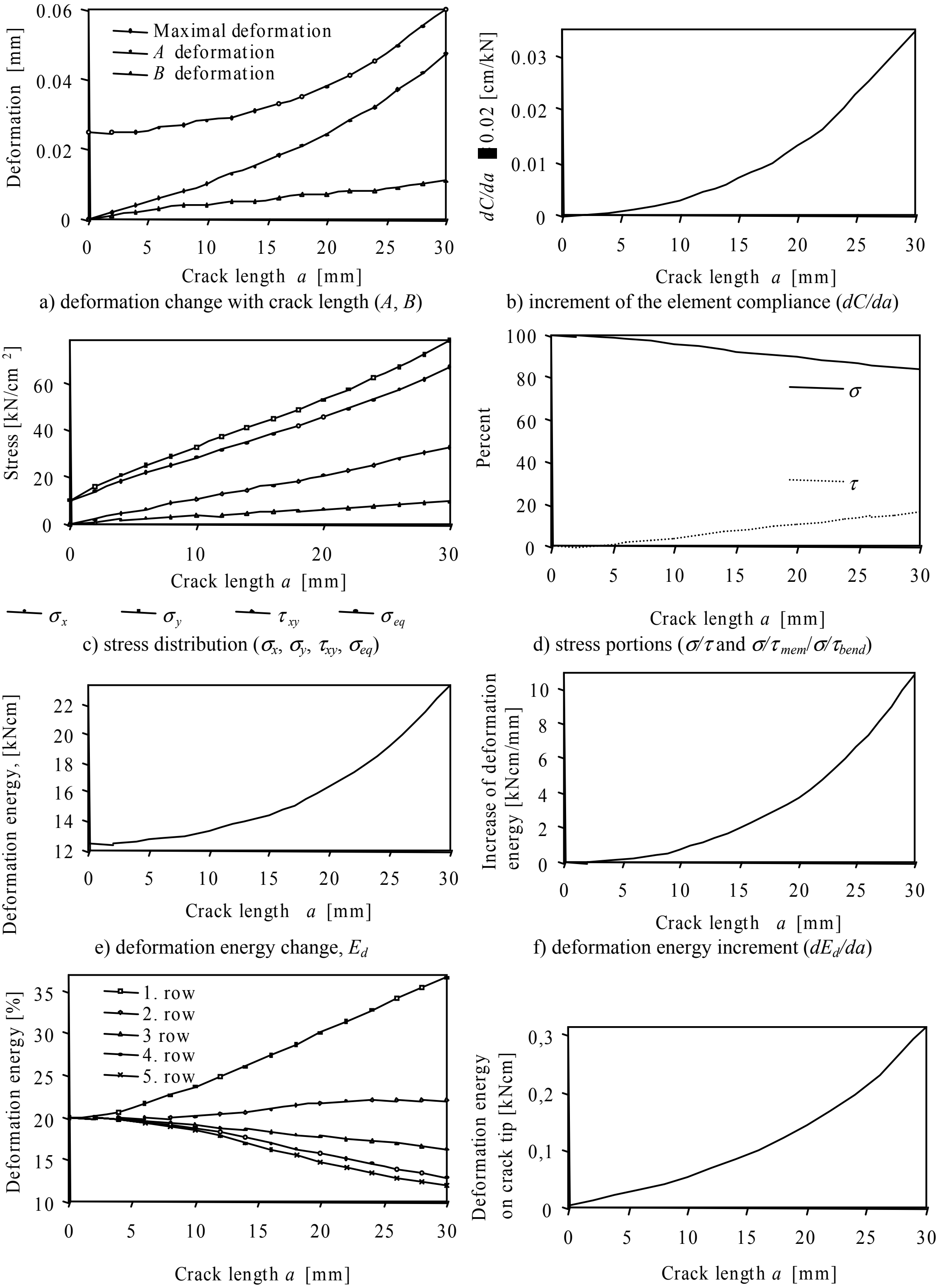

a) deformation change with crack length (A, B)

b) increment of the element compliance (dC/da)

c) stress distribution (σ_x, σ_y, τ_{xy}, σ_{eq})

d) stress portions (σ/τ and $\sigma/\tau_{mem}/\sigma/\tau_{bend}$)

e) deformation energy change, E_d

f) deformation energy increment (dE_d/da)

g) deformation energy change in zones

h) deformation energy on crack tip

Figure 2. Dependence of cracked plate parameters on crack length

A typical example is a plate of dimensions 100×100×1 cm with central through-crack exposed to nominal tensile stress of 10 kN/cm^2. The model of the cracked plate and stress field component distribution are shown in Fig. 1 for crack length of 25 mm. The dependence of different parameters on crack length is presented in Fig. 2.

In case of an embedded crack the computational model has to be of volume-type (see Fig. 3). The crack effect has to be considered in two directions (crack length and depth).

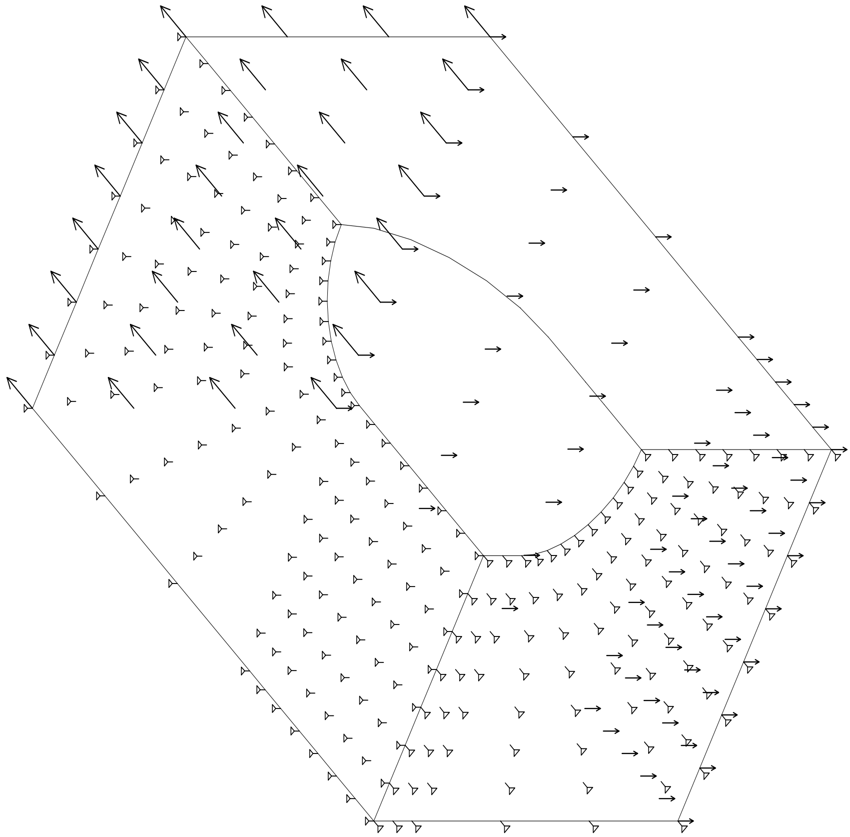

Figure 3. Computational volume model for a plate containing an embedded crack

3.2. Behaviour diagnostics of the rotary excavator bogie (FC Beocin)

Frequent cylinder failures of the support excavator SH400 in the Cement factory (FC) – Beočin, located beneath the flange of the radial-axial bearing (diameter D = 2.5 m) have caused bearing destruction, requiring behaviour diagnostics. Existent behaviour diagnostics were extended with the determination of flange warping. It has been shown that the bogie of the rotary excavator is exposed to very unfavourable stress and strain fields.

The base fine model (Fig. 4) verified the existance of stress-concentration. The stress value in the cylinder increased from 14 to 24.5 kN/cm^2 and in vertical plates from 10.5 to 28.3 kN/cm^2 (Fig. 5 and Table 1). Maximal deformation increased from 3 to 6.9 mm, and warping value from 0.3 to 0.75 mm. These values have substantially exceeded allowable values. The bogie modification could be done by adding the saw-plate between the cylinder and flange. The application of the saw-plate efficiently eliminates unfavourable behaviour of the cylinder and flange without perturbation of global behaviour of the considered construction.

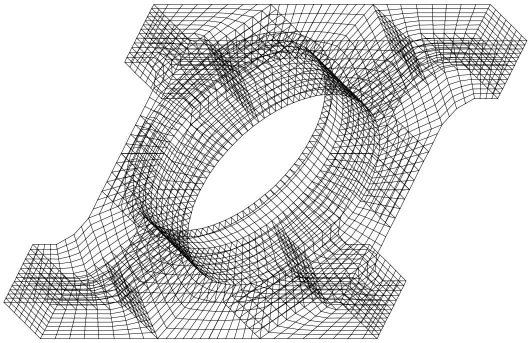

Figure 4. Fine model of excavator bogie

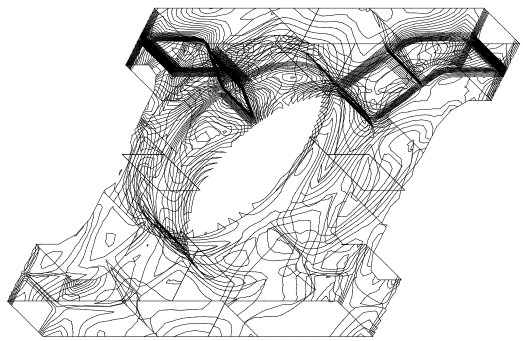

Figure 5. Stress field of bogie 0–28.3 kN/cm^2

Table 1. Contribution of stresses and strains in the bogie for base/modified model

Base/modified model	Stress distribution [%]		Distribution of strain energy [%]
	Membrane	Bending	
Upper horizontal plate	14.7/14.8	7.0/10.9	16.1/20.4
Lower horizontal plate	15. /15.7	6.2/6.3	18.7/20.9
Cilinder + saw-plate	18.7/15.5	12.8/8.3	18.7/12.6
Vertical plates	16.0/21.1	3.7/5.1	34.2/43.6
Flange	0.9/0.6	4.9/1.6	12.3/2.5
Total	65.3/67.7	34.7/32.3	100./100.

3.3. Failure anlysis of the radi-axial bearing of the rotary excavator C700S

During the warranty period, in service, radial-axial bearing of 5 m diameter failed due to damage of fixing on bucket wheel excavator C700 (Kolubara Metal Vreoci). The designer stated that the reason of failure was incomplete welding of diaphragms on the bogie. Finite element computation (Fig. 6) showed, apparently, that he was wrong and Kolubara-Metal had been released with significant expenses.

Analyses of the stress field (Fig. 7) showed presence of 16% bending stress in the computation model with 6 DOF and 11% in the reduced model (based on verified good concept of designed geometry). Large strain and stress concentration is found around supports. Obtained results showed that the effect of improper welding was negligible.

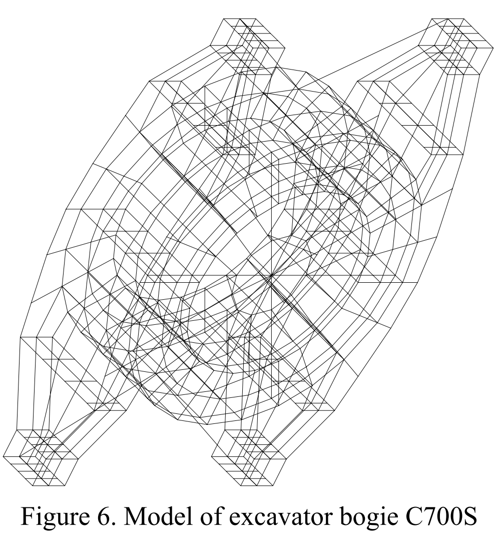

Figure 6. Model of excavator bogie C700S

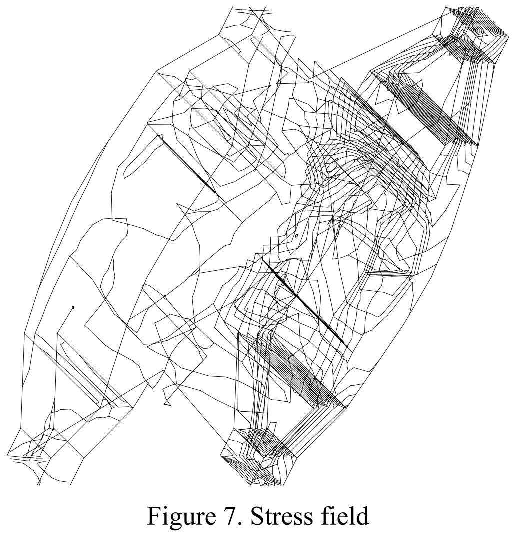

Figure 7. Stress field

Table 2. Strains and stresses

Computation results		Welded diaphragmas	Unwelded
Deformation [mm]	4 supports	2.389	2.42
	3 supports	2.46	2.49
Stress [kN/cm^2]	4 supports	5.73	5.76
	3 supports	6.27	7.43

Table 3. Reduced model

	3 DOF	6 DOF	membrane
Deformation [mm]	2.389	2.501	2.696
Stress [kN/cm^2]	5.73	6.74	6.25

3.4. Failure analysis and reconstruction of the excavator platform ARS Kopel

During service of slewing spreader platform ARS 1400/22+60+21 O&K, warping of some plates of the rotary platform (Fig. 8) occurred, requiring platform reconstruction.

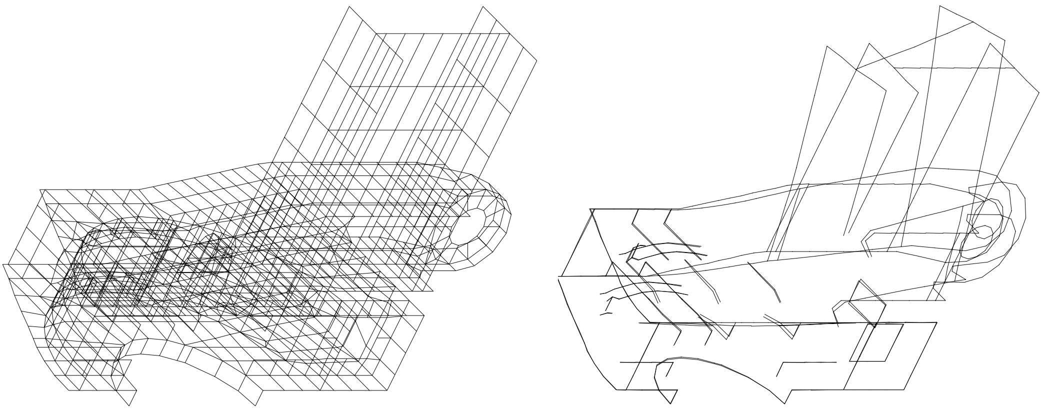

Figure 8. The half–model of the platform and deformation field

The largest stress value (Table 4 and Fig. 9), the largest deformation energy, and stress concentration were situated in the vertical plates. This was also experienced in service. Increase of vertical plate thickness eliminated stress concentration and decreased the stress. Static behaviour was confirmed by computation of free oscillations (Fig. 10).

Table 4. Percentual portions of stresses and deformation energy

Element	Load	Membrane/Bend	Deformation energy
Upper plate	1	18.8/5.8	15.2
	2	16.2/6.6	11.7
Lower plate	1	15.8/4.3	15.0
	2	15.0/4.9	12.5
Vertical plates	1	45.0/5.4	69.2 (39.7)
	2	46.6/5.3	75.1 (41.8)
Ribs of the upper plate	1	3.1/0.6	0.5
	2	3.6/0.7	0.6
Ribs of the lower plate	1	0.7/0.6	0.1
	2	0.6/0.6	0.1
Sum	1	83.6/16.7	100
	2	82.0/18.0	100

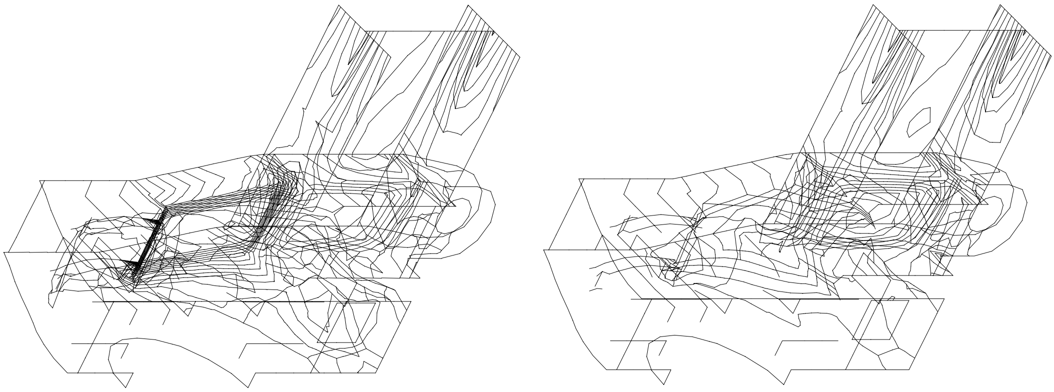

Figure 9. Stress fields of the existing (left) and reconstructed (right) model

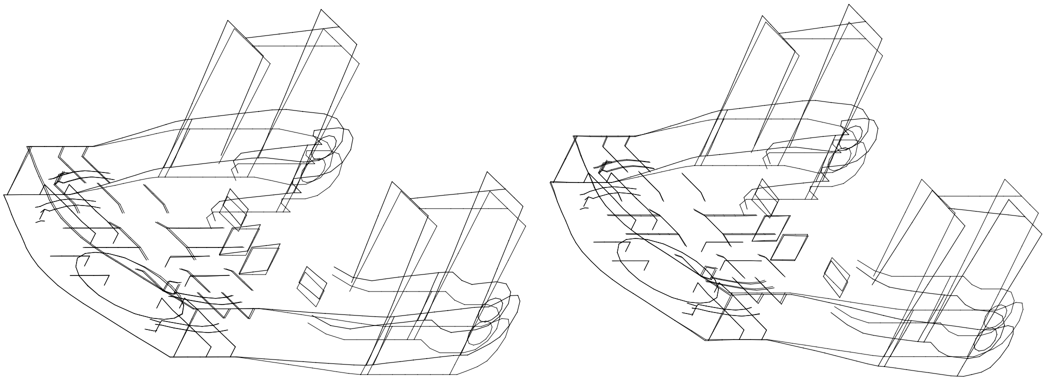

f_{01} = 27.0 Hz f_{02} = 29.59 Hz

Figure 10. First two main modes of oscillation

3.5. The modelling and computation of the excavator bogie-wheel

Operating wheel behaviour diagnostics, recovery and reconstruction of the excavator C700S O&K (Kolubara Metal Vreoci) are presented in Figs. 11–13, and in Table 5. The bogie-wheel is loaded in bending and torsion. The hollow shaft is of the greatest influence in the wheel behaviour.

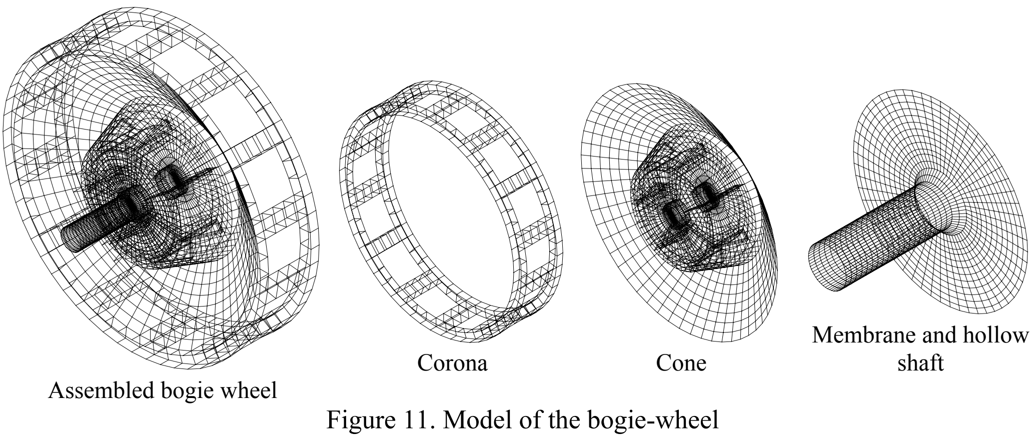

Figure 11. Model of the bogie-wheel

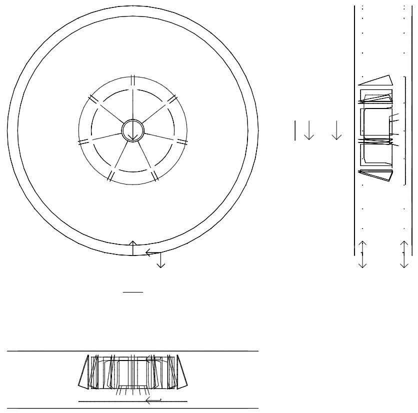

Figure 12. Contour, supports, and loading

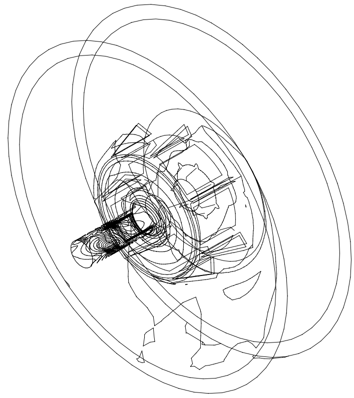

Figure 13. Stress field of the bogie-wheel

Table 5. Percentual portions of stresses and deformation energy

Element	Membrane/Bending stress		Deformation energy
Corona	0.8	0.5	2.3
Cone	14.1	2.5	7.4
Membrane	13.5	0.5	6.2
Hollow shaft	22.5	45.6	84.1
Sum	50.9	49.1	100

3.6. Diagnosed behaviour of the rotary excavator cantilever (C700S)

Fracture of some elements of the supporting cantilever of the bucket wheel excavator SchRs 630 (Kolubara Metal Lazarevac) appeared in service, due to the appearance of resonant frequencies with oscillation amplitudes up to 60 cm, disturbing the cantilever dynamic behaviour.

The construction consists of one beam element and three bar elements: tie, yoke, and cylinder, as modelled in Fig. 14. Strain energy is distributed as follows: beam 72.2%, tie 16.6%, cylinder 10.5%, and yoke 0.5% (Fig. 15).

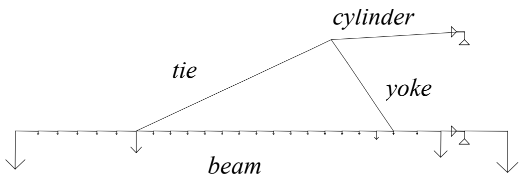

Figure 14. Plane model of the cantilever

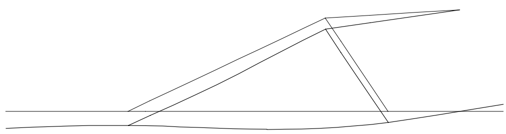

Figure 15. Cantilever strain – f_{max} = 10.4 cm

Static computation reveals that declination of the beam is too big at the joint support; the axial force in the tie and cylinder is high, but in the yoke is minor; bending moment in the part of the beam linked to the yoke is high; and strain energy of the beam is dominant.

Dynamic computation has shown that the first two frequencies are low, close to each other (Fig. 16) and coincide with the static deformation; the factor of dynamic amplification is too large; both the imaginary part of frequency characteristic and strain energy dominate in beam and in external masses (system is unstable), Tables 6–8, Figs. 17–19.

f_{01} = 1.58 Hz f_{02} = 1.81 Hz f_{03} = 4.30 Hz f_{04} = 8.25 Hz

Figure 16. First four main modes of oscillations

Table 6. Percentual portions of potential and kinetic energy

Structural elements	Potential/kinetic energy	
	f_{01} = 1.58 Hz	f_{02} = 1.81 Hz
beam	80/35	90/16
tie	12/3	6/1
cylinder	8/0	4/0
yoke	0/0	0/0
external mass	62	73

Table 7. Percentual distribution of the strain energy E_d

Elements	SA00	SA10	SA20	SA01	SA11	SA02	SA12
Σ	1418	647	709	669	310	551	287
beam	72.2	59.3	60.4	49.2	21.3	41.8	15.3
tie	16.8	3.4	2.6	26.8	8.3	28.5	10.2
cylinder	10.5	23.0	22.9	22.3	48.1	27.1	51.9
yoke	0.5	3.3	3.4	1.7	5.6	2.6	6
new tie	-	11.0	10.7	-	16.7	-	16.5
fill	-	-	0	-	-	-	-

Table 8. Natural frequencies of considered variants (in Hz)

	DA00	DA10	DA20	DA01	DA11	DA21	DB00	DB20
f_{01}	1.58	2.03	2.23	1.62	3.04	3.05	1.61	2.58
f_{02}	1.81	2.38	4.64	2.33	3.92	6.3	3.22	6.94
f_{03}	4.30	4.19	9.43	3.08	6.03	9.22	9.31	12.27

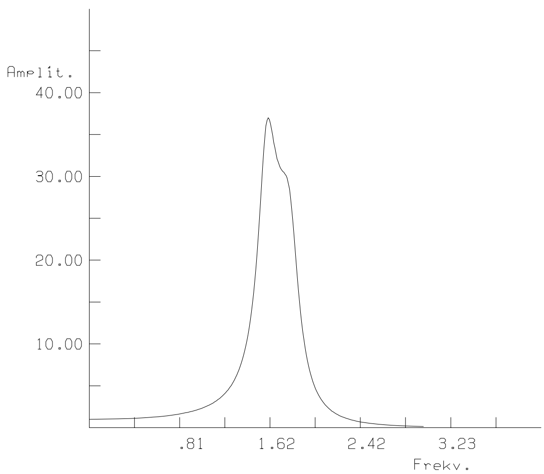

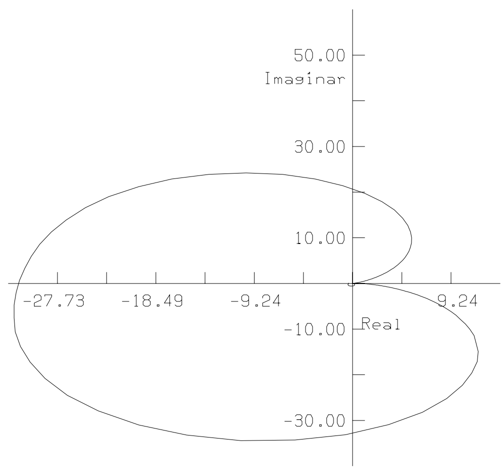

Figure 17. Frequency response for vertical excitation in the node of linking tie, yoke, and cylinder (left), and the response on the left part of the beam – DA00 (right)

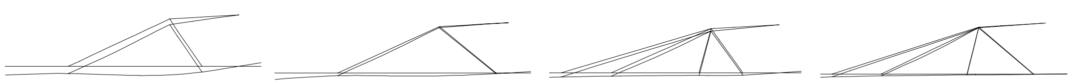

f_{max} = 10.4 cm f_{max} = 7.57 cm f_{max} = 5.55 cm f_{max} = 3.62 cm

Figure 18. Geometry and deformation of some model variants

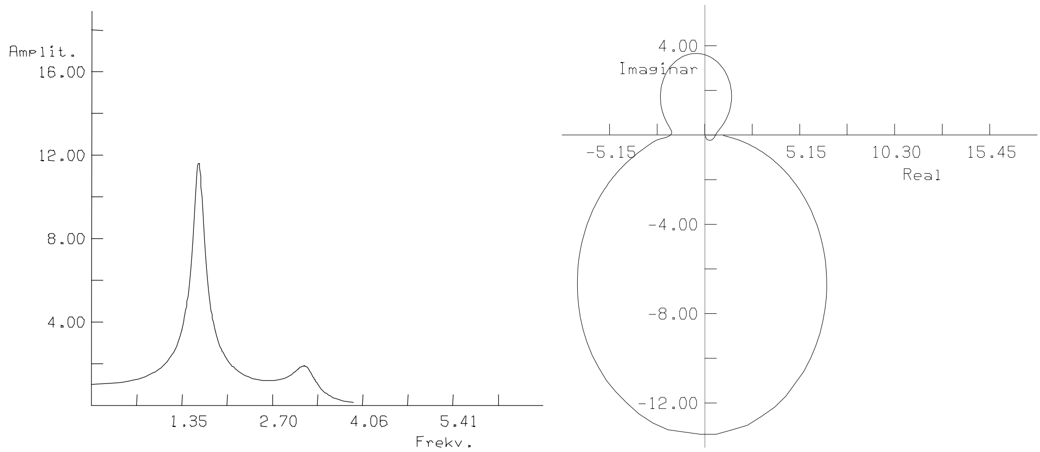

Figure 19. Frequency response – DB00

It is concluded that the implementation of new ties and the filling has been a reasonable solution in this case.

3.7. Crash effect analysis of the rail tank car for acid transportation

Three tank cars fell out of railway tracks in a crash. Elements of bogies and links between the cylinder and bed, and also the cylinder tank, have suffered local plastic deformation. The possibilities of future use of tank required some decision making and, accordingly, defining necessary operations for eliminating crash consequences. Models of deformed elements are presented in Fig. 20. The computational model is given in Fig. 21, and tank deformations and stress fields for critical elements are shown in Fig. 22.

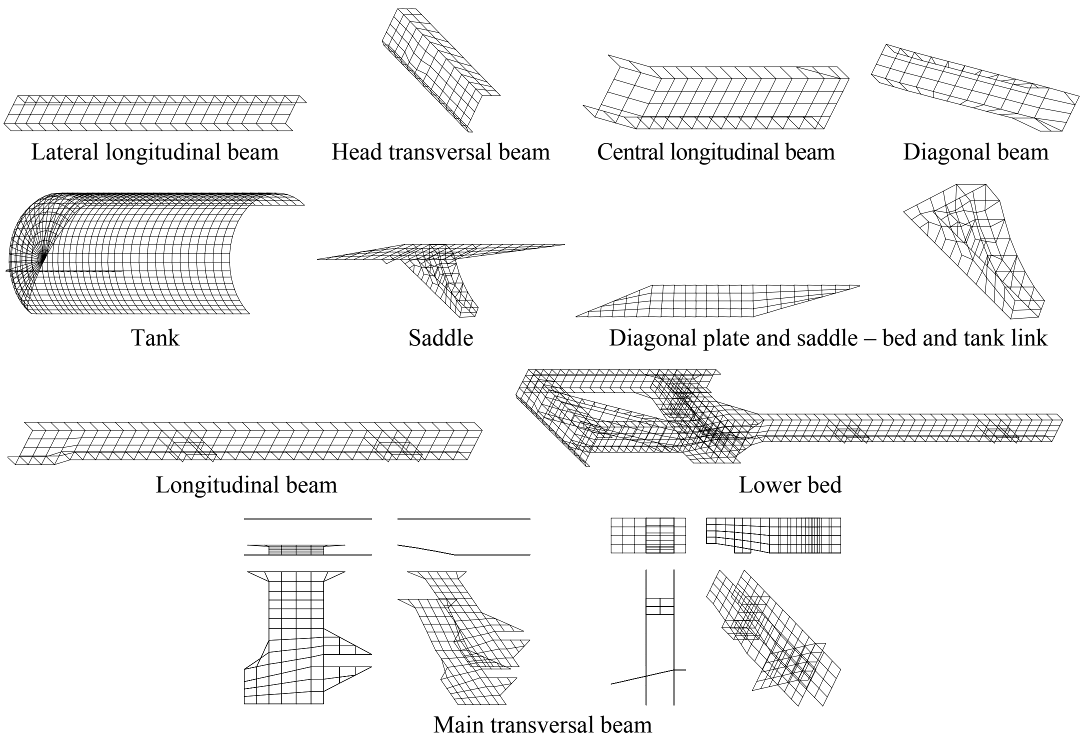

Figure 20. Models of deformed elements after tank car crash

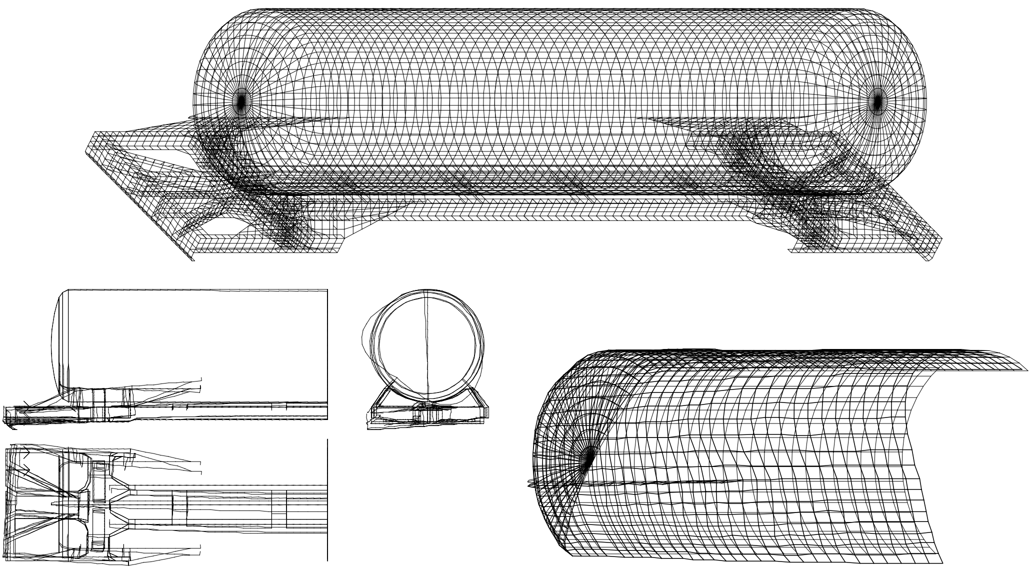

Figure 21. Computational models for tank car

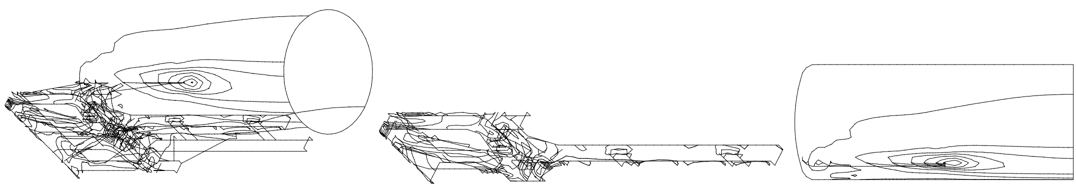

Stress field of tank, 0–20 kN/cm^2, step 2 | Stress field of the lower bed, 0–20 kN/cm^2, step 2 | Stress field of the tank, 0–14 kN/cm^2, step 2

Figure 22. Tank deformations in the moment of crash (left) and stress fields

The assumed load for calculation is the impact force of 600 kN on the tank car buffer. Equivalent maximum stress in the crash was of modest value, 20 kN/cm^2. Based on stress and strain fields, and on load distribution and strain energy, it is possible to conclude that the most important part of impact-energy was acquired by the car buffer. Nevertheless, compressed elements and elements of bed could lose geometrical stability. Based on previous consideration it was concluded that further tank exploitation is feasible.

3.8. Analysis of the behaviour of bogies on the train composition JZ 412-416

After several years of service, the electric-motor driven train composition JZ 412-416 (ŽTP Beograd), and the electric locomotives 441 and 461, and their bogies, exhibited some unfavourable behaviour.

The structure of the bogies consists of several parts as shown in Fig. 23.

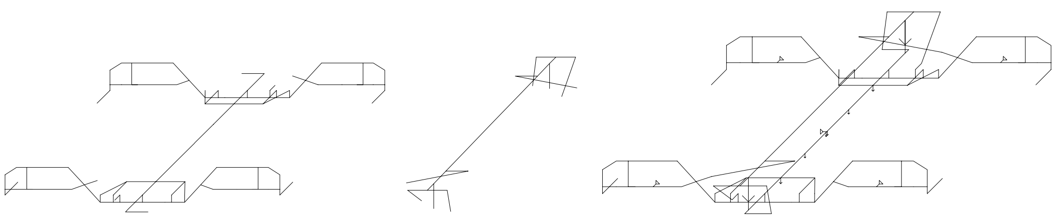

Frame, primary suspension and pull-bar | Cradle and secondary suspension | Model, loading, and supports of the bogie

Figure 23. Models of bogie compositions

The joint between the bogie and the stabiliser was unfavourably stressed at 29 kN/cm^2. The ratio between membrane and bending stress was 22/78, which is also unfavourable. Global behaviour of the construction, local behaviour, and stress concentration can be precisely obtained using plate model, Fig. 24. Obtained stress field is presented in Fig. 25.

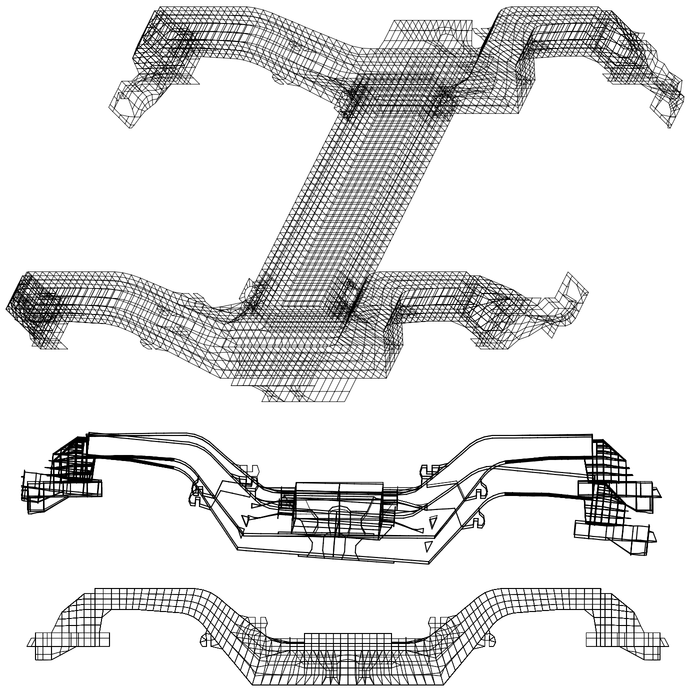

Figure 24. Plate model and deformation field

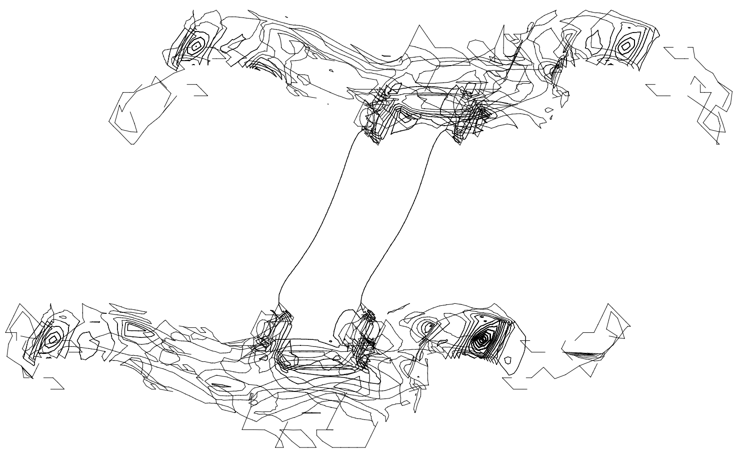

Figure 25. Stress field 0–6.6 kN/cm^2, with steps 0.5

3.9. Modelling of the failure and recovery of storage tank (*D* = 20 m, *H* = 20 m)

Failure of a storage tank occurred while proof pressure testing with air in plant “HIP,” in Pančevo. The structure consists of an internal storage tank anchored to the ground; the external tank is simply supported; with insulation (fiberglass) between the two tanks and pearlite between the roofs; anti-fire safety pipes. The tank model is given in Fig. 26, and elements for analysis in Fig. 27. Based on this, the tank has been syccessfully recovered.

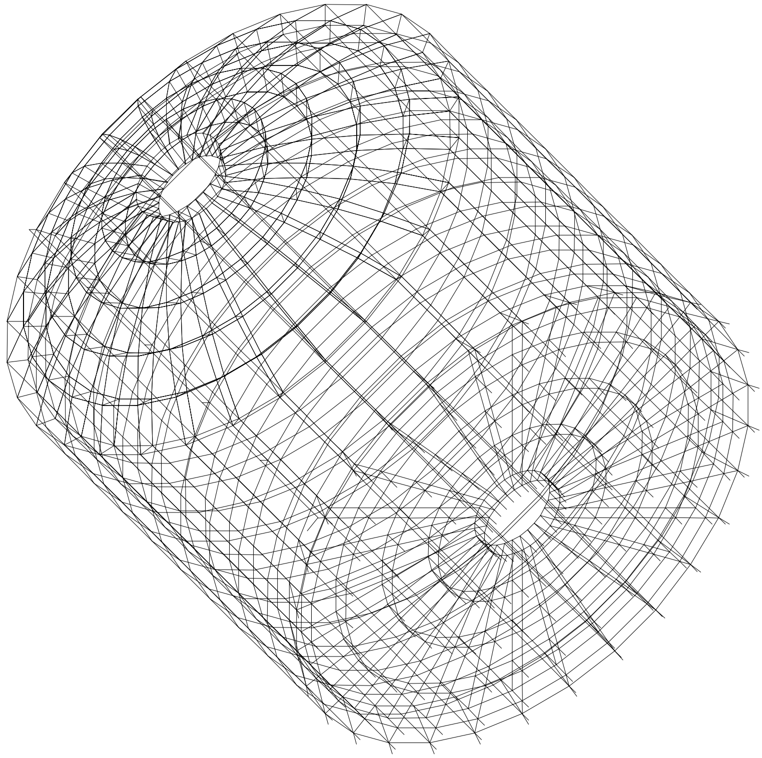

Figure 26. Model of the tank

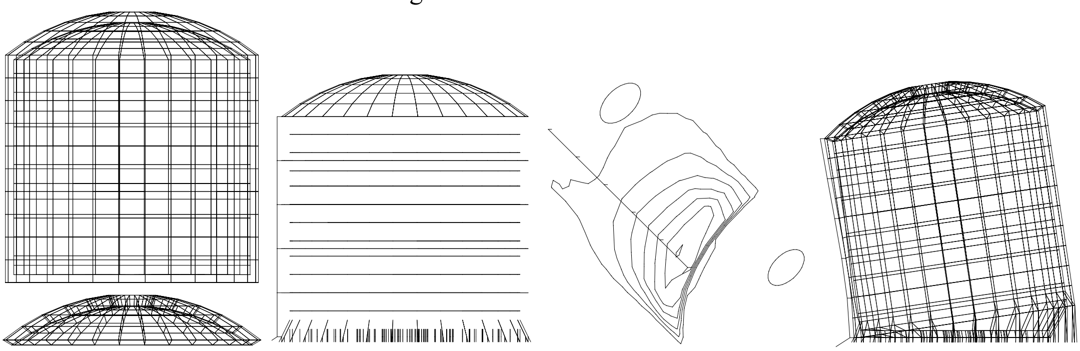

Tank model substructures

Stress field at the moment of failure

Deformation field at the moment of failure

Figure 27. Elements of analysis, enabling the recovery of tank

3.10. Stress field in a pressure vessel

After several years of service, cracks were detected in a pressure vessel exposed to internal pressure of 30 bar and temperature 200°C. The vessel, diamter D = 2000 mm, height H = 6000 mm, and wall thicknes t = 24 mm, has been used for coal drying in the company plant "Kolubara prerada" in Lazarevac. Stress analysis has been requested for the analysis of crack origin. It was found that an important part of strain energy is distributed in upper and lower parts of the shell (20.1% + 39.2% = 69.3%) and in upper (20.1%) and lower cupola (8.6%). Membrane stress is dominant (90.4%): in upper cupola 15.8%, in upper part of shell 24%; in lower part 19.2%; and in supports 27.7%. The computation showed bad stress distribution and corresponding poor behaviour of the pressure vessel.

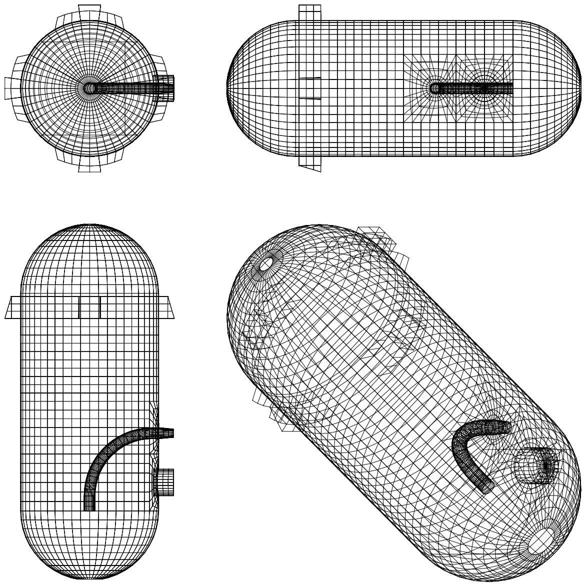

Figure 28. Model for stress analysis of cracked pressure vessel

3.11. Recovery of the rotary furnace

The computation of thermal and mechanical loading of the rotary furnace No. 3 in the Cement Factory in Beočin had been required for analysis of crack significance, detected in critical shell part (see Fig. 29).

Maximum stress and stress concentration are found to be around the elliptical hole (Fig. 30), the stress in the critical zone is very high (30 kN/cm^2), but only of membrane type (Table 11) and without stress concentrations. With this data, analysis is performed for two positions of the cone (old and new) and three shell thicknesses t (6, 8, and 2.5 cm), in five variants: model A – cone new position and $t = 6$ cm; model B – cone old position and $t = 6$ cm; model C – cone new position and $t = 8$ cm; model D – cone old position and $t = 8$ cm; model E – cone new position and $t = 2.5$ cm.

The analysis showed dominant effects of membrane stress and obtained results are stated as follows: the new position of the cone decreases stress for 5%; increase of plate thickness in the critical zone from 6 to 8 cm has decreased the stress for 5%, incorporation of the new ring in the critical zone is beneficial. When loading is applied to the whole ring, the maximal stress increases 30%.

The proposed recovery has been accomplished and the furnace was successfully placed back in service.

3.12. Reconstruction of sleeve at the entrance of limestone–mill “UNIDIAN”

The structure of limestone–mill “UNIDIAN”, Cement Factory in Beočin, consisted of a cylinder with two sleeves situated at saddle supports, was prone to failure. In order to eliminate the possibility of failure, the behaviour of the existing solution of the sleeve at the entrance has to be analysed by modelling the structure and sleeve in one cross-section (Fig. 31). Weak elements are the sleeve and support, since the existing saddle support unfavourably affects the sleeve. Welded joints must not be performed on the sleeve cylinder because of great bending stress (but if necessary, welding may be performed only in the longitudinal direction at cylinder ends). Sudden change in stiffness must be reduced by obtaining the influence when changing the sleeve cylinder thickness.

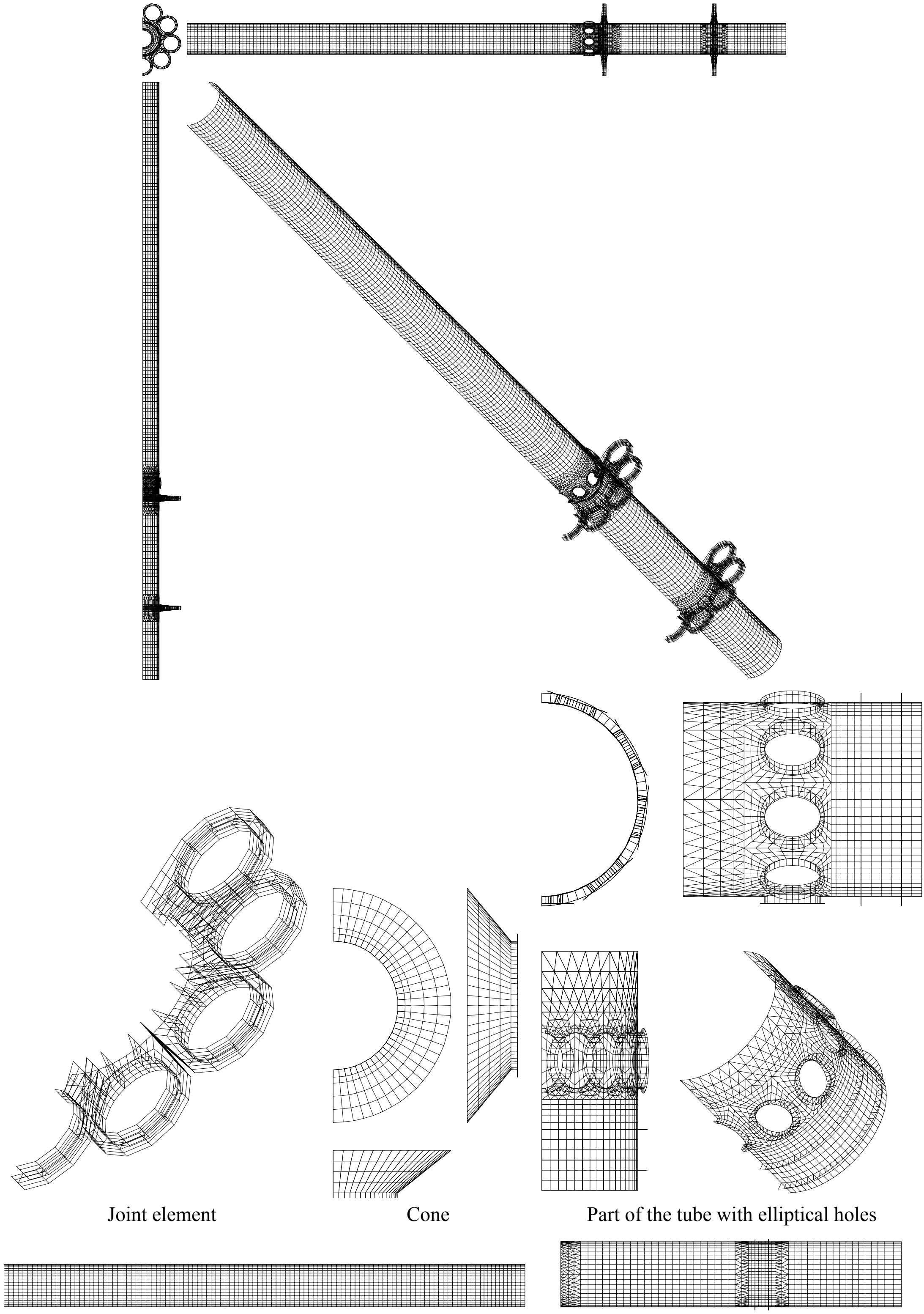

Figure 29. Models of the rotary furnace (up) and its parts

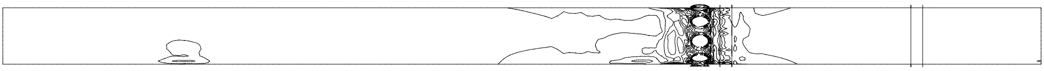

Stress field 0–40 kN/cm^2 with step 5

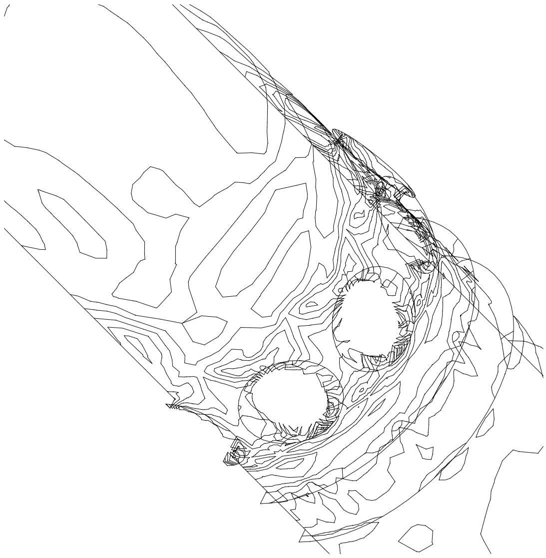

Stress field in the critical zone 0–40 kN/cm^2 with step 5

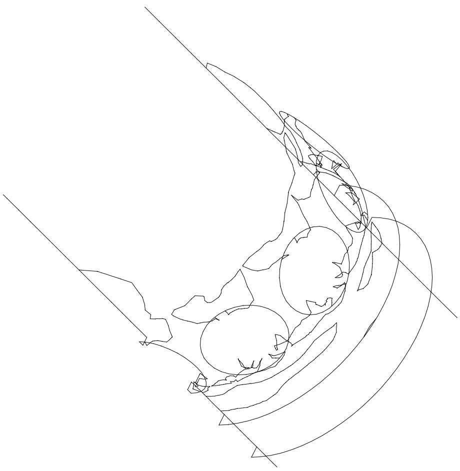

σ= 25 kN/cm^2

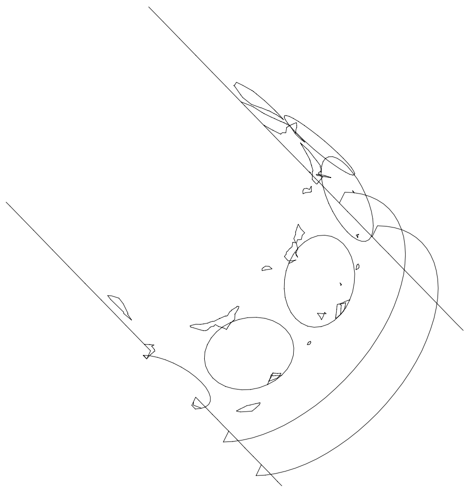

σ= 35 kN/cm^2

Figure 30. Partial stress of the critical zone

Table 11. Stress in the critical zone [kN/cm^2]

Variant	Membrane stress			Bending stress			Equivalent stress
	σ_x	σ_y	τ_{xy}	σ_x	σ_y	τ_{xy}	σ
A	28.81	-3.87	-1.60	-5.47	-1.64	-0.17	35.54
B	28.70	-5.35	-1.75	-6.81	-2.04	0.15	37.42
C	25.53	-3.66	-1.56	-5.62	-1.68	-0.20	32.26
D	25.51	-5.14	-1.72	-6.48	-1.95	0.19	33.86
E	40.25	-4.24	-1.63	-4.40	-1.32	-0.11	46.26

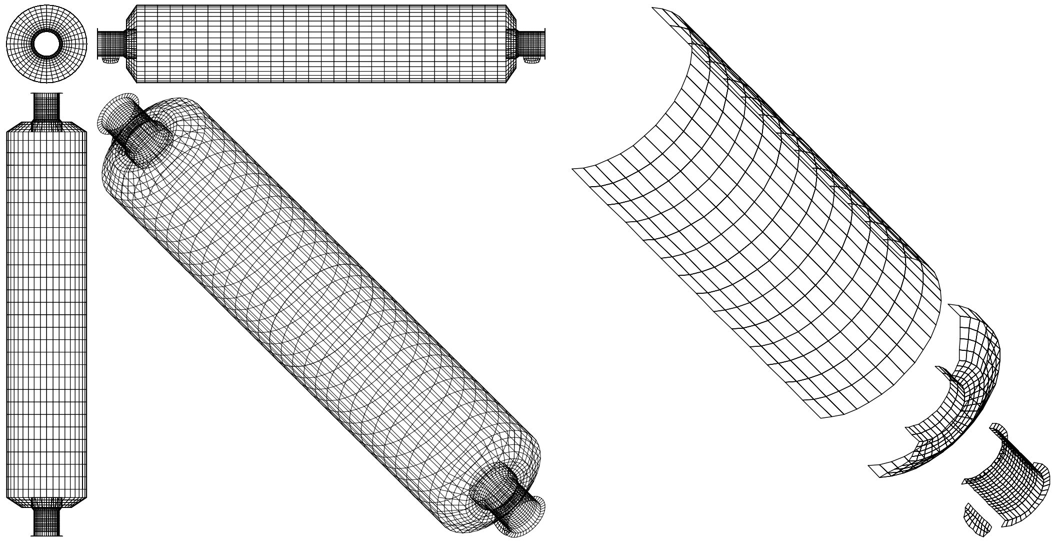

Model of the limestone-mill

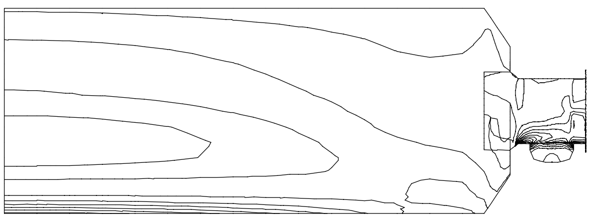

Stress field of sleeve and shell

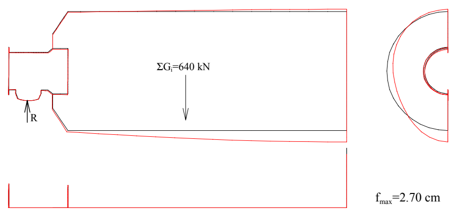

Model contour, loading and deformation

Figure 31. The analysis for reconstruction of the sleeve of limestone-mill “UNIDIAN”

Considered model variants are: changed sleeve cross-section area and thickness in the saddle support zone, δ_1 from 2.75 to 6 cm; and next to this zone, δ_2 from 4.5 to 7.5 cm (Fig. 32).

Based on computational results, presented in Fig. 33 and in Table 12, for this type of support, the thickness of the sleeve cylinder had dominant effect on the stress field. The stress value had decreased 3 times, the stress concentration is reduced, changes in stiffness are reduced and welding had been performed in the longitudinal direction. Model B, from Table 12, has been accepted and made, enabling the successful functioning of the sleeve.

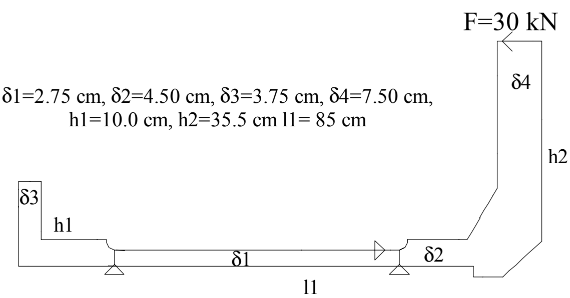

Figure 32. A variant of sleeve cross-section

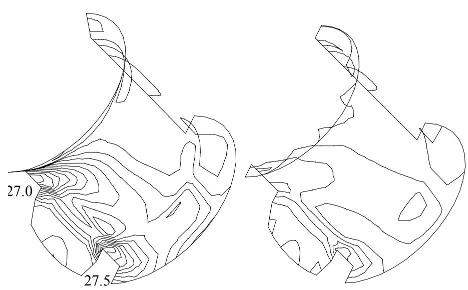

Stress 0–27.5 kN/cm^2 Stress 0–10 kN/cm^2

Figure 33. Stress field on old and new model

Table 12. Computational results

Models and variants	Thickness δ_1 [cm]	Thickness δ_2 [cm]	Max. D [cm]	Max. stress kN/cm^2	Max. stress sleeve
Model A var 1	2.75	4.50	2.70	27.5	27.5
var 2	4.05	5.75	2.66	16.9	15.0
var 3	6.00	7.75	2.62	16.9	10.0
Model B var 1	2.75	4.50	2.72	25.7	25.7
var 2	4.05	5.75	2.67	16.9	16.0
var 3	6.00	7.75	2.63	16.9	10.0
var 4	5.00	6.65	2.65	16.9	12.0
var 5	5.50	6.65	2.65	16.9	11.0
var 6	5.75	7.50	2.63	16.9	10.0
Model C var 1	4.50	4.50	2.68	16.9	16.0
var 2	5.75	5.75	2.65	16.9	11.5
Model D var 1	4.50	6.25	2.66	16.9	14.0
var 2	5.75	7.50	2.64	16.9	11.0

3.13. Recovery of the fractured tooth (containing cracks)

In order to define recovery procedures, if possible, two 3D models of 5 teeth (0 and 1 in Fig. 34) and the stress distribution have been analysed after gear-wheel failure in the Cement Factory mill, in Beočin. The behaviour of the fractured tooth part (170 mm in length) has been correlated to the entire tooth length of 650 mm behaviour (without cracks). Note that the position of the stress lines is similar in both cases (the stress in model 1 is about 20% higher than in model 0, Table 13). So it is concluded that the fractured tooth can be in function.

The fine 3D model consisted of 13 869 nodal points and 11 352 volumes. It confirmed the conclusion obtained using the first model.

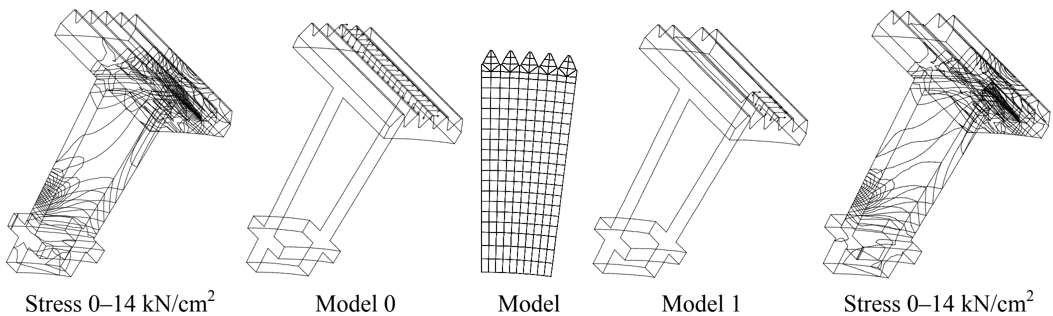

Figure 34. Models and stress fields in loading 2

Table 13. Stress ratios of models 0 and 1, at two loading conditions

Maximal stress [kN/cm^2]	Loading 1	Loading 2
Model 0/Model 1	7.8/10	26/32.8

To get more closer insight, the fine 2D model of a single tooth is also prepared and analysed. Obtained results are presented in Fig. 35 and in Table 14. The zone, which must not have cracks, is the area limited within the lines at a distance of about 25 mm from the top of the tooth and about 15 mm from the side of the tooth (see Fig. 36).

The fine 2D model of five teeth with appropriate supports and loads confirmed results obtained by the single tooth model.

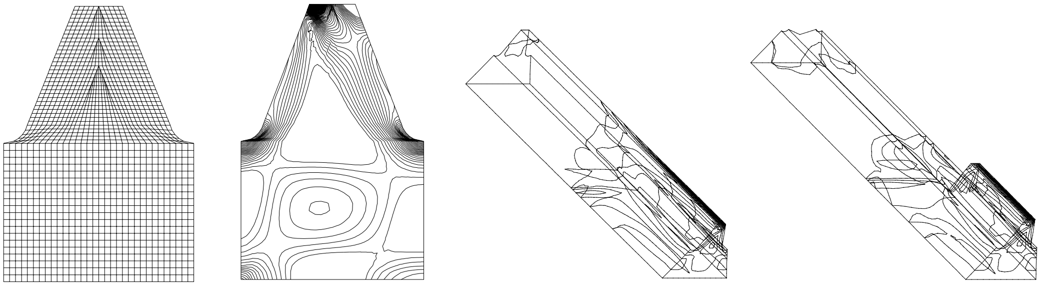

Fine 2D model | Stress lines 1–7 kN/cm^2 with step 0.1 | Model 0 | Model 1

Figure 35. Analysis of fractured tooth, stresses 0–37 kN/cm^2 with step 3, zones which have to be without cracks

Table 14. Percentual distribution of stress and deformation energy

Zones of the tooth	Stress		Deformation energy
	Normal	Shearing	
Bottom of the tooth	21	11	42
First zone from the side of the tooth, width 1 cm and height 1.5 cm	31	13	49
Second zone, width 5 mm and height 14 mm	9	5	6
Third zone, width 5 mm and height 0 mm	4	2	2
Middle of the tooth-triangle with base of 26 and height 28	3	1	1
Total	68	32	100

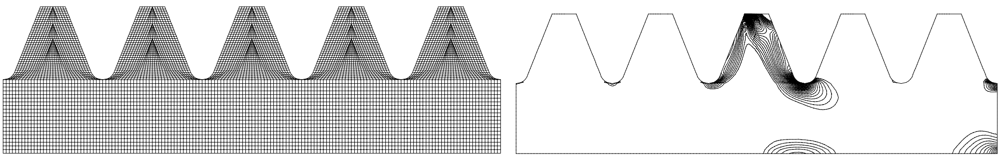

Figure 36. Fine 2D model of five teeth, stress lines 1–7 kN/cm^2, step 0.1, zones which have to be without cracks (right)

3.14. Recovery and reconstruction of excavator SchRs800 O&K structure

Substructures of the excavator SchRs800 O&K, operating in power plant Kostolac Drmno are consisted of: longitudinal shaped plates of the upper platform between top and bottom platform plate; cross plates and upper platform diaphragm between top and bottom plate of the upper platform; cylinder on the radial-axial bearing point; bottom platform plate; top platform plate; “П” column.

It has been proposed to recover and reconstruct the substructure in the following way: add around the existing cylinder a new one with diameter of 15 mm at distance of 25 mm from the old one and 240° around the periphery; to fit the curve beam of 40×80 mm cross-section on old cylinder external side and under the new one around the upper and lower cylinder perimeter and at a given angle; to reinforce part of longitudinal vertical external and internal plates to both pillar sides (thickness 15 mm) with additional plates 15 mm thick, and the diaphragm between pillar parts and cylinder with additional plates 15 mm thick; to add two diaphragms between the front vertical plate (connection with hydro-cylinder) and cylinder at 15° from linear axis (thickness 15 mm); to add four vertical locators between the cylinder, top and bottom platform plate, at 30°, 45°, 75° and 105° from hydro-cilinder linear axis connection; the existing location between the external vertical longitudinal plate, top and bottom platform plate (at 90° from linear axis) is to be transformed in the diaphragm with outlet (thickness 15 mm); in upper parts of the "Π" column frame insert two triangle locators 800×800×15 mm (three plates – front and back triangle, and longitudinal cross plate); on joint locator point for upper and lower pillar section add locators with vertical sections, that is horizontal partial plate with its locators 15 mm thick.

From three considered loading cases, the most severe one is selected as an example.

The excavator superstructure construction is shown in Fig. 37. Considerable improvement is achieved in the form of deformation and volume of the reconstructed excavator superstructure, as shown in Fig. 38. Stress field on both models is given in Fig. 39. Maximum stress is reduced for 27.27%. Stress concentration is minimized.

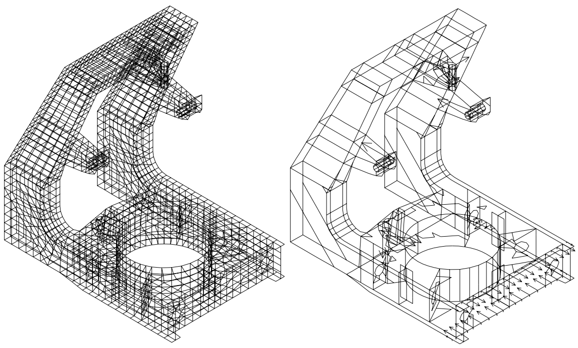

Figure 37. Excavator superstructure model

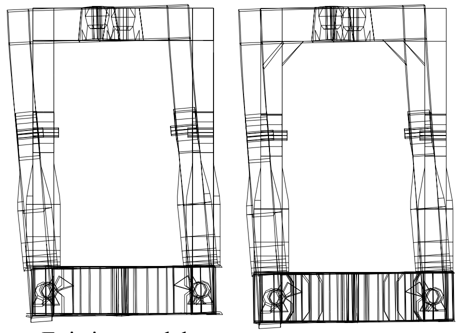

Existing model
f_{max} = 9.43 cm

Reconstructed model
f_{max} = 7.82 cm

Figure 38. Deformation field

Data for diagnostics of structural behaviour are given in Table 15. They reffer to membrane and bending stress distribution, and also to normal and shear stresses and superstructure construction strain energy for the first loading case. It is seen that the bottom plate and cylinder are unloaded and vertical plates are loaded, as requested.

The substructure recovery and reconstruction are successfully accomplished.

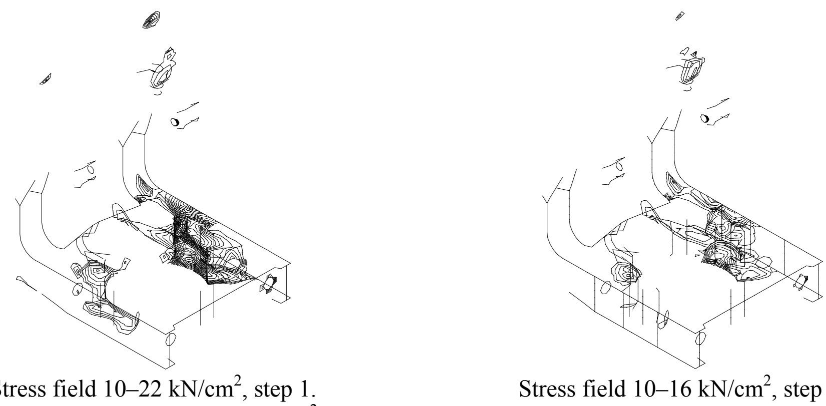

Stress field 10–22 kN/cm^2, step 1.
Existing model: σ_{max} = 22 kN/cm^2

Stress field 10–16 kN/cm^2, step 1.
Reconstructed model: σ_{max} = 16 kN/cm^2

Slika 39. Stress fields of excavator superstructure model

Table 15. Diagnostical data for structural behaviour of excavator superstructure

	σ_{max} [kN/cm^2]		memb/bend [%]		σ/τ [%]		E_d [%], [kNcm]	
	Existing	Recons	Existing	Reconstr.	Existing	Reconstr.	Existing	Recon
Longitudinal	17	13	15.6/2.8	15.2/2.6	12.4/6	12/5.8	16.3	17.9
Cross Plate	17	11	7.7/1	8.9/1.2	4.5/4.3	5.4/4.6	4.6	4.2
Cylinder	22	13	7/2.3	5/1.9	5.6/3.5	4.4/2	4.8	4.2
Bottom Plate	22	16	14.9/1.5	13.7/1.3	13/3.5	11.5/3	19.2	17
Top Plate	20	14	12.9/2.4	12.7/2	12.2/3.1	11.5/3.2	17.5	17.6
Column	14	13	27.8/3.9	28.3/4.3	20.5/11.4	21.2/11.3	29.3	28.1
Beams				2.4/.4		3/0.1	8.3	11.
Sum			86.1/13.9	86.3/13.7	68.2/31.8	69/31	13500	11200

3.15. The analysis of crack significance on rotary furnace ring

Cracks had been detected on the ring of furnace No 3 in Cement Factory Beočin. Crack significance analysis was required for the permission of continued service without repair. Inner diameter of the ring is 6000 mm, and thickness of 350 mm (Fig. 40). The ring 3D model is presented in Fig. 40, and the obtained displacement field in Fig. 41. The fine volume model produced 25% higher stress compared to plane ring model (Fig. 42).

Simulated crack depth on the volume model was 10.7 cm. On the planar model the simulated crack depth of 26.8 cm is accepted (10 cracks with a step of 2.68 cm). Structure with initial crack a = 10.7 cm has been analysed in Fig. 43, and crack growth effects on parameters of concern, including crack opening displacement (COD) and crack tip opening displacement (CTOD) is presented in Fig. 44.

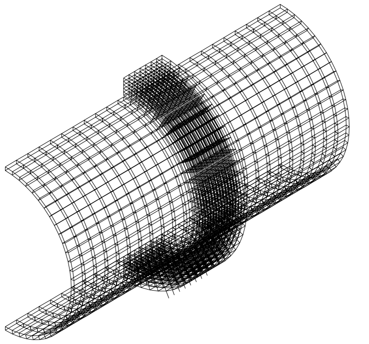

Figure 40. 3D coarse model of furnace ring

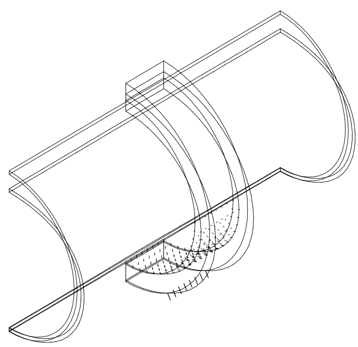

Figure 41. Displacement field, f_{max} = 0.5 cm (no crack)

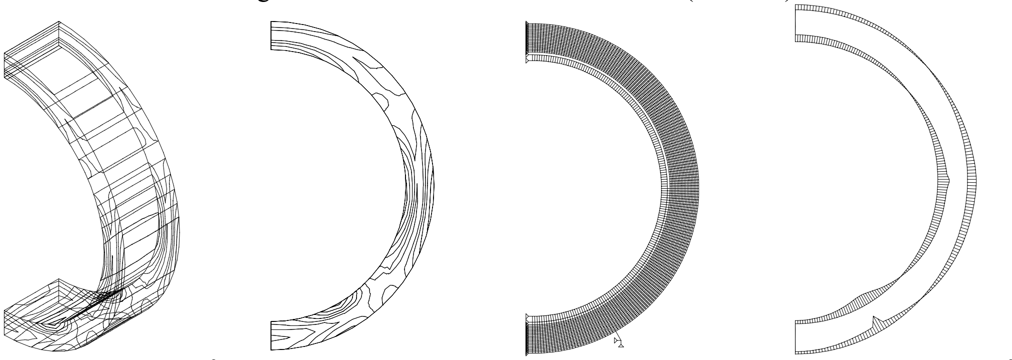

σ_{eq} = 0–4.25 kN/cm^2, step 1, without crack

2D model

σ_{max}^{eq} = 5.5 (10.5) kN/cm^2

Figure 42. Results for 2D ring model

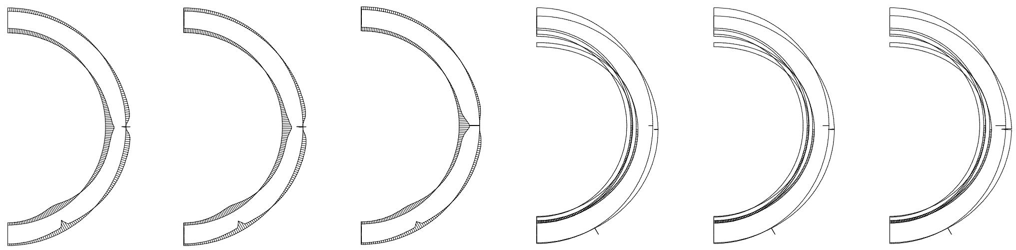

a_1, σ^u/σ^s = 6/6.5 a_2, σ^u/σ^s =7.5/7.5 a_3, σ^u/σ^s = 11/11 a_1, f = 0.544 cm a_2, f = 0.571 cm a_3, f = 0.65 cm

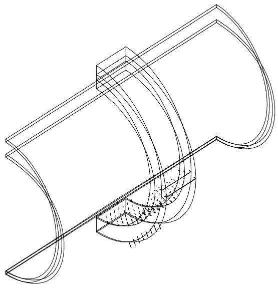

Crack a_1 = 10.7 cm, f_{max} = 0.55 cm

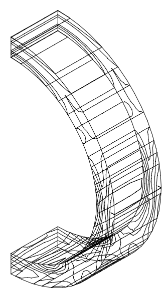

Crack a_1 = 10.7 cm, σ_{eq} = 0–4.375 kN/cm^2

Figure 43. Stress and deformation, for crack lengths a_1 = 10.7 cm, a_2 = 15.72 cm, a_3 = 26.8 cm

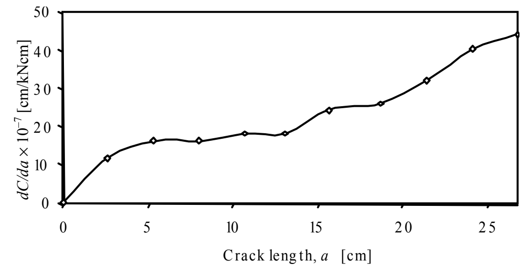

Increment of the element compliance, *dC/da*

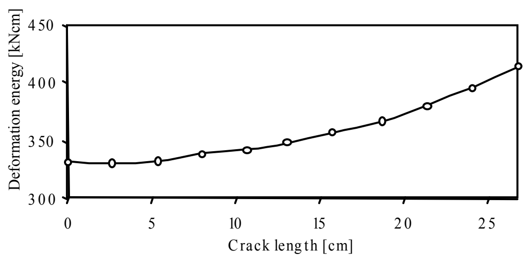

Deformation energy, E_d

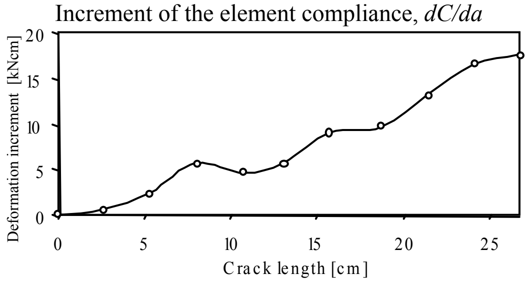

Increment of deformation energy, dE_d/da

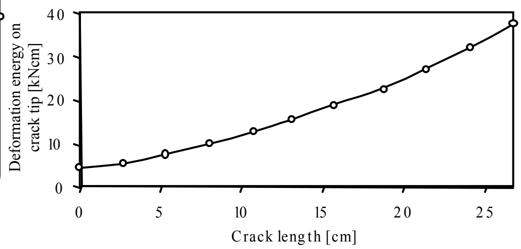

Deformation energy at the crack tip

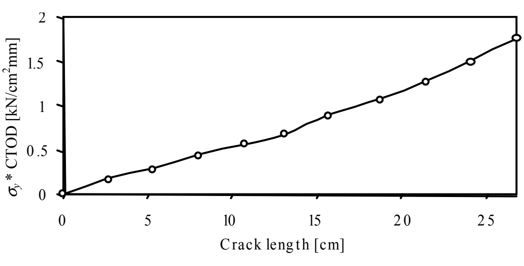

product σ_y*B

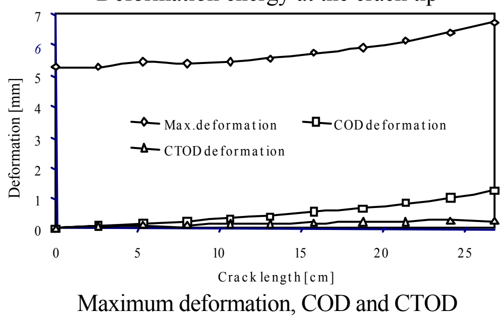

Maximum deformation, COD and CTOD

Figure 44. Crack growth effect on the behaviour of different parameters

Extended analysis of crack behaviour has concluded that the 5 cm crack is not dangerous, but from 5 to 13 cm it will grow in a stable manner and beyond 15 cm, an unstable crack growth may be expected. It is concluded that the furnace can be used with detected crack of 10.7 cm for the next six months. After this period, measurements have shown that the crack length has reached 20 cm and further service was not allowed.

3.16. Recovery of the rotary furnace ring

In order to improve the design of the rotary furnace ring in the Cement Factory of Popovac, model analysis has been performed. The half rotary furnace model is presented in Fig. 45. The results of stress and thermal loading analysis ($\Delta T = 100°C$) are shown in Fig. 45, and in Table 16.

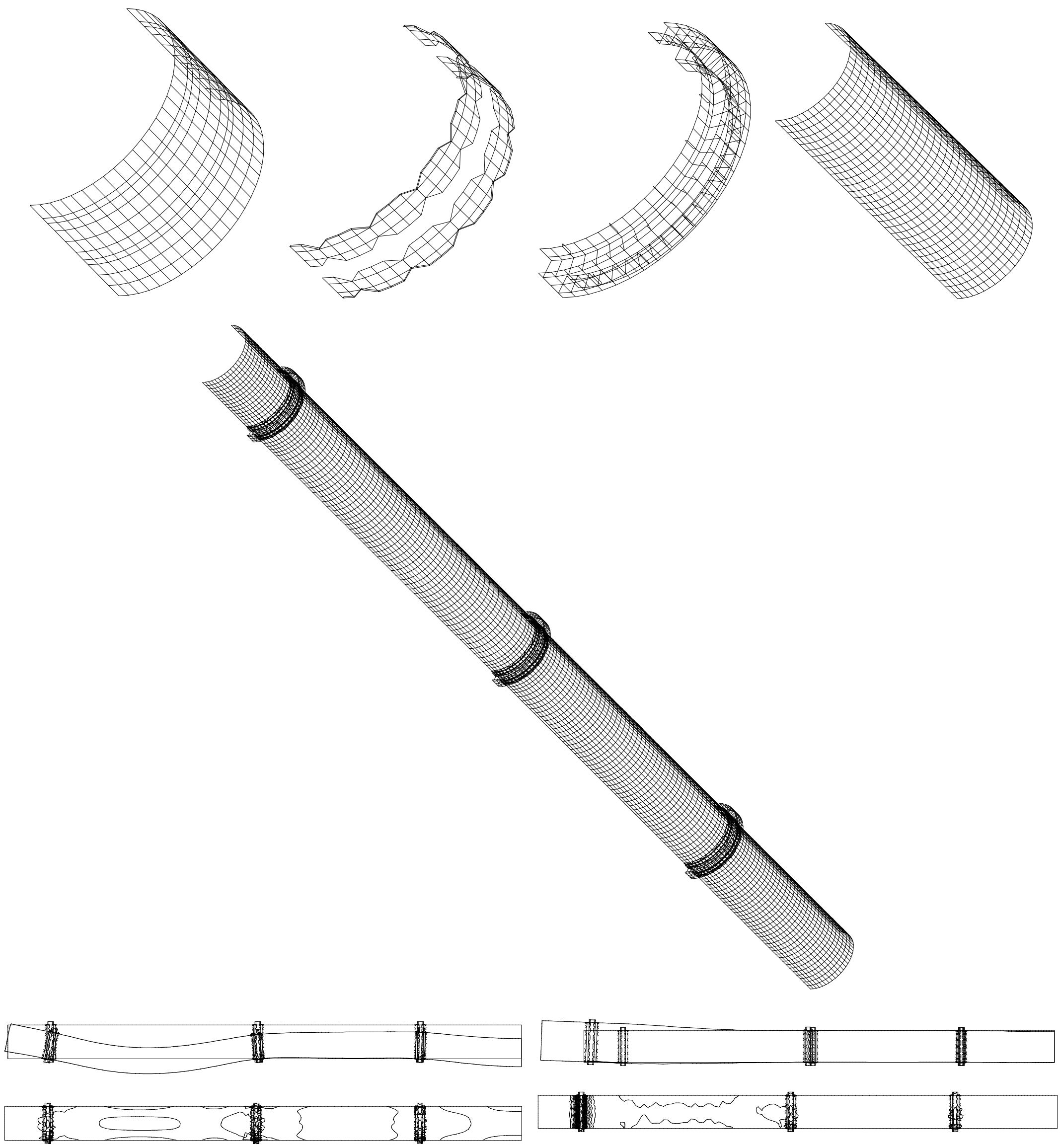

Dead load effect on deformation (f_{max} = 0.353 cm) and stress (0–3.5 kN/cm^2, step 0.5)

Dead and thermal load effect on deformation (f_{max} = 6.72 cm) and stress (0–15 kN/cm^2, step 1)

Figure 45. Model of the rotary furnace ring with deformation and stress

Table 16. Distribution of loading effects

Element	E_d^{abs}/E_d^{rel}	Memb/Bend	σ/τ
Shell	10.2/5	27.2/19	37.9/8.3
3.ring	49.5/23.5	6.8/9.6	14.6/1.7
Tooth (Gear), 3.ring	32.8/40.7	0.7/0.1	0.6/0.2
Element, 3.ring	5.3/4.9	5.2/11.3	13.7/2.8
Weld 3.ring.	2.1/25.8	2.6/5.8	7.1/1.3
1 + 2 ring	0.1/0.1	5.6/6.1	9.4/2.3
$\sum$	100/100	48.1/51.9	81.6/18.4

For the verification of obtained results, the results for existing and modified rings are compared in Fig. 46 and in Table 17 with the results obtained by the company Krupp–Polysius. It is possible to conclude that the results for the modified model are close to that of the Krupp–Polysius model.

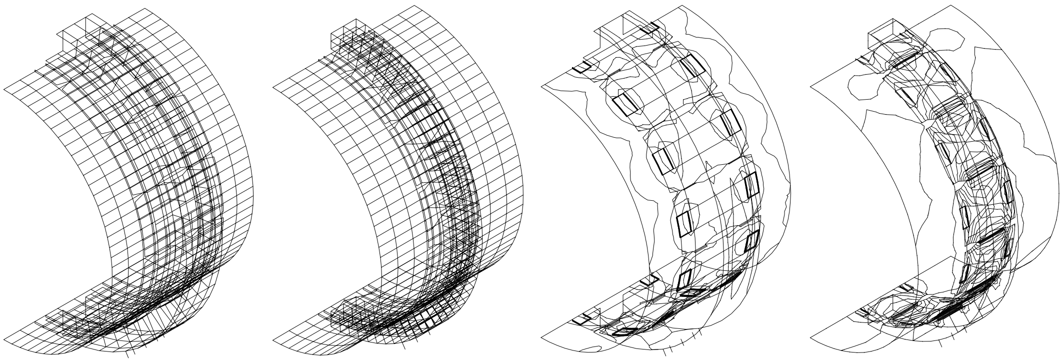

Modifed model   Krupp–Polysius model σ_{joint}^{eq} = 0–12.7 kN/cm^2, step 1 σ_{joint}^{eq} = 0–12.6 kN/cm^2, step 1

Figure 46. Compared modified and Krupp–Polysius models

Table 17. Results of calculation (model, deformation [cm], stress [kN/cm^2], energy)

Model	Modification model	Existing model	Krupp-Polysius model
Max. deformation	1.66	1.66	1.58
Max.$\sigma_{joint}^{eq}/\sigma_{element}^{eq}$	12.7/13	13.1/16.6	12.6/17.5
Shell $\sigma_{joint}^{eq}/\sigma_{element}^{eq}$	4/4.5	13.1/13.8	4/4.3
Weld $\sigma_{joint}^{eq}/\sigma_{elem}^{eq}$	12.7/13	13.1/13.8	12.6/14.8
Element $\sigma_{joint}^{eq}/\sigma_{elem}^{eq}$	9/10.5	8/10	12.6/17.5
Ring $\sigma_{joint}^{eq}/\sigma_{elem}^{eq}$	5/5.1	5/5.7	4.5/4.9
Tooth $\sigma_{joint}^{eq}/\sigma_{element}^{eq}$	- /2.5	- /3.9	- /3.3
Deformation energy [kNcm]	2400	2460	5330
Membrane/Bending [%]	51/49	43/57	34/66
σ/τ stress [%]	87.5/12.5	87.5/12.5	86/14

REFERENCES

1. Maneski, T., *Kompjutersko modeliranje i proračun struktura*, Monography in Serbian, Faculty of Mechanical Engineering, Belgrade. (1998)
2. Maneski, T., *Computer modelling and structural analysis*, Faculty of Mechanical Engineering, Belgrade. (2000)

3. Maneski, T., *Rešeni problemi čvrstoće konstrukcija*, Monography in Serbian, Faculty of Mechanical Engineering, Belgrade. (2002)
4. Maneski T., Milošević-Mitić V., Ostrić D., Postavke čvrstoće konstrukcija, Priručnik, Mašinski fakultet, Beograd (2002)
5. Zloković, Đ., Maneski, T., Nestorović, M., *Group supermatrix procedure in computing of engineering structures*, Structural Engineering Review, Vol. 6, No1, pp. 39-50. (1994)
6. Zloković, G., Maneski, T., Nestorović, M., *Group theoretical formulation of nonsymmetrical systems by the group supermatrix procedure*, Computers and Structures 71, pp. 637-649 (1999)
7. Maneski, T., *Rešeni problemi čvrstoće konstrukcija opreme u fabrikama cementa Beočin i Popovac*, Procesna tehnika (journal in Serbian), Belgrade. (2001)
8. Maneski, T., Aranđel, B., *Uticaj povećanja brzine kretanja na obrtno postolje elekro lokomotive JŽ 441*, (in Serbian) JUŽEL – 7th Conference, Vrnjačka Banja. (2001)
9. Maneski, T., *Mišljenje o konstruktivnom rešenju bidona sa potrebnim proračunom*, (in Serbian) Kolubara Prerada Vreoci, Faculty of Mechanical Engineering, Belgrade. (2001)
10. Babić, A., Maneski, T., Danojlić, V., *Okvir za reiženjering obrtnih postolja lokomotiva JŽ 441*, (in Serbian) X Conference – Železničko mašinstvo, Niš. (2002)
11. Maneski, T., Stefanović, D., Knežević, M., *Sanacija radnog točka bagera C700S*, V Yugoslav simposium with international participation MAREN2002, Faculty of Geology and Mining, Belgrade. (2002)
12. Maneski, T., Ivanković, M, Stanojević, D., *Rekonstrukcija rotacione peći 1000 t/dan FC Popovac*, International simposium Cement'02, Struga, Macedonia. (2002)
13. Sedmak, A., Maneski, T., Sedmak, S., *Primena koncepta integriteta konstrukcije na analizu stanja energetske opreme*, (in Serbian) Journal "Elektroprivreda," 1/02, Belgrade. (2002)
14. Maneski, T., Ignjatović, D., *Bucket Wheel Excavator SchRs 800 Reconstruction On Opencast Mine Drmno (Yugoslavia)*, Conference DIAGO 2003, VŠB-TU, Ostrava, Czech R. (2003)
15. Maneski, T., Bošnjak, S., Daničić, D., *Analiza popuštanja prstena oslonca rotacione peći br.3 u FC Beočin*, (in Serbian) journal "Procesna tehnika," Belgrade. (2003)

SINTAP – STRUCTURAL INTEGRITY ASSESSMENT PROCEDURE

Nenad Gubeljak, Faculty of Mechanical Engineering, Maribor, Slovenia
Uwe Zerbst, GKSS Research Centre, Institute of Materials Research, Geesthacht, Germany

INTRODUCTION

The SINTAP procedure is used in the interdisciplinary Brite-Euram project aimed to examine and unify the fracture mechanics based flaw assessment and has been propose as a procedure which should form the basis of future European standard [1]. Among many other publications a special issue of the journal *Engineering Fracture Mechanics* 67, 2000, pp. 479-668, contains a number of papers, which describe the main features of the SINTAP procedure. In the SINTAP procedure the implicit background assumption is that the component is defect-free. In this case, when assumed crack or crack-like flaw affects the load carrying capacity, the fracture mechanics principles have to be applied. Then the comparison between external effects and the material capacity has to be carried out on the basis of crack tip parameters such as the linear elastic stress intensity factor, K, the J integral or the crack tip opening displacement (CTOD). As a result, the fracture behaviour of the component can be predicted in terms of a critical applied load or a critical crack size.

Standard solutions for the crack tip parameters are available for specimens for measuring the material's resistance to fracture. As long as the deformation behaviour of the structural component is linear elastic, the relevant parameter in the component, K, is available in comprehensive compendia of K factor solutions [2,3,4,5]. If the component behaves in an elastic-plastic manner the situation is much more complex because the crack tip loading is additionally influenced by the deformation pattern of the material as given by its stress-strain curve. This makes the generation of handbook solutions an expensive task. To a limited extent this task has been accomplished for a few component configurations, [6]. SINTAP procedure also includes solutions for cracked plates, bars, and pipes of different loading configurations and crack positions. The overall structure of SINTAP is shown in Fig. 1. For more details see Refs. [7,8]. The aim of this lecture is to give a basic principle of SINTAP procedure, applied to a fractured forklift as an example.

1. SINTAP PROCEDURE

The SINTAP procedure is based on fracture mechanics principles, as shown in Fig. 2. If two of the input parameters are known, the third can be determined theoretically. This principle allows for different tasks of a fracture mechanics analysis:

- A crack is detected in a component during service. The question to be answered is whether this crack will lead to component failure or not. In certain circumstances the critical state can be avoided by reducing the load.
- In the design stage a component can be set-off with respect of a hypothetical crack, the dimensions and position of which have to be chosen such that the crack will be detected by non-destructive testing (NDT) in the final quality control, or in-service.
- Vice-versa, critical crack dimensions for subsequent NDT testing can be determined.

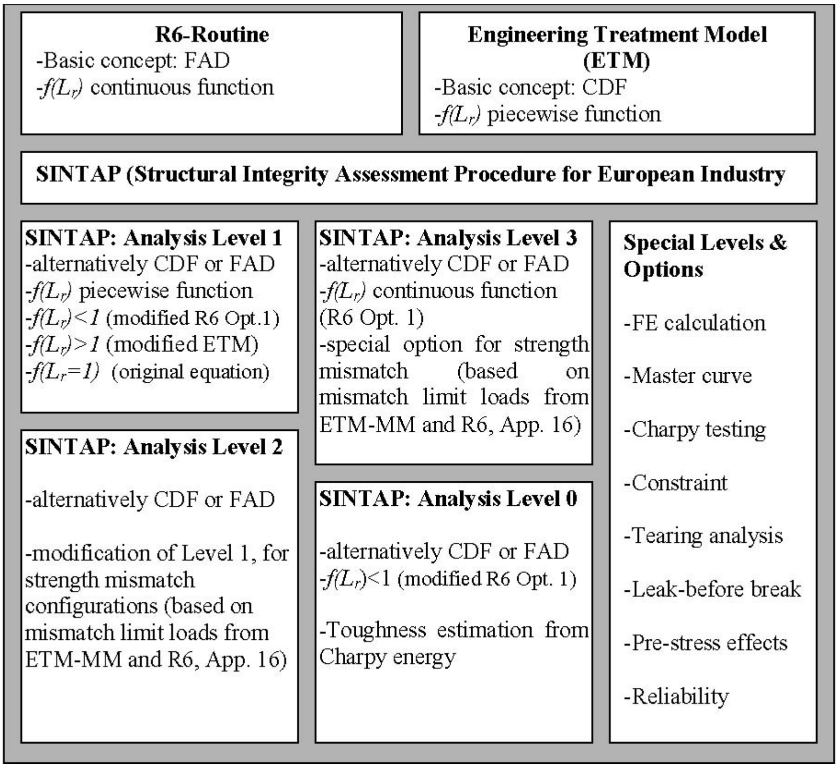

Figure 1. Overall structure of the SINTAP procedure, [9]

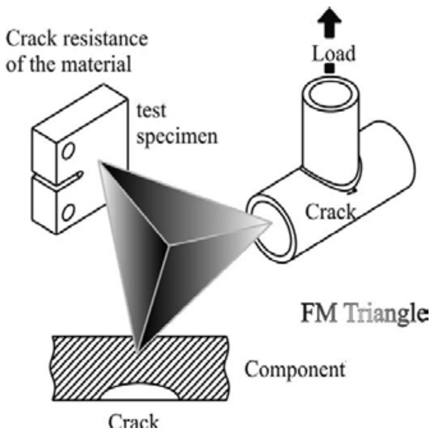

Figure 2. Fracture mechanics principles in design

The procedure for determining the critical crack size is illustrated in Fig. 3. Some basic items of SINTAP application will be addressed following this flow chart. Although some features and analysis steps shown in the flowchart will not be applied to fractured forklift analysis, they will be presented briefly because they provide important information for many other cases of failure analysis.

In order to determine a critical crack size the following input information is required:

- geometry and dimensions of the component,
- applied load, including secondary load components, such as residual stresses,
- information on crack type and orientation, and
- the stress-strain curve and fracture toughness of the material.

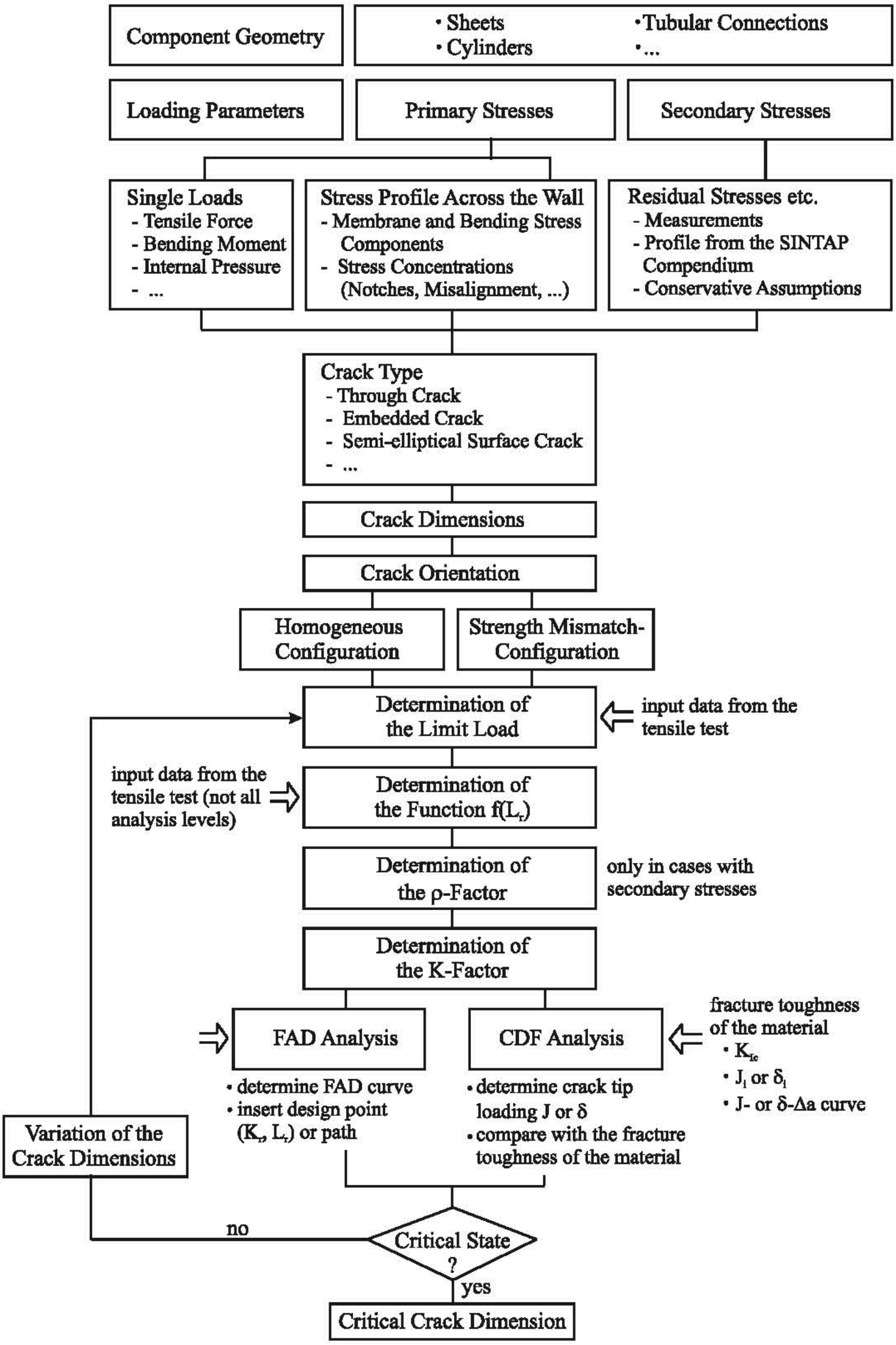

Figure 3. Flow chart for the determination of critical crack size using European SINTAP

1.1. Geometry and dimensions of the component

Component geometry and dimensions may vary, but from the analytical-handbook they are necessary for analysis. As an example, the geometry of the fractured fork is a thick plate (Fig. 4). The dimensions of the fractured cross section are shown in Fig. 5.

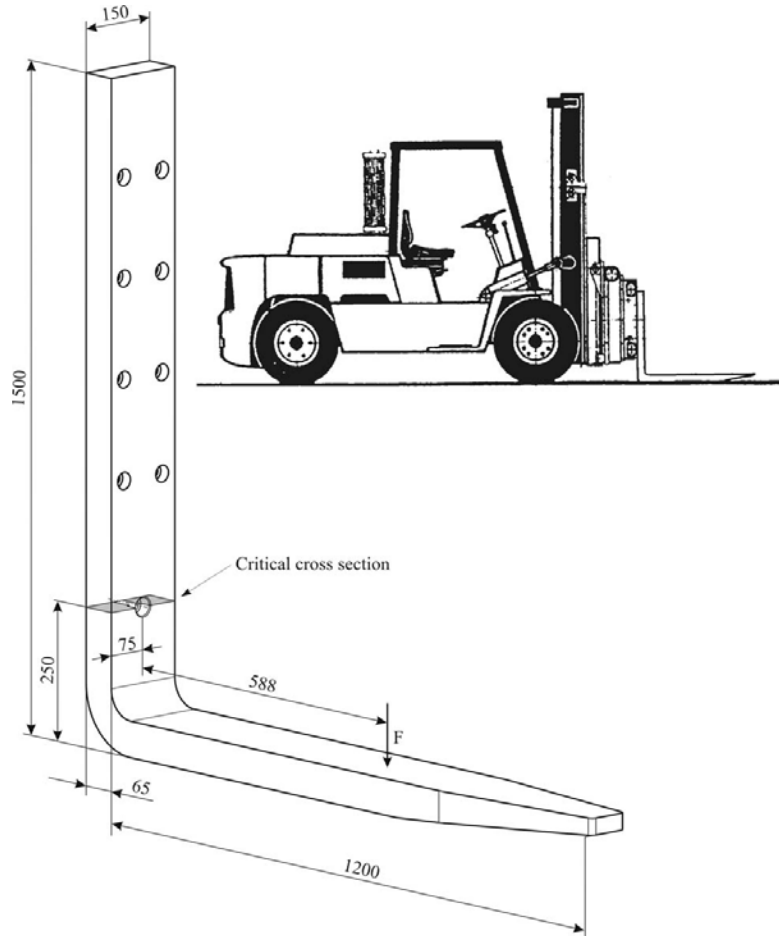

Figure 4. Geometry and dimensions of the fractured forklift (all measures in mm)

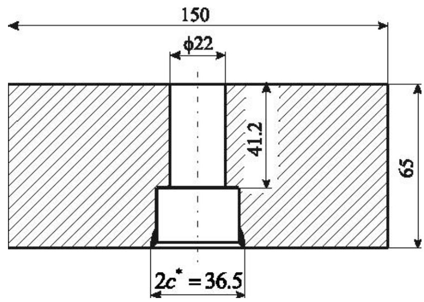

Figure 5. Geometry and dimensions of the fractured cross section (all measures in mm)

1.2. Applied load including secondary load components

In the SINTAP procedure the applied load can be introduced as a single load such as a tensile force, a bending moment, or internal pressure. The stress distribution analysis, i.e., determined by finite element method (FEM) is valuable, Fig. 6. Note that such a stress distribution profile refers to the component without crack. In the considered case of fractured fork, the loading type is predominant bending, that has allowed the application of a simple analytical model for determining bending stress. However, in order to also consider the membrane stress component, finite element analysis yielded the stress profile shown in Fig. 7, which is characterized by stress values σ_1 and σ_2 at the front and back surfaces of the plate. Based on these data, a bending stress and a membrane stress components are determined as: σ_b = 209 MPa; σ_m = 2 MPa.

These values correspond to one half of the design nominal load (35 kN) for the fork.

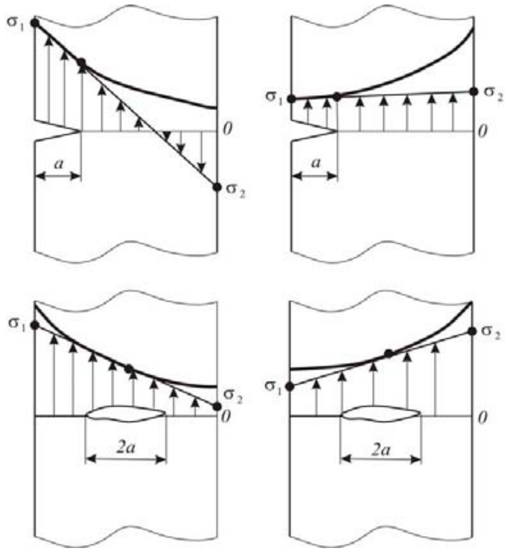

Figure 6. Distribution of membrane and bending stresses through thickness

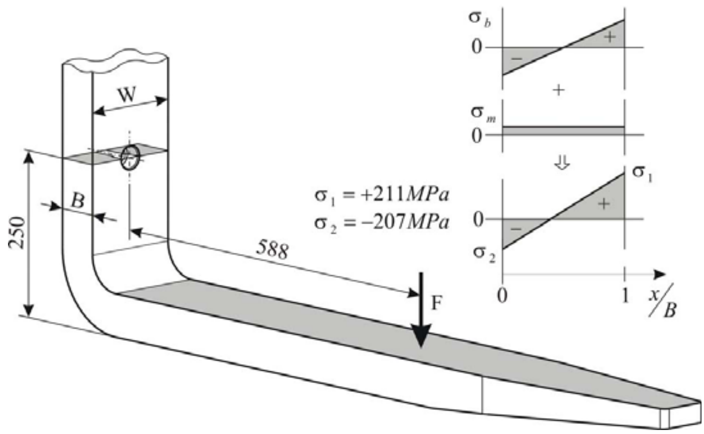

Figure 7. Stress distribution across the fork section containing the crack (all measures in mm). Membrane stress component: $\sigma_m = 0.5(\sigma_1 + \sigma_2)$. Bending stress component: $\sigma_b = 0.5(\sigma_1 - \sigma_2)$

In the present case only primary stresses had to be considered. In practice there are many cases, e.g., weldments – where these have to be completed by secondary stresses. In general, primary stresses arise from mechanical applied loads including the weight of the structure whereas secondary stresses are due to suspended stresses. Typical examples of secondary stresses are welding residual stresses. Secondary stresses are insignificant for common strength analyses because they are self equilibrating across the section. This is, however, no longer true when the same cross section contains a crack. In such a case, secondary stresses can be a major loading component which has to be considered in any analysis. In SINTAP, secondary stresses are taken into account in determining the K factor but not in determining the limit load, F_Y, or the degree of ligament plasticity, L_r.

1.2.1. Linear-elastic deformation behaviour

For linear-elastic deformation behaviour the crack tip loading can simply be determined by superposition of the K factor due to primary, and the K factor due to secondary stress, provided the crack opening mode is identical:

$$K_{\mathrm{I}} = K_{\mathrm{I}}^{p} + K_{\mathrm{I}}^{s} \tag{1}$$

1.2.2. Elastic-plastic deformation behaviour

In the general case, assessment is more complicated since interaction effects between primary and secondary stresses must be taken into account. Secondary stresses cannot cause plastic collapse, however, they may well contribute to plastic deformation. If they reach yield strength magnitude, the resultant crack tip loading is larger than $K_{\mathrm{I}}^{p} + K_{\mathrm{I}}^{s}$.

On the other hand, secondary stresses may be partly relieved due to relaxation effects introduced by ligament yielding. The interaction effect is modelled by a correction term ρ, which is defined in the Fracture Assessment Diagram (FAD) approach as:

$$K_r = \frac{K_{\mathrm{I}}^{p} + K_{\mathrm{I}}^{s}}{K_{mat}} + \rho \tag{2}$$

and in the Crack Driving Force (CDF) route as,

$$J = \frac{1}{E'}\left[\frac{K_{\mathrm{I}}^{p} + K_{\mathrm{I}}^{s}}{f(L_r) - \rho}\right]^2 \quad \text{or} \quad \delta = \frac{1}{E'\sigma_Y}\left[\frac{K_{\mathrm{I}}^{p} + K_{\mathrm{I}}^{s}}{f(L_r) - \rho}\right]^2 \tag{3,4}$$

The quantity ρ characterizes the difference between actual crack tip loading and crack tip loading which would result from simple superposition of K_{I}^{p} and K_{I}^{s}. By using

$$L_r = \frac{\sigma_{ref}^{p}}{\sigma_Y} \tag{5}$$

it is dependent on the ligament of plasticity, L_r (which is a function on primary loading), and on the magnitude of secondary stresses, and on the equation applied for $f(L_r)$. Therefore, it is possible to determine the correction term ρ from plot in Fig. 8.

Secondary stresses are not significant for analysis performed here, but they shall be mentioned without going into details. Note, that the SINTAP procedure gives guidance for the treatment of secondary stresses.

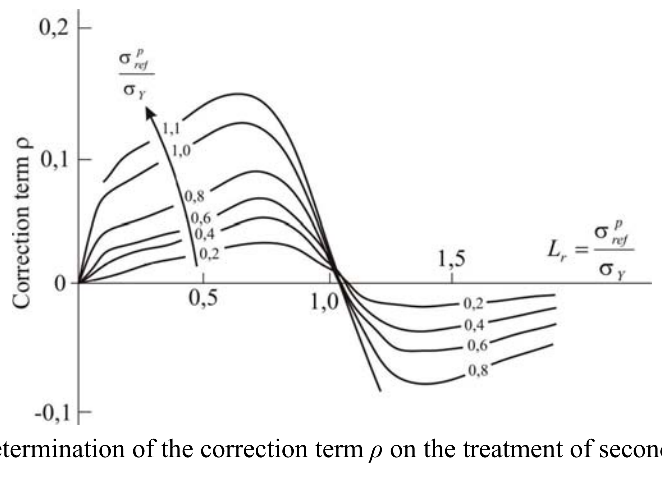

Figure 8. Determination of the correction term ρ on the treatment of secondary stresses

1.3. Crack type and orientation

Fracture mechanics analysis makes a difference between the through crack, embedded crack, and surface crack. Real crack shapes are idealized by substitute geometries such as rectangles, ellipses, and semi-ellipses. The idealization has to been done such that crack tip loading will be overestimated. Sometimes a crack or cluster of cracks have to be re-characterized if they interfere one with each other, or with a free surface. Real, irregular cracks are modelled by "ideal" straight, elliptical, or semi-elliptical cracks with dimensions defined by their envelope rectangles, as shown in Fig. 9. Most important is that the idealized flaws yield conservative results of FE analyses, as compared to the original crack. A cluster of multiple flaws may interact. If multiple cracks are located close to each other in the same cross section, they will be more severe than single cracks. This is taken into account by interaction criteria. If the spacing between single cracks is less than a certain value they have to be replaced by a larger crack, like if they have already coincided, as shown in Fig. 10. In a similar way the interaction effects between cracks on free surfaces are treated.

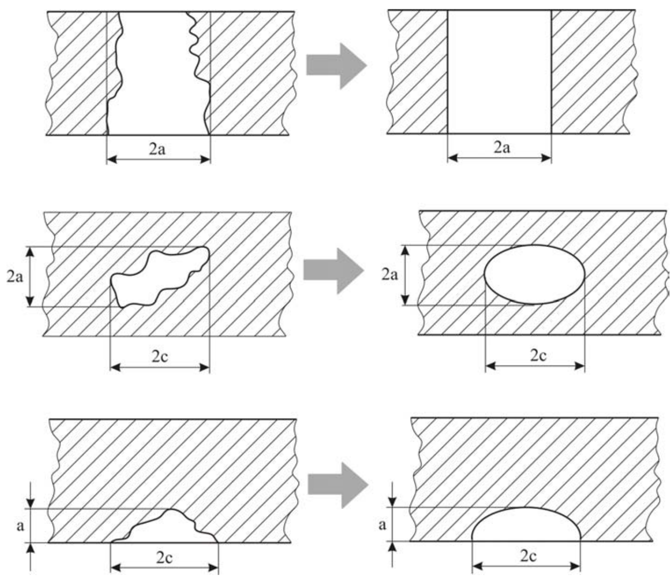

Figure 9. Defect idealisation

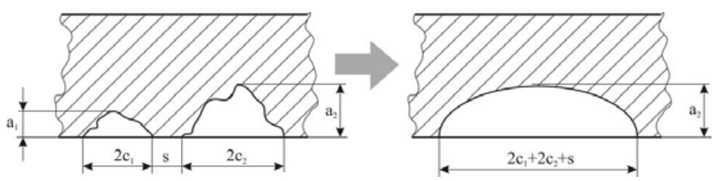

Interaction criterion ($c_1 < c_2$): s ≤ $2c_1$ for a_1/c_1 or $a_2/c_2 > 1$, s = 0 for a_1/c_1 and $a_2/c_2 \le 1$

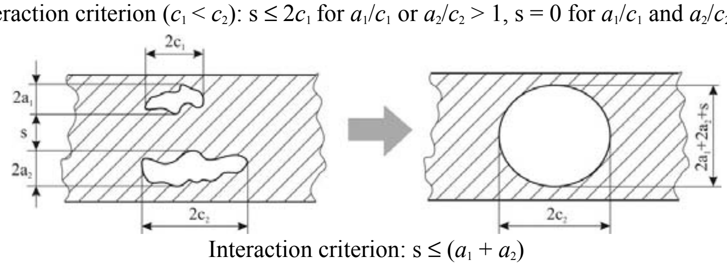

Interaction criterion: s ≤ ($a_1 + a_2$)

Figure 10. Defect idealisation of multiple flaws

In the present case of fork, the two edge cracks have been substituted by one through crack with dimensions which include the hole diameter as given in Fig. 11. For simplicity the crack is assumed to be of constant length, $2c$, over the wall thickness.

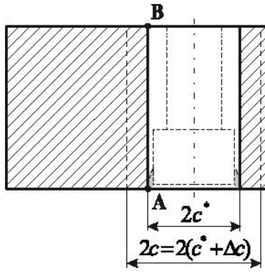

Figure 11. Definition of the idealized crack dimension $2c$

Usually, the crack plane is assumed to be perpendicular to the larger of the two principle stresses. In some cases, however, a real crack will not grow within this plane because of mechanical reasons, i.e. both principal stresses are of a magnitude of the same order, or because of the material heterogeneity. In such cases a more complicated mixed-mode analysis has to be carried out. In the present case the situation is quite simple because the maximum principle stress direction is identical to the axis of the fork.

In the flow chart in Fig. 3 the crack dimensions are introduced as input data. Actually, this refers to a default crack size, which is then varied iteratively. In each iteration step one should conclude whether the actual crack size is critical or not.

1.4. Homogeneous or strength mismatched configuration

Mismatch of strength means that in the welded joint, the base plate and the weld metal are of different strength, with the consequence of local strain concentrations within the weaker area if the yield strength of weld metal differs more than 10% from that of the base metal; if this difference is bellow 10%, the use of SINTAP procedure for homogeneous material (base plate) is recommended. The weld metal is commonly produced with yield strength, σ_{YW}, greater than that of the base plate, σ_{YB}. In Fig. 12b this case is designated as OverMatching (OM) with the mis-match factor M,

$$M = \frac{\sigma_{YW}}{\sigma_{YB}} > 1 \tag{6}$$

UnderMatching (UM) (Fig. 12a) is defined by

$$M < 1 \tag{7}$$

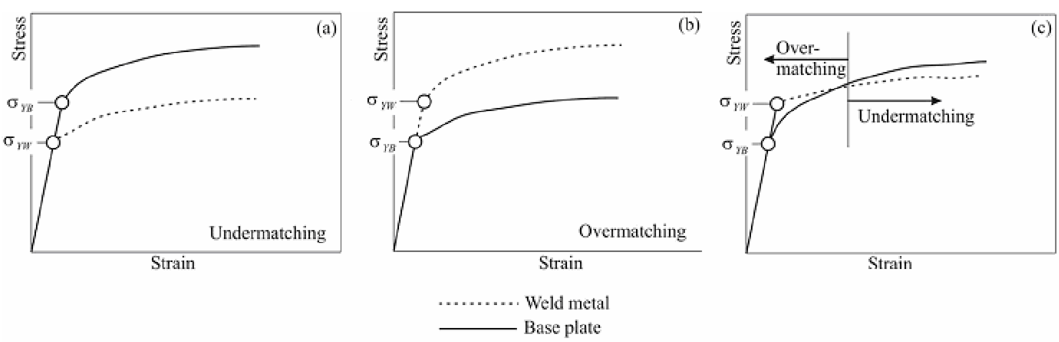

Figure 12. Definition of strength mismatched configuration

The mechanical consequences of mismatch are obvious from Fig. 13. Overmatching reduces the strain in the weld metal as compared to the base plate, thus leading to a shielding of a defect in the weld metal. Undermatching gives rise to a strain concentration in the weld metal.

There are, however, many cases where strength mismatch is of paramount interest. The mismatch plays an important role:

- in fracture toughness of the material (weld metal and base metal), (K_{mat}, J_{mat}, $CTOD_{mat}$),
- in stress intensity factor solution (K_I), in linear-elastic and elastic-plastic deformation behaviour, and
- in the limit load solution given by appropriate terms (F_Y, p_Y, σ_{ref}, etc.)

Therefore, the SINTAP procedure offers separate assessment options for the analysis of such cases. For the present example mismatch does not play any role.

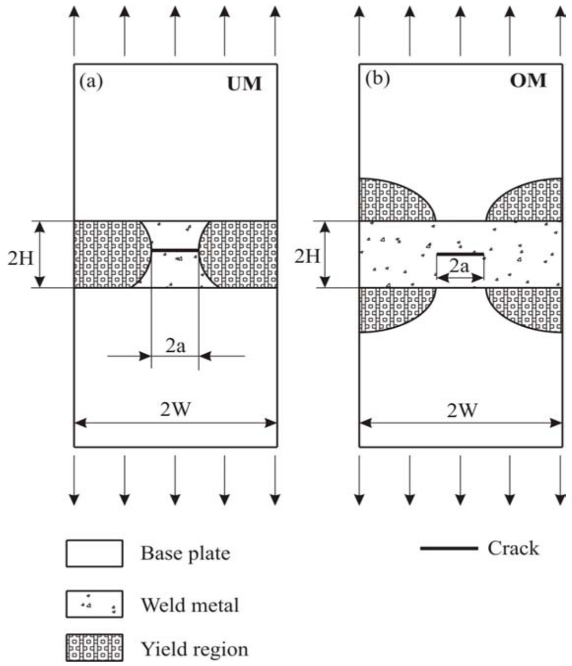

Figure 13. a) Undermatching (UM) gives rise to a strain concentration in the weld metal; b) Overmatching (OM) reduces the strain in the weld metal as compared to the base plate

1.5. Plastic limit load F_Y

The plastic limit load of the component with crack is one of the key parameters of the SINTAP analysis. Here some remarks are due. In solid mechanics the limit load is usually determined for ideally plastic materials. When the limit load is reached the deformation becomes unbounded over the cross section. Real materials, however, work harden with the consequence that the applied force can increase beyond the value given by the non-hardening limit load. Therefore, in the frame of a fracture mechanics analysis it has to be distinguished between a plastic collapse load which is identical to the maximum load which the structure with a crack can sustain and a net section yield load which refers roughly to that load at which the still unbroken ligament ahead of the crack is first fully plastic and the local load-deformation curve becomes nonlinear. This parameter as designated above is the plastic limit load F_Y. In practice it is usually determined under the assumption of an ideally plastic material inserting the yield strength as the maximum sustainable stress. This is supposed to represent the attainment of net section yielding, i.e. each point in the ligament ahead of the crack is supposed to have just reached the yield condition. This is correct for the ideally plastic material, however, for hardening materials some points are still under elastic deformation condition. Therefore, the thus determined value of F_Y represents a lower bound to the real yield load of component materials.

Within the SINTAP procedure a compendium of limit loads is provided. Other compilations are available in literature, e.g. in [11]. For cases, which are not covered by this compilation, conservative estimates are possible based on substitute geometries. In such cases the stress profiles in the components without crack are taken as input information.

Within the SINTAP procedure a loading parameter L_r is used which is defined as the ratio of the applied load F and the limit load F_Y, or respectively as the ratio of an applied net section stress σ_{ref} and the yield strength of the material, σ_Y, (Fig. 14):

$$L_r = F/F_Y = \sigma_{ref}/\sigma_Y \tag{8}$$

the latter being given as $\sigma_Y = R_{eL}$ for materials with, and $\sigma_Y = R_{p0.2}$ for materials without a Lüders plateau.

The reference stress of the plate geometry considered within this paper can easily be determined as

$$\sigma_{ref} = \frac{1}{1-(2c/W)}\left\{\frac{\sigma_b}{3} + \sqrt{\frac{\sigma_b^2}{9} + \sigma_m^2}\right\} \tag{9}$$

1.6. Stress intensity factor (*K* factor)

As in the case of the limit load, numerous solutions for K factors are available in compendia, e.g. [2,3]. The SINTAP procedure provides its own compilation of such solutions. Stress intensity factors can be determined for single loads such as forces, bending moments, internal pressures etc., as well as for stress profiles. The latter alternative allows handling geometrically complex components by using substitute structures, i.e. the stress profile is determined for the real structure without crack, whereas the determination of the K–factor is based on a simpler geometry like a plate, cylinder, etc. The K factor for the fork in the present paper was determined by

$$K_{\mathrm{I}}(c,F) = \sqrt{\pi c}\,(\sigma_m f_m + \sigma_b f_b) \tag{10}$$

where f_m and f_b are shape functions being defined for a plate with a through crack. They are $f_m^A = 1$ and $f_b^A = 1$ for point A, and $f_m^B = 1$ and $f_b^B = -1$ for point B.

1.7. Correction function *f*(L_r)

Under conditions of small scale yielding (roughly up to 0.6 times the limit load) a fracture mechanics analysis can be based on the linear-elastic K factor. This is, however, not possible for contained and net section yielding where the plastic zone is no more limited to a small region ahead of the crack tip. Under this condition any application of the K concept would lead to a significant underestimation of the real crack tip loading in terms of the J–integral or CTOD. Irrespective of this general statement the application of a formal K concept becomes possible when the linear-elastic K factor is corrected with respect of the yield effect. This is essential of the correction function $f(L_r)$. With respect of $f(L_r)$, the SINTAP procedure is structured in a hierarchic manner consisting of various analysis levels constituted by the quality and completeness of the required input information. Higher levels are more advanced than lower levels: they need more complex input information but the user is "rewarded" by less conservative results. An unacceptable result provides a motivation for repeating the analysis at the next higher level rather than claiming the component to be unsafe. The SINTAP standard analysis levels are:

Basic Level – Only the toughness, yield strength, and ultimate tensile strength of the material need to be known. Different sets of equations are offered for materials with and without Lüders plateau.

Mismatch Level – This is a modification of the Basic Level for inhomogeneous configurations such are strength–mismatched weldments.

Advanced or Stress-Strain Level – This requires toughness data and the complete stress-strain curve of the material. Both, homogenous and strength mismatched components can be treated.

There are additional levels:

Default Level – Only the yield strength of the material is required. The fracture resistance of the material can be conservatively estimated from Charpy data.

Constraint Level – Within this level, the effect of loss of constraint in thin sections or predominately tensile loading on fracture resistance is considered.

J–integral Analysis Level – This level includes a complete numerical analysis of defect structure.

In the present paper the Default, Basic and Advanced Levels are applied. The according equations $f(L_r)$ for ferritic steels without Lüders plateau are:

– <u>Default Level</u>

$$f(L_r)=\left[1+\frac{1}{2}L_r^2\right]^{-1/2}\left[0.3+0.7\exp\left(-0.6L_r^6\right)\right]\ \text{ for }\ 0\le L_r\le L_{r\,max} \tag{11}$$

$$L_{r\,max}=1+\left[\frac{150}{R_{p0.2}}\right]^{2.5},\ R_{p0.2}\ \text{ in MPa} \tag{12}$$

The fracture toughness is estimated in a conservative manner from Charpy data by

$$f(L_r)=\left[\frac{E\varepsilon_{ref}}{\sigma_{ref}}+\frac{1}{2}\frac{L_r^2}{\left(E\varepsilon_{ref}/\sigma_{ref}\right)}\right]^{-1/2}\quad \text{for }\ 0\le L_r\le L_{r\,max} \tag{13}$$

$$L_{r\,max}=\frac{\sigma_f}{\sigma_Y}\ \text{ with }\ \sigma_f=\frac{1}{2}(\sigma_Y+R_m)\ \text{ on the lower shelf, and by}$$

$$K_{mat}=K_{J0.2}=\sqrt{\frac{E(0.53\,\mathrm{KV}^{1.28})0.2^{0.133\,\mathrm{KV}^{0.256}}}{1000(1-\nu^2)}},\ \text{ on the upper shelf} \tag{14}$$

where K_{mat} is in MPa√m; specimen thickness B in mm; Charpy energy KV in J.

In addition, SINTAP offers a correlation for the ductile-to-brittle transition based on Charpy transition temperature for 28 J.

In the present analysis, Eq. (13) was applied for estimating fracture toughness from Charpy energy.

– <u>Basic Level</u>

$$f(L_r)=\left[1+\frac{1}{2}L_r^2\right]^{-1/2}\left[0.3+0.7\exp(-\mu L_r^6)\right]\ \text{ for }\ 0\le L_r\le 1 \tag{15}$$

$$\text{with} \quad \mu = \min \begin{cases} 0.001E/R_{p0.2} \\ 0.6 \end{cases} \tag{16}$$

and

$$f(L_r) = f(L_r = 1)L_r^{(N-1)/2N} \quad \text{for} \quad 1 \le L_r < L_{r\,max} \tag{17}$$

$$N = 0.3\left[1 - \frac{R_{p0.2}}{R_m}\right] \tag{18}$$

$$L_{r\,max} = \frac{1}{2}\left[\frac{R_{p0.2} + R_m}{R_{p0.2}}\right] \tag{19}$$

with $L_{r\,max}$ being the limit against plastic collapse.

– Advanced Level

$$f(L_r) = \left[\frac{E\varepsilon_{ref}}{\sigma_{ref}} + \frac{1}{2}\frac{L_r^2}{(E\varepsilon_{ref}/\sigma_{ref})}\right]^{-1/2} \quad \text{for} \quad 0 \le L_r \le L_{r\,max} \tag{20}$$

$$L_{r\,max} = \frac{\sigma_f}{\sigma_Y} \quad \text{with} \quad \sigma_f = \frac{1}{2}(\sigma_Y + R_m) \tag{21}$$

Different to the Levels above, $f(L_r)$ is a continuous function which follows the true stress–strain curve in a point-wise manner. Each value of σ_{ref} is assigned to an L_r value by

$$\sigma_{ref} = L_r \sigma_Y \tag{22}$$

The corresponding reference strain ε_{ref} is obtained from the true stress–strain curve as illustrated in Fig. 14. No distinction is necessary between materials with and without a Lüders plateau. On the other hand $\sigma_{ref}/\varepsilon_{ref}$ values have to be available at L_r = 0.7/0.9/0.98/ 1/1.02/1.1, and other values of L_r.

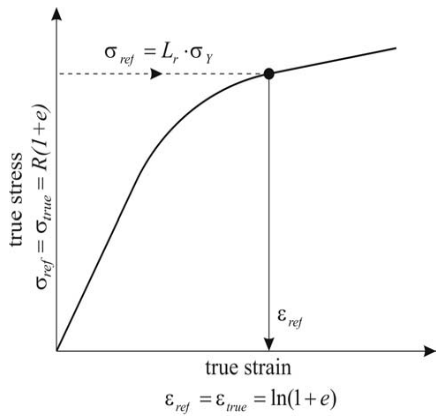

Figure 14. True stress and strain in terms of the loading parameter, L_r

1.8. The true stress–strain curve of the material

The engineering stress–strain curve of the material is shown in Fig. 15. Five tests were carried out but only the lowest curve was used for SINTAP analysis. The mechanical properties derived from these curves are summarized in Table 1. With σ and ε designating the engineering stress and strain, the true stress and strain values, σ_t and ε_t are determined by

$$\varepsilon_t = \ln(1+\varepsilon) \quad \text{and} \quad \sigma_t = \sigma(1+\varepsilon) \tag{23}$$

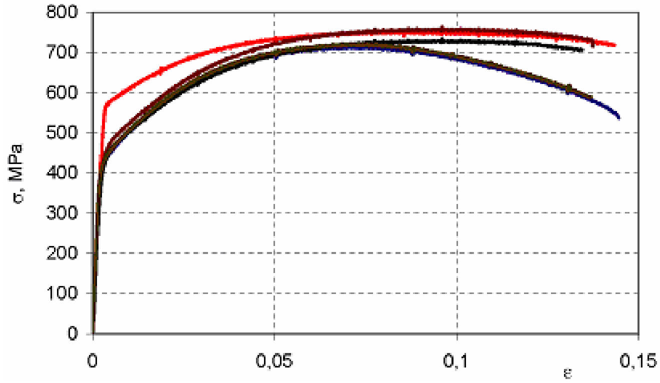

Figure 15. Engineering stress–strain curves of the fork material

Table 1. Mechanical properties obtained by tensile test and Charpy impact toughness values

E GPa	ν –	$R_{p0.2}$ MPa	R_m MPa	A_g %	A_t %	Z %	N –
2.1	0.3	446	720	6.89	14.95	53.60	0.176
		448	735	8.89	18.19	53.77	0.192
		578	754	7,.52	20.95	59.05	0.125
		474	764	9.72	19.48	55.81	0.187
		440	716	6.74	14.45	52.59	0.195

1.9. CDF versus FAD analyses

An important feature of the procedure is that the analyses can alternatively be based on a Failure Assessment Diagram (FAD) or on a Crack Driving Force (CDF) philosophy. Applying the FAD philosophy, a failure line is constructed by normalising the crack tip loading by the material's fracture resistance. The assessment of the component is then based on the relative location of a geometry dependent assessment point with respect to this failure line. In the simplest application the component is regarded as safe as long as the assessment point lies within the area enclosed by the failure line. It is potentially unsafe if it is located on or above the failure line. In contrast to this, in the CDF route the crack tip loading in the component is determined in a separate step. It is then compared with the fracture resistance of the material. If the crack tip loading is less than the fracture resistance, the component is safe, otherwise it is potentially unsafe.

Basic equations of FAD and CDF routes are set out in sub-sections 1.9.1 and 1.9.2 below.

1.9.1. FAD route

In the FAD route (Fig. 16), a failure assessment curve (FAC), K_r vs. L_r, is described by the equation

$$K_r = f(L_r) \tag{24}$$

To assess for crack initiation and growth, two parameters need to be calculated. The first one, K_r, is defined by

$$K_r = \frac{K_\mathrm{I}(a,F)}{K_{mat}} \tag{25}$$

where $K_\mathrm{I}(a,F)$ is the linear-elastic stress intensity factor of the defective component and K_{mat} is the fracture toughness.

The second parameter L_r is defined by

$$L_r = \frac{F}{F_Y} \tag{26}$$

where F_Y is the yield load of the cracked configuration.

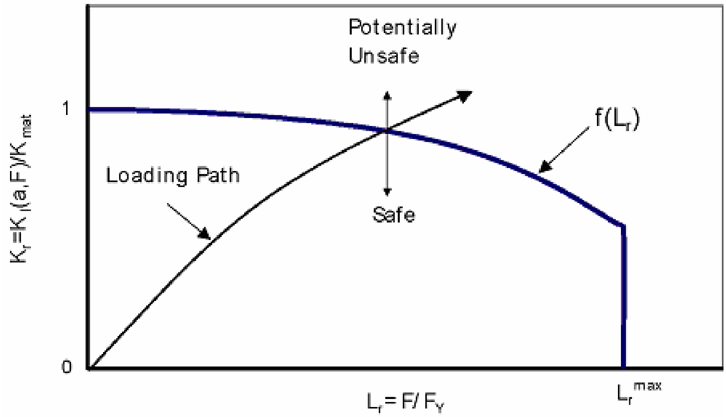

Figure 16. Failure assessment based on a FAD philosophy

1.9.2. CDF route

In the CDF route (Fig. 17), an applied parameter such as the *J*–integral or crack tip opening displacement (CTOD = δ) is determined, which characterises the stresses and strains ahead of the crack tip in a specimen or component:

$$J = J_e\left[f(L_r)\right]^{-2} \quad \text{or} \quad \delta = \delta_e\left[f(L_r)\right]^{-2} \tag{27, 28}$$

where J_e and δ_e are the elastic values of the crack tip parameters which can be deduced from the stress intensity factor $K_{\mathrm{I}}(a,F)$ as

$$J_e = \frac{[K_{\mathrm{I}}(a,F)]^2}{E'} \quad \text{or} \quad \delta_e = \frac{[K_{\mathrm{I}}(a,F)]^2}{E'\sigma_Y} \tag{29, 30}$$

with E' being Young's modulus in plane stress and $E/(1 - \nu^2)$ in plane strain. The quantity ν is Poisson's ratio.

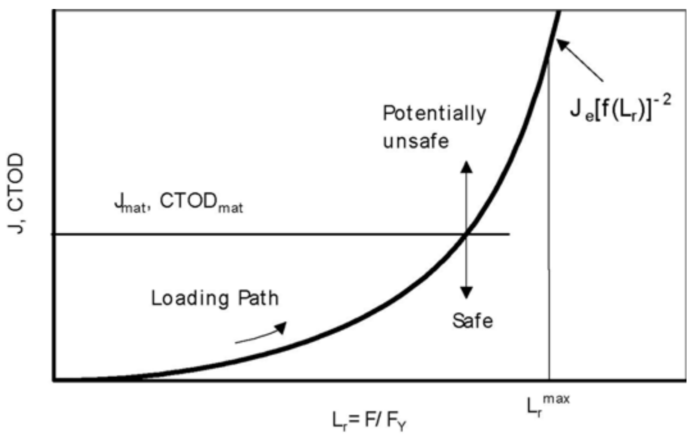

Figure 17. Failure assessment based on the CDF philosophy
(The function $f(L_r)$ is identical for the FAD and CDF routes)

In Eq. (2) the fracture resistance of the material is used in terms of the K factor, K_{mat}. This quantity is obtained formally from the J–integral or CTOD by

$$K_{mat} = \sqrt{\frac{J_{mat} E}{(1-\nu^2)}} = \sqrt{\frac{\sigma_y \delta_{mat} E}{(1-\nu^2)}} \tag{31}$$

The SINTAP procedure includes different analysis levels. The main difference between these levels is the function $f(L_r)$. It is defined such that lower levels can be applied even with relatively poor input information. Due to this, the output is more conservative as compared with more advanced levels which require more detailed input information, but "reward" the user with more realistic results. The Default Level is the lowest level of the SINTAP procedure. Its use is recommended only if no other data than the yield strength of the material and the Charpy data are available.

The function $f(L_r)$, which is the same for both FAD and CDF routes, is given by:

– In cases where the material exhibits a Lüders strain

$$f(L_r) = \left(1 + \frac{1}{2} L_r^2\right)^{-1/2} \quad \text{for } 0 \le L_r \le L_r^{max} \tag{32}$$

The cut-off L_r^{max} is defined in a conservative manner as

$$L_r^{max} = 1 \tag{33}$$

– If the material does not exhibit a Lüders strain, the failure assessment curve $f(L_r)$ is described by the equation

$$f(L_r) = \left(1 + \frac{1}{2} L_r^2\right)^{-1/2} \left[0.3 + 0.7 \exp(-0.6 L_r^6)\right] \quad \text{for } 0 \le L_r \le L_r^{max} \tag{34}$$

The cut-off L_r^{max} is defined slightly less conservatively as

$$L_r^{max} = 1 + \left(\frac{150}{R_{p0.2}}\right)^{2.5} \tag{35}$$

1.10. Fracture Toughness

The fracture toughness was determined in terms of the crack tip opening displacement CTOD (δ) according to the British standard BS 7448, Part 1, [10]. Four tests were carried out using three-point bend specimens at room temperature. The test setup is shown in Fig. 18, and a typical test record in Fig. 19. It shows typical pop-in behaviour. Pop-ins are cleavage fracture events disrupting the ductile tearing process. The crack is arrested subsequent to each pop-in. Note, however, that the specimen is subjected to displacement control in the test machine whereas in reality load control might occur. Usually the crack would not be arrested in such a case, but cause failure. Therefore, no benefit can be taken from the crack arrest following a pop-in which was specified as such by the test standard.

For SINTAP analyses the lowest of the pop-in fracture toughness values was chosen. This was $\delta_c = 0.02$ mm or corresponding $K_{mat} = 49.7$ MPa√m.

1.11. Charpy energy

Information on the Charpy energy is necessary for SINTAP Default Level assessment. Nine tests have been carried out at three temperatures. The result is summarised in Table 2. The SINTAP analysis was based on the minimum room temperature Charpy energy of 6 J.

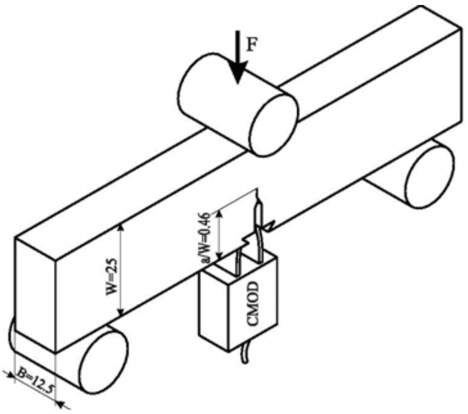

Figure 18. Test setup for determination of critical crack tip opening displacement

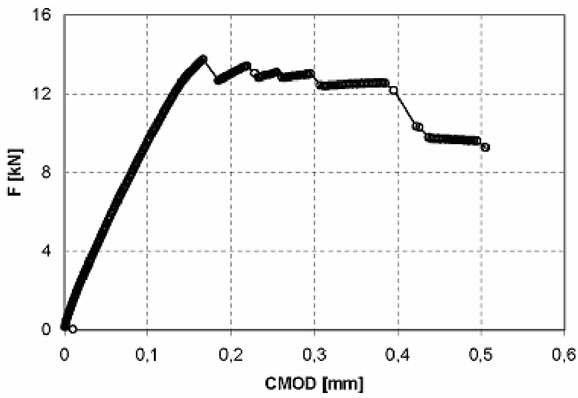

Figure 19. Typical test record of a CTOD test

Table 2. Charpy energy of the fork material at different temperatures

Charpy impact toughness J/80 mm^2		
+10°C	+20°C	+50°C
6; 6; 6	7; 6; 7	9; 8; 9

2. FAILURE ANALYSIS OF THE COMPONENT, RESULTS, AND DISCUSSION

The fork of a forklift is an example for using "Default" level, level "1" and level "3".

In Figs. 20 and 21 the CDF and FAD analyses are demonstrated for a crack size of 2*c* = 45.5 mm. This length corresponds to real crack length measured on the fractured surface of fork, as shown in Fig. 22. It is shown that the higher analysis levels yield less conservative results. The Default Level which uses fracture toughness values estimated from Charpy energy gives much lower critical loads than the higher levels.

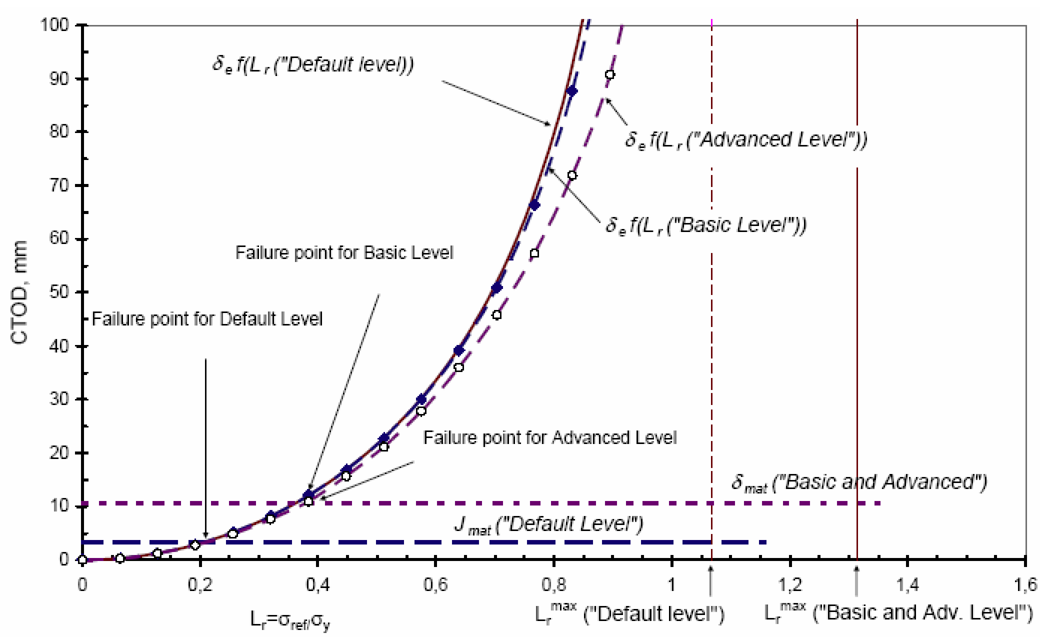

Figure 20. CDF analysis of Fork assuming a crack width of 2*c* = 45.5 mm. Failure is predicted for an applied load of 15 kN (Default Level), 27.38 kN (Basic Level), and 29.9 kN (Advanced Level)

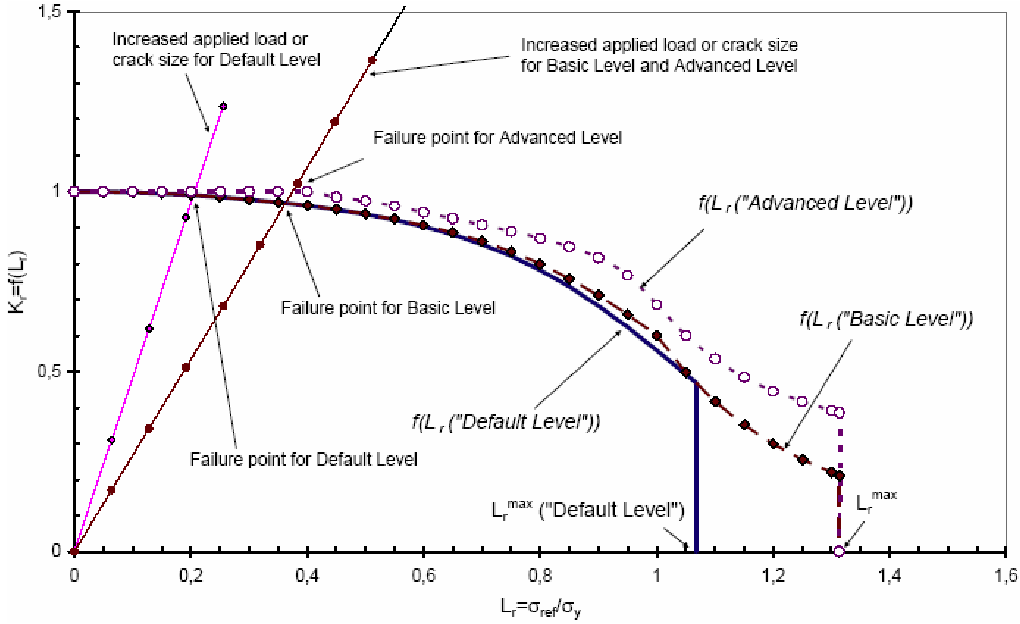

Figure 21. FAD analysis of the fork assuming a crack width of $2c$ = 45.5 mm. The predicted failure loads are identical to those obtained by the CDF analysis in Fig. 20

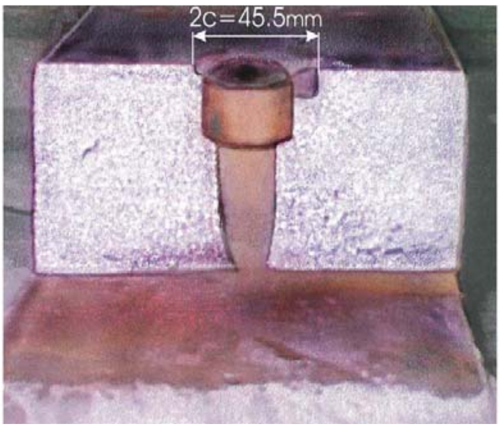

Figure 22. Real crack length measurement of the fractured fork

According to Fig. 3 the analysis was repeated for stepwise increased crack sizes $2c$. Critical crack size was then determined as the value of $2c$ that caused failure at half the nominal applied load the forklift was designed for. The bi-section was necessary because the forklift contained two forks.

As the final result, the critical crack size was determined to be:

- $2c$ = 10.35 mm (Default Level analysis)
- $2c$ = 33.2 mm (Basic Level analysis)
- $2c$ = 35.6 mm (Advanced Level analysis).

Compared to the real overall surface dimension of edge cracks, 45.5 mm, at failure (Fig. 22), the predictions were conservative by:

- 77.28% (Default Level analysis)
- 27.03% (Basic Level analysis)
- 21.75% (Advanced Level analysis),

this is not so much at the highest level because critical crack sizes are very sensitive with respect to the input information. At the highest level, the conservatism was mostly due to the simplified crack model used as substitute geometry (Fig. 11).

It can be concluded that failure occurred as the consequence of inadequate design and not of inadmissible handling, such as overloading. The failure could have been avoided by applying fracture mechanics in the design stage. The SINTAP algorithm was shown to be an easy, but suitable tool for this purpose.

CONCLUSIONS

The basic principle of the recently developed European SINTAP procedure has been reviewed. The SINTAP procedure contributes towards the development of a fitness for service standard of the European Committee for Standardization (CEN). The SINTAP procedure was applied to the failure analysis of a cracked component, and for predicting the critical size of cracks on both sides of a bore hole in a fork of a forklift. Assuming the loading by design, an overall critical crack size of 35.6 mm (including both cracks and the hole) was predicted at the highest analysis level, whereas the real fork had fractured in service after the overall crack size reached a length of 45.5 mm. This result has shown that inadequate design could give a sufficient account to failure without any need to imply further reasons such as inadmissible handling of the forklift in service. The results of the example also showed that SINTAP procedure gives reliable conservative results where conservatism (e.g. safety factor) decreases by increasing the quality of input data.

REFERENCES

1. SINTAP: Structural Integrity Assessment Procedure. Final Report. EU-Project BE 95-1462. Brite Euram Programme, Brussels. (1999)
2. Tada, H., Paris, P.C., Irwin, G.R., *The Stress Analysis of Cracks Handbook*. ASME Press, (1998)
3. Murakami, Y., et al. (Eds.), *Stress Intensity Factor Handbook*, Vol. 1&2 (1987), Vol. 3 (1992), Pergamon Press, Oxford.
4. Schwalbe, K-H., Kim, Y-J., Hao, S., Cornec, A., Koçak, M., *EFAM, ETM-MM96: the ETM method for assessing significance of crack-like defects in joints with mechanical heterogeneity (strength mismatch)*, GKSS Report 97/E/9. (1997)
5. Schwalbe, K-H., Zerbst, U, Kim, Y-J., Brocks, W., Cornec A., Heerens J., Amstutz H., *EFAM ETM 97: the ETM method for assessing crack-like defects in engineering structures*, GKSS Report 98/E/6. (1988)
6. Kumar, V., German, M.D., Shih, C.F., *An engineering approach for elastic-plastic fracture analysis*, EPRI-Report NP-1931, EPRI, Palo Alto, CA. (1981)
7. SINTAP Special issue of Engineering Fracture Mechanics, Vol. 67, Issue 6, pp. 476-668, Dec. 2000
8. Ainsworth, R.A., Bannister, A.C., Zerbst, U., *An overview of the European flaw assessment procedure SINTAP and its validation*, Int. J. Pres. Ves. & Piping, 77, pp. 869-876. (2001)
9. Zerbst, U., Hamann, R., Wohlschlegel, A., *Application of the European flaw assessment procedure SINTAP to pipes*, Int. J. Pres. Ves. & Piping, 77, pp. 697-702. (2000)
10. BS 7448: Part 2: 1997: *Fracture mechanics toughness tests, Part 2. Method for determination of K_{Ic}, critical CTOD and critical J values of welds in metallic materials*, British standards institution, London. (1997)
11. Miller, A.G., *Review of Limit Loads of Structures Containing Defects*. Int. J. Pres. Ves. & Piping, 32, pp. 197-327. (1988)

A NUMERICAL PROCEDURE FOR CALCULATION OF STRESS INTENSITY FACTORS AND ITS USE FOR LIFE ASSESSMENT OF STEAM TURBINE HOUSING OF THERMAL POWER PLANT

G. Jovičić, M. Živković, M. Kojić, S. Vulović
Faculty of Mechanical Engineering, Kragujevac, Serbia and Montenegro

INTRODUCTION

Studies of fracture mechanics emerged in the early twentieth century. Among a number of researchers, Griffith's idea of "minimum potential energy" provided a foundation for all later successful theoretical studies of fracture, especially for brittle materials. But it was not until after World War II that fracture mechanics developed as a discipline. Derived from Griffith's theorem, the concept of energy release rate, G, was first introduced by Irwin, in a form more useful for engineering applications. Irwin defined an energy release rate or the crack extension force tendency which can be determined from stress and displacement fields in the vicinity of the crack tip rather then from an energy balance for elastic solid as a whole, as Griffith suggested.

Conservation integrals in elasticity have been widely applied to fracture mechanics, among which the J integral is the most popular one. The J integral is path independent for elastic solids, and can be shown that the integral is identical to Irwin's energy release rate associated with the collinear extension of a crack in elastic solid [1].

1. DETERMINATION OF FRACTURE PARAMETERS IN THE PAK PROGRAM

1.1. Equivalent domain integral method (EDI)

Rice [1] defined a path-independent J-integral for two-dimensional crack problems in linear and nonlinear elastic materials. As shown in Fig. 1, J is the line integral surrounding a two-dimensional crack tip and is defined as

$$J_1 = \lim_{\Gamma_S \to 0} \int_{\Gamma_S} (W\delta_{1j} - \sigma_{ij} u_{i,1}) n_j d\Gamma \,, \;\; i,j = 1,2 \tag{1}$$

where W is the strain energy density given by

$$W = \frac{1}{2}\sigma_{ij}\varepsilon_{ij} = \frac{1}{2}C_{ijkl}\varepsilon_{kl}\varepsilon_{ij} \tag{2}$$

and n_j is the outward normal vector to the integration contour Γ_g around the crack tip (Fig. 1), σ_{ij} is the stress tensor, ε_{ij} is the strain tensor, C_{ijkl} is the constitutive tensor and u_i are components of the displacement vector.

Knowles and Stenberg [2] noted that this can be considered as the first component of a vector

$$J_k = \lim_{\Gamma_S \to 0} \int_{\Gamma_S} (W\delta_{kj} - \sigma_{ij} u_{i,k}) n_j d\Gamma \,, \;\; i,j,k = 1,2 \tag{3}$$

which is also path independent.

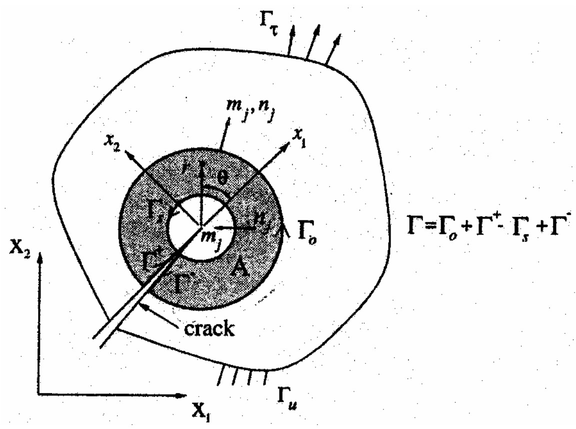

Figure 1. Conversion of the contour integral into an Equivalent Domain Integral method (EDI)

Helen and Blackburn [3] showed that

$$J = J_1 - iJ_2 = \frac{1}{E^*}(K_{\mathrm{I}}^2 + K_{\mathrm{II}}^2 + 2iK_{\mathrm{I}}K_{\mathrm{II}}) \tag{4}$$

where K_{I} and K_{II} are stress intensity factors for modes I and II, respectively. Thus, values of energy release rates (J_1 and J_2) for crack extension perpendicular and parallel to the crack, respectively, will be given by:

$$J_1 = \frac{K_{\mathrm{I}}^2 + K_{\mathrm{II}}^2}{E^*}$$
$$J_1 = \frac{-2K_{\mathrm{I}}K_{\mathrm{II}}}{E^*} \tag{5}$$

where

$$E^* = \begin{cases} E & \text{plane strain} \\ \dfrac{E}{1-\nu^2} & \text{plane stress} \end{cases}$$

Note that solution Eq. (5) is the intersection of a circle and hyperbola. Hence, there exists more than one pair of stress intensity factors.

The contour integral (1) is not in a form best suited for finite element calculations. The contour integral is therefore recasted into an equivalent domain form. The equivalent domain integral method (EDI) is an alternative way to obtain the J-integral. The contour integral is replaced by an integral over a finite-size domain. The EDI approach has the advantage that effects of variable body forces can easily be included. The standard J-contour integral given by Eq. (1) is rewritten, by introducing a weight function $q(x_1,x_2)$ into the EDI. Hence, the following contour integral is defined

$$\Psi = \int_\Gamma (W\delta_{1j} - \sigma_{ij}u_{i,1})m_j q d\Gamma \tag{6}$$

where the contour is $\Gamma = \Gamma_0 + \Gamma^+ - \Gamma_S + \Gamma^-$ (Fig. 1), m_j is an outward unit vector normal to the corresponding contour (i.e. $m_j = n_{jon}\Gamma_0$ and $m_j = -n_{jon}\Gamma_S$), and q is a weight function defined as $q = 1$ inside contour Γ, and $q = 0$ for the domain outside Γ (Fig. 2, Fig. 3b).

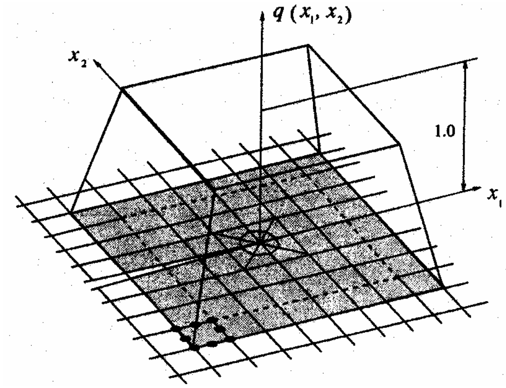

Figure 2. Weight function (q function)

Taking the limit $\Gamma_S \to 0$ leads to

$$\begin{aligned}&\lim_{\Gamma_S \to 0} \int_{\Gamma_0+\Gamma^+ +\Gamma^- -\Gamma_S} (W\delta_{kj} - \sigma_{ij}u_{i,,k})m_j q d\Gamma = \lim_{\Gamma_S \to 0} \int_{\Gamma_0+\Gamma^+ +\Gamma^- -\Gamma_S} (W\delta_{kj} - \sigma_{ij}u_{i,,k})m_j q d\Gamma = \\ &= \lim_{\Gamma_S \to 0} \int_{\Gamma_0+\Gamma^+ +\Gamma^-} (W\delta_{kj} - \sigma_{ij}u_{i,,k})m_j q d\Gamma - \lim_{\Gamma_S \to 0} \int_{\Gamma_S} (W\delta_{kj} - \sigma_{ij}u_{i,,k})m_j q d\Gamma\end{aligned} \tag{7}$$

Since $q = 0$ on Γ_0 and the crack faces are assumed to be traction–free, the above equation becomes

$$J_k = -\lim_{\Gamma_S \to 0} \Psi = \lim_{\Gamma_S \to 0} \int_{\Gamma} (W\delta_{kj} - \sigma_{ij}u_{i,k})m_j q d\Gamma \tag{8}$$

Applying the divergence theorem to Eq. (8), one can obtain the following expression

$$J_k = \int_A (\sigma_{ij}u_{i,k} - W\delta_{kj})q_{,j} dA + \int_A (\sigma_{ij}u_{i,k} - W\delta_{kj})_{,j} q dA \tag{9}$$

where A is the area enclosed by Γ. Note that the second term in the above equation must vanish for linear-elastic materials [4,5,6], and it follows

$$J_k = \int_A (\sigma_{ij}u_{i,k} - W\delta_{kj})q_{,j} dA \tag{10}$$

This expression is analogous to the one proposed for a surface integral based method to evaluate stress intensity factors [4].

In 3D case the J–EDI integral is converted into a volume integral [5–8] as

$$J_k = -\frac{1}{f}\int_V (W\delta_{kj} - \sigma_{ij}u_{i,k})q_{,j} dV \tag{11}$$

where $f = (2/3)\Delta$ with Δ being the thickness of the 3D element in the crack front direction.

1.2. Numerical evaluation of the J integral

The J–integral evaluation in the PAK program is based on the domain integration method described above. A direct evaluation of the contour integral is not practical in finite element analysis (FEA) due to difficulties in defining the integration path Γ. The conversion of the contour integral to the domain integral is exact for the linear elastic case and also for the nonlinear case, if unloading does not occur [4].

Since FEM calculations of displacements, strains, and stresses are based on the global coordinate system, the $(J_k)_{global}$ is evaluated first and then, if needed, transformed into $(J_k)_{local}$. The above expressions are represented by local coordinates x_k, (k = 1,2), which can be expressed in terms of global coordinates X_i by the transformation:

$$x_i = \alpha_{ij}(\theta) X_j,\ \alpha_{ij}(\theta) = \begin{pmatrix} \cos\theta & \sin\theta \\ -\sin\theta & \cos\theta \end{pmatrix} \tag{12}$$

The same transformation also holds for the J_k integral [10], i.e.,

$$\begin{Bmatrix} (J_1)_{local} \\ (J_1)_{local} \end{Bmatrix} = \begin{pmatrix} \cos\theta & \sin\theta \\ -\sin\theta & \cos\theta \end{pmatrix} \tag{13}$$

For sake of numerical implementation and computational efficiency within the FEM, Eq. (10) is evaluated in global coordinates.

When the material of the considered structure is homogeneous and body forces are absent, the finite element implementation of Eq. (10) becomes very similar to that of the contour integral. The only difference is the introduction of the weight function q, when Eq. (10) is used. With the isoparametric finite element formulation, the distribution of q within the elements is determined by a standard interpolation scheme with use of shape functions h_i:

$$q = \sum_{i=1}^{m} h_i Q_i \tag{14}$$

where Q_i are values of the weight function at nodal points, and m is the number of nodes. Spatial derivatives of q can be found by usual procedures for isoparametric elements.

The equivalent domain integral in 2D can be calculated as a sum of discretized values of Eqs. (10) and (11), [5]:

$$J_k = \sum_{\substack{\text{elements} \\ \text{in } A}} \sum_{p=1}^{P} \left[\left(\sigma_{ij} \frac{\partial u_i}{\partial X_k} - W\delta_{kj} \right) \frac{\partial q}{\partial X_j} \det\left(\frac{\partial X_m}{\partial \eta_n} \right) \right]_p w_p \quad i,j,k,m,n = 1,2 \tag{15}$$

and the equivalent domain integral in 3D [5,7] is

$$J_k = \frac{1}{f} \sum_{\substack{\text{elements} \\ \text{in } V}} \sum_{p=1}^{P} \left[\left(\sigma_{ij} \frac{\partial u_i}{\partial X_k} - W\delta_{kj} \right) \frac{\partial q}{\partial X_j} \det\left(\frac{\partial X_m}{\partial \eta_n} \right) \right]_p w_p \quad i,j,k,m,n = 1,3 \tag{16}$$

The terms within $[\cdot]_p$ are evaluated at Gauss points with use of Gauss weight factors, for each point, w_p. The present formulation is for a structure of homogeneous material in which no body forces are present. For the numerical evaluation of the above integral, the domain A is set from the set of elements about the crack tip. The domain A is set to contain all elements which have a node within a sphere of radius r_d about the crack tip. Figure 3 shows a typical set of elements for domain A. This figure shows the contour plot of the weight function q for the elements. The function q is then easily interpolated within the elements using the nodal shape functions, according to Eq. (14).

Function $q(x)$ can be interpreted as a rigid translation of nodes inside Γ, while nodes on Γ remain fixed. The set of nodes moved rigidly is referred to as the rigid region, and the function $q(x)$ as the shift function. PAK allows an automatic search for nodes of the rigid region. The first region consists of nodes of all elements connected to the crack tip node, i.e., $r_d = \max(\Delta x, \Delta y)$, where $(\Delta x, \Delta y)$ is the length of an element with crack tip. The second region or ring consists of all nodes in the first region and nodes of all elements connected to any node in the first region, i.e. $r_d = 2\max(\Delta x, \Delta y)$. Therefore, the contours of larger size domain are determined.

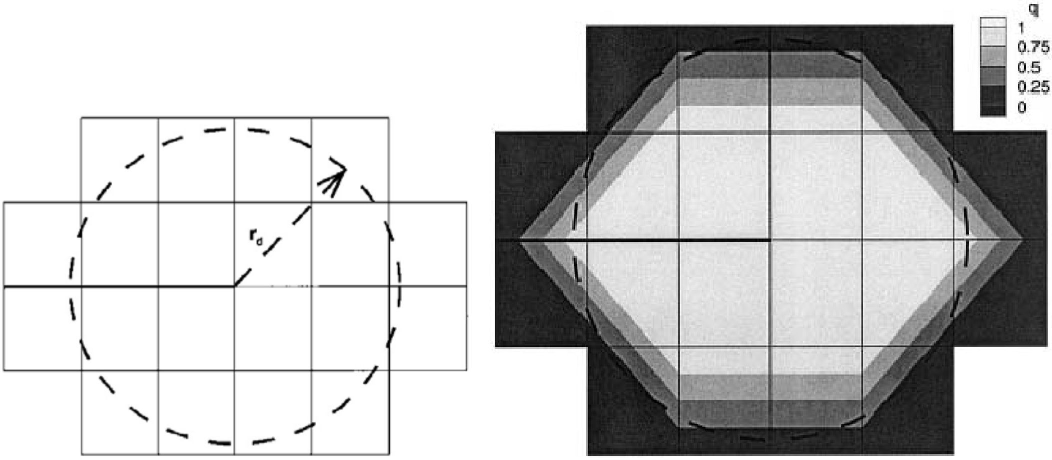

Figure 3. Weight function q on the elements

2. THE ESTIMATION OF FATIGUE LIFE

Unstable crack propagation occurs when one of the stress intensity factors K_α (α= I,II,III) is equal or greater than the experimentally determined material property K_c. The estimation of fatigue life can be updated for each crack extension. The crack growth equation provides a relation between the crack increment Δa and the increment in the number of load cycles ΔN. In case of cyclically loaded structures, the number of load cycles equivalent to the crack increment can be determined by a numerical integration of the governing crack growth equation [11].

The Paris law is a simple but very often used model of crack growth rate description in the linear region under mode I. This law has the form

$$\frac{da}{dN} = C\Delta K^m \tag{17}$$

where ΔK is the stress intensity factor range, and C and m are material constants. For most materials, m is between 2 and 7, while C is more material-dependent. A shortcoming of the Paris law is that it neglects the influence of the peak stress and the threshold range.

Growth of cracks under mode I and mode II was first systematically studied by Iida and Kobayashi [12]. Results of their experiments showed that even a small ΔK_{II} increase would significantly increase crack growth rate. However, they also observed that the crack tended to grow in the direction of minimum K_{II}. Some models take into account the mode II contribution. One way is by introducing an equivalent stress intensity factor $\Delta K_{\mathrm{I}eq}$ in the Paris equation

$$\frac{da}{dN} = C(\Delta K_{\mathrm{I}eq})^m \tag{18}$$

The maximum stress criterion can also be used to determine the equivalent mode I stress intensity factor, according to the following expression

$$K_{\mathrm{I}eq} = K_{\mathrm{I}} \cos^3 \frac{\theta_o}{2} - 3K_{\mathrm{II}} \cos^2 \frac{\theta_o}{2} \sin \frac{\theta_o}{2} \tag{19}$$

where θ_o denotes the direction in which the crack is likely to propagate relative to the crack tip coordinate system, and $\Delta K_{\mathrm{I}eq}$ is found to be the $K_{\mathrm{I}eq}$ range during one load cycle.

Tanaka [13] carried out experiments on cyclically loaded sheets of pure aluminium with initial cracks inclined to the tensile axis. As a by-product, the experiments formed the basis for a crack propagation law

$$\frac{da}{dN} = C(\Delta K_{eq})^m \tag{20}$$

where

$$\Delta K_{eq} = (\Delta K_{\mathrm{I}}^4 + 8\Delta K_{\mathrm{II}}^4)^{1/4} \tag{21}$$

The above equation was developed on the assumptions that
a) plastic deformation due to cyclic tension and transverse shear are not interactive, and
b) the resulting displacement field is the sum of displacements from the two modes.

3. NUMERICAL EXAMPLES FOR CALCULATION OF STRESS INTENSITY FACTORS

In this section, several examples of stress intensity factor calculation in case of crack under the assumption of plane strain and plane stress two-dimensional elasticity are presented. At the beginning a simple example of an edge crack is chosen to demonstrate the robustness of the above technique, and then results for more complicated geometries are presented. Results obtained with PAK will also be compared with results obtained by using the COSMOS program.

Example 1

In this example the stress intensity factor is determined for both modes of fracture (opening K_{I} and shear K_{II}) for a rectangular plate with an inclined crack edge subjected to uniform uniaxial tensile loading at the two ends.

Known data are given in Fig. 4.

σ = 1 psi
h = 2.5 in
W = 2.5 in
a = 1 in
E = 30×10^6 psi
ν = 0.3
ϕ = 45°
thickness = 1 in

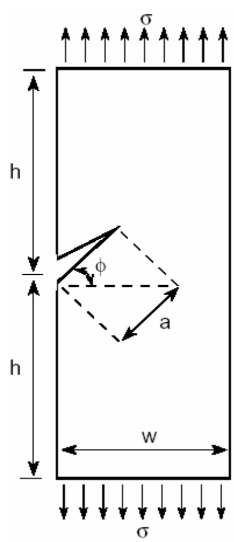

Figure 4. Model for testing

The full part has to be modelled since the model is not symmetric with respect to the crack. There is no restriction in proposed FE models, so that mesh can be either symmetric or non-symmetric with respect to the crack. However, the nodes in the two sides of crack cannot be merged in order to model the rupture area properly. Figure 5 shows the first and second region of integration for equivalent domain integral.

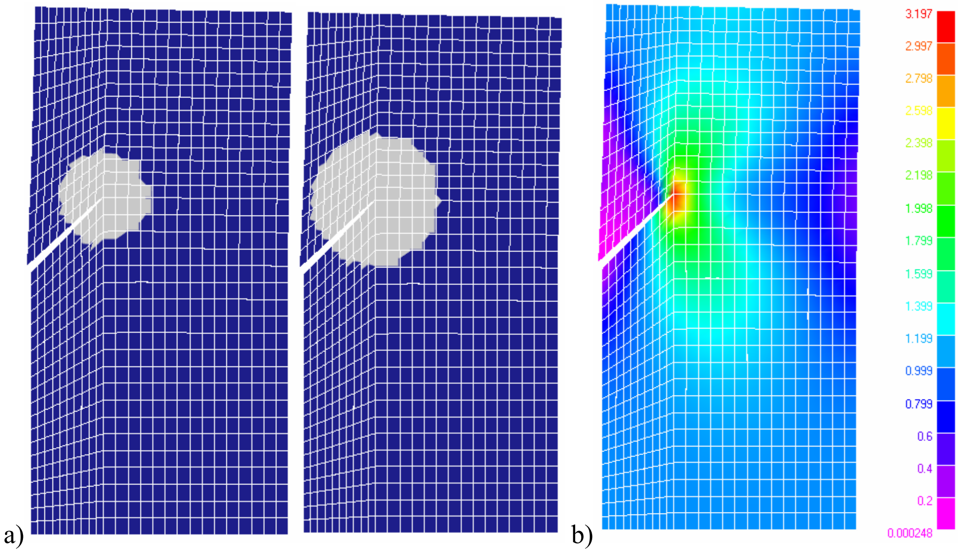

Figure 5. a) Domain integration for *J*–EDI. b) Von-Mises stress field

Results obtained by using *J*–EDI integral, incorporated in the PAK software, are compared with results carried out with COSMOS *J*–contour integral, and are shown in Table 1. Also, both sets of numerical results are compared with reference theoretical values. Comparison is given as N/A%.

Table 1. Comparison of results

		K_{I} (N/A%)	K_{II} (N/A%)
	Reference	1.85	0.88
8-node Element PAK	Path 1 Path 2	1.877 (1.4%) 1.907 (3.0%)	0.871 (1.0%) 0.907 (3.0%)
8-node element COSMOS	Path 1 Path 2	1.80 (2.7%) 1.79 (3.2%)	0.872 (0.9%) 0.874 (0.6%)

In order to present robustness of the *J*–EDI procedure, built into the PAK software, the above example was used with different radii r_d of the integration domain and the results are shown in Table 2. Radius r_d varied from 0.5% a to 90% a, where a denotes crack length. It can be concluded from Table 2 that results are insensitive to the choice of the *J*–integral domain integration radius.

Table 2. Values of the factor K_{I} for different integration domain radii

r_d (% of a)	5	15	25	35	45	55	65	75	85	90
K_{I}	1.810	1.864	1.807	1.877	1.906	1.9075	1.9071	1.9089	1.929	1.931
N/A(%)	2.1	0.75	2.3	1.4	3.0	3.1	3.08	3.20	4.20	4.37

It can be seen from the presented results that the error (N/A%) is small, even with a non-symmetrical grid with respect to the crack.

Example 2

In this example [14], the stress intensity factor of the crack located in the steam turbine housing 4 of TE Kolubara is calculated. After generating 2-D FE model of the lower housing part, together with insulation, the following steps were carried out:

- Calculation of the temperature field in nominal regime and corresponding stress field.
- Calculation of stress and deformation fields of the turbine for crack lengths (20–75 mm).
- Analysis of the influence of crack length on corresponding stress field as well as on the stress intensity factor.

For temperature field calculation, the 2-D grid consisted of 4400 8-node elements. Generated grid comprised the space of the turbine housing and insulation.

In Fig. 6 the stress field induced by temperature and internal pressure is shown. The effective stress for 2-D turbine model without insulation, for crack length 30 mm, is shown in Fig. 7.

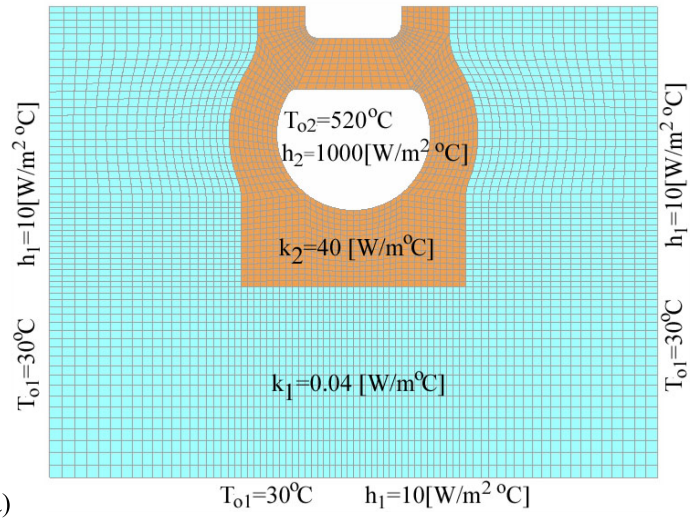

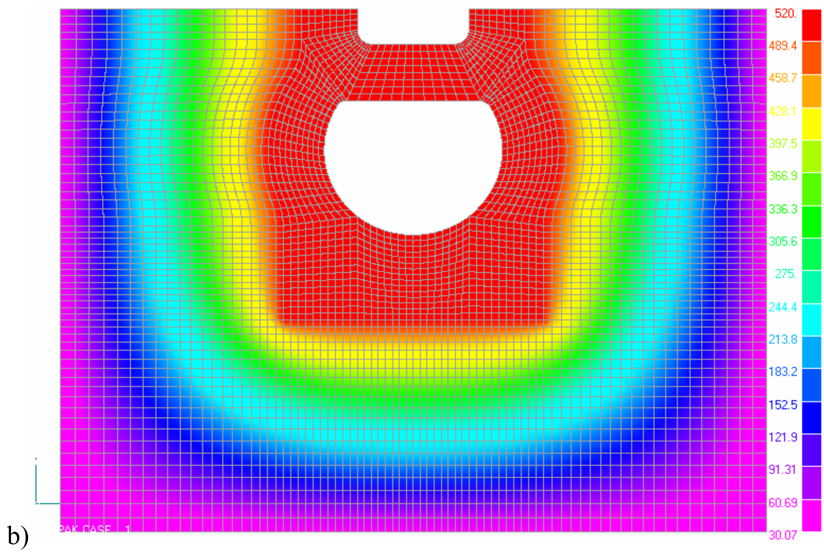

Figure 6. a) 2D model for calculation of the temperature field;
b) Temperature field of the turbine housing and insulation

Figure 8 shows the relationship between stress intensity factor K_I and crack length. It can be seen from Fig. 8 that by increasing crack depth from 20 mm to 40 mm, the stress intensity factor increases 30%. With crack length increase of over 50 mm, the stress intensity factor increases more rapidly.

Example 3

In this example [14], a 3-D analysis of the turbine housing is carried out. Using the original design documentation, the 3-D geometrical model of the turbine is generated. In this 3-D object, cracks with different lengths (90–375 mm) and depth (20–40 mm) are assumed and modelled. Calculations are performed to investigate the influence of crack length and depth on the value of maximum effective stress, as well as on the value of stress intensity factor.

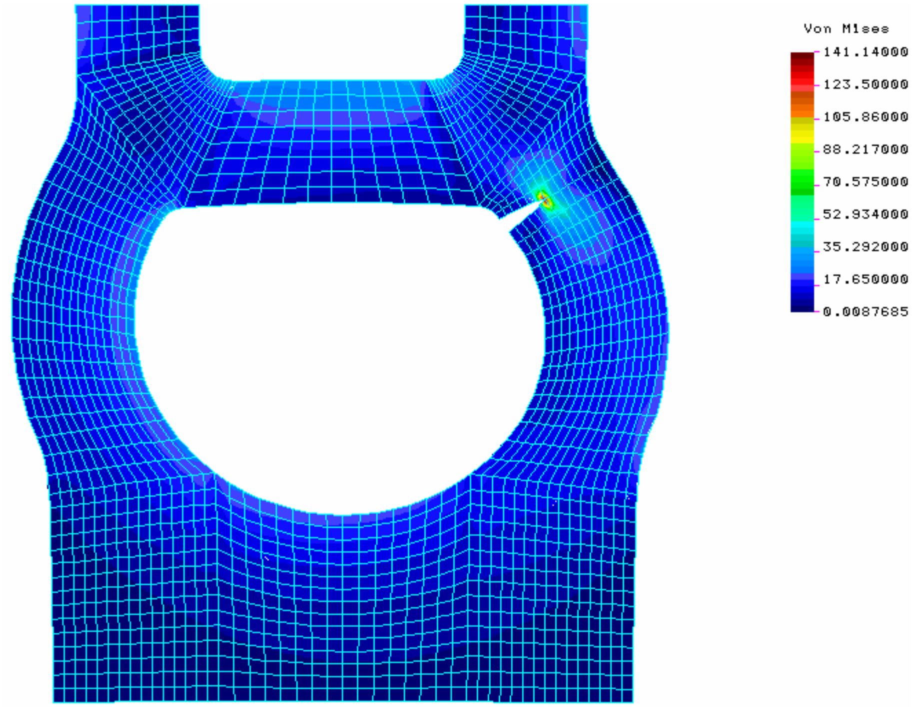

Figure 7. Effective stress field for crack length 30 mm

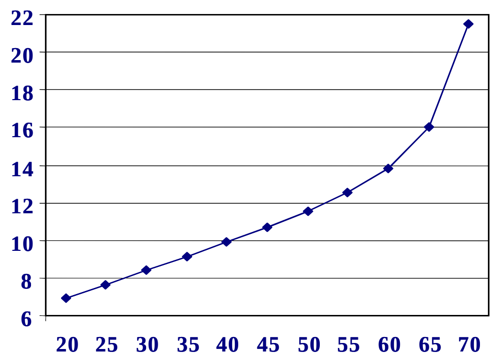

Figure 8. Relationship between stress intensity factor K_{I} and crack length

Boundary conditions: Lower part of the turbine housing has an axial plane of symmetry so that the 2-D model corresponds to the cross-section of that plane and the solid body of the housing.

For calculation of the temperature field, boundary conditions of thermal conduction according to Fig. 6 are used. In order to reduce the number of elements in the 3-D grid, the critical quarter of the turbine is modelled. It is worth to emphasize that the cracks are located in that quarter as well as the steam intake with sharp edges that induce the stress concentration. In Fig. 9 the 3-D model is shown. The calculated relationship between maximum effective stress and crack length for different crack depth is shown in Fig. 10. It can be seen from Fig. 10 that variation in crack length from 90 mm to 375 mm, for constant crack depth, did not significantly affect the effective stress. On the other hand, increase of crack depth, for constant crack length, leads to a 15 to 30% increase in effective stress. Figure 11 shows the effective stress field in vicinity of the crack (375×30).

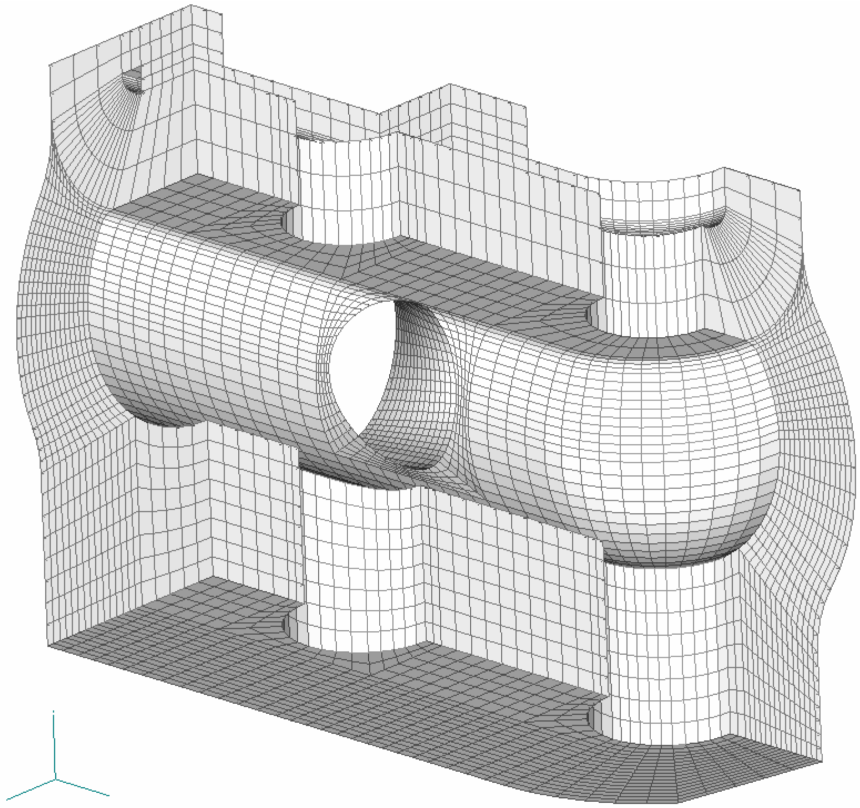

Figure 9. The 3-D model

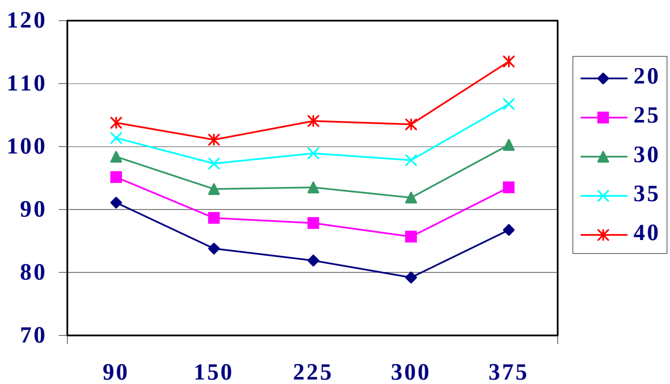

Figure 10. Relationship between maximum effective stress and crack length for different crack depth

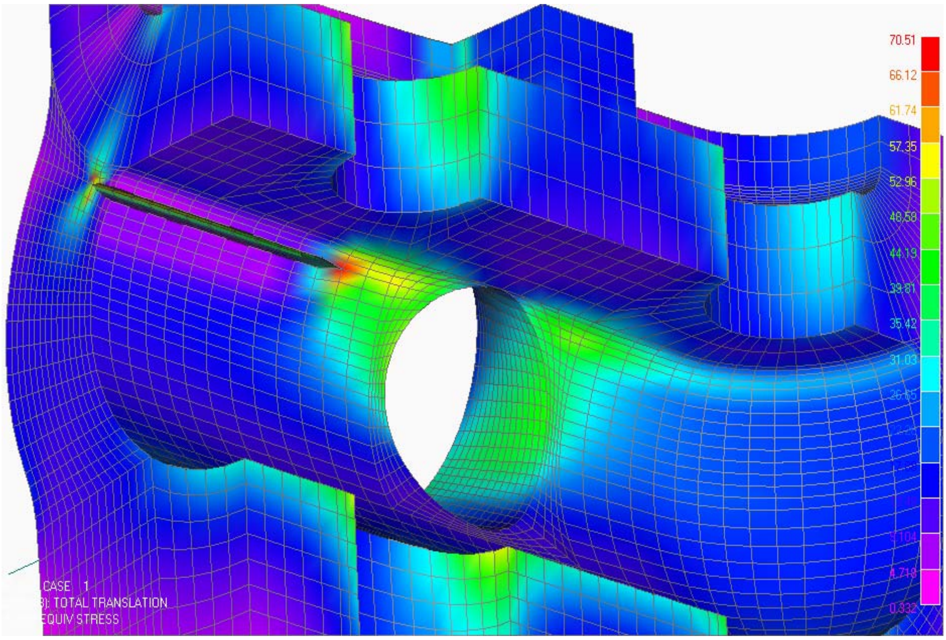

Figure 11. Field of the effective stress in the vicinity of the crack (375×30)

Dependence of stress intensity factor on crack length and depth is shown in Fig. 12. It is observed that increase in crack depth from 20 to 40 mm, for constant crack length, leads to the increase of stress intensity factor from 15 to 30%.

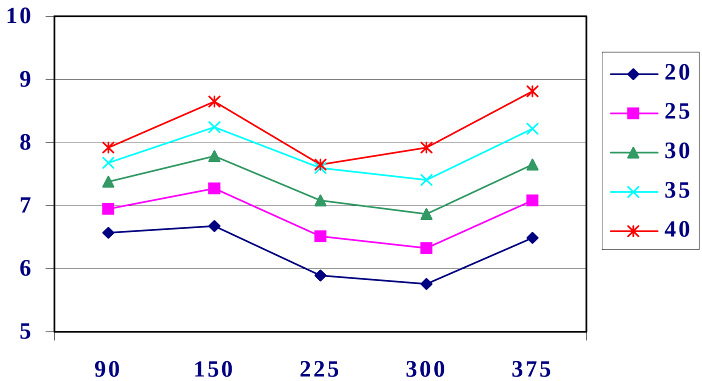

Figure 12. Dependence of stress intensity factor on crack length and crack depth (20, 25, 30, 35, and 40 mm)

CONCLUSIONS

Based on the equivalent domain integral (EDI) method, very robust, efficient and reliable procedure for numerical estimation of stress intensity factors is obtained. Application of the *J*–EDI integral is suitable because it relies on use of domain integrals rather than contour integrals. Obtained numerical results show a small influence of the choice of *J*-integral domain integration on the value of stress intensity factor. In addition to relatively simple test cases, the analysis of complex 3-D problems is presented. The analysis shows that a stable crack growth is predicted in nominal regime of the analyzed structure, while 2-D analysis shows a rapid increase of the stress intensity factor for crack depth increase over 50 mm.

REFERENCES

1. Rice, J.R., *A Path Independent Integral and Approximate Analysis of Strain Concentration by Notches and Cracks*, Journal of Applied Mechanics, 35, pp. 379-386. (1968)
2. Knowles, J., Sternberg, E., *On a class of conservation laws in linearized and finite elastostatics*, Arch. Rat. Mech. Anal., 44, pp. 187-211. (1972)
3. Hellen, T., Blackburn, W., *The calculation of stress intensity factor for combined tensile and shear loading*, Int. J. Fract., 11, pp. 605-617. (1975)
4. V.E. Saouma, Fracture Mechanics, Dept. of Civil Environmental and Architectural Engineering, University of Colorado, Boulder, CO, 80309-0428. (2000)
5. Kojić, M., Živković, M., Jovičić, G., Vlastelica, I., Đorđević, V., *Mehanika loma-Teorijske osnove i numeričke metode rešavanja*, Studija, Mašinski fakultet Kragujevac, Laboratorija za inženjerski softver. (2003)
6. Moes, N., Dolbow, J., Belytschko, T., *A Finite Element Method for Crack Growth Without Remeshing*, Int. J. Numer. Meth. Engn., 46, pp. 131-150. (1999)
7. Cung-Yi Lin, *Determination of the Fracture Parameters in a Stiffened Composite Panel*, PhD Thesis, North Carolina State University. (2000)
8. Enderlein, M., Kuna, M., *Comparison of finite element techniques for 2D and 3D crack analysis under impact loading*, International Journal for Solids and Structures, 40. (2003)
9. Kim, Y.J., Kim, H.G., Im, S., *Mode decomposition of three-dimensional mixed-mode crack via two-state integral*, International Journal of Solids and Structures, 38, pp. 6405-6425. (2001)
10. Kim, J-H., Paulino, G., *T-stress, mixed-mode stress intensity factors, and crack initiation angles in functionally graded materials: a unified approach using the interaction integral method*, Comp. Method Appl. Mech. Engng. 192, pp. 1463-1494. (2003)
11. Andersen, M.R., *Fatigue Crack Initiation and Growth in Ship Structures*, PhD Thesis, Department of Naval Architecture and Offshore Engng, Technical University of Denmark. (1998)
12. Iida, S., Kobayashi, A.S., *Crack-Propagation Rate in 7075-T6 Plates under Cyclic Tensile and Transverse Shear Loadings*, Journal of Basic Engineering, pp. 764-769. (1969)
13. Tanaka, K., *Fatigue Crack Propagation from a Crack Inclined to the Cyclic Tensile Axis*, Engineering Fracture Mechanics, 6, pp. 493-507. (1974)
14. Živković, M., Kojić, M., Slavković, R., Vulović, S., Đorđević, V., Vujanac, R., *Analiza prslina u kućištu turbine 4 TE Kolubara*, Mašinski fakultet Kragujevac, Laboratorija za inženjerski softver. (2002)
15. Živković, M., Kojić, M., Slavković, R., Vulović, S., Đorđević, V., *Procena preostalog radnog veka bubnja kotla TE "Nikola Tesla"-A2, 210MW*, Elaborat, Mašinski fakultet Kragujevac, Laboratorija za inženjerski softver. (2002)

RELIABILITY AND SAFE SERVICE OF STRUCTURES

Milosav Ognjanović, Faculty of Mechanical Engineering, Belgrade, S&Mn

INTRODUCTION

The failure process consists of the part taking place from the occurrence of cracks and the part covering crack spreading. The crack spreading process is determined by many known parameters and has been studied in fracture mechanics. The process of crack occurrence is not known enough and is stochastic. It takes place chaotically, the finite cycles number may vary even several times at completely identical fatigue conditions. In case of high strength steel the crack spreading speed is great, thus the participation of the finite cycles number in the course of crack spreading in the total finite cycles number is small. The cycles number of stress fluctuation until the occurrence of a crack, which is stochastic (chaotic), dominates. Those are the basic reasons why mathematical statistics is used in the analyses and calculations of machine parts loaded in this way. This approach always presents a possible practical solution when physical laws have not been completely clarified and when deterministic methods are not applicable. Due to the stochastic behaviour of the failure process, i.e. the critical stress, and also due to stochastic work conditions, i.e. service stresses, two solutions are used in practice. One consists of the application of safety factor which entails "bridging over" the distribution range of these stresses and elimination of risks of every possible failure. The other consists of using statistical indicators which make possible entrance into the range of "controlled" risk at the occurrence of failure which is expressed by the respective probability – reliability. The rationality of design solutions is small in the first case, and the mass and dimensions are big. In the second case along with the risk of a smaller number of machine parts failed, a significant reduction of dimensions and mass are also achieved, and the design solutions become more compact.

In order to establish a relation between the probability of service conditions (load and stress) and the probability of failure under such conditions, extensive experimental data from both ranges are required. The service conditions are defined by the regime of exploitation, i.e. the stress spectrum in the length of service. These spectrums, i.e. regimes, are obtained by measurements, follow-ups, analyses, and statistical research of service conditions of machine systems of respective types in typical exploitation conditions. The failure probability is determined on the basis of a large number of tested samples of machine parts until fracture. Only based on extensive statistical data and theoretical knowledge is it possible to establish a reliability model of respective machine system components. It is based on empiricism and is a good substitute for not well understood fatigue process, as well as for the stochastics of exploitation conditions.

1. SAFETY FACTOR AND RELIABILITY CORRELATION

The safety factor is the ratio of critical stress (at which failure begins) and work stress which is the consequence of service load acting on the machine part. Failure does not occur if in each possible case the work stress is less than the critical. Neither the critical nor the work stresses are determinant values. The determinant values are stochastic values which dissipate by rule within a wide range (Fig. 1). The safety factor is the ratio of the mean (most probable) value of critical stress and the highest work stress, which can be expected in the work process. There is also a possibility for the occurrence of circumstances which cannot be foreseen, thus work stress can be somewhat greater, but this is not likely. The machine part has absolutely been used, and the safety in work satisfied, if the safety factor is such that the highest possible value of work stress is lower than the minimal possible value of critical stress. This condition has been satisfied if the dissipation presented in Fig. 1 (curve 1) is covered by the value of the safety factor. This value is $S = 1.25\ldots2.5$. Lower limits may be used when data about the critical and work stresses are well known and reliable.

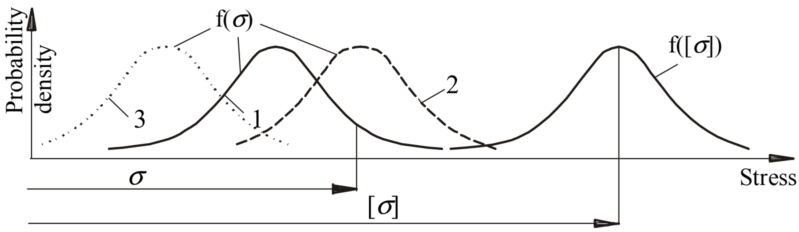

Figure 1. Relation between service stress distribution $f(\sigma)$ and critical stress distribution $f([\sigma])$ in safety factor determination

Large values of safety factor create conditions for work stress to be significantly smaller than the critical one (curve 3 in Fig. 1). The increased distance between the curves of the distribution of critical and work stress does not increase the probability that failures will not occur. This probability is close to zero when these curves are close to each other (the curve of work stress distribution 1). With increase in safety factor there is an increase in dimensions, and the safety remains the same. High values of the safety factor contribute to irrational use of mass of machine parts, and make the design solution large and massive. In machine systems where mass reduction is of increased significance for the materialization of the function, rationality is achieved by acting on all factors on which the machine part mass depends, and thus also onto the safety factor. In these machine systems it is not sufficient that the safety factor be on the lower limit which provides the condition that there is no probability for failure to occur. A risk is taken that in a smaller number of machine systems, some of which failed. After failures they are replaced by new ones, and the risk taken enables the reduction of safety factor below the indicated lower limits and reduction of dimensions, i.e. mass of chosen parts and the entire machine system. The risk of failure is unreliability, and the probability for failure not to occur in the course of service length is the reliability. Calculation on the basis of limited risk that failure may still happen is a transition from the range of complete safety into the range of reliability. The curves of work distribution (2) and critical stresses in Fig. 1 overlap partly. The ends of these curves are with small (low) probability density and overlap on the wide range of stress. The difference between critical and service stress is thereby significantly reduced and dimensions decrease with a relatively small “risk” of failure. The safety factor determined for the state of partial overlapping of curves of the distribution of the working and critical stress is significantly smaller than the minimal required for the provision of full safety. This contributes to significant mass reduction according to the diagram in Fig. 1. This value of safety factor may be valid for orientational determination of allowed stress for the reliability range. A more precise calculation of allowed stress is determined on the basis of known distribution of the working and critical stresses and for the chosen value of reliability.

The elementary reliability relates to the possibility of occurrence of certain kinds of defects, i.e. failures. The unreliability, $F_p = 1 - R$, is a complex probability of the occurrence probability of service stress, and of the probability of failure at that stress. For fracture to occur due to fatigue, it is necessary that stress occurs in the machine part and that the possibility of fatigue (fracture) exists at that stress. Fracture occurs if both indicated conditions are satisfied, i.e. the probability represents the integral of the product of the density of these probabilities and is proportional to the overlapping area in Fig. 2a. The integration is obtained numerically and turns into the sum of the product of the density of stress probability f_i and failure probability P_{Ri} which represents the cumulative (integral) probability of critical stress.

$$F_p = \sum_{i=1}^{k} p_i P_{Ri}\ ; F_p = \sum_{i=1}^{k} f_i P_{Ri}\ ;\ F_p = \int_{-\infty}^{+\infty} f(\sigma) f([\sigma]) d\sigma$$

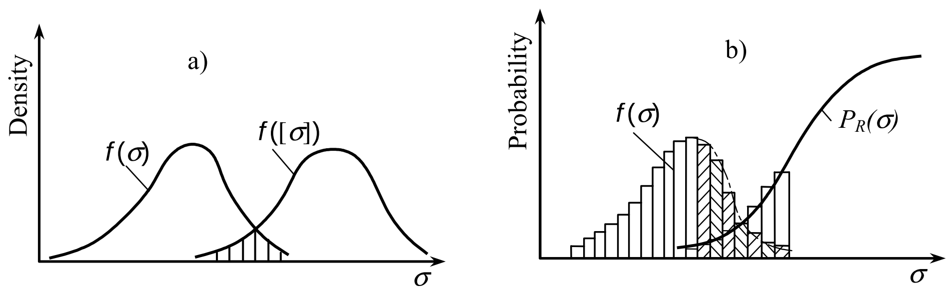

Figure 2. Relation of the probabilities of service and critical stresses and reliability determination

If the number of different service stresses i is small, the probability density f_i turns into the statistical weight p_i. It can be determined as the ratio of stress fluctuation σ_i cycles number in the length of service $n_{\Sigma i}$ and the total number of stress cycles in the length of service n_Σ, i.e. as $p_i = n_{\Sigma i}/n_\Sigma$. If a machine part is exposed to a fluctuating stress of constant amplitude, the statistic weight, i.e. the possibility of the occurrence of such stress is $p(\sigma) = n_\Sigma/n_\Sigma = 1$, thus the unreliability is equal to failure probability $P_R(\sigma)$. If a machine part is exposed to stresses of different amplitudes (Fig. 3), the statistical weight of each is $p_i = n_{\Sigma i}/n_\Sigma$ ($n_\Sigma = \sum n_{\Sigma i}$). In that proportion, the failure probabilities P_{Ri} have an impact on the unreliability F_p (Fig. 2b and Fig. 3). The unreliability is equal to the sum of products of statistic weight and failure probability for each one of the stress values.

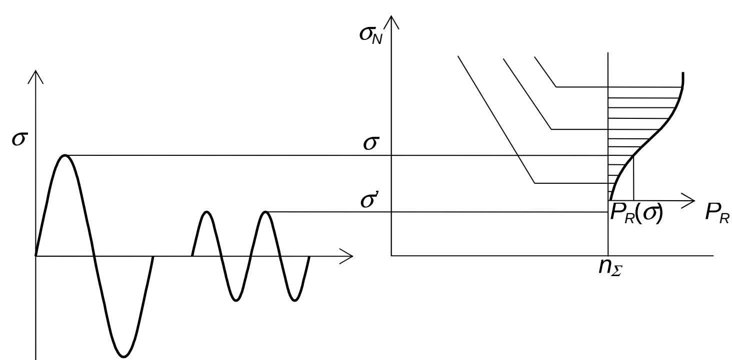

Figure 3. The relation of failure probability and work stress in the range of infinite life strength

The presented procedure enables cumulative probability F_p to be obtained for variable stress amplitude, based on the function of distribution of failure probability P_{Ri} for constant stress amplitude. This approach is acceptable for most defects of which it is necessary to fulfil two conditions: that the cause of defect exists and that this cause is capable of producing the defect. This means at the same time that functions presented in Fig. 2 are mutually independent. In fractures due from fatigue, these two curves are not independent. The position of the function of failure probability distribution P_R depends on the shape of probability density $f(\sigma)$ function. If the function $f(\sigma)$ is asymmetrical so that the density maximum centre is towards lower stress values, that is a light exploitation regime. For light regimes the function P_R moves towards the zone of greater values of critical stresses. The curves $f(\sigma)$ and P_R become mutually distant for such work conditions, and unreliability F_p is reduced. In case of heavy exploitation regimes, the process is opposite. In order to take into consideration relation between distributions of service and critical stresses, it is necessary to introduce into consideration the failure probability for service fatigue strength. Figure 4 shows the function and the range of distribution of the failure probability for the service fatigue strength.

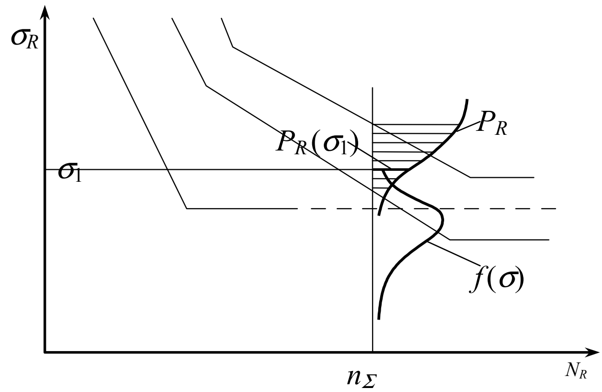

Figure 4. The relation of stress distribution $f(\sigma)$ and failure probability P_R for service fatigue strength

The service fatigue strength σ_R is the largest stress σ_1 in the stress spectrum $f(\sigma)$ which leads to failure after N_R stress cycles of all amplitude values. Thus, σ_R is by nature the greatest stress from the stress spectrum, marked by σ_1. The service fatigue strength may be determined transforming the Wöhler's curve by applying the damage accumulation hypothesis or by experiments. The failure probability is determined for the respective stress spectrum in which the largest stress is σ_1, thus for the given spectrum $f(\sigma_1) = 1$, and the unreliability $F_p = P_R(\sigma_1)$.

Starting from the fact that service and critical stresses must be treated as statistical values, the possible approaches in the calculation of carrying capacity, safety factor, and reliability are as follows. The least correct calculation is based on using the safety factor as an indicator of the ratios of these stresses. It is expected that the safety be complete thereby, and the dimensions are significantly greater in comparison to other ways of calculation. A more precise approach with controlled risk is based on using indicators of elementary reliability. In the fatigue of the machine parts to fracturing, distributions of service and critical stresses are in mutual dependence. By introducing this effect also, the calculation precision is additionally increased and the exploitation, i.e. unit carrying capacity of machine parts is also increased.

2. STRESS SPECTRUMS AND EXPLOITATION REGIMES

Figure 5 shows the possible analogous random function of stress fluctuation with marked values of change, i.e. stress change ranges $\sigma_s = 2\sigma_a$, where σ_a is the stress amplitude. The mean values σ_m around which stress fluctuates, are also variable. It is necessary to make a selection of values of the changes and their mean values, classify them into classes and determine the number of occurrences of each of the values of changes. If the analogous (uninterrupted) time function is digitalized, it transforms into a set of numerical values in small time intervals Δt, as presented in Fig. 5a. The program for processing digital values compares each one of them with the previous one and determines the values of neighbouring extremes – minimum and maximum, and calculates the spans $\sigma_{si} = \sigma_{\mathrm{maxi}} - \sigma_{\mathrm{mini}}$. The span is calculated only at the increase of stress so that the cycles are not doubled. The calculated spans can be classified by their value and by mean stress values. For the purpose of simplification, further analysis relates only to spans. Figure 5b shows that the calculated values of the spans are classified in certain classes – fields of equal value. For example, the first class, for $i = 1$, would include all spans $\sigma_{si} = 0...20$ N/mm^2, and the second for $i = 2$ would include spans $\sigma_{s2} = 20...40$ N/mm^2, and the third for $i = 3$, $\sigma_{s3} = 40...60$ N/mm^2 etc.

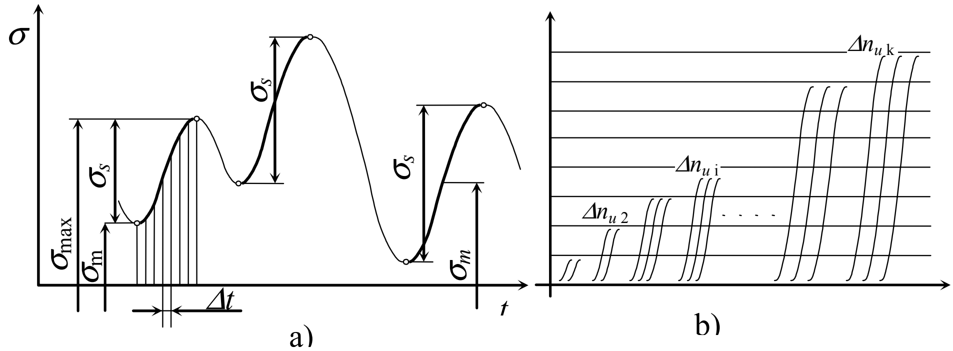

Figure 5. Processing (classification) of the stress amplitudes

Statistical processing of obtained results of stress spans (amplitude) classification consists of determining the rule by which their values behave. If stress classes are marked by $i = 1,2,3...k$ and if in each class there is a $\Delta n_{u1}, \Delta n_{u2},...\Delta n_{uk}$, the span occurrence $\sigma_{s1}, \sigma_{s2},...\sigma_{sk}$, i.e. amplitude $\sigma_{a1}, \sigma_{a2},...\sigma_{ak}$, the frequency of occurrence of each class is

$$f_i = \frac{\Delta n_{ui}}{n_u}\ ;\ n_u = \sum_{i=1}^{k} \Delta n_{ui}$$

In the graphical form the frequency of the occurrence of stress classes represents a histogram of probability density (Fig. 6a) which may transform into a histogram of cumulative probability (Fig. 6b), following the expression

$$F_i = \sum_{i=1}^{k} f_i = \sum_{i=1}^{k} \frac{\Delta n_{ui}}{n_u}$$

These empirical values are translated in the most efficient manner into an analytical form by using Weibull's function

$$F(x) = 1 - e^{-\left(\frac{x}{\eta}\right)^{\beta}}\ ,\ \text{i.e.}\ F(\sigma_a) = 1 - e^{-\left(\frac{\sigma_a}{\eta}\right)^{\beta}}$$

where the independent variable x is substituted by the stress amplitude σ_a. The parameters of this distribution are η and β, which may be determined in the simplest way by graphical method. It is necessary to transform Weibull's function into the form of a straight line for this purpose. This is achieved by double logarithm of the transformed form of Weibull's function

$$F(x)=1-e^{-\left(\frac{x}{\eta}\right)^{\beta}}, \text{ i.e. } F(\sigma_a)=1-e^{-\left(\frac{\sigma_a}{\eta}\right)^{\beta}}$$

$$\ln\ln\frac{1}{1-F(\sigma_a)}=\ln\left(\frac{\sigma_a}{\eta}\right)^{\beta}=\beta\ln\sigma_a-\beta\ln\eta$$

and substitution $Y=\ln\ln\frac{1}{1-F(\sigma_a)}$; $X=\ln\sigma_a$; $a=\beta$; $b=-\beta\ln\eta$

from where it follows that $Y = aX + b$ is the equation of the straight line in the coordinate system with the respective logarithmic scale.

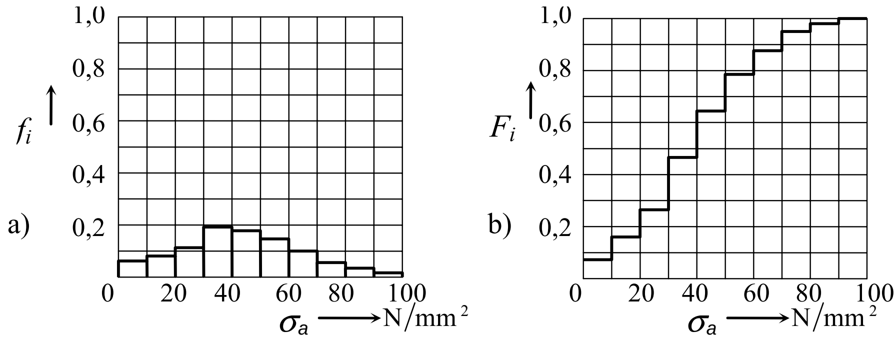

Figure 6. Histograms of the probability density and the cumulative function

Figure 7 shows the coordinate system with uniform scale on the coordinates X and Y (upper and right scale). Starting from expressions for $X = \ln\sigma_a$ and $Y = \ln\ln\{1/[1 - F(\sigma_a)]\}$ and from this uniform scale, values have been calculated for σ_a and for $F(\sigma_a)$, the values of which are given on the lower and left scale. This is how the Weibull's coordinate system is obtained. Experimental (empirical) values of cumulative probability $F(\sigma_a)$ are entered for each class of stress amplitudes σ_a. A series of points is obtained which follow closely the straight line. After entering, this set of points is approximated by a straight line. Coordinates X and Y enable determination of parameters in the equation of the straight line, a and b, and thereby also the parameters of Weibull's distribution, η and β. After approximating experimental points by a straight line, the parameter η expressed in the stress units is read in the intersection of the straight line with the X axis, i.e. that is the stress value for the probability $F(\sigma_a) = 0.632$. Dimensions of parameter η are same as σ_a, thus in expression $F(\sigma_a)$ the ratio σ_a/η is a dimensionless value. Parameter $\beta = 1.3$ is the part on the Y axis for $\Delta X = 1$ and represents a dimensionless value.

The greatest stress fluctuations have the greatest effect on fatigue of the material. The number of their occurrences, i.e., the frequency of occurrence is small. In this sense, a more correct and clear presentation offers the logarithmic form of the cumulative function shown in Fig. 8. The values of function $H(\sigma_a) = 1 - F(\sigma_a) = 1...0$ are multiplied with a suitable number of stress cycles $n_b = 106$. The multiples are logarithmic for each value σ_a and values $\log(H(\sigma_a)n_b)$ are obtained between 1...6. This is the number of the logarithmic units on the logarithmic axis with the scale from 100 to 106 stress cycles (Fig. 8). With this transformation the cumulative function $F(\sigma_a)$ has been translated into the logarithmic form, where the range of large stress amplitudes has been spread out onto about 2/3 of the horizontal axis, and the field of small and medium stress amplitudes has been compressed onto 1/3.

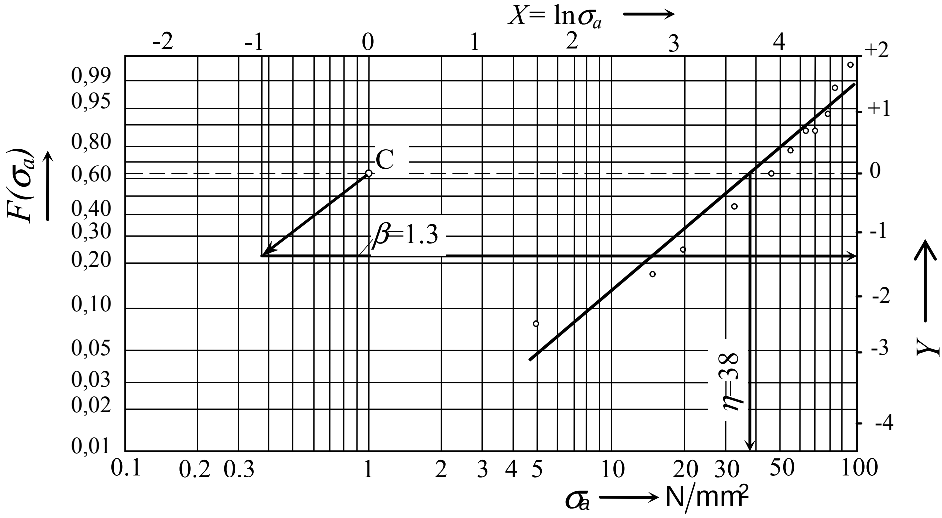

Figure 7. Parameters of Weibull’s function determination for stress amplitude distribution

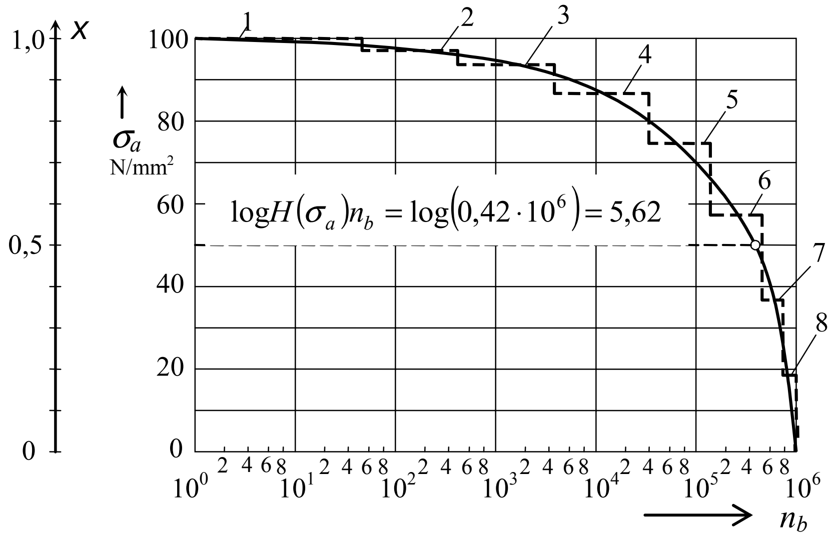

Figure 8. Logarithmic presentation of the stress spectrum

The continuous shape of the logarithmic curve is not suitable for use in calculations or for endurance testing. The step-like shape is more suitable for this purpose. The optimal number of steps (stress levels) is eight. The division is formed by forming more steps in the range of greater values of stress amplitudes (differences in stress levels are smaller), and in the range of smaller amplitudes there are less steps with greater differences in level. After the division it is possible to create a tabular form, i.e. a table filled up with values which are read from the graphical presentation (Fig. 8).

In Table 1, i denotes stress level σ_{ai}, i.e. σ_i, where σ_{a1}, i.e. just σ_1 is the largest stress in the stress spectrum. The relative variable $x_i = \sigma_i/\sigma_1 = 0...1$ enables a permanent ratio to be kept between stress levels. The number of cycles (occurrences) of each of the stress levels is determined by reading the values of horizontal parts on the step-like diagram (Fig. 8). Their sum for k stress levels satisfies the condition

$$n_b = \sum_{i=1}^{k} \Delta n_{bi} \ .$$

Table 1. Presentation of the stress spectrum in Fig. 8

i	1	2	3	4	5	6	7	8
σ_{ai} N/mm^2	100	98	94	87	74	57	38	19
$x_i=\sigma_{ai}/\sigma_{a1}$	1	0.98	0.94	0.87	0.74	0.57	0.38	0.19
Δn_{bi}	50	450	3500	36000	110000	450000	200000	200000

The Stress Spectrum is an ordered set of stress amplitudes of the value n_b which shows the participation of each of the stress amplitudes σ_i in the selected number of cycles n_b. It is a statistical (ordered) presentation of random stress fluctuation, it enables a pattern in behaviour to be defined in the random process and respective calculations and tests to be completed. The stress spectrum is determined by the value n_b, the relative variable x_i, and the largest stress σ_1. The number of stress levels may also be greater but also significantly less than eight. It can be obtained by statistical processing of empirical data obtained from random function, as has been shown above, or starting from the known cumulative growing function of stress amplitudes $F(\sigma_a)$. Besides this, the stress spectrum can be obtained by combining the deterministic and statistical approach. In the course of service length the machine system may operate with different loads (stresses). The load values (stresses) may be calculated and it is also possible to estimate the possible number of cycles of each one of them. By joining the blocks of stress cycles defined by the value and number of cycles, a set of blocks is obtained. By proportional reduction of the total number of cycles to n_b and blocks to Δn_{bi}, a stress spectrum is obtained. This spectrum need not satisfy the above given conditions by all its features, but it may be used both for testing and for calculations, and also for estimates of the service regime. The mentioned possibilities of stress spectrum formation do not give the same degree of precision. The choice is made depending on the aims and possibilities of realization.

Machine systems (of the same design) may be exposed to the action of service loads (stresses), the value of which reaches some upper acceptable limit. In some exploitation conditions this limit may be reached extremely rare, i.e. loads (stresses) are most often below this limit. In some other exploitation conditions the loads (stresses) may be most frequently close to the upper limit. The exploitation regime in this sense represents the statistical estimate of the presence of stress amplitudes from the same set of their values, depending on exploitation conditions. This estimate may be made with the help of the function of probability density $f(\sigma_a)$, the cumulative growing function $F(\sigma_a)$, and the logarithmic function of the stress spectrum (Fig. 8). It is possible to speak of light (l) medium (m) and heavy exploitation regime (h). The light regime entails big participation of small stress amplitudes, only exceptionally they can be equal to the largest. As per Fig. 9a, maximum probability density is for $x_m = 0.2$, i.e. $\sigma_a = 0.2\sigma_{a1}$. In the case of medium exploitation regime the participation of higher amplitudes increases, and they are most often with amplitudes $\sigma_a = 0.5\sigma_{a1}$ ($x_m = 0.5$), whereby the participation of the high stress amplitudes in the heavy regime is increased ($\sigma_a = 0.8\sigma_{a1}$) on account of the decreasing presence of small amplitudes. By further increase of the severity of the exploitation regime all amplitudes become equal to the highest. That is the regime with a constant stress amplitude ($x_m = 1$). If Weibull's distribution function of stress amplitude $F(\sigma_a)$ is known, the appraisal of the severity of the exploitation regime may be made if the amplitude with the highest occurrence frequency is determined. Another derivative of the function $F(\sigma_a)$ equated to zero determines the extreme of the function maximum $f(\sigma_a)$, where

$$\sigma_{am} = \eta \sqrt[\beta]{(\beta-1)/\beta}\ \text{, i.e. } x_m = \sigma_{am}/\sigma_{a1}\ .$$

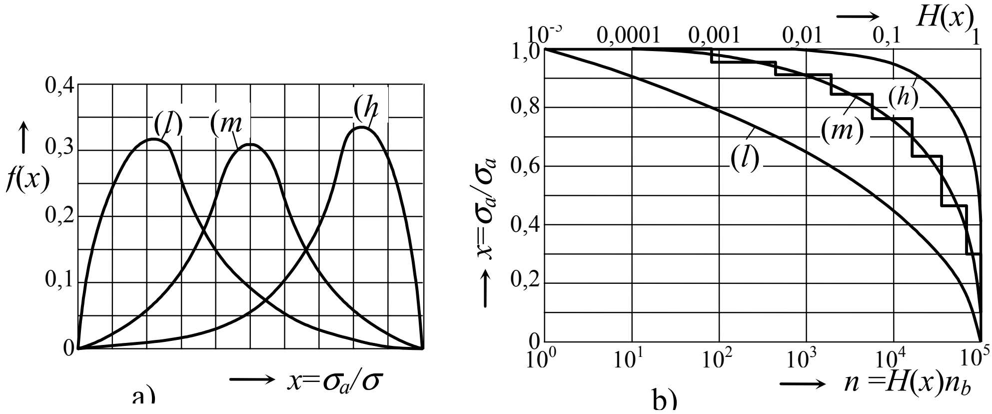

Figure 9. Characteristic representatives of light (l), medium (m) and heavy (h) exploitation regimes

Upon analysis of conditions of different machine systems, big differences have been determined in the heaviness of the exploitation regime. It depends on exploitation conditions, the aims of which the machine system was developed, its function. In vehicles for example, the installed engine power is by rule great so as to enable acceleration within short time, and so that this power could be used in sudden circumstances for the performance of short lasting operations with big loads. In the stationary driving regime, a relatively small part of the installed power is used. In the statistical sense, small stress amplitudes are dominant, and the large ones are present only in exceptional circumstances. Thus the stress amplitudes, i.e. the work regime of vehicles, are a typical example of the light exploitation regime. The other extreme is represented by machine systems where it is endeavoured in the stationary work state to achieve maximum capacity and productivity. Ore mills in flotation or in cement plants are typical representatives. In filling these systems it is endeavoured in the stationary work regime to reach the maximum and use the maximum installed power as well as the carrying capacity of the system parts. The stress amplitudes are by rule close to the highest, and the exploitation regime is heavy. The work regime in the mining plants is just somewhat lighter. Other machine systems operate with regimes which are between these border cases.

The stress spectrum based on which it is possible to estimate the exploitation regime may also be obtained in a simpler way. Instead of determining the time functions of stress amplitudes as is given in the previous text, the approach may also be simplified. It is possible to make estimates and tentative calculations so as to determine what part of the work time will the machine system work at full power and then what time will it be using less power expressed in percentages. Based on this, it is possible to obtain load blocks which, when put in order by value, give an ordered set of stress levels similar to the presentation in Fig. 8, the number of stress levels need not be eight, it may be any other number. The set of stress changes in service length or in the sample of this service length transforms in this way into an ordered set of fluctuations, which represents the stress spectrum. It may be used for reliability calculation and also for testing.

3. FAILURE PROBABILITY OF MACHINE PARTS

Fracture due to fatigue is a result of a complex and stochastic process, and the stress finite cycle number is a statistical value which can be estimated only on the basis of the law of probability. Fatigue is a process which has not been studied sufficiently theoretically to be defined by analytical forms which would make possible the calculation of the stress finite cycles number. There are several hypotheses about the fatigue process course, i.e. the crack occurrence process. When a crack occurs it becomes the source of additional stress concentration, it spreads gradually until the occurrence of complete fracture. The total finite cycles number up to the fracture N equals the sum of the stress cycle number until the occurrence of the crack N' and the stress cycle number in the course of crack spreading N'' ($N = N' + N''$). The crack spreading process has been studied to a significant degree. This process differs to a high degree, or completely from processes which take place in the material structure up to the occurrence of cracks. This process is stochastic, insufficiently studied and it brings a stochastic component into total stress finite cycles up to fracture. In case of soft and tougher materials (steels) the period of crack spreading is relatively long, i.e. it may be longer than the period up to the occurrence of the crack. Calculations in the sense of forecasts of service length of machine parts with cracks in such cases may have a certain practical significance. In high strength steels the number of stress cycles up to the occurrence of cracks is relatively big, and crack spreading is very fast, thus the calculations in relation to crack spreading are not of great practical use.

Up to the occurrence of cracks a process takes place which may be presented most closely by some assumptions with Markov's process (Fig. 10). If the process evolved in one direction, there would be a change at each stress change, from state j into state $j + 1$ which entails an increase of the crystal dislocation (fatigue degree). Thus by an one direction process from state 0 (without fatigue), state m would be reached, which entails the occurrence of cracks. This would practically be a deterministic process, thus based on the required energy for the creation of the dislocation, it would be possible to calculate the required stress cycles number for the occurrence of cracks. The process is not one-directional, thus from state j, a transition into state $j + 1$, or into state $j - 1$ is possible. Whether the process is moving forwards or backwards depends to a large degree on the stress cycle number that will be required for the occurrence of cracks. The transition probably does not take place, so that transitions occur into neighbouring states, instead skipping of states is more likely. Big stress amplitudes, probably in large jumps, contribute to the advancing of the fatigue process. Some smaller stress amplitudes may bring an advanced fatigue process back to some state close to the initial one. It has been proven that small stress changes (less than $0.5\sigma_D$) do not bring about an increase in the fatigue, but instead cause relaxation. Depending on the sequence (mixing) of big and small stress amplitudes the fatigue process may, under same testing conditions, advance faster or more slowly. The relation of the biggest and smallest stress cycles number up to fracture under the same testing conditions (same stress value and change, same form, material and other test sample features, etc.) amounts to $N_{max}/N_{min} = 3...5$ or even more. This can be attributed only to the indicated stochastics of the fatigue process.

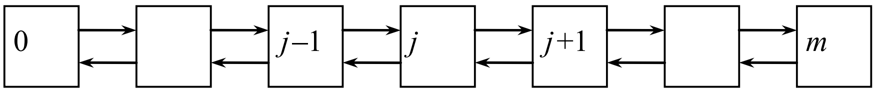

Figure 10. The statistical model of the fatigue process as defined by a series of current states

The failure probability is a cumulative probability that a machine part will fail under a certain stress by a certain stress cycle number. This is also the probability that at a certain stress cycle number, failures will occur at certain stresses. The failure probability is calculated on the basis of statistical processing of the testing results. That is the ratio of the number of failed test samples (parts) under certain conditions and the number of tested parts under such conditions. It is necessary to choose for testing, the stress values to which the test samples, i.e. parts are to be exposed, then the number of pieces which are to be tested, and the manner of achieving (simulating) the stress fluctuation. The number of pieces (test samples or parts) z_Σ to be tested on each one of the chosen stress levels should be sufficiently big so that, based on the sufficiently big set, it would be possible to deduce statistical conclusions. A set greater than $z_\Sigma = 20$ test samples or parts is considered as sufficiently big. This testing work takes a lot of time with significant energy consumption, and the tested parts are not for further use. It is therefore endeavoured to reduce as much as possible the number of pieces to be tested. The smallest number of pieces which still makes possible the deduction of statistical conclusions is $z_\Sigma = 8$. For these small samples the failure probability is not defined as the ratio of the number of failed z_i and tested pieces z_Σ, i.e. as $P_R = z_i/z_\Sigma$, but as by some of the approximate expressions

$$P_R = \frac{z_i}{z_\Sigma + 1}\,;\; P_R = \frac{z_i - 0.5}{z_\Sigma}\,;\; P_R = \frac{z_i - 0.33}{z_\Sigma - 0.33}$$

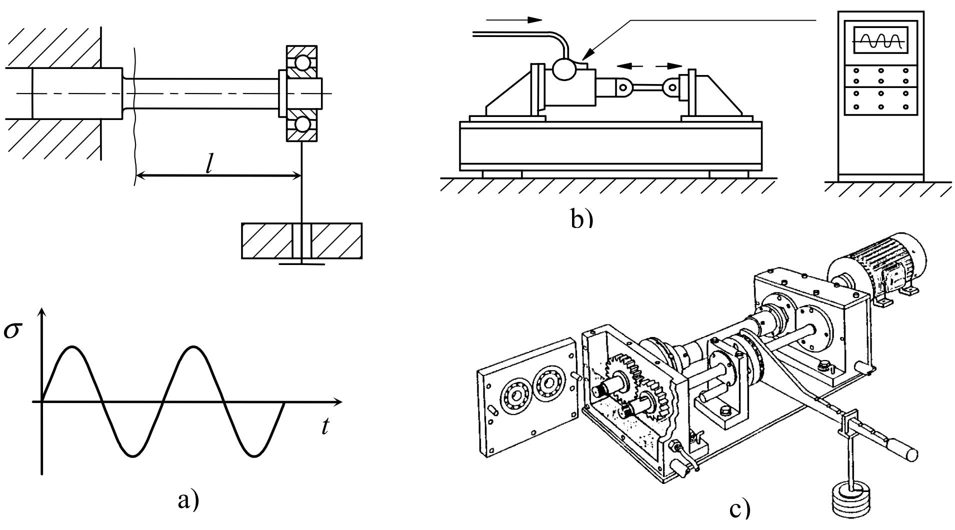

Figure 11. Some of the possibilities of simulation of the variable stress: a) rotary bending, b) axial load through hydraulic machines, c) back to back system with power circulation

The manner of achieving (simulating) the fluctuating stress is another of the significant issues which must be resolved at the performance of research. Figure 11 shows some of the possibilities of achieving the fluctuating stress with constant amplitude. Rotating test samples exposed to rotating bending (Fig. 11a) are simply loaded with calibrated weights through roller bearings. Due to the rotation of test samples, reverse stress changes are achieved, and the crack at fracturing spreads out circularly. The number of finite cycles number is equal to the number of rotations of the test sample. Figure 10b shows the manner of introducing the longitudinal force in the testing of the engine screw, piston rods, and other similar parts exposed to longitudinal variable forces. The change of force occurs through hydraulic machines with a change of force of sufficiently high frequency. The rotating machine parts such as gears, shafts, couplings, etc. are tested with the help of devices with closed power circuits (Fig. 11c). Two identical pairs of gears, i.e. transmissions are conjugated in the circuit ("back to back"). The load is achieved by flexible deformation of parts in the circuit, in stationary state, with the moment created by the weight on the lever of appropriate length. In such a state, screws are tightened on the coupling, weights and levers are removed, and the "conserved" load–stress in the parts remains in the circuit, which remains also in the state of rotation. The number of stress cycles is the same as the number of rotations.

4. FAILURE PROBABILITY IN THE RANGE OF FINITE LIFE STRENGTH

In the logarithmic coordinate system the fatigue strength curve – Wöhler's *S–N* curve is a straight line. By logarithm of exponential equations $\sigma_N^m N = C$, we get $m\log\sigma_N + \log N = \log C$, and by substituting $y = \log\sigma_N$, $x = \log N$, $\log C = C_1$, it follows that $my + x = C_1$. The straight line is defined by two points. It is sufficient to perform the testing for two stress levels and use these results for determination of required data for any stress level using equations of the indicated straight line.

For the realization of the testing process it is necessary to choose two stress levels to which the test samples will be exposed to, and choose the number of test samples (parts) which are to be tested at chosen stress levels. The difference between chosen stress levels should be as big as possible so that the direction of the obtained straight line is as precise as possible. The upper level should be as close as possible to the yield strength without entering the plasticity range. The lower level should be as close as possible to the endurance limit, without entering the range of dissipation of the endurance limit. The decision about the values of these stresses is made on the basis of experiences gained in previous research work or on the basis of testing one or a few pieces. Figure 12 gives an example of research results of rotating test samples related to bending. The test was performed at reversed stress $\sigma_{N1} = F_1 l/W = 973$ N/mm^2 ($F_1 = 1500$ N) and $\sigma_{N2} = F_2 l/W = 810$ N/mm^2 ($F_2 = 1250$ N). To each one of these stresses, $z_\Sigma = 10$ test specimens were exposed. In the range of finite life strength, the failure (fracture due to fatigue) occurs after some finite number of cycles, in the case of all test specimens. Finite numbers of cycles are the result of the stochastic process and are realized by the law of coincidence. After classification into the growing series of numbers, a set of values is obtained of these numbers, *N*, given in the table in Fig. 12. For two stress levels, two sets of finite cycles numbers are obtained by testing. The failure probability for each one is a cumulative probability $P_R = z_i/z_\Sigma$, where z_i is the number of failed specimens at the finite numbers of cycles, which are smaller or equal to the number *N* for which the probability is calculated, z_Σ – total number of tested specimens with stress for which the probability is calculated. This expression is valid for big samples (big sets z_Σ). For small samples, the above indicated approximate expressions are used. The most suitable for applications is the first expression which has been used for calculation of failure probability in the table in Fig. 12. The failure probabilities, P_R, determined in this way have been entered in Weibull's coordinate mesh, and the set of points for stress $\sigma_{N1} = 973$ N/mm^2 and for $\sigma_{N2} = 810$ N/mm^2 have been approximated by straight lines. The parameters of Weibull's distribution have been determined following the methodology, presented in Section 2. The obtained values of parameters for stress σ_{N1} = 973 N/mm^2 are η = 105 000 cycles, β = 3.8 and for stress σ_{N2} = 810 N/mm^2, η = 950 000 cycles, β = 2.6. For these parameters and for respective stress levels of Weibull's distribution, the failure probabilities are

$$P_R(N) = 1 - e^{-\left(\frac{N}{105000}\right)^{3.8}} \; ; \; P_R(N) = 1 - e^{-\left(\frac{N}{950000}\right)^{2.6}}$$

z_i	N for σ_N in N/mm^2		$P_R = \frac{z_i}{z_\Sigma + 1}$
	σ_{N1} = 973	σ_{N1} = 810	
1	52380	331500	0.091
2	76800	419800	0.182
3	82315	512320	0.273
4	82530	650030	0.364
5	87820	768000	0.455
6	89930	905320	0.545
7	102415	102865	0.636
8	123300	113460	0.727
9	131050	121350	0.818
10	175200	1383000	0.909

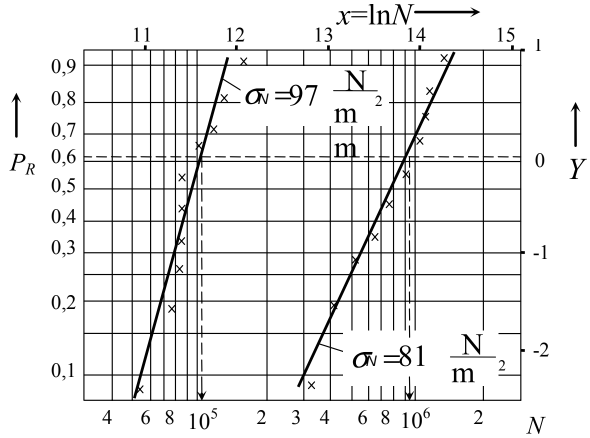

Figure 12. Distribution of failure probability in the range of finite life strength

5. FAILURE PROBABILITY IN THE RANGE OF INFINITE–LIFE STRENGTH

In the range of the infinite–life strength, the distribution of failure probability is defined for a fixed stress cycles number up to fracture, and the independent variable is stress, i.e. fatigue strength σ_N. The realization of the test process of this probability is preceded by the decision making about the fixed number of stress cycles up to which the tests are to be conducted, as well as the decision about the stress level number for which sets of z_Σ specimens (parts) are to be tested. The stress cycle number up to which the specimens are tested is a post infinite life limit number of cycles N_{DV}. That is the number of stress cycles for which it is known for sure that it is greater than the infinite life limit N_D, but it is not too large, so that tests should not become too long-lasting. The test specimens which fracture at the number of cycles $N < N_{DV}$ are classified as failed test specimens' z_i at a respective stress value (level), and those that do not fail up to N_{DV} are classified in the group that have not failed $z_\Sigma - z_i$. At higher stress levels (closer to finite-life strength) of the same number of test samples z_Σ, there is a greater number of failed samples z_i. With decrease of the stress level there is a decrease in the number of failed specimens, and the number of specimens that endure the N_{DV} cycles increases.

The problem of stress level selection is more complex. The decision is made about the number of stress levels, their density, and stress values. If the value of the endurance limit σ_D (σ_{lim}) and the value of the dissipation range are known, several stress levels are uniformly distributed in that range, such as for example σ_{N3}, σ_{N4}, σ_{N5}, σ_{Nk} (Fig. 13a). This is the stress level method, following which further tests take place on z_Σ specimens and the calculation of the failure probability $P_R = z_i/(z_\Sigma + 1)$. If the value of infinite-life strength is not known in advance, the level method cannot be applied, i.e. this method must be preceded by application of the step method. Following the step method, after each tested specimen the stress level changes, with which the next specimens will be tested. If a test tube fails before reaching the fixed post-limit cycle number N_{DV} the next one will be tested with the first lower stress level. If it does not fail, it is considered that the stress was small, thus the next one is tested with a greater stress. By “oscillating” on the steps (Fig. 13b), the endurance limit is defined. The number of tested, z_Σ, and the number of failed, z_i, specimens on each stress level, is obtained by counting. For the number of tested specimens z_Σ to be sufficiently big, it is necessary that the total number of tested specimens (parts) at all stress levels is sufficiently big. Even in such case at extreme levels (the lowest and the highest), the number of tested pieces is small, i.e. less than the limit number for the deduction of statistical conclusions. For a sufficient number z_Σ to be achieved on these stress levels also, additional specimens (parts) are tested. In this way a combination is made of the step method and the level method. The value of infinite life strength (endurance limit) and the magnitude of the dissipation range are firstly determined with the help of the step method and then additionally, the level method is completed for the purpose of determining failure probability $P_R = z_i/(z_\Sigma + 1)$.

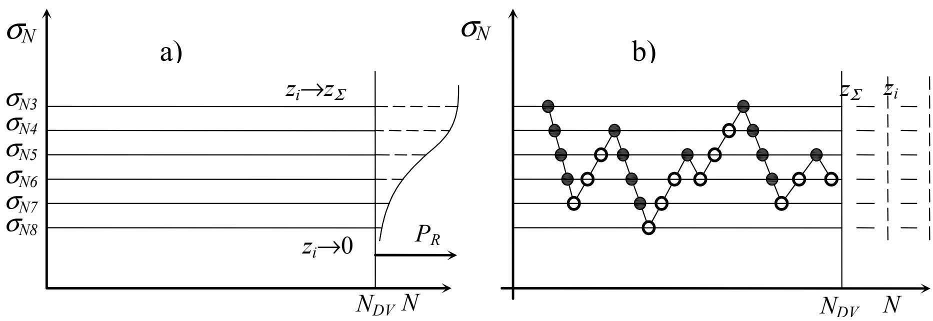

Figure 13. Failure probability testing in the range of infinite–life strength
a) level method, b) step method

$N_{DV} = 5 \cdot 10^6$			
F N	σ_N N/mm^2	z_i	$P_R = \dfrac{z_i}{z_\Sigma + 1}$
1200	777	9	0.818
1150	746	5	0.454
1100	713	4	0.363
1050	680	1	0.090

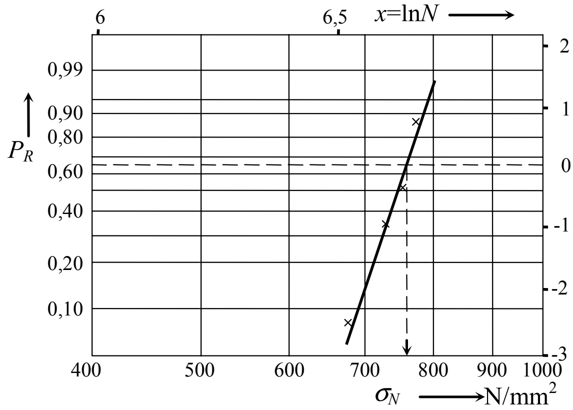

Figure 14. Definition of the parameters of Weibull’s distribution for the failure probability in the range of infinite–life strength

The calculated failure probabilities P_R are entered into Weibull’s coordinate mesh for respective stress values σ_N. After approximating this set of points by a straight line, parameters are obtained of this distribution, η and β. Figure 14 gives an example of test results of rotating specimens (Fig. 11a) with calculated failure probabilities. With approximated straight line, parameters $\eta = 760$ N/mm^2 (for the probability $P_R = 0.632$) and $\beta = 23$ (the part on the ordinate for $\Delta X = 1$) are obtained. For these parameters the Weibull’s distribution of failure probability for $N_{DV} = 5 \cdot 10^6$ is

$$P(\sigma_N) = 1 - e^{-\left(\frac{\sigma_N}{760}\right)^{23}}$$

In the absence of more precise information, this function of distribution of failure probabilities may be valid for all cycle numbers which are greater than infinite life limit N_D.

6. THE FIELD OF THE BASIC FATIGUE STRENGTH DISSIPATION

It is possible to form the field of fatigue strength dissipation by using functions of failure probability obtained by testing two stress levels in the range of finite-life strength and for the infinite-fatigue-life. That field covers all stress levels and numbers of cycles. This range is by rule limited by lines with failure probabilities P_R = 0.1 and 0.9, and the line with failure probability P_R = 0.5 is most frequently in use. By using the indicated three distributions of failure probability, it is possible to calculate cycle numbers, i.e. stresses which correspond to the indicated probabilities and that means

$$N = \eta\sqrt[\beta]{-\ln(1-P_R)}\ ;\ \sigma_N = \eta\sqrt[\beta]{-\ln(1-P_R)}$$

with the use of respective parameters η and β. In this way points are determined for stress levels σ_{N1} and σ_{N2} and for the number of stress cycles N_{DV}. The calculated coordinates have been entered into the coordinate system with logarithmic axes, Fig. 15. By joining the points with the same probability P_R, border curves are obtained P_R = 0.1, P_R = 0.9 as well as the middle line for P_R = 0.5. The failure probability distributions have been presented on stress levels σ_{N1} = 973 N/mm^2, σ_{N2} = 810 N/mm^2 and for $N_{DV} = 5\cdot10^6$. Based on border lines, it is possible to define distributions for any stress σ_N and for any number of stress cycles N.

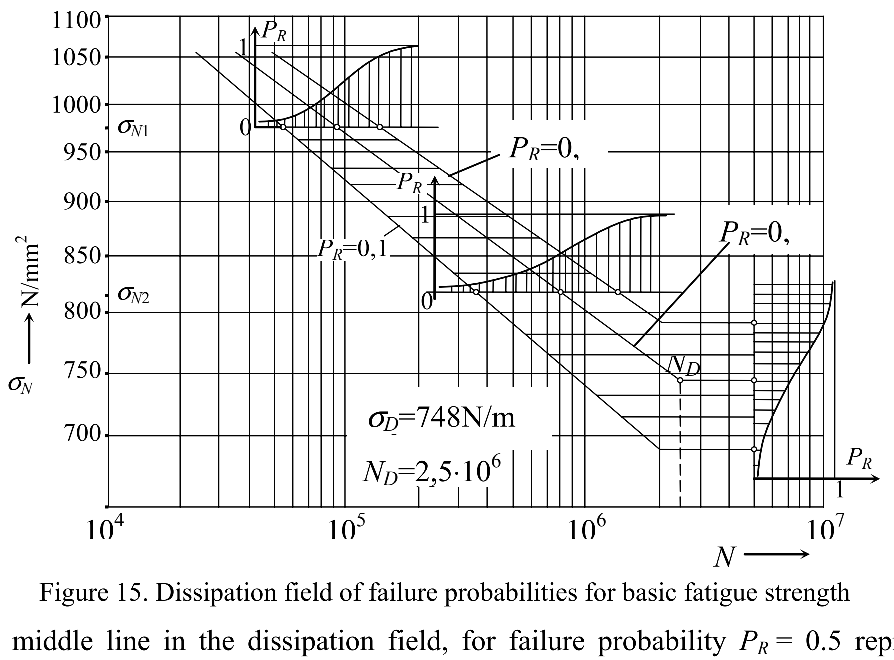

Figure 15. Dissipation field of failure probabilities for basic fatigue strength

The middle line in the dissipation field, for failure probability P_R = 0.5 represents Wöhler's *S–N* curve. It is defined by three parameters σ_D (σ_{lim}), N_D and m. The coordinates of breaking point are $\sigma_D = \sigma_{lim}$ = 748 N/mm^2 and $N_D = 2.5\cdot10^6$ and are defined by reading from the diagram. The exponent by which the inclination of Wöhler's curve is defined is obtained on the basis of coordinates of points on this line, i.e.

$$\sigma_D^m N_D = \sigma_{N1}^m N_{1(0.5)}\,;\; m\log\sigma_D + \log N_D = m\log\sigma_{N1} + \log N_{1(0.5)}$$

$$m = \frac{\log(N_{1(0.5)}/N_D)}{\log(\sigma_D/\sigma_{N1})} = \frac{\log(0.095\cdot 10^6/2.5\cdot 10^6)}{\log(748/973)} = 12.43$$

It is possible to calculate in the same way the exponents, *m*, for border lines for probabilities P_R = 0.1 and 0.9. They differ little from the value of this exponent for P_R = 0.5 as the dissipation range spreads gradually from higher to lower stresses. In absence of more precise information it is possible to take that lines for P_R = 0.1, 0.5, and 0.9 are mutually parallel, and that exponents *m* are mutually equal.

The infinite fatigue life strength is reduced with the reduction of material strength, also with increase of structural non-homogeneity, and with increase of stress concentration, etc. With reduction of infinite fatigue life strength (endurance limit) with respect to static strength, the exponent *m* decreases. If the endurance limit is increased by surface reinforcement and if it approaches static strength, the exponent *m* increases (as in the indicated example). The infinite life limit N_D may be decreased with decrease of σ_D, but more often it stays the same.

7. FAILURE PROBABILITY FOR SERVICE FATIGUE STRENGTH

The service fatigue strength σ_R follows the curve in the double logarithmic coordinate system (Fig. 16a). By approximating this slightly curved line with a broken up straight line, a line is obtained with two breaking points, the coordinates of which are presented in the figure as equations of the parts of these lines. The coordinates of the breaking point σ_{R0}, N_{R0} and the exponent *q* are parameters of the service fatigue strength curve. The position of the curve in the coordinate system depends on the weight of the work regime. In case of the light one (*l*), the curve is shifted to the right, i.e. towards the range of extremely high numbers of cycles up to fracture N_R. With an increase of the heaviness of the regime, the service fatigue strength curve approaches the Wöhler's (*w*).

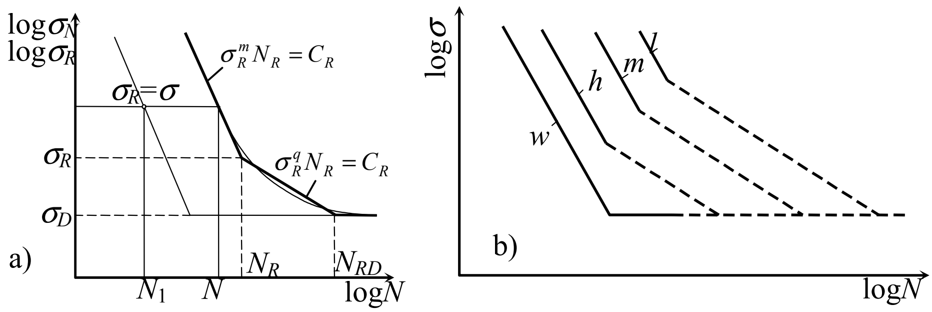

Figure 16. Service fatigue strength curves: a) approximation by broken straight line; b) the impact of the heaviness of work regime onto the relation of the curve of service and basic strength

The testing of service fatigue strength and failure probability for service fatigue strength is quite complex in comparison with this testing of basic strength. Two basic additional problems are imposed here. One relates to the manner of creating loads (stress) in the course of testing, the other relates to the choice of stress level for testing. The stress spectrum is an ordered set of stress changes. By ordering this set, the sequence has been lost and the impact of small and big changes has been mixed up. Gassner has suggested a solution for this problem. Following his suggestion, the ordered set should be mixed again so that the simulation effect is as close as possible to the effect of real random function of stress fluctuation. The simulation of each of the amplitudes should not be performed so as to finish firstly with one amplitude and then go onto the other. Each amplitude should be simulated from the beginning in small blocks, which will be repeated several times up to failure of the tested object. This will have a positive effect on getting closer to the effect of the sequence of stress fluctuation to the real state. He suggested a diagram following which it is necessary to make a simulation of stress change (Fig. 17) which is obtained by transforming the stress spectrum. As the stress spectrum value $n_b = 10^6$ or 10^5 is too big, fracture may occur before the simulation on spectrum is completed, i.e. at $N_R < n_b$ or at a little bigger cycle number N_R than n_b. In order to avoid this possibility, the stress change simulation should be performed in blocks N_B which are by the cycle number much smaller than the unit spectrum of stress n_b. The block of cycles is obtained by proportional decrease of the cycle numbers in the stress spectrum. The proportion for this transformation is

$$\frac{\Delta N_{Bi}}{\Delta n_{bi}} = \frac{N_B}{n_b}\ ;\ \Delta N_{Bi} = \Delta n_{bi}\frac{N_B}{n_b}\ ;\ n_b = \sum_{i=1}^{k}\Delta n_{bi}\ ;\ N_B = \sum_{i=1}^{k}\Delta N_{Bi}$$

The simulations are materialized by starting from some stress level from the spectrum (block) centre. Upon completion of the simulation of stress level σ_4, for example, with the number of cycles ΔN_{B4}, a transition is made onto a higher stress level σ_3 and so on up to σ_1, and then from the biggest stress level towards smaller ones as presented in Fig. 17. If block N_B is smaller, it will be repeated several times up to fracturing, i.e. the number of repetitions is $y = N_R/N_B$. Better mixing of big and small stress amplitudes suits the greater number of repetitions. Too big number of repetitions of blocks imposes the need for the unacceptable big number of stress level change in the course of the testing process. This problem may be resolved by electronic, i.e. program management of stress level changes.

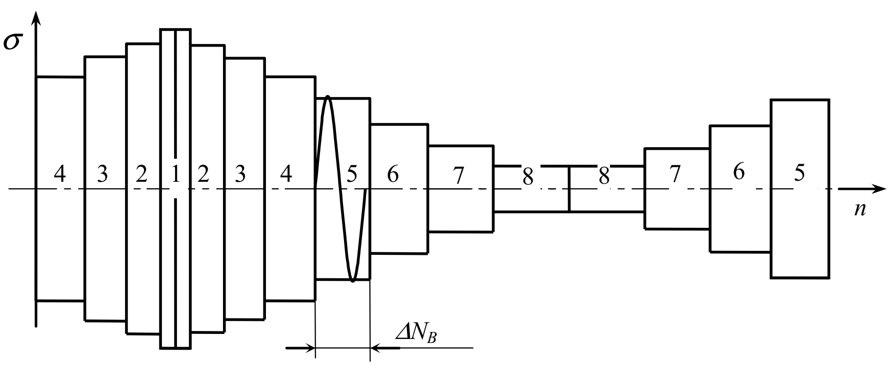

Figure 17. The sequence of cycle blocks of stress in testing of service fatigue strength (Gassner's diagram)

For the determination of failure probability for service fatigue strength, test results are required for three stress levels σ_R, i.e. σ_1. Two levels are required for the determination of the direction of the lower part on the service fatigue strength curve. The upper part of this broken straight line is parallel with the line of the basic (Wöhler's) strength. Testing is necessary for one stress level for the purpose of determination of the position (distance) of this part from the line of basic strength. The highest stress level σ_R' is chosen in such a manner that all stress levels in the stress spectrum are greater than the infinite life strength. The lowest stress level in the spectrum must thereby be significantly above the infinite life strength, so that the greatest stress in the spectrum σ_R' is in the zone of the upper part of the service strength. The second level of the greatest stress in the spectrum σ_R'' should be in the upper region of the lower part. This condition is achieved if stress levels in the stress spectrum are so adjusted that at least one stress level (the lowest) is under the level of infinite life strength. The third level of the greatest stress in the spectrum σ_R''' should be on the level close to and above the range of infinite life strength dissipation. For each of the chosen three levels of greatest stress in the stress spectrum (service fatigue strength) a set of z_Σ test specimens is tested. Fractures occur at different numbers of cycles N_R, following the same principle as in the range of finite life strength. Classified by values, cycle numbers N_R may be presented as in the table in Fig. 18. The calculated failure probabilities P_R for the respective cycle numbers are entered into corresponding Weibull's coordinate mesh. After approximating with a straight line, parameters of these distributions are determined. In the example in Fig. 18, for service fatigue strength levels σ_R', σ_R'',σ_R''', the functions of distribution of failure probabilities are:

$$P_R(N_R)=1-e^{-\left(\frac{N_R}{1.2\cdot 10^6}\right)^{3.1}}\ ;\ P_R(N_R)=1-e^{-\left(\frac{N_R}{1.3\cdot 10^7}\right)^{1.95}}\ ;\ P_R(N_R)=1-e^{-\left(\frac{N_R}{2.5\cdot 10^8}\right)^{1.4}}$$

z_i	N_R			P_R
	σ'_R	σ''_R	σ'''_R	
1	$N_{R\min}$	$N_{R\min}$	$N_{R\min}$	0.09
2	–	–	–	–
3	–	–	–	–
.	–	–	–	–
.	–	–	–	–
z_Σ	$N_{R\max}$	$N_{R\max}$	$N_{R\max}$	0.9

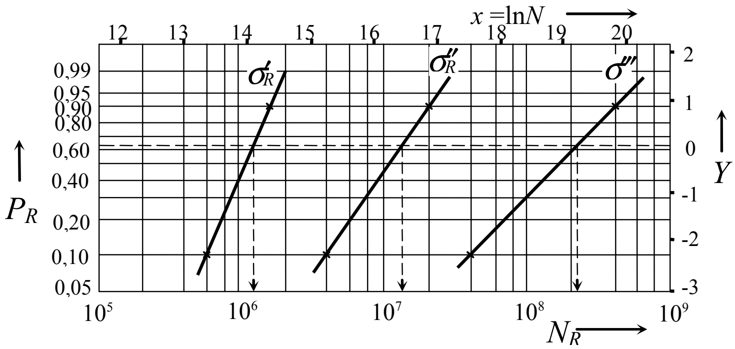

Figure 19. Distribution functions of the failure probability for service fatigue strength

Using the formed distribution functions, it is possible to calculate on each of the three service fatigue strength levels the cycle numbers N_R for failure probabilities P_R = 0.1, 0.5, and 0.9 from the expression obtained by the logarithm of Weibull's function of failure probability $N_R = \eta\sqrt[\beta]{-\ln(1-P_R)}$. By joining the points with the same failure probability a dissipation range is formed by the lines for the probability P_R = 0.1 and 0.9 (Fig. 19).

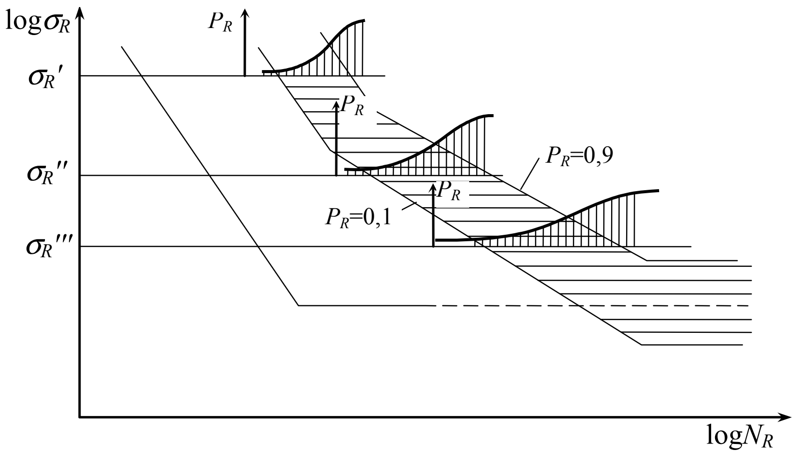

Figure 19. Dissipation of experimental data for service fatigue strength

By joining the points at the levels of service fatigue strength σ_R'' and σ_R''' a dissipation range is formed around the lower part of the service fatigue strength line. For the points on the level σ_R' parallel with the line for time strength forms the dissipation range around the upper part of the service fatigue strength. The third region overlaps with the dissipation region of the failure probability for infinite life strength. Based on the obtained border curves it is possible to determine the functions of the distribution of the failure probabilities for any level of service fatigue strength σ_R and for any cycle number up to failure N_R. It is also possible to determine the coordinates of the breaking points of the service fatigue strength curve for the respective failure probability as well as the respective exponent of the service fatigue strength curve q.

CONCLUSIONS

The fatigue process of machine parts has not been studied sufficiently, particularly in the part until cracks occur. Besides this, the process is stochastic, i.e. hard to predict either by applying theoretical or empirical methods. Those are the reasons why experimental results and mathematical statistics in the form of probability indicators – reliability are used in practical applications.

The indicator of the possibility for the occurrence of fracture on a certain place at a certain time in machine systems is elementary reliability. It represents the controlled risk of the designer to allow such a place for the possibility of failure with the aim of rationalizing the dimensions in comparison with the complete safety which is expressed by the safety factor.

The procedure for the determination of the elementary reliability is simple and has been presented in the initial part of the work. The gathering of the information required for the calculation of this reliability is a big problem. Extensive research is required for the purpose of statistic generalization. Procedures which enable rationalization in the scope of the testing process have been presented in this work.

REFERENCES

1. Haibach, E., *Betriebsfestigkeit – Verfahren und Daten zur Bauteilberechnung*, VDI-Verlag
2. Leitch, R., *Reliability Analysis for Engineers – An Introduction*, Oxford scientific publications, Oxford University Press. (1995)
3. Savić, Z., Janković, M., *Prilog proučavanju dinamičke izdržljivosti zubaca zupčanika pri promenljivom opterećenju*, Zbornik radova sa svetskog simpozijuma o zupčanicima i zupčastim prenosnicima, Kupari-Dubrovnik, Vol B, pp. 305-319. (1978)
4. Savić, Z., *Pouzdanost – viši stepen tačnosti provere čvrstoće elemenata konstrukcija*, Zbornik radova sa naučno-stručnog skupa "Istraživanje i razvoj mašinskih elemenata i sistema – IRMES-95", Niš, pp. 2-10. (1995)
5. Savić, Z., Ognjanović, M., Janković, M., *Osnovi konstruisanja –Zbirka zadataka*, Naučna knjiga Beograd, 1981, 1986, 1988, 1991.
6. Todorović, J., Zelenović, D., *Efektivnost sistema u mašinstvu*, Naučna knjiga Beograd. (1981)
7. Ivanović, G., Stanivuković, D., *Pouzdanost tehničkih sistema – Zbirka rešenih zadataka*, Mašinski fakultet, Beograd. (1987)
8. Tošić, M., Terzić, I., Gligorijević, R., Ognjanović, M., *Failure improf glow-discharge-nitrided steel rotary specimens*, Journal of Surface and Coating Technology, No.63, pp. 73-83. (1994)
9. Ognjanović, M., Gligorijević, R., *Fatigue strength of nodular connecting rods*, Proceedings of the International Conference on Fatigue and Stress of Engineering Materials and Components, Imperial College London. (1988)

10. Ognjanović, M., *Fatigue and failure probability of shafts under operating conditions*, International Journal for Vehicle Mechanics, Engines and Transportation Systems, Mobility Vehicle Mechanics, Vol.21, No 4, pp. 43-50. (1995)
11. Ognjanović, M., *Gear Failure and Reliability in Resonance Conditions*, Proceedings of the International Congress "Gear Transmissions 95", Sofia, Vol. 2, pp. 85-88. (1995)
12. Ognjanović, M., Ristivojević, M., Milić, M., *Lomovi pogonskih vratila-osovina električnih lokomotiva*, Časopis "Železnica", No 1-2, pp. 23-28. (1997)

PREDICTION OF THE FRACTURE AND FATIGUE PROPERTIES OF WELDED JOINTS BY HEAT-AFFECTED-ZONE SIMULATION

Vladimir Gliha, Faculty of Mechanical Engineering, Maribor, Slovenia

INTRODUCTION

Welding is the best practical way of joining two or more metallic pieces to make them act permanently as a single piece. Elements of huge steel constructions and heavy machinery are mostly joined by fusion welding, using arc welding with the consumable electrodes. Arc fusion welding is an efficient and simple joining technique enabling high commercial effects because of achievable good quality joints produced in workshop conditions (industrial production) as well as on-site (erection).

Many metallic structures are made of steel. Nowadays, high strength low alloy (HSLA) structural steels are increasingly used all over the world. They have some fundamental practical advantages over plain carbon structural steels as higher strength and improved toughness, and due to good weldability are extraordinary well suited to design and manufacture welded products which will be subjected to the most demanding conditions. If designers, technologists, and inspectors are really familiar with all peculiarities of processing these steels, a painless confrontation of industry with the world market is guaranteed. The successful competition in this market is then quite possible.

A serious problem when welding with the HSLA structural steels is to ensure the adequate toughness of all zones in the joint. Besides, some kinds of weld defects are always present in commercial welded joints. Existence of defects and weak zones at the same time can promote fracture of the welded joint during production, testing by loading, or in normal exploitation. Failure occurs with crack initiation. Crack initiation is the consequence of an over-critical interaction between stresses and inconveniently oriented crack-like defects. The basic function of welded joints is jeopardised if any kind of the crack, which could not be arrested, initiates during loading. The final result of this process is namely disintegration of the joint. The type of interaction between stresses and defects mainly depends on the character of the loading, on the temperature, and effects of environment. Thus, the effects of cyclic mechanical loading on welded joints are different than effects of static, quasi-static, or dynamic loading.

Feasibility to prepare samples with the microstructure of potential weak zones of welded joints which extensions enable mechanical testing were a welcome step to the experimental studies of welded joint properties and effects of welding on metals. Such an approach is possible because of the available equipment which is purposely designed for these tasks, i.e. thermal cycle simulators. This computer controlled equipment is used for the simulation of thermal conditions during welding on samples of the material with the appropriate starting microstructure. The fracture and fatigue properties of different zones in welded joints will be successfully predicted if appropriate specimens are made of these samples and tested in accordance with their size. The limited size of specimens is the main obstacle in the intention to determine relevant welded joint properties by testing. The size of samples with the simulated microstructure depends on the heating and cooling capacities of the simulator as well as on the material, peak temperature of the thermal cycle, and necessary size of the zone with simulated microstructure.

The lecture presents most important results of researches performed in the Research and Development Institute of Metalna in Maribor, and in the Welding Laboratory of Mechanical Engineering Faculty, Maribor, in the last 15 years, from since the thermal cycle simulator was available. Some other results, obtained in the researches with our participation are also included. Those results are used to explain applied approaches to study fracture and fatigue properties of welded joints in HSLA structural steels.

1. WAYS TO TEST THE STRENGTH OF WELDED JOINT

Static and dynamic strength of welded structures with crack-like defects can be evaluated using different types of precracked specimens. The reliability of these results, obtained experimentally, depends mostly on the shape and size of specimens used.

1. In order to assess the actual strength of workshop-quality welded structures, full-size models are loaded up to fracture, or to plastic yielding. These so-called proof tests of full-scale samples are sometimes used in series production. Different types of proof tests include strain- or displacement-measurement tests and fracture or burst tests. Tests performed on structures with a crack prepared in the area of the lowest fracture resistance provide reliable fracture-toughness data. The effect of structural shape and the effects of residual stresses are included in experimental fracture-toughness data. In the case of special-order production of huge welded structures (cranes, bridges, halls, boilers, pressure vessels) full-scale tests are extremely expensive and are not often used. Such well documented tests had been performed in the past on two models of the penstock for the reversible hydro-electric power plant in Bajina Bašta [1-4].
2. In order to assess a real strength of workshop-quality welded joints, large, welded precracked specimens are tested in pure tension. These specimens, known as wide plates (WP), belong to the group of large-scale fracture-toughness specimens. The effects of residual stresses, always present in the non-stress relieved welded joints, are similar to those in welded structures if base metal thickness and welding technology are the same.
   Some WP tests were recently conducted in the brittle-to-ductile fracture transition-temperature range on a single-bevel, K butt-welded joint in a HSLA structural steel [5-7].
3. Small-scale fracture-mechanics specimens are usually used to assess the apparent fracture toughness of different zones in welded joints. Some of those specimens are standardised; others are not. The size of standardised specimens depends on welded joint thickness. Specimens are easy to prepare, the experiments are simple, quick and cheap, and loadings are low; just opposite to the situation described in both previous points. Unfortunately, the effect of residual stresses is practically absent from fracture-toughness data due to limited size of the sampled welded joint. Residual stresses are almost totally removed during welded joint cutting and specimen machining.

For the study of the properties of the heat-affected-zone (HAZ), the welded joint shape can be specially designed to allow the test of particular HAZ sub-zone. Single-bevel welded joints are appropriate because the crack tip can be positioned in the interesting HAZ sub-zone across the weld-joint thickness. The so-called composite notch is used for fracture-mechanics specimens of double-bevel, X, or V butt-welded joints. So obtained joint weakest link is presented in [8]. This type of specimen is also suitable to test fracture properties of simulated microstructure of welded joints.

2. THERMAL CONDITIONS IN WELDING PROCESS

Structural steels belong to polycrystalline metals. In general, properties of polycrystalline metal depend on its microstructure. Microstructure is a function of chemical composition, thermal history, and starting microstructure. The same situation is with different zones of welded joints in steels.

Each fusion welded joint consists of two materials: the weld metal (WM) and HAZ, whereas, WM is solidified mixture of fused filler and base metal (BM) if welding with consumable electrodes is applied. HAZ is actually BM in which the microstructure is altered due to the welding thermal effect. Fusion line defines the limits of both materials (Fig. 1).

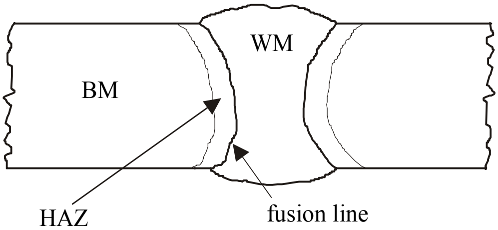

Figure 1. Specific zones in a fusion welded joint (BM, WM, and HAZ)

Joining by fusion welding can be performed either in a single run (single pass welding) or using two or more passes to realize the joint (double- or multi-pass welding).

In case of single pass welding, the microstructure of the weld metal is more or less uniform, but the microstructure of HAZ depends on the peak temperature of the thermal cycle and its cooling time. The heating sequence of welding cycle is not important, whilst the sequence of the highest temperatures and the cooling sequence, especially the cooling rate, are decisive for the final microstructure. The first and second sequences have effects on grain growth while the second and third sequences – on the micro-constituents that have been formed [9]. Cooling rate for carbon structural steels is usually expressed as $\Delta t_{8/5}$. This is the cooling time in the temperature range 800–500°C when austenite decomposes into microconstituents stable at lower temperatures.

The expressions from reference [10] were used to design appropriate cooling sequence at a particular point in the vicinity of the heat source during seam welding. Three-dimensional heat flow is assumed.

For defined $\Delta t_{8/5}$ and temperature of the material T_0 (either ambient/preheating temperature or inter-pass temperature) an appropriate net heat input, Q, is calculated as:

$$Q = \frac{2\pi\lambda\Delta t_{8/5}}{\dfrac{1}{500 - T_0} - \dfrac{1}{800 - T_0}} \tag{1}$$

where λ is the thermal conductivity.

If the peak temperature of the thermal cycle caused by welding, T_p, is fixed, the distance R from the point in the HAZ to the line where the heat source is travelling during a weld-pass deposition can be calculated as:

$$R = \sqrt{\frac{2Q}{\pi e \rho c (T_p - T_0)}} \tag{2}$$

where c and ρ are the heat capacity and the density, respectively.

Thus, for the known R, Q and T_0, the temperature course in the cooling sequence of the thermal cycle was designed for use on a computer-controlled thermal cycle simulator as:

$$T(t) = T_0 + \frac{Q}{2\pi\lambda t} e^{-\frac{R^2}{4Dt}} \tag{3}$$

where D is the diffusivity and t is the time.

Microstructure of the former single cycle zones can be retransformed in the case of multi-pass welding. Subsequent thermal cycles that reheat these materials over Ac_1 temperature represent the newest thermal history. Microstructure of the weld metal and HAZ in the vicinity of those weld passes is therefore changed and the properties are now different (Fig. 2).

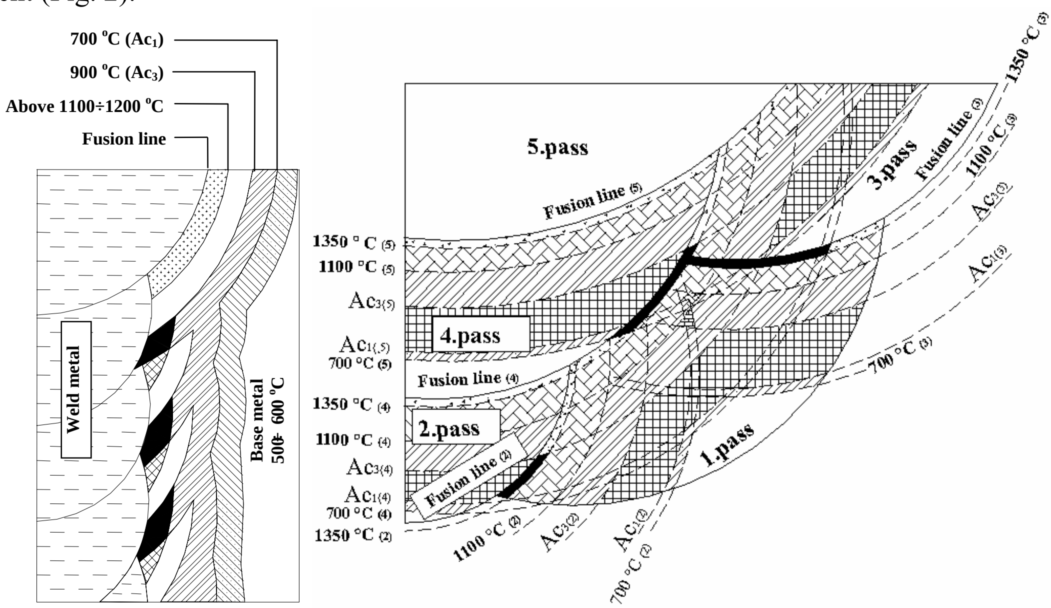

Figure 2. Different zones formed in the heat-affected-zone (left) and in the weld metal (right) of a multi-pass welded joint, therefore having different properties

3. SIMULATIONS AND MICROSTRUCTURE EVALUATION

Different shapes of samples have been used on different simulators: cylindrical samples on Gleeble simulators (Fig. 3a [11]), rectangular ones on Smitweld simulators. A thermocouple is leant against the sample or welded to it in its mid-length. Type of thermocouple is chosen according to its resistivity against the highest temperature of the thermal cycle applied and its duration.

Dilatation can be measured during the thermal cycles. Combining the results of dilatation curves analysis and of metallographic examination, continuous-cooling-transformation time (CCT) diagrams can be designed. They are valid under welding conditions.

The material for simulation is cut from steels (BM) and welded joints (WM). An example of the single-pass WM sampling, prepared for simulation is shown in Fig. 4 [12].

Samples of the base metal or single cycle weld metal are heated to temperature T_p, that should be below the melting point of the material concerned, as rapid as necessary (the highest heating rate depends on the simulator's capacity) and then cooled immediately or after some delay. Immediate cooling is typical for real welding. Holding at peak temperature for a few seconds is convenient for deeper metallurgical studies because effects of heating by welding are in this way much more clear and more stressed. The consequence of such a weld thermal cycle simulation in the limited length of the specimen mid-part is a uniform microstructure over the whole cross-section of the sample (Fig. 3b [11]).

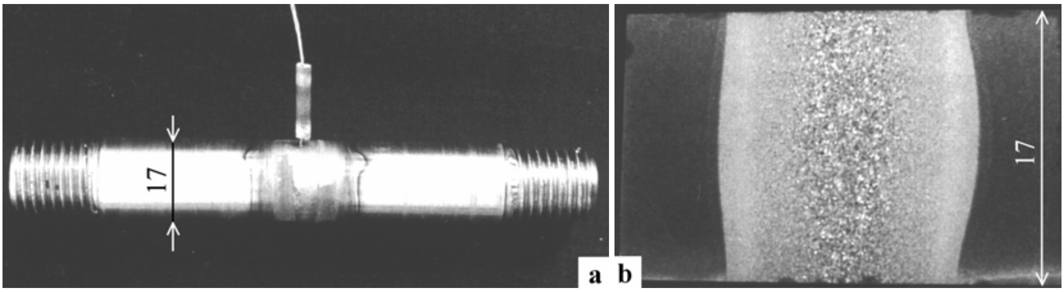

Figure 3. Sample with a simulated microstructure of HAZ (a).
Macrograph made in the middle of the sample (b).

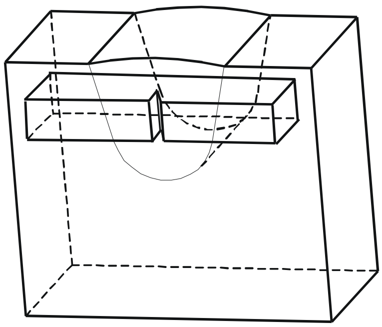

Figure 4. Sample with the starting microstructure of the weld metal

Two examples of welding simulation performed on thermal cycle simulator are shown in Fig. 5. Both diagrams show thermal conditions close to the fusion line, where during welding the temperature attained almost melting point of the steel Nionicral 70 at least once. The T_p exceeded 1350°C during single thermal cycle. Coarse grain HAZ is formed (CGHAZ). During the double thermal influence, the T_{p1} exceeded 1350°C too, but then the T_{p2} (peak temperature of the subsequent weld pass) attained the temperature range in-between Ac_1 and Ac_3 temperatures (780°C). Dilatometric curves are recorded. Their analysis show at which temperatures austenite begins to decompose (indexes *s*) and at which temperature the decomposition is finished (indexes *f*). In Fig. 5, *M* means martensite, whilst *B* means bainite.

Continuous-cooling-transformation diagrams represent the microstructure that will form during welding at different distances from the fusion line at different cooling rates. Chemical composition and peak temperatures are already taken into account.

An example of CCT diagrams in the region of the coarsest grain is shown in Fig. 6 for two different steels: HSLA steel Nionicral 70, and StE 355 Ti, fine-grained steel, micro-alloyed with Ti. The first CCT diagram is taken from Ref. [13] whilst the second one from Ref. [14]. Both diagrams are valid under welding conditions for CGHAZ, since the temperature of thermal cycles exceeded at least 1350°C, and cooling corresponds to real welding. Such a thermal cycle is shown in the upper diagram in Fig. 5.

The microstructure of CGHAZ at higher cooling rates (shorter $\Delta t_{8/5}$) in Nionicral 70 is martensitic (Fig. 6–left). At medium rates the bainitic-martensitic microstructure is found in the CGHAZ. As longer is $\Delta t_{8/5}$, the proportion of bainite in CGHAZ is greater. At very slow cooling ($\Delta t_{8/5} \geq 400$ s) smaller portion of ferrite is already present in the predominantly bainitic microstructure of CGHAZ. All is reflected in the Vickers hardness of formed microstructure (numbers in circles). Maximum hardness of martensitic CGHAZ depends on the carbon content of steels. It can be calculated (C ≅ 0.09%) as,

$$HV_{\max} = 802 \times \%C + 305 \tag{4}$$

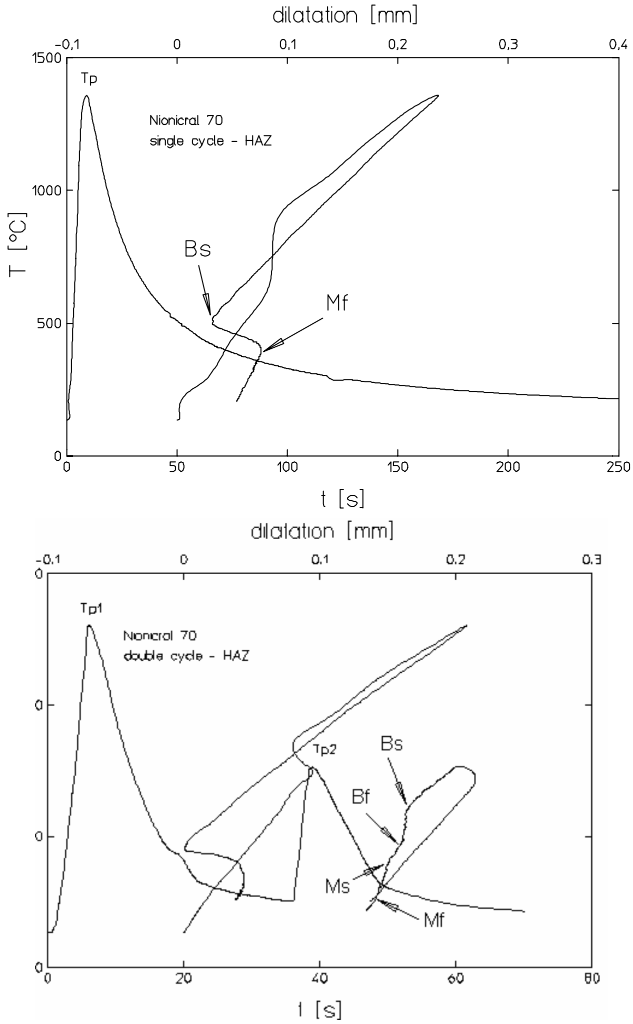

Figure 5. Thermal conditions at fusion line simulated for single-(top) and double-pass welding (bottom)

For the steel StE 355 Ti, the obtained CCT diagram is different (Fig. 6–right). This can be attributed to significant differences in chemical compositions of these two steels and the effect of applied manufacturing technologies.

An example of CCT diagrams for two different zones in double-cycle HAZ at the fusion line valid under welding conditions is shown in Fig. 7 [13]. In the first thermal cycle the microstructure of CGHAZ is formed. The applied maximum temperature of the subsequent thermal cycles exceeded Ac_3 temperature ($T_{p2} \cong 955$°C), left diagram in Fig. 7, and attained temperature range Ac_1–Ac_3, right diagram in Fig. 7. Cooling corresponds to real welding. At higher cooling rates, martensitic HAZ will hardly exist if $T_{p2} \cong 955$°C and will never exist if $T_{p2} \cong 780°C$. Bainite in both double-cycle HAZs is formed at shorter $\Delta t_{8/5}$ than in CGHAZ (Fig. 6–left). Smaller portion of ferrite is already present at much higher cooling rates than in the case of CGHAZ. All this is reflected in Vickers hardness of formed HAZs (numbers in circles). The obtained CCT diagram that corresponds to $T_{p2} \cong 780°C$ is valid only for the retransformed part of the former CGHAZ. The rest of microstructure is tempered former single cycle CGHAZ.

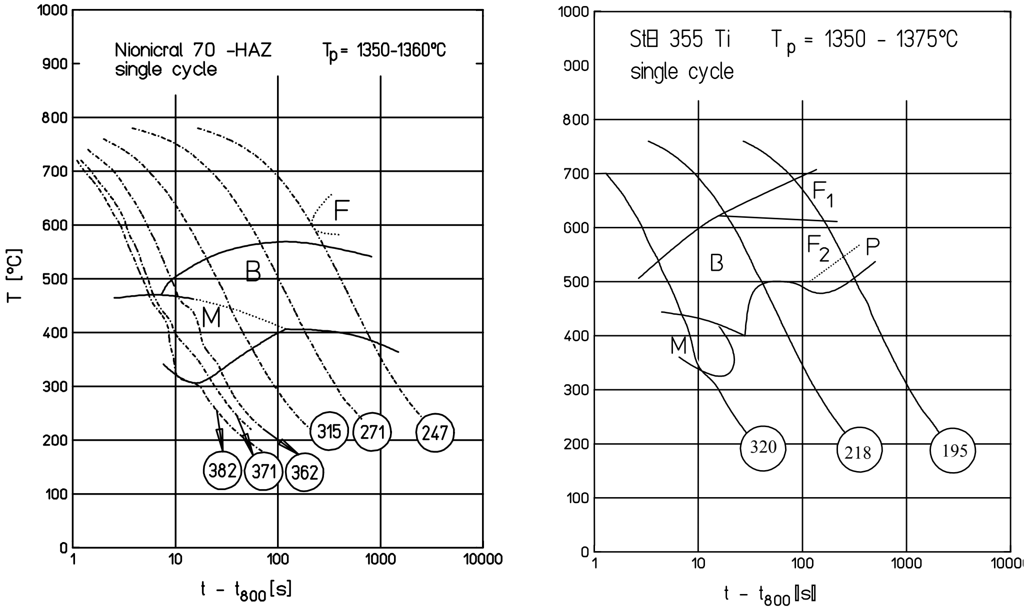

Figure 6. Continuous-cooling-transformation (CCT) diagrams valid for CGHAZ of two steels: HSLA steel Nionicral 70 (left) and StE 355 Ti, fine-grained steel, microalloyed with Ti (right)

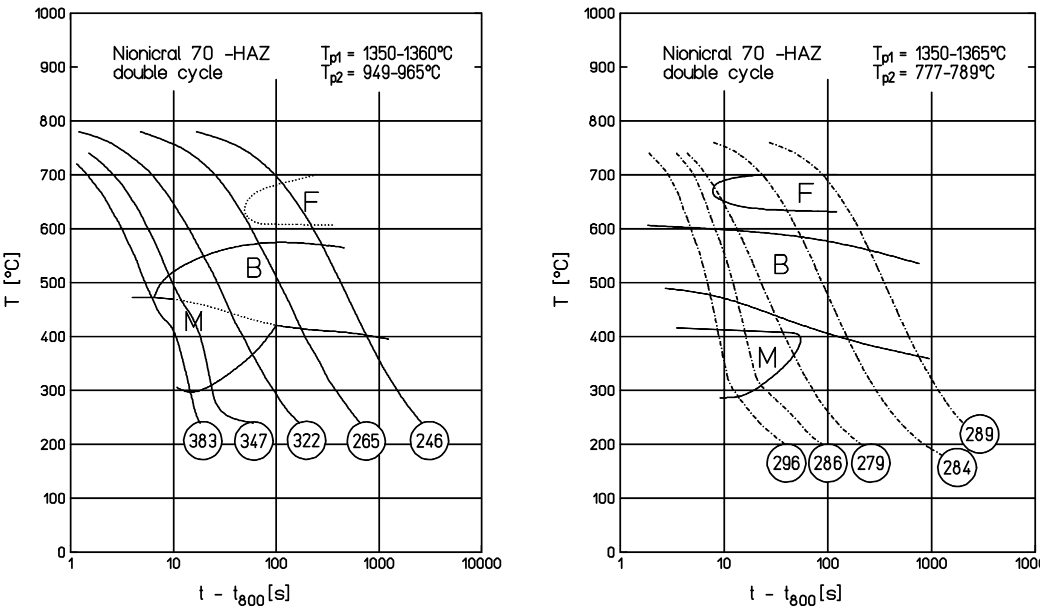

Figure 7. Continuous-cooling- transformation (CCT) diagrams valid for different double-cycle heat-affected-subzones close to fusion line of HSLA steel Nionicral 70. Due to differences in peak temperatures T_{p2} the microstructures are not the same.

4. MECHANICAL PROPERTIES OF SIMULATED MATERIAL

Hardness of the simulated microstructure is not difficult to measure. Actual hardness data are available from real welded joints, too. Brinell hardness of a single cycle HAZ for HSLA steel Ninonicral 70 is shown in Fig. 8–left [13]. Peak temperature, $T_p \cong 700°C$ represents Ac_1 temperature of the steel, whereas T_p approaching 1400°C represents the zone close to the fusion line. The hardest is the CGHAZ. Impact toughness of the same HAZ as that in Fig. 8–left, is shown in Fig. 8–right [13]. The hardest zone of HAZ, i.e. the CGHAZ, has the lowest toughness.

It is an easy task to determine impact toughness on simulated microstructures. Size of the sample is so defined that standard Charpy specimens can be machined. The region with the simulated microstructure is a few millimetres long and located in the middle of the sample, and the V-notch can be positioned at this point (Fig. 9–left). As an example, Charpy impact toughness vs. temperature (S curve) for the simulated microstructure of a CGHAZ of HSLA Nionicral 70 steel [15] is shown in Fig. 9–right.

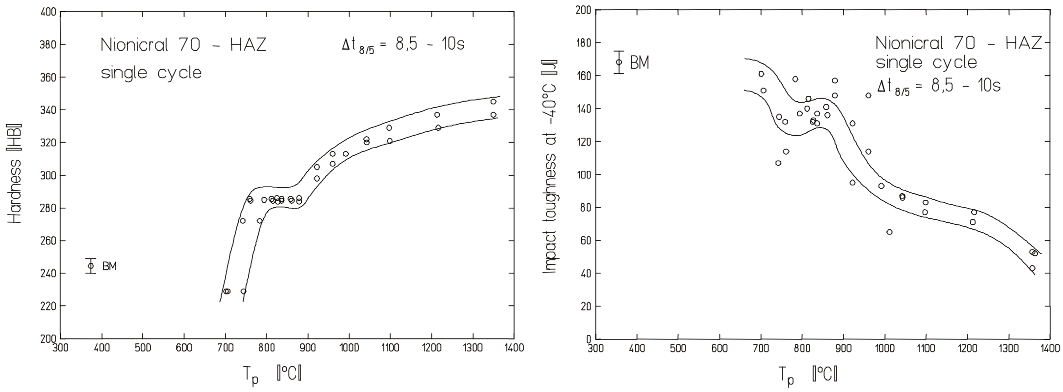

Figure 8. Hardness HB (left) and V notch Charpy impact toughness at –40°C (right) for specimens, simulated at different temperatures T_p, meaning across the whole width of the HAZ

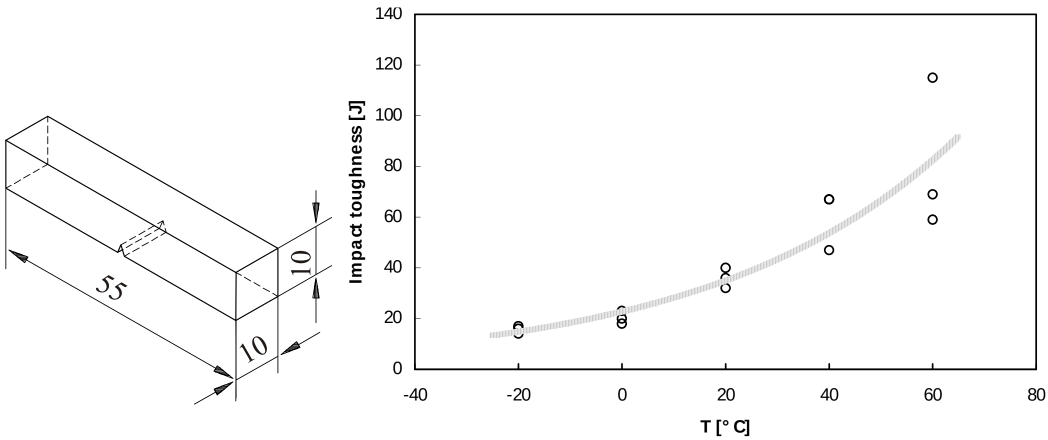

Figure 9. Charpy specimen machined from the sample with simulated microstructure of the CGHAZ (left), and its S-curve (right)

The relation between impact toughness and cooling rate can be studied as shown in Fig. 10–left for HSLA Nionicral 70 steel, and the relation between impact toughness and peak temperature of subsequent thermal cycle, as shown by an example for the same steel, in Fig. 10–right [13].

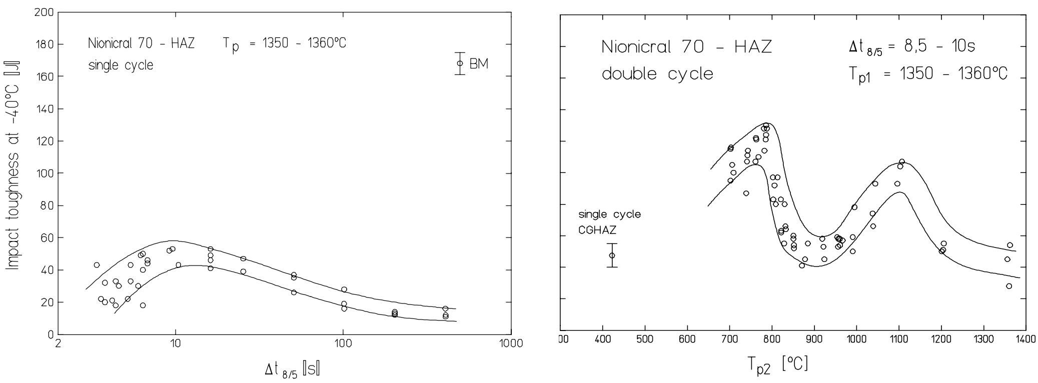

Figure 10. Impact toughness against $\Delta t_{8/5}$ for a single cycle CGHAZ (left), and against T_{p2} for HSLA structural steel Nionicral 70 (right). Double-cycle HAZ was previously CGHAZ.

Measurement of mechanical properties (yield strength and ultimate tensile strength) and rheological material properties of different zones of welded joints is pretty complicated. Standard gauge-length of tensile specimen has be at least 10 times longer than the diameter. Simulated microstructure exists only in the middle of the sample, therefore some adapted tensile specimens should be used. An experimental set-up is sketched in Fig. 11.

Hourglass-shaped specimens were used in reference [13]. The load, F, the load-line displacement, Δl, and circumference, πD, had been measured during specimen loading. Change of circumference can be used for the determination of decreasing cross-section diameter D. The circumference enabled calculating true strain during tensile testing, because standard strain measurement in the longitudinal direction of the specimen is not possible here.

The diagram with load (F) transformed into engineering stress (σ_0) versus load-line displacement (Δl) enabled determining ultimate tensile stress, R_m, if the value σ_{0m} is known. Fracture stress, σ_f, is expressed by σ_{0f} (Fig. 12–top). The engineering strain (ε_0) is calculated via change of specimen's current diameter, D , and yield stress, $R_{p0.2}$, on the basis of $\sigma_{0p0.2}$ (Fig. 12–bottom).

Strength coefficient A and plastic strain exponent n are determined using logarithmic dependence of true stress against true strain (Fig. 13).

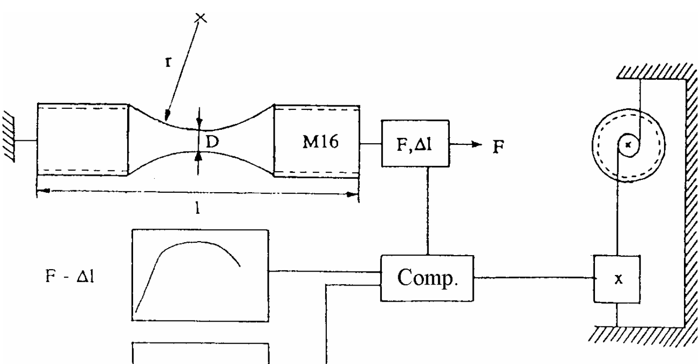

Figure 11. Experimental determination of mechanical and rheological properties of material with the simulated microstructure

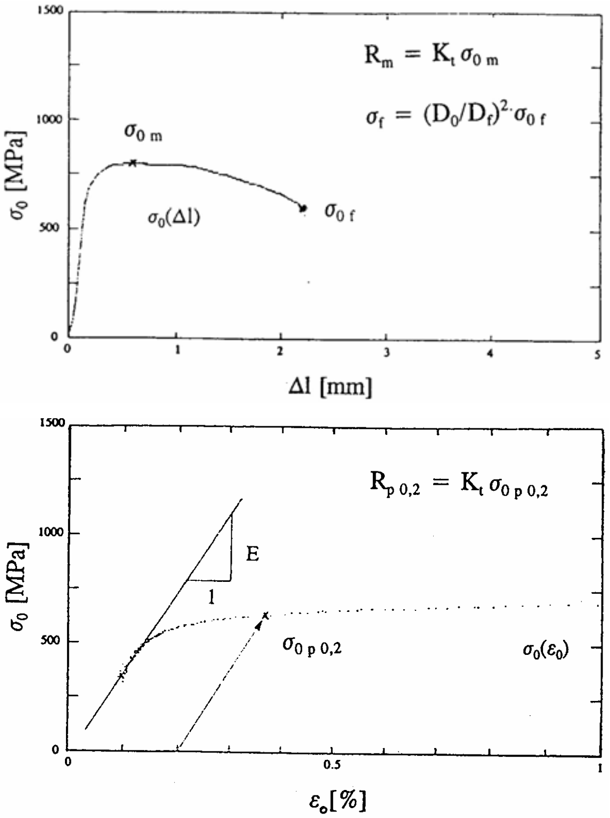

Figure 12. Engineering stress σ_0 versus load-line displacement Δl diagram (top), and engineering stress σ_0 versus engineering strain ε_0 diagram (bottom)

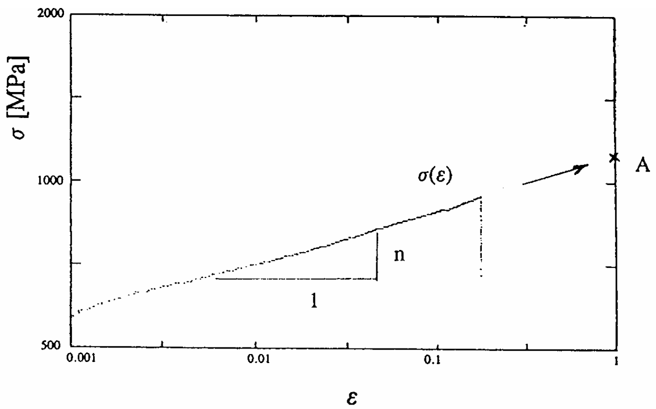

Figure 13. Logarithmic dependence true stress–true strain for determination of strength coefficient A and plastic strain exponent n

5. FRACTURE PROPERTIES OF SIMULATED MATERIAL

Two types of precracked small-scale fracture toughness specimens were used to determine fracture properties of simulated microstructures that can be found in welded joints: round tensile and three-point-bend specimens, presented in Fig. 14.

The reachable size of specimen actually depends on the heating and cooling capacity of the used simulator. Therefore, specimens made from samples with simulated microstructure of the appropriate sub-zone of the weld are hardly large enough for standard testing of fracture toughness K_{Ic} [16,17].

Only provisional fracture toughness values are available when specimens do not fulfill the size criteria in standards which depend on fracture and mechanical properties of the tested material. The only exceptions are the extremely brittle sub-zones of welded joints.

Otherwise, adequate methods should be introduced to evaluate either the provisional fracture toughness data or original experimental diagrams. These approaches are of greatest interest because just the most brittle sub-zones are decisive for the integrity of the whole welded structure.

When simulation is performed, the prepared microstructure exists only at the mid-length of the samples. The crack should be positioned there. Besides, fracture toughness should not be influenced by crack preparation.

The round tensile specimens $\phi 10\times 120$ mm (Fig. 14–left) were circularly machine pre-notched to 1.5 mm in the region of the simulated microstructure of HAZ. The specimens were loaded by rotational bending to produce approximately 2 to 2.5 mm deep ring-shaped fatigue pre-cracks. Minimum to maximum cycle loading ratio $R = -1$ was applied. The maximum stress intensity factor, $K_{\max}$, was kept below 70% of the minimum expected K_{Ic} [18], which could be measured using a specimen with $D = 10$ mm. $K_{\max}$ was established as:

$$K_{\max} = 0.7K_{Ic} = 0.7\sqrt{\frac{D}{1.5}} \times R_p{}^{app} = 0.0572 \times R_p{}^{app} \tag{5}$$

The approximate yield strength, $R_p{}^{app}$, was determined from hardness data using formulas from [17]. The $R_p{}^{app}$ and K_{max} values in Eq. (5) are expressed in MPa and in MPa·m$^{1/2}$, respectively. The final proportion of the net-to-gross diameter of the specimen was 0.5 to 0.6.

Tensile specimens were loaded up to fracture. If diameter D fulfilled the condition given in [18], plane-strain fracture toughness, K_{Ic}, would be expressed by using the following relation:

$$K_I = \frac{F}{\pi d^2}\sqrt{2\pi d}\left[1 + \frac{1}{2}\frac{d}{D} + \frac{3}{8}\left(\frac{d}{D}\right)^2 - 0.363\left(\frac{d}{D}\right)^3 + 0.731\left(\frac{d}{D}\right)^4\right]\sqrt{1 - \frac{d}{D}} \tag{6}$$

Two different F–LLD (Δl) diagrams recorded by fracture toughness testing are shown in Fig. 15 [19]. The left one is linear and enables direct K_{Ic} determination, whilst the right one is not valid for K_{Ic} determination, according to standards.

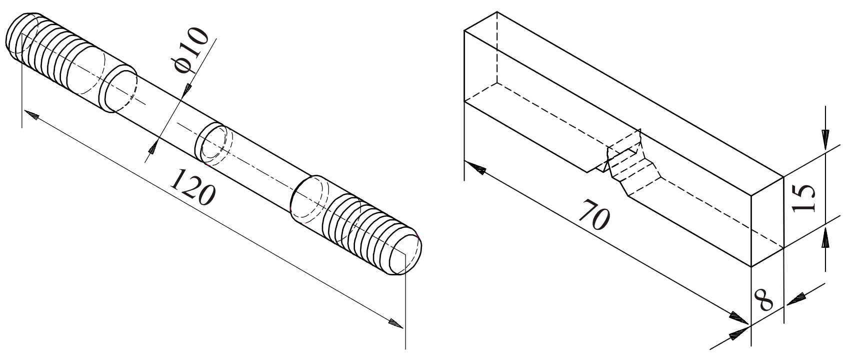

Figure 14. Round tensile specimen (left), and three-point-bend specimen (right)

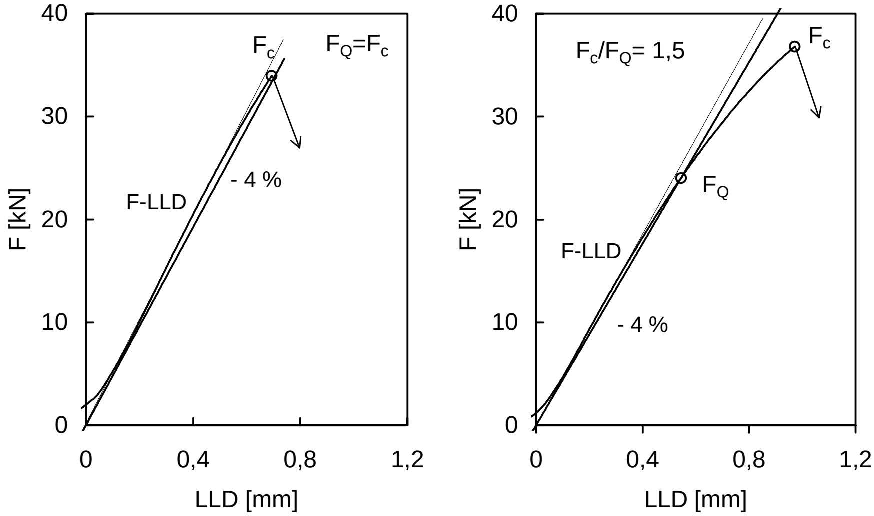

Figure 15. Acceptable linear (left), and non-linear *F–LLD* (Δl) diagrams. Only acceptable linear behaviour can be used for plane-strain fracture toughness K_{Ic} determination

The three point bend specimens, 8×15×70 mm in size (Fig. 14–right), were machine pre-notched for 5 mm on one side in the region of the simulated microstructure. The specimens were loaded using repetitive bending at a loading ratio $R \leq 0.1$ to form fatigue pre-crack 2.5 mm in crack length to width ratio a/W of about 0.5. The maximum stress-intensity factor, K_{max}, during precracking that ensures a negligible influence on fracture toughness was determined according to the standard in reference [20].

Specimens can be loaded up to fracture (Fig. 15), or during stable crack growth with significant pop-in effect (Fig. 16–left) or, even beyond maximum load F_m (Fig. 16–right) [13].

In case of stable crack growth, the single specimen method can be used by applying the potential drop method (Fig. 17–left) [13], or compliance measurement technique (Fig. 17–right) [21].

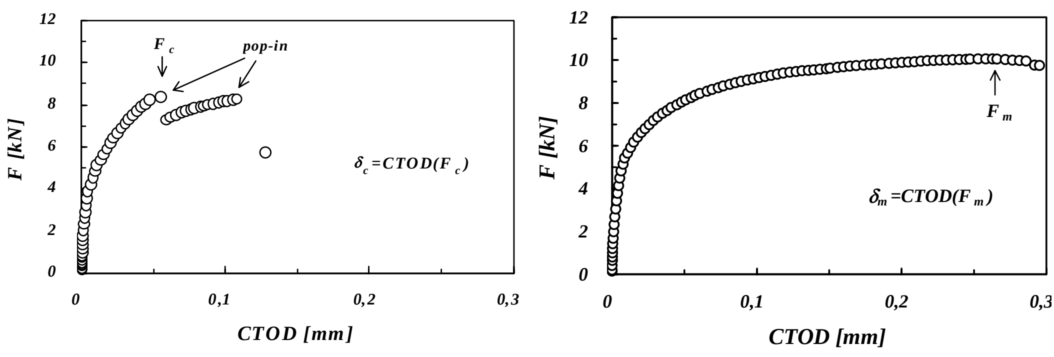

Figure 16. Fracture mechanics experiments: quasi-brittle fracture initiation occurred, expressed by typical pop-in (left); stable-crack growth, with expessed plastic behaviour (right)

An appropriate crack tip opening displacement (CTOD) value (δ_i, δ_c or $\delta_{0.2}$) can be calculated after determined position of crack initiation (F_i), as follows [20]:

$$\delta = \frac{(1-\mu^2)\,K^2}{2R_pE} + \frac{0.4\,(W-a)}{0.4W+0.6a}\mathrm{CMOD}_p \tag{7}$$

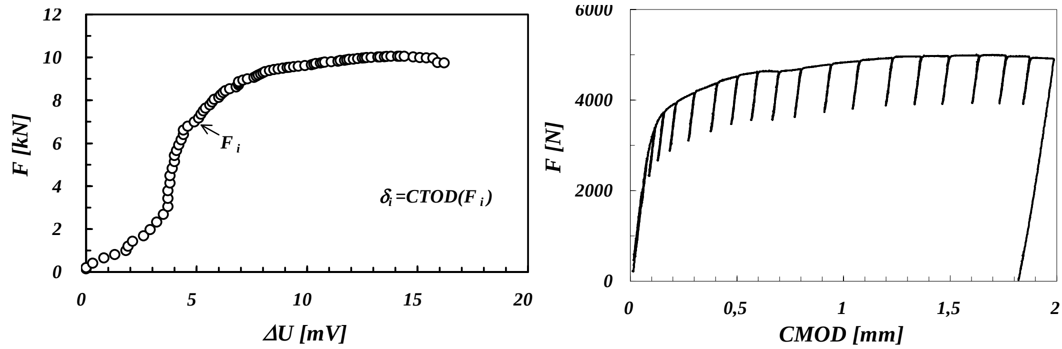

Figure 17. Detection of crack initiation by the potential drop method (left), and the compliance method (right)

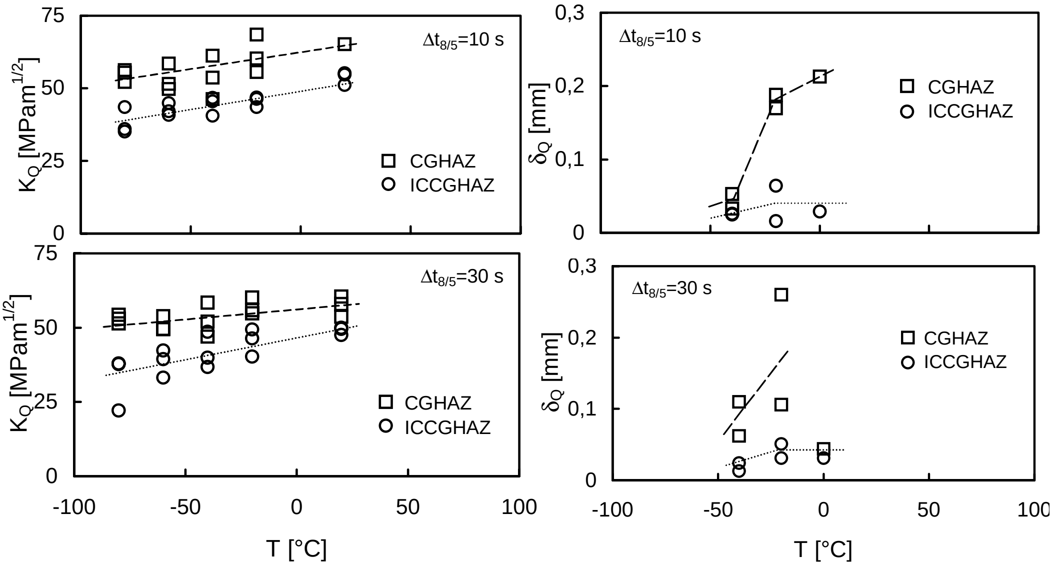

Figure 18. Provisional stress intensity factor, K_Q, determined on round tensile specimens (left), and provisional crack-tip opening displacement, δ_Q, determined on three-point-bend specimens (right), for $\Delta t_{8/5}$ = 10 s (above) and for $\Delta t_{8/5}$ = 30 s (below)

Series of tests were performed at different temperatures on specimens shown in Fig. 14. In general, two HAZ sub-zones from welds in the HSLA structural steel Niomol 490K were treated [21]. The provisional fracture toughness results, K_Q, for round tensile specimens are given in Fig. 18–left, and δ_Q–values for three-point-bend specimens in Fig. 18–right. Mostly the size of specimens was not sufficient for K_{Ic} measurement, especially bend specimens, because the following conditions were not fulfilled:

$$D \geq 1.5\left(\frac{K_{\mathrm{I}c}}{R_p}\right)^2; \quad B \geq 2.5\left(\frac{K_{\mathrm{I}c}}{R_p}\right)^2 \tag{8}$$

where D and B are the round tensile specimen diameter [18], and the rectangular three-point bend specimen thickness [16], respectively, whereas R_p is the yield strength.

For further evaluation, the experimental force vs. load-line displacement diagrams (*F–LLD*) and force vs. crack-mouth opening displacement diagrams (*F–CMOD*) were adapted according to the equivalent-energy method, the idea described in reference [22] and shown in Fig. 19.

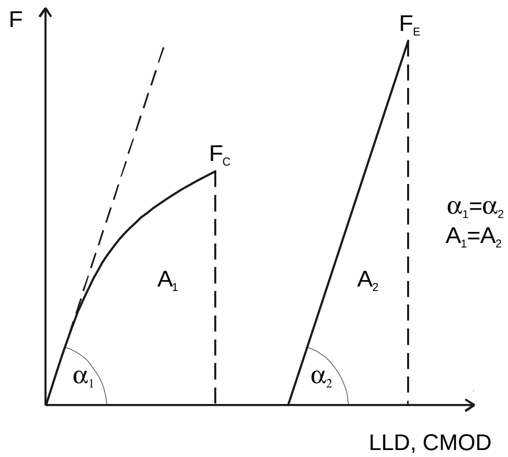

Figure 19. Recorded non-linear diagram up to fracture at F_c and the appropriate fictive linear diagram. The same deformation energy consumption is assumed. The fictive load F_E is looked for

The work necessary for brittle or quasi-brittle fracture of specimens was searched for. The fictitious critical load, F_E, is used to calculate the approximate fracture-toughness value K_{EE}:

$$F_E = \sqrt{2tg\alpha A_1} \; ; \quad K_{EE} = \frac{YF_E}{B\sqrt{W}} \tag{9}$$

where the area under the actual diagram, A_1, represents the work done to the specimen up to fracture, and angle α is initial slope of the diagram. The equality of areas A_1 and A_2 is assumed; B and W are specimen dimensions, whilst Y is the compliance factor depending on a/W ratio.

The result of final evaluation is shown in Figs. 20 and 21 [21].

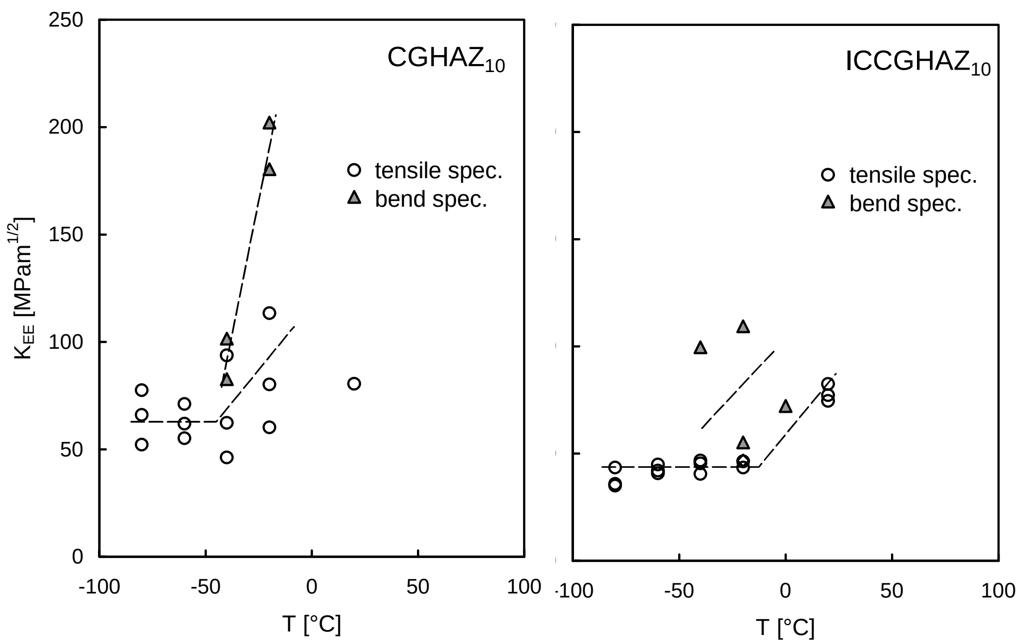

Figure 20. Approximate fracture toughness values K_{EE} of $CGHAZ_{10}$ and $ICCGHAZ_{10}$

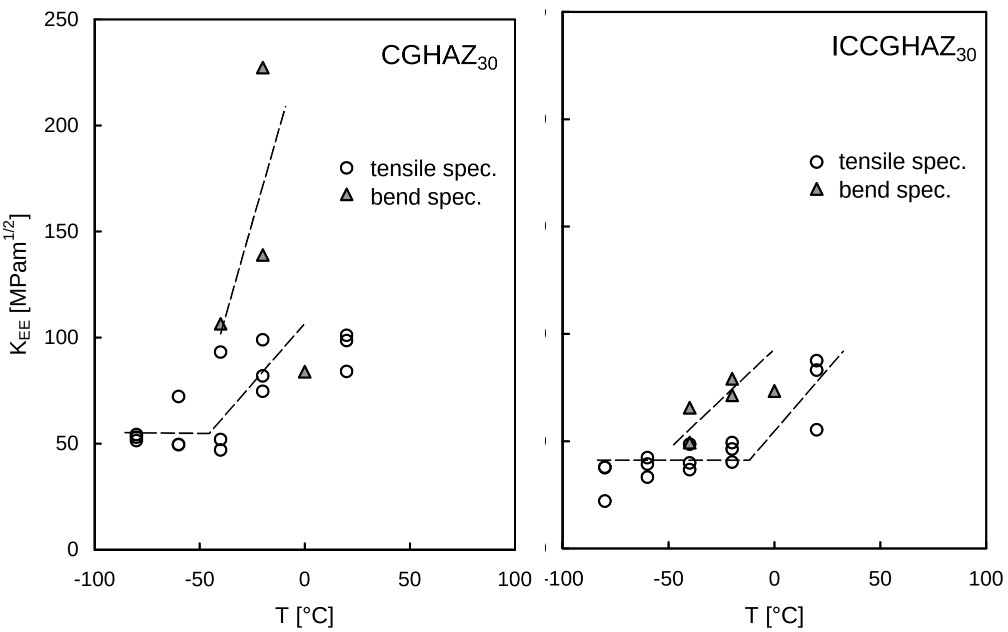

Figure 21. Approximate fracture toughness values K_{EE} of $CGHAZ_{30}$ and $ICCGHAZ_{30}$

The K_{EE} values of both ICCGHAZs agree fairly well across the whole temperature range of CTOD testing (–40 to 0°C). The agreement between K_{EE} values of both CGHAZs is acceptable only at –40°C, but not at higher temperatures. However, values in Figs. 20 and 21, which are derived from diagrams recorded by CTOD testing, are in general, in spite of adaptation, less optimistic than the others. The reason is the characteristic geometry of both fracture toughness specimens.

Experimental fracture toughness results are always influenced by plastic zone size, irrespective of the degree of non-linearity of *F–LLD* diagrams. In case of perfectly linear diagrams, the developed plastic zone size is limited and the influence is almost negligible. Nevertheless, the effect of the same size of plastic zone is higher on tensile specimens than on three-point bend specimens. The reason is the actual size and the peculiarity of circular cross-sections in comparison with rectangular ones. The size of the net cross-section of both specimens depends on the size of the pieces of steel that can be prepared on simulators and on the specimens' shape.

When a limited, but not a negligible, plastic zone is developed, another approach is available for the evaluation of material fracture toughness; this is known as plastic zone correction method [23]. The plastic zone size assessed at the moment of fracture is added to the actual crack length. A more realistic fracture toughness is calculated according to the usual formulae. By using a crack length correction, the specimen cross-section is fictitiously reduced.

An increase in crack length changes the specimen cross-section. The consequence of the plastic zone development results in a reduction of net diameter, d, of tensile specimens with a round cross-section, and of the net width (ligament), $W - a$, of specimens with a rectangular cross-section. The increase in crack length is approximated simply with the plastic zone size, r_y, since $r_y << d$ and $r_y << W - a$. However, the relative cross-section reduction for both types of specimens is not the same, despite the same plastic-zone size and the same stress state. The expression for round tensile specimens is shown in Eq. (10) whereas for three-point-bend specimens in Eq. (11).

$$S = \frac{\pi d^2}{4} \quad \rightarrow \quad \frac{dS}{S} = -\frac{4r_y}{d} \tag{10}$$

$$S = B(W-a) \quad \rightarrow \quad \frac{dS}{S} = -\frac{r_y}{W-a} \tag{11}$$

Taking into account actual dimensions of both types of specimens ($5 \leq d \leq 6$ mm and $W - a \cong 7.5$ mm) the ratio of relative cross-section reductions is:

$$\frac{dS}{S}_1 : \frac{dS}{S}_2 = \frac{4(W-a)}{d} = 5 \text{ to } 6 \tag{12}$$

The effect of plastic zone size on experimentally determined fracture toughness would be 5 to 6 times higher on tensile specimens than on three-point bend specimens. Actually, results at –40°C agree better than shown in Figs. 20 and 21. The discrepancy at higher temperatures is more significant.

The final result is that both types of small-scale fracture mechanics specimens are useful for assessing fracture toughness if fracture toughness is extremely low, i.e. whenever embrittlement caused by welding finds expression in a very low fracture toughness of the HAZ.

6. FATIGUE PROPERTIES OF SIMULATED MATERIAL

Two types of specimens were used to determine some fatigue properties of simulated microstructure found in HAZ of welded joints. They are shown in Fig. 22.

Simulated microstructure exists at the mid-length of the samples. The appropriate shape of specimens and the type of loading must be taken into consideration. Strength of HAZ can be higher than the strength of the base metal. In general, fatigue properties increase with strength. Relevant fatigue properties will be available only if the fatigue process takes place in the mid-length of the specimen.

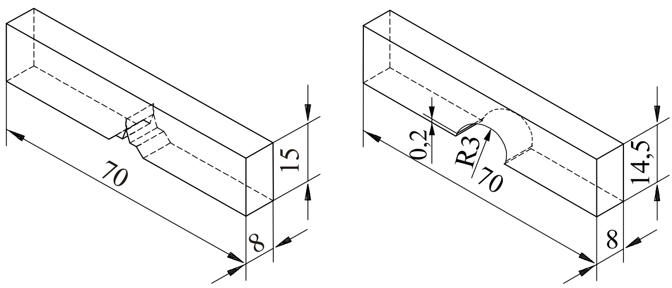

Figure 22. The appropriate specimen for measurement of fatigue crack propagation rate (left), and for the endurance limit (right) in HAZ

Single-edged specimens were used to determine fatigue crack propagation rate in the materials of simulated microstructure. Specimens were loaded in pure bending on resonant loading machine. The obtained propagation rate, da/dN, determined for two different CGHAZs vs. stress intensity range, ΔK, is shown in Fig. 23–left [13].

A notch 3.2 mm deep with radius $R = 3.0$ mm causes stress concentration with factor $K_t = 1.74$ [24,25], the level encountered in real welds [26]. The notched specimens were used for experimental determination of endurance limit. Surfaces at the bottom of the notch were either smooth or weakened with Vickers indentations. They actually modelled surface defects, of the size comparable with the size of grains in CGHAZ. An example of the endurance limit, $\Delta\sigma_{eBn}$, against the cooling time, $\Delta t_{8/5}$, is shown in Fig. 23–right [13].

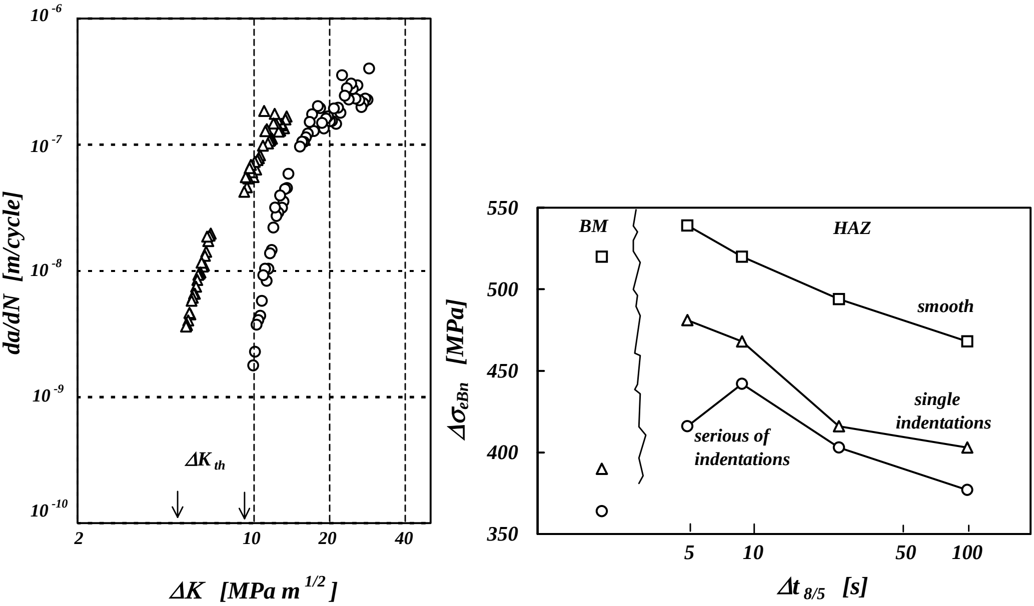

Figure 23. The fatigue crack propagation rate (left), and three courses of the endurance limit

Two types of surface defects were considered: single Vickers indentations and series of Vickers indentations. The size of each indentation was either $d \cong 110\ \mu m$ or $d \cong 220\ \mu m$. Both kinds of artificial defects are schematically presented in Fig. 24–left [27,28]. Equivalent geometrical parameters (EGP) of these artificial defects were calculated. Defect size and stress gradient were also taken into account [13]. They are shown in Fig. 24–right.

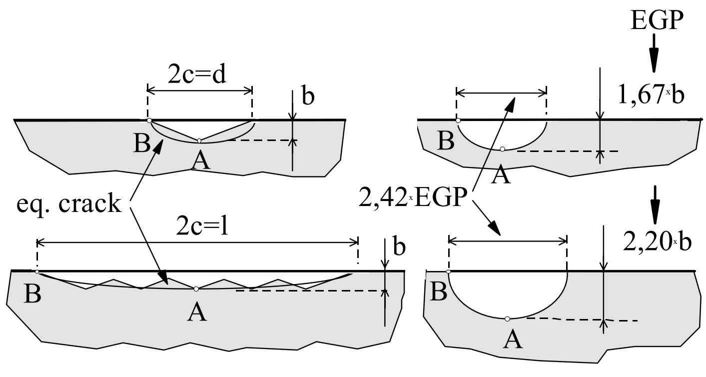

Figure 24. Single (upper left) and series of Vickers indentations (left down) used as artificial surface micro-defects and appropriate designed equivalent geometrical parameters (EGP) that describe the effect of defects on fatigue strength (right)

Experimentally determined fatigue strength, i.e. endurance limit of materials, of twelve different structures found in HAZ, from both single cycle CGHAZs and double cycle HAZs that initially, after the first cycle were CGHAZs, are presented in Fig. 25 [13,28] in double logarithmic coordinates. Endurance limit of simulated HAZ with the sizes of defects at the right side of the diagram resembles the influence of long cracks. The slopes approach one half, which is typical for linear elastic fracture mechanics.

In order to consider the significance of material strength for fatigue behaviour, the threshold stress intensity factor range is normalised with the strength of the material.

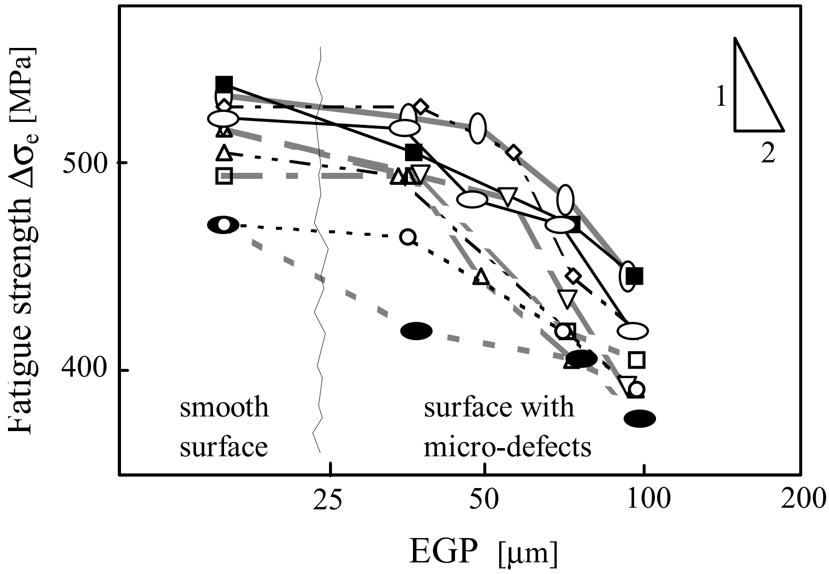

Figure 25. The fatigue strength for twelve different structures in HAZ

The final conclusion of this research was that the threshold stress intensity factor range, ΔK_{th}, of discussed HAZ zones depend on their ultimate tensile strength, R_m, and on the size of artificial defects expressed by EGP. Their relations are expressed by two empirical formulas: in Eq. (13) the Goodman criterion is applied, whereas in Eq. (14) the criterion of Gerber is used,

$$\Delta K_{th} = (1.20 \times 10^{-3} R_m + 0.485)\,\mathrm{EGP}^{0.35} \tag{13}$$

$$\Delta K_{th} = (1.13 \times 10^{-3} R_m + 0.730)\,\mathrm{EGP}^{0.33} \tag{14}$$

The effect is clearly shown in Fig. 26.

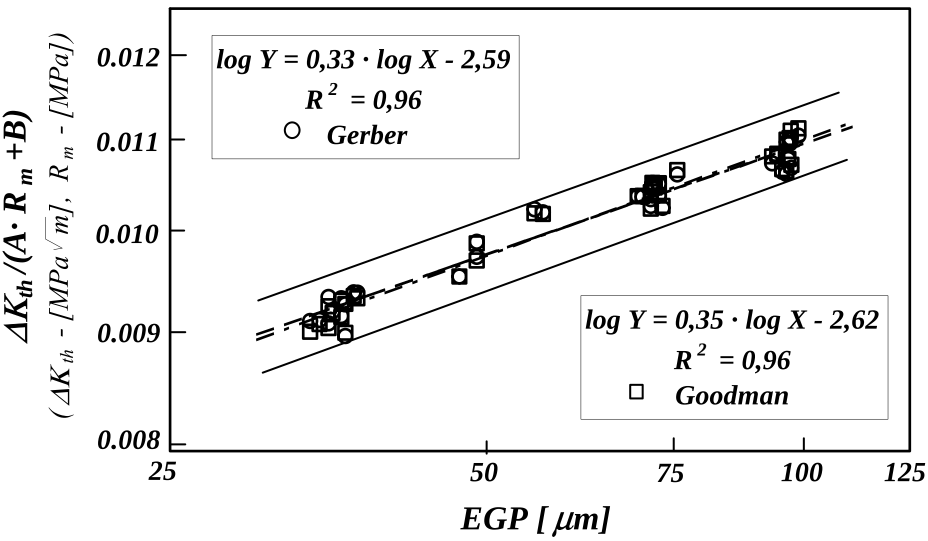

Figure 26. The threshold stress intensity factor range normalised with the strength of the material

REFERENCES

1. Grabec, I., Mužič, P., Kuder, J., Gliha V., *Use of Acoustic Emission in Testing Strength of Welded Structures*, Strojniški vestnik, 24 (3-4), pp. 1-11. (1978)
2. Gliha, V., Kuder, J., Rak, I., Grabec, I., *Kritičnost uniformiranih ravninskih diskontinuitet na modelu visokotlačnega cevovoda RHE Bajina Bašta (Critical state of uniform planar discontinuities on the model of high pressure penstock RHE Bajina Bašta)*, Strojniški vestnik, 26 (7-8), pp. 160-169. (1979)
3. Sedmak, S., Sedmak, A., *An Experimental Investigation into the Operational Safety in a Welded Penstock by a Fracture Mechanics Approach*, Fatigue Fract Eng M, 18 (5), pp. 527-538. (1995)
4. Kuder, J., Raztresen, J., Rak, I., Gliha, V., *The Use of Fracture Mechanics and Model Testing for Assurance of the Safety of Penstocks*, Welding in the World, 27 (1/2), pp. 19-35. (1998)
5. Rojko, D., *Določitev lomne žilavosti na velikih preizkušancih in primerjava lomne žilavosti na standardnih preizkušancih*, Univeza v Mariboru, Fakulteta za strojništvo, Magisterij, Maribor. (2000)
6. Gliha, V., Rojko, D., *The Pre-Cracking of Wide Plate Specimens*, International Journal of Pressure Vessels and Piping, in press
7. Rojko, D., Gliha, V., *The CTOD Testing using Wide Plate Specimens*, in preparation
8. Gubeljak, N., *The Fracture Behaviour of Specimens with a Notch Tip Partly in the Base Metal of Strength Mis-Match Welded Joints*, Int J of Fracture, 100, pp. 169-181. (1999)
9. Easterling, K., *Introduction to the Physical Metallurgy of Welding*, Butterworths. (1983)
10. Karlsson, L., *Thermal Stresses in Welding*, Thermal Stresses I, Edited by R.B.Hetnarski, Elsevier Science Publisher. (1986)
11. Vojvodič-Tuma, J., Rak, I., Vehovar, L., *Optimiranje varjenja jekla Niomol 490K za izdelavo zahtevnih konstrukcij*, Poročilo o projektu štev. L2-8538-0206-97/99, IMT Ljubljana. (1999)
12. Rojko, D., *Izoblikovanje mikrostruktur večvarkovnega zvara s stališča termičnega vpliva varjenja*, Univeza v Mariboru, Fakulteta za strojništvo, Doktorat, Maribor. (2003)
13. Gliha, V., *Analiza nosilnosti homogenih večvarkovnih zvarnih spojev pri utrujanju z ozirom na vplive parametrov varjenja in gradnje vara*, Univerza v Ljubljani, Naravoslovnotehniška fakulteta, Doktorat, Ljubljana. (1998)
14. Rak, I., Gliha, V., Koçak, M., *Weldability and Toughness Assessment of Ti-Microalloyed Offshore Steel*, Metallurgical and Materials Transactions A, 28A, January, pp. 199-206. (1997)
15. Gliha, V., Burzić, Z., Pašić, S., Manjgo, M., Vuherer, T., *Experimental analysis of resistance to the impact of heat affected zone of HSLA steel*, 2nd DAAAM International Conference on Advanced Technologies for Developing Countries – ATDC'03, Tuzla. (2003)
16. BS 7448-1: Fracture Mechanics Toughness Test, Part 1. Method for Determination of K_{Ic}, Critical CTOD and Critical J Values of Metallic Materials. (1991)
17. ASTM E 399-90: Standard Test Method for Plane-Strain Fracture Toughness of Metallic Materials. (1997)
18. Wei, S., Tingshi, Z., Daxing, G., Dunkang, L., Poliang, L., Xiaoyun, Q., *Fracture Toughness Measurement by Cylindrical Specimens with Ring-Shaped Crack*, Engineering Fracture Mechanics, 16, No.1, pp. 69-82. (1982)
19. Gliha, V., Vuherer, T., Ule, B., Vojvodič-Tuma, J., *The Fracture Resistance of Simulated HAZ Areas in a HSLA Structural Steel*, in the course of publication
20. BS 7448-2: Fracture Mechanics Toughness Test, Part 2. Method for Determination of K_{Ic}, Critical CTOD and Critical J Values of Welds in Metallic Materials. (1997)
21. Gliha, V., Vuherer, T., Pucko, B., Ule, B., Vojvodič-Tuma, J., *An evaluation of steel embrittlement caused by welding*, Materials and Manufacturing Processes, Vol.19, No. 2, pp. 139-157. (2004)
22. ASTM E 992-84: Standard Practice for Determination of Fracture Toughness of Steels Using Equivalent Energy Methodology. (1989)
23. Schwalbe, K.-H., *Bruchmechanik metallischer Werkstoffe*, Carl Hanser Verlag. (1980)
24. Peterson, R.E., *Stress Concentration Factors*, Wiley. (1974)

25. Noda, N-A., Nisitani, M., *Stress Concentration of a Strip with a Single Edge Notch*, Engineering Fracture Mechanics, 2, pp. 223-238. (1987)
26. Gliha, V., Toplak, D., *Fatigue Strength of a Butt Welded HSLA Structural Steel with Backing*, 5th International Fracture Mechanics Summer School, Dubrovnik, Yugoslavia. (1989)
27. Gliha, V., *Influence of Small Surface Discontinuities at the Weld Toe on Bending Fatigue Strength*, 11th Biennial European Conference on Fracture, Poiters-Futuroscope, France. (1996)
28. Gliha, V., *Fatigue Strength of Material at the Weld Toe in the Presence of Surface Micro-Defects*, 12th Biennial Conference on Fracture, Sheffield, UK. (1998)

APPLICATION OF FRACTURE MECHANICS IN ASSESSMENT OF STRUCTURAL INTEGRITY

Aleksandar Sedmak, Faculty of Mechanical Engineering, Belgrade, S&Mn
Marko Rakin, Faculty of Technology and Metallurgy, Belgrade, S&Mn

INTRODUCTION

Fracture mechanics is a scientific discipline related to cracks and their effects on the behaviour of various materials and structures. Fracture mechanics (originally referred to as crack mechanics) started to develop at the beginning of the XX century, with the papers of Inglis on stress concentration [1] and Griffith, on energy releasing rate [2]. In the fifties Irwin established foundations of linear elastic fracture mechanics by introducing the stress intensity factor and its critical value [3,4]. At that time fracture mechanics registered first significant successes in practice by explaining failure of Liberty ships and Comet jet airplanes [5]. Further development of this scientific discipline included its expansion to the elastic-plastic field, using the analysis of a plastic zone in front of a crack tip [5,6] and the introduction of proper parameters – crack tip opening displacement [7] and *J* integral [8]. As a matter of course, the development of fracture mechanics in some other important fields such as fatigue, [9], creep [10], and corrosion [11] followed.

Practical application of fracture mechanics is from the very beginning based on the interpretation of its parameters; on one hand, they represent loading and structural geometry, and on the other they represent material properties and its resistance to crack growth. In that way the triangle of fracture mechanics has been established, Fig. 1, enabling fracture mechanics to become one of the foundations of a new discipline – structural integrity. In other words, instead of only handling fracture analysis, fracture mechanics has become an important tool in the hands of engineers whose job is to prevent fracture.

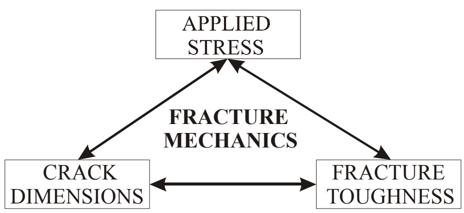

Figure 1. Fracture mechanics triangle

Fracture mechanics has brought significant changes in engineering practice. As an example to illustrate this statement, the problem with the Alaska pipeline and application of the fracture-safe principle in design may be mentioned. In case of the pipeline from Alaska to the rest of the USA, the fracture mechanics criteria were adopted instead of traditional standards on admissible defects in a welded joint [12]. Namely, when non-destructive testing revealed a large number of defects in round welded joints which, according to the then effective standards, should have been repaired, the question of economic justification, i.e. necessity of repair, arose. Therefore, the institution in charge, following the requirement of the company that installed the pipeline, addressed to the National Institute of Standards and Technology (then the National Bureau of Standards – NBS) for help. Detailed analysis of fracture mechanics parameters, based on the concept of crack tip opening displacement, covered assessment of the crack growth driving force on one hand, and resistance of the material (weld metal) to crack growth [13-16] on the other hand. The results of that research were officially accepted, so that the scope of repair was dramatically reduced, due to which unnecessary costs were avoided as well as risks of occurrence of new defects caused by repair welding. Thanks to that research it was concluded that the analysis of fracture mechanics is an acceptable base for admissible exception from the existing standards under certain circumstances, if such analysis provides convincing and conservative (safe) assessment of structural integrity. It should also be emphasized that this level of application of fracture mechanics was reached not only through this detailed investigation, but also through preceding intensive development of fracture mechanics as a scientific discipline.

It is thus obvious that the fundamental change that fracture mechanics has brought into engineering practice is the recognition of the fact that existence of cracks and similar defects cannot be avoided, and that their effects on structural integrity should be analysed. The basic role of fracture mechanics is to mathematically connect three variables (stress, defect dimensions, and fracture toughness), as shown in Fig. 1, which enables evaluation of the third, based on two known variables. For example, if the stress is known, based on loading and structural geometry, and the fracture toughness of the material of the structure based on tests, then one can define critical defect size. In practice, it also frequently happens that methods of non-destructive tests (NDT) reveal a crack or a similar defect in a structure, for which critical stress is subsequently defined, based on known fracture toughness of the material, or either the minimal fracture toughness of the material is subsequently defined based on the stress state of a structure. This concept can be applied already in the phase of structural design, if one assumes existence of cracks, dimensions of which correspond to the sensitivity of the NDT equipment.

The methodology of application of fracture mechanics depends on available data of material properties, effects of surrounding media and external loading of a structure. In case of static loading, one should recognize the material behaviour described as linear elastic ('relatively small-scale yielding') from the behaviour of the material whose plastic properties should not be neglected. In the first case, linear elastic fracture mechanics (LEFM) is applied, while in the second case, depending on the form of plastic yielding, various methods of elastic plastic fracture mechanics (EPFM) are applied. In case of dynamic loading, one should also recognise linear elastic from elastic plastic behaviour of the material, where the fatigue is of particular significance as a typical mechanism of crack growth under cyclic external loading. Finally, ambient effects could be crucial, due to elevated temperatures or corrosion.

1. APPLICATION OF LINEAR ELASTIC FRACTURE MECHANICS

The application of LEFM is based on the stress intensity factor, K_{I}, which on one hand represents loading and structural geometry, including crack dimensions, and on the other, its critical value, $K_{\mathrm{I}c}$, represents the material property. Based on this interpretation of LEFM parameters and Griffith's energy criterion, one can establish simple dependencies for the assessment of structural integrity.

$$K_{\mathrm{I}} \leq K_{\mathrm{I}c} \text{ – structural integrity is not threatening,} \tag{1a}$$

$$K_{\mathrm{I}} > K_{\mathrm{I}c} \text{ – structural integrity is threatening due to possibility of brittle fracture} \tag{1b}$$

2. APPLICATION OF ELASTIC-PLASTIC FRACTURE MECHANICS

There are few ways to take into account material plasticity in assessment of structural integrity, all of which are based on application of crack tip opening displacement or *J* integral, as appropriate parameters of elastic-plastic fracture mechanics. Crack tip opening displacement (CTOD), although without clear theoretical base, has a wide practical application, mainly due to the simplicity of determination. On the other hand, the *J* integral requires a more complex procedure for determination, but as an energy parameter based on fundamental laws of continuum mechanics has equally important practical application.

2.1. Designed CTOD curve

Using theoretical hypothesis of Wells [7] on linear dependence of CTOD vs. remote strain (stress) in a zone of large-scale yielding (LSY), as well as on the dependence of critical value of CTOD (δ_{crit}) vs. strain in the fracture of wide plates with two-edge cracks (ε_f), obtained by analysis under conditions of relatively small-scale yielding (SSY), Burdekin and Stone have defined the non-dimensional parameter Φ [17]:

$$\Phi = \frac{\delta_{crit}}{2\pi\varepsilon_y a} = \left(\frac{\varepsilon_f}{\varepsilon_y}\right)^2 \text{ for } \frac{\varepsilon_f}{\varepsilon_y} \leq 0.5\,;\ \Phi = \frac{\delta_{crit}}{2\pi\varepsilon_y a} = \frac{\varepsilon_f}{\varepsilon_y} - 0.25 \text{ for } \frac{\varepsilon_f}{\varepsilon_y} > 0.5 \tag{2}$$

where ε_y – yield strain. Graphical presentation of designed CTOD curve, Fig. 2, enables its simple application. Namely, if for a certain structure, a point located above the projected curve is obtained, it is considered to be fracture-free, as $\varepsilon \leq \varepsilon_f$ and $\delta > \delta_c$. In that case computation of the ordinate of that point is based on material data (δ_c, ε_y) and crack length (a), and the abscissa of the point is computed according to external loading reduced to deformation:

$$\varepsilon = \frac{1}{E}\left[k_t(P_m + P_b) + S\right] \tag{3}$$

where P_m and P_b are primary membrane- and bending stresses, increased by stress concentration coefficient, k_t. S is a secondary (residual or thermal) stress, and E, the elasticity modulus.

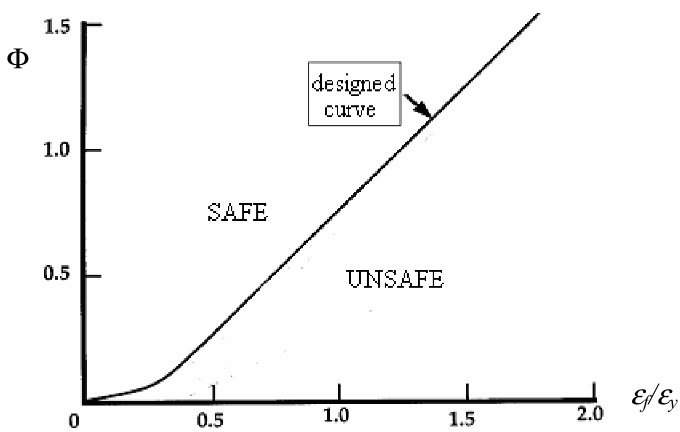

Figure 2. Designed CTOD curve

2.2 Failure analysis diagram

Structures made of ductile materials are less susceptible to brittle fracture, and therefore may fracture by plastic collapse. The mechanism of plastic collapse is not covered by designed CTOD curve, so its analysis requires a more general, two-parameter approach, realized through the Failure Analysis Diagram (FAD). This diagram represents the boundary curve, constructed according to the modified model of a yielding track for a passing-through crack on an infinite plate, [18]:

$$\frac{K_{eff}}{K_{\mathrm{I}}} = \frac{\sigma_c}{\sigma}\left[\frac{8}{\pi^2}\ln\sec\frac{\pi}{2}\frac{\sigma}{\sigma_c}\right]^{1/2} \tag{4}$$

where $K_{\mathrm{I}} = \sigma\sqrt{\pi a}$, K_{eff} was introduced instead of δ ($K_{eff}^2 = \delta\sigma_Y E$), and yield stress σ_Y was replaced by plastic collapse stress σ_c as a more convenient yield criterion for actual structures. As a final step, non-dimensional variables $S_r = \sigma/\sigma_c$ and $K_r = K_{\mathrm{I}}/K_{\mathrm{I}c}$ are defined, where it is supposed that K_{eff} equals to the fracture toughness of the material, so that Eq. (4) becomes:

$$K_r = S_r\left[\frac{8}{\pi^2}\ln\sec\left(\frac{\pi}{2}S_r\right)\right]^{-1/2} \tag{5}$$

If the material is completely ductile, the structure fails due to plastic collapse at $S_r = 1$, while for fracture of a completely brittle material $K_r = 1$. In all other cases there is an interaction between plastic collapse and brittle fracture, so that K_r and S_r are less than 1, and the pairs of corresponding values make a boundary curve, Fig. 3.

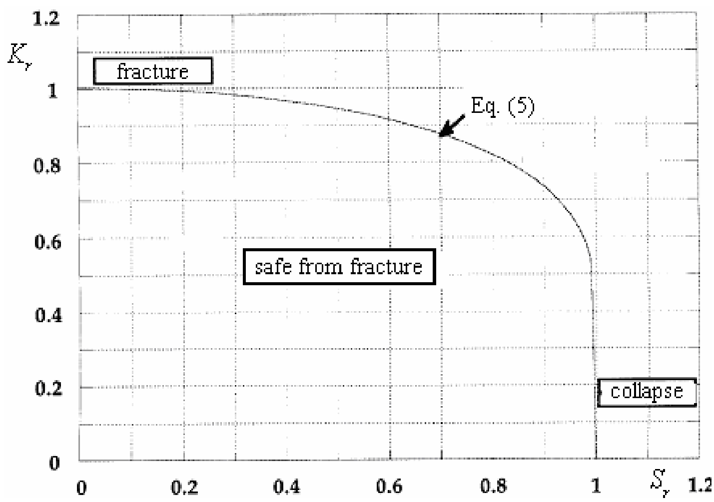

Figure 3. Failure analysis diagram

Stresses necessary for determination of K_r and S_r are divided as on the design CTOD curve, into primary and secondary ones, and in determining S_r only the primary stresses are taken into account, as the secondary stresses do not affect structural collapse.

It should be mentioned that the application of FAD is not limited to K, also J or δ can be placed on the ordinate, as well as the numerous modifications of this diagram such as 'level III' expanding the zone of plastic yield collapse, or 'level I' which simplifies it, as defined in Procedure 6493 [20].

2.3. The PD6493 procedure

The original PD6493 procedure [19] was based on designed CTOD curve. This methodology had a few disadvantages: e.g. the equation for crack growth driving force was mainly empirical and had varying level of conservative approach. Corrected equations for the crack growth force became available with R6 and EPRI procedures, while the projected CTOD curve was already widely applied. Thus in 1991, the PD6493 was modified [20], so that previous solutions remained (in level I), while simultaneously, improvements were introduced (levels II and III). What all three levels of PD6493 have in common is the method of determination of stress state and crack size. The latest version from the year 1999 is BS 7910:1999, *Guidance on methods for assessing the acceptability of flaws in metallic structures* (incorporating Amendment 1).

2.3.1. Crack size

In order to be able to analyze a crack, one should present it in some of the forms for which analytical solutions do exist. Cracks are divided into passing-through and partially-passing, the latter being divided into surface and hidden types, Fig. 4. If there are more cracks, the increase of stress intensity factor should be taken into account, while at very close distances the cracks join into a single one, Fig. 5. The procedure of crack analysis also includes its projection in the plane normal to the direction of main stress, and the description of a rectangle, the dimensions of which are taken as its basic dimensions.

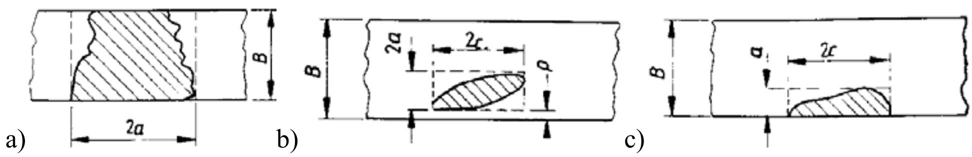

Figure 4. Cracks: a) passing through, b) partially passing hidden crack, c) partially passing surface crack

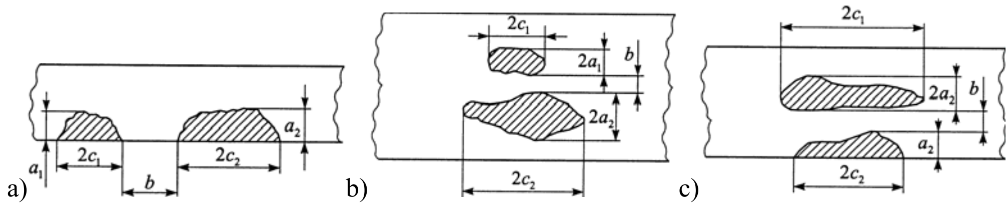

Figure 5. Reduction of cracks to one: a) 2 surface cracks, b) 2 hidden cracks, c) 1 hidden, 1 surface

a)	b)	c)
$b < c_1 + c_2 \Rightarrow a = \max(a_1, a_2)$	$b \le a_1 + a_2 \Rightarrow a = a_1 + a_2 + b/2$	$b \le a_1 + a_2 \Rightarrow a = 2a_1 + a_2 + b$
$2c = 2(c_1 + c_2) + b$	$2c = \max(2c_1, 2c_2)$	$2c = \max(2c_1, 2c_2)$

2.3.2. Stress state

In considering the stress state on the location of a crack, the following stresses (the sum of which makes representative total stress) are taken into account, Fig. 6:

– membranous stress, P_m, as a component of uniformly distributed primary stress;
– bending stress, P_b, as a component of primary stress, varying across section thickness;
– secondary stress, Q, as a self-balancing stress, e.g. thermal and residual stresses;
– stress increase, F, on locations of local discontinuities (irregular shape or non-axiality).

Analytical solutions for plates and cylinders with a partially-passing surface crack correspond to linear distribution of stresses across the thickness on which tensile and bending stresses are defined as $P_m = (P_{\min} + P_{\max})/2$ and $P_b = (P_{\min} - P_{\max})/2$, where $P_{\min}$ and $P_{\max}$ are minimal and maximal stresses in the section, Fig. 6a. Care should be taken not only about the stress distribution, but also about the division of loading into primary and secondary loading. Primary stresses mainly occur due to exterior loading and moments, while secondary stresses are most frequently the result of effects of non-uniform heating and cooling, e.g. welding–induced stresses that are localized and self–balancing. Unlike secondary ones, primary stresses may lead to yield fracture, if sufficiently strong. Secondary stresses contribute to fracture, if tensile, with sufficiently high values and close to a crack.

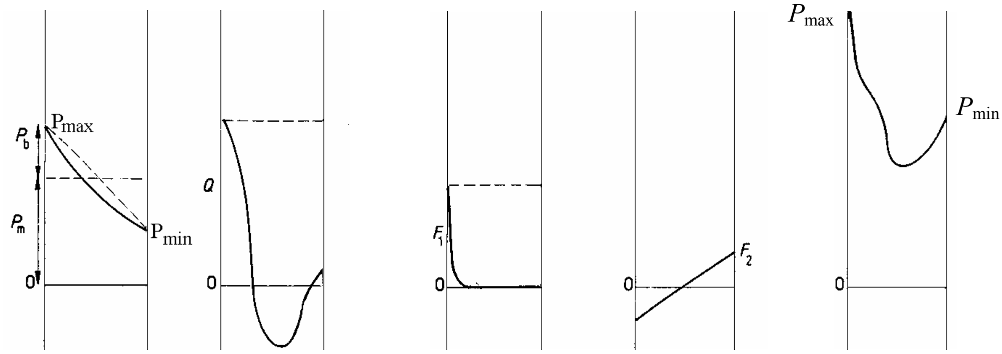

a) primary, b) secondary, c) irregular distribution, d) non-axiality, e) total stress

Figure 6. Schematic presentation of stress distribution across the section

3. EXAMPLES OF STRUCTURAL INTEGRITY ASSESSMENT

3.1. Pressure vessels at hydroelectric power plant 'Bajina Bašta'

This example is a typical problem if regular control of NDT reveals 'unacceptable' defects according to standard JUS ISO 5817 [12], as was the case with welded joints of vessels for compressed air in hydroelectric power plant 'Bajina Bašta' [21].

Thus, e.g., the vessel No. 970 had two defects marked as 'unacceptable,' one of which from the photo 970-64 (see Fig. 7), was again ultrasonically examined, which definitely confirmed incomplete penetration 60 mm long and 2 mm wide. By defect length, in this case, is to be understood the dimension in the direction of welded joint (longitudinal joint, photo No.64, near the upper circular seam, Fig. 7), while the width of the defect is its size in the direction of weld thickness. This defect was chosen as one of three 'critical,' both because of dimensions and location. Namely, as far as dimensions are concerned, it was the largest defect, and most dangerous because of its location, as it spread near the change from cylindrical shell to torus–spherical dish cover, where local bending exists.

Vessel No.971 had 11 defects marked unacceptable, according to Report No.2/98 of Goša Institute, among which defect from Photo No.971-57 was chosen as critical, the lack of side wall fusion 10 mm long, located in central circular welded joint (Fig. 7). Detailed ultrasonic inspection did not reveal this defect, but it was still taken into account.

Vessel No.973 had one defect marked as unacceptable. In comparison with defects in the two above specified vessels, this one was less dangerous, both in size and location (circular welded joint).

Vessel No.974 had 3 defects marked as unacceptable, according to Report No.5/98 of Goša Institute. Visual control showed the three defects were in fact defects in shape, i.e. caused by the lack of fusion between two passes, or interpass cold lap. As those three defects were located on the circular joint, they were under relatively small influence of stress, so that their effect on vessel safety was negligible. Besides, those three defects could have been eliminated by grinding, with small reduction of thickness at the grinding area, which had no significant influence on vessel safety [22].

Vessel No.976 had 5 defects marked as unacceptable, according to Report No.6/98 of Goša Institute, out of which defects from Photos No.24 and No.38 were again, ultrasonically inspected. Based on additional ultrasonic inspection, it was concluded that two slags from Photo No.976-24 were not connected, and that the defect from Photo No.976-38 was in fact offset or mismatch, i.e. shape defect (507). Having this in mind, as well as the size and location of defects found in vessel No.976, it was concluded that all five defects in vessel No.976 were less dangerous than those marked "critical" in vessels 970 and 971.

Vessel No.978 had 5 defects marked as unacceptable, out of which the defect from Photo No.35 was additionally ultrasonically inspected. Additional ultrasonic inspection showed that dimensions of this defect were not 'critical'; but incomplete penetration No.402, 25 mm long, from Photo No.978-14 was chosen as one of three critical defects, although additional ultrasonic inspection failed to register it. The width of this defect, the value of 2 mm was adopted that, according to the documentation of vessel No.978, corresponded to the predicted size of the weld metal root, and at the same time was the upper sensitivity limit for ultrasonic examination.

Based on a survey of radiograms with 'unacceptable' defects, and on additional ultrasonic examination and analysis of the condition of vessels, the defects found in vessels No.970 (defect No.970-64), incomplete penetration 60 mm long and 2 mm wide, 978 (incomplete penetration 978-14, 25 mm long and 2 mm wide), and 971 (lack of side wall fusion – 971-57, 10 mm long), Fig. 7.

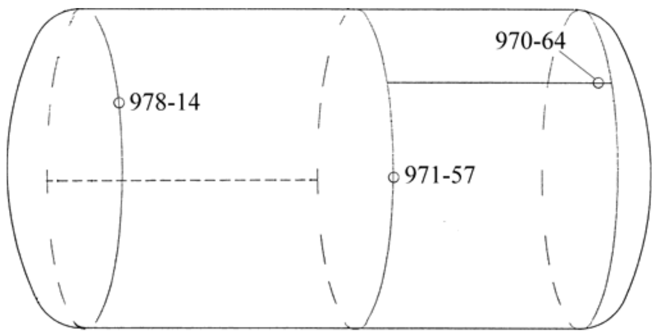

Figure. 7. Vessels of hydroelectric power plant 'Bajina Bašta' – location of main defects

3.1.1. The analysis of critical defects using the methods of fracture mechanics

The defects marked as 'critical' were analyzed using methods of fracture mechanics, by applying conservative approach. Therefore, all three were considered as cracks: defects No.970-64 and 978-14 as surface cracks (partially passing through the thickness, while defect No.971-57 was considered a line crack (passing through the entire thickness). In this way an extremely conservative assessment was adopted for defect 971-57, in order to check the behaviour of the vessel, even in such a case.

In order to determine stress intensity factors, one should know the external loading and geometry. Fracture toughness in this case could not have been determined and conservative assessment of its value was used instead. Care was also taken for the possibility of corrosion and fatigue, as well as of effects of residual stresses and the vicinity of dish cover, or openings. The analysis of 'critical' defects is given herein.

The data, essential for the analysis of defect No.970-64 are as follows:

– vessel geometry (thickness $t = 50$ mm, mean diameter $D = 2150$ mm);

– material of vessel cylindrical shell: NIOVAL 50 (low-alloyed steel of increased strength)
– crack geometry (60 mm long, 2 mm wide, direction–along the weld, location–root of longitudinal weld metal, adjacent to the circular weld–dish cover connection, far away from the openings);
– loading (internal pressure) p = 81 bar, residual stress σ_R = 200 MPa–the highest value – transversal to weld, based on experience with similar material and vessel [23];
– weld metal fracture toughness is 1580 MPa√mm, as minimum value according to [24].

Having in mind the conservative approach in the analysis of critical defects, it has been assumed that defect No.970-64 spreads over the entire length of the cylindrical part of vessel. In that case, the problem is observed in the section transversal to longitudinal direction of vessel, Fig. 8, where the influence of the curve is negligible (justifiable for 50 mm thickness and diameter of 2150 mm). The crack dimension, defined as 60 mm length exists no more in the analysis and the dimension so far defined as width becomes the length (2 mm). Thus the problem is reduced to a tensile plate, the dimensions of which are significantly larger than the crack length, where non-symmetry caused by the location of crack is neglected (the crack centre is 22.5 mm away from the lower side of the plate, and 27.5 mm away from its upper side). The idea of such a conservative approach is to prove in the simplest way that structural integrity is not threatened.

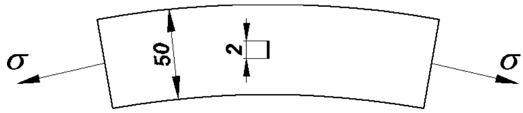

Figure 8. Section scheme in which crack No.970-64 is analyzed

If we assume that the remote stress is a sum of circumferential stress induced by internal pressure ('boiler formula') and cross-sectional residual stress in the middle of a weld, the following is obtained for the stress intensity factor:

$$K_{\mathrm{I}} = \left(\frac{pR}{t} + \sigma_R \right) \sqrt{\pi a} = \left(\frac{8.1 \cdot 1075}{50} + 200 \right) \sqrt{\pi} = 663 \ \mathrm{MPa} \sqrt{\mathrm{mm}} \tag{6}$$

Having in mind that the obtained value of K_{I} is only 42% of a minimal value of $K_{\mathrm{I}c}$ (1580 MPa√mm), it may be concluded that there is no risk of brittle fracture. This conclusion is also valid even if one assumes the crack length to be twice of the measured (thus taking into account measuring inaccuracy), since in that case K_{I} = 937 MPa√mm, which is 59% of the minimal value of $K_{\mathrm{I}c}$, still providing sufficient safety against brittle fracture.

Defect No.978-14 (incomplete penetration, 25 mm long and 2 mm wide, in a circular weld connecting the lower dished cover) is presented as a surface crack, but it is assumed for this crack too, that it spreads over the entire circumference of the vessel. The data essential for analysis (with the same material as in previous analysis) are:
– vessel geometry (thickness t = 42 mm, mean diameter D = 1958 mm);
– crack geometry–25 mm long, 2 mm wide, direction–along the weld, location–root of circular weld metal connecting the dish cover, far from the openings;
– loads (internal pressure p = 78 bar, residual stress σ_R = 200 MPa, same as with defect No.970-64).

In this case the problem is observed in the section transversal to circumferential direction of the vessel, Fig. 9. The section is presented simplified, since even the part belonging to the dish cover is shown as a plane, justly disregarding curve effects. Moreover, it is ignored that the stress in the torus part of the dish cover differs from the stress in a cylindrical part of the vessel, since in the torus area adjacent to the cylindrical part the stress is pressure, and not dangerous for crack growth. Thus, non-symmetry in the problem, caused by the location of crack is ignored, and same as in the previous case. If the sum of longitudinal stress, caused by internal pressure (‘boiler formula’), and transversal residual stress in the centre of the seam is assumed to be the remote stress, than the following is obtained for stress intensity factor:

$$K_{\mathrm{I}} = \left(\frac{pR}{2t} + \sigma_R\right)\sqrt{\pi a} = \left(\frac{7.8 \cdot 979}{84} + 200\right)\sqrt{\pi} = 515 \ \mathrm{MPa}\sqrt{\mathrm{mm}} \tag{7}$$

which is 32% of the critical value ($K_{\mathrm{I}c}$ = 1580 MPa√mm), and does not threat the vessel. For twice this crack length, K_{I} = 728 MPa√mm = 45%$K_{\mathrm{I}c}$ is obtained.

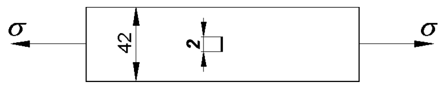

Figure 9. Section scheme in which crack No.978-14 is analyzed

Defect No.971-57 (lack of penetration, 10 mm long, in a circular weld at the middle of the vessel) has from the very beginning been presented as a passing-through crack, as the other dimension remains unknown. The data important for the analysis are as follows:

– pressure geometry (thickness t = 50 mm, mean diameter D = 2075 mm);
– crack geometry (10 mm long, direction–along seam, location–circular weld metal in the middle of the vessel, far from the openings;
– loads–internal pressure p = 81 bar, residual stress σ_R = 175 MPa – transversal to weld, away from weld centre, based on experience with similar material and vessel [22].

As in the previous case, the problem is presented by a plate under tension, not in the cross section, but as a “separate” part of the cylinder, Fig. 10. If the remote stress is assumed as a sum of the longitudinal, pressure induced stress (“boiler formula”), and the transversal residual stress, away from the weld centre, the stress intensity factor is:

$$K_{\mathrm{I}} = \left(\frac{pR}{2t} + \sigma_R\right)\sqrt{\pi a} = \left(\frac{8.1 \cdot 1075}{100} + 175\right)\sqrt{5\pi} = 1039 \ \mathrm{MPa}\sqrt{\mathrm{mm}} \tag{8}$$

which is 66% of critical value ($K_{\mathrm{I}c}$ = 1580 MPa√mm) and does not threat the vessel. Even if one assumes twice the crack length, the stress intensity factor (K_{I} = 1465 MPa√mm for $2a$ = 20 mm) remains below critical value (92%).

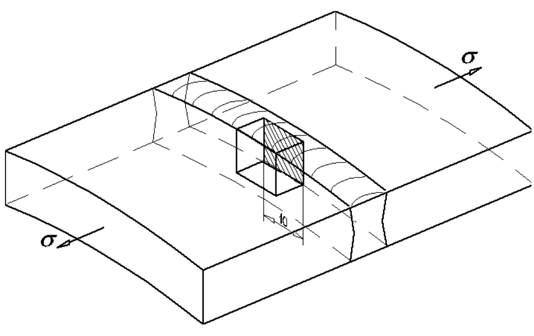

Figure 10. Cylindrical part scheme in which crack No.971-57 is analyzed

Further analysis includes plastic material behaviour, i.e. the application of FAD. In that case the K_R parameter has already been defined: 0.59 for defect No.978-14 and 0.92 for defect No.971-57. For evaluation of the S_R parameter, one should define the stress in the net section from primary loading (internal pressure), while the secondary stress is not taken into account [25].

Net section stress for defect No.970-64 is $\sigma_n = 1.08pR/t$, where the 1.08 factor takes into account the weakening of the 50 mm section thickness due from a 4 mm long crack, so that the following is obtained:

$$S_R = \frac{\sigma_n}{\sigma_F} = 2\left(\frac{1.08pR}{t}\right)\Big/\left(R_{eH} + R_M\right) = 2\left(\frac{1.08\cdot 8.1\cdot 1075}{50}\right)\Big/\left(500+650\right) = 0.33 \tag{9}$$

where data for R_{eH} and R_M were taken from the project documentation for base metal (for weld metal they do not differ much). Effects of the vicinity of the dish cover have been ignored, as the discontinuity occurring causes significant change of stress in a torus part of the dish cover, but not in the cylindrical part [18].

The stress in net section of defect No.978-14 is $\sigma_n = 1.05pR/2t = 95$ MPa, with the section weakening coefficient of 1.05 (the 2 mm long crack for thickness of 42 mm), so that the following is obtained:

$$S_R = \frac{\sigma_n}{\sigma_F} = \frac{95}{575} = 0.17 \tag{10}$$

The influence of the vicinity of the dish cover is again taken to be negligible [18].

The net section stress for defect No.971-57 is $\sigma_n = 1.05pR/2t = 87$ MPa, where section weakening coefficient is not taken into account as its influence is negligible, so that the following is obtained:

$$S_R = \frac{\sigma_n}{\sigma_F} = \frac{87}{575} = 0.15 \tag{11}$$

Based on values obtained for K_I/K_{Ic} and σ_n/σ_F, the points (0.33; 0.59), (0.17; 0.45), and (0.15; 0.92) are plotted in the failure analysis diagram (FAD), all located in the safe part of the diagram, Fig. 11.

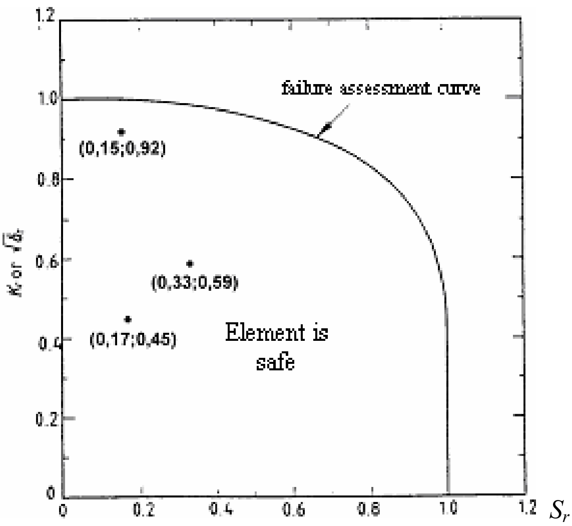

Figure 11. Failure analysis diagram for damaged vessels

Having in mind the conservatism of this analysis in all its aspects, it may be concluded that the vessels are safe not only from brittle fracture, but from the plastic collapse, too. It is essential to note that the FAD enables simple analysis of the integrity that may reliably establish whether a component is fracture-safe or not, on condition that the geometry and loading are presented in a conservative way. On the other hand, if the integrity cannot be proved, this does not mean that the component is useless, but that additional, more complex analyses are necessary.

3.2. The pipeline at hydroelectric power plant 'Perućica'

During the period from 1995 to 1996 the pipeline was subjected to inspection a few times, using various methods of non-destructive testing which, among others, revealed longitudinal defects (cracks) in longitudinal welded joints II and III, where bent sheet pieces were inserted on the part of increased thickness (50 mm), Fig. 12a. Having in mind the dimensions of cracks, the crack in the joint III, Fig. 12b, was taken for analysis, as more dangerous.

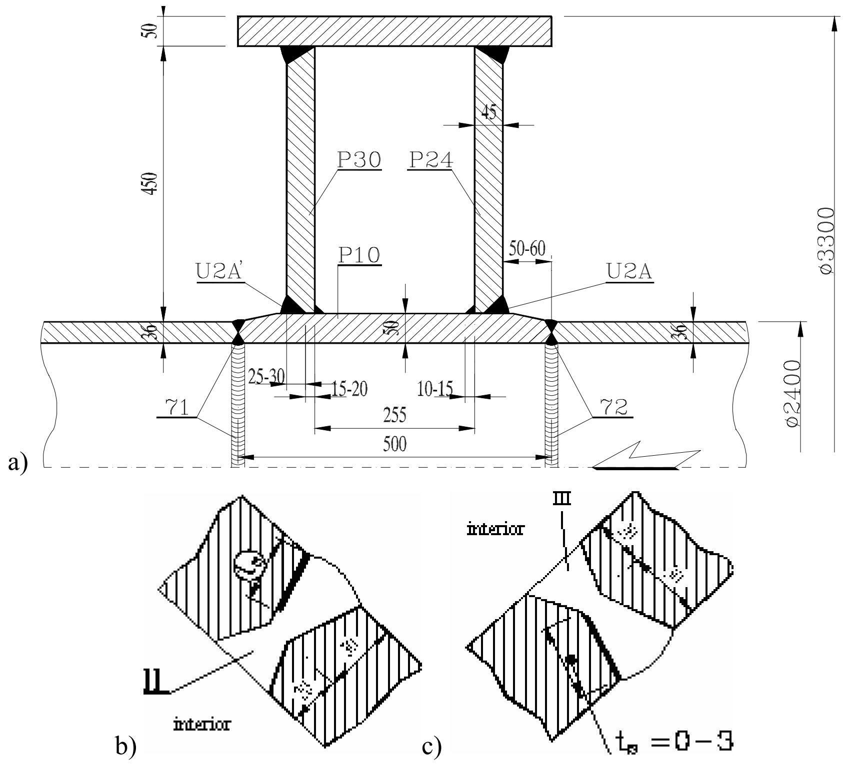

Figure 12. Detail of the pipeline (a) with cracks in joints II (b), and III (c)

The crack III is presented as a surface crack, partially passing through weld thickness. The data relevant to the analysis are:

- pipeline geometry (thickness t = 50 mm, diameter D = 1200 mm);
- material of the vessel cylindrical part – CRN 460 (NIOVAL 47, low-alloyed steel of increased strength);
- crack size (450 mm long, 0–30 mm deep, direction–along weld, location–fusion zone);
- loading (internal pressure p = 6 MPa, circumferential stress $\sigma_t = pR/t$ = 144 MPa, residual stress σ_R = 200 MPa – maximum value–transversal to weld;
- weld metal fracture toughness, i.e. of heat affected zone (HAZ), minimum value 1580 MPa√mm (50 MPa√m), and based on experience with the similar base metal.

Considering the conservative approach in the analysis of critical failures, crack III is assumed to have 30 mm depth over the entire observed length. In this case the problem should be considered in the section oriented transversally to the longitudinal direction of the vessel, where the curvature effect is ignored and quite justifiable for 50 mm thickness and 2400 mm diameter. The analysis becomes two-dimensional (plain strain) and the problem is considered as a plate under tension with an edge crack. If the remote stress is assumed to be the sum of circumferential stress induced by internal pressure ('boiler formula') and the residual stress in the weld centre, the stress intensity factor is as follows:

$$K_{\mathrm{I}} = 1.12\left(\frac{pR}{t} + \sigma_R\right)\sqrt{\pi a} = 1.12\left(\frac{6\cdot 1200}{50} + 200\right)\sqrt{\pi 30} = 3741\ \mathrm{MPa}\sqrt{\mathrm{mm}} \qquad (12)$$

In case that the residual-stress effects are ignored, the following is obtained:

$$K_{\mathrm{I}} = 1.12\left(\frac{pR}{t}\right)\sqrt{\pi a} = 1.12\left(\frac{6\cdot 1200}{50}\right)\sqrt{\pi 30} = 1565\ \mathrm{MPa}\sqrt{\mathrm{mm}} \qquad (13)$$

which is close to brittle fracture (ratio $K_{\mathrm{I}}/K_{\mathrm{I}c} = 0.99$ shows there is practically no reserve regarding the risk of brittle fracture, not even if residual stresses are ignored. In the net section stress $\sigma_n = 2.5pR/t + \sigma_R$, where factor 2.5 is taken into account because of section weakening from a 30 mm long crack in 50 mm thickness. Thus, the following is obtained:

$$S_R = \frac{\sigma_n}{\sigma_F} = 2\frac{\frac{2.5pR}{t} + \sigma_R}{R_{eH} + R_M} = 2\frac{\frac{2.5\cdot 6\cdot 1200}{50} + 200}{500 + 650} = 0.97 \qquad (14)$$

Based on values obtained for $K_{\mathrm{I}}/K_{\mathrm{I}c}$ and σ_n/σ_F, it is obvious that the point (0.99; 0.97) is located deeply within the unsafe region, Fig. 13.

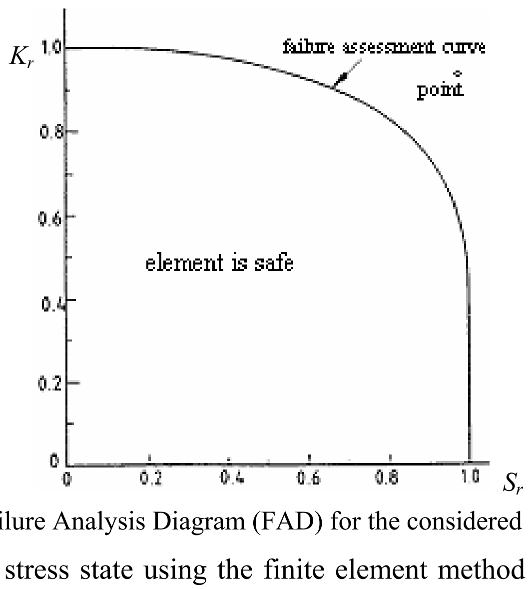

Figure 13. Failure Analysis Diagram (FAD) for the considered pipeline crack

The calculation of stress state using the finite element method (FEM) is made based on the model shown in Fig. 14 (a quarter of inserted pipe). The results of analysis presented in Tab. 1 show that the collar decreases stresses from 144 MPa to 80 MPa, in the region of pipe parts 250 mm away from the middle of the collar, which corresponds to the location of joints with cracks. However, even with so reduced operating stress, the corresponding point in FAD drops into an unsafe region, as the value for S_r modifies to 0.7, while the value of K_r remains unmodified (0.99). However, one should have in mind that only three-dimensional calculation could accurately determine the stress state of such complex geometry, which is certainly less favourable than the one obtained.

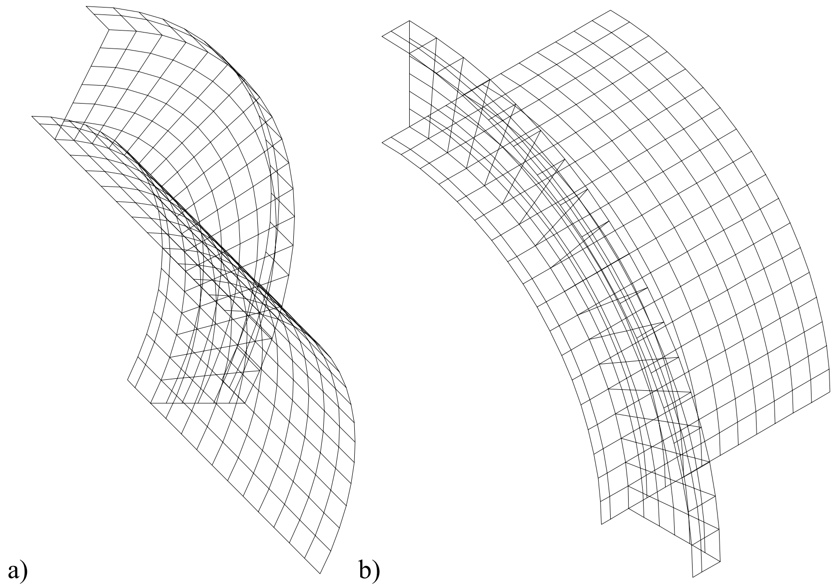

Figure 14. Two isometric views of the FE model, (a) and (b)

Table 4. Stresses at characteristic points along the bifurcation axis – with upper plate on the collar

distance from collar centre	σ_x^m (MPa)	σ_y^m (MPa)	τ_{xy}^m (MPa)	σ_x^s (MPa)	σ_y^s (MPa)
a (350 mm)	136.2	95.4	0	1.8	5.4
b (250 mm)	95.4	79.8	0	–23.4	–78.6
c (100 mm)	75	69.6	0	–12.6	–42
d (0 mm)	72	69.6	0	–0.6	–1.8

σ_x^m–longitudinal normal membranous stress; σ_y^m–circumferential normal membranous stress, τ_{xy}^m–tangential membranous stress, σ_x^s–longitudinal normal bending stress, σ_y^s–circumferential normal bending stress

CONCLUSION

Structural integrity is a relatively new scientific and engineering discipline, which includes state analysis and diagnostics of the behaviour and weakening, and life time assessment and revitalization of structures [26]. It means that, besides common situations in which structural integrity should be accessed when non-destructive testing detects a defect, this discipline also includes stress-state analysis of crack-free structures, mostly by the finite element method. In that way an accurate and detailed distribution of displacements, strains, and stresses is obtained, making it possible to establish the 'weak' points in a structure, even before a crack appears. This approach is very important for structures exposed to operating conditions typical for crack initiation, such as fatigue, creep, and corrosion.

REFERENCES

1. Inglis, C.E., *Stresses in a plate due to the presence of cracks and sharp corners*, Proc. Inst. Naval Arch. 55, pp. 219-241. (1913)
2. Griffith, A.A., *The phenomena of rupture and flow in solids*, Phil. Trans. Roy. Soc. London. A, 221, pp. 163-198. (1920)

3. Irwin, G.R., Kies, J.A., *Fracturing and fracture dynamics*, Welding Journal. Res. Sup. 31 (2), pp. 95s-100s. (1952)
4. Irwin, G.R., Kies, J.A., *Critical energy rate analysis of fracture strength*, Welding Journal. Res. Sup. 33 (4), pp. 193s-198s. (1954)
5. Irwin, G.R., *Plastic zone near a crack and fracture toughness*, Proc. 7th Sagamore Research Conf. on Mechanics & Metals Behavior of Sheet Material, Vol.4, pp. 463-478, Racquette Lake, NY. (1960)
6. Dugdale, D.S., *Yielding of steel sheets containing slits*, J. Mech. Phys. Solids, 8, pp. 100-104. (1960)
7. Wells, A.A., *Application of fracture mechanics at and beyond general yielding*, British Welding Journal, 11, pp. 563-570. (1963)
8. Rice, J.R., *A path independent integral and the approximate analysis of strain concentration by notches and cracks*, J. Appl. Mech. 35, pp. 379-386. (1968)
9. Paris, P.C., Gomez, R.E., Anderson, W.E., *A rational analytic theory of fatigue*, The Trend in Engineering, 13 (1), pp. 9-14, University of Washington. (1961)
10. Landes, J.D., Begley, J.A., *A fracture mechanics approach to creep crack growth*, ASTM STP 590, pp. 128-148, Philadelphia, ASTM. (1976)
11. Speidel, M.O., *Theory of stress corrosion cracking in alloys*, J.C. Scully (ed.), NATO Scientific Affair Division. Brussels, pp. 345-354. (1970)
12. JUS ISO 5817, *Elektrolučno zavarivanje čelika – uputstvo za ocenu nivoa kvaliteta*, JUS. (in Serbian) (1997)
13. Reed, R.P., Schramm, R.E., *Entry level inspection of pipeline circular welded joints with accent to non-destructive testing*, (in Serbian) Monograph of the 3rd International Fracture Mechanics Summer School (IFMASS 3), Ed. S. Sedmak, pp. 319-338. (1985)
14. Read, D.T., *Fracture mechanics analysis and curves of allowed flaw size for surface cracks in pipelines*, (in Serbian), *ibid.* 12, pp. 319-338. (1985)
15. Reed, R.P., et al., *Fitness-for-service criteria for pipeline girth-weld quality*, Final Report to the U.S. DOT, NBS, Boulder, CO, USA. (1983)
16. Hicho, G.E., *Assessing the significance of blunted flaws in quality inspection of welded pipelines for service entry level*, (in Serbian), *ibid* 12, pp. 339-353. (1985)
17. Burdekin, F.M., Dawes, M.G., *Practical use of linear elastic and yielding fracture mechanics with particular reference in pressure vessels*, Proc. of the Institute of Mechanical Engineering Conference, London, pp. 28-37. (1971)
18. Bednar, H.H., *Pressure Vessel Design Handbook*, Van Nostrand Reinhold Comp., New York, NY. (1986)
19. PD6493:1980, *Guidance on methods for assessing the acceptability of flaws in fusion welded structures*, London: British Standard Institution. (1980)
20. PD6493:1991, *Guidance on methods for assessing the acceptability of flaws in fusion welded structures*, London, BSI. (1991)
21. Reports 1–8/98, Goša Institute, S. Palanka, (in Serbian). (1998)
22. Report No.12-10-12.03/98, Faculty of Mechanical Engineering, Belgrade (in Serbian). (1998)
23. Adžiev, T., *Contribution to studying the influence of residual stresses on the fracture resistance of welded structures containing a crack*, (in Macedonian), Doctoral Thesis, Faculty of Mechanical Engineering, Skopje. (1988)
24. Gerić, K., *Crack initiation and growth in high strength steel welded joints*, (in Serbian) Doctoral Thesis, Faculty of Technology and Metallurgy, Belgrade. (1997)
25. Hertzberg, R.W., *Deformation and Fracture Mechanics of Engineering Materials*, John Wiley & Sons, New York, NY. (1996)
26. Maneski, T., Sedmak, A., *Structural integrity*, (in Serbian), Journal of the Society for Structural Integrity and Life, Belgrade, Vol.1, No.2, pp. 107-110. (2001)